ASME
SETTING THE STANDARD

Transactions of the ASME, Journal of Heat Transfer (ISSN 0022-1481) is published monthly by The American Society of Mechanical Engineers, Three Park Avenue, New York, NY 10016. Periodicals postage paid at New York, NY and additional mailing offices. POSTMASTER: Send address changes to Transactions of the ASME, Journal of Heat Transfer, c/o THE AMERICAN SOCIETY OF MECHANICAL ENGINEERS, 22 Law Drive, Box 2300, Fairfield, NJ 07007-2300. **CHANGES OF ADDRESS** must be received at Society headquarters seven weeks before they are to be effective. Please send old label and new address.

Journal of Heat Transfer

Published Monthly by ASME

VOLUME 131 • NUMBER 5 • MAY 2009

RESEARCH PAPERS

(Contents continued on inside back cover)

This journal is printed on acid-free paper, which exceeds the ANSI Z39.48-1992 specification for permanence of paper and library materials. ♾™
♻ 85% recycled content, including 10% post-consumer fibers.

Journal of Heat Transfer Volume 131, Number 5 MAY 2009

TECHNICAL BRIEFS

The ASME Journal of Heat Transfer is abstracted and indexed in the following:

Applied Science and Technology Index, Chemical Abstracts, Chemical Engineering and Biotechnology Abstracts (Electronic equivalent of Process and Chemical Engineering), Civil Engineering Abstracts, Compendex (The electronic equivalent of Engineering Index), Corrosion Abstracts, Current Contents, E & P Health, Safety, and Environment, Ei EncompassLit, Engineered Materials Abstracts, Engineering Index, Enviroline (The electronic equivalent of Environment Abstracts), Environment Abstracts, Environmental Engineering Abstracts, Environmental Science and Pollution Management, Fluidex, Fuel and Energy Abstracts, Index to Scientific Reviews, INSPEC, International Building Services Abstracts, Mechanical & Transportation Engineering Abstracts, Mechanical Engineering Abstracts, METADEX (The electronic equivalent of Metals Abstracts and Alloys Index), Petroleum Abstracts, Process and Chemical Engineering, Referativnyi Zhurnal, Science Citation Index, SciSearch (The electronic equivalent of Science Citation Index), Theoretical Chemical Engineering

Numerical Simulation of the Effects of a Thermally Significant Blood Vessel on Freezing by a Circular Surface Cryosurgical Probe Compared With Experimental Data

Genady Beckerman

Avraham Shitzer[1]
e-mail: mersasa@tx.technion.ac.il

David Degani

Department of Mechanical Engineering,
Israel Institute of Technology,
Haifa, Israel 32000

The dynamic thermal interaction between a surface cryosurgical probe (heat sink) and an embedded cylindrical tube (heat source), simulating a thermally-significant blood vessel, has been studied. The cryoprobe was operated by liquid nitrogen while the embedded tube was perfused by water at a constant inlet temperature. Previous experimental data were obtained in a phase-changing medium (PCM) made of 30%/70% by volume mashed potato flakes/distilled-water solution. A parametric study was conducted without the embedded tube, and with flow rates of 30 ml/min and 100 ml/min in the tube, while cooling rates at the tip of the cryoprobe were maintained at $-4°C/min$, $-8°C/min$, or $-12°C/min$. Numerical thermal analysis was performed by ANSYS7.0 and showed good conformity to the experimental data. The results quantify the effects of these parameters on both the shape and extent of freezing obtained in the PCM. For 20 min of operation of the cryoprobe, water temperatures inside the tube remained well above the freezing point for all assumed operating conditions. Frozen volumes of the $0°C$ isotherm, approximating the "frozen front," and the $-40°C$ isotherm, representing the "lethal temperature," were smallest for the combination of highest cooling rate at the cryoprobe and the highest flow rate in the tube, ($-12°C/min$ and 100 ml/min). The results indicate that both the flow rates in the embedded tube, and the cooling rates applied at the cryoprobe, have similar qualitative effects on the size of the PCM frozen volumes; increasing either one will cause these volumes to decrease. Under the conditions of this study the effects of flow rate in the tube are more pronounced, however, effecting relative frozen volumes decreases by about 10–20% while those of the cooling rate at the cryoprobe are in the range of 7–14%. [DOI: 10.1115/1.3001035]

1 Introduction

The purpose of the cryosurgical treatment is to destroy as many cells as possible inside a given tissue volume while causing minimal damage to the surrounding healthy cells. Cryosurgery is typically applied by cryoprobes, which are usually operated by liquid nitrogen, high pressure Argon gas, or by a closed-loop cooling cycle. The cryoprobe may be needlelike when inserted into the tissue or flat-surface for the treatment of superficial tumors.

Despite the progress made by cryosurgery, it still lags behind other current surgical techniques used to treat malignant tissues. The reason for this stems mainly from the inability of the procedure to ensure complete eradication of the malignant tissue volume. Many factors play roles in this uncertainty among which is the presence of thermally-significant blood vessels in the vicinity of the tumor. These vessels act as heat sources that compete with the effects of heat extraction by the cryoprobe. Over the years, numerous experimental [1–3] and analytical [4–10] studies have been performed into cryosurgical applications. Trezek [11] and Rubinsky [12] provided state-of-the-art reviews of the subject. Neither of these studies, however, had considered the effects of a thermally-significant blood vessel on the temperature field, which develops during cryosurgery. Several analytical and numerical solutions of similar problems, i.e., freezing in the vicinity of a single tube buried below a planar boundary from which freezing initiates, were attempted, e.g., Refs. [13–15].

Zhang et al. [16] developed a 2D steady state model of a single finite length large blood vessel embedded in the center of a cylindrical tissue region, which is being frozen on its curved surface. They obtained an analytical solution to this unrealistic geometry for biological tissues and calculated temperature distributions in the tissue and the blood vessel. Also presented separately are the results of an experimental study simulating the thermal effects of two counter-current blood vessels embedded in a gel. A surface contacting copper cylinder, precooled by LN_2, was used to freeze the test rig. Clinical type cryoprobes were not used nor were the measured data correlated with model results. Deng and Liu [17,18] developed a finite difference algorithm to study the effects of a large blood vessel, simulated by a cylindrical duct in the vicinity of an embedded cryoprobe [17], on the transient temperature profiles during cryosurgery. Their results indicated that the heat source, which is embodied by the cylindrical duct, may have significant effects depending on cryoprobe configuration. In a subsequent study [18], more realistic vascular models were simulated and the results showed that these models produced significant temperature differences for the same cryoprobe configuration. Re-

[1]Corresponding author.

Contributed by the Heat Transfer Division of ASME for publication in the JOURNAL OF HEAT TRANSFER. Manuscript received May 30, 2008; final manuscript received July 29, 2008; published online March 20, 2009. Review conducted by Giulio Lorenzini.

cently, Deng et al. [19] used infrared thermometry to study the effects of both a single embedded large blood vessel and a counter-current vessel pair on the temperature field produced by an inserted 5 mm OD cryoprobe operating on LN_2. Experiments were conducted both in vitro (gel) and in vivo (rabbit ear and stomach). Multiple infrared surface thermograms demonstrate the different temperature distribution patterns produced by various cryoprobe positionings relative to the embedded blood vessels. The authors conclude that the heating caused by warm blood flowing in the large vessels can produce steep temperature gradients in the tissue undergoing cooling, thereby preventing tissue regions adjacent to them from being frozen.

Neither of these studies had addressed the application of a finite surface cryoprobe from which the freezing front emanates, in contrast to the embedded needle-type cryoprobe. An experimental study by Chayut and Shitzer [20] indicated significant thermal effects of the flow inside an embedded tube (heat source) that simulated the blood vessel (an artery or a vein), both on the shape and the extent of the frozen region produced by a surface cryoprobe. Slowing down of the flow inside the heat source and the possibility of initiation of freezing inside it were also indicated under the conditions of that study. In a subsequent experimental study, Massalha and Shitzer [21] investigated the effects of a simulated thermally-significant blood vessel on the temperature field that developed in a phase-changing medium (PCM) due to the application of a surface cryoprobe. This class of problems is governed by a number of parameters including the number of blood vessels, their dimensions, locations and orientations in the PCM relative to the cryoprobe, blood flow rate, type of blood flow—pulsatile or steady—size and type of the surface cryoprobe, its operational mode, etc. Massalha and Shitzer [21] limited their study to varying only the flow rate in the embedded tube while all other parameters were maintained constant.

The anatomical and physical complexities of the cryosurgical process limit the applicability of an analytical approach for simulating the problem. This suggests the application of a numerical approach. Numerous publications deal with cryosurgery-related problems by using finite-element techniques due to its ability to deal with complex geometries, variable properties and boundary conditions. Rubinsky and Cravalho [22] implemented a finite-element technique, which allows the application of an adaptive grid for tracking the freezing front. Oung and Tamma [23] developed a one-dimensional finite-element model to deal with the problem of multiple-interface freezing fronts, which is based on the enthalpy formulation for a fixed grid. The method is relatively easy to implement because the location of the freezing front in this formulation is not one of the variables. Bhattacharya et al. [24] developed a fixed grid finite-element approach for the generalized phase-change problem for mushy regions, also based on the enthalpy formulation.

The objective of the present study is to analyze numerically the thermal interaction between a flat circular surface cryoprobe and a tissuelike medium inside which, close and parallel to the probe's surface, passes an embedded water-perfused tube, simulating a blood vessel. Solutions of the transient temperature fields are obtained using a commercial code (ANSYS7.0), by coupling the solution of the energy equation for the tissuelike PCM and the equation governing the thermal field developing inside the embedded tube, using the sequential weak coupling approach. The results for the case without the embedded tube and for two different flow rates in the tube, are compared with available experimental data [21] and show good conformity.

2 Experiments

2.1 Experimental Setup. A detailed description of the experimental setup is given by Massalha and Shitzer [21]. Only the essential details are repeated here.

The setup consisted of the following four subsystems.

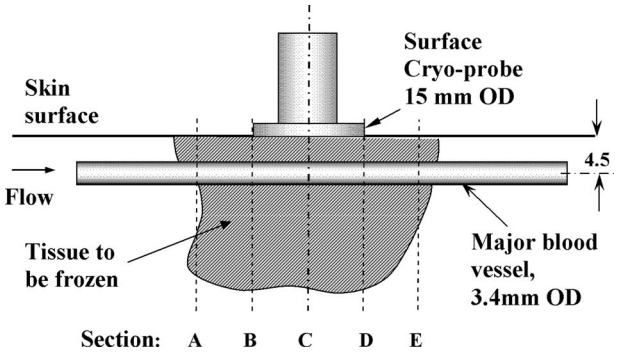

Fig. 1 Schematic of the experimental setup showing temperature measuring sections A–E

2.1.1 Cryosurgical System. The system consisted of a liquid nitrogen (LN_2) storage Dewar, a flat, circular, surface cryoprobe (brass, 15 mm in diameter) connected to a delivery tube, and a PC-based control and data acquisition system. The cooling rate at the tip of the cryoprobe was controlled by offsetting portions of the cooling effect delivered by the LN_2 to the tip of the cryoprobe by means of an electrical resistance wire wound around the stem of the cryoprobe [21].

2.1.2 The PCM Test Section. The test section consisted of a rectangular support frame, made of two Plexiglas plates, which held both the embedded tube (the "heat source") and the thermocouple wires. The embedded tube, simulating large blood vessels in the human body, was made of a rigid acrylic circular tube 4.8/3.4 mm in diameter. The tube was perfused by water at a constant inlet temperature. The test section was filled with the PCM (30% mashed potato flakes and 70% distilled-water solution by volume) and was placed in an inner cylindrical metal container, which was fitted, flushed at the top, inside an insulated outer cylindrical container. The free volume between the bottom and sides of the two containers was used for circulating temperature-controlled water to maintain a constant temperature at the outer surfaces of the PCM contained inside the inner container.

2.1.3 The Water Circulating System. Constant temperature water was supplied to the embedded tube and into the volume between the outer and inner containers. Water flow rate in the embedded tube was continuously monitored by a turbine flow meter.

2.1.4 Temperature Measuring System and Test Procedure. A total of 32 Teflon-coated chromel-alumel thermocouples (TCs), made of 0.4/0.25 mm wires, were used: 28 to monitor the temperatures of the PCM and the remaining 4 to monitor the temperatures of the water flowing through the embedded tube. The thermocouple junctions were arranged in the PCM on a single plane perpendicular to the embedded tube and coinciding with the centerline of the cryoprobe (Section C, Fig. 1). Placement was done at alternate symmetrical lateral locations on a 5×5 mm^2 grid to minimize thermal perturbations, as shown in Fig. 2. The thermocouple wires were connected to a PC through a multiplexer and were scanned every 10 s at a rate of 25 samples/s. In order to obtain detailed temperature measurements in the PCM, while minimizing the thermal perturbations caused by placing multiple TCs, the following temperature measuring procedure was adopted. Five temperature measurement sections, A–E, 7.5 mm apart and perpendicular to the embedded tube, were specified (Fig. 1). In each subsequent test, which started with the PCM at the same uniform initial temperature [21], the cryoprobe was placed alternately at one of the specified sections, with the TCs always remaining in section C. This procedure allowed gathering detailed temperature data from all five sections while minimizing the thermal perturbation in the PCM.

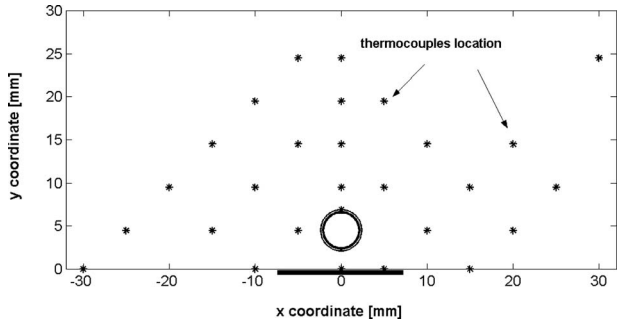

Fig. 2 Positioning of the thermocouple junctions on a 5 ×5 mm² grid in the PCM at each measuring section A–E

2.2 Experimental Procedure. Three series of freezing experiments were performed:

(1) without the embedded tube,
(2) with 30 ml/min water flow rate in the tube, and
(3) with 100 ml/min water flow rate in the tube

The three freezing experiments consisted each of five subexperiments with the cryoprobe positioned alternately at each of the five sections A–E, as noted in section (d) above. Prior to each subexperiment, test section temperatures were brought to the same initial level with standard deviations for all 28 thermocouples in the range of $\pm 0.87 - \pm 1.03\,^{\circ}\mathrm{C}$ [21]. The $-8\,^{\circ}\mathrm{C/min}$ cooling rate at the tip of the cryoprobe was established initially for each experiment by monitoring the probe tip's temperature variations. Freezing experiments lasted typically 20–22 min until the probe temperature reached $-160\,^{\circ}\mathrm{C}$. In all cases, the cooling rate provided by the cryoprobe had been monitored continuously, as explained above.

3 Numerical Analysis

The heat transfer problem in the phase-changing medium is governed by the heat equation expressed by the enthalpy formulation

$$\frac{\partial H}{\partial t} = \nabla \cdot (k \nabla T) \tag{1}$$

where t is the time, k is the thermal conductivity, T is the temperature, and H is the volumetric enthalpy from

$$H = \int_{T_{\mathrm{ref}}}^{T} \rho c_p dT \tag{2}$$

The problem is solved in a parallelepiped domain (see Fig. 3 showing half the domain) subject to the following boundary and initial conditions (the vertex of the axes coinciding with the center of the flat part of the cryoprobe and the y-axis pointing perpendicular to the cryoprobe):

$$\partial T/\partial x = 0 \quad \text{at} \quad x = 0 \tag{3}$$

$$T = \text{const} \quad \text{at} \quad x = 50 \text{ mm} \tag{4}$$

$$T = f(t) \quad \text{under the cryoprobe} \quad \text{at} \quad y = 0 \tag{5a}$$

$$\partial T/\partial y = 0 \quad \text{elsewhere} \quad \text{at} \quad y = 0 \tag{5b}$$

$$T = \text{const} \quad \text{at} \quad y = -100 \text{ mm} \tag{6}$$

$$T = \text{const} \quad \text{at} \quad z = \pm 50 \text{ mm} \tag{7}$$

The continuity conditions on the tube surface,

$$T_{\text{tube surface}} = T_{\text{contacting medium}} \tag{8a}$$

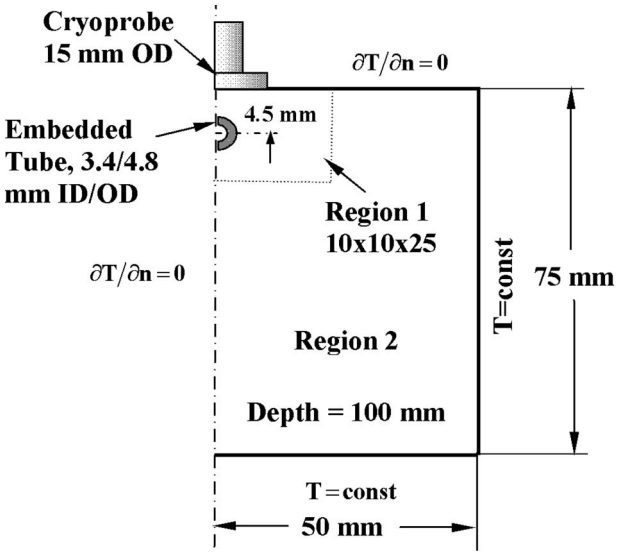

Fig. 3 Schematic of the numerical solution domain

$$\text{Heat Flux}_{\text{tube surface}} = \text{Heat Flux}_{\text{contacting medium}} \tag{8b}$$

The initial condition,

$$T = \text{const} \quad \text{at} \quad t = 0 \tag{9}$$

Constant temperature conditions initially inside the solution domain (Eq. (9)) and on the sides and bottom surface of the parallelepiped (Eqs. (4), (6), and (7)), were set at 34 °C, consistent with the conditions of the experimental phase [21]. Similarly, the upper surface of the domain was assumed thermally insulated except for the circular segment contacting the cryoprobe, where a time-dependent temperature variation was imposed (Eq. (5*a*)), both applied in accordance with the experimental conditions [21].

A finite-element Galerkin method coupled with Newton–Raphson time step iterations was applied by ANSYS7.0 to solve the heat transfer problem. This package handles the phase-change problem by an enthalpy formulation [25]. Thermophysical properties of the PCM (30%/70% by volume mashed potato flakes—distilled-water solution) are listed in Table 1. The thermal conductivity, density, and specific heat are each assumed to have constant but different values in the two phases. Linear variation between these values was assumed in the phase-change temperature range [26]. The solution domain, which simulated the experimental system, is shown in Fig. 3. The outer dimensions of this domain were

Table 1 Thermophysical properties of the PCM (30%/70% mashed potatoes flakes—distilled water solution) applied in the numerical solution

Property	Value
Thermal conductivity of the unfrozen phase	0.561 W/m K
Thermal conductivity of the frozen phase	1.95 W/m K
Thermal conductivity of the tube wall	0.33 W/m K
Density of the unfrozen phase	1124 kg/m³
Density of the frozen phase	1046 kg/m³
Density of the tube wall	960 kg/m³
Density of the fluid (water) in the tube	997 kg/m³
Specific heat of the unfrozen phase	3.4 MJ/kg K
Specific heat of the frozen phase	1.88 MJ/kg K
Specific heat of the tube wall	2.26 MJ/kg K
Specific heat of the fluid (water) in the tube	4.0 MJ/kg K
Phase change temperature range	−1−−8 °C
Latent heat of solidification	233 MJ/m³ K

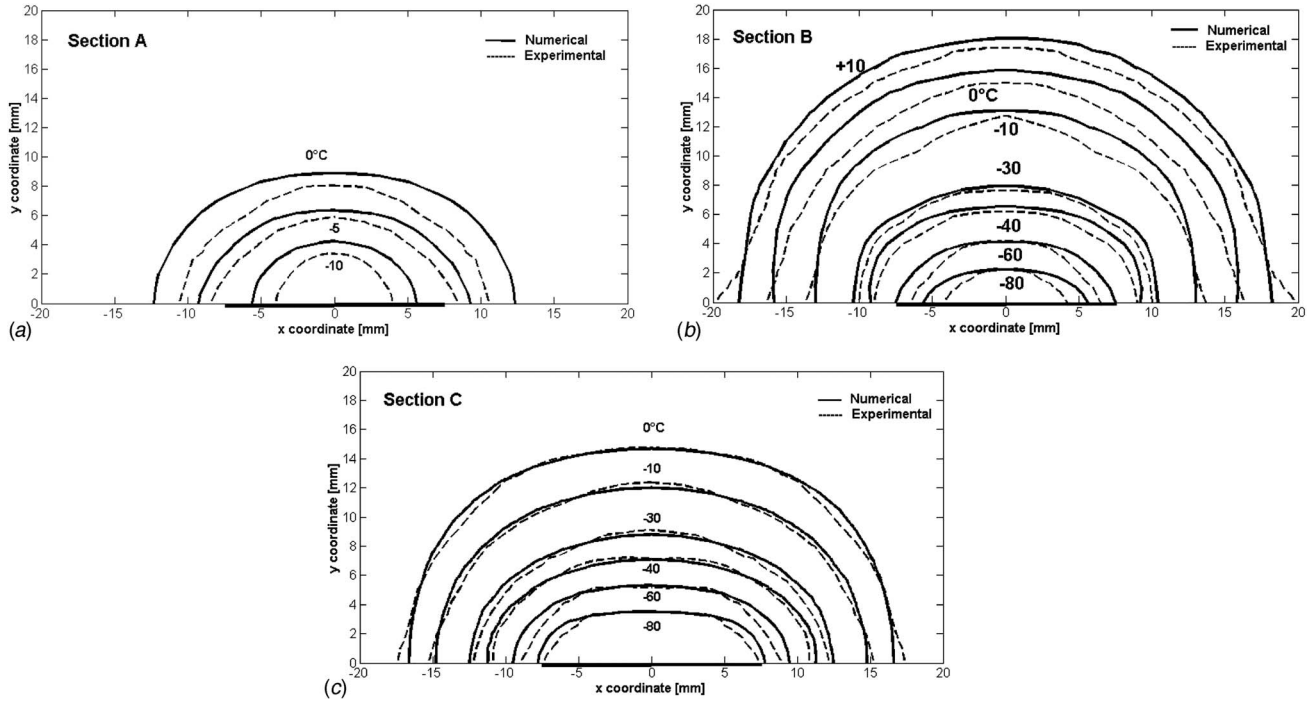

Fig. 4 Comparison of measured and computed isotherms in the PCM after 20 min of operation without the embedded tube. Probe cooling rate: −8°C/min.

established by numerical trials to ensure the satisfaction of the boundary conditions.

The entire solution domain was divided into two regions: one containing the PCM, which was further divided into two subregions for improving the accuracy in the vicinity of the cryoprobe (Fig. 3), and the other containing the embedded tube (the fluid region). At the interface between the fluid and PCM regions, temperature and heat flux continuity conditions were imposed. A fully developed laminar flow profile was assumed in the embedded tube ($Re \leq 820$). The solution of problems in which the two different regions interact thermally is handled in ANSYS by a "sequential weak coupling" algorithm. Accordingly, solutions are obtained separately for the energy equations in the PCM and in the fluid. Temperature and heat flux boundary conditions are imposed at the boundary between the PCM and the fluid regions at each time step. Iterations continue until the matching conditions satisfy an assumed convergence criterion, for each time step.

4 Results and Discussion

Results are presented by two sets of figures. Figures 4 and 5 compare measured and calculated temperatures in the PCM while Figs. 6–12 present calculated effects of various operating parameters on temperature fields, both in the PCM and in the embedded tube.

Figure 4 compares isothermal contours obtained without the embedded tube in three sections—A, B, and C—in the PCM. Temperature distributions in the remaining two sections, D and E, were close to those in sections B and A, respectively, due to symmetry and are therefore omitted from the presentation. The data shown were obtained after 20 min of operation and cryoprobe cooling rate of −8°C/min. These operating conditions were repeated in all subsequent experiments with the embedded tube. Measured data were interpolated to produce isothermal contours, as described by Massalha and Shitzer [21]. In the center section C, coinciding with the cryoprobe centerline, both measured and calculated lower isotherms are rather flat and ellipsoidal-like. This is due to the shape of the cryoprobe at this section, which is projected like a 15 mm wide strip. Higher isotherms, located at increasing distances from the cryoprobe, assume more circularlike shapes. Similar results are observed at section B, which is situated at the edge of the cryoprobe, 7.5 mm from the center. At section A, located outside the contact area with the cryoprobe, 15 mm from its center, isothermal contours shown are all circularlike with much higher temperatures, as is to be expected. The degree of conformity of the measured and calculated results is variable among the sections. The closest conformity is obtained in the center section C and the least in the farthest section A. This may be due to measurement inaccuracies, the interpolation method used, the assumption of perfect thermal insulation at the surface of the PCM, and the certain differences in initial conditions in all five subexperiments.

Figure 5 compares results obtained in all five sections, A–E, with the inclusion of the embedded tube. Water flow rate in the tube was the highest employed: 100 ml/min. In this figure, the presence of the embedded tube is quite pronounced and distorts the shape of the isothermal contours. The most distortions by the tube are in its immediate vicinity, as is to be expected. Conformity of measured and calculated results is quite good with some deviations observed in the farthest downstream location, section E. Effects of flow direction in the embedded tube are manifested by comparing the symmetrically located upstream sections A and B with those of their respective downstream locations E and D. Additional experimental results are presented in Ref. [21].

As noted above, the following Figs. 6–12, present only calculated effects of various operating parameters on temperatures, all shown for cases that included the embedded tube. Figure 6 shows the advancement of two isothermal contours: −40°C and 0°C at section C for a 100 ml/min flow rate in the tube and different times of operation. These isotherms were chosen since the former is assumed to represent the "lethal" temperature for cryosurgery of the prostate [27] while the latter closely simulates the boundary of the frozen region. In this, and the subsequent two figures, a somewhat larger concentric circle is drawn around the embedded tube

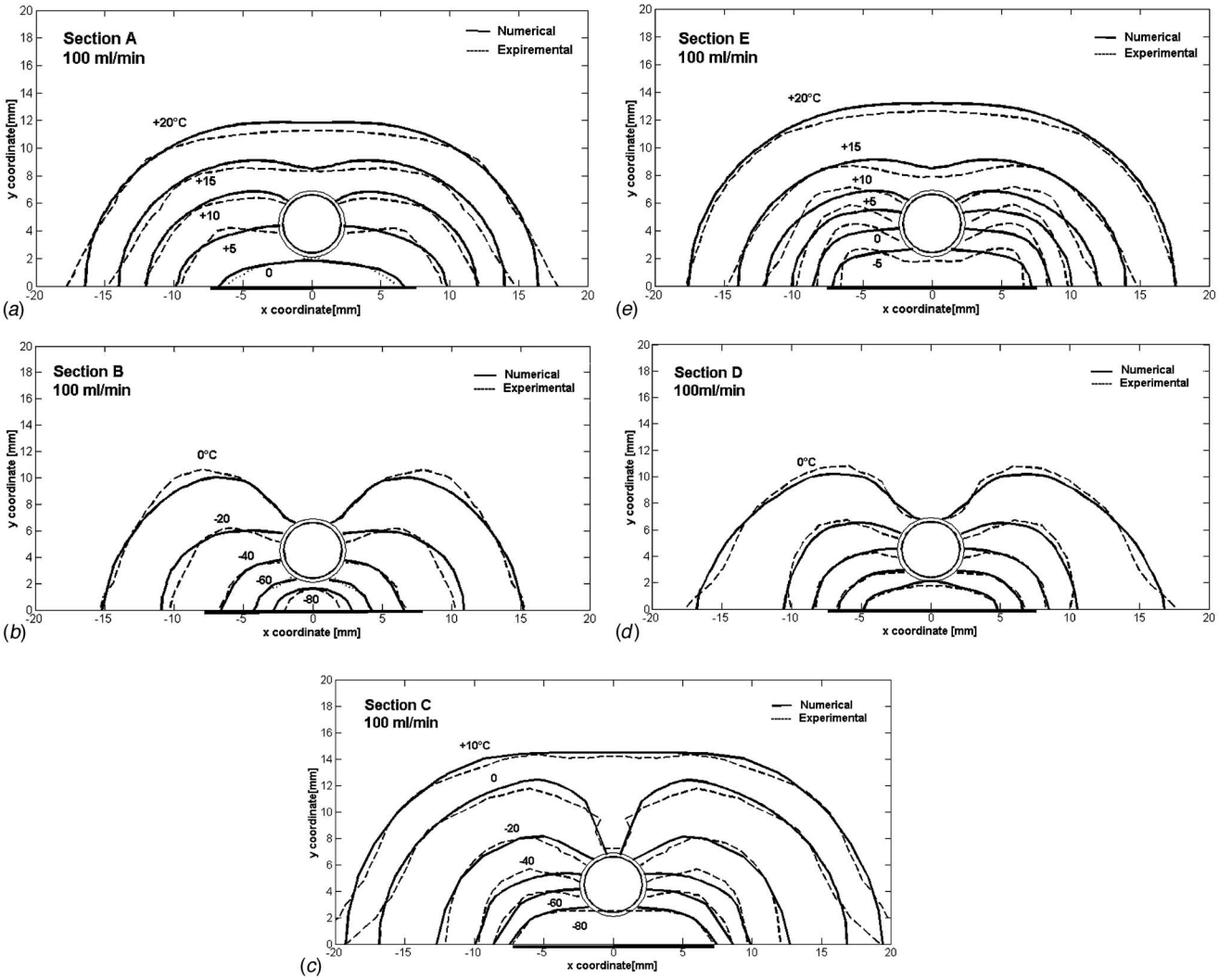

Fig. 5 Measured and computed isotherms in sections A–E in the PCM after 20 min of operation. Probe cooling rate: −8°C/min. Embedded tube flow rate: 100 ml/min.

to which all isotherms are drawn. Details of the temperature distributions in the region between these two circles, in the tube wall, and inside it, are shown in Fig. 9. As seen in Fig. 6, the effects of the embedded tube, which acts as a heat source, are quite pronounced in its immediate vicinity, as is to be expected. In fact, the fronts of both isotherms do not completely detach from the surface of the embedded tube in times shorter than 20 min. A yet unfrozen area is observed above the tube for the duration of operation.

Figure 7 compares the effects of flow direction of the warm

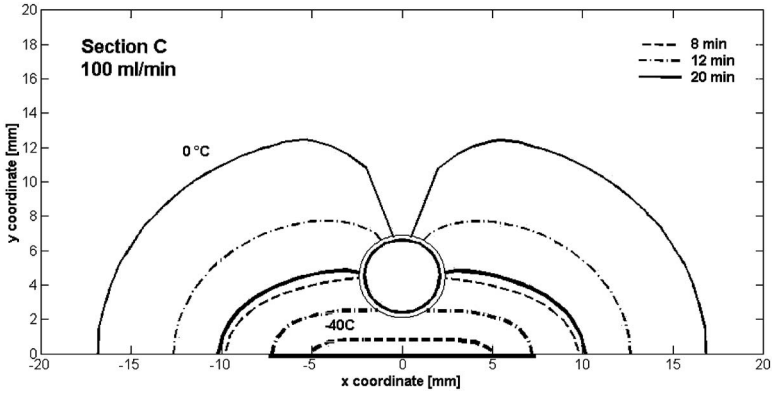

Fig. 6 Computed advancements of the 0°C and −40°C isothermal fronts at section C for embedded tube flow rate of 100 ml/min. Probe cooling rate: −8°C/min.

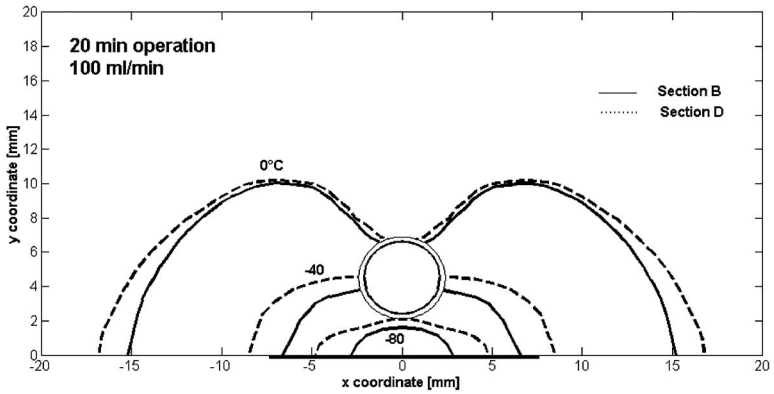

Fig. 7 Computed comparison of three isothermal fronts in sections B (upstream) and D (downstream) after 20 min of operation. Probe cooling rate: −8°C/min. Embedded tube flow rate: 100 ml/min.

water in the embedded tube, simulating blood flow on the symmetrically located sections B (upstream) and D (downstream). The effects of the somewhat warmer fluid at the upstream section B are manifested in the retardation of the advancements of all three shown isotherms. This effect is relaxed somewhat as the fluid arrives at section D, after having lost heat due to its interaction

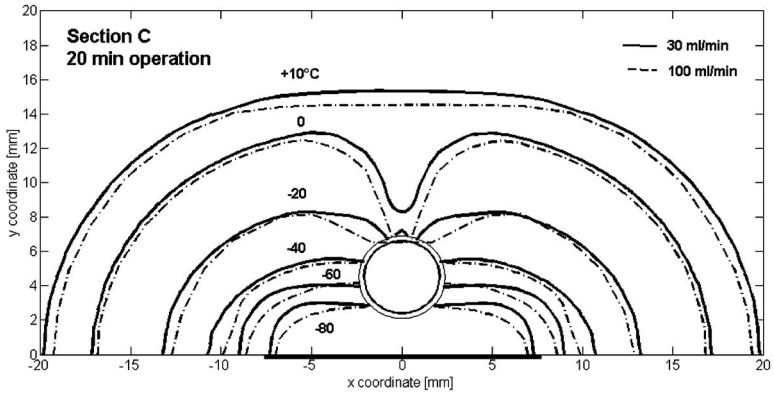

Fig. 8 Computed effects of embedded tube flow rates on isothermal fronts location at section C after 20 min of operation. Probe cooling rate: −8°C/min.

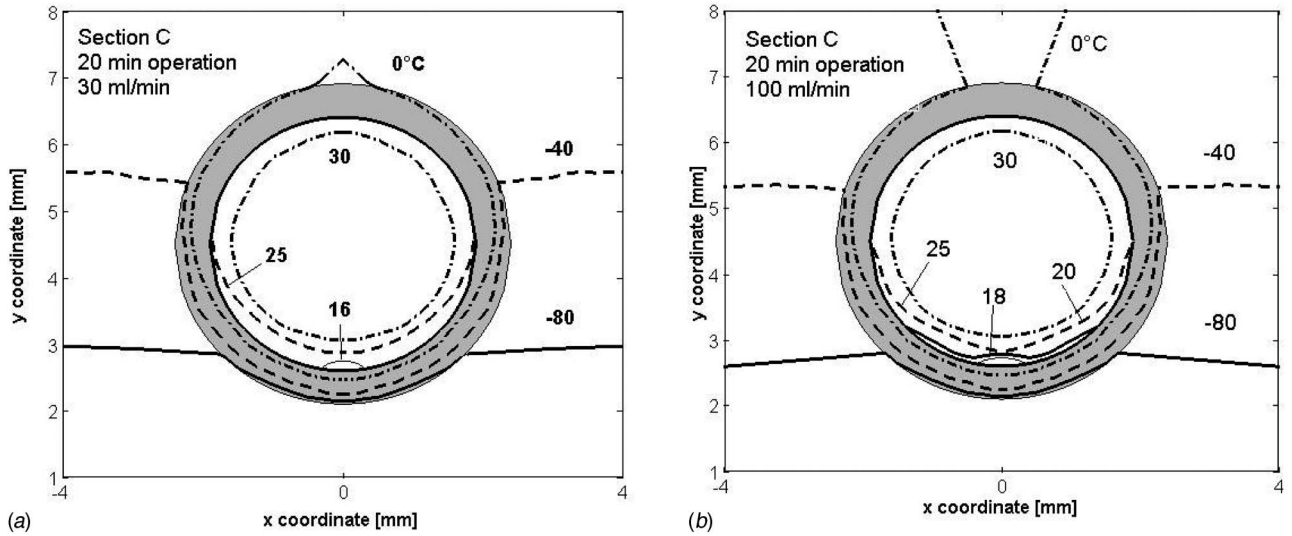

Fig. 9 Computed effects of flow rates in the embedded tube on the temperature field inside the tube and its wall and in the PCM at section C after 20 min of operation. Probe cooling rate: −8°C/min; temperatures in degrees centigrade.

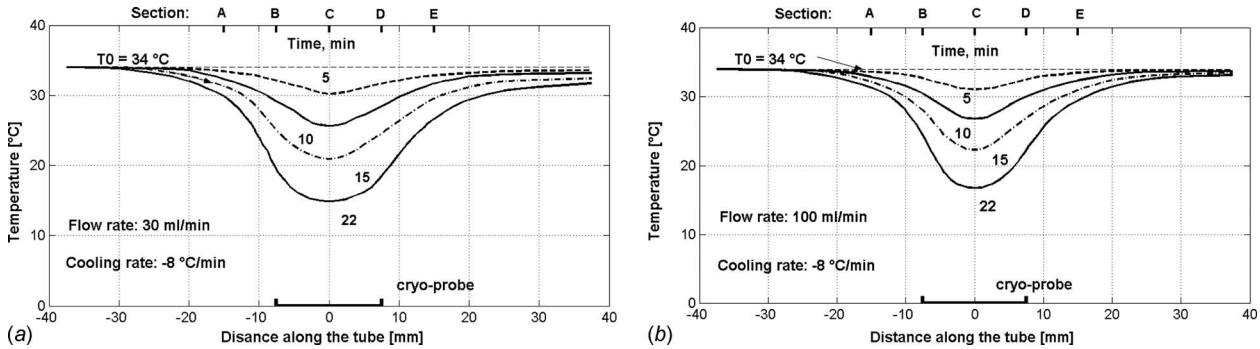

Fig. 10 Computed effects of flow rates in the embedded tube on the axial temperature variations along the tube centerline. Probe cooling rate: –8°C/min.

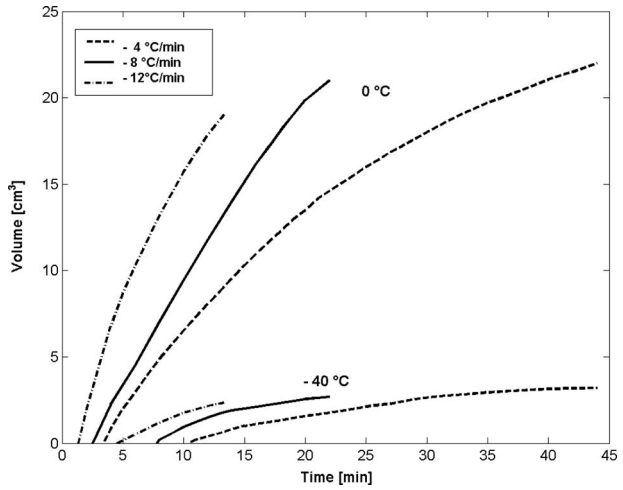

Fig. 11 Computed evolution of the volumes enclosed by 0°C and –40°C isotherms for three different probe cooling rates without the embedded tube. Final probe temperature: –142°C.

with the colder PCM. Also seen is the attenuation of this effect with respect to the 0°C isotherm in the areas close to the side of the tube farthest from the cryoprobe where the fluid temperatures are highest. The advancement of the lower isotherms shown is noticeably different in the area between the cryoprobe and the tube. This is primarily due to the thermal competition between the heat sink (cryoprobe) and the heat source (tube).

Figures 8–10 show the effects of fluid flow rate in the embedded tube, after 20 min of operation, on temperatures in the PCM, in the tube's wall, and in the flowing water. Figure 8 shows the location of a number of isotherms in section C. As a general rule, all isotherms develop farther in the PCM, the lower is the flow rate in the tube. For the conditions shown, a separation of the 0°C isotherm is observed adjacent to the area of the tube farthest from the cryoprobe, for the higher flow rate in the tube. This observation is highlighted in Fig. 9. A similar separation was reported by Massalha and Shitzer [21].

Figure 9, showing the effects of water flow rates, focuses on the temperatures of the water inside the tube, in the tube's wall and in the adjacent PCM. In the area inside the tube closest to the cryoprobe, isothermal contours appear similar for both flow rates, indicating the dominance of the cryoprobe in this area. Outside the

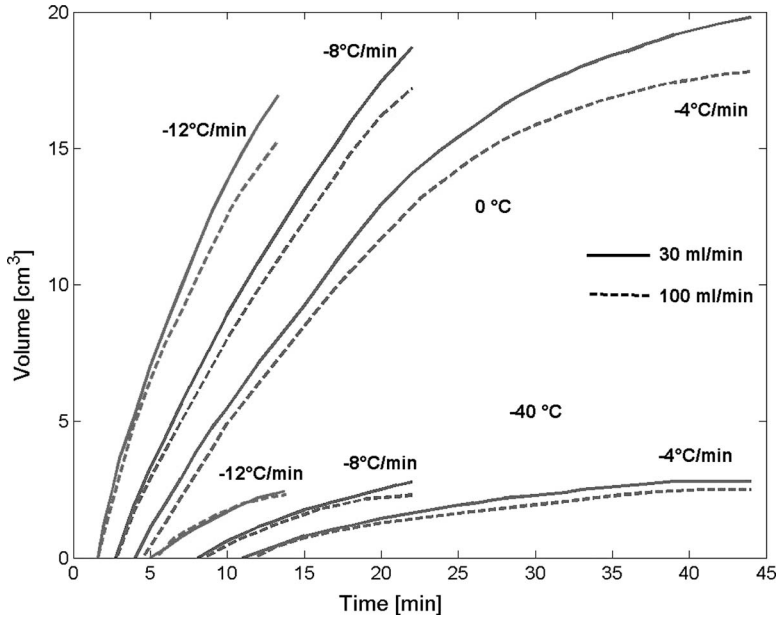

Fig. 12 Computed effects of flow rates in the embedded tube and probe cooling rates on the evolution of the volumes enclosed by the 0°C and –40°C isotherms. Final probe temperature: –142°C.

Table 2 Minimal calculated fluid temperatures (°C) inside the embedded tube

Cooling rate / Flow rate	−4°C/min	−8°C/min	−12°C/min
30 ml/min	14.16	14.93	16.22
100 ml/min	15.92	16.82	18.46
Duration of operation, s	2640	1320	880

tube, however, the effects of the flow rate are expressed clearly. One effect is the upwards "bending" of the −80°C isotherm by the higher flow rate (100 ml/min) compared with the downwards bending by the lower flow rate. The other noticeable difference is with regard to the 0°C isotherms. Inside the tube's wall and closer to the cryoprobe, these isotherms appear rather similar for both flow rates. Deviations appear in areas farther away from the cryoprobe. For the lower flow rate (30 ml/min), this isotherm had already moved sideways from the apex of the tube while it still enclosed a triangularlike area in this region for the higher flow rate, as was noted above.

These effects are further demonstrated in Fig. 10, showing the axial temperature distributions at the centerline of the tube. The effects of the different flow rates are quite noticeable in the downstream areas with water temperatures almost regaining their initial levels for the higher flow rate, for all times shown. Temperature differences of up to about 3°C develop over time at these downstream areas for the lower flow rate. A similar qualitative result was reported by Massalha and Shitzer [21]. Table 2 lists minimal temperatures calculated for the water in the embedded tube for the two studied flow rates and for the various cooling rates studied at the cryoprobe. Temperatures differed by up to 2°C due to the higher flow rate compared with those of the lower flow rate. While these minimal temperatures are well above the freezing point of the fluid, under different flow conditions, freezing inside the tube may also occur [20].

To further quantify the effects of the different cryoprobe cooling rates and water flow rates, calculated frozen volumes enclosed by several isothermal surfaces are presented in Figs. 11 and 12. Results are shown for an identical final cryoprobe temperature of −142°C {=34°C minus (8°C/min*22 min)}, which dictated different operation times (see Table 2) for the different cooling rates studied. Figure 11 compares the volumes enclosed by the lethal temperature, −40°C, and by the "frozen front" temperature 0°C for the case without the embedded tube, and for three different cooling rates: −4°C/min, −8°C/min, and −12°C/min. It is seen that the initiation of each of these volumes is delayed, by as much as about 10 min for the lethal temperature at the slowest cooling rate. Final volumes attained in all the cases, for both shown isotherms are very close although cooling durations were different to achieve an identical final temperature at the cryoprobe. This suggests that the advancement of isothermal fronts in an infinite medium, due to the local application of a circular surface cryoprobe, is strongly dominated by the product of cooling rate and the time of application.

Qualitatively similar results are observed in Fig. 12 for the same two isothermally enclosed volumes, with the inclusion of the embedded tube. Differences in the final volumes attained for the same cooling rate are mainly due to the heating effects of the flow rates in the tube with the higher flow rate delaying the advancement over that of the lower, as is to be expected.

Table 3 summarizes these results for all cases considered. For both isothermal surfaces shown, 0°C and −40°C, the smallest enclosed volumes are those for the highest cooling rate at the cryoprobe (−12°C/min), which is applied for the shortest duration as explained above, coupled with the highest flow rate in the tube. For this combination of operating parameters, volumes are smaller by 20.4% and 21.4% for these two isotherms, respectively, as compared with the case without the embedded tube. For the case without the tube, volumes enclosed by the 0°C and −40°C isotherms are smaller by 13.2% and 12.5%, respectively, for the highest cooling rate in comparison to the lowest (−4°C/min). At the intermediate cooling rate of −8°C/min and the highest flow rate of 100 ml/min, these differences are considerably higher at 18.9% and 17.2%, respectively.

5 Conclusion

This study considers the combined effects of a surface cryoprobe, operated by liquid nitrogen, and a thermally-significant blood vessel, embodied by an embedded tube positioned in the PCM in the vicinity of the cryoprobe. Data were collected in a series of previous experiments conducted in a PCM made of 30%/70% solution of mashed potato flakes and distilled-water. An interactive numerical solution of the dynamic temperature fields in the PCM and in the embedded tube was developed using ANSYS7.0. The predicted results compared well with the experimental data of a previous study [21] and facilitated a parametric study of two operating parameters: cooling rates applied at the probe (−4°C/min, −8°C/min, and −12°C/min) and flow rates in the embedded tube (without the tube, 30 ml/min and 100 ml/min). The results demonstrate that, for an identical final temperature at the tip of the cryoprobe and the resulting different application times, both the flow rates in the embedded tube and the cooling rates applied at the cryoprobe have similar qualitative effects on the size of the PCM frozen volumes; increasing either one will cause these volumes to decrease. The effects of flow rate in the tube are more pronounced, however, effecting relative frozen volumes decreases by about 10–20% while those of the cooling rate at the cryoprobe are in the range of 7–14%. For the case without the tube, volumes enclosed by the 0°C and −40°C isotherms were smaller by 13.2% and 12.5%, respectively, for the highest cooling rate compared with the lowest (−12°C/min versus −4°C/min). At the intermediate cooling rate of −8°C/min, volumes enclosed by these isotherms are considerably higher at 18.9% and 17.2%, respectively, when compared with the case without the tube.

Results of this study should be useful during the planning stages of cryosurgical procedures, which are to be applied in the vicinity of thermally-significant blood vessels.

Table 3 Frozen volumes (cm^3) enclosed by the 0°C and −40°C isothermal surfaces for various flow rates in the embedded tube and cooling rates at the cryoprobe. Final cryoprobe temperature: −142°C.

Cryoprobe cooling rate		−4°C/min		−8°C/min		−12°C/min	
Isotherm		0°C	−40°C	0°C	−40°C	0°C	−40°C
Flow rate	No flow	22.0	3.2	20.6	2.9	19.1	2.8
	30 ml/min	19.8	2.9	18.4	2.8	16.6	2.5
	100 ml/min	17.9	2.6	16.7	2.4	15.2	2.2

References

[1] Walder, H. A. D., 1971, "Experimental Cryosurgery," *Cryogenics in Surgery*, H. Von Leden and W. G. Cahan, eds., Medical Examination Publishing Co., Flushing, NY, pp. 150–181.

[2] Rabin, Y., and Shitzer, A., 1996, "A New Cryosurgical Device for Controlled Freezing, Part 1: Setup and Validation Tests," Cryobiology, **33**, pp. 82–92.

[3] Larson, T. R., Robertson, D. W., Corica, A., and Bostwick, D. G., 2000, "In Vivo Interstitial Temperature Mapping of the Human Prostate During Cryosurgery With Correlation With Histopathological Outcomes," Urology, **55**, pp. 547–552.

[4] Cooper, T. E., and Trezek, G. J., 1970, "Analytical Prediction of the Temperature Field Emanating From Acryogenic Surgical Cannula," Cryobiology, **7**, pp. 79–93.

[5] Rubinsky, B., and Shitzer, A., 1976, "Analysis of a Stefan-Like Problem in a Biological Tissue Around a Cryosurgical Probe," ASME J. Heat Transfer, **98**, pp. 514–519.

[6] Comini, G., and Del Giudice, S., 1976, "Thermal Aspects of Cryosurgery," ASME J. Heat Transfer, **98**, pp. 543–549.

[7] Keanini, R. G., and Rubinsky, B., 1992, "Optimization of Multiprobe Cryosurgery," ASME J. Heat Transfer, **114**, pp. 796–801.

[8] Weill, A., Shitzer, A., and Bar-Yoseph, P., 1993, "Finite Element Analysis of the Temperature Field Around Two Adjacent Cryo-Probes," ASME J. Biomech. Eng., **115**, pp. 374–379.

[9] Rabin, Y., 1998, "Uncertainty in Temperature Measurements During Cryosurgery," Cryo Letters, **19**, pp. 213–224.

[10] Rabin, Y., 2003, "Cryoheater as a Means of Cryosurgery Control," *Proceedings of the IMECE'03*, Washington, D.C., Nov. 15–21, Paper No. IMECE-41100.

[11] Trezek, G. J., 1985, "Thermal Analysis for Cryosurgery," *Heat Transfer in Medicine and Biology: Analysis and Applications*, A. Shitzer and R. C. Eberhart, eds., Plenum, New York, pp. 239–259.

[12] Rubinsky, B., 2000, "Cryosurgery," Annu. Rev. Biomed. Eng., **2**, pp. 157–187.

[13] Lunardini, V. J., 1983, "Approximate Phase-Change Solutions for Insulated Buried Cylinders," ASME J. Heat Transfer, **105**, pp. 25–33.

[14] Sadegh, A. M., Jiji, L. M., and Weinbaum, S., 1987, "Boundary Integral Equation Technique With Application to Freezing Around a Buried Pipe," Int. J. Heat Mass Transfer, **30**, pp. 223–232.

[15] Negiz, A., Hastaoglu, M. A., and Heidemann, R. A., 1995, "Three-Dimensional Transient Heat Transfer From a Buried Pipe: Solidification of a Stationary Fluid," Numer. Heat Transfer, Part A, **28**, pp. 175–193.

[16] Zhang, Y. T., Liu, J., and Zhou, Y. X., 2002, "Pilot Study on Cryogenic Heat Transfer in Biological Tissues Embedded With Large Blood Vessels," Forsch. Ingenieurwes., **67**, pp. 188–197.

[17] Deng, Z. S., and Liu, J., 2005, "Effect of Configuration Between Cryoprobe and Large Blood Vessels on the Tissue Freezing During Cryosurgery," *Proceedings of the Engineering in Medicine and Biology Society, IEEE-EMBS*, pp. 490–493.

[18] Deng, Z. S., and Liu, J., 2006, "Numerical Study of the Effects of Large Blood Vessels on Three-Dimensional Tissue Temperature Profiles During Cryosurgery," Numer. Heat Transfer, Part A, **49**, pp. 47–67.

[19] Deng, Z. S., Liu, J., and Wang, H. W., 2008, "Disclosure of the Significant Thermal Effects of Large Blood Vessels During Cryosurgery Through Infrared Temperture Mapping," Int. J. Therm. Sci., **47**, pp. 530–545.

[20] Chayut, Y., and Shitzer, A., 1996, "Simulating the Effects of a Large Blood Vessel on the Temperature Field Around a Surface Cryoprobe," *Proceedings of the ASME Advances in Heat and Mass Transfer in Biotechnology*, L. J. Hayes and S. Clegg, eds., pp. 21–22, Paper Nos. HTD-337, BED-34.

[21] Massalha, L., and Shitzer, A., 2004, "Freezing by a Flat, Circular Surface Cryoprobe of a Tissue Phantom With an Embedded Cylindrical Heat Source Simulating a Blood Vessel," ASME J. Biomech. Eng., **126**, pp. 736–744.

[22] Rubinsky, B., and Cravalho, E. G., 1981, "A Finite Element Method for the Solution of One-Dimensional Phase Change Problems," Int. J. Heat Mass Transfer, **24**, pp. 1987–1989.

[23] Ouyang, T., and Tamma, K. K., 1996, "Finite Element Simulations Involving Simultaneous Multiple Interface Fronts in Phase Change Problems," Int. J. Heat Mass Transfer, **39**, pp. 1711–1718.

[24] Bhattacharya, M., Basak, T., and Ayappa, K. G., 2002, "A Fixed Grid Finite Element Based Enthalpy Formulation for Generalized Phase Change Problems: Role of Superficial Mushy Region," Int. J. Heat Mass Transfer, **45**, pp. 4881–4898.

[25] http://www.ansys.com/products/multiphysics-features.asp

[26] Bonacina, C., Comini, G., Fasano, A., and Primicerio, M., 1974, "On the Estimation of Thermophysical Properties in Nonlinear Heat Conduction Problems," Int. J. Heat Mass Transfer, **17**, pp. 861–867.

[27] Saliken, J. C., Donnelly, B. J., and Rewcastle, J. C., 2002, "The Evolution and State of Modern Technology for Prostate Cryosurgery," Urology, **60**, pp. 26–33.

A Hybrid Large Eddy Simulation/Filtered Mass Density Function for the Calculation of Strongly Radiating Turbulent Flames

Abhilash J. Chandy
School of Mechanical Engineering,
Purdue University,
West Lafayette, IN 47907-2088

David J. Glaze
Sandia National Laboratories,
P.O. Box 5800,
Albuquerque, NM 87185

Steven H. Frankel
School of Mechanical Engineering,
Purdue University,
West Lafayette, IN 47907-2088

Due to the complex nonlinear coupling of turbulent flow, finite-rate combustion chemistry and thermal radiation from combustion products and soot, modeling, and/or simulation of practical combustors, or even laboratory flames undergoing strong soot formation, remain elusive. Methods based on the determination of the probability density function of the joint thermochemical scalar variables offer a promising approach for handling turbulence-chemistry-radiation interactions in flames. Over the past decade, the development and application of the filtered mass density function (FMDF) approach in the context of large eddy simulations (LES) of turbulent flames have gained considerable ground. The work described here represents the first application of the LES/FMDF approach to flames involving soot formation and luminous radiation. The initial focus here is on the use of a flamelet soot model in an idealized strongly radiating turbulent jet flame, which serves to detail the formulation, highlight the importance of turbulence-radiation interactions, and pave the way for the inclusion of a soot transport and finite-rate kinetics model allowing for quantitative comparisons to laboratory scale sooting flames in the near future. [DOI: 10.1115/1.3082405]

Keywords: LES, FMDF method, soot, turbulence-radiation interactions

1 Introduction

It is well known that flame-generated soot particles considerably enhance radiative heat losses, reducing thermal efficiencies of many power systems, such as gas turbines and diesel engines [1], and furthermore lead to air pollution [2]. This emphasizes the need for innovative approaches, both experimental (e.g., Ref. [3]) and computational (e.g., Ref. [4]), to aid in the design of cleaner combustors that can satisfy stricter emission standards for particulates such as soot.

The treatment of the associated luminous thermal radiation and turbulence-radiation interactions (TRI) is one of the main challenges with regard to strongly radiating flames. Joint composition probability density function (PDF) method [5], offers an attractive means of handling nonlinear turbulent thermochemical interactions. For example, in the joint scalar PDF transport equation method the chemical source term appears in closed form, since it is a function of the thermochemical composition, which is an independent variable. This feature of the joint scalar PDF method carries over to other aspects of combustion physics, including soot chemistry and radiation, providing a means of accounting for the effects of turbulent fluctuations on these processes.

2 Background

Monte Carlo based PDF methods [5] have gained in popularity in past years, in particular with regard to Reynolds-averaged Navier–Stokes (RANS) predictions of nonequilibrium turbulent flame phenomena such as extinction/reignition dynamics [6,7]. The main challenge there is related to the development of consistent and robust mixing models and their influence on the predictions [8,6].

Several RANS studies focusing on TRI have been performed earlier [9–11]. These studies employed either the joint velocity-composition PDF or a joint composition PDF to conclude that the inclusion of the absorption coefficient-temperature correlation alone may increase radiative heat flux by a significant amount ($>45\%$). Analogous PDF transport techniques have been developed for large eddy simulation (LES) only recently. In the context of LES, the solution of the filtered mass density function (FMDF) transport equation by stochastic Monte Carlo simulation as a subgrid scale (SGS) modeling approach was formulated for turbulent reacting flows by Jaberi et al. [12], and has since been used for turbulent flames in the absence of radiation [13,14]. With respect to any radiative transfer calculation (thermal radiation from gas or soot), to the author's knowledge, this is the first study that applies a Monte Carlo PDF model in the context of LES to strongly radiating turbulent flames.

To reduce the computational effort, a simplified soot model based on a flamelet state relationship is employed. Such a relationship assumes the soot volume fraction to be perfectly correlated with mixture fraction. Although there is some experimental evidence to support this view [15], the soot concentration is not simply related to mixture fraction, since the soot chemistry is comparatively slow and its diffusive transport is negligible. The focus of the current study is, however, to demonstrate the effectiveness of the FMDF method in accurately treating SGS TRI and it is assumed that observations and conclusions related to TRI effects are unlikely to change even with a detailed soot model.

Contributed by the Heat Transfer Division of ASME for publication in the JOURNAL OF HEAT TRANSFER. Manuscript received April 29, 2007; final manuscript received September 16, 2008; published online March 16, 2009. Review conducted by Yogesh Jaluria. Paper presented at the Western States Combustion Meeting, San Diego, CA, March 2007.

3 Formulation

3.1 LES Model. The filtered Navier–Stokes equations are given by

$$\frac{\partial \langle \rho \rangle_l}{\partial t} + \frac{\partial \langle \rho \rangle_l \langle u_i \rangle_L}{\partial x_i} = 0 \tag{1}$$

$$\frac{\partial \langle \rho \rangle_l \langle u_j \rangle_L}{\partial t} + \frac{\partial \langle \rho \rangle_l \langle u_i \rangle_L \langle u_j \rangle_L}{\partial x_i} = -\frac{\partial \langle p \rangle_l}{\partial x_j} + \frac{\partial \langle \tau_{ij} \rangle_l}{\partial x_i} - \frac{\partial \tau_{u_i u_j}}{\partial x_i} \tag{2}$$

where ρ, u_i, and p are the mixture density, mixture velocity, and pressure, respectively. In the above equations $\langle \ldots \rangle_l$ is obtained by applying a high-pass scale filter that happens to be the grid itself [16], while $\langle \ldots \rangle_L$ is a density-weighted, or Favre-filtered, quantity that can be defined from this grid filter function as $\langle f(\boldsymbol{x},t) \rangle_L \equiv \langle \rho f \rangle_l / \langle \rho \rangle_l$.

The filtered viscous stress tensor, $\langle \tau_{ij} \rangle_l$, is approximated in terms of resolved filtered quantities, and the SGS stress tensor, $(\tau_{u_i u_j})$, is closed in this study using a version of the Lagrangian dynamic SGS model of Meneveau et al. [17]. This model is based on the Smagorinsky eddy-viscosity model, and the model coefficient in the eddy-viscosity determination is evaluated dynamically (as a function of time and space) so that it adjusts to the local flowfield conditions, following the Lagrangian dynamic Smagorinsky approach of Germano et al. [18]. More details can be found in Refs. [17–19].

Spatial derivatives appearing in the closed Favre-filtered equations are discretized using a sixth-order compact finite difference scheme [20]. The two grid points nearest to the boundaries of the computational domain employ a fifth-order explicit scheme that has been tuned for stability when combined with our choice of sixth-order compact interior scheme [21]. In addition, a sixth-order compact pentadiagonal low-pass filter is applied to the entire solution at each time step to remove this destabilizing high-wavenumber noise [20]. With regard to time advancement, the semidiscrete system, representing the modeled LES transport equations, is advanced from time level n to time level $n+1$ using the standard fourth-order Runge–Kutta method [22].

Physical boundary conditions are implemented using the characteristic-based approach of Poinsot and Lele [23] for compressible viscous flows, modified for multicomponent reacting chemical species [24]. The jet flames are simulated in a rectangular adiabatic free-slip duct. The sidewalls only provide weak confinement to the flow, since they are chosen far enough from the jet to minimize direct interaction [25]. The downstream boundary is treated as a subsonic outflow. Details related to the implementation of these boundary conditions can also be found in Ref. [19].

3.2 FMDF Solver

3.2.1 FMDF Transport Equation. The FMDF can be defined as

$$F_L(\boldsymbol{\psi};\boldsymbol{x},t) \equiv \int_{-\infty}^{+\infty} \rho(\boldsymbol{x}',t)\zeta[\boldsymbol{\psi},\boldsymbol{\phi}(\boldsymbol{x}',t)]G(\boldsymbol{x}'-\boldsymbol{x})d\boldsymbol{x}' \tag{3}$$

where $\boldsymbol{\phi}(\boldsymbol{x},t)$ is the vector of thermochemical variables, and $\boldsymbol{\psi}$ is the corresponding sample space. The term $\zeta[\boldsymbol{\psi},\boldsymbol{\phi}(\boldsymbol{x}',t)]$ is called the fine-grained density, defined as [5]

$$\zeta[\boldsymbol{\psi},\boldsymbol{\phi}(\boldsymbol{x}',t)] = \delta[\boldsymbol{\psi}-\boldsymbol{\phi}(\boldsymbol{x},t)] \equiv \prod_{\alpha=1}^{M+1} \delta[\psi_\alpha - \phi_\alpha(\boldsymbol{x},t)] \tag{4}$$

where δ is the delta function. The fine-grained density has the physical interpretation of the joint PDF of a single realization of a measurement. Equation (3) thus represents the density-weighted spatially-filtered probability density of all possible measurements of subgrid composition at location $\boldsymbol{x}$ and time t.

An exact transport equation for the FMDF can be derived directly from the instantaneous scalar transport equation yielding

$$\frac{\partial F_L(\boldsymbol{\psi};\boldsymbol{x},t)}{\partial t} + \frac{\partial [\langle u_i(\boldsymbol{x},t)|\boldsymbol{\psi}\rangle_l F_L(\boldsymbol{\psi};\boldsymbol{x},t)]}{\partial x_i} = \frac{\partial}{\partial \psi_\alpha}\left[\left\langle \frac{1}{\hat{\rho}(\boldsymbol{\phi})}\frac{\partial J_i^\alpha}{\partial x_i}\middle|\boldsymbol{\psi}\right\rangle_l F_L(\boldsymbol{\psi};\boldsymbol{x},t)\right] - \frac{\partial [S_\alpha(\boldsymbol{\psi})F_L(\boldsymbol{\psi};\boldsymbol{x},t)]}{\partial \psi_\alpha} \tag{5}$$

where $\alpha=1,2,\ldots,M$ corresponds to each of the M chemical species, and $\alpha=M+1$ represents the total enthalpy. The scalar flux vector is thus

$$J_i^\alpha = -\gamma_\alpha \frac{\partial \phi_\alpha}{\partial x_i} \tag{6}$$

with γ_α equal to either ρD_α for chemical species transport or $\rho\alpha_s$ for enthalpy transport, where D_α is the molecular diffusivity for species, α and α_s is the thermal diffusivity with each functions of temperature and species composition. The source term S_α in the above equation is equal to the mass fraction source term S_{ϕ_α} for $\alpha=1,2,\ldots,M$ or S_{rad} for $\alpha=M+1$.

The convective term (second term in the left hand side (LHS) of Eq. (5)) is modeled in a manner consistent that is conceptually analogous to the gradient transport hypothesis defined above. The conditionally-filtered term (first term in the right hand side (RHS) of Eq. (5)) represents the SGS molecular mixing rate, which is much more sensitive to model choices than the convection term and employs the use of the so-called mixing model [8] (also see Sec. 3.2.3).

3.2.2 Monte Carlo Solution of FMDF. Due to the high dimensionality of the FMDF equation, the computational cost of numerically solving it using traditional finite difference techniques makes their use impractical. Instead, through the use of Itô calculus, Eq. (5) may be transformed from its deterministic form into a system of stochastic differential equations (SDEs) [5,12], which govern the evolution of a large sample of these Monte Carlo particles having a probability distribution identical to the original FMDF.

In a simulation, for a small ensemble volume ΔV with N_p number of particles within, any Favre-filtered variable can be approximated through the FMDF as

$$\langle Q \rangle_F \approx \frac{\sum_{n=1}^{N_p} w^{(n)} Q(\boldsymbol{\phi}^{(n)})}{\sum_{n=1}^{N_p} w^{(n)}} \tag{7}$$

where $w^{(n)}$ is a weighting factor assigned to each particle. These approximations approach exact equations, as the averaging volumes approach zero and the number of particles in each volume approaches infinity. For the present work, the averaging volume is taken to be the finite difference grid cell volume.

Statistical noise in the filtered temperature field can lead to oscillations in the filtered pressure calculated with the equation of state. Since derivatives of the pressure are used in the finite difference solver, this can destabilize the numerical solution [12]. As an alternative coupling technique [26,14], a redundant equation for sensible enthalpy is carried along with continuity and momentum equations in the finite difference solver. The filtered source term in this equation can be directly calculated from the reaction rates obtained through integration of the particle scalars with.

3.2.3 Molecular Mixing Model: Interaction by Exchange With the Mean. The mixing model employed here is interaction by exchange with the mean (IEM) [27], whose particle method implementation takes the following form:

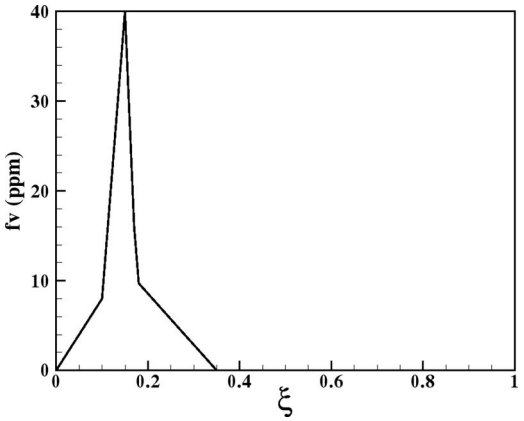

Fig. 1 The soot-state relationship showing soot volume fraction in ppm as a function of mixture fraction, ξ

$$\phi_\alpha^+(t_0+\Delta t)=\phi_\alpha^+(t_0)-(1-e^{-C_\Omega \Delta t/\tau_m})(\phi_\alpha^+(t_0)-\langle\phi_\alpha\rangle_L) \tag{8}$$

where $\langle\phi_\alpha\rangle_L$ is the local mean scalar value interpolated to the particle position, and the subgrid molecular mixing time scale is $\tau_m=(\gamma+\gamma_t)/(\langle\rho\rangle_l\Delta_G^2)$, with C_Ω being a free model parameter that is nominally set to a value of 4 for the present work [12]. With the use of the flamelet soot model here, soot is assumed to be a function of the mixture fraction and hence assumed to be in the gas phase. With this assumption in place, the use of a mixing model, such as the IEM (or modified curl (MC) or Euclidean minimum spanning tree (EMST)), that is entirely tuned for gas-phase diffusion processes to model the diffusive transport of soot, seems appropriate.

3.3 Soot Model. There are various soot models, from empirical to detailed ones, available in the literature [28]. However, a full 3D reacting flow computation involving a detailed soot model along with a detailed representation of the associated radiative loss is computationally very expensive. So in order to reduce computational effort, a simplified soot model based on a soot-state relationship was employed. The relation is given by $f_v=f(\xi)$, where f_v is the soot volume fraction and ξ is the mixture fraction. The functional relationship for an acetylene flame [29] is given in Fig. 1.

3.4 Radiation Closure Model. Assuming wavelength independence (gray approximation) and negligible scattering, the radiative source term can be written as

$$S_{\text{rad}}=-\nabla\cdot\mathbf{q}^R=\kappa\left(\int_{4\pi} I d\Omega-4\pi I_b\right) \tag{9}$$

with the corresponding filtered form of the radiative source term is given by

$$\langle S_{\text{rad}}\rangle_F=-\nabla\cdot\langle\mathbf{q}\rangle_F^R=\int_{4\pi}\langle\kappa I\rangle_L d\Omega-4\pi\langle\kappa I_b\rangle_F \tag{10}$$

where $\mathbf{q}^R$ denotes the radiative flux, I is the intensity, I_b is the black-body intensity or Planck function, Ω denotes solid angle, and κ is the spectrally averaged absorption coefficient. The contribution due to radiation from the gas-phase species is also assumed to be negligible compared with that from soot, in which case the absorption coefficient is given by the relation [30], $\kappa=3.83 f_v C_0 T/C_2$, where C_2 is chosen to be 0.014388 m K and C_0 is chosen to be 7 [31,30]. Furthermore, the Planck function, I_b is given the black-body emission function

$$I_b=\frac{\sigma T^4}{\pi} \tag{11}$$

where σ is the Stefan–Boltzmann coefficient given by 5.67×10^{-8} J/m^2 K^4 s. With scattering from the radiative medium assumed to be negligible, the radiative intensity is governed by the radiative transfer equation (RTE) for an absorbing-emitting medium, a presentation of which is provided next.

The mathematical form of the RTE that is solved in the LES formulation here is the *filtered* RTE (FRTE) and is given by

$$\frac{d\langle I\rangle_L}{ds}=\langle-\kappa I\rangle_L+\langle\kappa I_b\rangle_F \tag{12}$$

The filter in the above equation is implicit, as the LES grid itself acts as a filter and no explicit filter is applied to the RTE. The discrete ordinates method (DOM) is the method chosen here to solve the filtered RTE. A new parallelizing technique for the implementation of the DOM in 3D turbulent reacting flows was formulated and tested in one of our recent articles [32] to permit more efficient radiation calculations. The filtered form of the volume-averaged intensity, $I_{P,r}$, is given by

$$\langle I_{P,r}\rangle_L=\frac{\langle\kappa V\gamma I_{b,r}\rangle_F+|\xi_r|A_x\langle I_{x_i,r}\rangle_L+|\eta_r|A_y\langle I_{y_i,r}\rangle_L+|\mu_r|A_z\langle I_{z_i,r}\rangle_L}{\langle\kappa\rangle_L V\gamma+|\xi_r|A_x+|\eta_r|A_y+|\mu_r|A_z} \tag{13}$$

where V is the control volume, ξ_r, η_r, and μ_r are the direction cosines of direction r. The subscripts x, y, and z are used to denote face-averaged values, while the subscript i stands for radiation intensities entering the control volume, and A_x, A_y, and A_z are face areas whose normals are in the x, y, and z directions. The parameter γ relates the incoming and outgoing radiation intensities to the volume-averaged intensity (equations found in Ref. [30]) and is assigned a value of 1, which corresponds to a step scheme or an upwind scheme. Two nondimensional parameters are introduced through the nondimensionalization of the RTE, and they are the Boltzmann number given by $\text{Bo}=\rho_o U_o C_{p,o}/\sigma T_o^3$ and a nondimensional absorption coefficient given by $K_{\text{ab}}=L_o T_o 3.83 C_o/C_2$. $T_o=298.15$ K is the reference temperature, U_o is the reference velocity, given by $U_o=U_j-U_c$, and L_o is the reference length scale chosen to be D.

4 Physical Problem Description

The problem under consideration in this study consists of a turbulent jet of pure fuel injected at a velocity of $U_j=20$ m/s into a coflow of air at velocity $U_c=4$ m/s, both being at reference temperature, T_o. For all the simulations conducted here, the Re of the cold jet is 5000, based on the central fuel jet diameter and velocity.

Idealized chemistry is employed here, where the fuel, oxidizer, and product species are related through the single-step irreversible reaction $F+r\text{Ox}\rightarrow(1+r)P$, where r is the mass stoichiometric oxidizer/fuel ratio. An Arrhenius-type reaction is assumed, and two controlling nondimensional parameters are revealed from the nondimensionalization of the reaction rate expressions—the Damköhler number, $\text{Da}=(A_f\rho_o L_o)/(U_o W_{\text{Ox}})$ and the Zeldovich number, $\text{Ze}=E_A/\mathcal{R}T_o$.

Since acetylene flames are known to produce large amounts of soot, the idealized chemistry employed here is one that mimics a one-step acetylene-air chemical mechanism, and the value of r is thus chosen to be 13.2, based on the stoichiometric value of a single-step acetylene-air chemical mechanism. The Da, Ze, and Ce values are chosen to be 10, 5, and 5, respectively, with the definitions of these parameters described above. The first set of studies analyzes the importance of the consideration of radiation in calculations of heavily sooting flames by comparing the following cases: (1) without radiation, (2) with an approximate optically thin model that neglects self-absorption, and (3) with the discrete

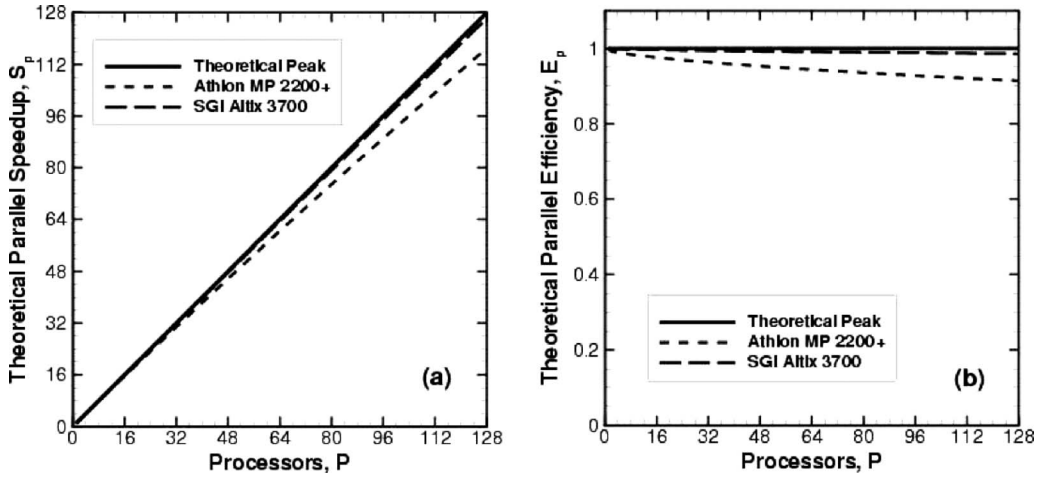

Fig. 2 Theoretical (*a*) speedup and (*b*) parallel efficiency for an LES using the FMDF closure model

ordinates method. These cases will be referred to as the WORAD, OTM, and DOM cases, respectively. The second set of studies assess SGS turbulence-radiation interactions or TRI in such flames with radiation being closed by the DOM. Comparisons are made between two cases, where the Planck function in the radiation source term is estimated from fine-grained quantities and from mean quantities and are referred to as the "DOM with TRI" and "DOM without TRI" cases, respectively. Also for all these cases, Bo is set to 2000 and K_{ab} is set to 10,000.

5 Subgrid Scale Turbulence-Radiation Interactions

In LES, with filter-scale TRI being treated accurately, on a SGS level, due to the strongly nonlinear dependence of radiative properties on temperature and species concentrations, $\langle\kappa(T,\phi_\alpha)I\rangle_L$ does not equal $\langle\kappa(T,\phi_\alpha)\rangle_L\langle I\rangle_L$ and $\langle\kappa(T,\phi_\alpha)I_b\rangle_F$ does not equal $\langle\kappa(T,\phi_\alpha)\rangle_F\langle I_b\rangle_F$ in Eq. (12), making these two terms unclosed. In the context of LES/FMDF, all statistics of composition variables including species and temperature are known at every instant, which helps in closing $\langle\kappa(T,\phi_\alpha)I_b\rangle_F$. Closure of the term, $\langle\kappa(T,\phi_\alpha)I\rangle_L$, requires on the other hand complete information of the statistics among the intensity variables, which of course is unavailable with the DOM, since the RTE that is solved is in filtered form. However, one of the most common approximations made in open literature on TRI is the optically thin eddy approximation, as described by Kabashnikov and Myasnikova [33], and later arguments supporting this were also put forth by Song and Viskanta [34]. The rationale behind this assumption is that the instantaneous local intensity at a point is formed over a path traversing several turbulent eddies, i.e., $\langle\kappa(T,\phi_\alpha)I\rangle_L = \langle\kappa(T,\phi_\alpha)\rangle_L\langle I\rangle_L$ or with the use of the FMDF model here $\langle\kappa(T,\phi_\alpha)I\rangle_L = \langle\kappa(T,\phi_\alpha)\rangle_F\langle I\rangle_L$.

6 Results and Discussion

This section presents results from LES/FMDF simulations of heavily sooting turbulent flames and the objective is to assess the importance of SGS TRI in such flames. All the computations presented here use a domain of size $40\times8\times8$ with a grid of $180\times70\times70$ where the above domain size values are nondimensional. The number of particles in the smallest cell of the domain was chosen in all these cases as 25.

For the purpose of a scaling analysis, Fig. 2 illustrates the parallel speedup, $S_p = T_{\text{serial}}/T_{\text{parallel}}$, and the parallel efficiency, $E_p = S_p/p$, for two architectures—a research cluster of dual AMD Athlon MP 2200+machines with gigabit Ethernet interconnects and the SGI Altix 3700, which serves as an example of a high-end supercomputer. Network and CPU performances for the Athlon cluster are based on actual measurements, while those for the Altix 3700 are estimated from available marketing information and relative SPECfp2000 performance benchmarks for the two architectures. The LES/FMDF code exhibits nearly linear speedup due to the large quantity of calculations required for the FMDF model, essentially indicating that this code is more CPU-bound than network-bound.

The computations were performed on our in-house research cluster, the Athlon MP 2200+ and the Xeon Linux "tungsten" cluster at National Center for Supercomputing Applications (NCSA). Typical calculations on the Xeon cluster were conducted on 64 processors, and the total simulation execution time was 59 wall clock h for 100 nondimensional time units, of which 35% accounts for the communication time. Each nondimensional time unit here is given by $t^* = tL_o/(U_j - U_c)$. The time for cases with radiation using DOM consumed an additional 50% of wall clock h on 64 processors.

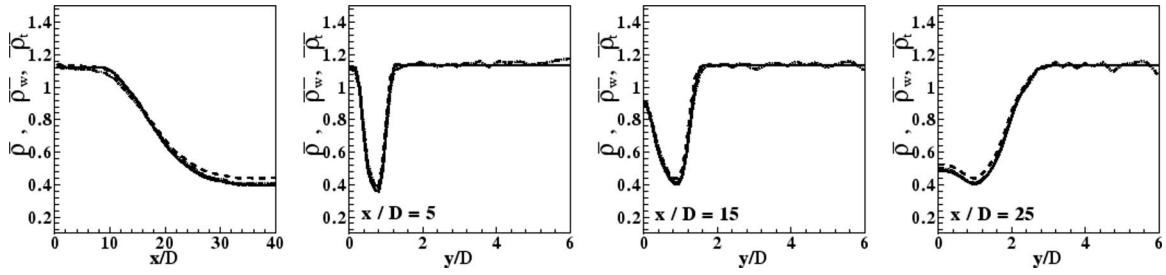

Fig. 3 Assessment of consistency in the time-averaged filtered density profiles at centerline-axial (column 1) and three different radial locations (columns 2–4) from calculations of the DOM case. Lines: solid: $\langle\rho\rangle_L$, dashed: $\langle\rho\rangle_{L,w}$, and dash-dot: $\langle\rho\rangle_{L,t}$.

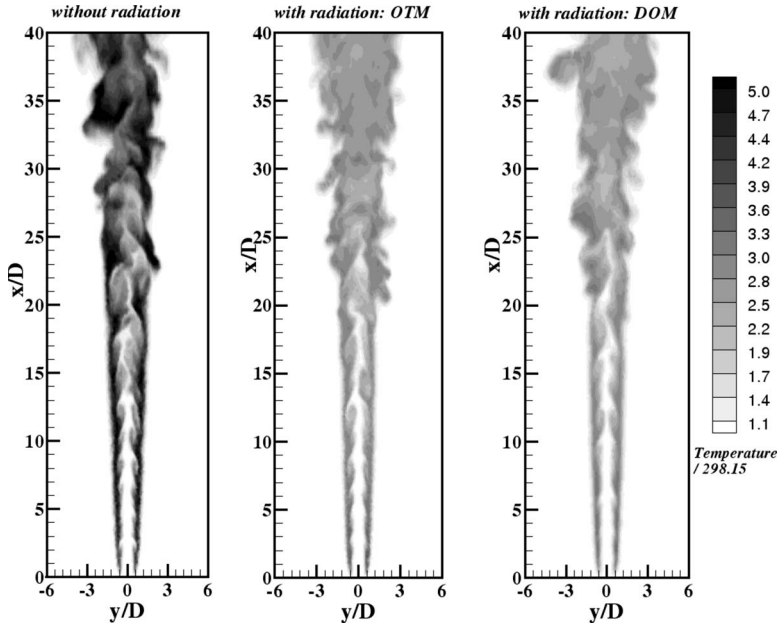

Fig. 4 Instantaneous cross section through the jet centerline of the nondimensional temperature from LES/FMDF computations of the three cases—WORAD (left), OTM (middle), and DOM (right)

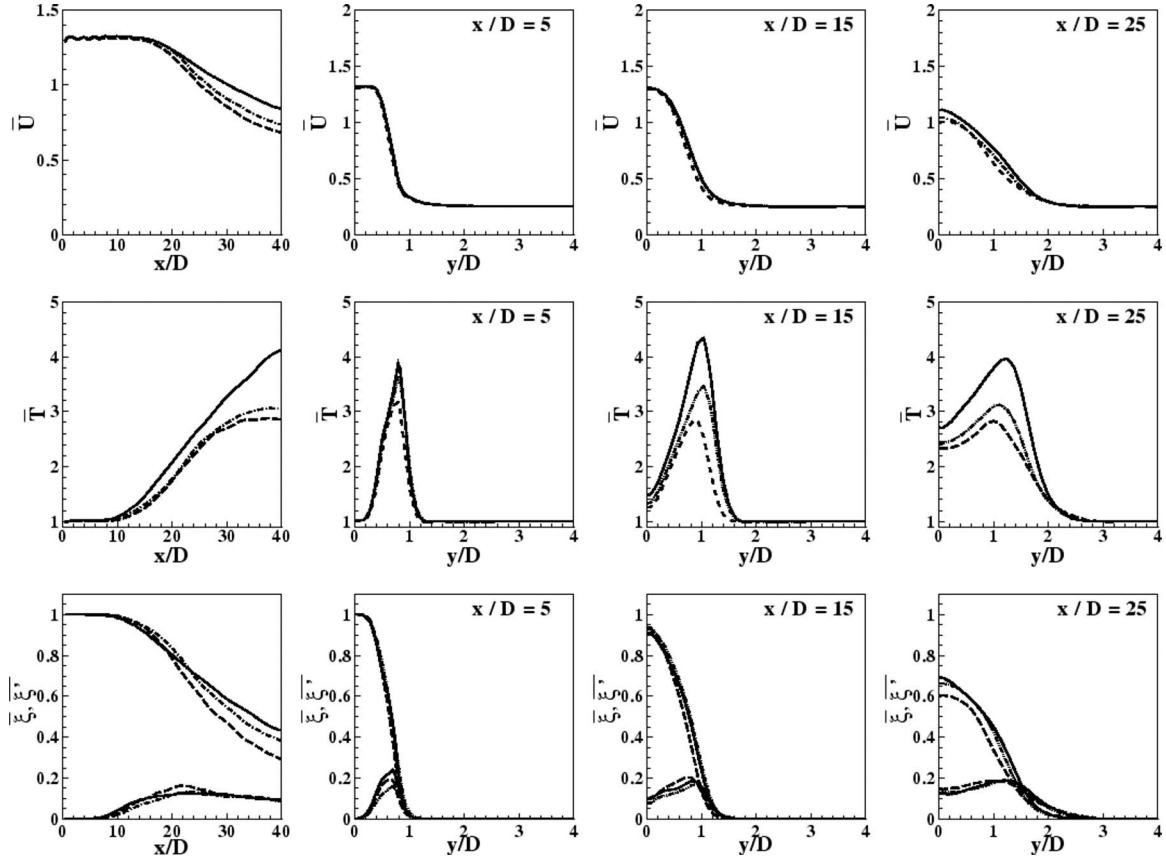

Fig. 5 Axial (column 1) and radial profiles (columns 2–4) of mean filtered nondimensional velocities, nondimensional temperatures, and mixture fraction along with its rms from LES/FMDF computations of the three cases—WORAD (solid lines), OTM (dashed lines), and DOM (dash-dot lines)

6.1 Consistency of the Feedback System. In the current implementation, density can be evaluated using three redundant densities. First, there is a filtered density that is associated with the finite difference solver that is obtained from the continuity equation—$\langle\rho\rangle_L$. Second, a filtered value of the density can be calculated from the weights through the relation

$$\langle\rho\rangle_{L,w} \approx \frac{\Delta m}{\Delta V}\sum_{n=1}^{N_p} w^{(n)} \tag{14}$$

Third, a fine-grained density can be calculated from the thermochemical state of a particle using the ideal gas law and can then be used to find a filtered density based on thermochemical properties using the relation

$$\frac{1}{\langle\rho\rangle_{L,t}} = \frac{\sum_{n=1}^{N_p} w^{(n)}/\rho_w^{(n)}}{\sum_{n=1}^{N_p} w^{(n)}} \tag{15}$$

where $\rho_w^{(n)} = P_o/(R^{(n)}T^{(n)})$, P_o being the operating pressure, R being the gas constant for the mixture, and T being the temperature. Consistency requires that $\langle\rho\rangle_l = \langle\rho\rangle_{L,w} = \langle\rho\rangle_{L,t}$. The robustness of the FMDF method can be improved by ensuring a time-accurate consistency of these densities [35].

Figure 3 presents the degree of consistency for the DOM case. Clearly for the DOM case, the densities are consistent with very slight oscillations in the particle weight-based density in the far-field region of the jet. These are due to the fewer number of particles in this region, which might not be significant since gradients are low in these regions.

6.2 Importance of Radiation. Contours of temperature on a slice across the jet centerline are presented in Fig. 4, for the WORAD, OTM, and DOM cases. Under the optically thin approximation the radiation source term is calculated as

$$S_{\text{rad}} = 4\kappa\sigma(T_{\text{surr}}^4 - T^4) \tag{16}$$

where T_{surr} is the surrounding medium temperature and is chosen to be the reference temperature here. The model is based on an optically thin assumption at the scale of the computation and hence self-absorption effects are neglected. Although, this form of the source term captures the nonlinearity in the temperature term, the radiative energy loss from the soot may be slightly overestimated due to any positive correlation between soot volume fraction and temperature in soot-promoting high-temperature fuel-rich regions. However, probably due to the simplicity in its implementation, this model has been widely employed in studies of soot and gas thermal radiation [36,37].

The noticeable feature in Fig. 4 is that there is almost a 50% reduction in temperatures with the inclusion of radiation in the DOM and OTM cases. As expected, OTM overpredicts the radiative heat loss and hence underpredicts the temperature compared with DOM. This is due to the fact that self-absorption effects are neglected.

Profiles of velocity, temperature, and mixture fraction are shown in Fig. 5. Reduction in temperature due to radiative effects in the OTM and DOM cases causes an increase in density, which in turn decreases the axial velocity. Such differences affect the mean mixture fraction as well, more so, downstream of the jet.

A better quantitative comparison of the two radiation models is presented with the help of profiles of radiative source term and

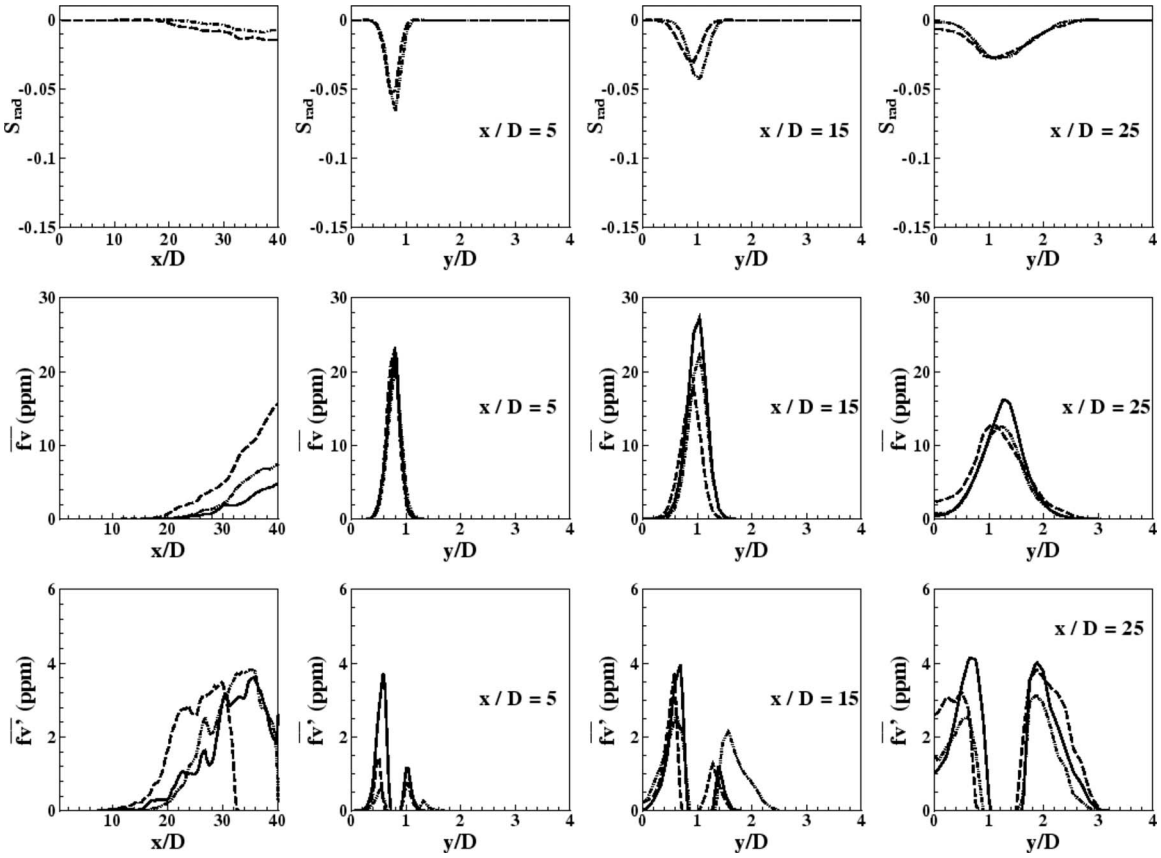

Fig. 6 Axial (column 1) and radial profiles (columns 2–4) of mean filtered radiative source term (S_{rad}) and the soot volume fraction (f_v) along with its rms from LES/FMDF computations of the OTM (dashed lines) and DOM (dash-dot lines) cases

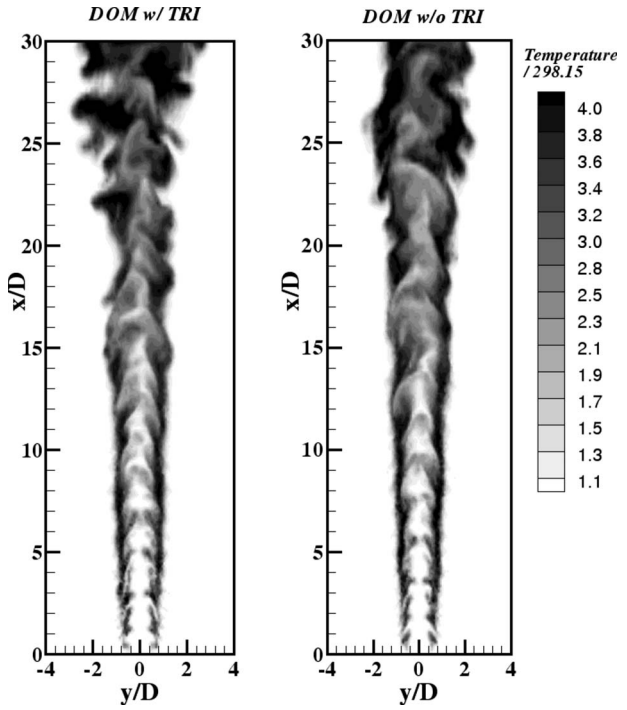

Fig. 7 Instantaneous cross section through the jet centerline of the nondimensional temperature from LES/FMDF computations of the two cases—with TRI (left) and without TRI (right)

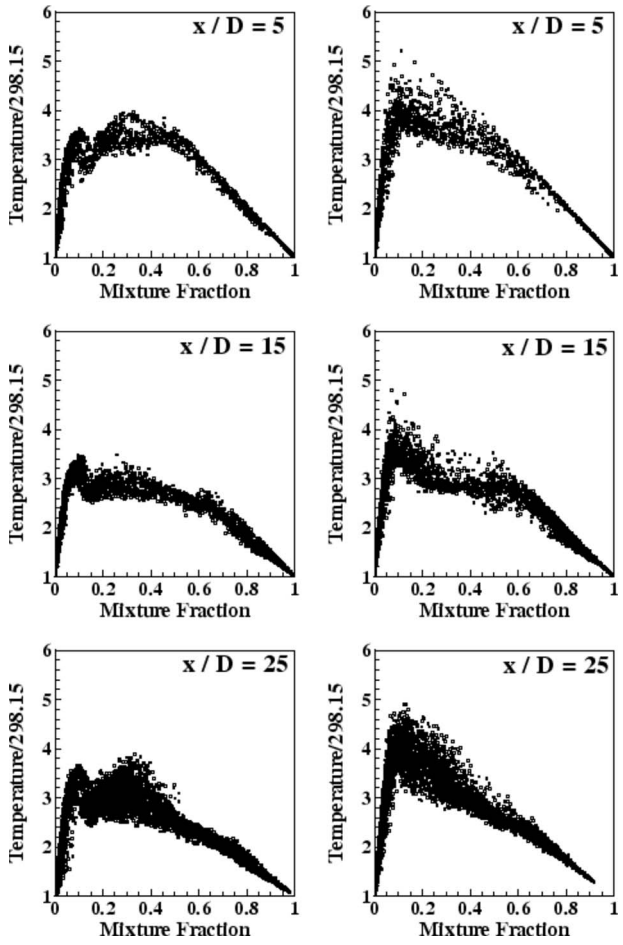

Fig. 8 Scatter plots of nondimensional temperature against mixture fraction at the axial locations x/D=5, 15, and 25 from LES/FMDF computations of the two cases—with TRI (left) and without TRI (right)

soot volume fraction in Fig. 6. The overprediction of radiative heat loss by OTM is evident in the profiles of the mean radiation source term downstream of the jet. Besides it should also be noted that the radiation heat loss at each axial location peaks where the soot volume fraction peaks, indicating the effect of thermal emission from the soot layer. Soot forms in thin layers and soot fluctuations (rms of soot volume fraction, f_v') are large and almost 1/3 of the mean values. The highly intermittent nature of the soot process can be clearly seen in the behavior of the rms of the soot volume fraction. This behavior is in qualitative agreement with several previous experimental and numerical studies of strongly radiating turbulent flames [38–40].

6.3 Importance of Subgrid Scale Turbulent-Radiation Interactions. The importance of SGS TRI is presented in this subsection. Comparisons are made between two cases—one where DOM is employed and full SGS TRI are considered ($\langle\kappa(T,Y_\alpha)I_b\rangle_F$ is evaluated directly) and the other with DOM and all SGS TRI are ignored ($\langle\kappa(T,Y_\alpha)I_b\rangle_F=\langle\kappa(T,Y_\alpha)\rangle_F\langle I_b\rangle_F$. An explanation related to these correlations was provided in Sec. 5.

Figure 7 compares instantaneous contours of temperature for the cases with and without SGS TRIs. The legends in these figures indicating "w TRI" and "w/o TRI" refer to computations with and without SGS TRIs, respectively. Although, there appears to be only slight differences in the flame structure, the most obvious difference is that the flame gets colder if SGS TRI is considered. This can also be confirmed from the scatter plots of temperature versus mixture fraction in Fig. 8. Scatter plots at various axial locations clearly show that ignoring SGS TRI increases the overall temperature of the flame.

Profiles of the mean filtered radiative source term shown in Fig. 9 indicate that the consideration of TRI increases the overall radiative heat loss and the difference becomes more significant downstream. In the DOM without TRI case, the contribution due to emission in the radiative source term is determined from mean property values. This filters much of the inherent turbulent fluctuations in temperature and species mass fraction, and hence reduces the radiative emission from the core of the flame. Thus, due to the suppressed radiative heat loss, the temperature ends up being higher when SGS TRIs are ignored. Such effects are expected to be larger when turbulent fluctuations are larger, as in high Re cases, or downstream of a jet, as in the case presented here.

7 Conclusions

A hybrid large eddy simulation/filtered mass density function approach was presented to calculate strongly radiating turbulent flames, with the radiation heat source from the simplified soot model. The discrete ordinates method was employed to close radiative transfer. Idealized chemistry and properties were used, and parameters were chosen to match those of a one-step acetylene-air mechanism.

Redundant densities were compared to illustrate the consistency of the implementation. Comparisons of instantaneous snapshots and time-averaged statistics were made between three cases: the first being a calculation without a radiation model, the second, an OTM based on the assumption that self-absorption effects are negligible, and the third, using the detailed DOM to calculate thermal radiation contribution from soot. While radiative emission resulted in highly reduced temperatures, thus altering the flame structure significantly, subtle differences were also observed between the simplified and detailed radiation models suggesting the importance of absorption effects in such flames. Also presented were LES/FMDF calculations coupled with DOM to assess the

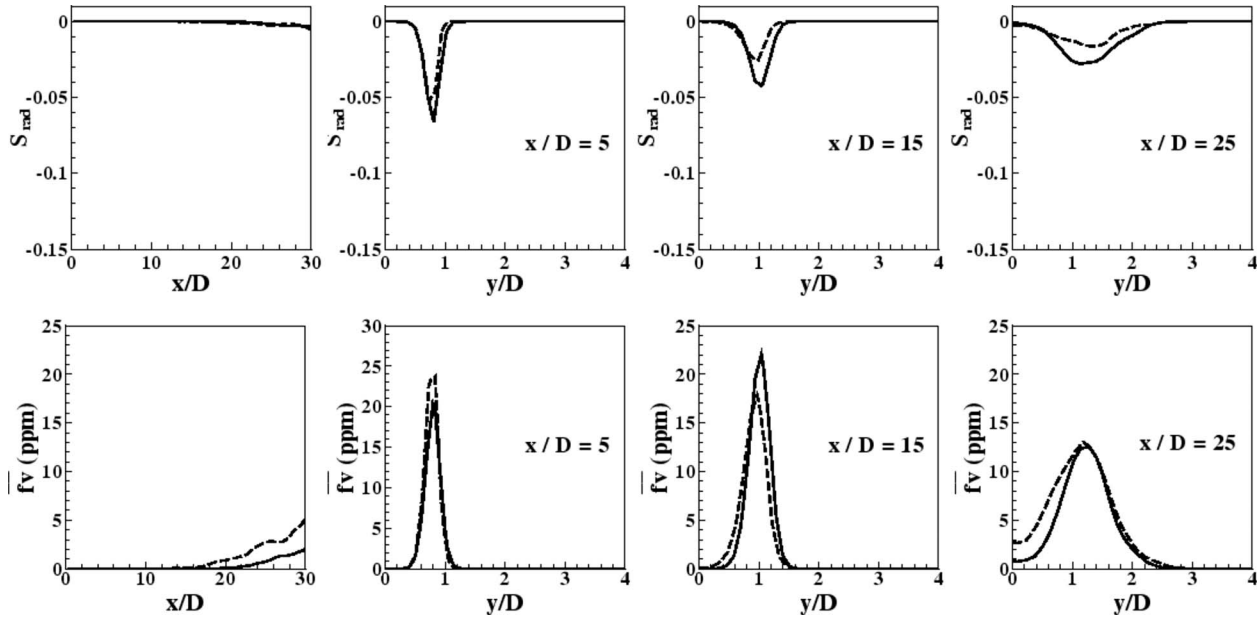

Fig. 9 Axial (column 1) and radial profiles (columns 2–4) of mean filtered radiative source term (S_{rad}) and the soot volume fraction (f_v) along with its rms from LES/FMDF computations of the two cases—with TRI (solid lines) and without TRI (dashed lines)

importance of subgrid scale turbulence-radiation interactions. Neglect of SGS TRI increased temperatures, due to the estimation of the emission term from mean properties. Hence, these results further emphasized the unique advantage of PDF methods, where nonlinear interactions, in this case the radiative source term, were treated accurately.

Acknowledgment

The authors would like to acknowledge the National Center for Supercomputing Applications (NCSA) for providing computing resources for conducting the calculations, which are presented in this paper.

References

[1] Yang, B., and Koylu, U. O., 2005, "Detailed Soot Field in a Turbulent Non-Premixed Ethylene/Air Flame From Laser Scattering and Extinction Experiments," Combust. Flame, **141**, pp. 55–65.
[2] Jacobson, M., 2001, "Strong Radiative Heating Due to the Mixing State of Black Carbon in Atmospheric Aerosols," Nature (London), **409**, pp. 695–697.
[3] Mungekar, H., and Atreya, A., 2006, "Flame Radiation and Soot Emission From Partially Premixed Methane Counterflow Flames," ASME J. Heat Transfer, **128**, pp. 361–367.
[4] Zheng, Y., Barlow, R. S., and Gore, J., 2003, "Measurements and Calculations of Spectral Radiation Intensities for Turbulent Non-Premixed and Partially Premixed Flames," ASME J. Heat Transfer, **125**, pp. 678–686.
[5] Pope, S. B., 1985, "PDF Methods for Turbulent Reacting Flows," Prog. Energy Combust. Sci., **11**, pp. 119–192.
[6] Xu, J., and Pope, S. B., 2000, "PDF Calculations of Turbulent Nonpremixed Flames With Local Extinction," Combust. Flame, **123**, pp. 281–307.
[7] James, S., Anand, M. S., Razdan, M. K., and Pope, S. B., 2001, "In Situ Detailed Chemistry Calculations in Combustor Flow Analyses," ASME J. Eng. Gas Turbines Power, **123**, pp. 747–756.
[8] Fox, R. O., 2003, *Computational Models for Turbulent Reacting Flows*, Cambridge University Press, Cambridge, England.
[9] Mazumder, S., and Modest, M. F., 1999, "A PDF Approach to Modeling Turbulence-Radiation Interactions in Nonluminous Flames," Int. J. Heat Mass Transfer, **42**, pp. 971–991.
[10] Li, G., and Modest, M. F., 2003, "Importance of Turbulence-Radiation Interactions in Turbulent Diffusion Jet Flames," ASME J. Heat Transfer, **125**, pp. 831–838.
[11] Aksit, I. M., and Moss, J. B., 2006, "A Hybrid Scalar Model for Sooting Turbulent Flames," Combust. Flame, **145**, pp. 231–244.
[12] Jaberi, F. A., Colucci, P. J., James, S., Givi, P., and Pope, S. B., 1999, "Filtered Mass Density Function for Large-Eddy Simulation of Turbulent Reacting Flows," J. Fluid Mech., **401**, pp. 85–121.
[13] Sheikhi, M. R. H., Drozda, T. G., Givi, P., Jaberi, F. A., and Pope, S. B., 2005, "Large Eddy Simulation of a Turbulent Nonpremixed Piloted Methane Jet Flame (Sandia Flame D)," Proc. Combust. Inst., **30**, pp. 549–556.
[14] Raman, V., and Pitsch, H., 2005, "LES/Filtered Density Function Simulation of Turbulent Combustion With Detailed Chemistry," Annual Research Briefs, Center for Turbulence Research, NASA Ames/Stanford University, pp. 297–308.
[15] Sivathanu, Y., and Faeth, G. M., 1990, "Soot Volume Fractions in the Overfire Region of Turbulent Diffusion Flames," Combust. Flame, **81**, pp. 133–149.
[16] Sagaut, P., 2006, *Large Eddy Simulation for Incompressible Flows: An Introduction*, 3rd ed., Springer, New York.
[17] Meneveau, C., Lund, T., and Cabot, W., 1996, "A Lagrangian Dynamic Subgrid-Scale Model of Turbulence," J. Fluid Mech., **319**, pp. 353–385.
[18] Germano, M., Piomelli, U., Moin, P., and Cabot, W. H., 1991, "A Dynamic Subgrid-Scale Eddy Viscosity Model," Phys. Fluids A, **3**(7), pp. 1760–1765.
[19] Glaze, D. J., 2006, "Large Eddy Simulation of a Turbulent Jet Diffusion Flame Using the Filtered Density Mass Function Model," Ph.D. thesis, Department of Mechanical Engineering, Purdue University.
[20] Lele, S. K., 1992, "Compact Finite Difference Schemes With Spectral-Like Resolution," J. Comput. Phys., **103**, pp. 16–42.
[21] Carpenter, M. H., Gottlieb, D., and Abarbanel, S., 1993, "The Stability of Numerical Boundary Treatments for Compact High-Order Finite-Difference Schemes," J. Comput. Phys., **108**, pp. 272–295.
[22] Hoffman, J. D., 1992, *Numerical Methods for Engineers and Scientists*, McGraw-Hill, New York.
[23] Poinsot, T. J., and Lele, S. K., 1992, "Boundary Conditions for Direct Simulations of Compressible Viscous Flows," J. Comput. Phys., **101**, pp. 104–129.
[24] Pakdee, W., and Mahalingam, S., 2003, "An Accurate Method to Implement Boundary Conditions for Reacting Flows Based on Characteristic Wave Analysis," Combust. Theory Modell., **7**, pp. 705–729.
[25] Amielh, M., Djeridane, T., Anselmet, F., and Fulachier, L., 1996, "Velocity Near-Field of Variable Density Turbulent Jets," Int. J. Heat Mass Transfer, **39**(10), pp. 2149–2164.
[26] Muradoglu, M., Pope, S., and Caughey, D., 2001, "The Hybrid Method for the PDF Equations of Turbulent Reactive Flows: Consistency Conditions and Correction Algorithms," J. Comput. Phys., **172**, pp. 841–878.
[27] Dopazo, C., and O'Brien, E. E., 1974, "An Approach to the Autoignition of a Turbulent Mixture," Acta Astronaut., **1**, pp. 1239–1266.
[28] Kennedy, I. M., 1997, "Models of Soot Formation and Oxidation," Prog. Energy Combust. Sci., **23**, pp. 95–132.
[29] Gore, J. P., 1986, "A Theoretical and Experimental Study of Turbulent Flame Radiation," Ph.D. thesis, Department of Mechanical Engineering, Pennsylvania State University.
[30] Modest, M. F., 2003, *Radiative Heat Transfer*, Academic, New York.
[31] Kent, J. H., and Honnery, D., 1987, "Soot and Mixture Fraction in Turbulent Diffusion Flames," Combust. Sci. Technol., **54**, pp. 383–397.
[32] Chandy, A. J., Glaze, D. J., and Frankel, S. H., 2007, "Parallelizing the Discrete Ordinates Method (DOM) for Three-Dimensional Radiative Heat Transfer Calculations Using a Priority Queuing Technique," Numer. Heat Transfer, Part B, **52**, pp. 33–49.
[33] Kabashnikov, V. P., and Myasnikova, G. I., 1985, "Thermal Radiation in Turbulent Flows-Temperature and Concentration Fluctuations," Heat Transfer-

Sov. Res., **17**, pp. 116–125.
[34] Song, T., and Viskanta, R., 1987, "Interaction of Radiation With Turbulence: Application to a Combustion System," J. Thermophys. Heat Transfer, **1**(1), pp. 56–62.
[35] Pitsch, H., 2006, "Large Eddy Simulation of Turbulent Combustion," Annu. Rev. Fluid Mech., **38**, pp. 453–482.
[36] Brookes, S. J., and Moss, J. B., 1999, "Predictions of Soot and Thermal Radiation Properties in Confined Turbulent Jet Diffusion Flames," Combust. Flame, **116**, pp. 486–503.
[37] Singh, J., Patterson, R. I. A., Kraft, M., and Wang, H., 2006, "Numerical Simulation and Sensitivity Analysis of Detailed Soot Particle Size Distribution in Laminar Premixed Ethylene Flames," Combust. Flame, **145**, pp. 117–127.
[38] Sivathanu, Y. R., Gore, J. P., and Dolinar, J., 1991, "Transient Scalar Properties of Strongly Radiating Jet Flames," Combust. Sci. Technol., **76**, pp. 45–66.
[39] Steinberger, C. J., Vidoni, T. J., and Givi, P., 1993, "Compositional Structure and the Effects of Exothermicity in a Nonpremixed Planar Jet Flame," Combust. Flame, **94**, pp. 217–232.
[40] Coppalle, A., and Joyeux, D., 1994, "Temperature and Soot Volume Fraction in Turbulent Diffusion Flames: Measurements of Mean and Fluctuating Values," Combust. Flame, **96**, pp. 275–285.

Investigation of Hierarchically Branched-Microchannel Coolers Fabricated by Deep Reactive Ion Etching for Electronics Cooling Applications

J. P. Calame[1]
e-mail: jeffrey.calame@nrl.navy.mil

D. Park

R. Bass

Electronics Science and Technology Division,
Naval Research Laboratory,
Washington, DC 20375

R. E. Myers
ATK Mission Research,
Newington, VA 22122

P. N. Safier
S&J Solutions LLC,
Alexandria, VA 22314

The removal of high heat fluxes from BeO ceramic and GaN-on-SiC semiconductor dies using hierarchically branched-microchannel coolers is investigated, in order to examine the impact of the number of branching levels on performance. The microchannel coolers are made by lithography and deep reactive ion etching of single crystal silicon. The test dies contain a dc-operated resistive zone that approximates the spatially averaged heat flux that would appear in low-temperature cofired ceramic microwave circuit packages and in monolithic microwave integrated circuits. For the particular geometric constraints selected for the study (three source/exhaust channels, $\sim 5 \times 5$ mm^2 die footprint, 200 μm deep channels in a 400 μm thick silicon wafer), the optimum performance is achieved with three hierarchical levels of branched-channel size. A heat flux of 1.5 kW/cm^2 is removed from the 3.6×4.7 mm^2 resistive zone of the BeO-based die, at a surface temperature of 203°C. When attached instead to a high thermal conductivity GaN-on-SiC die with a 1.2×5 mm^2 resistive zone, a heat flux of 3.9 kW/cm^2 is removed from the resistive zone at 198°C surface temperature. The total water flow rate is 275 ml/min in both situations. The experimental results are found to be in reasonable agreement with finite element simulations based on idealized estimates of convection coefficients within the channels. For the three-channel size configuration, an effective heat transfer coefficient in the range of 12.2–13.4 W/cm^2 K (with respect to a 20°C bulk fluid temperature) is inferred to be present on the top of the microchannel cooler, based on simulations and derived values obtained from the experimental data.
[DOI: 10.1115/1.3001017]

Keywords: microchannel cooler, constructal theory, fractal geometry, constructal trees, electronic cooling, single phase, forced convection, GaN, SiC

1 Introduction

In recent years, there has been considerable interest in high heat flux cooling for electronics, in particular, for emerging classes of semiconductor chips used in computers, microwave amplifiers, and power switching electronics [1,2]. Localized heat fluxes are expected to approach or exceed 1 kW/cm^2 in such applications, and research on schemes to provide effective thermal management at this level is necessary. Single-phase microchannel coolers are one candidate for such applications [3–5], although in simple straight channel geometries they often need a relatively high fluid flow rate or have a large pressure drop (or both) to achieve a high heat transfer coefficient. This can become a problem in systems applications, such as in phased array radars, where there are large numbers of active devices to be cooled. One strategy under investigation, variously known as hierarchically branched-microchannel coolers or fractal channel coolers, seeks to optimize the heat transfer from a volume or surface while minimizing the fluid flow and pressure drop [6–8]. Such schemes seek to imitate the fractal branching patterns found in nature [9], as in animal vascular and bronchial (or gill) systems, to create a large surface area in a small volume.

Probably the largest series of contributions to the ideas and literature on heat transfer in such hierarchical systems, and methods of synthesizing and optimizing hierarchical networks, is by Bejan [7,10,11]. Bejan coined the term "constructal theory" to describe the synthesis process, and using these methods a wide range of layered and volumetric branched-channel designs have been proposed and examined [10–14]. Other researchers have made significant contributions, including Chen and Cheng [8,15] who examined heat transfer in layered networks of Mandelbrot trees [9], and Pence and co-workers [16–18], who have done a number of theoretical and experimental studies of fractal geometry cooling networks, including developing new computationally based methodologies for optimizing heat transfer. Important contributions have also been made by Brunschwiler et al., who employed hierarchical treelike branchings of both fluid source and fluid return channels in microscale jet impingement cooling [19].

In this paper, a detailed experimental and simulation study of one particularly simple class of hierarchically branched-microchannel cooler is presented, with a goal of providing effective cooling of low-temperature cofired ceramic microwave chip packages and emerging GaN-on-SiC semiconductors for high power microwave amplifiers. As background on the cooling needs of such semiconductors and typical chip geometries, the reader is

[1]Corresponding author. Present address: Naval Research Laboratory, Code 6843, 4555 Overlook Ave. SW, Washington, DC 20375.

Contributed by the Heat Transfer Division of ASME for publication in the JOURNAL OF HEAT TRANSFER. Manuscript received April 16, 2008; final manuscript received September 10, 2008; published online March 20, 2009. Review conducted by Roger Schmidt.

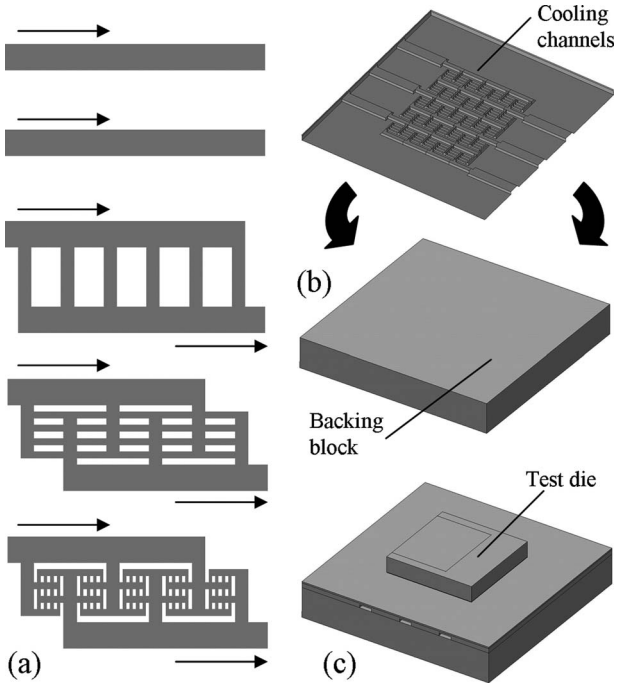

Fig. 1 (*a*) Schematic showing the conceptual evolution of a hierarchically branched cooling channel network, obtained by adding successive levels of cross channels to an initial network of parallel channels; (*b*) illustration of the assembly of a hierarchically branched-microchannel cooler by placing a slab containing the channels onto a backing block; (*c*) top view of the completed test package showing a heat source testing die that is attached to the top surface of the microchannel cooler

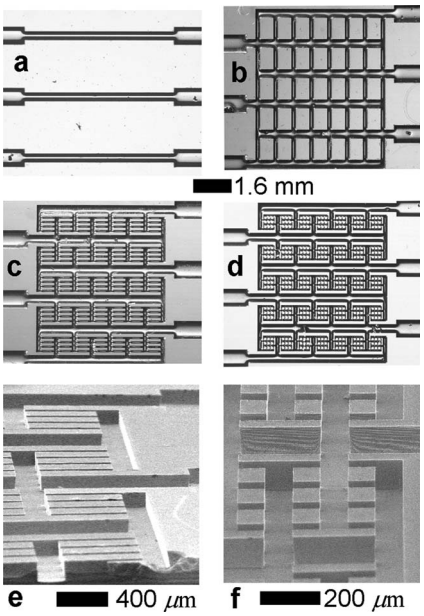

Fig. 2 Optical micrographs of the family of hierarchically branched-microchannel coolers made by DRIE showing the undersides of the central region of the etched silicon slabs. Shown are the (*a*) one-channel, (*b*) two-channel, (*c*) three-channel, and (*d*) four-channel size configurations. Scanning electron micrographs of the (*e*) three-channel and (*f*) four-channel size configurations are also provided.

referred to Refs. [20–22], including experimental studies with ordinary microchannel coolers [23]. Although a wide variety of hierarchically branched cooling channel geometries and materials are possible for this application, the present investigation is focused on the simple scheme shown schematically in Fig. 1(*a*). Essentially, at each stage in the hierarchical progression, an additional level of cross-channels is added. This style of branched geometry was described by Bejan and Errera [24], and it is the logical extension of ordinary straight microchannel coolers. However, rather than focusing on optimization of the channel sizes, the investigation in the present paper seeks to study the impact of the number of branching levels (at fixed ratios of channel size) on high heat flux thermal performance, in a materials system and layout that are compatible with lithographic fabrication and the intended application. In the investigations, a sequence of hierarchically branched-channel coolers are fabricated and attached to test ceramic and semiconductor chips (dies) that are capable of generating high heat fluxes, as shown schematically in Figs. 1(*b*) and 1(*c*). The details of these procedures are described in Sec. 2 of this paper. Next, results from experimental studies of the heat transfer are presented and compared with simplified finite element simulations in Sec. 3. In Sec. 4, the heat transfer coefficients produced by the various microchannel coolers are evaluated and interpreted. This paper concludes with a summary in Sec. 5.

2 Fabrication Details and Experimental Test Setup

Silicon, with channels fabricated by contact photolithography and deep reactive ion etching (DRIE) [25], was selected for the microchannel cooler material [26]. The use of silicon ensures ultimate compatibility with lithographic mass production, while providing a reasonable thermal conductivity (κ=150 W m^{-1} K^{-1}) and a good expansion match to ceramics and other semiconductors. To ensure that only a single masking and etching sequence is needed, all channels need to be of the same depth. Although channel depths to 400 μm are occasionally reported for DRIE structures, 200 μm was selected as a more practical value to preserve channel shapes and avoid erosion of the patterning resist. Next, the overall wafer thickness gets set by mechanical considerations on the low side and by the need to avoid excessive thermal resistance on the high side; 400 μm was selected as a compromise. The ratio between channel widths in the hierarchical branching sequence is a free parameter; a constant factor of 2 reduction in width was selected. Finally, all channels within a given level of the hierarchy were evenly spaced, and the largest channel spacing was selected to give three inlet and three exhaust channels under the footprint of interest for microwave packages ($\sim 5 \times 5$ mm^2).

The fabrication procedure of the microchannel coolers began by spin-coating a $\sim$100 mm diameter (4 in.), 400 μm thick double-sided polished 100-oriented silicon wafer with a layer of positive photoresist (S1827, Shipley Corp., Marlborough, MA). The deposition conditions were 3000 rpm for 60 s, followed by baking at 120°C for 2 min, which produced a 2.7 μm thick film. Using a Karl-Suss MJB3 deep ultraviolet aligner and a mask, various microchannel coolers with the different channel branching configurations were exposed and developed onto the substrate. At the conclusion of this lithography sequence, the silicon associated with each of the desired channel patterns is bare, while the other parts of the silicon remain coated with protective photoresist. The 200 μm deep channel network was etched into the patterned substrate using the Bosch process in a Plasmalab System-100 fluorine-based inductively coupled plasma/reactive ion etcher (Oxford Instruments, Oxfordshire, UK). Following etching, the remaining photoresist was removed by chemical dissolution, and the wafer was cut with a diamond dicing saw into individual microchannel cooler pieces. Each piece had transverse dimensions of 12.70×12.70 mm^2.

Optical micrographs of the family of hierarchically branched-microchannel coolers made by DRIE are shown in Figs. 2(*a*)–2(*d*). The micrographs show the undersides of the central region of the etched silicon slabs. The configuration in Fig. 2(*a*)

will be referred to as the one-channel size configuration; the principal channels in the center are 400 μm wide. Note that the wider entrance and exit channels on either side, which are 800 μm wide to allow lower pressure drop in serving the central region, are not included in the nomenclature for channel size count. Figure 2(*b*) shows the two-channel size configuration, with 400 μm wide principal channels and 200 μm wide cross channels. The three-channel size configuration in Fig. 2(*c*) starts with a layout similar to the two-channel design, but it includes an additional level of 100 μm wide cross channels. The four-channel size configuration further augments the branching with yet another level of channels, in this case 50 μm wide. Scanning electron micrographs of some of the details of the three-channel and four-channel configurations are shown in Figs. 2(*e*) and 2(*f*), respectively. Profilometry measurements confirmed that the channels in all configurations were between 195 μm and 200 μm deep.

The top (unetched) surfaces of the silicon microchannel coolers were metallized by electron beam evaporation of 25 nm of Ti, followed by 25 nm of Pt, and finally 400 nm of Au. This was done in order to allow the die attach of resistive heat sources for testing. Commercial 100 Ω chip resistors consisting of a BeO die ($5.76 \times 5.76 \times 1.03$ mm^3) having a 3.6 mm long by 4.7 mm wide resistive coating on the top surface, along with gold contact stripes on either end of the resistive zone, were obtained. The dies also had a robust bottom surface Ti/Au metallization. Each configuration of microchannel cooler had one of these BeO-based resistors attached to it using 96%Sn–3.5%Ag–0.5%Cu solder. The attachment was done in a glovebox under N_2 gas at 245°C using Kester 951 flux, followed by washing in methyl alcohol. The die attach thickness was measured to be 25 ± 5 μm. A photograph showing a die that has been attached to the metallized top of a microchannel cooler is shown in Fig. 3(*a*). The dies are centered with respect to the top surface of the microchannel cooler, but on the BeO dies themselves the resistive zone is not centered, but rather it is shifted completely over toward one edge.

For testing, the microchannel coolers were placed on top of a $12.70 \times 12.70 \times 2.00$ mm^3 polished silicon block; the top surface of the block will ultimately act as the bottom surface for the microchannels. This was depicted in Fig. 1(*b*). The combination of the 400 μm thick silicon microchannel cooler and its 2 mm thick backing silicon block are mounted into a gasketed acrylic holder and manifold assembly (test cell), described in detail in a previous paper [23]. The holder uses a brass top plate having a large hole that allows clearance for (and access to) the heat source die on the microchannel cooler top surface. The internal structure of the test cell is polished and designed to fit snugly around the microchannel cooler/backing block to a tolerance of 10 μm or better in the transverse dimensions. Furthermore, the gaskets and o-rings apply vertical pressure (~1 MPa) to eliminate leaks above and below the combination of the microchannel cooler and the backing block (as well as between the two in the nonchannel regions). However, there will still be interfacial thermal contact resistance at this location, which will be discussed later in the paper. Once assembled, the test cell is connected to a water-based chiller/gear pump/deionizer system with a constant 20°C outlet temperature. The flow through the microchannel cooler loop is measured with an experimentally calibrated turbine-based electronic flowmeter. Pressures are measured at the fluid inlet and outlet ports of the test cell, along with the inlet-to-outlet temperature differential. Detailed information on the properties, calibration, and accuracy of the pumping/diagnostic system are provided elsewhere [23].

Electrical leads were mounted to the contact stripes of the resistive dies using silver paint. A 0.50 mm diameter, ungrounded sheath, type J thermocouple was placed on the center of the resistive zone of the die using a drop of silver paint (smaller than the sheath diameter). As the resistive zone has only a very thin top passivation layer, and quite high voltages (to ~160 V) are used to energize the die, the entire thermocouple and battery-powered

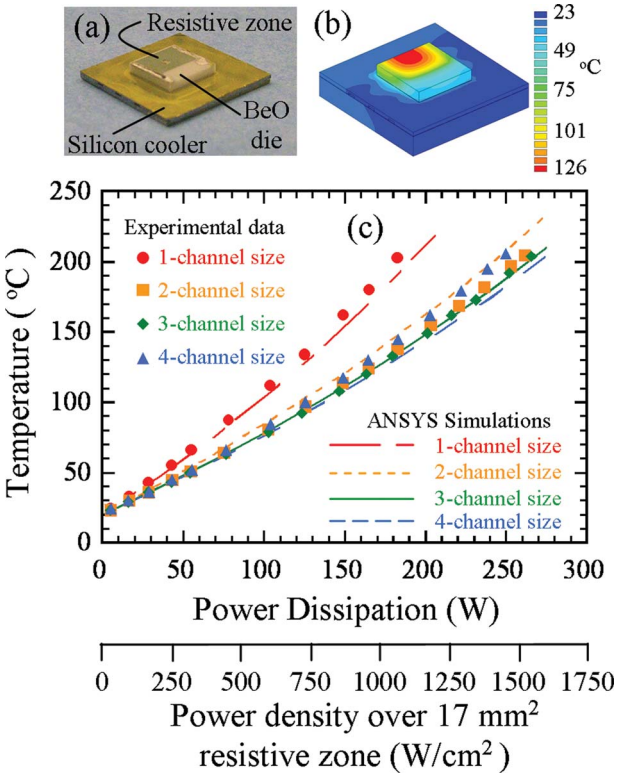

Fig. 3 (*a*) Photograph of a hierarchically branched-channel cooler with an attached BeO-based heat source die; (*b*) ANSYS simulation of temperatures in the three-channel size configuration at 1 kW/cm^2 dissipation in the resistive zone; (*c*) experimental resistive zone temperature versus power dissipation data (symbols) and ANSYS simulations (lines) for the various channel configurations

thermocouple meter assembly are floating relative to ground and are enclosed in an insulating plastic box. To make thermal measurements, a desired energizing voltage was applied to the resistive zone, and the surface temperature was monitored until steady state was reached. The temperature measurement accuracy was ±0.5°C. The combination of the energizing voltage (measured at the die using four-terminal techniques) and current was used to compute the power being dissipated in the resistive zone. Between measurements, the power was removed, and the surface temperature was allowed to cool back to the bulk fluid temperature. The process was repeated using higher and higher energizing voltages, to create a complete data set.

3 Experimental Results and Simulation

Experimental results for resistive zone surface temperature versus dissipated power are shown for the various microchannel cooler/resistive die packages in Fig. 3(*c*) by the symbols. The data points were obtained at 275 ml/min total flow rate in each configuration. The measured dissipated power, combined with the known 17 mm^2 area of the resistive zone, is used to obtain the localized heat flux, which is provided as a second horizontal axis in the plot. Operating conditions were restricted to keep surface temperatures below ~200°C to avoid damaging the resistive material.

The one-channel size configuration results in a surface temperature of 190°C at 1 kW/cm^2 resistive zone dissipation (170 W power). By going to the two-channel size configuration, the surface temperature at 1 kW/cm^2 is reduced considerably to 129°C. A small additional reduction in surface temperature, to 124°C, is obtained using the three-channel size configuration. However, in the package with the four-channel size configuration, the tempera-

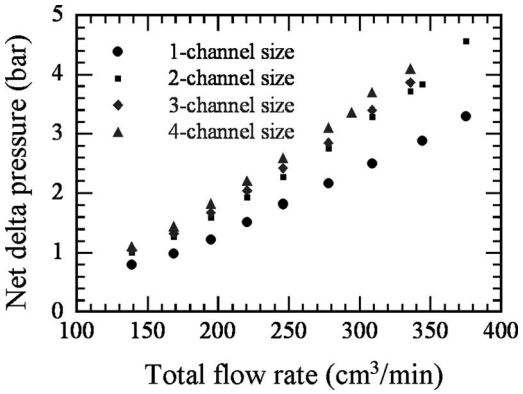

Fig. 4 Experimentally measured differential pressure versus flow data for the various channel configurations

ture at 1 kW/cm^2 increases considerably to 136°C. This is worse than even the two-channel size result. Clearly, from an experimental standpoint, there is a limit to the benefit of subdividing the channels.

The fact that the four-channel size configuration is in excess of the optimum is also made clear from pressure drop ΔP versus flow data, which is shown in Fig. 4 for each configuration. These curves show the net pressure drop across the microchannel cooler, obtained by the differential pressure measurements across the test cell and subtracting out the minor flow-dependent contributions from the fittings and manifolds of the acrylic holder. All curves exhibit the expected quadratic dependence between ΔP and flow rate. Looking first at the one-channel size configuration, one sees that the pressure drop at 275 ml/min is 2.01 bar. The two-channel size configuration has $\Delta P=2.60$ bar, and going to three-channel sizes very slightly increases ΔP to 2.69 bar. A more significant increase, to $\Delta P=2.96$ bar, occurs in the four-channel size configuration. Therefore, going from three-channel size configuration to the four-channel size configuration is clearly counterproductive, since one will suffer from an increase in pressure while simultaneously obtaining a higher, rather than a lower, temperature.

Finite element thermal modeling was undertaken with the ANSYS code (ANSYS Inc., Canonsburg, PA) for each of the configurations. The goal was to not only provide a comparison between simulations and experiments but also to enable estimation of the effective heat transfer coefficient that each configuration can apply to the bottom of the heat source die. Since the top surface of the silicon microchannel cooler (beneath the die attach) is inaccessible to experimental measurements, one must partially rely on modeling to understand the heat flux, temperature, and effective heat transfer coefficient behavior at this location. These quantities are particularly important for evaluating the prospective use of the hierarchical channel concept for cooling other types of electronic chips and packages in various practical applications.

The package with the one-channel size microchannel cooler was modeled in ANSYS using a number of element types and sizes to handle the various geometric size scales. The BeO die was meshed primarily with ten node tetrahedron elements (tets) with edge lengths of ~470 μm near the resistive zone increasing to ~580 μm edge length pyramidal elements near the bottom of the die. The thin die attach was meshed with $\sim 580\times 580\times 25$ μm^3 20-node brick elements. The 400 μm thick silicon slab containing the DRIE-etched channels had a complex tetrahedral and pyramidal mesh with ~580 μm edge length near the bottom of the die and in adjacent regions on the top surface, decreasing to 200 μm at the cooling channel walls. The rear backing silicon block was meshed with tets with 200 μm edge length near the channels, and the meshing was gradually coarsened (expansion factor 1.2) to edge lengths near 1.3 mm at the bottom of the backing block and in other regions remote from the channels. The total number of elements in the entire model of the one-channel configuration-based package was ~27,000.

Temperature-dependent thermal conductivities were assigned to the BeO and silicon materials using lookup tables based on data in the literature [27]. In these data, the room temperature (20°C) thermal conductivity of BeO was 280 $W\,m^{-1}\,K^{-1}$, falling off approximately as $T^{-1.24}$, with T the temperature in K. Similarly, the silicon room temperature thermal conductivity was 150 $W\,m^{-1}\,K^{-1}$, falling off approximately as $T^{-1.26}$. A thermal conductivity of 57 $W\,m^{-1}\,K^{-1}$ was assigned for the die attach [28]. One key issue in the experimental setup is the nonbonded mechanically pressed contact between the silicon slab containing the channels and the silicon backing block. There will be interface thermal resistance at this location due to imperfections at this contact. For the purposes of modeling, the value of interface thermal resistance R was estimated based on the work of Prasher [29], as

$$R=\frac{1.53\sigma}{\kappa_{\text{int}}}\left(\frac{H}{P_c}\right)^{0.097} \tag{1}$$

where σ is the surface roughness, P_c is the contact pressure, H is the elastic modulus of the silicon (150 GPa), and κ_{int} is the thermal conductivity of the interface material. In this case, stagnant water is assumed to fill the interface, with $\kappa_{\text{int}}=0.6$ $W\,m^{-1}\,K^{-1}$ at 20°C. The computed value of R with 1 MPa contact pressure and with 1 μm surface roughness is 8.1×10^{-6} $m^2\,K\,W^{-1}$, corresponding to an interface thermal conductivity $h_{\text{int}}=1/R$ of 12.3 $W\,cm^{-2}\,K^{-1}$. This value was used in ANSYS at the silicon-to-silicon interface, independent of temperature.

With the exception of the cooling channel walls and the resistive zone of the die, all external surfaces of the model were treated as thermally insulating. The channel walls were assigned a convection coefficient as a boundary condition in ANSYS. Specifically, for the one-channel size configuration at 275 ml/min total flow, the linear flow velocity in each of the three principal $d=400$ μm wide by $t=200$ μm tall channels is ~19 m/s, corresponding to a Reynolds number Re of 5100, which is turbulent. This assumes that each channel has a hydraulic diameter D equal to four times the channel area divided by the channel perimeter, which works out to $D=2td/(t+d)=270$ μm for the channel dimensions. Using a friction factor f approximated by

$$f=(1.58\ \ln \text{Re}-3.28)^{-2} \tag{2}$$

and the Petukov–Kirrillov correlation [30] for Nusselt number Nu

$$\text{Nu}=\frac{(f/2)\text{RePr}}{1.07+12.7\sqrt{f/2}(\text{Pr}^{2/3}-1)} \tag{3}$$

one obtains a channel wall convection coefficient $h_{\text{wall}}=\text{Nu}\,\kappa_f/D$ of 11.3 $W\,cm^{-2}\,K^{-1}$, where κ_f is the thermal conductivity of the water. A similar calculation for the $d=800$ μm wide inlet/outlet channels gives $h_{\text{wall}}=6.23$ $W\,cm^{-2}\,K^{-1}$. A fluid bulk temperature T_B of 20°C was assumed in both cases, and the bulk fluid temperature changes that occur while traversing the channels were neglected.

The simulation results for the one-channel configuration are shown by the alternating long/short dashed line in Fig. 3(*c*). The results are in very good agreement with the experimental data, with the simulation giving a temperature rise (relative to T_B) only about 5% too low. Also of note in both the simulation and the data is the concave upward curvature; this is due to the thermal conductivity of the BeO and to a lesser extent the silicon, decreasing with increasing temperature.

Simulations were also performed using ANSYS for the packages employing the two-, three-, and four-channel configurations. The finite element models employed progressively finer meshing to accommodate the smaller and more detailed channel geometries. The total number of elements in the model of the two-channel-based package was ~30,600, while in the three- and four-channel

based packages the element counts were, respectively, ~40,800 and ~62,300. A number of severe simplifying approximations were made in estimating the flow velocities and convection coefficients in these more complex geometries. First, only an average flow velocity was estimated for each channel size, and this was used to compute a uniform convection coefficient for all channel walls of that size. Hence spatial variations in flow or convection coefficient along a given channel are not included. Second, only simple correlations for computing convection coefficients were employed throughout a channel, hence developing boundary-layer flow effects associated with entry into a channel after a branch, turning corners, and other distortions in flow were not included in the computation of convection coefficients. Third, turbulent conditions were generally assumed in the various channels during the initial group of simulations (Eqs. (2) and (3)), regardless of the value of Re. The rationale is that the violent turbulent flow existing in the largest channels may not have time or space to damp out within the short smaller channels, particularly with the extra disruptions caused by the 90 deg bends. Recent experimental work by Peixinho and Mullin [31] on quantifying the spatial/temporal quenching of turbulence by reducing Re in pipe flow provides some support for this conjecture. Those authors document the indefinite persistence of pre-existing turbulent perturbations at Re as low as 1750, which is significantly below the Re ~ 2500 typically associated with turbulent flow. Of greater relevance, they find that even in lower Re regimes where quenching toward laminar flow is clearly occurring, the probabilistic decay has a spatial half-life of ~3300/(1750-Re) hydraulic diameters. If such a scaling was to remain valid down to Re ~ 1000, then the half-life would be ~4.4D, which would imply the existence of residual turbulent motion in at least the first level of cross channels. A notable exception to the turbulent assumption was made for the smallest channels in the modeling of the four-channel size configuration, in which the fully developed (FD) laminar Nu is greater than the turbulent value predicted by Eq. (3). In that case the larger FD laminar Nu was used instead, on the assumption that the turbulent correlation is completely invalid at such Re values. (Alternative assumptions will be investigated later in the paper for comparison, including using FD laminar flow or simultaneously developing (SD) laminar flow in all the levels of cross channels.) The fourth approximation was that bulk fluid temperature rises were ignored, i.e., T_B was held fixed at 20°C in all the channels. With these various combined simplifying assumptions, channel wall convection coefficients of 11.3 W cm^{-2} K^{-1}, 5.1 W cm^{-2} K^{-1}, 3.4 W cm^{-2} K^{-1}, and 3.0 W cm^{-2} K^{-1} were computed and used during the initial group of simulations for the 400 μm, 200 μm, 100 μm, and 50 μm wide channels, respectively. A convection coefficient of 6.23 W cm^{-2} K^{-1} continued to be used in the 800 μm wide feed/exhaust channels. As an example of a typical simulation result, a contour plot of the temperatures in the three-channel package at 1 kW/cm^2 resistive zone dissipation is pictured in Fig. 3(*b*).

The simulations for the more complex geometries are shown by the additional three lowermost curves in Fig. 3(*c*). Like the one-channel configuration, the data all have the curvature due to temperature-dependent thermal conductivities. The simulation for the two-channel configuration (short dashed line) gives temperatures somewhat above the experimental data (squares). The error in the predicted temperature rise is about 8%. For the three-channel configuration, the simulation (solid line) and the experimental data (diamonds) are essentially identical. However, in the case of the four-channel configuration (medium dashed line), significant departures occur, with the simulated temperature rise being 12% below the data (triangles). Furthermore, the simulations fail to predict the observed decline in performance relative to the three-channel configuration.

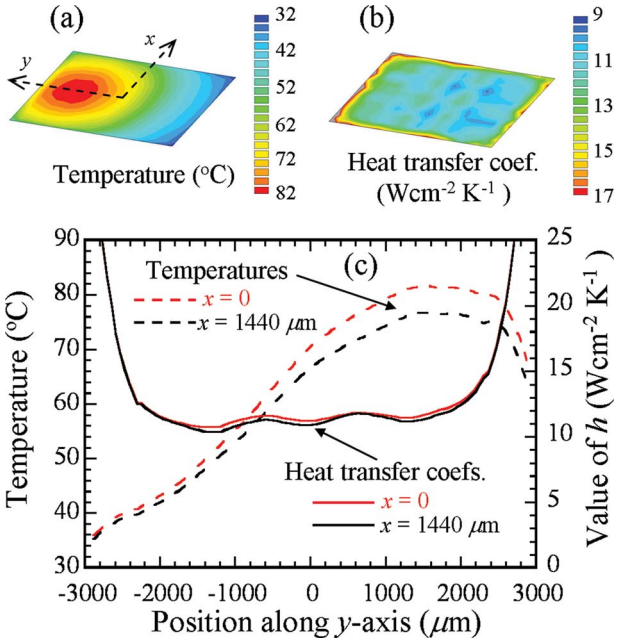

Fig. 5 (*a*) **Map of the simulated temperatures present on the top silicon surface of the three-channel size hierarchically-branched cooler configuration (beneath the die footprint), when 1 kW/cm^2 is being dissipated in the resistive zone of the overlying die; (*b*) corresponding map of simulated local heat transfer coefficients, and (*c*) plot of temperature and local heat transfer coefficient along the *y*-direction at two different *x* locations within these maps**

4 Discussion

In order to better understand the performance of the various microchannel coolers and, in particular, to enable such coolers to be considered for practical applications, it is useful to evaluate the heat transfer coefficient that they create on their top surface for a given value of T_B. For example, if they are considered for cooling commercial semiconductor chips, one would like to be able to use such a heat transfer coefficient as a rear boundary condition for the chip-level simulation, to avoid modeling the complex geometry of the cooler structure in every subsequent simulation. Also, computing the heat transfer behavior at the top of the microchannel cooler surface (or extracting it as a derived parameter based on the experimental data) is important for correctly gauging the impact of the number of channel sizes on thermal performance, since the high thermal resistance of the thick BeO die tends to make the resistive zone surface temperature relatively insensitive to the applied heat transfer coefficient. This also tends to obscure the potential benefit in applications with thinner more highly thermally conductive semiconductor dies, such as SiC.

For a purely simulation-based approach, one can compute the heat transfer coefficients from the ANSYS simulations by examining the temperatures and heat fluxes present at the top silicon surface of the microchannel cooler (directly below the die attach under the footprint of the die). This is done by taking a "slice" through the solved ANSYS model using cutting surface-defining and mapping postprocessing functions. Such a map of the top-of-silicon temperature distribution is shown in Fig. 5(*a*) for the three-channel size configuration as an example, when 1 kW/cm^2 is being dissipated in the resistive zone of the overlying die. The map only covers the area beneath the die footprint. A plot of the temperature T_s versus position along the *y*-axis is shown in Fig. 5(*c*) by the upper dashed line. The temperature distribution is lopsided because the resistive zone on the top of the overlying die is not centered (as seen in Fig. 3(*a*)). The lower dashed line shows the temperature profile along the *y*-direction at an *x*-position of

1440 μm, which is about halfway to the edge of the map (and exhibits somewhat lower temperatures). A similar two-dimensional map and linear sampled curves were created from ANSYS for the vertical heat flux (F_z, not shown). From this, a map and curves of local heat transfer coefficient $h(x,y)$ that is being generated by the microchannel cooler (with respect to the bulk coolant temperature T_B=20°C) can be computed via

$$h(x,y) = \frac{-F_z(x,y)}{T_s(x,y) - T_B} \tag{4}$$

A map of this local heat transfer coefficient is depicted in Fig. 5(*b*), and the dependence along the *y*-axis is shown in Fig. 5(*c*) at x=0, and x=1440 μm by the upper and lower solid curves, respectively. Apart from the sharply rising tails right near the locations corresponding to the die edges at ±2880 μm (a common numerical artifact in finite element modeling associated with edges), the local values of h are quite uniform across the map for this three-channel size configuration. Similar simulations and analyses (not shown) were performed for the one-, two-, and four-channel size configurations, and high uniformity in h was likewise found for the two- and four-channel size situations. The one-channel size configuration had significant nonuniformity in h(~50%) due to the sparse coverage by the channels.

Spatially averaged values of heat transfer coefficients were evaluated in a number of ways for each of the configurations. The simplest method merely took the average of h along the *y*-axis (with x=0), restricting the averaging to $h<20$ W cm^{-2} K^{-1} to avoid the edge effects. The results are shown by the squares in Fig. 6(*a*). With this method, the computed values of h approximately double (from 5 W cm^{-2} K^{-1} to 10 W cm^{-2} K^{-1}) in going from the one- to two-channel configuration, followed by a more modest increase to 12 W cm^{-2} K^{-1} in the three-channel case, and finally suffering a very small decline in the four-channel configuration. For an alternative method, the quantity T_s-T_B was averaged along the *y*-axis and was used in conjunction with the known average heat flux passing through the entire mapped area. This average flux is 518 W/cm^2, based on the 1 kW/cm^2 being dissipated over the resistive zone and multiplication by the ratio of the area of the resistive zone to the entire die footprint area. The results of this calculation of h are shown by the diamonds in Fig. 6(*a*). A further extension of this concept was to average the value of T_s-T_B over the entire surface and to employ this with the 518 W/cm^2 surface-averaged heat flux, giving the results shown by the open circles. The final method of computation was to take the complete surface average (over the entire map) of the local $h(x,y)$ given by Eq. (4). This result is depicted by the triangles in the figure.

A direct experimental measurement of h at this location is not possible, of course, since the surface in inaccessible. However, it is possible to create an experiment-derived value of average h with a simple auxiliary ANSYS simulation in conjunction with the measured temperature data. Specifically, a finite element model of only the BeO die and the underlying die attach was constructed, with 1 kW/cm^2 dissipation placed on the resistive zone. A heat transfer coefficient h_{avg}, in conjunction with rejection to a bulk temperature of 20°C, was used as a boundary condition on the bottom of the die attach layer. A sequence of iterative simulations was performed, in which h_{avg} was adjusted until the simulated resistive zone temperature matched the experimental value. These results for h_{avg} are plotted by the solid circles in Fig. 6(*a*).

Overall, the simulated values of heat transfer coefficient computed with the various averaging methods are in reasonable agreement with the experiment-derived values in most aspects, especially when the extreme nature of the modeling simplifications is considered. Overall agreement is excellent for the one-channel size configuration and reasonable for the three-channel configuration. However, although the simulations do seem to show a slowing or a leveling off of the incremental improvement beyond the three-channel configuration, the experiment has a sharp decline in performance that is not properly captured by the simulations. In addition, to a large extent the experiments show the leveling off occurring earlier, between the two- and three-channel configurations, while the simulations show an initially slower but steadier rise through this region. In spite of these shortcomings, the simulations agree with experiment in showing that about a factor of 2 increase in heat transfer coefficient can be achieved in this type of package by using the branching channel methodology.

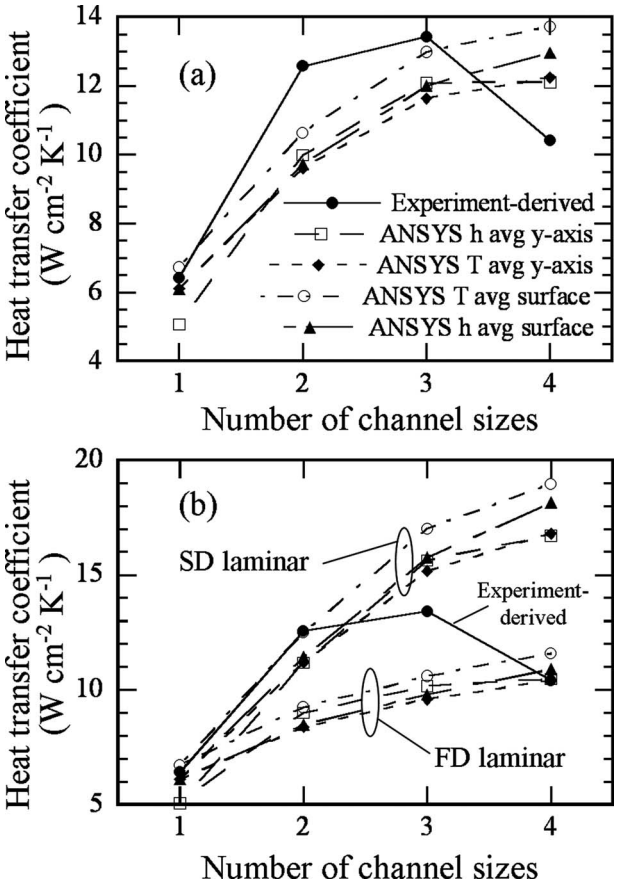

Fig. 6 (*a*) Plot of the average heat transfer coefficient (on the top of the silicon microchannel cooler surface, under the die footprint) as a function of the number of channel sizes in the configuration. Experiment-derived values are shown by the solid circle symbols/solid lines, along with ANSYS simulations using various averaging strategies and assuming turbulent conditions (in all channels except the smallest in the 4-channel configuration); (*b*) similar comparison between experiment-derived values and ANSYS simulations that are performed assuming FD and SD laminar conditions in all levels of cross channels (primary channels remain turbulent).

Since the assumption of the persistence of turbulent conditions into the cross channels is speculative, additional sets of ANSYS simulations were performed with alternative laminar assumptions for comparison. For a second group of simulations, turbulent conditions in the primary 400 μm wide channels were still assumed (h_{wall}=11.3 W cm^{-2} K^{-1}), but all smaller channels were assumed to be described by FD laminar conditions. Channel wall convection coefficients of 1.1 W cm^{-2} K^{-1}, 1.8 W cm^{-2} K^{-1}, and 3.0 W cm^{-2} K^{-1} were computed for the 200 μm, 100 μm, and 50 μm wide channels, respectively [32]. A turbulent convection coefficient of 6.23 W cm^{-2} K^{-1} continued to be used in the 800 μm wide feed/exhaust channels. After performing the new ANSYS thermal simulations, postprocessing procedures analogous to those involved in creating Figs. 5 and 6(*a*) were performed. The

results are shown in Fig. 6(*b*) by the group of curves labeled as FD laminar. The various schemes for obtaining an average heat transfer coefficient over the top surface of the silicon (beneath the die footprint) noted in the legend of Fig. 6(*a*) were used again in Fig. 6(*b*). The experiment-derived values of h_{avg} are replicated in Fig. 6(*b*) for convenience, albeit on a different ordinate scale. The FD laminar simulations of overall heat transfer coefficient are significantly below the experiment-derived values for the two- and three-channel size configurations, while agreement is excellent for the four-channel size configuration.

Because the cross channels have relatively small ratios of length to hydraulic diameter, a third set of simulations using SD laminar flow assumptions [33] in the 50–200 μm wide channels were also performed. The correlations of Churchill and Ozoe [34] were used to obtain a multiplicative enhancement factor for h_{wall} with respect to the values for FD laminar flow. Although this correlation was developed for circular tubes, the use of the multiplicative enhancement formalism with a rectangular channel Nusselt number [32] (instead of Nu for circular tubes) is believed to provide a suitable correction that agrees well with other investigations in the literature [35]. Since such developing flow values of h_{wall} are position dependent, an average was taken over the channel length. The enhancement factors were computed to be ~7.7×, 4.8×, and 4.8× the FD laminar values, for 200 μm, 100 μm, and 50 μm wide channels, respectively, yielding h_{wall} values of 8.3 W cm^{-2} K^{-1}, 8.9 W cm^{-2} K^{-1}, and 14.3 W cm^{-2} K^{-1}. The simulated results are shown in Fig. 6(*b*) with the group of curves labeled as SD laminar. In comparison to the experiment-derived values, the agreement is excellent for the two-channel size configuration, but the simulations are significantly higher than experiment for the three- and four-channel size configurations. Together, the various FD and SD laminar simulations in Fig. 6(*b*) can be seen to bracket the experiment-derived values of h_{avg}. However, neither comes close to reproducing the overall trend as well as the simulations in Fig. 6(*a*). Most likely there is a complicated distribution of turbulent, laminar, and various transitional flows present in the channel network, and future research using numerical fluid dynamics modeling will be required to provide a better understanding and more accurate calculations. In addition, the increase in flow area from one branch level to the next can create flow distribution problems and increased pressure drop, which would be particularly important in the four-channel size configuration and may explain the experimental falloff in performance relative to the three-channel size configuration.

To further explore the overall heat transfer coefficient calculations in Fig. 6(*a*), and to provide a demonstration of the suitability of a DRIE-fabricated hierarchical channel cooler in an application of current interest, an additional experiment with a GaN-on-SiC die was done in the three-channel size configuration. The three-channel size geometry was selected for this final study since it was the best performing of the various geometries. A high thermal conductivity 4*H*-SiC die, 5 mm×5 mm×380 μm thick, was epitaxially coated with thin GaN and AlGaN layers to form a 1.2 mm long by 5 mm wide resistive zone as described in a previous publication [23]. This die, when operated as a dc resistor, can simulate the localized heat fluxes that would occur with integrated microwave amplifiers of similar physical size and in the identical material system. The GaN-on-SiC die was attached to a metallized three-channel size microchannel cooler using ~6 μm of 96%Sn–3.5%Ag–0.5%Cu solder, followed by mounting and testing in a manner analogous to the testing of the BeO-based dies.

The experimental results of peak GaN temperature versus the electrical power dissipated in the resistive zone are shown by the solid circles in Fig. 7. The total water flow rate was 275 ml/min. Very high localized heat fluxes were achieved with this configuration due to the high thermal conductivity SiC die acting as its own heat spreader and due to the relatively small physical size of the active resistive zone. The highest dissipated power studied was 234 W over the resistive zone (3.9 kW/cm^2), which resulted in a GaN temperature of 198 °C. A full ANSYS simulation including the entire hierarchical channel cooler, die, die attach, and rear backing block was performed analogously to those described earlier for the BeO-based dies. Turbulent correlations were used in all channels. The thermal conductivity curve assumed for the SiC in the simulations had a value of 475 Wm^{-1} K^{-1} at 300 K [36], with a $T^{-1.3}$ functional roll-off (T in K) [36,37]. The results of the simulations are shown by the solid line in Fig. 7, and they are in excellent agreement with the data.

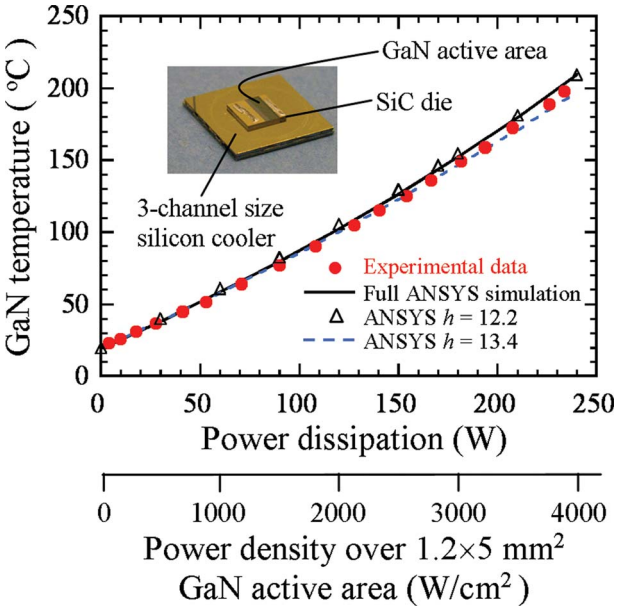

Fig. 7 Experimentally measured GaN temperature versus power dissipation data (solid circles) for a GaN-on-SiC heat source die that is attached to the three-channel size hierarchically branched-channel cooler along with ANSYS simulations. A photograph of the package is shown in the inset.

To investigate the validity of the heat transfer coefficients determined previously from the BeO die experiments, two additional simple ANSYS simulations that included only the GaN-on-SiC die and the die attach were performed. In the first case, the average of the heat transfer coefficients determined via simulation for the three-channel size configuration in Fig. 6(*a*) (12.2 W cm^{-2} K^{-1}, bulk rejection temperature 20 °C) was applied as a boundary condition to the bottom of the die attach. The results are nearly indistinguishable from the full ANSYS simulation, and a few points are shown by the triangles in Fig. 7 to illustrate this. In the second case, the "experimental" value of h from Fig. 6 for the three-channel size configuration (13.4 W cm^{-2} K^{-1}) was used instead, and the results are shown by the dashed line in Fig. 7. The latter simplified simulation is just slightly below the experimental values. Taken together, the extra experiment and simulations verify that an average heat transfer coefficient of between 12.2 W cm^{-1} K^{-1} and 13.4 W cm^{-2} K^{-1} is present on the top surface of the three-channel size hierarchical channel cooler, and that the performance with the GaN-on-SiC die is consistent with the BeO die-based experiments.

Finally, since earlier experiments [23] with conventional microchannel coolers used the same types of GaN-on-SiC heat source dies, it is possible to compare their behavior to the three-channel size hierarchical channel cooler under high heat flux conditions. Specifically, the die that was mounted to the three-channel size hierarchical channel cooler could handle 2.0 times the power dissipation for a given GaN temperature, compared with a die mounted to a conventional silicon microchannel cooler having

seven 500 μm wide by 1.4 mm tall channels (when both setups were operated at 275 ml/min total flow). Achieving comparable power dissipation performance in the conventional case requires increasing the flow rate to near 1.9 l/min (0.5 gallon/min), which is about seven times the flow rate needed for the hierarchical channel cooler. The reduction of flow exhibited by the hierarchical channel coolers is particularly important for systems applications such as phased array radars with many devices needing cooling. However, the improved performance is due to a combination of factors besides merely using the hierarchical channel geometry, including the ability to place channels much closer to the die underside and to use fewer, smaller main feed/exhaust channels (all by virtue of microfabrication). Further refinement of the relative importance of the various factors contributing to the reduced flow requirement and improved power dissipation will need additional comparative simulations and experiments in a wider range of geometries.

5 Summary and Conclusions

Experiments on removing high heat fluxes from BeO ceramic and GaN-on-SiC semiconductor dies using hierarchically branched-microchannel coolers have been performed, in order to examine the impact of the number of branching levels on performance. The microchannel coolers were made from single crystal silicon by contact photolithography and DRIE. The BeO-based dies contained a topside patterned resistive metal coating and the SiC dies contained an AlGaN/GaN heterostructure; in each case, these coatings were operated as a direct current resistor, providing a localized heat source. The dimensions of the dies and the localized heat sources in the BeO and GaN-on-SiC dies were sized to represent the spatially averaged heat flux that would appear in low-temperature cofired ceramic microwave circuit packages and monolithic microwave integrated circuits, respectively.

For the particular geometric constraints selected for the study (three source/exhaust channels, $\sim 5 \times 5$ mm^2 die footprint, 200 μm deep channels in a 400 μm thick silicon wafer), the optimum performance was achieved with three levels of branched-channel size (i.e., main channels, followed by cross channels, further followed by another set of cross channels). With this type of microchannel cooler configuration, a heat flux of 1.5 kW/cm^2 was removed from the 3.6×4.7 mm^2 resistive zone of the BeO-based die, at a surface temperature of 203°C. When attached instead to a high thermal conductivity GaN-on-SiC die with a 1.2×5 mm^2 resistive zone, a heat flux of 3.9 kW/cm^2 was removed at 198°C surface temperature. In these situations, the average heat fluxes appearing on the rear of the die (at the top of the microchannel cooler) were 780 W/cm^2 and 960 W/cm^2, respectively, and the total water flow rate was 275 ml/min.

The experimental results were found to be in reasonable agreement with finite element simulations based on highly idealized estimates of convection coefficient within the channels. For the three-channel size configuration, an effective heat transfer coefficient in the range of 12.2–13.4 W cm^{-2} K^{-1} (with respect to a 20°C bulk fluid temperature) was inferred to be present on the top of the microchannel cooler, based on simulations and derived values obtained from the experimental data. This value is about twice as good as that obtained for the one-channel size configuration. Furthermore, the 12.2–13.4 W cm^{-2} K^{-1} heat transfer coefficient in the three-channel size configuration was found to be consistent with the experiments using both types of dies over a wide power range, giving further support to its accuracy. However, the experimentally observed decline in performance in going from a three-channel size to a four-channel size configuration was not exhibited by the simulations, which tended to predict only leveling off in performance. A much more sophisticated fluid-mechanical model of the flow within the branched channels, and thus the inclusion of a position-dependent local convection coefficient and bulk temperature rise within the various channels, would be expected to improve the accuracy of the simulations. Calculations of this type, using the FLUENT code, have been recently described in the literature for solving the conjugate problem of dendritic convective channels in a disk receiving a heat flux on its top surface [38]. Such an undertaking for the configurations studied in the present paper would be a good topic for future research, along with optimization of the heat transfer performance using the sophisticated model.

Acknowledgment

This work was supported by the Office of Naval Research.

Nomenclature

d = channel width
D = channel hydraulic diameter
f = friction factor
F_z = vertical heat flux
h = heat transfer coefficient
h_{avg} = experiment-derived average heat transfer coefficient
h_{int} = interface thermal conductivity
h_{wall} = convection coefficient on channel wall
H = elastic modulus
Nu = Nusselt number
P_c = contact pressure
Pr = Prandtl number
R = interface thermal resistance
Re = Reynolds number based on channel hydraulic diameter
t = channel height
T = temperature
T_B = bulk fluid temperature
T_s = local temperature within an analysis surface

Greek Symbols

ΔP = differential pressure drop
κ = thermal conductivity
κ_{int} = thermal conductivity of an interface material
κ_f = thermal conductivity of the cooling fluid
σ = surface roughness

References

[1] Garimella, S. V., 2006, "Advances in Mesoscale Thermal Management Technologies for Microelectronics," Microelectron. J., **37**(11), pp. 1165–1185.
[2] Kandlikar, S. G., and Bapat, A. V., 2007, "Evaluation of Jet Impingement, Spray, and Microchannel Chip Cooling Options for High Heat Flux Removal," Heat Transfer Eng., **28**(11), pp. 911–923.
[3] Tuckerman, D. B., and Pease, R. F. W., 1981, "High Performance Heat Sinking for VLSI," IEEE Electron Device Lett., **2**, pp. 126–129.
[4] Sobhan, C. B., and Garimella, S. V., 2001, "A Comparative Analysis of Studies on Heat Transfer and Fluid Flow in Microchannels," Microscale Thermophys. Eng., **5**, pp. 293–311.
[5] Qu, W., and Mudawar, I., 2002, "Experimental and Numerical Study of Pressure Drop and Heat Transfer in a Single-Phase Micro-Channel Heat Sink," Int. J. Heat Mass Transfer, **45**, pp. 2549–2565.
[6] Bejan, A., and Errera, M. R., 1997, "Deterministic Tree Networks for Fluid Flow: Geometry for Minimal Flow Resistance Between a Volume and One Point," Fractals, **5**, pp. 685–695.
[7] Bejan, A., 2001, "The Tree of Convective Heat Streams: Its Thermal Insulation Function and the Predicted 3/4-Power Relation Between Body Heat Loss and Body Size," Int. J. Heat Mass Transfer, **44**, pp. 699–704.
[8] Chen, Y., and Cheng, P., 2002, "Heat Transfer and Pressure Drop in Fractal Tree-Like Microchannel Nets," Int. J. Heat Mass Transfer, **45**, pp. 2643–2648.
[9] Mandelbrot, B. B., 1982, *The Fractal Geometry of Nature*, Freeman, New York.
[10] Bejan, A., 2000, *Shape and Structure, From Engineering to Nature*, Cambridge University Press, Cambridge, UK.
[11] Bejan, A., and Lorente, S., 2006, "Constructal Theory of Generation of Configuration in Nature and Engineering," J. Appl. Phys., **100**, p. 041301.
[12] Bejan, A., 2003, "Constructal Tree-Shaped Paths for Conduction and Convection," Int. J. Energy Res., **27**, pp. 283–299.
[13] da Silva, A. K., Lorente, S., and Bejan, A., 2004, "Constructal Multi-Scale Tree-Shaped Heat Exchangers," J. Appl. Phys., **96**(3), pp. 1709–1718.
[14] Wechsatol, W., Lorente, S., and Bejan, A., 2003, "Dendritic Heat Convection on a Disk," Int. J. Heat Mass Transfer, **46**, pp. 4381–4391.
[15] Chen, Y., and Cheng, P., 2005, "An experimental Investigation on the Thermal

Efficiency of Fractal Tree-Like Microchannel Nets," Int. Commun. Heat Mass Transfer, **32**, pp. 931–938.
[16] Pence, D. V., 2002, "Reduced Pumping Power and Wall Temperature in Microchannel Heat Sinks With Fractal-Like Branching Channel Networks," Microscale Thermophys. Eng., **6**(4), pp. 319–330.
[17] Alharbi, A. Y., Pence, D. V., and Cullion, R. N., 2003, "Fluid Flow through Microscale Fractal-Like Branching Channel Networks," ASME J. Fluids Eng., **125**(6), pp. 1051–1057.
[18] Alharbi, A. Y., Pence, D. V., and Cullion, R. N., 2004, "Thermal Characteristics of Microscale Fractal-Like Branching Channels," ASME J. Heat Transfer, **126**(5), pp. 744–752.
[19] Brunschwiler, T., Rothuizen, H., Fabbri, M., Kloter, U., Michel, B., Bezama, R. J., and Natarajam, G., 2006, "Direct Liquid Jet-Impingement Cooling With Micro-Sized Nozzle Array and Distributed Return Architecture," *Proceedings of the Tenth Intersociety Conference on Thermal and Thermomechanical Phenomena in Electronics Systems (ITHERM'06)*, IEEE, Piscataway, NJ, pp. 196–203.
[20] Kopp, B. A., Oullette, E., and Billups, A. J., 2000, "Thermal Design Considerations for Wide Bandgap Transistors," Microwave J., **43**, pp. 110–118.
[21] Kopp, B. A., Billups, A. J., and Luesse, M. H., 2001, "Thermal Analysis and Considerations for Gallium Nitride Microwave Power Amplifier Packaging," Microwave J., **44**, pp. 72–82.
[22] Calame, J. P., Myers, R. E., Wood, F. N., and Binari, S. C., 2005, "Simulations of Direct Die Attached Microchannel Coolers for the Thermal Management of GaN-on-SiC Microwave Amplifiers," IEEE Trans. Compon. Packag. Technol., **28**, pp. 797–809.
[23] Calame, J. P., Myers, R. E., Binari, S. C., Wood, F. N., and Garven, M., 2007, "Experimental Investigation of Microchannel Coolers for the High Heat Flux Thermal Management of GaN-on-SiC Semiconductor Devices," Int. J. Heat Mass Transfer, **50**, pp. 4767–4779.
[24] Bejan, A., and Errera, M. R., 2000, "Convective Trees of Fluid Channels for Volumetric Cooling," Int. J. Heat Mass Transfer, **43**, pp. 3105–3118.
[25] O'Brien, G. J., Monk, D. J., and Najafi, K., 2001, "Sub-Micron High Aspect Ratio Silicon Beam Etch," Proc. SPIE, **4592**, pp. 315–325.
[26] Colgan, E. G., Furman, B., Gaynes, M., Graham, W. S., LaBianca, N. C., Magerlein, J. H., Polastre, R. J., Rothwell, M. B., Bezama, R. J., Choudhary, R., Marston, K. C., Toy, H., Wakil, J., Zitz, J. A., and Schmidt, R. R., 2007, "A Practical Implementation of Silicon Microchannel Coolers for High Power Chips," IEEE Trans. Compon. Packag. Technol., **30**(2), pp. 218–225.
[27] King, J. A., 1988, *Materials Handbook for Hybrid Microelectronics*, Artech House, Dedham, MA, pp. 106–492.
[28] Mhiaoui, S., Sar, F., and Gasser, J. D., 2007, "Electrical and Thermal Conductivities and Thermopower of Some Lead Free Solders (LFS) in the Liquid and Solid State," J. Non-Cryst. Solids, **353**, pp. 3628–3632.
[29] Prasher, R., 2006, "Thermal Interface Materials: Historical Perspective, Status, and Future Directions," Proc. IEEE, **94**(8), pp. 1571–1586.
[30] Petukhov, B. S., and Kirillov, V. V., 1958, "Heat Exchange for Turbulent Flow of Liquid in Tubes," Teploenergetika (Moscow, Russ. Fed.), **5**, pp. 63–68.
[31] Peixinho, J., and Mullin, T., 2006, "Decay of Turbulence in Pipe Flow," Phys. Rev. Lett., **96**, pp. 094501.
[32] Morini, G. L., 2000, "Analytical Determination of the Temperature Distribution and Nusselt Numbers in Rectangular Ducts With Constant Axial Heat Flux," Int. J. Heat Mass Transfer, **43**, pp. 741–755.
[33] Bejan, A., 2003, "Forced Convection: Internal Flows," *Heat Transfer Handbook*, A. Bejan and A. D. Kraus, eds., Wiley, Hoboken, NJ, Chap. 5.
[34] Churchill, S. W., and Ozoe, H., 1973, "Correlations for Forced Convection With Uniform Heating in Flow over a Plate and in Developing and Fully Developed Flow in a Tube," ASME J. Heat Transfer, **95**, pp. 78–84.
[35] Lee, P. S., Garimella, S. V., and Liu, D., 2005, "Investigation of Heat Transfer in Rectangular Microchannels," Int. J. Heat Mass Transfer, **48**, pp. 1688–1704.
[36] Jenny, J. R., Muller, S. G., Powell, A., Tsvetkov, V. F., Hobgood, H. M., Glass, R. C., and Carter, C. H., Jr., 2002, "High-Purity Semi-Insulating 4H-SiC Grown by the Seeded-Sublimation Method," J. Electron. Mater., **31**(5), pp. 366–369.
[37] Sarua, A., Ji, H., Hilton, K. P., Wallis, D. J., Uren, M. J., Martin, T., and Kuball, M., 2007, "Thermal Boundary Resistance Between GaN and Substrate in AlGaN/GaN Electronic Devices," IEEE Trans. Electron Devices, **54**(12), pp. 3152–3158.
[38] Wang, X. Q., Mujumdar, A. S., and Yap, C., 2006, "Numerical Analysis of Blockage and Optimization of Heat Transfer Performance of Fractal-like Microchannel Nets," ASME J. Electron. Packag., **128**, pp. 38–45.

Predicting Heat Transfer in Long R-134a Filled Thermosyphons

M. H. M. Grooten
e-mail: c.w.m.v.d.geld@tue.nl

C. W. M. van der Geld

Department of Mechanical Engineering,
Technische Universiteit Eindhoven,
Postbus 513,
5600 MB Eindhoven, The Netherlands

When traditional air-to-air cooling is too voluminous, heat exchangers with long thermosyphons offer a good alternative. Experiments with a single thermosyphon with a large length-to-diameter ratio (188) and filled with R-134a are presented and analyzed. Saturation temperatures, filling ratios, and angles of inclination have been varied in wide ranges. A higher sensitivity of evaporation heat transfer coefficients on reduced pressure than in previous work has been found. Measurements revealed the effect of pressure or the saturation temperature on condensation heat transfer. The condensate film Reynolds number that marks a transition from one condensation heat transfer regime to another is found to depend on pressure. This effect was not accounted for by correlations from the literature. New correlations are presented to predict condensation and evaporation heat transfer rates. [DOI: 10.1115/1.3000969]

Keywords: heat pipe, thermosyphon, heat exchanger, R-134a

1 Introduction

The heat transfer in thermosyphons is based on a continuous cycle of the vaporization and condensation processes. The thermosyphon, or heat pipe if equipped with a wick inside, is heated at the evaporator, which causes evaporation of a part of the fluid. The vapor flows to the condenser, where the fluid condenses while giving off its latent heat, caused by cooling from the outside. The condensate flows back to the heated section along the wall by gravitation or capillarity, which closes the cycle. The process is schematically shown in Fig. 1, which also defines the angle with the vertical, β, and the adiabatic region.

Thermosyphons are used to foster heat transfer between two gas streams in certain conditions [1,2]. Our studies [3,4] have focused on heat pipe equipped air-to-air heat exchangers in which two plate heat exchangers are coupled with multiple thermosyphons. Since air-to-air plate exchangers require quite some space, the heat pipes applied need to be long. This is the reason why the present study focuses on 3 m long thermosyphons with a length-to-diameter ratio of 187.5. Vasiliev [5,6] gave an overview of applications of heat pipes and thermosyphons, including heat pipes for application in space. Long thermosyphons appear not to have been investigated yet. The single thermosyphon of the present study is filled with R-134a as a working fluid for application reason explained below.

The commercial use of heat exchangers equipped with long heat pipes is the following. Stand-alone electricity power generators are usually cooled with ambient air. Particularly in warmer countries, heat pipe equipped heat exchangers provide an alternative for air-to-air heat exchangers at low air temperature differences. Advantages of heat pipes are high heat recovery effectiveness, compactness, absence of moving parts, light weight, relative economy, absence of external power requirements, pressure tightness, and absence of cross-contamination between streams and reliability [7,8].

Especially during nights in warmer countries, system temperature may drop considerably. The filling with R-134a as a working fluid prevents freezing. R-134a as a working fluid in thermosyphons was hardly investigated up to the present study.

The goal of this research is to measure evaporation and condensation heat transfer in a long R-134a filled thermosyphon, to assess the merits of existing predictive methods for heat transfer in thermosyphons, and, if necessary, to adapt existing models in a physically consistent way in order to accommodate the new experimental findings with the long thermosyphon.

2 Experimental

The total length of the thermosyphon is 3 m, of which the evaporator L_{evap} is 1.20 m, the condenser L_{cond} is 1.45 m, and the adiabatic section is 0.35 m. The tube is made of copper, 16 mm outer diameter and 0.8 mm wall thickness, with a smooth inner surface. The length-to-diameter ratio is large: 187.5. The working fluid is R-134a. Experiments are performed with filling ratios of 25%, 62%, and 100%. The filling ratio is defined as

$$F_e = \frac{V_f}{V_{\text{evap}}} \tag{1}$$

where the evaporator volume, V_{evap}, is $\pi r_i^2 L_{\text{evap}}$, where r_i is 7.2 mm, and the volume of fluid, V_f, is the volume of liquid plus the volume that would be obtained if the vapor would be condensed to liquid. Before filling the tube, the tube is at vacuum. After filling only R-134a liquid and vapor fill the pipe. The pressure after the evacuation process is less than 6 Pa due to residual inert gases. The mass of R-134a added at vacuum is measured with 0.1 g accuracy.

Thermocouples (K-type, 0.75 °C in accuracy) are welded at the outer wall of the tube to measure the axial temperature distribution. A thermocouple is soldered at every 190 mm. The K-type thermocouples are coupled with a IOtech 16 bit signal converter. To avoid deviations in temperature measurements due to the thermocouple location on the perimeter, the inclination of the thermosyphon is sideways. All thermocouples are mounted in front. Temperature differences over the perimeter of the thermosyphon, which are to be expected due to a partial dryout at inclination, have no effects on measurements. All thermocouples are calibrated in situ by an isothermal run. Mean deviations between the thermocouples at the condenser, evaporator, and adiabatic section are within 0.3 °C.

At the evaporator end, the pressure is measured with a manometer at a frequency of 100 Hz. The manometer accuracy is 2% after calibration in the range of 0–40 bar, typically 0.5 bar accurate. The manometer output is averaged and read at 1 Hz. A 16 bit signal converter is applied for data acquisition. At the top, a Pt-100 of 0.06 m probe depth is mounted into the tube to measure the saturation temperature.

Contributed by the Heat Transfer Division of ASME for publication in the JOURNAL OF HEAT TRANSFER. Manuscript received March 31, 2008; final manuscript received September 16, 2008; published online March 20, 2009. Review conducted by Louis C. Chow.

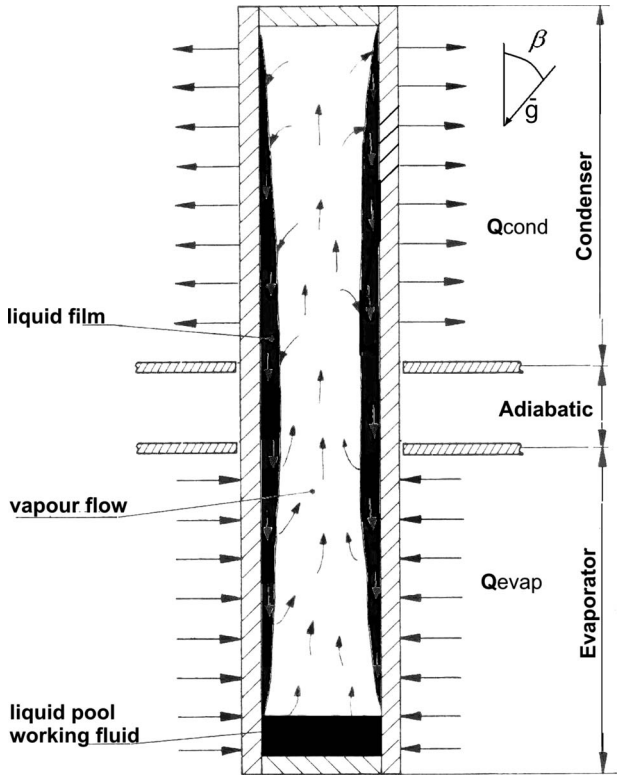

Fig. 1 Schematic view of a thermosyphon

The experimental apparatus is shown schematically in Fig. 2. An electric heater is attached at the evaporator outer wall, consisting of three 4 mm diameter heater elements, 1.20 m heated length of 650 W each, distributed equally over the perimeter and placed in the axial direction. To enhance the thermal contact between the heater elements and the tube, thermal pasta is applied equally over the length of the heaters. Together with equally spaced hose clips around the heater elements, all mounted with a 3 N m moment, the heat input can be regarded as uniform over the evaporator length. The heat input by the electric heater is controlled by a Wattmeter and measured with 1% accuracy of the measured value, typically within 1 W. A 20 mm layer of polyethylene foam insulation surrounds the condenser section with the water jacket. The evaporator section with the heater elements is surrounded by a 40 mm glass wool insulation to minimize heat losses to the environment. The heat losses are measured with a heat flux sensor with an accuracy of 5 W/m^2, positioned on the outside of the insulation.

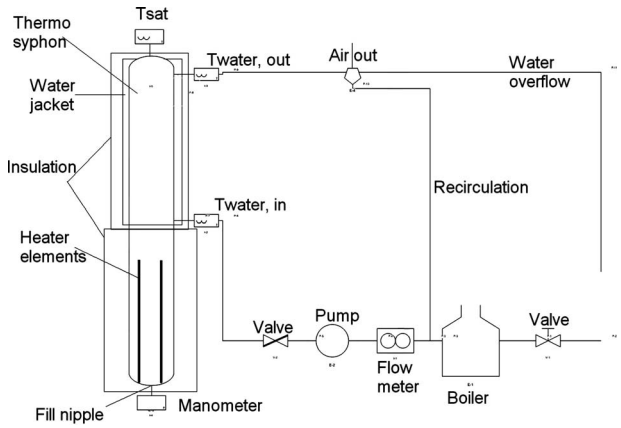

Fig. 2 Schematic view of the experimental setup

The heat loss to the surrounding can be calculated to be 0.5% of the heat input at worst. The heat flow rate at both the condenser and the evaporator is corrected for these heat losses to the environment.

Tap water flows through the water jacket surrounding the condenser for cooling. The tap water flow is measured by a flow meter, suitable for flow velocities of 0–1 m/s and flow rates of 0–0.18 l/s within 0.01 l/s accuracy.

The temperature of the water is measured upstream and downstream the water jacket with two Pt-100 sensors. All Pt-100 sensors are calibrated with accuracy better than 0.1°C for the temperature range of 0–100°C. The rejected heat at the condenser is calculated according to Eq. (2) after the substitution of the appropriate values for tap water,

$$Q = \dot{m} \cdot (h_{\text{in}} - h_{\text{out}}) = \dot{m} \cdot (c_{p,\text{in}} T_{\text{in}} - c_{p,\text{out}} T_{\text{out}}) \tag{2}$$

The two Pt-100 sensors for measuring tap water inlet and outlet temperature at the condenser are corrected for an offset obtained from an isothermal run. The uncertainties of all measured and calculated parameters are estimated according to Ref. [9].

Measurements are performed at inclination angles β from 0 deg to 87 deg. The angle is determined at 0.2 deg accuracy. High cooling water temperatures are to be achieved to indirectly vary the saturation temperature inside the thermosyphon between 20°C and 75°C. This corresponds with pressures of 5.7–20.6 bar. A boiler enables preheating of the condenser cooling water. The cooling inlet temperature, the cooling water mass flow rate, and the heat input of the heater elements at the evaporator are controlled, which enables control of the saturation temperature. At the top of the condenser, all air possibly caught in the cooling water system exits with a water overflow to a sink.

3 Experimental Results

The following results will be presented:

- Heat transfer dependencies on saturation temperature in the range of 20–75°C for the vertical orientation, β=0 deg, and a filling ratio F_e of 62%.
- Heat transfer dependencies on the angle of inclination in the range of 0–87 deg for a filling ratio of 62% and for a saturation temperature of 20°C.
- Heat transfer dependencies on filling ratios in the range of 25–100% for a saturation temperature of 20°C and for a vertical orientation.

3.1 Effects of Saturation Temperature on Phase Change Heat Transfer. The measurements were performed at steady state, and it typically took 20 min to reach a steady state condition. Measurements were done at each condition during 5 min to check the steady state condition and to guarantee proper averaging. Figure 3 shows a typical example of the thermosyphon wall temperature histories during a measurement. This figure shows that the variation is less than 0.1°C. Effects of axial conduction through the copper wall are negligible compared with the axial heat transfer of the thermosyphon.

Figure 4 shows the heat flow rate measured from the temperature difference over the water outlet and water inlet at the condenser side and the electric heater at the evaporator side. The error bars on the measured condenser heat flow rates account for the accuracies of the cooling water flow meter and cooling water temperature difference measurements on a 95% confidence interval. At steady state these heat flow rates should be equal. Figure 4 shows that this is the case. The measurements in Fig. 4 are the results of the thermosyphon at a vertical position with a filling ratio of F_e=62% and for saturation temperatures of 20°C, 35°C, 40°C, 55°C, 65°C, and 75°C. Other angles of inclination and filling ratios gave similar results.

Figure 5 presents the mean wall temperature difference between the evaporator and the condenser. The mean condenser temperature is defined as the average of the four thermocouples at the

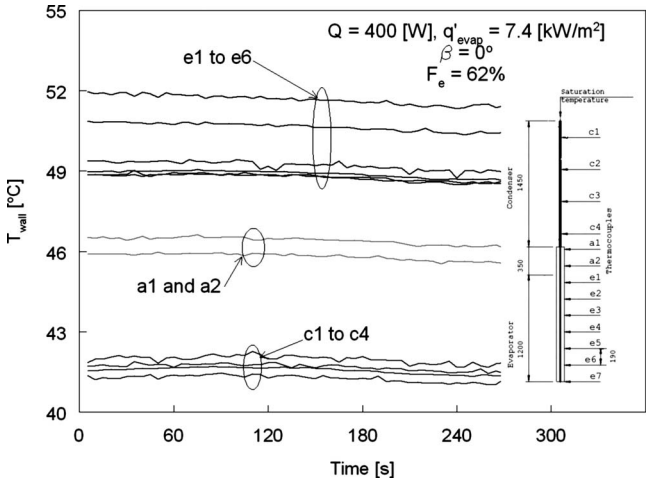

Fig. 3 Typical histories of wall temperatures, Q=400 W for vertical orientation, F_e=62%

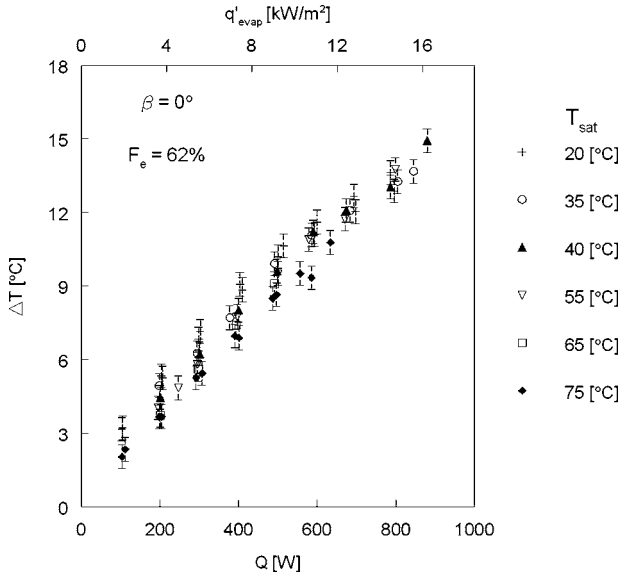

Fig. 5 Measured mean temperature differences between evaporator and condenser versus heat flow rate and evaporator heat flux for various saturation temperatures at F_e=62% and for vertical orientation. The evaporator heat flux scale is linear.

condenser wall, and the mean evaporator temperature is the averaged wall temperature of the six thermocouples at the evaporator wall. The variation in each thermocouple is less than 0.1 °C. The temperature difference between the condenser and the evaporator increases with increased heat flux.

To calculate heat transfer coefficients for the condensation and evaporation processes, both the wall temperatures and the saturation temperatures need to be known. In our experiments, the saturation temperature is measured with an inside Pt-100, but many authors [10,11] took the adiabatic section temperature as the saturation temperature. Figure 6 gives a typical example of the differences in saturation temperature depending on whether the saturation temperature is obtained with the intruding Pt-100 (called Saturation), the averaged adiabatic wall temperature (called Adiabatic), or the Antoine relation (called Pressure sensor). It follows from Fig. 6 that the adiabatic wall temperature is not always the same as the inner saturation temperature. Agreement is only observed at high heat transfer rates, exceeding 400 W, corresponding with heat fluxes at the evaporator of 7.4×10^3 W/m^2. The measured saturation temperature has a systematic error at heat transfer rates below 400 W. Possibly, condensation at the intruding Pt-100 occurs, resulting in too low temperatures. The saturation temperature is alternatively calculated from the measured saturation pressure with the Antoine relation, Eq. (3). However, this is less accurate, taking the accuracy of the pressure measurement into account, which is typically 0.5 bar,

$$T = \frac{B}{A - \ln(p)} - C \tag{3}$$

with A=10.52, B=2484, and C=263.1, pressure in bar, and T in °C.

The same discrepancies between the saturation temperature, adiabatic wall temperature, and saturation temperature obtained from pressure measurements are observed at lower saturation temperatures and other filling ratios and inclination angles. Care needs to be taken when zooming in on the evaporation or conden-

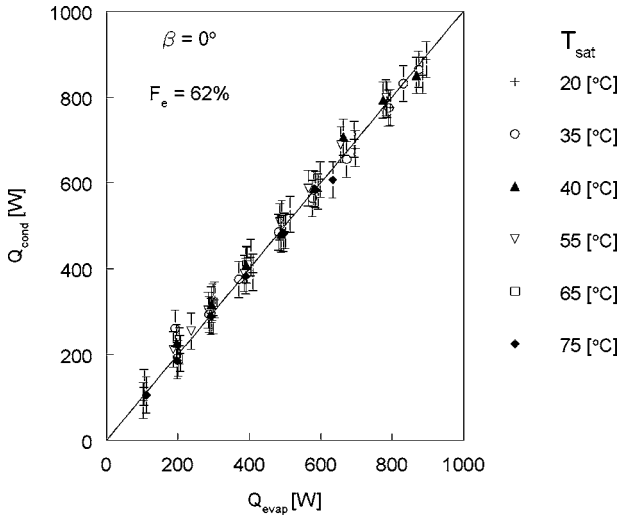

Fig. 4 Comparison of measured heat flow rates at evaporator and condenser at F_e=62%, vertical orientation, for various saturation temperatures, A_{evap}=0.0543 m^2, and A_{cond}=0.0656 m^2

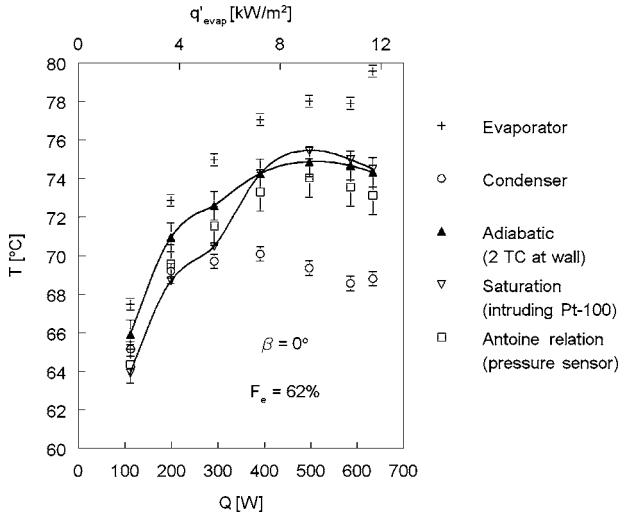

Fig. 6 Typical deviation in measurements of the saturation temperature with several methods, compared with the mean evaporator and condenser temperatures. Lines are given to guide the eye.

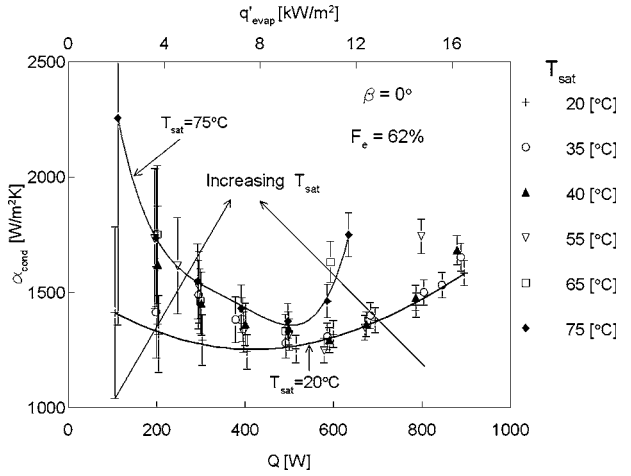

Fig. 7 Measured heat transfer coefficient condenser side for various saturation temperatures, F_e=62%, and vertical orientation. Lines are given to guide the eye.

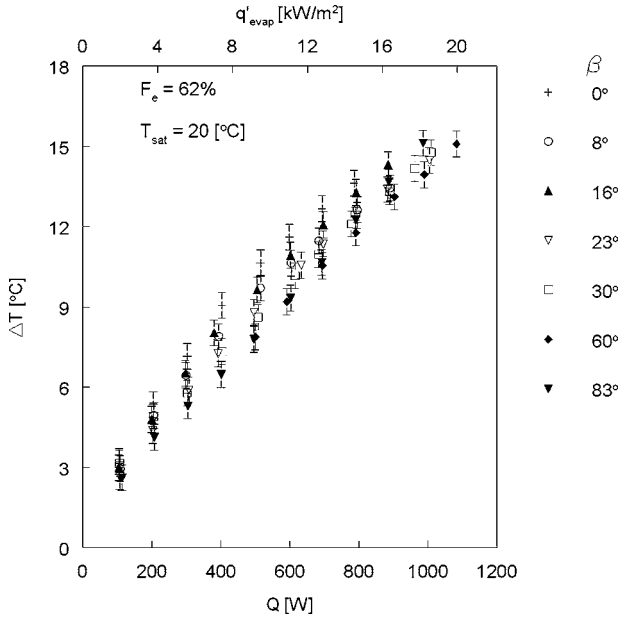

Fig. 9 Measured mean temperature differences between evaporator and condenser for various inclination angles, F_e =62%, and T_{sat}=20°C

sation process separately because in order to calculate heat transfer coefficients accurately at the condenser and evaporator, a correct temperature difference between the condenser, saturation and evaporator is of great importance. In view of Fig. 6, the adiabatic wall temperature measured with two thermocouples has been selected for further analysis of the condensation and evaporation processes.

The measured mean heat transfer coefficient α at the condenser side is now defined by Eq. (4), and that at the evaporator side is defined by Eq. (5),

$$\alpha_{\text{cond}} = \frac{Q}{A_{\text{cond}}(T_{\text{adiabatic}} - T_{\text{cond}})} \tag{4}$$

$$\alpha_{\text{evap}} = \frac{Q}{A_{\text{evap}}(T_{\text{evap}} - T_{\text{adiabatic}})} \tag{5}$$

Here A_{cond}=0.0656 m^2 and A_{evap}=0.0543 m^2.

This yields the results in Figs. 7 and 8. Note the difference from the results in Fig. 5, which showed a temperature difference between the evaporator and condenser. Heat transfer coefficients for *condensation* first decrease for increased heat transfer rate and then increase. A minimum in condensation heat transfer coefficient of 1300 W/m^2 K exists around a heat transfer rate of 500 W. At heat transfer rates up to 400 W, a higher saturation temperature is beneficial for condensation heat transfer, for example, 1800 W/m^2 K at 200 W for T_{sat}=75°C versus 1400 W/m^2 K at 200 W for T_{sat}=20°C. Note the high errors at low heat flow rates in Figs. 7 and 8. This follows from the definitions of α in Eqs. (4) and (5) and the accuracy of the temperature measurements in Sec. 2. The heat flow rate is in the order of 10^2 W. The area is in the order of 10^{-2} m^2, and the temperature difference is in the order 1°C.

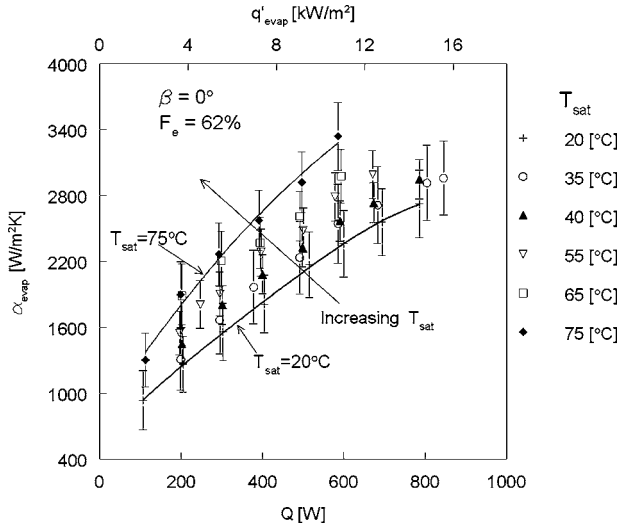

Fig. 8 Measured heat transfer coefficient evaporator side for various saturation temperatures, F_e=62%, and vertical orientation. Lines are given to guide the eye.

Heat transfer coefficients for *evaporation* increase from 1000 to approximately 3000 W/m^2 K with increasing heat transfer rates (see Fig. 8). With increasing saturation temperatures, the heat transfer coefficient for evaporation increases at a given heat transfer rate. In general, higher heat transfer coefficients are measured at the evaporator side than at the condenser side.

3.2 Effects of the Angle of Inclination With the Vertical on Phase Change Heat Transfer. Similar steady state measurements as shown in Figs. 3 and 4 are performed for a constant saturation temperature of 20°C for various angles of inclination. Measurements are performed at a filling ratio of 62%, at inclination angles of 0 deg, 8 deg, 16 deg, 30 deg, 60 deg, and 83 deg. Not shown, but also performed, are measurements at 75°C at angles of 0 deg, 60 deg, 83 deg, and 87 deg. Figure 9 shows the mean temperature difference between the condenser and evaporator.

Coefficient α_{cond} is found to be in the range of 1300–2200 W/m^2 K (see Fig. 10). Figure 10 shows that condensation heat transfer at low heat transfer rates increases with an increase in the inclination angle at constant saturation temperature. This dependency vanishes at heat transfer rates above 800 W.

At the highest heat flow rate found, the condensation heat transfer coefficient levels off at inclination angles larger than 60 deg. Possibly, the condenser is flooded by liquid rushing up from the evaporator, as observed by Gross [12]. A typical axial vapor velocity is 1 m/s.

Heat transfer coefficients at the evaporator side increase from 1000 to almost 4000 W/m^2 K at an increasing heat flow rate (see

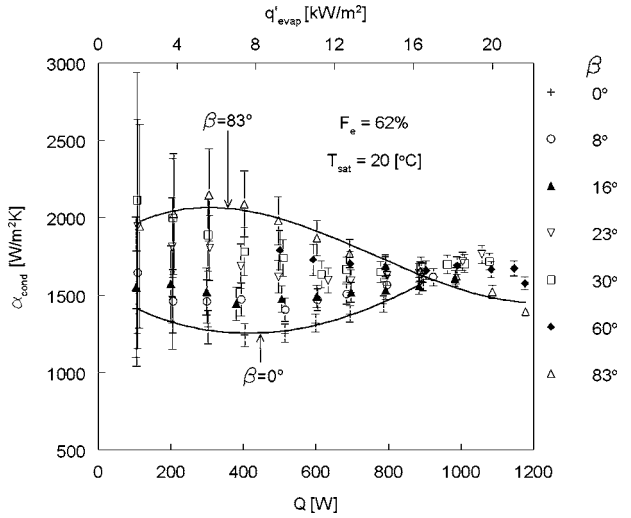

Fig. 10 Measured heat transfer coefficient condenser side for various inclination angles, F_e=62%, and T_{sat}=20°C. Lines are given to guide the eye.

Fig. 11). The heat transfer coefficient at the evaporator side does not show a clear dependency on the angle of inclination.

3.3 Effects of the Filling Ratio on Phase Change Heat Transfer. Similar steady state measurements as shown in Figs. 3 and 4 are performed for various filling ratios. The saturation temperature and angle of inclination are kept constant at 20°C and vertical, respectively. All previous measurements were performed at a filling ratio of 62%, which resulted in a good working of the thermosyphon system up to the operating limit. A filling ratio of 100% is chosen to see the dependency on overfilling the thermosyphon, where a filling ratio of 25% results in a forced dryout within the working temperature range. The temperature difference between the condenser and evaporator at constant heat flux at a filling ratio of 25% is systematically higher compared to filling ratios of 62% and 100%. The lowest filling ratio of 25% has the highest heat transfer resistance. Further overfilling from 62% to 100% hardly affects the behavior of the thermosyphon.

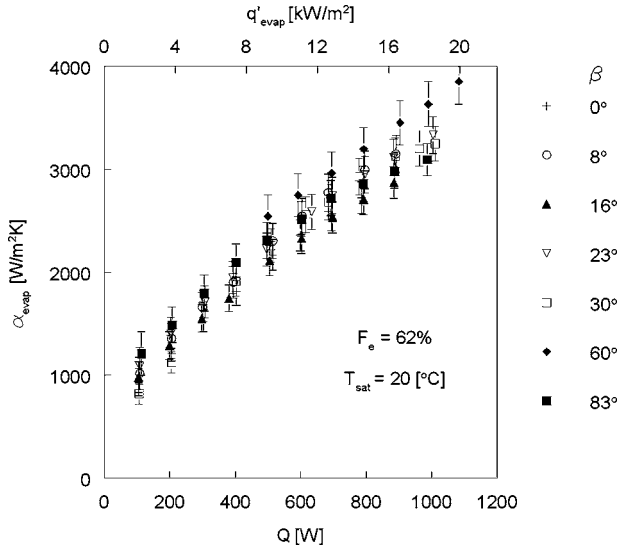

Fig. 11 Measured heat transfer coefficient evaporator side for various inclination angles, F_e=62%, and T_{sat}=20°C

4 Analysis

In general, higher heat transfer coefficients for evaporation than for condensation are measured. Boiling at the inner wall of the thermosyphon results in bubbles escaping from the liquid pool at the evaporator section, which is typical of nucleate boiling. The liquid at the wall is refreshed in this way, and diffusion plays a less important role in boiling than in condensation. It will be investigated below whether the concrete trends measured for the long thermosyphon can be predicted with existing correlations for short thermosyphons.

The large length-over-diameter ratio of the present thermosyphon makes it necessary to investigate the possibility of occurrence of geometry determined physical phenomena, such as liquid entrainment and confined boiling. There exists an operational heat flux limit of thermosyphons at which liquid entrainment comes into play. Such entrainment limits in thermosyphons are extensively described in the literature (see, for example, Ref. [13]). The operating conditions for our measurements were selected such that liquid entrainment did not occur. Recently we performed measurements at the same operating conditions with a transparent thermosyphon with the same wetting characteristics as R-134a on copper [4]. It has been shown in these measurements that in the condensation area a liquid film exists and that only occasionally does droplet splashing into the liquid film occur in the adiabatic region between the evaporator and condenser areas.

Confinement boiling may cause special flow patterns to occur in a thermosyphon [14,15]. Capillary flow effects in the internal flow in a thermosyphon are usually indicated by a low value of the Bond number, defined as $\sqrt{\rho_l \cdot g \cdot d^2/\sigma}$, with σ as the surface tension coefficient and d as the diameter. Typical values of the Bond number in our experiments are in the range of 16–34. For our working fluid, R-134a, it was recently demonstrated that the typical problems related to confined flow boiling do not occur in a pipe with the same diameter as the one used for our thermosyphon [16]. It is concluded that existing correlations for short thermosyphons should, in principle, be applicable to our measuring conditions. This is further investigated below.

A clear separation of the evaporation and the condensation processes increases accuracy in the prediction of phase change heat transfer. Gross [12] reviewed models of heat transfer in film condensation and experiments of heat transfer in the condensation process in thermosyphons, as well as the evaporation process [17]. However, the databases on which correlations for condensation and boiling heat transfer in thermosyphons were based do not contain the working fluid R-134a and were obtained with tubes that are short compared with our thermosyphon. In addition, quite some scatter among data was found, and, in particular, the effect of pressure remained unclear. Extrapolation of existing correlations to the present situation with R-134a and a 3 m long tube is therefore somewhat awkward; it yielded unsatisfying results, as will be shown below.

Many models generally applicable to filmwise condensation heat transfer and pool boiling heat transfer exist in the literature, some of which are possibly applicable to heat transfer in thermosyphons. Most important models will be examined below.

4.1 Condensation Heat Transfer. To analyze condensation heat transfer, it is convenient to introduce a film Reynolds number [18,19],

$$\mathrm{Re}_f = \frac{4\dot{m}_{\mathrm{cond}}}{\mu_f} \tag{6}$$

with

$$\dot{m}_{\mathrm{cond}} = \frac{Q}{\Delta h_{fg} \pi d_i} \tag{7}$$

where $\dot{m}_{\mathrm{cond}}$ is the mass flow rate of condensate per unit perimeter.

The Nusselt number reads

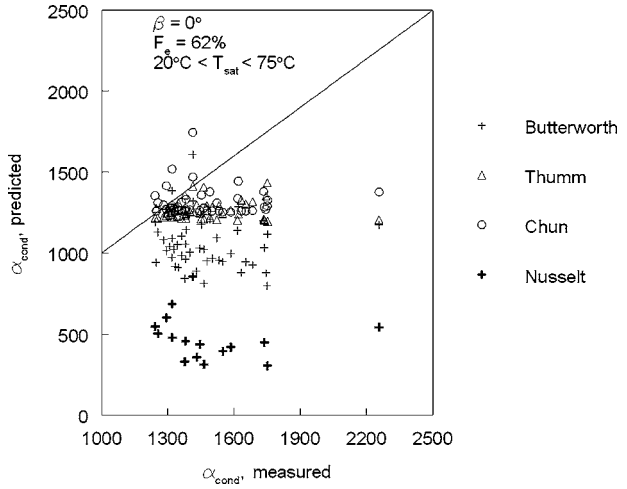

Fig. 12 Comparison of measured and predicted heat transfer coefficient condenser sides for various models at various saturation temperatures, vertical orientation, and F_e=62%

$$\overline{\mathrm{Nu}} = \frac{\alpha_{\mathrm{cond}} L}{\lambda_f} \tag{8}$$

with a typical length scale [12,20], as is common in film condensation theory,

$$L = \left(\frac{\nu^2}{g}\right)^{1/3} \tag{9}$$

Some models for condensation heat transfer of liquid films of vertical surfaces are now reviewed. The Nusselt model [18] yields

$$\alpha_{\mathrm{cond}} = 1.47 \mathrm{Re}_f^{-1/3} \left(\frac{\rho_f(\rho_f - \rho_v)g}{\mu_f^2}\right)^{1/3} \lambda_f \tag{10}$$

The model of Butterworth [18] yields

$$\alpha_{\mathrm{cond}} = \left(\frac{\mathrm{Re}_f}{1.08\mathrm{Re}_f^{1.22} - 5.2}\right)\left(\frac{\rho_f(\rho_f - \rho_v)g}{\mu_f^2}\right)^{1/3} \lambda_f \tag{11}$$

The model of Thumm et al. [20] for heat transfer in film condensation of water in a vertical tube with countercurrent vapor flow corrects the Nusselt model given by Eq. (10) for turbulent condensate film flow at high Re_f.

Chun and Kim [19] presented the following correlation for filmwise condensation heat transfer on vertical surfaces:

$$\overline{\mathrm{Nu}} = 1.33\ \mathrm{Re}_f^{-1/3} + 9.56 \cdot 10^{-6}\ \mathrm{Re}_f^{0.89}\ \mathrm{Pr}^{0.94} + 8.22 \times 10^{-2} \tag{12}$$

valid for $10 \leq \mathrm{Re}_f \leq 3.1 \times 10^4$ and $1.75 \leq \mathrm{Pr} \leq 5.0$. The models reviewed above are found not to be valid for 3 m long R-134a filled thermosyphons. This will be explained below.

Figure 12 shows a comparison of measured and predicted heat transfer coefficients by the models of Nusselt, Butterworth, Thumm et al. [20], and Chun and Kim [19] for saturation temperatures of 20–75 °C and for a filling ratio of 62%. Existing correlations underpredict our data. This underprediction can be removed by accounting for the dependency of a transition Reynolds number, $\mathrm{Re}_{f,\mathrm{trans}}$, on reduced pressure, as will be explained below.

The model of Butterworth enhances the model of Nusselt by taking laminar wavy film condensate heat transfer into account. Butterworth still predicts lower heat transfer coefficients than the ones measured. Both models do not catch the effects of countercurrent vapor flow, which affects the liquid film thickness and waviness. These models show a trend for the effect of saturation temperature on condensation heat transfer, which is opposite to the one observed in our measurements. Extrapolated to our specific application, the model of Thumm et al. [20] does not agree well with the present measurements.

From the work of Cavallini et al. [21], it follows that condensation heat transfer coefficients of refrigerants inside a plain round tube are affected by saturation temperature, which is directly related to reduced pressure. The correlation of Chun and Kim [19], Eq. (12), does not take this dependency into account. We modified this correlation and used the reduced pressure to account for a dependency of the minimum Nusselt number in a way described below.

The following correlation for the measured data presented in Sec. 3.1 is proposed:

$$\overline{\mathrm{Nu}} = (3.52 \pm 0.14) \cdot p_{\mathrm{reduced}}^{0.46} \cdot \mathrm{Re}_f^{-1/3} + (1.8 \pm 0.2) \times 10^{-4} \cdot p_{\mathrm{reduced}}^{-0.42} \cdot \mathrm{Re}_f^{0.74} \tag{13}$$

with

$$p_{\mathrm{reduced}} = \frac{p}{p_c}$$

All uncertainties in Eq. (13) are for a 95% confidence interval. The new correlation (Eq. (13)) is valid for a vertical R-134a filled thermosyphon with

$$200 \leq \mathrm{Re}_f \leq 5000$$

$$0.1411 \leq p_{\mathrm{reduced}} \leq 0.5811$$

Fit statistics are F=45 and r^2=0.51, caused by the scatter of measured data at low heat flow rates. The correlation coefficient r^2 is defined by [22]

$$r^2 = \sum_{i=1}^{N} (\hat{y}_i - \bar{y})^2 \Bigg/ \sum_{i=1}^{N} (y_i - \bar{y})^2 \tag{14}$$

where N is the number of measurements with outcome y_i, $\hat{y}_i$ are the corresponding predictions with the fit function, and $\bar{y}$ is the average of the set $\{y_i\}$. The number of parameters used in the fit, k, of course, affects the quality of the fit. Whereas the correlation coefficient should preferably have a value close to 1, the parameter F should at the same time have a maximum value,

$$F = \left\{ \sum_{i=1}^{N} (\hat{y}_i - \bar{y})^2 \Bigg/ \sum_{i=1}^{N} (y_i - \hat{y}_i)^2 \right\} \cdot (N-k)/(k-1) \tag{15}$$

Figure 13 shows a comparison of measured and predicted heat transfer with the new correlation (Eq. (13)) for various saturation temperatures, a vertical position, and a filling ratio of 62%.

At small Re_f, the film is laminar and becomes thicker at increasing Re_f. If heat transfer is mainly by conduction through the thin condensate film, the heat transfer decreases with increasing film thickness. This is accounted for in the first term of Eq. (13). Above a transition Reynolds number, $\mathrm{Re}_{f,\mathrm{trans}}$, the film flow becomes wavy and turbulent, which increases heat transfer. To account for this heat transfer enhancement, usually special "wave factors" are suggested to correct Nusselt's theory (Eq. (10)) (see the review by Gross [12]). To account for heat transfer enhancement at Reynolds numbers above the transition Reynolds number, the second term of Eq. (13) is introduced in a similar way as Chun and Kim did [19]. The form of Eq. (13) prevents discontinuity for the prediction of condensation heat transfer at transitional Reynolds numbers. The $\mathrm{Re}_{f,\mathrm{trans}}$ number, where a transition from laminar to turbulent film flow and a minimum in condensate film heat transfer occur, is dependent on Pr in the model of Chun and Kim [19]. However, from the new measurements, the following are found:

- For low Reynolds numbers, an increased reduced pressure (thus an increase in saturation temperature) leads to enhanced heat transfer.

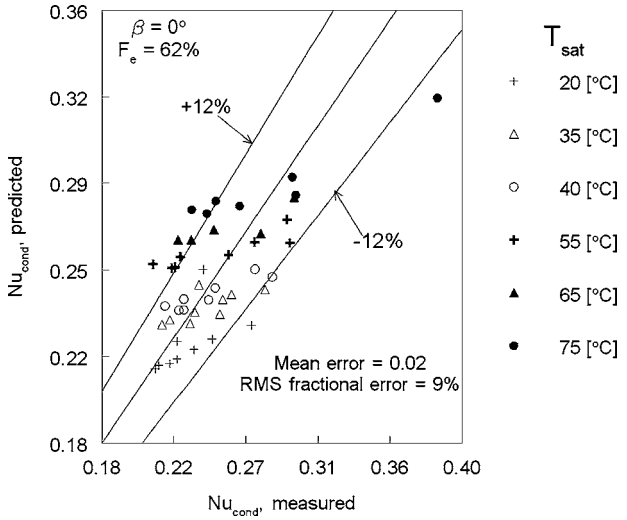

Fig. 13 Film condensation heat transfer in a vertical thermosyphon, F_e=62%, vertical orientation, and accuracy of present correlation (Eq. (13))

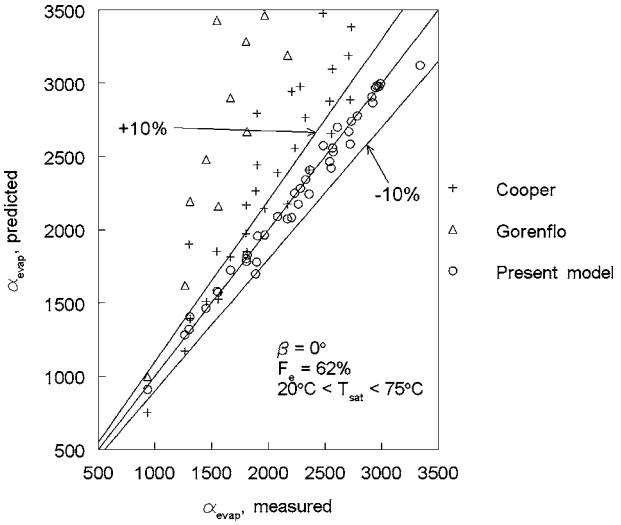

Fig. 15 Comparison of measured and predicted heat transfer coefficient evaporator sides for various models at various saturation temperatures, vertical orientation, and F_e=62%

- The Reynolds number where the second term of Eq. (13) starts to get significant, $\mathrm{Re}_{f,\mathrm{trans}}$, depends on the reduced pressure.

The above mentioned effects of the reduced pressure are clearly shown in Fig. 14.

The reduced pressure also occurs in the second term of Eq. (13), a modification of the correlation of Chun and Kim [19], because of the second observation. It occurs in the first term because this term dominates at low Reynolds numbers and because of the first observation. That the exponent accounting for the dependency on pressure in the second term is negative (−0.42) is because an increase in pressure in the case of a wavy and/or turbulent condensate film flow reduces heat transfer. The exponent for the reduced pressure in the first term is found by a separate fit of the measured data for Re_f below the $\mathrm{Re}_{f,\mathrm{trans}}$ at the corresponding reduced pressure. All data at Re_f above the $\mathrm{Re}_{f,\mathrm{trans}}$ at the corresponding reduced pressure are fitted separately to find the exponents for Re_f and p_{reduced} in the second term of Eq. (13). Note that the product of the constant and the reduced pressure term in the first term of Eq. (13), i.e., $(3.52 \pm 0.14) \cdot p_{\mathrm{reduced}}^{0.46}$, is in the order of 1, as is common in literature for laminar film condensation.

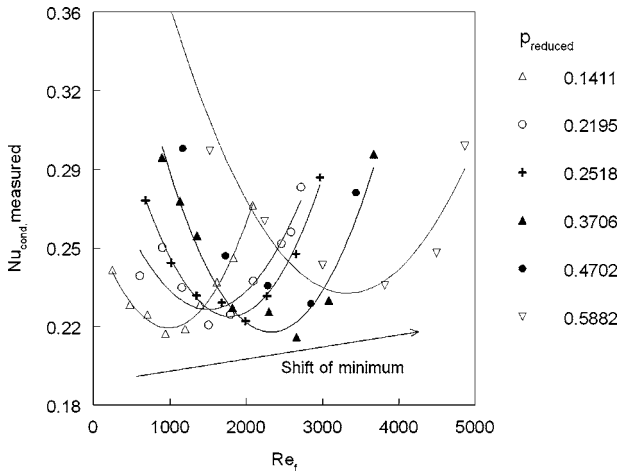

Fig. 14 Condensation heat transfer versus film Reynolds number for various reduced pressures

4.2 Evaporation Heat Transfer. Two pool boiling models for evaporation of refrigerants are now examined: Cooper and Gorenflo [23]. Both models take the dependency of the evaporation heat transfer coefficient on the saturation pressure into account via an explicit parameter. The Cooper model is

$$\alpha_{\mathrm{evap}} = 55 p_{\mathrm{reduced}}^{0.12-0.4343\ln(R_p)} (-0.4343 \ln(p_{\mathrm{reduced}}))^{-0.55} \times M^{-0.5} q^{0.67} \tag{16}$$

with p_{reduced} as the reduced pressure, p/p_c (p_c is 4.06 MPa for the fluid R-134a used here), R_p as the surface roughness in micrometers (typically 1 μm), M as the molecular weight of the condensate in kg/kmol (typically 102 kg/kmol for R-134a), and q as the heat flux in the $\mathrm{W/m^2}$ evaporator area. The Gorenflo model is

$$\alpha_{\mathrm{evap}} = 4500 F_{PF} (q/20\,000)^{0.9-0.3 p_r^{0.3}} \times (R_p/0.4)^{0.133} \tag{17}$$

with

$$F_{PF} = 1.2 p_{\mathrm{reduced}}^{0.27} + 2.5 p_{\mathrm{reduced}} + p_{\mathrm{reduced}}/(1 - p_{\mathrm{reduced}})$$

Both models for evaporation heat transfer examined are found not to be valid for 3 m long R-134a filled thermosyphons. The new measurements show that the sensitivity of the evaporation heat transfer coefficient on reduced pressure is clearly larger than as represented by the power of 0.12 of Cooper [23]. Gross [17] found a power of 0.7 for the heat flux, and Cooper found a power of 0.67, but for the large L over D value of our measurements a power of 0.52 is found. Figure 15 shows a comparison of the measured heat transfer coefficient at the evaporator with the one predicted with the new correlation (Eq. (18)) presented below and with the models of Cooper and Gorenflo. Cooper (Eq. (16)) predicts well the heat transfer coefficients for evaporation at 20 °C, but heat transfer at higher temperatures is overestimated. Gorenflo (Eq. (17)) overestimates the heat transfer coefficients in all cases. The length of our thermosyphon leads to flow phenomena that are not readily caught by a correlation for shorter tubes. Gross [17] already showed how complicated it is to correlate all available boiling heat transfer data of thermosyphons: 88.5% of the data were only predicted within ±50% accuracy.

For the present measurements of Sec. 3.1, the following equation is found to do well:

$$\alpha_{\mathrm{evap}} = (28 \pm 3) \cdot p_{\mathrm{reduced}}^{(0.24 \pm 0.01)} \cdot q^{(0.52 \pm 0.01)} \tag{18}$$

with q as the heat flux at the evaporator. All uncertainties are at a 95% confidence interval. The fit statistics are F=1178 and r^2

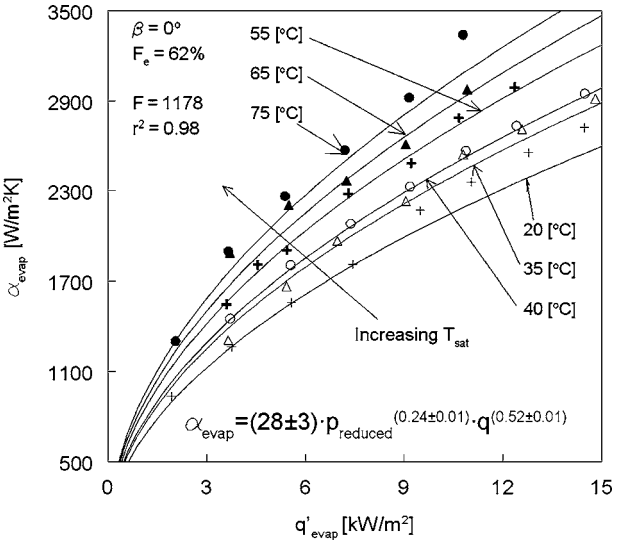

Fig. 16 Comparison of measured and predicted heat transfer coefficient evaporator sides with the present correlation (Eq. (18)) at various saturation temperatures, vertical orientation, and F_e=62%. See Fig. 13 for the legend.

=0.98. Figure 16 shows the prediction of the heat transfer coefficients with the new correlation at various saturation temperatures.

5 Conclusions

The evaporation and condensation heat transfer in a 3 m long R-134a filled thermosyphon, with L/D ratio of 188, have been investigated in a wide operating range. Knowledge of these heat transfer characteristics facilitates future design of air-to-air heat exchangers equipped with thermosyphons of this length, as explained in the introduction. Evaporation heat transfer coefficients have been measured to be in the range of 1000–3000 W/m^2 K. Condensation heat transfer coefficients have been measured to be in the range of 1300–2300 W/m^2 K.

The following new trends have been observed:

- The effect of pressure, or T_{sat}, on condensation heat transfer enhancement is twofold.
- For low condensate film Reynolds number, Re_f, an increase in pressure leads to an increase in heat transfer, a tendency that is familiar.
- The Reynolds number that marks the transition from this low Reynolds number heat transfer regime to another regime with a different tendency, $Re_{f,trans}$, depends on pressure.
- The effect of pressure, or T_{sat}, on evaporation heat transfer is higher for the long R-134a filled thermosyphon than that measured previously for all other, shorter, thermosyphons.

Existing correlations underpredict our data particularly because of these effects of pressure. For this reason, new correlations for condensation and evaporation heat transfer coefficients have been presented.

Physical explanations for the trends observed have been presented. The dependency of $Re_{f,trans}$ on pressure only transpires if accurate data in a wide range are carefully examined, and the authors are confident that this dependency applies to all thermosyphons with similar filling fluids and, more importantly, with similar L over D ratios.

Acknowledgment

The support of H. Hagens of VDL Klima BV, The Netherlands in facilitating the experimental work is greatly appreciated.

Nomenclature

A = surface area, m^2
F_e = filling degree
L = length, m
M = molecular weight, kg/kmol
Nu = Nusselt number
Pr = Prandtl number
Q = heat flow rate, W
R_p = typical surface roughness, μm
Re = Reynolds number
T = temperature, °C
V = volume, m^3
c_p = heat capacity at constant pressure, J/(kg K)
d = diameter, m
g = acceleration due to gravity, m/s^2
Δh_{fg} = enthalpy of evaporation, J/kg
$\dot{m}$ = mass flow rate, kg/s
p = pressure, Pa
$p_{reduced}$ = reduced pressure
q = heat flux, W/m^2
r = radius, m

Greek

α = heat transfer coefficient, $W/(m^2 K)$
β = inclination angle to the vertical, deg
λ = thermal conductivity, W/(m K)
μ = dynamic viscosity, Pa s
ν = kinematic viscosity m^2/s
ρ = mass density, kg/m^3
σ = surface tension, N/m

Subscripts

cond = condenser
evap = evaporator
f = fluid
i = inner
l = liquid
sat = saturation
v = vapor

References

[1] Noie, S. H., 2006, "Investigation of Thermal Performance of an Air-to-Air Thermosyphon Heat Exchanger Using ε-NTU Method," Appl. Therm. Eng., **26**(5–6), pp. 559–567.
[2] Noie-Baghban, S. H., and Majideian, G. R., 2000, "Waste Heat Recovery Using Heat Pipe Heat Exchanger (HPHE) for Surgery Rooms in Hospitals," Appl. Therm. Eng., **20**(14), pp. 1271–1282.
[3] Hagens, H., Ganzevles, F. L. A., Van der Geld, C. W. M., and Grooten, M. H. M., 2007, "Air Heat Exchangers With Long Heat Pipes: Experiments and Predictions," Appl. Therm. Eng., **27**(14–15), pp. 2426–2434.
[4] Grooten, M. H. M., Van der Geld, C. W. M., and Van Deurzen, L. G. M., 2008, "A Study of Flow Patterns in a Thermosyphon for Compact Heat Exchanger Applications," *Proceedings of the Fifth International Conference on Transport Phenomena in Multiphase Systems, HEAT*, Bialystok, Poland, D. Butrymowicz, T. Skiepo, and J. Goscik, eds., Vol. 2, pp. 323–328.
[5] Vasiliev, L. L., 2005, "Heat Pipes in Modern Heat Exchangers," Appl. Therm. Eng., **25**(1), pp. 1–19.
[6] Vasiliev, L. L., 1998, "State-of-the-Art on Heat Pipe Technology in Former Soviet Union," Appl. Therm. Eng., **18**(7), pp. 507–551.
[7] Dunn, P. D., and Reay, D. A., 1994, *Heat Pipes*, 4th ed., Pergamon, New York.
[8] Wadowski, T., Akbarzadeh, A., and Johnson, P., 1991, "Characteristics of a Gravity Assisted Heat Pipe Based Heat Exchanger," Heat Recovery Syst. CHP, **11**(1), pp. 69–77.
[9] Kline, S. J., and McKlintock, F. A., 1953, "Describing Uncertainties in Single-Sample Experiments," Mech. Eng. (Am. Soc. Mech. Eng.), **75**, pp. 3–8.
[10] Abou-Ziyan, H. Z., Helali, A., Fatouh, M., and Abo El-Nasr, M. M., 2001, "Performance of Stationary and Vibrated Thermosyphon Working With Water and R-134a," Appl. Therm. Eng., **21**, pp. 813–830.
[11] Payakaruk, T., Terdtoon, P., and Ritthidech, S., 2000, "Correlations to Predict

Heat Transfer Characteristics of an Inclined Closed Two-Phase Thermosyphon at Normal Operating Conditions," Appl. Therm. Eng., **20**, pp. 781–790.
[12] Gross, U., 1992, "Reflux Condensation Heat Transfer Inside a Closed Thermosyphon," Int. J. Heat Mass Transfer, **35**(2), pp. 279–294.
[13] Peterson, G. P., and Bage, B. K., 1991, "Entrainment Limitations in Thermosyphons and Heat Pipes," ASME J. Energy Resour. Technol., **113**, pp. 147–153.
[14] Tadrist, L., 2007, "Review on Two-Phase Flow Instabilities in Narrow Spaces," Int. J. Heat Fluid Flow, **28**, pp. 54–62.
[15] Bonjour, J., and Lallemand, M., 1998, "Flow Patterns During Boiling in a Narrow Space Between Two Vertical Surfaces," Int. J. Multiphase Flow, **24**, pp. 947–960.
[16] Chen, L., Tian, Y. S., and Karayiannis, T. G., 2006, "The Effect of Tube Diameter on Vertical Two-Phase Flow Regimes in Small Tubes," Int. J. Heat Mass Transfer, **49**(21–22), pp. 4220–4230.
[17] Gross, U., 1990, "Pool Boiling Heat Transfer Inside a Two-Phase Thermosyphon: Correlation of Experimental Data," Proceedings of the Ninth International Heat Transfer Conference, Jerusalem, Israel, Vol. 2, pp. 57–62.
[18] Marto, P. J., 1998, "Condensation," *Handbook of Heat Transfer*, 3rd ed., W. M. Rohsenow, J. P. Hartnett, and Y. I. Cho, eds., McGraw-Hill, New York, pp. 14.4–14.15.
[19] Chun, M. H., and Kim, K. T., 1991, "A Natural Convection Heat Transfer Correlation for Laminar and Turbulent Film Condensation on a Vertical Surface," *Proceedings of the Joint ASME/JSME Thermal Engineering Conference*, Vol. 2, pp. 459–464.
[20] Thumm, S., Phillipp, Ch., and Gross, U., 2001, "Film Condensation of Water in a Vertical Tube With Countercurrent Vapour Flow," Int. J. Heat Mass Transfer, **44**, pp. 4245–4256.
[21] Cavallini, A., Censi, G., Del Col, D., Doretti, L., Longo, G. A., Rossetto, L., and Zilio, C., 2003, "Condensation Inside and Outside Smooth and Enhanced Tubes: A Review of Recent Research," Int. J. Refrig., **26**, pp. 373–392.
[22] Schmidt, J., Giesbrecht, H., and Van der Geld, C. W. M., 2007, "Void Fraction and Distributions in Upward Pipe Flow of Gas and a High-Viscous Liquid," Int. J. Multiphase Flow, **34**(1), pp. 363–374.
[23] Collier, J. G., and Thome, J. R., 1994, *Convective Boiling and Condensation*, 3rd ed., Clarendon, Oxford, pp. 148–169.

Experimental Investigation of the Effects of Fluid Properties and Geometry on Forced Convection in Finned Ducts With Flow Pulsation

B. O. Olayiwola
e-mail: b.olayiwola@bci.uni-dortmund.de

P. Walzel
Chair
e-mail: p.walzel@bci.uni-dortmund.de

Mechanical Process Engineering,
Faculty of Biochemical and Chemical Engineering,
Technische Universität Dortmund,
Emil-Figge Strasse 68,
44227 Dortmund, Germany

An experimental study was conducted on the effects of flow pulsation on the convective heat transfer coefficients in a flat channel with series of regular spaced fins. Glycerol-water mixtures with dynamic viscosities in the range of 0.001–0.01 kg/ms were used as working fluids. The device contains fins fixed to the insulated wall opposite to the flat and smooth heat transfer surface to avoid any heat transfer enhancement by conduction of the fins. Pulsation amplitude $x_o = 0.37$ mm and pulsation frequencies f in the range of $10\ Hz < f < 47\ Hz$ were applied, and a steady-flow Reynolds number in the laminar range of $10 < Re < 1100$ was studied. The heat transfer coefficient was found to increase with increasing Prandtl number Pr at a constant oscillation Reynolds number Re_{osc}. The effect of the d_h/L ratio was found to be insignificant for the system with series of fins and flow pulsation due to proper fluid mixing in contrast to a steady finned flow. A decrease in heat transfer intensification was obtained at very low and high flow rates. The heat transfer was concluded to be dynamically controlled by the oscillation.
[DOI: 10.1115/1.2970068]

Keywords: heat transfer, flow pulsation, finned channels, thermal boundary layers

1 Introduction

The augmentation of convective heat transfer has become a subject of interest in recent times because of its implications in numerous natural phenomena and engineering applications, such as in nuclear power reactors, microreactor systems, and electronic devices. One of the techniques that have been adopted is the combination of pulsating flow and series of sharp edges in ducts. With this technique, it is possible to decouple fluid mixing and heat transfer performance from the mean flow velocity [1]. According to Ni and Gough [2], the fluid mechanical conditions for this kind of system were described to be complex, with similar magnitudes of both axial and radial velocity components.

In general, pulsating equipment may be classified into two main types: (a) one where pulsation is generated by the alternating motion of some intrinsic elements in a column or channel such as in a reciprocating plate column and (b) another where oscillation is produced by the hydraulic transmission of a perturbation to the liquid contained in a column or channel using, e.g., positive displacement pumps to introduce the feed into the system [3].

Several research works have been made on the combined effects of oscillatory flow and fins or baffles in ducts or channels on heat transfer intensification. In the work of Zhang et al. [4], a numerical study of the laminar natural convection on a vertical baffle plate subjected to a periodic oscillation was performed. It was found that the heat transfer intensification increases with increasing dimensionless oscillation frequency and amplitude but decreases with the Grashof number. Chang and Shiau [5] also performed a numerical study on the effects of a single horizontal baffle and flow pulsation on the heat transfer characteristics of opposing mixed convection in a parallel vertical open channel. The heat transfer coefficient was observed to increase with increasing pulsation magnitude for a low Prandtl number Pr fluid [5]. In addition, the heat transfer coefficient was found to increase with increasing Prandtl number Pr at a constant pulsation amplitude. A better heat transfer was found to be generated in the channels containing series of baffles/fins coupled with flow pulsation. A significant heat transfer enhancement was reported for an orifice-type baffled tube with flow oscillation at low net flow rates in Refs. [1,6] using conducting baffles with reverse oscillations. The same observation was reported in Refs. [7–9] using series of nonconducting fins in a flat channel. The influence of the pulsation amplitude was reported to be of small significance on the heat transfer coefficient [1]. However, the pulsation amplitude was found to significantly influence the heat transfer coefficient in Refs. [8,9]. It is important to consider the dependence of the heat transfer coefficients as well as the intensification factor on the Prandtl number Pr and the effects of the diameter to length ratio of the duct.

This paper provides information on the effects of these parameters on the heat transfer coefficients as well as on the intensification factor over a wide range of the laminar flow regime using nonconducting fin geometry and oscillations generated upstream of the flow. The fins were arranged on the insulated wall opposite to the smooth and plain heat transfer surface only to interact with the flow of the working fluid. This enhances the convective heat transfer coefficient without significant gain from the heat conducting effect of the fins. Hence, a separation of the conducting effect and the flow effect is possible.

2 Parameters Affecting the Heat Transfer Coefficients

Since the device contains fins that are regularly spaced and assuming that the flow is fully developed such that the flow pat-

Contributed by the Heat Transfer Division ASME for publication in the JOURNAL OF HEAT TRANSFER. Manuscript received August 24, 2007; final manuscript received May 13, 2008; published March 16, 2009. Review conducted by Bengt Sunden.

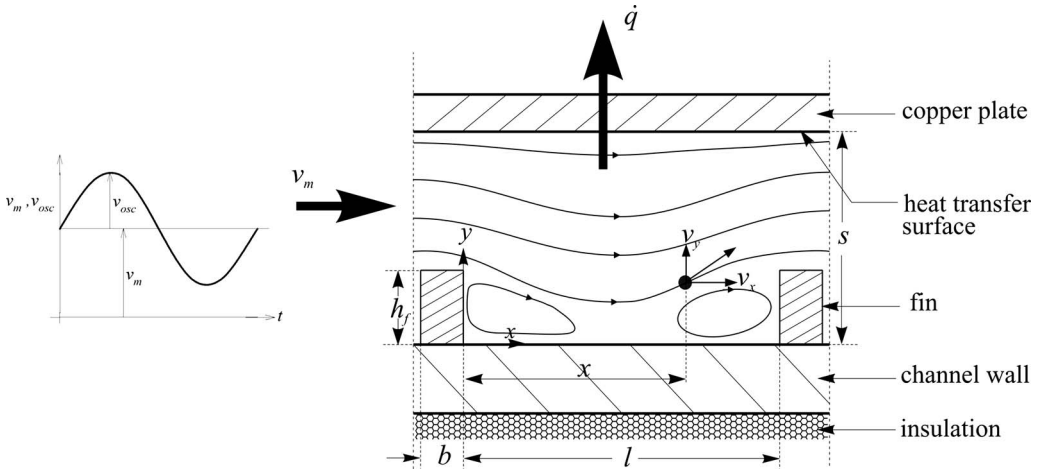

Fig. 1 Description of the flow behavior

terns are repeated in the duct, a simple module, which is the space between two fins in the duct, can be used to describe the flow behavior in the system.

Figure 1 shows the modular description of the flow patterns. Heat is exclusively transported from the working fluid to the upper channel wall. The fins were positioned on the lower channel wall, which is insulated from the environment and through which no heat transfer takes place. The heat conducting effects of the fins are suppressed by the insulation.

For conditions where there is flow in the finned duct but no superimposition of pulsation, the heat transfer coefficient within the device depends on the mean flow velocity v_m, the fluid properties ρ, μ, λ, and C_p, and the geometrical parameters, i.e., h_f, $d_h \approx 2s$, l, b, and L. As described in standard literatures, the heat transfer coefficient expressed in nondimensional terms by the Nusselt number Nu can therefore be stated to depend on the mean Reynolds number Re, the Prandtl number Pr, and the geometrical parameters. A laminar flow condition allows for a combination of Re and Pr to obtain the Peclet number $Pe = Re\,Pr$ [10]. For a combination of flow pulsation and sharp edges in ducts, the flow becomes complex, and two more parameters, i.e., pulsation amplitude x_o and frequency f, are added as independent parameters. The heat transfer coefficient then depends on the mean Reynolds number Re, the oscillation Reynolds number Re_{osc}, the Prandtl number Pr, and the geometric parameters.

3 Heat Transfer Measurements

The experimental setup is as shown in Fig. 2. The device has an active length of $L = 900$ mm and a lateral extension of $B = 90$ mm. The channel is positioned horizontally and contains 53 fins mounted at the lower wall of the channel in a spacing of $l = 15$ mm. The fins were bars with a height of $h_f = 3$ mm and a thickness of $b = 2$ mm.

The fins are fixed on the insulated wall opposite to the plain and smooth heat transfer plate in order to avoid direct heat conduction by the bars. The cooling and working fluids are separated by a copper plate with a thickness of $\delta = 6$ mm. The distance between the copper plate and the lower wall of the channel resulted in a channel width of $s = 8$ mm. It was initially intended to arrange the copper plate below the fin plate in order to obtain a stable density layering when cooling the working fluid from below. Unfortunately, air was entrapped between the fins and could not be removed. The channel therefore had to be operated with the cooling wall (copper plate) above the finned wall.

However, trials proved that the additional heat transfer due to unstable thermal layering and natural convection within the working range is insignificant. The distance between the copper plate and the upper wall of the channel resulted in a passage for the

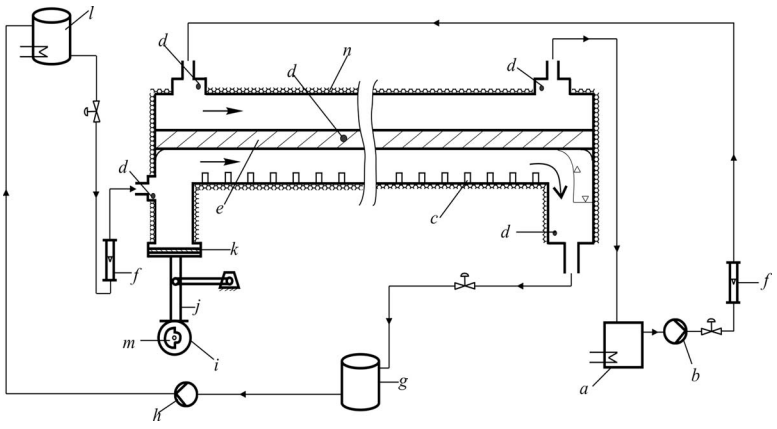

Fig. 2 Experimental setup for heat transfer measurements. (*a*) cryostat; (*b*) centrifugal pump; (*c*) fin (*d*); PT 100 sensor; (*e*) copper plate; (*f*) ratometer; (*g*) collection vessel; (*h*) hose pump; (*i*) motor; (*j*) connecting rod; (*k*) diaphragm; (*l*) overhead tank; (*m*) unbalanced mass; and (*n*) insulation.

coolant of $H=10$ mm. The hydraulic diameter d_{H_c} for this compartment again corresponds approximately to twice the gap width, i.e., $d_{H_c}=20$ mm.

The experiments were carried out with three different glycerol-water mixtures of 23 wt %, 43 wt %, and 52 wt % glycerol and an isopropanol-water mixture with a dynamic viscosity of 0.0025 kg/ms was used as the cooling medium. The flow direction of the mixture and the coolant was concurrent, as shown in Fig. 2.

The working fluid flowed from an overhead tank through a control valve placed upstream of a rotameter measuring the flow rate of the medium and into the heat exchanger. The overhead tank contains an immersed coil heater to maintain the temperature of the mixture. In addition, a stirrer was provided for a proper mixing of the working fluid to make sure that the fluid with a constant inlet temperature enters the device. A Colora cryostat Type KT505 was used to cool the inflow coolant to the desired temperature and to keep it constant throughout the experiments. The cooled isopropanol-water mixture was conveyed into the heat exchanger by a centrifugal pump through a flowmeter. The flow rate of the coolant was kept constant at 1977 l/h for all the experiments. The inlet temperature of the coolant was in the range of 2.4–2.9 °C, and the operation led to coolant outlet temperatures in the range of 3.1–4.0 °C. The exiting coolant was then recycled back into the cryostat. The mixture inlet temperatures were in the range of 19–23 °C, and the outlet temperatures were in the range of 11–18 °C. The cooled glycerol-water mixture was collected in a vessel and recycled back into the overhead tank with the use of a hose pump. Wall temperatures covered the range of 5.8–10.0 °C depending on the adjustment. All temperatures were measured with PT 100 sensors. The analog signals of the temperature measurements were converted to a digital type using an NI-DAQ™mx Base card, which is a NI USB device. The channels were connected to the card using a single-ended mode. The data were displayed on the PC and recorded in a ASCII file type.

Pulsation was transferred to the working fluid by a vibrating rubber diaphragm. Depending on the frequency range, the rubber diaphragm was driven by a motor with unbalanced masses ($f>15$ Hz) or a crank drive ($f<15$ Hz). The motor was placed upstream of the channel. It produced a circular vibration, and by a coupling mechanism the circular oscillation of the motor was converted to a linear vertical oscillation with an up and down movement of the diaphragm. The pulsation amplitude within the channel was determined by photographic means (observing tracks of tracer particles under a zero main flow condition) through the transparent sidewalls of the channel. The pulsation frequency corresponds to the rotational speed of the motor controlled by a frequency transform. The adjusted frequency was measured by a stroboscope. At the exit of the channel, an air pillow was allowed to eliminate the oscillation in the discharged line.

A steady-flow Re range of $100 \leq \mathrm{Re} \leq 1000$ was investigated. The frequency f of the pulsation was varied between 10 Hz and 47 Hz, and the pulsation amplitude x_o was 0.37 mm. All the experiments were carried out at constant geometrical parameters, i.e., a relative fin height of $h_f/d_h=0.204$, a relative fin spacing of $l/d_h=1.021$, and a relative fin thickness of $b/d_h=0.136$. Mixtures of glycerol and water with Prandtl numbers Pr in the range of $10<\mathrm{Pr}<80$ were used as the working fluids. For a particular fluid type, the experiments were carried out for both steady and unsteady finned flows using the same flow rate setting.

4 Determination of Heat Transfer Enhancement

By heat balance over the entire system after steady state conditions had been reached for each adjustment, the overall heat transfer coefficient U was obtained. This equals the steady rate of the heat flux $\dot{q}$ from the mixture through the wall into the cooling medium, i.e.,

$$\dot{q} = U\Delta T_{\mathrm{lm}} = \frac{\dot{m}_w \bar{C}_{p_w}(T_{w_{\mathrm{out}}} - T_{w_{\mathrm{in}}})}{A_s} \tag{1}$$

where ΔT_{lm} is the logarithmic mean temperature difference over the entire device, A_s is the heat transfer area, $\dot{m}_w$ is the mass flow rate of the working fluid, $\bar{C}_{p_w}$ is the mean specific heat capacity determined at the average temperature of the mixture, $T_{w_{\mathrm{in}}}$ is the measured inlet flow temperature of the medium, and $T_{w_{\mathrm{out}}}$ is the measured outlet temperature of the mixed working fluid at the outlet.

The heat transfer coefficient on the coolant side, $h_c = \mathrm{Nu}_c k_c/d_{H_c}$, was calculated from the modified equation of Petukhov and Popov for the transition and fully developed turbulent flow with diameter to length effects [11]. All the physical properties of the coolant were determined at its bulk mean temperature, i.e., arithmetic mean of both inlet and outlet temperatures. The correction factor μ_c/μ_{ws} was approximately taken to be 1. The change in the coolant temperature was narrow, and the viscosity change was assumed to be insignificant.

When the values from PT 100 sensors had been steady, the temperature data were taken for a certain time duration. The heat transfer coefficient $h^*_{w_p}$ due to pulsation in the working fluid section was then calculated from the recorded database on the series resistance for heat transfer from fluid to fluid separated by a wall (see, e.g., Ref. [12]),

$$h^*_{w_p} = \frac{1}{\dfrac{1}{U} - \dfrac{1}{h_c} - \dfrac{\delta}{k_{\mathrm{Cu}}}} \tag{2}$$

where h_c is the heat transfer flux related to the logarithmic temperature difference between the wall surface and the coolant and $h^*_{w_p}$ is the heat transfer flux related to the logarithmic temperature difference between the working fluid and the wall surface.

The mean heat transfer coefficient due to the pulsation of the working fluid was then calculated. The same was done for the mean heat transfer coefficient at a nonpulsed condition. The heat transfer enhancement factor, thus defined as the ratio of the working fluid heat transfer coefficient obtained in a pulsed flow h_{w_p} to that obtained in a steady flow h_{w_o} at the same flow rate, was then obtained. This is defined thus as

$$E = \frac{h_{w_p}}{h_{w_o}} \tag{3}$$

5 Results and Discussion

The experiments were repeated to determine the reproducibility of the results. In order to determine the relationship between the sets of arrays, a statistical analysis was carried out by the determination of the correlation coefficient between the data sets. A correlation coefficient of approximately 0.99 was found for majority of the data.

Figures 3(*a*) and 3(*b*) show the dependence of the heat transfer coefficient of the working fluid at the copper plate on the steady Reynolds number Re for different Prandtl numbers Pr for a steady finned flow and a pulsating finned flow, respectively. The oscillation Reynolds number $\mathrm{Re}_{\mathrm{osc}}=200$ was held constant at a constant pulsation amplitude of $x_o=0.37$ mm. The pulsation frequencies f of 10.7 Hz, 23.2 Hz, and 46.7 Hz were used in order to obtain data for constant Prandtl numbers Pr of 15, 37, and 78, respectively. All geometrical parameters are constant; i.e., $d_h/L=0.0163$, $h_f/d_h=0.204$, $l/d_h=1.021$, and $b/d_h=0.136$.

The heat transfer coefficient is seen to increase consistently with increasing main flow Reynolds number Re due to increased convective flow. At a very low Reynolds number Re, the influence of the Prandtl number Pr on the heat transfer coefficients ceases.

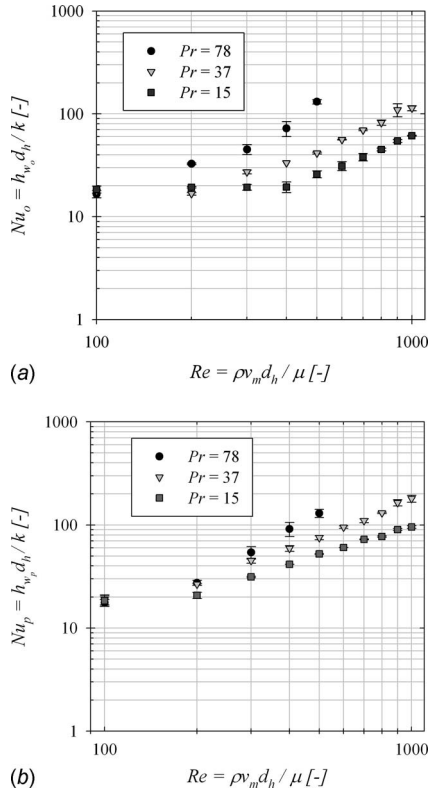

Fig. 3 Dependence of the heat transfer coefficient on the Reynolds number Re for different Prandtl numbers Pr: (*a*) $Re_{osc}=0$, (*b*) $Re_{osc}=200$, and $x_o/d_h=0.025$

In Fig. 3(*a*), the reason for the receding effect of the flow velocity at a very low Reynolds number Re is the increase in the boundary layer thickness where only conduction of heat is possible. The transport of the heat out of the pulsated zone is reduced with reduced convective flow velocity (Fig. 3(*b*)). The system then becomes more determined by the convection and less determined by the ratio of the hydrodynamic boundary layer to the thermal boundary layer. With increasing Pr, the heat transfer coefficient expressed by the Nusselt number Nu_p for the two conditions of flow increases at $Re > 100$. This is qualitatively similar to what was reported in Ref. [8] for pipe and slit systems. Furthermore, the work of Chang and Shiau [5] using a fluid with $Pr=0.71$ also reveals an increase in Nu with increasing Re.

The influence of the Prandtl number Pr on the heat transfer enhancement E at constant $Re_{osc}=200$ and $x_o/d_h=0.025$ for a given Re is shown in Fig. 4. For the three Re and Prandtl numbers $Pr < 40$, the enhancement E increases with increasing Prandtl number Pr. A decrease in E was obtained for the Prandtl number $Pr \geq 40$. This can be attributed to the viscous force on the fluid, which dampens the effect of the fluid pulsation. In Ref. [5], $Nu=20$ was obtained at $Re=250$ for $Pr=15$ using a plate with a single horizontal baffle and flow pulsation to study mixed convection in a parallel vertical open channel and $Nu=10$ when there is no flow pulsation.

Figure 5 shows the dependence of the heat transfer enhancement on Pe at constant oscillation Reynolds numbers Re_{osc} of 200 and 500 using the same working fluid with $Pr=15$. In this case, $x_o/d_h=0.025$, $d_h/L=0.0163$, $h_f/d_h=0.204$, $l/d_h=1.021$, and $b/d_h=0.136$, and only the oscillation frequency changes.

With increased Re_{osc} from 200 to 500, the maximum heat enhancement E_{max} is increased from approximately 2.1 to 2.5. This is due to the increase in the ratio of the maximum oscillation celerity v_{osc} to the mean flow velocity v_m, referred to as κ in Ref. [8]. In addition, the position of E_{max} shifts toward lower Peclet

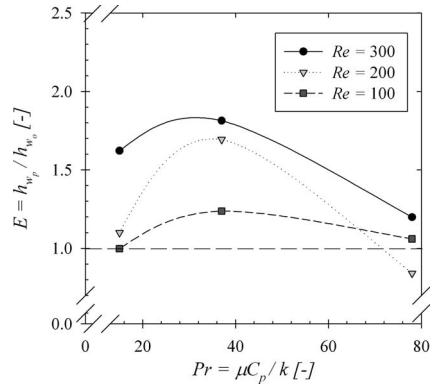

Fig. 4 Influence of the Prandtl number Pr on the heat transfer enhancement at constant $Re_{osc}=200$ and $x_o/d_h=0.025$

numbers Pe. The results of Refs. [1,6–9] qualitatively substantiate the dependence of the heat transfer enhancement on flow rates or Pe. In Ref. [1], heat transfer enhancements $E=1.83$ and $E=4.0$ at $Re_{osc}=300$ and $Re=300$ and $Re_{osc}=200$ and $Re=130$, respectively, used an oscillatory baffled system with a fluid whose viscosity is about three times higher than ours. In addition, using the same kind of system as in Ref. [1], Mackley et al. [6] also reported $E=1.22$ for $Re_{osc}=200$ and $Re=300$ and $E=1.78$ for $Re_{osc}=500$ and $Re=300$. In our system and at these conditions, as in Ref. [6], we obtained $E=1.62$ and 1.98, respectively. A maximum heat enhancement E_{max} of about 2.5 was reported in Refs. [8,9]. The same qualitative observations regarding the dependence of heat transfer enhancement on the Reynolds number were made in Ref. [13], even though the experimental setup was such that there was no pulsation of the flow. The increased Re_{osc} leads to an increased fluid mixing and significant heat transfer from the working fluid into the cooling medium. From the flow visualization, the flow recirculation was found upstream of the fins in addition to the downstream recirculation eddies at this E_{max} for $Re_{osc}=500$.

For laminar flow in smooth ducts, the heat transfer coefficient expressed by the Nusselt number Nu is known to depend approximately on the one-third power of the ratio of the hydraulic diameter to the length of the duct for $Re\,Pr > 10$ [14]. Grace suggested the same dependence for the heat transfer performance of a Kenic mixer [15]. Figure 6 shows the dependence of the heat transfer coefficient on d_h/L for a steady finned flow. Below $Re=200$, the heat transfer coefficient does not show a significant dependence on the d_h/L. At $Re > 200$, the heat transfer coefficient monotonically increases with increasing Reynolds number Re. When d_h/L is doubled, the curve is shifted higher. This is quantitatively simi-

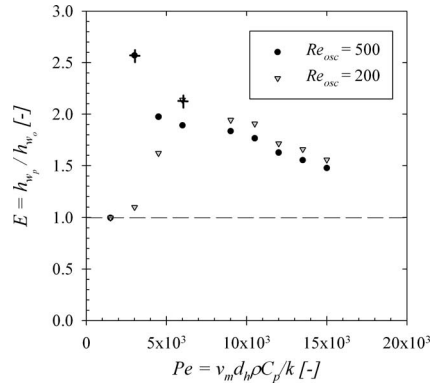

Fig. 5 Dependence of the heat transfer enhancement on the Peclet number Pe at constant Re_{osc} for $Pr=15$, $x_o/d_h=0.025$, $d_h/L=0.0163$, $h_f/d_h=0.204$, $l/d_h=1.021$, and $b/d_h=0.136$

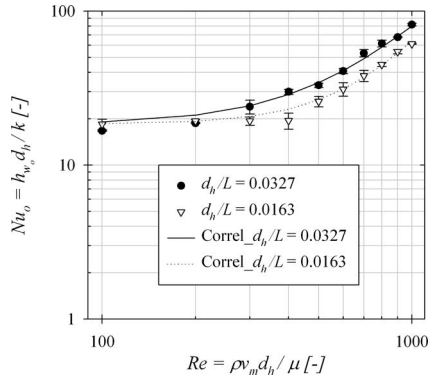

Fig. 6 Effect of d_h/L on heat transfer coefficients for a steady finned flow: Pr=15, h_f/d_h=0.204, l/d_h=1.021, and b/d_h=0.136

lar to was reported in Ref. [10]. From our proposed correlation (Eq. (4)), the heat transfer performance for the finned channel was also found to depend on the one-third power of the diameter to length ratio of the duct for higher Re > 200. This is shown in Fig. 6. The higher exponent of the Reynolds number Re can then be attributed to the presence of the nonconducting fins, which were only used to redirect the flow. In addition, at every fin position the real channel diameter is reduced by 37.5%. The fluid at this position undergoes significant acceleration,

$$\mathrm{Nu}_O = 18.42 + C(\mathrm{Re})^n(\mathrm{Pr})^{0.33}\left(\frac{d_h}{L}\right)^{0.33}$$

$$\text{for } 100 \le \mathrm{Re} \le 1000 \text{ and } \mathrm{Pr} = 15$$

$$n = 2.5 \text{ and } C = 2.3 \times 10^{-6} \text{ for } d_h/L = 0.0163$$

$$n = 1.95 \text{ and } C = 1.1 \times 10^{-4} \text{ for } d_h/L = 0.0327 \qquad (4)$$

With superimposition of pulsation on the fluid flowing into the finned duct, the heat transfer coefficient shows no significant dependence on the diameter to length ratio. This can be explained by a repeated rearrangement of the thermal boundary layer when both flow pulsation and fins are combined. Figure 7 shows the results of the experiments and our proposed correlation (Eq. (5)) obtained for the system with combined conditions of flow pulsation and fins,

$$\mathrm{Nu}_p = 7.29 + 0.00388(\mathrm{Re\ Pr})^{1.046}$$

$$\text{for } x_o/d_h = 0.025,\ 100 \le \mathrm{Re} \le 1000 \text{ and } \mathrm{Pr} = 15 \qquad (5)$$

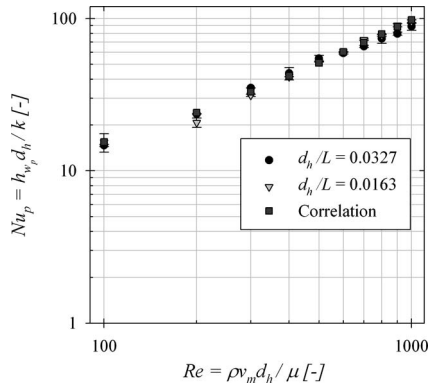

Fig. 7 Effect of d_h/L on heat transfer coefficients for a pulsating finned flow at $\mathrm{Re_{osc}}$=200: Pr=15, x_o/d_h=0.025, h_f/d_h=0.204, l/d_h=1.021, and b/d_h=0.136

From the proposed correlation of Nu_p (Eq. (5)), the exponents of Re and Pr are more than the usual 0.33 of the correlations for a steady laminar flow in smooth ducts. This suggests that the heat transfer is dynamically controlled. In addition, it can be concluded that the thermal boundary layers are frequently destroyed and renewed as a result of pulsation leading to increased thermal diffusivity and higher heat transfer.

6 Conclusions

The results of the heat transfer coefficients revealed that the system is dynamically controlled by oscillation. The diameter to length ratio of the channel d_h/L was found to significantly influence the heat transfer coefficients for a steady finned flow. For a pulsating flow in finned ducts, the influence of the d_h/L ratio was not significant due to enhanced fluid mixing and repeated thermal boundary layer rearrangement as a result of flow pulsation. There is no significant influence of the Prandtl number Pr on the heat transfer coefficients at very low Re. With increasing Prandtl number Pr, the heat transfer coefficient increases. In addition, the heat transfer coefficient monotonically increases with increasing main Reynolds number Re. For a given pulsation amplitude x_o and oscillation Reynolds number $\mathrm{Re_{osc}}$, the heat transfer intensification was found to increase until we reach a Prandtl number of Pr=40, after which a decrease in the intensification factor was obtained. Within the experimental limits, a maximum heat transfer enhancement $E_{\max}$ of 2.5 was obtained. In general, a decrease in $E_{\max}$ was obtained at low and high flow rates.

Acknowledgment

The authors would like to acknowledge the financial support of the Matching Fund Scholarships of the DAAD.

Nomenclature

x_o = pulsation amplitude (m)
f = pulsation frequency (Hz)
d_{H_c} = coolant-side hydraulic diameter (m)
d_h = working fluid-side hydraulic diameter (m)
L = active length (m)
B = lateral extension (m)
l = fin spacing (m)
δ = thickness of the copper plate (m)
s = working fluid-side width (m)
H = coolant-side width (m)
h_f = fin height (m)
b = fin thickness (m)
v_m = mean flow velocity (m/s)
v_{osc} = maximum oscillation velocity (m/s)
U = overall heat transfer coefficient ($\mathrm{W/m^2\,K}$)
h = heat transfer coefficient ($\mathrm{W/m^2\,K}$)
A_s = heat transfer area ($\mathrm{m^2}$)
T = temperature (K)
ΔT_{lm} = log-mean temperature (K)
$\dot{q}$ = heat flux ($\mathrm{W/m^2}$)
$\bar{C}_p$ = mean specific heat capacity (J/kg K)
k = thermal conductivity (W/m K)
μ = dynamic viscosity (kg/ms)
ρ = density ($\mathrm{kg/m^3}$)

Dimensionless Numbers

$E = h_{w_p}/h_{w_o}$ = heat transfer enhancement factor
$\mathrm{Nu} = hd_h/k$ = Nusselt number
$\mathrm{Pe} = v_m d_h \rho C_p/k$ = Peclet number
$\mathrm{Pr} = \mu C_p/k$ = Prandtl number
$\mathrm{Re_{osc}} = 2\pi f A \rho d_h/\mu$ = oscillation Reynolds number
$\mathrm{Re} = \rho v_m d_h/\mu$ = Reynolds number

Subscripts

c = coolant
max = maximum
m = mean
o = nonpulsating
p = pulsating
w = working fluid
ws = copper surface
Cu = copper

References

[1] Mackley, M. R., and Stonestreet, P., 1995, "Heat Transfer and Associated Energy Dissipation for Oscillatory Flow in Baffled Tubes," Chem. Eng. Sci., **50**(14), pp. 2211–2224.

[2] Ni, X., and Gough, P., 1997, "On the Discussion of the Dimensionless Groups Governing Oscillatory Flow in Baffled Tube," Chem. Eng. Sci., **52**(18), pp. 3209–3212.

[3] Reis, N., 2006, "Novel Oscillatory Flow Reactors for Biotechnological Applications," Ph.D. thesis, Escola de Engenharia, Universidade do Minho.

[4] Zhang, X., Maruyama, S., and Yamaguchi, H., 2005, "Laminar Natural Convection Heat Transfer From a Vertical Baffled Plate Subjected to a Periodic Oscillation," J. Heat Transfer, **127**, pp. 733–739.

[5] Chang, T., and Shiau, Y., 2005, "Flow Pulsation and Baffle's Effects on the Opposing Mixed Convection in a Vertical Channel," Int. J. Heat Mass Transfer, **48**, pp. 4190–4204.

[6] Mackley, M. R., Tweddle, G. M., and Wyatt, I. D., 1990, "Experimental Heat Transfer Measurements for Pulsatile Flow in Baffled Tubes," Chem. Eng. Sci., **45**(5), pp. 1237–1242.

[7] Olayiwola, B., and Walzel, P., 2006, "Convective Heat Transfer Intensification in Laminar Duct Flow," *Proceedings of the ASME 2006 Second Joint U.S.-European Fluids Engineering Summer Meeting*, Miami, July 17–20.

[8] Olayiwola, B., and Walzel, P., 2008, "Cross-Flow Transport and Heat Transfer Enhancement in Laminar Pulsed Flow," Chem. Eng. Process., **47**, pp. 929–937.

[9] Olayiwola, B., and Walzel, P., 2007, "Flow Pulsation Modified Duct Surface for Process Heat Transfer Intensification," Int. J. Chem. React. Eng., **5**(A71).

[10] Gnielinski, V., 1994, *VDI-Wärmeatlas (GVC)*, VDI-Verlag GmbH, Düsseldorf.

[11] Knudsen, J. G., Hottel, H. C., Sarofim, A. F., Wankat, P. C., and Knaebel, K. S., 1997, *Heat and Mass Transfer: Perry's Chemical Engineers' Handbook*, 7th ed., McGraw-Hill, New York.

[12] Levenspiel, O., 1998, *Engineering Flow and Heat Exchange*, Plenum, New York.

[13] Rowley, G. J., and Patankar, S. V., 1984, "Analysis of Laminar Flow and Heat Transfer in Tubes With Internal Circumferential Fins," Int. J. Heat Mass Transfer, **27**(4), pp. 553–560.

[14] Sieder, E. N., and Tate, G. E., 1936, "Heat Transfer and Pressure Drop of Liquids in Tubes," Ind. Eng. Chem., **28**(12), pp. 1429–1435.

[15] Grace, C. D., 1971, "'Static Mixing' and Heat Transfer," Chem. Process Eng., **52**(7), pp. 57–59.

J. Miwa

Y. Asako[1]
e-mail: asako@tmu.ac.jp

Department of Mechanical Engineering,
Tokyo Metropolitan University,
Hachioji, Tokyo, 192-0397, Japan

C. Hong
Department of Mechanical Engineering,
Tokyo University of Science,
Yamazaki, Noda, Chiba, 278-8501, Japan

M. Faghri
Department of Mechanical Engineering and
Applied Mechanics,
University of Rhode Island,
Kingston, RI 02881-0805

Performance of Gas-to-Gas Micro-Heat Exchangers

Heat transfer performance of two-stream parallel and counter-flow gas-to-gas micro-heat exchangers are investigated numerically. Flow passages are plane channels with heights in the range of 10–100 μm and selected lengths of 12.7 mm and 25.4 mm. Numerical methodology is based on the arbitrary-Lagrangian-Eulerian method. Computations were performed to find the effects of capacity ratio, channel height, and length on the heat transfer characteristics of micro-heat exchangers. To results are presented in the form of temperature contours, bulk temperatures, total temperatures, and heat flux variation along the channel. It was found that the temperature inversion occurs under certain conditions. Also, the effectiveness and the number of transfer units approach and the estimation of the heat exchange rate were discussed. The range of parameters where the predicted effectiveness agrees with the numerical result were investigated.
[DOI: 10.1115/1.3013828]

Keywords: heat exchanger, microscale, gas-to-gas, effectiveness, Ntu

Introduction

Since the early work by Tuckerman and Pease [1] on high performance heat sinks for very large scale integrated chip (VLSI), numerous experimental and numerical investigations have been undertaken on fluid flow and heat transfer characteristics of micro-channels. It is well known that gaseous flow characteristics in a micro-channel are affected by the combined effects of rarefaction (the slip on the surface), surface roughness, and compressibility. The compressibility effect on the fluid flow characteristics have been addressed by many researchers, e.g., Prud'homme et al. [2], Berg et al. [3], Guo and Wu [4], Sayegh et al. [5], and Sun and Faghri [6]. Recently, Asako et al. [7–9] performed experimental and numerical investigations to find the effect of compressibility for a wide range of Re and Ma numbers in plane micro-channels and tubes. It was found that $f \cdot \mathrm{Re}$ (the product of friction factor and Reynolds number) is a function of the Ma number in the quasi-fully developed region for cases where gaseous flow was accelerated.

A number of investigations on the heat transfer characteristics of gaseous flow in a plane micro-channels and a micro-tube have been conducted. Guo [10] performed numerical investigations on heat transfer characteristics of gaseous flow in a micro-channel. Asako et al. [11–15] conducted numerical investigations of heat transfer characteristics of gaseous flow in micro-channels and micro-tubes for both cases of constant wall temperature and heat flux.

Gas-to-gas heat exchangers are used for heat recovery of hot exhaust air in catalytic processes and industrial drying plants. Applications can be found in micro-reactors that are used in the fine chemical process industry. Since gas-to-gas heat exchangers occupy a large space in various energy systems, it is required to reduce its size.

The focus of previous investigators, i.e., Halbritter et al. [16] and Brandner et al. [17], was on liquid-to-liquid heat exchangers. The friction loss in this case is quite large and the pressure decreases along the channel. However, for gas-to-gas heat exchangers, the flow accelerates due to the gas expansion and thermal energy conversion to kinetic energy. This results in a static temperature decrease of the gas. There is a possibility that the averaged static temperature of a hot gas becomes lower than that of a cold gas near the exit. Therefore, the performance of micro-heat exchangers may differ from that of conventional sized heat exchangers. A careful search of the literature failed to disclose any prior study for the heat exchange performance of gas-to-gas micro-heat exchangers. This has motivated the present study.

Formulation

Description of the Problem. The problem is modeled as a two-stream heat exchanger, as shown in Fig. 1. Figures 1(*a*) and 1(*b*) show parallel and counter-flow cases, respectively. In Fig. 1(*a*), chambers at the stagnation temperatures $T_{\mathrm{stg}H}$ and $T_{\mathrm{stg}C}$ and the stagnation pressures $p_{\mathrm{stg}H}$ and $p_{\mathrm{stg}C}$ are attached to the upstream sections. The outer walls of the passages are adiabatic. As a preliminary study, the thickness of the partition plate between the passages is assumed to be zero. In this case, the temperature variation in the partition plate in the x-direction is the maximum. The effect of the thickness of the partition plate on the heat exchange characteristics will be investigated in the forthcoming publication. The computation was conducted for a steady two-dimensional laminar flow of an ideal gas. In Fig. 1(*b*), the hot chamber is attached to the right side of the heat exchanger.

The governing equations can be expressed as

$$\frac{\partial \rho u}{\partial x} + \frac{\partial \rho v}{\partial y} = 0 \tag{1}$$

$$\frac{\partial \rho u u}{\partial x} + \frac{\partial \rho u v}{\partial y} = -\frac{\partial p}{\partial x} + \mu\left(\frac{\partial^2 u}{\partial x^2} + \frac{\partial^2 u}{\partial y^2}\right) + \frac{\mu}{3}\frac{\partial}{\partial x}\left(\frac{\partial u}{\partial x} + \frac{\partial v}{\partial y}\right) \tag{2}$$

$$\frac{\partial \rho u v}{\partial x} + \frac{\partial \rho v v}{\partial y} = -\frac{\partial p}{\partial y} + \mu\left(\frac{\partial^2 v}{\partial x^2} + \frac{\partial^2 v}{\partial y^2}\right) + \frac{\mu}{3}\frac{\partial}{\partial y}\left(\frac{\partial u}{\partial x} + \frac{\partial v}{\partial y}\right) \tag{3}$$

$$\frac{\partial \rho u i}{\partial x} + \frac{\partial \rho v i}{\partial y} = -p\left(\frac{\partial u}{\partial x} + \frac{\partial v}{\partial y}\right) + \lambda\left(\frac{\partial^2 T}{\partial x^2} + \frac{\partial^2 T}{\partial y^2}\right) + \Phi \tag{4}$$

[1]Corresponding author.

Contributed by the Heat Transfer Division of ASME for publication in the JOURNAL OF HEAT TRANSFER. Manuscript received January 25, 2008; final manuscript received September 30, 2008; published online March 18, 2009. Review conducted by Sai C. Lau. Paper presented at the 2006 ASME International Mechanical Engineering Congress (IMECE2006), Chicago, IL, November 5–10, 2006.

where

$$\Phi = 2\mu\left[\left(\frac{\partial u}{\partial x}\right)^2 + \left(\frac{\partial v}{\partial y}\right)^2\right] - \frac{2\mu}{3}\left(\frac{\partial u}{\partial x} + \frac{\partial v}{\partial y}\right)^2 + \mu\left(\frac{\partial u}{\partial y} + \frac{\partial v}{\partial x}\right)^2 \tag{5}$$

The equation of the state for the ideal gas is expressed by

$$i = \frac{1}{\gamma - 1}\frac{p}{\rho} = \frac{R}{\gamma - 1}T \tag{6}$$

Furthermore, with the assumptions of a no slip boundary condition, uniform inlet velocity, pressure and density, and specified pressure p_{out} at the outlet, the boundary conditions can be expressed as follows:

(a) On the walls.

For $y = \pm h$, : $u = v = 0$, $\partial T/\partial y = 0$

For $y = 0$, : $u = v = 0$, $(\partial T/\partial y)_{y=0^+} = (\partial T/\partial y)_{y=0^-}$

(b) At the inlet of passages

For hot passage, : $u = u_{inH}$, $v = 0$, $p = p_{inH}$, $\rho = \rho_{inH}$, $i = i_{inH}$

For cold passage, : $u = u_{inC}$, $v = 0$, $p = p_{inC}$, $\rho = \rho_{inC}$, $i = i_{inC}$

(c) At the outlet of both passages,

For both passages, : $p = p_{out}$ (7)

It can be shown that the slip effect of channels with height is in the range of 10–100 μm is negligibly small [18].

Velocity, pressure, and density at the inlet of the channel are obtained by the stagnation treatment given by Karki [19]. Stagnation pressure can be expressed in terms of the inlet pressure, velocity, and specific internal energy, as follows:

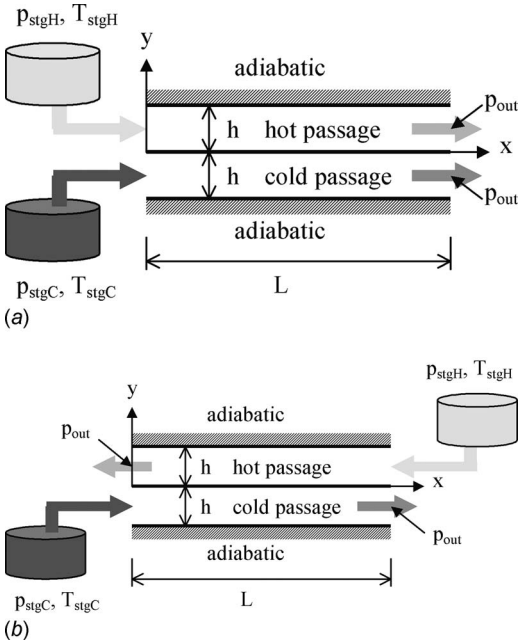

Fig. 1 A schematic of a problem (*a*) parallel-flow (*b*) counter-flow

Table 1 Cell size effect on heat exchange rate

Cell	$\dot{Q}$ (W/m)	Change
100×20	184.479	−0.10%
100×30	185.107	0.24%
200×20	184.671	—
200×30	185.318	0.35%
400×20	184.673	0.001%
400×30	184.947	0.15%

$$p_{stg} = p_{in}\left[1 + \frac{1}{2}\frac{|u_{in}|^2}{\gamma i_{in}}\right]^{(\gamma/\gamma-1)} \tag{8}$$

Also, from the ideal gas law, the relationship for pressure and density between stagnation and inlet point can be expressed as

$$\frac{p_{stg}}{{\rho_{stg}}^{\gamma}} = \frac{p_{in}}{{\rho_{in}}^{\gamma}} \tag{9}$$

Static pressure at the inlet can be obtained from a linear extrapolation from the interior of the computational domain. By substituting the extrapolated pressure and the stagnation pressure into Eq. (9), the inlet density is obtained. Then, using the equation, the specific internal energy at the inlet can be found. Finally, the inlet velocity can be determined by substituting these values into Eq. (8). The procedure is repeated until convergence is achieved.

Reynolds Number and Mach Number. Attention will now be focused on the calculation of the Reynolds and Mach numbers that will be defined as

$$\mathrm{Re} = \frac{2\dot{m}}{\mu} = \frac{|\bar{u}|D_h}{\mu/\bar{\rho}}, \quad \mathrm{Ma} = \frac{|\bar{u}|}{\sqrt{\gamma(\gamma-1)\bar{i}}} \tag{10}$$

where $\dot{m}$ is the mass flow rate per unit depth and D_h is the hydraulic diameter (=2h). $\bar{u}$, $\bar{\rho}$, and $\bar{i}$ are the average velocity, density, and specific internal energy at the cross section of a passage.

$$\bar{u} = \frac{1}{h}\int u dy, \quad \bar{\rho} = \int \rho u dy \Big/ \int u dy$$

$$\bar{p} = \frac{1}{h}\int p dy, \quad \bar{i} = \frac{1}{\gamma - 1}\frac{\bar{p}}{\bar{\rho}} \tag{11}$$

Numerical Solutions. The numerical methodology is based on the Arbitrary-Lagrangian-Eulerian (ALE) method proposed by Amsden et al. [20]. The detailed description of the ALE method is documented in the literature and will not be presented. The computational domain is divided into quadrilateral cells. The velocity components are defined at the vertices of the cell and other variables such as pressures, specific internal energy, and density are assigned at the cell centers. The number of cells in the x-direction was 200, 400, or 600 depending on the height of the passage and the gas velocity. The cell size gradually increases in x-direction from the inlet to the middle of the passage, and it gradually decreases to the outlet. The number of cells in the y-direction of each passage was fixed at 20 or 30. The cell size effect on the heat exchange rate was supplementary examined for a case of $h = 100$ μm and $\mathrm{Ma}_{outH} \approx \mathrm{Ma}_{outC} \approx 0.3$. The results are tabulated in Table 1. The change in the heat exchange rate on the basis of 200×20 cells is quite small. The majority of the computations were conducted with 200×20 cells for each passage. The computation for a small passage and high velocity flows were performed with increased number of cells. The cell size effect for a single passage is well documented in Ref. [9].

The ALE method is a time marching method. The value of 10^{-9} was chosen for the minimum time step. The convergence for the

Table 2 Parameters

h	10 μm, 20 μm, 50 μm, 100 μm
L	12.7 mm, 25.4 mm
T_{stgH}	350 K
T_{stgC}	300 K
P_{stgH}	($Ma_{outH} \approx 0.1-0.15$, 0.15–0.3, 0.3–0.6, 0.6–0.8)
P_{stgC}	($Ma_{outC} \approx 0.1-0.15$, 0.15–0.3, 0.3–0.6, 0.6–0.8)
P_{out}	100 kPa

time increment was confirmed by inequalities $|\Delta\dot{m}/\dot{m}| < 10^{-10}$, where $\Delta\dot{m}$ represents a change in the mass flow rate per time step. The value of 10^{-4} was used for the convergence criterion of the Newton–Raphson iteration in the interior loop of the ALE method.

The computations were performed for the stagnation temperatures of $T_{stgH}=350$ K and $T_{stgC}=350$ K for both parallel and counter-flow cases with air as the working fluid. When air temperature ranges from 250 K to 350 K, C_p, μ, and λ of air vary from 1.005 kJ/(kg K) to 1.019 kg/(kJ K), from 1.59×10^{-5} Pa s to 2.025×10^{-5} Pa s, and from 0.0226 W/(m K) to 0.0293 W/(m K), respectively. The changes in these values are relatively small. Therefore, constant properties are assumed except for the density. The thermo-physical properties of $R=287$ J/(kg K), $\gamma=1.4$, $\mu=1.862\times10^{-5}$ Pa s, and $\lambda=0.0261$ W/(m K) at 300 K were used for the computations. The selected channel heights h were 10 μm, 20 μm, 50 μm, and 100 μm, and the selected channel lengths were 12.7 mm and 25.4 mm. The computations were conducted for cases where both channel heights are identical. All combinations of the channel heights and lengths were computed. The outlet pressure maintained at an atmospheric condition $p_{out}=10^5$ Pa. The stagnation pressures p_{stgH} and p_{stgC} were varied between 1.2×10^5 Pa and 2×10^6 Pa and were selected in such a way that the computed Mach numbers at the outlet ranges from 0.07 to 0.8. The Reynolds numbers calculated were in the range from 20 to 3800. Re number of 3800 is out of the conventional laminar flow range. However, there is a possibility that the flow is laminar since the relaminarization due to the flow acceleration has been reported (e.g., Ref. [21,22]). The channel heights, lengths, and the stagnation pressures are listed in Table 2. A total of 128 cases were computed for each case.

Results of Parallel-Flow

Temperature Contours. Temperature contour plots for the typical combination of high and low flows in each passage are presented in Fig. 2. Figures 2(*a*)–2(*d*) are the results of $h=50$ μm and $L=12.7$ mm. The mass flow rate per unit depth of each passage can be calculated from Reynolds number using Eq. (10). Figure 2(*a*) is the result for the case where flows in both passages are low. In this case, no temperature decrease near the outlets is observed. In the case of fast flows, the temperature decrease can be seen near the outlet of the cold passage in Fig. 2(*b*), near the outlet of the hot passage in Fig. 2(*c*), and near the outlets of the both passages in Fig. 2(*d*). This is due to the energy conversion to the kinetic energy. As seen in Fig. 2(*c*), it is obvious that the average temperature of the cross section of the hot passage is lower than that of the cold passage near the outlet due to the temperature decrease. This temperature inversion is only observed in the case of the combination of high flow in the hot passage and low flow in the cold passage of all heights. The temperature contours for $h=10$ μm and 20 μm are not plotted in the figure. However, in most cases of $h=10$ μm and 20 μm, the temperature near the corner of the inlet and the adiabatic wall of the hot passage becomes higher than the stagnation temperature because of the viscous heat generated.

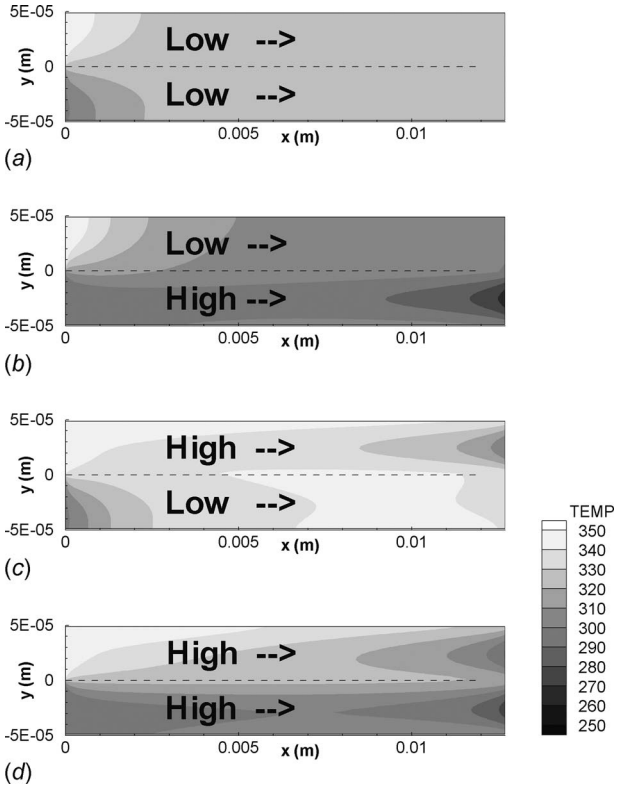

Fig. 2 Contour plots of temperature ($h=50$ μm and $L=12.7$ mm); (*a*) $Re_H=168.7$ ($Ma_{outH}=0.081$) and $Re_C=170.5$ ($Ma_{outC}=0.082$), (*b*) $Re_H=177.4$ ($Ma_{outH}=0.082$) and $Re_C=1458.5$ ($Ma_{outC}=0.643$), (*c*) $Re_H=1326.4$ ($Ma_{outH}=0.622$) and $Re_C=163.6$ ($Ma_{outC}=0.080$), and (*d*) $Re_H=1360.2$ ($Ma_{outH}=0.625$) and $Re_C=1425.0$ ($Ma_{outC}=0.641$)

Bulk Temperature. Attention will now be turned to the bulk temperature of the fluid (averaged static temperature at a cross section) T_b, and it is defined as

$$T_b = \int \rho C_p u T dy \Big/ \int \rho C_p u dy \tag{12}$$

The T_b for each of the four cases in Fig. 2 is plotted as a function of x/L in Fig. 3. As seen in Fig. 3(*a*), when both flows are low, the bulk temperature of the hot passage decreases gradually, in con-

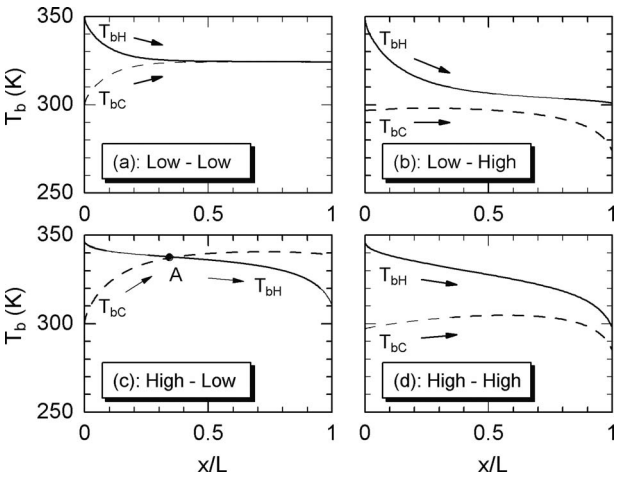

Fig. 3 Bulk temperature for $h=50$ μm and $L=12.7$ mm

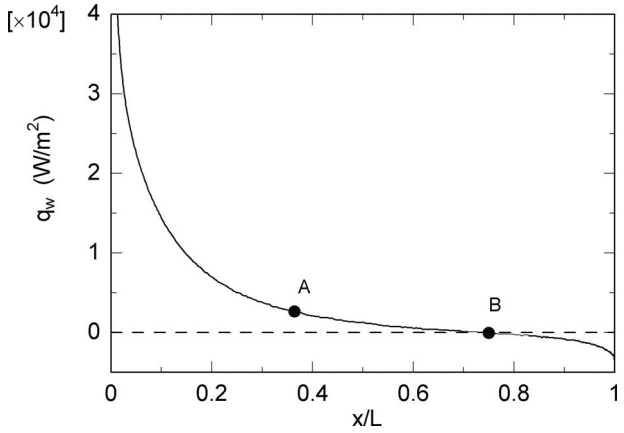

Fig. 4 Heat flux from hot passage to cold passage for case of Fig. 2(*c*)

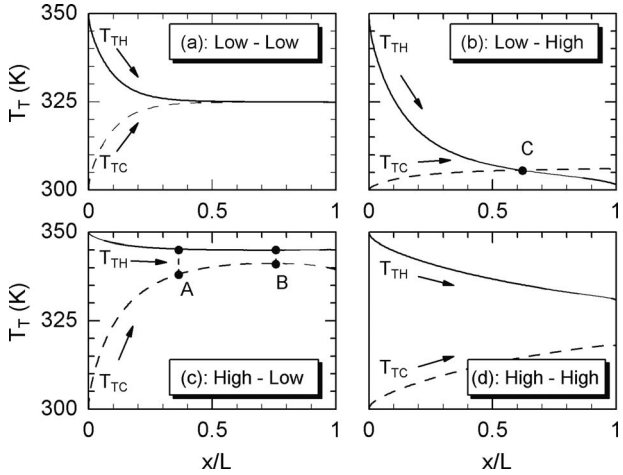

Fig. 5 Total temperature for $h=50$ μm and $L=12.7$ mm

trary, the bulk temperature of the cold passage increases gradually. The result shows similar trends of temperature responses as in a conventional sized heat exchanger. However, when the flow in the hot passage is much higher than that in the cold passage (Fig. 3(*c*)), both bulk temperatures cross at point A. In this case, the bulk temperature of the cold passage is higher than that of the hot passage in the downstream section from point A. This is due to the energy conversion. Temperature inversion is observed for all cases of $\mathrm{Re}_H > \mathrm{Re}_C$ ($\mathrm{Ma}_{\mathrm{out}H} > \mathrm{Ma}_{\mathrm{out}C}$) with the exception of $h=100$ μm. In the case of $h=100$ μm, temperature inversion is observed only in the cases of $\mathrm{Re}_H \gg \mathrm{Re}_C$ ($\mathrm{Ma}_{\mathrm{out}H} \gg \mathrm{Ma}_{\mathrm{out}C}$) because the relative passage length is short.

Heat Flux. The heat flux from the hot passage to the cold passage for the case of high and low flows (Fig. 3(*c*)), is plotted in Fig. 4. As shown in Fig. 3(*c*), the bulk temperature of the hot passage is lower than that of the cold passage in the downstream section from point A. However, the heat flux from the hot passage to the cold passage still takes a positive value beyond point A. The heat flux takes a negative value beyond point B. This result suggests that in the case of the gas-to-gas micro-heat exchanger, the bulk temperature (the averaged static temperature at the cross section) is not suitable for a characteristic temperature of heat transfer from the hot passage to the cold passage.

Total Temperature. Attention will now be turned to the total temperature of the fluid T_T, and it is defined as

$$T_T = \frac{\int \rho C_p u T dy + \int \rho u \frac{u^2}{2} dy}{\int \rho C_p u dy} \tag{13}$$

The values of T_T for all four cases in Fig. 2 are plotted as the function of x/L in Fig. 5. In the case of high and low flows (Fig. 5(*c*)), where the bulk temperature inversion is observed, the total temperature of the cold passage continually increases in the section from points A to B, and the total temperature of the hot passage continually decreases in the same section. Since the heat flux from the hot passage to the cold passage in the section from points A to B is positive, the total temperature response in this section is physically explained. The total temperature of the cold passage decreases beyond point B, and the total temperature of the hot passage increases beyond point B. These temperature responses can be physically explained from the negative heat flux in this section.

As seen in Fig. 5(*b*), total temperatures crosses at point C. Flow in the hot passage is much slower than that in the cold passage. The heat balance of the flows in the hot and cold passages can be confirmed by the total temperatures at the inlets and outlets of both passages. In this case, the heat balance is satisfied and the phenomenon is physically explained. The total temperature inversion is observed in 38 cases of $\mathrm{Re}_H < \mathrm{Re}_C$ ($\mathrm{Ma}_{\mathrm{out}H} < \mathrm{Ma}_{\mathrm{out}C}$) with the exception of $h=100$ μm. In the case of $h=100$ μm, the total temperature inversion is not observed because of the relatively short passage length.

Ntu and ε. The number of transfer units Ntu, the effectiveness ε and the capacity ratio R_c, are often used for the heat exchange performance analysis of heat exchangers. Those are defined as [23]

$$\mathrm{Ntu} = \frac{\mathrm{KA}}{(\dot{m}c_p)_{\min}}, \quad \varepsilon = \frac{\dot{Q}}{(\dot{m}c_p)_{\min}(T_{T\mathrm{in}H} - T_{T\mathrm{in}C})}$$

$$R_c = \frac{(\dot{m}c_p)_{\min}}{(\dot{m}c_p)_{\max}} \tag{14}$$

where K is the overall heat transfer coefficient, and $\dot{Q}$ is the heat transfer rate per unit depth and are expressed as

$$K = \frac{\dot{Q} \ln \frac{T_{\mathrm{out}H} - T_{\mathrm{out}C}}{T_{\mathrm{in}H} - T_{\mathrm{in}C}}}{(T_{\mathrm{out}H} - T_{\mathrm{out}C} - T_{\mathrm{in}H} + T_{\mathrm{in}C})} \frac{1}{A} \tag{15}$$

$$\dot{Q} = (\dot{m}c_p)_H (T_{T\mathrm{in}H} - T_{T\mathrm{out}H}) = (\dot{m}c_p)_C (T_{T\mathrm{out}C} - T_{T\mathrm{in}C}) \tag{16}$$

Substituting Eq. (15) into Eq. (14), we obtain

$$\mathrm{Ntu} = \frac{\dot{Q} \ln \frac{T_{\mathrm{out}H} - T_{\mathrm{out}C}}{T_{\mathrm{in}H} - T_{\mathrm{in}C}}}{(\dot{m}c_p)_{\min}(T_{\mathrm{out}H} - T_{\mathrm{out}C} - T_{\mathrm{in}H} + T_{\mathrm{in}C})} \tag{17}$$

Note that the static temperature is used to calculate the effectiveness ε and the heat transfer rate $\dot{Q}$ in a conventional sized heat exchanger analysis. However, the kinetic energy is not negligible when flow is high. In such a case, the total temperatures should be used to calculate the effectiveness ε and the heat transfer rate.

The effectiveness is obtained from the computed total temperatures at the inlet and the outlet for all cases. The effectiveness obtained is below unity with the exception of two cases of $h=10$ μm whose Ma numbers are $\mathrm{Ma}_{\mathrm{out}H} < 0.1$ and $\mathrm{Ma}_{\mathrm{out}C} = 0.6-0.8$. In this case, the flow in the cold passage is high and the static temperature at the outlet decreases. This results in temperature decrease in the hot passage. The static temperature contour near the outlet is presented in Fig. 6. Note that Fig. 6 is concentrated near the outlet and the scale of the x-direction differs from that in Fig. 2. The static temperature at the midheight of the outlet

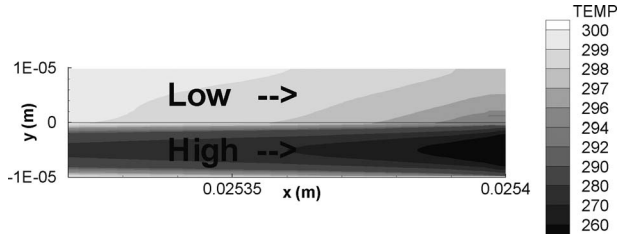

Fig. 6 Temperature contour near outlet for $h=10\ \mu$m, $L=25.4$ mm, $Re_H=26.1$ ($Ma_{outH}=0.06$), and $Re_C=416.4$ ($Ma_{outC}=0.792$)

of the cold passage is below 250 K. This results in the static temperature decrease in the hot passage. The static temperature at the outlet of the hot passage is below 300 K. Since the flow in the hot passage is low, the total temperature is almost equal to the static temperature. Then, T_{ToutH} is below T_{TinC} and the effectiveness becomes greater than unity. The highest effectiveness obtained is 1.07.

Although, we do not know for sure, the static temperature or the total temperature is more suitable for the calculation of the transfer unit Ntu, the total temperatures at the inlet and outlet are used to calculate the number of transfer unit. Note that in the case of Fig. 5(*b*) where the total temperature inversion is observed, the value of the fraction in logarithmic function of Eq. (17) takes a negative value and the Ntu value cannot be obtained. The value of the fraction takes a negative value in 38 cases of $Re_H<Re_C$ ($Ma_{outH}<Ma_{outC}$) of $h=10\ \mu$m, 20 μm, and $h=50\ \mu$m. The value of the fraction takes a positive value in all cases of 100 μm. The effectiveness ε for all the calculable cases are plotted in Fig. 7 as a function of Ntu. In the case of the parallel-flow, ε is expressed by Ntu and R_c as [23]

$$\varepsilon = \frac{1}{1+R_c}[1-\exp\{-\mathrm{Ntu}(1+R_c)\}] \tag{18}$$

The correlations given by Eq. (18) are also plotted in Fig. 7 with R_c as a curve parameter. Since ε and Ntu of the calculable cases satisfy the correlation of Eq. (18), it is natural that ε and Ntu obtained from the simulation results agree with Eq. (18).

Therefore, if the overall heat transfer coefficient K can be estimated accurately, the heat exchange rate of a two-stream parallel-flow gas-to-gas micro-heat exchanger can be estimated via Eq. (18) for the calculable cases. The heat transfer coefficient for parallel plates with one wall at a uniform temperature and the other wall insulated was obtained by many researchers [24] and one of the correlations by Mercer et al. [25] is

$$\mathrm{Nu}_m = 4.86 + \frac{0.32(4x^*)^{-1.2}}{1+0.24(4x^*)^{-0.7}\,\mathrm{Pr}^{0.17}} \tag{19}$$

where $x^*=(x/D_h\mathrm{RePr})$ The averaged heat transfer coefficients of the hot and cold passages α_{mH} and α_{mC}, are obtained from Eq. (19). Then, substituting those values into the following equation, the overall heat transfer coefficient K is obtained.

$$\frac{1}{K} = \frac{1}{\alpha_{mH}} + \frac{1}{\alpha_{mC}} \tag{20}$$

Substituting K into Eq. (14), the number of transfer units Ntu can be obtained. Finally, the effectiveness ε is obtained from Eq. (18). The ratio of the estimated effectiveness and the simulated resultn $\varepsilon_{est}/\varepsilon_{sim}$ is plotted in Fig. 8 as a function of the capacity ratio R_c. There is a trend that the estimated effectiveness ε_{est} is greater than the simulated one ε_{sim} in the cases of $Re_H<Re_C$ ($Ma_{outH}<Ma_{outC}$). In the cases of $Re_H>Re_C$ ($Ma_{outH}>Ma_{outC}$), the ε_{est}, is less than the ε_{sim}. When the capacity ratio R_c, is in the range of 0.5–1, the effectiveness can be estimated within $\pm 10\%$ in error. The estimation error decreases with increasing the capacity ratio. When the capacity ratio is unity, the effectiveness can be estimated within $\pm 2\%$ in error.

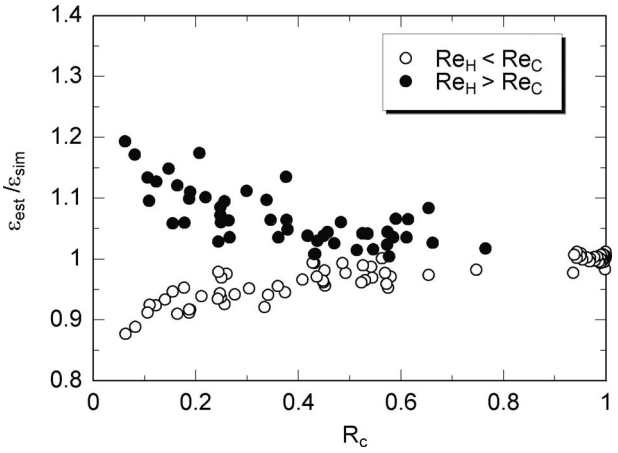

Fig. 8 Ratio of estimated effectiveness and the simulated result $\varepsilon_{est}/\varepsilon_{sim}$ as a function of R_c

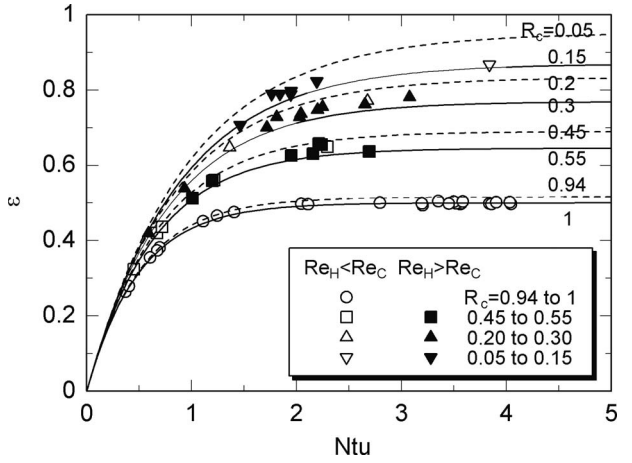

Fig. 7 Effectiveness ε as a function of Ntu

Results of Counter-Flow

Temperature Contours. Temperature contour plots for the typical combination of high and low flows in each passage are presented in Fig. 9. Figures 9(*a*)–9(*d*) are the results of $h=50\ \mu$m and $L=12.7$ mm. The mass flow rate per unit depth of each passage can be calculated from Reynolds number using Eq. (10). Figure 9(*a*) is the result for the case where both flows are low. In this case, no temperature decrease near the outlets is observed. In the case of high flows, the temperature decrease can be seen near the outlet of the cold passage in Fig. 9(*b*), the outlet of the hot passage in Fig. 9(*c*), and the outlets of the both passages in Fig. 9(*d*). This is due to the energy conversion to the kinetic energy. The temperature contours for $h=10\ \mu$m and 20 μm are not plotted in the figure. However, in most cases of $h=10\ \mu$m and 20 μm, the temperature near the corner of the inlet and the adiabatic wall of the hot passage (upper right corner of the figures) becomes higher than the stagnation temperature because of the viscous heat generation.

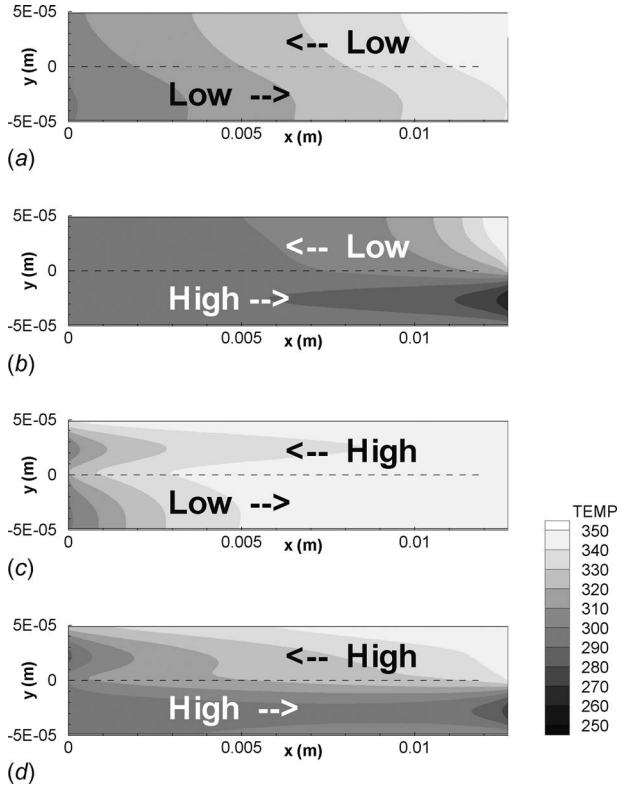

Fig. 9 Contour plots of temperature for parallel-flows (h =50 μm and L=12.7 mm); (*a*) Re_H=168.4 (Ma_{outH}=0.079) and Re_C=171.0 (Ma_{outC}=0.084), (*b*), Re_H=180.0 (Ma_{outH}=0.083) and Re_C=1472.0 (Ma_{outC}=0.643), (*c*) Re_H=1320.0 (Ma_{outH}=0.671) and Re_C=162.3 (Ma_{outC}=0.081), and (*d*) Re_H=1360.9 (Ma_{outH}=0.621) and Re_C=1430.4 (Ma_{outC}=0.640)

Bulk Temperature. The T_b for each of the four cases in Fig. 9 is plotted as a function of x/L in Fig. 10. As seen in Fig. 10(*a*), when both flows are low, the bulk temperature of the hot passage decreases linearly, in contrary, the bulk temperature of the cold passage increases linearly. The result shows similar trends of temperature responses as in a conventional sized two-stream heat exchanger model. However, when the flow in the hot passage is much higher than that in the cold passage (Fig. 10(*c*)), both bulk temperatures cross at point A. In this case, the bulk temperature of the cold passage is higher than that of the hot passage in the right

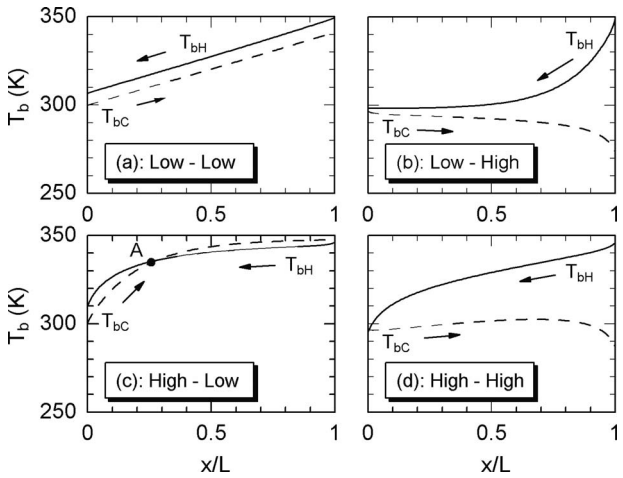

Fig. 10 Bulk temperature for h=50 μm and L=12.7 mm

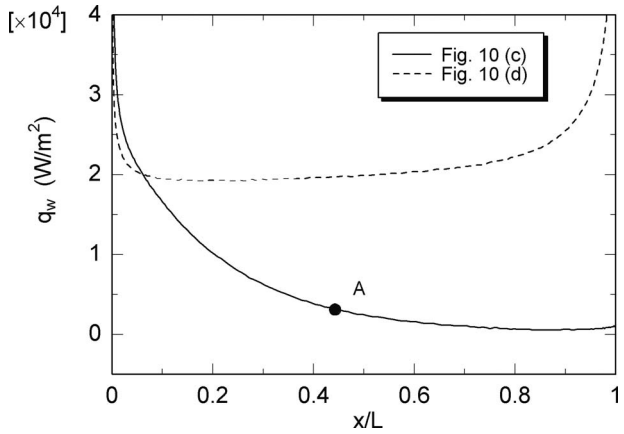

Fig. 11 Heat flux from hot passage to cold passage for case (*c*) of L=12.7 mm

hand side of point A. That is, the bulk temperature of the hot passage is lower than that of the cold passage at the inlet of the hot passage. In this case, the inlet velocity of the hot passage is 89.2 m/s (Ma_{inH}=0.239), the bulk temperature decreases about 4 K due to the energy conversion into kinetic energy. However, the gas velocity becomes 0 on the partition plate. The gas temperature recovers to 350 K near the plate. Then, the temperature of the flow in the cold passage approaches 350 K and the temperature inversion occurs. This type of temperature inversion is observed in the cases of $Re_H \gg Re_C$ ($Ma_{outH} \gg Ma_{outC}$), when the height of the passage is 50 μm.

There is another type of temperature inversion. This type of temperature inversion can be seen at the outlet of the hot passage in Fig. 10(*d*). This type of temperature inversion occurs at the location very close to x=0. The temperature decreases at the outlet of the hot passage due to the energy conversion when the flow in the hot passage is high. This type of temperature inversion occurs in the cases of $Re_H \gg Re_C$ ($Ma_{outH} \gg Ma_{outC}$) and h =100 μm, in the cases of Ma_{outH} and $Ma_{outC} > 0.6$ and h =50 μm, and in most cases of h=10 μm and 20 μm.

Heat Flux. The heat fluxes from the hot passage to the cold passage for the cases in Figs. 10(*c*) and 10(*d*) are plotted in Fig. 11. As shown in Fig. 10(*c*), the bulk temperature of the hot passage is lower than that of the cold passage in the right section from point A. However, the heat flux from the hot passage to the cold passage takes a positive value in the right section from point A. Also, the heat flux for the case of Fig. 10(*d*) takes a positive value near x/L=0 where the bulk temperature inversion is observed. These results suggest that in the case of the gas-to-gas micro-heat exchanger, the bulk temperature (the averaged static temperature at the cross section) is not suitable for a characteristic temperature of heat transfer from the hot passage to the cold passage.

Total Temperature. The values of T_T for four cases of Figs. 9(*a*)–9(*d*) are plotted as the function of x/L in Fig. 12. In the case of *c*, where the bulk temperature inversion occurs, the total temperature of the cold passage continually increases in the right section from point A and the total temperature of the hot passage continually decreases in the same section. Since the heat flux from the hot passage to the cold passage in the right section from point A is positive, this total temperature response in this section is physically explained.

As seen in Fig. 12(*b*), the total temperatures cross at point C. The total temperature inversion is observed in a case where the flow in the hot passage is much lower than that in the cold passage. The heat balance of the flows in the hot and cold passages can be confirmed by the total temperatures at the inlets and outlets

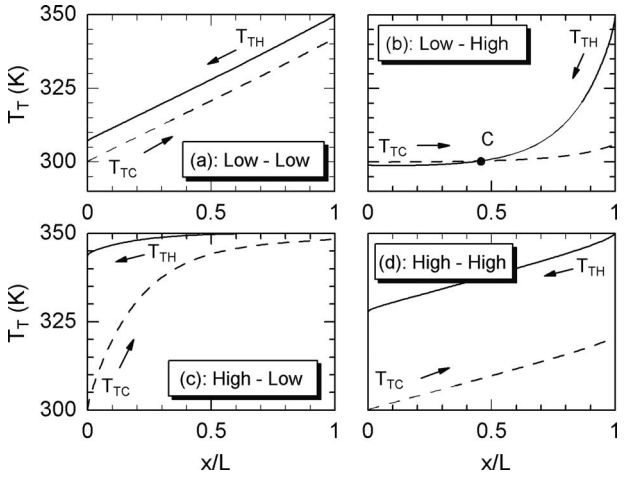

Fig. 12 Total temperature for h=50 μm and L=12.7 mm

of both passages. In this case the heat balance is satisfied. The flow in the cold passage is high and the static temperature at the inlet decreases. This results in a temperature decrease in the flow at the outlet of the hot passage. The static temperature contour near the outlet of the hot passage (the inlet of the cold passage) is presented in Fig. 13. Note that Fig. 13 is concentrated near x=0 and the scale of the x-direction differs from that in Fig. 9. The static temperature at the inlet of the cold passage is below 300 K, since the flow is high. This results in the temperature decrease in the hot passage. The static temperature at the outlet of the hot passage becomes below 300 K, as shown in Fig. 13. Since the flow in the hot passage is low, the total temperature is almost equal to the static temperature. Then, T_{ToutH} becomes lower than T_{TinC}.

Figure 12(c) shows the total temperature response for the case where the flow in the hot passage is much higher than that in the cold passage. No temperature inversion occurs in the cases of h =50 μm and 100 μm. However, the total temperature inversion occurs in the cases of h=10 μm and 20 μm. The total temperature near the outlet of the cold passage for h=10 μm is plotted in Fig. 14(a). The static temperature contour near the outlet of the cold passage (the inlet of the hot passage) for this case is presented in Fig. 14(b). The Ma number at the outlet of the cold passage is 0.162 and the Ma at the inlet of the hot passage is 0.066. The dynamic temperature of the flow at the outlet of the cold passage is about 3 K. Therefore, the total temperature of the flow in the cold passage is beyond 350 K. Then, the T_{ToutC} becomes slightly higher than T_{TinH}.

Ntu and ε. The effectiveness is obtained from Eq. (14) by using the computed total temperatures at the inlet and outlet for all cases. The effectiveness obtained for some cases are greater than unity. This happens when the total temperature inversion occurs, $T_{ToutH} < T_{TinC}$ or $T_{TinH} < T_{ToutC}$. The former temperature inversion occurs in the cases of $\mathrm{Re}_H < \mathrm{Re}_C$ ($\mathrm{Ma}_{outH} < \mathrm{Ma}_{outC}$) when the

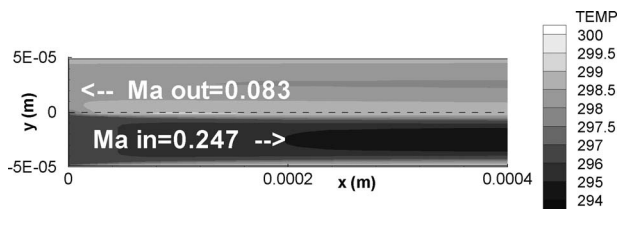

Fig. 13 Temperature contour near x=0 of Fig. 12(b) (h =50 μm and L=12.7 mm) [Re_H=180.0 (Ma_{outH}=0.083) and Re_C =1472.0 (Ma_{outC}=0.643)]

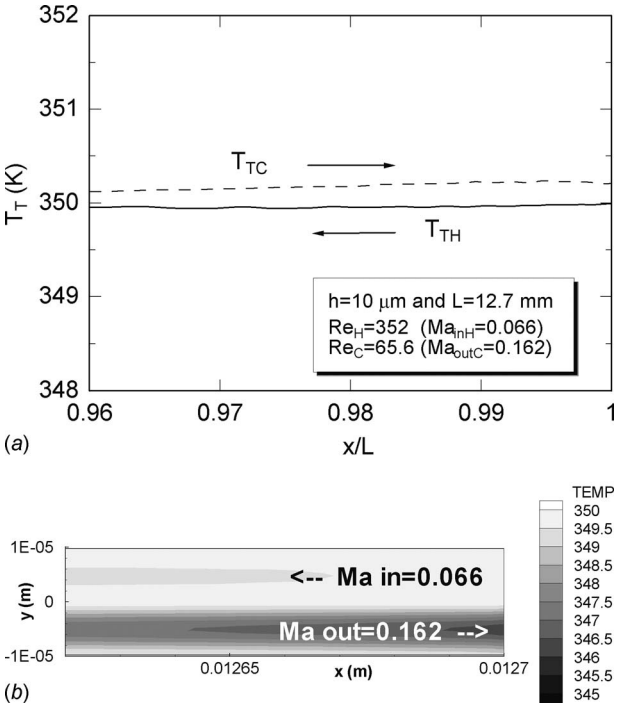

Fig. 14 Total temperature and temperature contour near x=L for h=10 μm and L=12.7 mm [Re_H=352.0 (Ma_{outH}=0.0747) and Re_C=65.6 (Ma_{outC}=0.162)]; (a) total temperature (b) temperature contour

height of the passage is 10 μm or 20 μm and in the cases of $\mathrm{Ma}_{outH} < 0.1$ and $\mathrm{Ma}_{outC} > 0.4$ when the height of the passage is 50 μm. This type of the temperature inversion occurs in 27 cases out of 128 cases. The latter temperature inversion occurs in 11 cases of $\mathrm{Re}_H > \mathrm{Re}_C$ ($\mathrm{Ma}_{outH} > \mathrm{Ma}_{outC}$) when the height of the passage is 10 μm or 20 μm. In those cases, the effectiveness becomes greater than unity.

The total temperatures at the inlet and outlet are used to calculate the number of transfer unit. Note that the value of the fraction in logarithmic function of Eq. (17) takes a negative value and Ntu value cannot be obtained when the total temperature inversion occurs $T_{ToutH} < T_{TinC}$ or $T_{TinH} < T_{ToutC}$. In the case of the counterflow, when the total temperature inversion occurs, the Ntu value is uncalculable and also the effectiveness becomes greater than unity. The effectiveness ε for all the calculable cases are plotted in Fig. 15 as a function of Ntu. In the case of the counterflow, ε is expressed by Ntu and R_c as [23]

$$\varepsilon = \frac{1 - \exp\{-\mathrm{Ntu}(1 - R_c)\}}{1 - R_c \exp\{-\mathrm{Ntu}(1 - R_c)\}} \quad (R_c \neq 1)$$

$$\varepsilon = \frac{\mathrm{Ntu}}{1 + \mathrm{Ntu}} \quad (R_c = 1) \tag{21}$$

The correlations given by Eq. (21) are also plotted in Fig. 15 with R_c as a curve parameter. Since ε and Ntu of the calculable cases satisfy the correlation of Eq. (21), it is natural that ε and Ntu obtained from the simulation results agree with Eq. (21).

Therefore, if the overall heat transfer coefficient K can be estimated accurately, the heat exchange rate of a two-stream counterflow gas-to-gas micro-heat exchanger can be estimated via Eq. (21) for the calculable cases. The averaged heat transfer coefficients of the hot and cold passages α_{mH} and α_{mC} are obtained from Eq. (19). Then, substituting those values into Eq. (20), the overall heat transfer coefficient K is obtained. Substituting K into Eq. (14), the number of transfer units Ntu can be obtained. Fi-

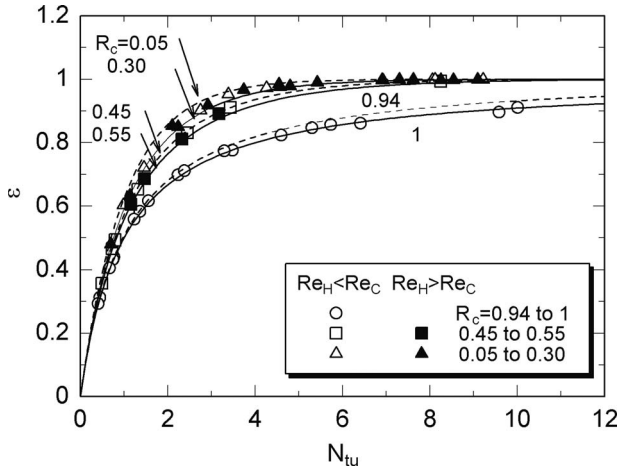

Fig. 15 Effectiveness ε as a function of Ntu

nally, the effectiveness ε is obtained from Eq. (21). The ratio of the estimated effectiveness and the simulated result $\varepsilon_{est}/\varepsilon_{sim}$ is plotted in Fig. 16 as a function of the capacity ratio R_c. There is a trend that the ratio of the estimated effectiveness and the simulated result $\varepsilon_{est}/\varepsilon_{sim}$ ranges from 0.86–1.03 in the cases of $Re_H < Re_C$ ($Ma_{outH} < Ma_{outC}$). In the cases of $Re_H > Re_C$ ($Ma_{outH} > Ma_{outC}$) the ratio ranges from 0.97–1.05. The effectiveness obtained from Eq. (14) is always below unity and it cannot be estimated for the case of $\varepsilon > 1$. In the case of the counter-flow, the estimation error does not depend on the capacity ratio.

Concluding Remarks

Two-stream gas-to-gas micro-heat exchanger has been investigated numerically. The computations were performed to obtain the heat exchange performance of a micro-heat exchanger. The following conclusions are obtained.

Parallel-Flow

(1) The bulk (static) temperature of the flow in the hot passage becomes lower than that of the cold passage) for all cases of $Re_H > Re_C$ ($Ma_{outH} > Ma_{outC}$) with the exception of $h = 100$ μm. In the case of $h = 100$ μm, the temperature inversion is observed in only the cases of $Re_H \gg Re_C$ ($Ma_{outH} \gg Ma_{outC}$).

(2) The total temperature of the flow in the hot passage 1 becomes lower than that of the cold passage for all cases of $Re_H < Re_C$ ($Ma_{outH} < Ma_{outC}$) with the exception of $h = 100$ μm.

(3) The effectiveness ε is greater than unity in the case of $Ma_{outH} < 0.1$ and $Ma_{outC} = 0.6–0.8$ and $h = 10$ μm.

(4) The effectiveness of a two-stream gas-to-gas micro-heat exchanger in the range of $0.5 < R_c < 1$ can be estimated via Eq. (18) within $\pm 10\%$ in error when the overall heat transfer coefficient K is obtained from Eqs. (19) and (20).

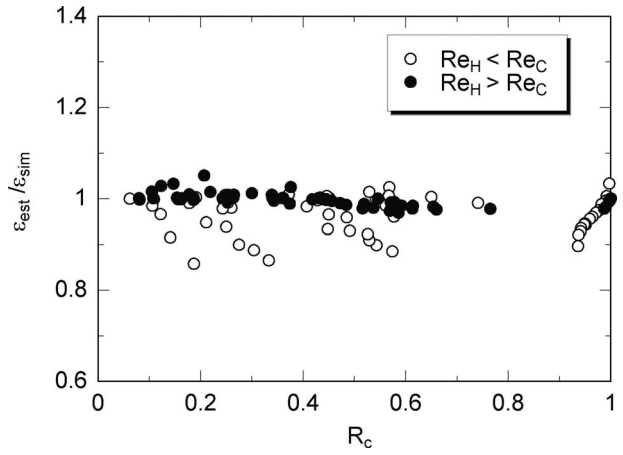

Fig. 16 Ratio of estimated effectiveness and the simulated result $\varepsilon_{est}/\varepsilon_{sim}$ as a function of R_c

Counter-Flow

(1) The bulk (static) temperature inverse occurs and there are two types of the bulk temperature inverse $T_{boutH} < T_{binC}$ and $T_{binH} < T_{boutC}$.

(2) There are two types of the total temperature inversion $T_{ToutH} < T_{TinC}$ and $T_{TinH} < T_{ToutC}$. The former temperature inversion occurs in the cases of $Re_H < Re_C$ ($Ma_{outH} < Ma_{outC}$) when the height of the passage is 10 μm or 20 μm, in the cases of $Ma_{outH} < 0.1$ and $Ma_{outC} > 0.4$ when the height of the passage is 50 μm. The latter temperature inversion occurs in the cases of $Re_H > Re_C$ ($Ma_{outH} < Ma_{outC}$) when the height of the passage is $h = 10$ μm or 20 μm.

(3) The effectiveness ε becomes greater than unity when the total temperature inversion occurs.

(4) The effectiveness of a two-stream gas-to-gas micro-heat exchanger for the cases of $Re_H > Re_C$ ($Ma_{outH} > Ma_{outC}$) can be estimate via Eq. (21) within $-3–5\%$ in error, for the cases of $Re_H < Re_C$ ($Ma_{outH} < Ma_{outC}$) within $-14–3\%$ in error, respectively, when the overall heat transfer coefficient K is obtained from Eqs. (19) and (20).

Acknowledgment

Financial support from the Japan Society for the Promotion of Science (Grant-in-Aid for Scientific Research (C) Contract No. 18560209) is greatly acknowledged.

Nomenclature

A = heat transfer area per unit depth (=L), m
c_p = specific heat, J/(kg K)
D_h = hydraulic diameter, m
h = channel height, m
i = specific internal energy, J/kg
K = overall heat transfer coefficient, W/(m^2 K)
L = channel length, m
Ma = Mach number, Eq. (10)
$\dot{m}$ = mass flow rate per unit depth, kg/(m s)
Nu_m = average Nusselt number, $=\alpha_m D_h/\lambda$
Ntu = number of transfer units
Pr = Prandtl number
p = pressure, Pa
$\dot{Q}$ = heat transfer rate per unit depth, W/m
q_w = heat flux from hot passage to cold passage, W/m^2
R = gas constant, J/(kg K)
R_c = capacity ratio
Re = Reynolds number, Eq. (10)
T = temperature, K
T_b = bulk temperature, Eq. (12)
T_T = total temperature, Eq. (13)
u, v = velocity components, m/s
x, y = coordinates, m
α_m = average heat transfer coefficient, W/(m^2 K)
ε = effectiveness
ϕ = dissipation function, Eq. (5)
γ = specific heat ratio

λ = thermal conductivity, W/(m K)
μ = viscosity, Pa s
ρ = density, kg/m^3

Subscripts

C = cold passage
est = estimation value
H = hot passage
in = inlet
max = maximum value
min = minimum value
out = outlet
sim = simulation result
stg = stagnation value

References

[1] Tuckerman, D. B., and Pease, R. F. W., 1981, "High-Performance Heat Sinking for VLSI," IEEE Electron Device Lett., **5**, pp. 126–129.
[2] Prud'homme, R. K., Chapman, T. K., and Browen, J. R., 1986, "Laminar Compressible Flow in a Tube," Appl. Sci. Res., **43**, pp. 67–74.
[3] Berg, H. R., Seldam, C. A., and Gulik, P. S., 1993, "Compressible Laminar Flow in a Capillary," J. Fluid Mech., **246**, pp. 1–20.
[4] Guo, Z. Y., and Wu, X. B., 1997, "Compressibility Effect on the Gas Flow and Heat Transfer in a Micro Tube," Int. J. Heat Mass Transfer, **40**(13), pp. 3251–3254.
[5] Sayegh, R., Faghri, M., Asako, Y., and Sunden, B., 1999, "Direct Simulation Monte Carlo of Gaseous Flow in Micro-Channel," 33rd National Heat Transfer Conference, Paper No. HTD99-256.
[6] Sun, H., and Faghri, M., 2000, "Effect of Rarefaction and Compressibility of Gaseous Flow in Micro Channel Using DSMC," Numer. Heat Transfer, Part A, **38**, pp. 153–158.
[7] Asako, Y., Pi, T., Turner, S. E., and Faghri, M., 2003, "Effect of Compressibility on Gaseous Flows in Micro-Channels," Int. J. Heat Mass Transfer, **46**, pp. 3041–3050.
[8] Asako, Y., Nakayama, K., and Shinozuka, T., 2005, "Effect of Compressibility on Gaseous Flows in a Micro-Tube," Int. J. Heat Mass Transfer, **48**, pp. 4985–4994.
[9] Hong, C., Asako, Y., Turner, S. E., and Faghri, M., 2007, "Friction Factor Correlation for Gas Flow in Slip Flow Region," J. Fluids Eng., **129**, pp. 1268–1276.
[10] Guo, Z. Y., 2000, "Size Effect on Flow and Heat Transfer Characteristics in MEMS," *Proceedings of the International Conference on Heat Transfer and Transport Phenomena in Micro-Scale*, pp. 24–31.
[11] Asako, Y., 2004, "Heat Transfer Characteristics of Gaseous Flows in a Micro-Tube," Therm. Sci. Eng., **12**(5), pp. 31–37.
[12] Asako, Y., and Toriyama, H., 2005, "Heat Transfer Characteristics of Gaseous Flows in Microchannels," Microscale Thermophys. Eng., **9**(1), pp. 15–31.
[13] Hong, C., and Asako, Y., 2007, "Heat Transfer Characteristics of Gaseous Flows in a Microchannel and a Microtube With Constant Wall Temperature," Numer. Heat Transfer, Part A, **52**, pp. 219–238.
[14] Hong, C., Asako, Y., and Lee, J. H., 2007, "Heat Transfer Characteristics of Gaseous Flows in Micro-Channel With Constant Heat Flux," Int. J. Therm. Sci., **46**, pp. 1153–1162.
[15] Hong, C., and Asako, Y., 2006, "Heat Transfer Characteristics of Gaseous Flows in Micro-Channels With Negative Heat Flux," Fourth International Conference on Nanochannels, Microchannels and Minichannels, Paper No. ICMM2006-96163.
[16] Halbritter, A., Schygulla, U., Wenka, A., and Schubert, K., 2004, "Comparison of Numerical Simulation and Experimental Results for Crossflow and Counterflow Microchannel Heat Exchangers," Second International Conference on Microchannels and Minichannels, Paper No. ICMM2004-2438.
[17] Brandner, J., Henning, J., Schygulla, U., Wenka, A., Zimmermann, S., and Schubert, K., 2005, "Comparison of Crossflow Micro Heat Exchangers With different Micro Structure Designs," Third International Conference on Microchannels and Minichannels, Paper No. ICMM2005-75072.
[18] Hong, C., Asako, Y., and Lee, J., 2008, "Poiseuille Number Correlations for High Speed Microflows," J. Phys. D: Appl. Phys., **41**(10), pp. 1–10.
[19] Karki, K. C., 1986, "A Calculation Procedure for Viscous Flows at All Speeds in Complex Geometries," Ph.D. thesis, University of Minnesota, Minneapolis.
[20] Amsden, A. A., et al., 1980, "SALE a Simplified ALE Computer Program for Fluid Flow at All Speeds," Los Alamos Scientific Laboratory Report No. LA-8095.
[21] Kreskovsky, J. P., Shamroth, S. J., and McDonald, H., 1974, "Parametric Study of Relaminarization of Turbulent Boundary Layers on Nozzle Wall," *NASA* Paper No. CR-2370.
[22] Murphy, H. D., Chambers, F. W., and Mceligot, D. M., 1983, "Laterally Converging Flow Part 1. Mean Flow," J. Fluid Mech., **127**, pp. 379–401.
[23] Mills, A. F., 1992, *Heat Transfer*, Irwin, Boston.
[24] Shah, R. K., and London, A. L., 1978, "Laminar Flow Forced Convection in Ducts," *Advances in Heat Transfer Supplement 1*, Academic, New York.
[25] Mercer, W. E., et al., 1967, "Laminar Forced Convection in the Entrance Region Between Parallel Flat Plates," ASME J. Heat Transfer, **89**, pp. 251–257.

Air-Side Surface Wettability Effects on the Performance of Slit-Fin-and-Tube Heat Exchangers Operating Under Wet-Surface Conditions

L. Liu
e-mail: lliu9@illinois.edu

A. M. Jacobi
e-mail: a-jacobi@illinois.edu

Department of Mechanical Science and Engineering,
University of Illinois,
1206 West Green Street,
Urbana, IL 61801

A study of condensate retention and the attendant thermal-hydraulic effect associated with changes in air-side surface wettability is presented for a series of slit-fin-and-tube heat exchangers of identical geometry with controlled wettability covering a wide range of contact angles. An experiment in which the retained mass of air-side condensate was measured under dynamic conditions is described, and the results are analyzed using conventional thermal-hydraulic measurements of j and f. The data demonstrate that for the heat exchangers used in this study, the j factor is not strongly influenced by condensate retention, but the friction factor is significantly reduced for surfaces of increased wettability. Hydrophilic heat exchangers retain much less air-side condensate than do the hydrophobic heat exchangers, and the amount of retention is found to depend on the air-side Reynolds number (Re_{dh}) and the rate of latent heat transfer (Q_l). Based on an assumption of filmwise condensation, a new model for predicting the mass of retained condensate is described and compared with the steady-sate retention data. The model is successful in predicting retained condensate over a wide range of tested conditions. The potential of this new approach and possible refinements that will add engineering value are discussed. [DOI: 10.1115/1.2994722]

Keywords: condensation, retention, wettability, heat exchangers, aluminum, contact angle, fin-and-tube

1 Introduction

In many air-cooling systems, the heat exchanger operates with its surface temperature below the dew point of conditioned air. As a result, moisture from the air stream condenses and accumulates on the surface of the heat exchanger, until it is removed by the air-flow forces or gravity. Condensate retained on heat exchangers can reduce the air-side heat-transfer coefficient, increase core pressure drop, and adversely affect indoor air quality. Therefore, it is important to understand how much condensate is retained on the heat-transfer surface and how it affects the heat transfer and pressure-drop performance of the heat exchanger.

Enhancement of the surface wettability can reduce the contact angle of water condensing on the surface and improve the condensate drainage, which is usually achieved by surface coating or plasma treatment in application. Types of coatings on aluminum fins as well as their wetting mechanisms have been well documented by Hong and Webb [1]. Min et al. [2] provided data of contact angles for several available commercial coatings and investigated their long-term wetting characteristics on heat exchangers. Min and Webb [3] reported contact angles on aluminum, copper, and two commercial coatings on aluminum. They also observed and measured the condensate retention formed on these surfaces and found out that the weight of condensate retained per unit area was an approximate function of the receding contact angles. Condensation experiments were conducted by Shin and Ha [4] using fin-and-tube heat exchangers with three different shapes and two different wettabilities. Their work showed that a reduction in water retention can be achieved significantly by improving surface wettability and by changing the design of a heat exchanger with a lower number of fins and fins with slant ends. Very recently, it has been demonstrated that radical changes in the wettability of aluminum—the most common fin material in these applications—can be achieved through the use of anisotropic microscale surface features, and that such changes can significantly reduce the maximum size of droplets retained on the surface [5].

The effects of surface coatings on the thermal-hydraulic performance of the heat exchangers have also attracted the interest of researchers. Wang and Chang [6] reported the heat- and mass-transfer characteristics of fin-and-tube heat exchangers with and without hydrophilic coating. They concluded that the hydrophilic coating had a negligible effect on the sensible heat-transfer coefficient, but the pressure drop was 15–40% lower than for surfaces without a coating. They also observed that there were no detectable changes of the sensible heat-transfer coefficients with a change in inlet relative humidity, while the pressure drop for the hydrophilic surfaces was sensitive to the inlet condition. Hong and Webb [7] studied the effect of different coating type on wavy, lanced, and louver fin geometries and arrived at similar conclusions. The coating had no effect on sensible heat-transfer coefficient for all fin geometries tested, and the wet pressure drops were reduced by 45% and 15%, respectively, for louver and wavy fins at a 2.5 m/s frontal air velocity. Wang et al. [8] compared the air-side performance of compact fin-and-tube heat exchangers under wet-surface conditions with and without a hydrophilic coating. The data suggested that the heat-transfer performance for the hydrophilic surface is lower than for the corresponding uncoated

Contributed by the Heat Transfer Division of ASME for publication in the JOURNAL OF HEAT TRANSFER. Manuscript received December 7, 2007; final manuscript received June 18, 2008; published online March 18, 2009. Review conducted by Bengt Sunden. Paper presented at the 22nd IIR International Congress of Refrigeration, August 21–26, 2007.

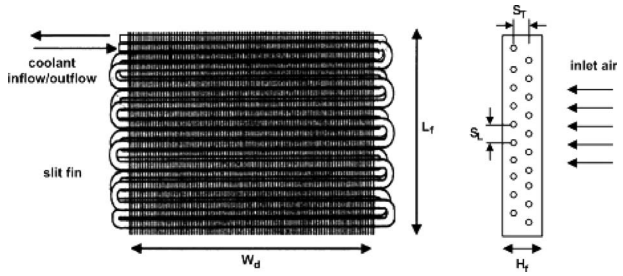

Fig. 1 Schematic showing the geometry of the test slit-fin round-tube heat exchangers; dimensions are provided in Table 1

surface, and the degradation may be as large as 20% for a fin spacing of 1.2 mm. The pressure drop for the hydrophilic surface was always lower than for the corresponding uncoated surface, with a maximum reduction of 40% for the plain-fin geometry. A new method using plasma gas to form a hydrophilic surface on fin stock was introduced by Kim et al. [9]. Their experiments showed a long-term reduction in pressure drop of 25% for heat exchangers after the plasma treatment, while at a fixed air frontal velocity, the air-side heat-transfer coefficient was essentially unaffected by the coating. In these studies, fin surface wettability of heat exchanger specimens was manipulated by different coatings and procedures. However, it is the surface wettability (contact angle) that matters, but not how that is acquired.

Early work aimed at predicting the amount of retained condensate on heat exchangers was focused on annular-finned tubes with filmwise condensation from a pure quiescent vapor. Beatty and Katz [10] proposed a simple model accounting for gravity-dominated drainage. The model showed reasonable agreement with data. However, Rudy and Webb [11] demonstrated that in many cases the agreement broke down. They argued that surface tension forces are significant for the integral-fin tube and should be included in the drainage modeling. Rudy and Webb [11] developed an improved model of drainage, which was also restricted to the annular-fin geometry, with filmwise condensation from a pure vapor. These early models do not extend trivially to condensation on air-cooling surfaces. Jacobi and Goldschmidt [12] developed a model for the retention of water condensate from a moist-air flow over an annular-fin geometry. Although the model was simple, it recognized the forces relevant to condensate bridging and explained the observed j and f behaviors with $\mathrm{Re}_{\mathrm{dh}}$. More recently, Korte and Jacobi [13] proposed a model of droplet retention on heat-transfer surfaces and provided the first comparisons of retention data to predictions for a plain-fin-and-tube heat exchanger. They found the maximum droplet size (the size of the largest droplet retained on a fin) to be a key parameter in condensate retention. A series of studies of droplet shape and retentive forces [14–16] led to a more comprehensive model by El Sherbini and Jacobi [17]. In contrast to this approach based on understanding maximum droplet size, Zhong et al. [18] proposed a fluid dynamics model to understand the drainage of water from complex air-side surfaces, and they compared this approach to experimental data.

Although wet-surface performance has been studied extensively, there is limited information in the open literature on condensate retention and drainage behavior and the influence of surface wettability. It is uncommon to find retention data reported along with thermal-hydraulic performance, much less a characterization of surface wettability. Moreover, even the most recent condensate retention models cannot address condensate behavior on emerging superhydrophobic or superhydrophilic surfaces. As our ability to engineer such surfaces with chemical and morphological modification grows, our understanding of condensate retention and its effects must be extended if we hope to exploit such technologies in heat exchanger design. In this article, we report an investigation of condensate drainage and retention associated with changes in surface wettability. The thermal-hydraulic effect will also be examined, in order to build a more complete picture of the relationships between wettability, retention, and performance. Finally, we will propose and validate a condensate retention model applicable for hydrophilic heat exchangers.

Table 2 Wettability description of the tested heat exchangers

Specimen	Advancing contact angle θ_A (deg)	Receding contact angle θ_R (deg)	Surface treatment
1	~30	~0	Plasma treating
2	~50	~0	Plasma treating
3	~110	~0	Plasma treating
4	~85	~42	Untreated

2 Methods

2.1 Experimental Apparatus and Instrumentation. Four slit-fin round-tube heat exchangers with identical geometry and different wettabilities were tested in this study. A geometric description of the heat exchangers is provided in Fig. 1, with dimensional information listed in Table 1. As shown in Table 2, two heat exchangers were treated to be hydrophilic, through a plasma coating process ($\theta_A \sim 30$ deg and $\theta_A \sim 50$ deg, respectively); the third one shows a large contact angle hysteresis ($\theta_A \sim 110$ deg and $\theta_R \sim 0$ deg) after treatment, and the fourth one represents the wettability of an untreated aluminum surface ($\theta_A \sim 85$ deg and $\theta_R \sim 42$ deg). It has been observed by Kim et al. [9] that the contact angles measured on the untreated heat exchangers gradually decrease with increasing numbers of wet/dry cycles, while the wettability of the aluminum fins after plasma treatment appears to be robust.

The closed-loop wind tunnel used in these experiments is shown schematically in Fig. 2. The airflow was conditioned with resistance heaters (up to 8 kW) and a steam injection system providing up to 12 kg/h of steam, regulated using chilled-mirror dew-point sensors and a proportional-integral-derivative contoller (PID controller). The air flow was drawn by an axial fan and a variable speed drive through honeycomb flow straighteners, screens, and a 9:1 area contraction into the test section at rates up to about 20 $\mathrm{m}^3/\mathrm{min}$. A 6-junction equally spaced thermocouple grid ($\pm 0.1\,^\circ\mathrm{C}$) was used to measure the air temperature at the heat exchanger inlet, and a 12-junction grid was used at the heat exchanger outlet ($\pm 0.1\,^\circ\mathrm{C}$). The dew-point upstream and downstream of the heat exchanger was measured using conventional chilled-mirror hygrometers, with an uncertainty less than $\pm 0.2\,^\circ\mathrm{C}$. Pressure drop across the heat exchanger was measured with an electronic pressure transducer (± 0.2 Pa). A single-phase mixture of ethylene glycol and water was supplied by a gear pump to cool the heat exchanger during the experiments. The temperature of the coolant was regulated using a chiller system and moni-

Table 1 Heat exchanger dimensions

N_t	W_d (mm)	L_f (mm)	H_f (mm)	F_p (mm)	t (mm)	L_s (mm)	D_o (mm)	S_T (mm)	S_L (mm)
20	313	209	25	1.20	0.13	9.53	7.37	12.7	20.8

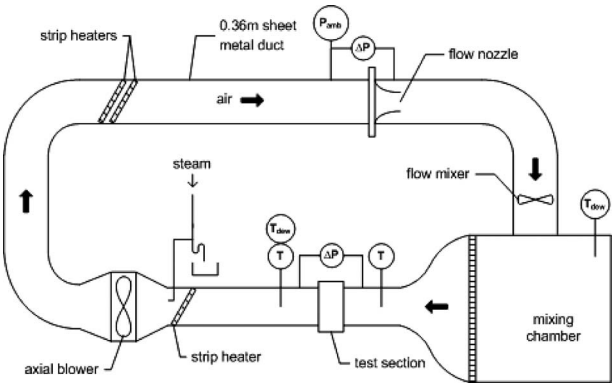

Fig. 2 Wind tunnel for thermal-hydraulic measurements and condensate retention experiments

tored using immersion resistance temperature detectors (RTD's) ($\pm 0.03°C$) at the inlet and exit of the heat exchanger. A Coriolis-effect mass flow meter was used to measure the coolant flow rate. During an experiment, the data acquisition system would sample instruments throughout the test and log data to a text file for subsequent analysis.

The test section shown schematically in Fig. 3 allowed a transient measurement of the condensate retention on the test specimen. The heat exchanger was suspended in the wind tunnel with a nonabsorbing strap. The strap is grid-structured with holes on allowing water to pass through and be drained from the heat exchanger. An electronic balance with reported uncertainty of ≤ 0.1 g was placed under the test section to record the mass retention on the specimen. Flexible plastic film was used to insulate the heat exchanger and allow its movement for the mass measurement. Coolant inlet and outlet tubes were kept as flexible as possible to reduce the weight measurement uncertainty, and horizontal supports were introduced to mitigate friction interference. Balance calibration was conducted before every single retention test by recording readings for calibration weights. Deviation from the calibration weight was found to be less than 5% for moderate

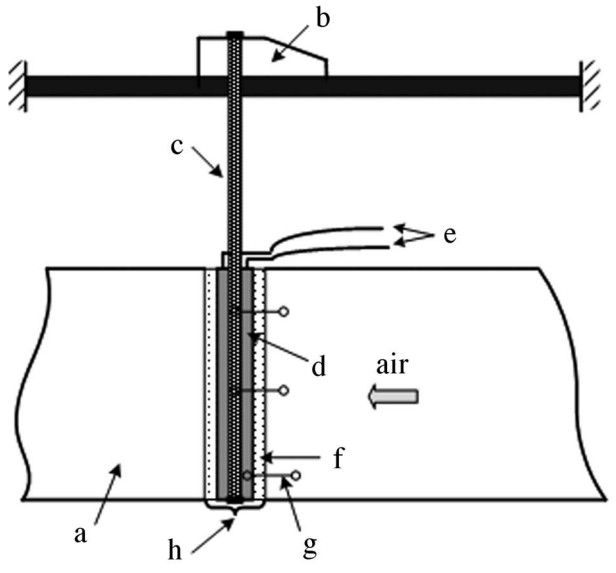

Fig. 3 Heat exchanger test section. This design allows the real-time measurement of retained condensate, along with conventional thermal-hydraulic measurements. (*a*) wind tunnel; (*b*) electronic balance; (*c*) strap; (*d*) heat exchanger; (*e*) coolant supply; (*f*) flexible plastic film; (*g*) horizontal support; (*h*) drainage holes.

face velocities but as high as approximately 10% at an air face velocity of about 3 m/s. A linear calibration curve was fitted and used to record data in subsequent testing.

2.2 Experimental Procedure and Data Interpretation. Heat-transfer, pressure-drop, and dynamic retention data for different specimens were recorded over a range of operating conditions. For thermal-hydraulic measurements, tests were conducted with an inlet coolant temperature of $4.4°C$ and an inlet air temperature of $23.9°C$. The inlet dew point was held at approximately $18.3°C$, and air-side face velocities were spanned from about 0.7 m/s to 2.3 m/s. When dynamic condensate retention data were obtained, the range of experimental conditions was expanded in order to investigate the effects of various parameters on the amount of condensate retained on air-side surface. Therefore, inlet air temperature was adjusted between $23.9°C$ to $35.0°C$, and upstream dew point ranged from $12.8°C$ to $21.1°C$. The experimental program spanned air-side face velocities from about 0.7 m/s to 3.5 m/s, and inlet coolant temperatures ranged from $-1.1°C$ to $4.4°C$.

An experiment was initiated by bringing the air flow to the desired temperature, velocity, and relative humidity and then suddenly starting the coolant flow, which had been preconditioned to the desired temperature. The electronic balance would record the mass retention on the test heat exchanger every 0.2 s. After a brief transient period at the beginning of each test (normally half an hour and varying with different surface characteristics and operating conditions), it would arrive at a steady state. At steady state, the amount of water condensing onto the surface from the incoming air is equal to the amount of water removed by gravity and air flow. After an experiment arrived at the steady state, reading of the electronic balance as well as all conditions remained constant within their experimental uncertainty throughout the rest of the test. The experimental conditions were carefully set and monitored to ensure that the temperature of entire heat-transfer surface was below the dew-point temperature throughout the experiment. That is, the fully wet condition was ensured for every single test.

The temperature and flow-rate data sampled during an experiment were first used to determine the steady-state heat-transfer coefficient. Among several different approaches found in the literature, the log mean enthalpy difference (LMED) method for simultaneous heat and mass transfer described by Threlkeld [19] was adopted. Enthalpy differences were used instead of temperature differences for interpreting the total air-to-coolant heat-transfer rate.[1] Fin efficiencies were determined using the sector method (with 32 sectors per tube), as addressed by Hong and Webb [21] and extended by Kim and Jacobi [22] for slit-fin geometry applications. The coolant-side transfer coefficient was calculated from a self-developed correlation, using the Wilson-plot method [23] and overall heat-transfer coefficients measured at different coolant mass flow rates [24]. Conduction resistance through the tube wall was calculated assuming steady one dimensional conduction, and the fin-tube contact resistance was neglected. The air-side and coolant-side heat-transfer rates were calculated using the mass flow rates and enthalpy (temperature) changes for the moist-air (coolant) flow:

$$Q_{\text{air}} = m_a(h_{a,\text{in}} - h_{a,\text{out}}) \tag{1}$$

$$Q_c = m_c C_{p,c}(T_{c,\text{out}} - T_{c,\text{in}}) \tag{2}$$

where $h_{a,\text{in}}$ and $h_{a,\text{out}}$ are the enthalpies of inlet and outlet air, which can be determined with known moist-air temperature, pressure, and dew point. Only data with air-to-coolant energy balance within 10% were used for heat-transfer coefficient evaluation, and the air-side and coolant-side heat-transfer rates were averaged for the data reduction. Reduction procedures were programed with all

[1]The correction factor F was evaluated to be ~ 0.98, which is typical to operating conditions in this study [20].

of the measured data into a commercial software package, engineering equation solver (EES), and the air-side heat-transfer coefficient was solved in an iterative way.

Once the air-side heat-transfer coefficient was determined, data interpretation followed the methods detailed by the ARI Standard for condensing heat exchangers. Correlations for air-side Colburn j factors and Fanning friction factors were provided as a function of the air-side Reynolds number. The j and f factors were determined from temperature, mass flow, pressure-drop, and geometrical data using the following equations:

$$j = \frac{\mathrm{Nu}}{\mathrm{Re_{dh}Pr}^{1/3}} = \frac{h}{Gc_{\mathrm{pa}}}\mathrm{Pr}^{2/3} \tag{3}$$

with

$$G = \frac{\dot{m}_a}{A_{\min}} \tag{4}$$

and

$$f = \frac{2\Delta P_{HX}\rho_a}{G^2}\left(\frac{A_{\min}}{A_T}\right) - (1+\sigma^2)\left(\frac{\rho_{\mathrm{up}}}{\rho_{\mathrm{down}}} - 1\right)\left(\frac{A_{\min}}{A_T}\right)\left(\frac{\rho_a}{\rho_{\mathrm{up}}}\right) \tag{5}$$

with

$$\sigma = \frac{A_{\min}}{A_{\mathrm{front}}} \quad \text{and} \quad \rho_a = \frac{\rho_{\mathrm{up}} + \rho_{\mathrm{down}}}{2} \tag{6}$$

2.3 Modeling Condensate Retention on Hydrophilic Heat Exchangers. When the condensation of water occurs on a hydrophilic surface, it takes a filmwise mode rather than the dropwise mode observed on hydrophobic heat-transfer surfaces. Therefore, the droplet-based approach of the previous retention modeling work is of dubious validity for heat exchangers with good wettability because the force-balance approach with an empirical basis for droplet size distribution [13,17] does not capture the basic physics of the filmwise mode. A mechanistic model of condensate retention in the filmwise mode might shed light on the heat-transfer mechanisms and could provide insight into the influence of surface temperature, air face velocity, on heat-transfer rate and retention. A film-based model is therefore desired for predicting retention on these hydrophilic heat exchangers.

In order to develop a model of the condensate mass retained on the heat exchanger surface, we begin by considering a thin continuous film of condensate retained on the fins and adopt the following assumptions: (1) the condensate film spreads out on all fin surfaces and remains stable and unbroken; (2) the fins are too far apart for interfin condensate bridging to occur. Later, we will discuss the possible refinements and modifications to the model that might be useful in relaxing these restrictions.

Consider laminar film condensation occurring on one single vertical fin, as described in Fig. 4. The fin is surrounded by a mixture of air and water vapor with a forced gas flow orthogonal to gravity. The fin surface is maintained at a constant temperature, which is below the saturation temperature of the moist air, and at a steady state a constant-density liquid film forms and drains by gravity and liquid-vapor shear. Under these assumptions,

$$M = \rho_l \int_{A_T} \delta(x,y)\,dA \tag{7}$$

In Eq. (7), M is the total mass of retained condensate on the heat exchanger, ρ_l is the mass density of liquid water, and $\delta(x,y)$ is the condensate film thickness. The integration is performed over the entire surface area of the heat exchanger (A_T), which is the summation of the fin area and tube area. It should be noted that an expression for $\delta(x,y)$ will be developed for the vertical fin and applied over A_T. As such, the tube surface is not distinguished from fin surface for condensate evaluation. Because the tube area is usually a small portion of the total (5.4% for the heat exchanger used in this article), this approximation does not have a large impact on the final result.

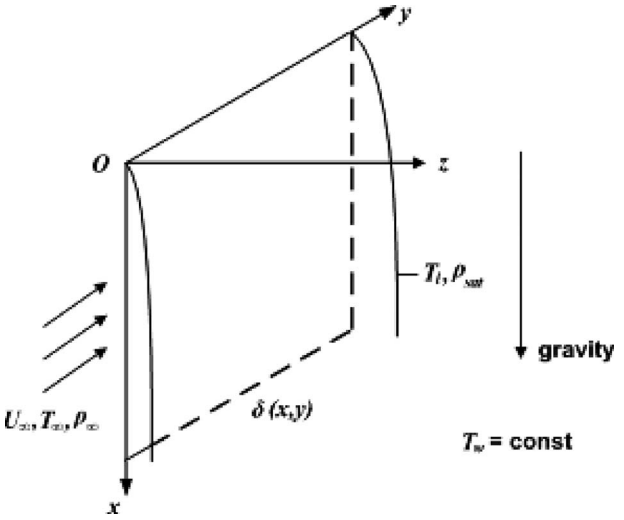

Fig. 4 Problem description: laminar film condensation on a vertical fin

The model is now pursued by developing an expression for film thickness function $\delta(x,y)$, which has been of classical interest in heat transfer. Pioneering work was reported by Nusselt [25], who considered the simple case of pure-vapor condensation on a vertical surface with viscous forces balancing gravity (no shear at the liquid-vapor interface). When a noncondensable gas is present (air in this case), the solution is usually pursued using two-phase boundary layer equations for momentum, energy, and species. Koh et al. obtained similarity solutions for the two-phase boundary layer equations on a vertical surface under free convection alone [26] and forced convection alone [27], and others used approximate or numerical methods [28–30]. Unfortunately, a simple similarity solution does not exist in combined convection (forced and free convection) because a single similarity transformation cannot capture the x, y, and z dependences. Approximate methods are usually less amenable to generalization, and the expense of a numerical approach might vitiate its utility.

Because an analytical approach is preferred, and because a simple solution does not exist for combined convection, the limiting conditions of no air flow ($\mathrm{Re_{dh}} \to 0$) and an infinite air velocity ($\mathrm{Re_{dh}} \to \infty$) will be used as asymptotic solutions and Churchill's method [31] will be used to interpolate between these limiting cases. In this way, a relatively simple and general analytical expression for $\delta(x,y)$ will be developed for the mixed-convection case.

2.3.1 High Reynolds Number Limit. When the air-side Reynolds number is very large, a balance between viscous forces in the liquid film and shear at the liquid-vapor interface prevails, and drainage by gravity can be neglected. The problem becomes a laminar film condensation under forced convection, as shown schematically in Fig. 5, and the film thickness $\delta(y)$ increases along with the direction of incoming flow.

At low mass-transfer rates, mass conservation for the liquid film can be written as

$$\rho_l \frac{d}{dy}\int_0^{\delta(y)} u(y,z)\,dz = h_m(y)(\rho_\infty - \rho_{\mathrm{sat}}(T_i)) = \frac{q(y)}{h_{fg}} \tag{8}$$

In Eq. (8), $u(y,z)$ is the y-velocity distribution in the liquid layer, $h_m(y)$ is the mass-transfer coefficient, ρ_∞ and $\rho_{\mathrm{sat}}(T_i)$ are the water vapor densities in the air flow and at saturation conditions at the interface, $q(x)$ is the local latent heat transfer, and h_{fg} is the heat

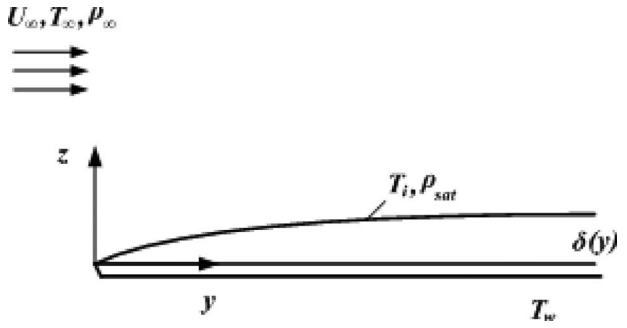

Fig. 5 Film condensation under forced convection

of condensation. With Nusselt's assumptions [25] that the effects of both energy convection and fluid acceleration within the condensate layer can be neglected, the momentum balance for the liquid layer can be written as

$$\frac{\partial^2 u}{\partial z^2} = 0 \tag{9}$$

The boundary conditions that must be satisfied by Eq. (9) are

$$z = 0, \quad u = 0 \tag{10a}$$

$$z = \delta(y), \quad \tau(y) = \mu_l \frac{\partial u}{\partial z} \tag{10b}$$

Because the liquid film is assumed to be very thin, it is reasonable to assume that the air flow imparts shear on a flat surface through a laminar boundary layer (again, assuming a low mass-transfer rate), thus

$$\tau(y) \approx \tau_w = 0.332 U_\infty \left(\frac{\rho \mu U_\infty}{y}\right)^{1/2} \tag{11}$$

Equation (11) is from similarity solution for air flow over a flat plate, and ρ and μ without subscript are the properties of incoming air, which is a mixture of air and water vapor.

From Eq. (9) and its boundary conditions, the velocity distribution in the liquid $u(y,z)$ is determined to be

$$u(y,z) = \frac{0.332 U_\infty}{\mu_l}\left(\frac{\rho \mu U_\infty}{y}\right)^{1/2} z \tag{12}$$

With Eq. (12), the integral of Eq. (8) can be evaluated. After rearranging, the film thickness is found to be

$$\delta(y) = \left[\frac{4\mu_l D_h^{3/2} \rho}{0.332 \rho_l \mu^2 h_{fg} \sigma^{3/2}}\right]^{1/2} \frac{q(y)^{1/2}}{\mathrm{Re}_{\mathrm{dh}}^{3/4}} y^{3/4} \tag{13}$$

In Eq. (13) the air-side Reynolds number ($\mathrm{Re}_{\mathrm{dh}}$) and surface ratio ($\sigma$) are defined as

$$\mathrm{Re}_{\mathrm{dh}} = \frac{\rho D_h U_{\max}}{\mu} \tag{14}$$

$$\sigma = \frac{A_{\min}}{A_{\mathrm{front}}} = \frac{U}{U_{\max}} \tag{15}$$

In order to obtain the mass retention on entire heat-transfer surface, we integrate both sides of Eq. (13) over the heat exchanger core depth H_f (i.e., along with the direction of air flow). Noting

$$M = \rho_l A_T \frac{1}{H_f} \int_0^{H_f} \delta(y) dy \tag{16a}$$

$$Q_l = A_T \frac{1}{H_f} \int_0^{H_f} q(y) dy \tag{16b}$$

and that $\delta(y)$ and $q(y)$ are both power-law functions of y, the result of integration is obtained to be

$$M = C_1 Q_l^{1/2} / \mathrm{Re}_{\mathrm{dh}}^{3/4} \tag{17a}$$

$$C_1 = \frac{2}{3}(H_f \cdot D_h)^{3/4} \left(\frac{2\mu_l \rho_l \rho A_T}{0.332 \mu^2 h_{fg} \sigma^{3/2}}\right)^{1/2} \tag{17b}$$

In Eqs. (17*a*) and (17*b*), C_1 is a function of the liquid-vapor properties and geometrical parameters of the heat exchanger; however, for a specified geometry, the property changes are very small over the range of air-cooling conditions motivating this work. Therefore, for simplicity, C_1 is treated as a constant in subsequent calculations.

2.3.2 Low Reynolds Number Limit. As $\mathrm{Re}_{\mathrm{dh}} \to 0$, air flow vanishes and a balance between viscous forces in the liquid layer and gravity prevails. Liquid-vapor shear is neglected, and the condensate is removed by gravity. This problem is classical laminar film condensation and film thickness $\delta(x)$ will only increase in the direction of gravity (x). An analysis similar to that of Sec. 2.3.1 gives the following result (provided without elaboration):

$$M = C_2 Q_l^{1/3} \tag{18a}$$

$$C_2 = 0.8 \left(\frac{\mu_l \rho_l}{g h_{fg}}\right)^{1/3} (3 L_f A_T^2)^{1/3} \tag{18b}$$

Again, C_2 is considered as a constant. (Note that C_1 and C_2 are not dimensionless.)

2.3.3 Interpolation Using Churchill's Method. Mass retention for intermediate Reynolds numbers is found by interpolating between the limiting the cases given in Eqs. (17*a*) and (18*a*) using Churchill's method [31] and the final expression is obtained to be

$$M = C_1 Q_l^{1/2} \mathrm{Re}_{\mathrm{dh}}^{-3/4} \left[1 + \left(\frac{C_1 Q_l^{1/6} \mathrm{Re}_{\mathrm{dh}}^{-3/4}}{C_2}\right)^n\right]^{-1/n} \tag{19}$$

Although the constants C_1 and C_2 are derived (Eqs. (17*b*) and (18*b*)), the model will be closed by allowing them to be determined from experimental data along with n.

3 Results and Discussion

In this section, the thermal-hydraulic data (conventional j and f factors) of the tested heat exchangers will be presented first, followed by the dynamic and steady-state condensate retention results. The effects of surface wettability on the heat exchanger performance and mass retention will then be discussed. Finally, a comparison will be drawn between the measured steady-state retention data and the predictions from the filmwise condensation modeling. Through a standard error-propagation calculation, the uncertainty in j factors was found to be about $\pm 5\%$ at low air-side Reynolds number ($\mathrm{Re}_{\mathrm{dh}} \sim 100$) and about $\pm 19\%$ at high air-side Reynolds number ($\mathrm{Re}_{\mathrm{dh}} > 400$), which is mostly from the uncertainty of upstream and downstream dew-point measurements. The uncertainty in f is about $\pm 5\%$ at low air-side Reynolds numbers and less than $\pm 4\%$ at high air-side Reynolds numbers. The accuracy of pressure transducers is the major source for uncertainty in the f results. The uncertainty in retention mass (M) measurements was estimated to be less than $\pm 5\%$ under steady-state conditions, mainly due to the small fluctuations caused by discrete shedding behavior.

3.1 Air-Side Thermal-Hydraulic Performance. Air-side heat-transfer and pressure-drop results under fully wet conditions are presented in the form of sensible j factors and f factors as functions of air-side Reynolds number $\mathrm{Re}_{\mathrm{dh}}$ in Figs. 6 and 7. The

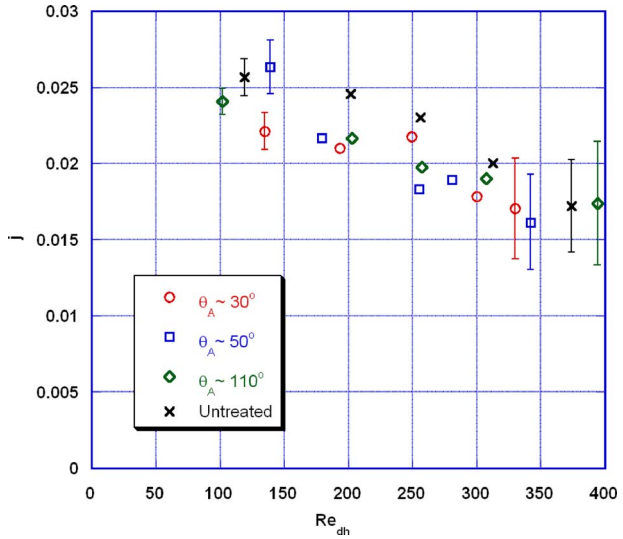

Fig. 6 Colburn *j* factors versus Re_{dh} under fully wet test conditions

data suggest that the specimens treated to improve wettability show slightly lower Colburn j factors than do the untreated heat exchanger (Fig. 6), but the difference is almost within the experimental uncertainty. Figure 7 shows that the two hydrophilic specimens ($\theta_A \sim 30$ deg and $\theta_A \sim 50$ deg, respectively) display much lower f factors than does the untreated one, and specimen 3($\theta_A \sim 110$ deg) has the highest friction factors. The condensation occurring on specimens 1 and 2 is essentially filmwise, and that occurring on specimens 3 and 4 is more dropwise in nature. Therefore, droplets on the surfaces of specimens 3 and 4 present a larger projected area to the flow and might even form interfin bridges and block the air flow. In support of this explanation, the friction factors for specimens 3 and 4 are more sensitive to the air-side Reynolds number compared with hydrophilic specimens, implying that under increased liquid-vapor shear the droplet number density as well as its distribution will be significantly affected for dropwise condensation, whereas the thin water film on hydrophilic heat exchangers is not significantly affected. The reason why the f factors for specimen 1($\theta_A \sim 30$ deg) are slightly higher than for specimen 2($\theta_A \sim 50$ deg) is not clear, but it may be due

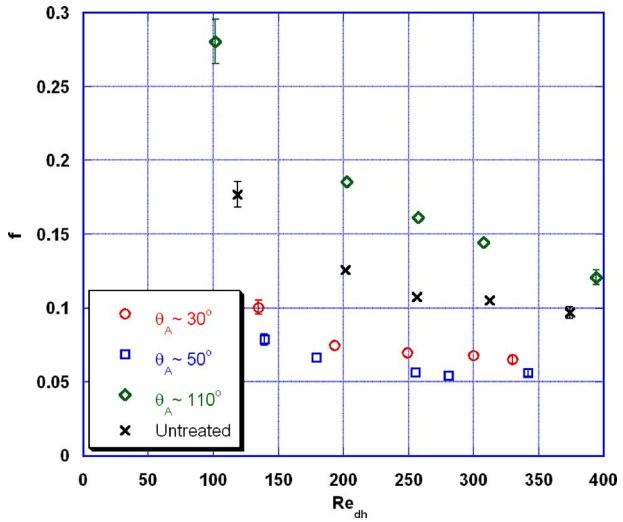

Fig. 7 Fanning *f* factors versus Re_{dh} under fully wet test conditions

to the experimental uncertainties, since these two specimens have very similar surface characteristics and their behaviors are expected to be close. From Figs. 6 and 7, it is clear that the heat exchanger area goodness (j/f) for the hydrophilic specimens is more than twice that of the hydrophobic specimens. These data indicate that operating at a fixed pressure drop, the hydrophilic specimens would provide a significant increase in heat duty at identical operating conditions.

For a single plain surface, because dropwise condensation prevents the buildup of an insulating liquid film and provides a large portion of bare surface area for heat transfer, it is widely reported that dropwise condensation can offer higher rates of heat transfer than filmwise condensation. However, the situation is more complicated for condensation occurring on the air-side surface of an evaporator. In most cases, the j factor also depends on the geometry of the heat exchanger. For example, if a heat exchanger has offset-strip or louvered fins, droplet retention will sometimes deteriorate the inherent boundary layer restarting effect of the interrupted surface and cause a degradation in heat transfer. Also, for heat exchangers with very tight fin pitch—as the specimens tested in this study ($F_p \sim 1.2$ mm)—droplet bridging occurs on a large portion of the surface. Condensate retained in the space between adjacent fins severely blocks the air-flow passage. As a result, no obvious difference in j factors for the hydrophilic and hydrophobic specimens is observed in Fig. 6.

In summary, for the heat exchangers tested in this study, the heat-transfer performance is not strongly influenced by the condensate retention, but pressure drop is significantly reduced by the enhancement of surface wettability. These results are similar to those observed by Wang et al. [8] and demonstrate that manipulating the surface wettability can remarkably reduce the pressure drop of heat exchangers without deleteriously affecting heat transfer. This behavior might result in reduced fan power and reduced fan noise, or at fixed pressure drop filmwise condensation might allow higher air-side velocities and an attendant increase in heat transfer.

3.2 Dynamic Condensate Retention Data. Two sets of real-time retention measurements for the heat exchangers are given in Fig. 8, where data are presented for two fixed blower frequencies[2] and otherwise identical operating conditions ($T_{a,\text{in}}=23.9\,^\circ\text{C}$, $T_{c,\text{in}}=4.4\,^\circ\text{C}$, $DP_{\text{up}}=18.3\,^\circ\text{C}$, and $\dot{m}_c=0.056$ kg/s). As shown in Fig. 8, the heat exchangers were initially dry; over time condensate accumulated on the air-side heat-transfer surface. As the mass of retained condensate increased, gravitational and flow forces eventually overcame surface-tension retaining effects and condensate would start to drain from the heat exchanger. When the rate of deposition is balanced by shedding, a steady-state value of mass retention is achieved, as shown in Fig. 8. In spite of using chilled-mirror dew-point sensors and a PID controller, the dew point in the wind tunnel sometimes fluctuated (by 2 °C at most). Thus, one must exercise caution not to draw too much from the details of the results in Fig. 8, especially over long periods of time. The general behavior is most important.

It is obvious that under the same operating conditions, specimen 1($\theta_A \sim 30$ deg) and specimen 2($\theta_A \sim 50$ deg) retain much less condensate than do the other two specimens, which are relatively more hydrophobic. This behavior is due to the filmwise condensation on the hydrophilic heat exchangers. Moreover, the water film is very thin, and much more uniform, which reduces the possibility of bridging to occur between the adjacent fins. The reduced retention on hydrophilic specimens is congruent with the explanation for the reduced friction factors in Fig. 7.

It is noteworthy that the time required to achieve steady-state condensation for more hydrophobic heat exchangers (specimens 3

[2]During the experiments, the accumulation of condensate changed the friction factor. The experiments were conducted at two fixed blower frequencies: 42 rpm corresponds to a dry-surface $Re_{dh} \sim 250$ and 50 rpm corresponds to $Re_{dh} \sim 350$.

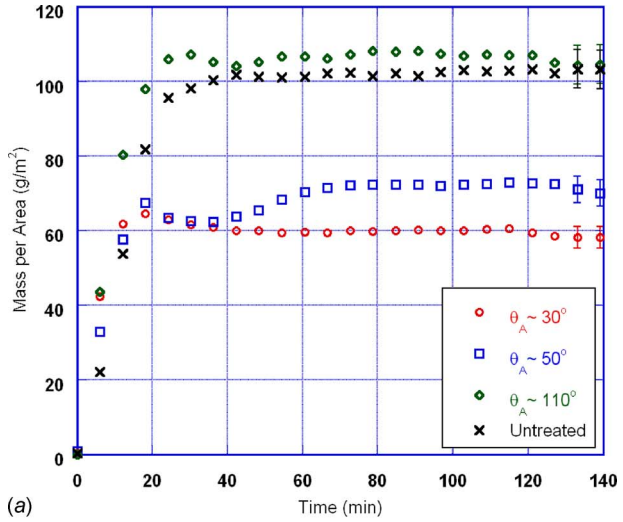

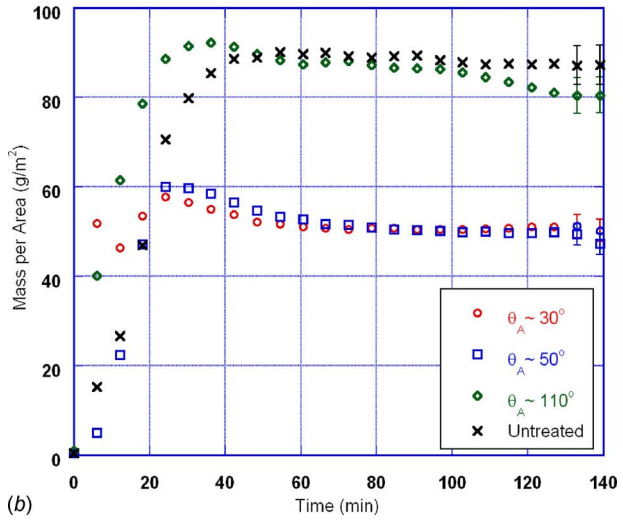

Fig. 8 The mass of retained condensate on the tested heat exchangers as a function of time. These data were obtained under conditions: $T_{a,in}$=23.9 deg, $T_{c,in}$=4.4°C, DP_{up}=18.3°C, and $\dot{m}_c$=0.056 kg/s: (*a*) air blower frequency 42 rpm or dry-surface Re_{dh}~250; (*b*) air blower frequency 50 rpm or dry-surface Re_{dh}~350

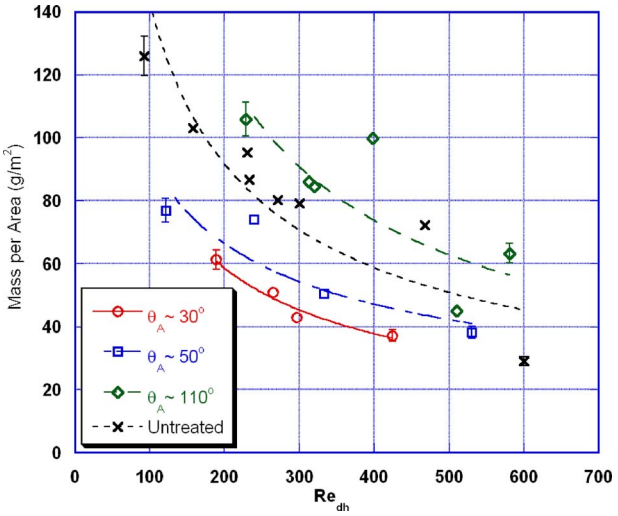

Fig. 9 With similar latent heat transfer Q_l/A_T~115 W/m², mass retention decreases with air-side Reynolds number (least-squared-error power-law fits to data shown to enhance readability)

and 4) is usually longer than for the hydrophilic ones (specimens 1 and 2). This behavior may be manifested simply because the more hydrophobic heat exchangers retain much more condensate at steady state, which takes more time to accumulate if the deposition rates are similar. The dropwise condensation, which is much less uniform and unstable than a thin condensate film, may require a longer time to attain a stationary condensate distribution needed for steady state.

Comparing Fig. 8(*a*) to Fig. 8(*b*), it can be concluded that increasing the air blower frequency, i.e., increasing the air face velocity (or air-side Reynolds number) causes a reduction in the mass retention. By increasing the air blower frequency from 42 rpm (*a*) to 50 rpm (*b*), the steady-state retention of specimens 1 and 2 decreased from about 65 g/m² to 50 g/m², and the retention for specimens 3 and 4 decreased from more than 100 g/m² to approximately 85 g/m². This behavior will be discussed further in Sec. 3.3.

3.3 Steady-State Condensate Retention. The mass retention data in the steady-state region of the real-time retention measurement were averaged for each individual experiment to provide steady-state mass retention data for different specimens over a range of air and coolant temperatures, flow rates, and humidity. The influence of each parameter on the mass retention was investigated. It was found that the amount of condensate retained on the heat exchanger increases as the air-side Reynolds number decreases, the relative humidity increases, the coolant temperature decreases, and the coolant mass flow rate increases. Again, the wettability of the fin surface also plays an important role. Under similar operating conditions, the hydrophilic specimens 1 and 2 always retain much less condensate than do specimens 3 and 4, which are relatively more hydrophobic.

The effects on steady-state retention as discussed in the previous paragraph can be simplified by noting that the trends all follow an increased retention with an increased latent heat-transfer rate. For that reason, and with the hope of further clarifying the trends in the data, the steady-state retention data in Fig. 9 are provided for cases with similar Q_l. Figure 9 shows that, for heat exchangers with similar latent heat-transfer rate, mass retention decreases with air-side Reynolds number, and with similar air-side Reynolds number, mass retention increases with the amount of latent heat transfer Q_l (Fig. 10). These results and the success of using an M/A_T dependence on Q_l in plotting the data are easily explained by referring to Eq. (13), which is developed from the filmwise condensation model. At a fixed Re_{dh}, increasing the heat flux (say by lowering the coolant circulating temperature) will increase the film thickness, which in turn increases retention. On the contrary, a higher air-side Reynolds number increases shear at the liquid-vapor interface, causing an increased flow of the condensate film toward the exit face of the heat exchanger and a decrease in retention. Finally, it is also clear that the more hydrophilic surfaces (specimens 1 and 2) retain less condensate than do the more hydrophobic surfaces (specimens 3 and 4) under all conditions.

3.4 Comparison Between Modeled and Measured Retentions. The observed fact that mass retention is a function of air-side Reynolds number and latent heat transfer supports the modeling procedure (Eqs. (17*a*) and (18*a*)). With the retention behavior formulated for the limiting cases of very small and very large air-side Reynolds numbers, the retention data (spanning Re_{dh} from about 100 to 600) were correlated using Eq. (19) and parameters C_1, C_2, and n were found to minimize the least-squared error (Table 3). If applied to the entire data set, C_1=2.17, C_2=0.51, n=0.339, and the rms deviation becomes 26.7%. The resulting predictions of retained condensate are compared with the experimen-

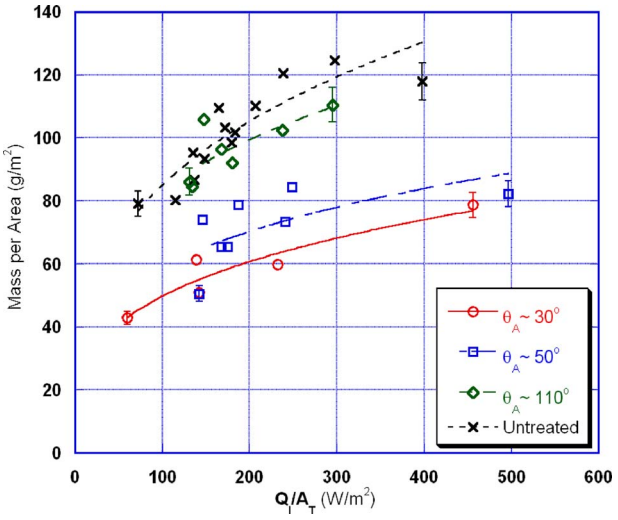

Fig. 10 With similar air-side Reynolds number $Re_{dh}\sim 275$, mass retention increases with the amount of latent heat transfer (least-squared-error power-law fits to the data shown to enhance readability)

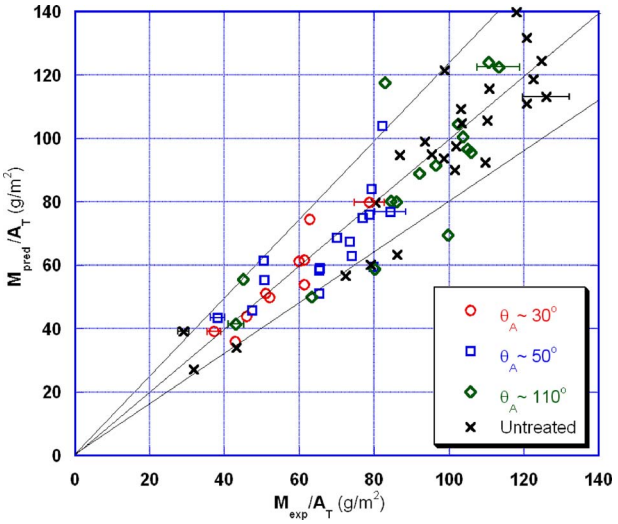

Fig. 11 The retained condensate mass retention predicted by the model compared with experimental data. The lines indicate ±20% from experiments, and the rms deviation of the predictions from the experiments is 14.6%.

tal results in Fig. 11. Figure 11 shows that Eq. (19) works well for predicting the mass retention on the tested heat exchangers under most conditions. Figure 11 also shows that the model does a better job for specimen 1 ($\theta_A\sim 30$ deg) and specimen 2 ($\theta_A\sim 50$ deg) compared with the other two specimens. The rms deviation of the modeled retention from the experimental measurements was 12.5% for specimens 1 and 2, but it was 15.8% for specimens 3 and 4. It should be anticipated that the model is more successful for specimens that are hydrophilic because it is based on an assumed filmwise condensation, and these results are congruent with that expectation.

This new model differs fundamentally from earlier attempts to predict condensate retention in air-cooling applications [13,17], in that it relies on an important simplification in constructing the relationship $M=f(\mathrm{Re}_{dh},Q_l)$ of Eq. (19). A continuous stable film of condensate on each fin surface was assumed to exist. Certainly, the tubes and slits on the fin surface interrupt the water film. Moreover, this model does not account for interfin bridging effects, and at the fin pitch of these heat exchangers ($f_p=1.2$ mm) condensate might form bridges. This model is expected to work best for plain-fin hydrophilic heat exchangers with a large fin spacing; nevertheless, it has been demonstrated to provide predictions with engineering value for more complex fins at a relatively tight fin spacing.

Clearly, this simple filmwise model does not capture the complex physics of retention on these heat exchangers because the condensate dynamics are known to include droplet and bridge formation on untreated aluminum heat exchangers. The relative success of the model, these complexities notwithstanding, probably implies that Eq. (19) somehow embodies the salient features of the physics. We believe that the results as given in Figs. 9 and 10, as well as the trends of those data that can be explained through Eq. (19), strongly suggest that the Re_{dh} and Q_l dependence of M is the most important dependence. By isolating their effects as in Eq. (19), we might think of Re_{dh} as providing for drainage and Q_l as providing for deposition.

Table 3 Constants for Eq. (19)

Specimen	C_1	C_2	n
1	4.67	0.03	0.566
2	4.14	0.11	0.367
3	4.94	0.42	0.309
4	1.08	0.57	0.579

4 Summary and Conclusion

This study reports the experimental data for condensate retention and thermal-hydraulic results for slit-fin round-tube heat exchangers with identical geometry and differing surface wettability. The effects of wettability are reported, and conventional methods have been used to provide air-side j and f factors. A link between retained condensate and thermal-hydraulic performance is established. For the first time, the effects of air and coolant temperatures, velocities, relative humidity, and surface wettability are all examined for their impact on the amount of condensate retention on the air side of heat exchangers. The significant experimental findings are summarized as follows: (1) Under the same operating conditions, hydrophilic heat exchangers retained less water than heat exchangers that are more hydrophobic; (2) enhancing the wettability of the fin surface significantly reduced the wet-surface pressure drop without decreasing the sensible heat-transfer coefficient; (3) condensate retention increased with smaller air-side Reynolds numbers and with a higher relative humidity of the air, a lower coolant circulating temperature, and a larger coolant mass flow rate. In other words, the retained condensate mass increased with latent heat-transfer rate and decreased with air-side Reynolds number.

Based on a laminar filmwise condensation analysis, a model for predicting the mass of retained condensate on hydrophilic heat exchangers was presented. The model was successful in predicting the magnitude and trends of condensate retention for the heat exchanger specimens over a wide range of tested conditions. The current model is restricted by the assumption of continuous and stable laminar film condensation on the fin surface. It also neglects all of the effects of interfin interactions. Nevertheless, the model gives predictions with engineering value and could be used for evaluating the condensate retained on a heat exchanger with the latent heat-transfer estimated. Future refinements of this modeling could involve the tube effects and consider condensate bridging impact.

Acknowledgment

We are grateful for assistance from LG Electronics Co. for providing the heat exchanger samples and for financial support from

the Air Conditioning and Refrigeration Center (ACRC) at the University of Illinois.

Nomenclature

A_{front} = frontal area of the heat exchanger
$A_{\min}$ = minimum flow area
A_T = total surface area
C_p = specific heat
D_h = hydraulic diameter
D_o = outside tube diameter
f = Fanning friction factor
F_p = fin pitch
G = mass flux at minimum flow area
h = heat-transfer coefficient
$h_{a,\text{in}}$ = enthalpy of inlet air
$h_{a,\text{out}}$ = enthalpy of outlet air
H_f = heat exchanger core depth
h_{fg} = heat of condensation
h_m = mass-transfer coefficient
j = Colburn j factor
k = thermal conductivity
L_f = fin length
L_s = length of slit between tubes
M = condensate retention
$\dot{m}$ = mass flow rate
Nu = Nusselt number
N_t = number of tubes
NTU = number of transfer units
Pr = Prantdl number
Q_{air} = air-side heat-transfer rate
Q_c = coolant-side heat-transfer rate
Q_l = total latent heat-transfer rate
q = local latent heat flux
Re = Reynolds number
S_L = longitudinal tube spacing
S_T = transverse tube spacing
St = Stanton number
T = temperature
t = fin thickness
u = y-velocity in the liquid film; Fig. 5
$U_{\max}$ = air velocity based on minimum flow area
W_d = width of the heat exchanger

Greek Symbols

δ = film thickness
θ = contact angle
μ = dynamic viscosity
ρ = density
σ = surface ratio $A_{\min}/A_{\text{front}}$
τ = shear stress
ΔP = air-side pressure drop across the heat exchanger

Subscripts

HX = heat exchanger
A = advancing (contact angle)
R = receding (contact angle)
a = air
c = coolant
l = liquid water
w = wall
up = upstream of the heat exchanger
down = downstream of the heat exchanger
∞ = incoming air properties
sat = saturation
dh = hydraulic diameter

References

[1] Hong, K., and Webb, R. L., 2000, "Wetting Coatings for Dehumidifying Heat Exchangers," HVAC&R Res., **6**(3), pp. 229–239.
[2] Min, J., Webb, R. L., and Bemisderfer, C. H., 2000, "Long-Term Hydraulic Performance of Dehumidifying Heat-Exchangers With and Without Hydrophilic Coatings," HVAC&R Res., **6**(3), pp. 257–272.
[3] Min, J., and Webb, R. L., 2001, "Studies of Condensate Formation and Drainage on Typical Fin Materials," Exp. Therm. Fluid Sci., **25**, pp. 101–111.
[4] Shin, J., and Ha, S., 2002, "The Effect of Hydrophilicity on Condensation Over Various Types of Fin-and-Tube Heat Exchangers," Int. J. Refrig., **25**, pp. 688–694.
[5] Sommers, A. D., and Jacobi, A. M., 2006, "Creating Micro-Scale Surface Topology to Achieve Anisotropic Wettability on an Aluminum Surface," J. Micromech. Microeng., **16**, pp. 1571–1578.
[6] Wang, C. C., and Chang, C. T., 1998, "Heat and Mass Transfer for Plate Fin-and-Tube Heat Exchangers, With and Without Hydrophilic Coating," Int. J. Heat Mass Transfer, **41**, pp. 3109–3120.
[7] Hong, K., and Webb, R. L., 1999, "Performance of Dehumidifying Heat Exchangers With and Without Wetting Coating," ASME J. Heat Transfer, **121**, pp. 1018–1026.
[8] Wang, C. C., Lee, W. S., Sheu, W. J., and Chang, Y. J., 2002, "A Comparison of the Airside Performance of the Fin-and-Tube Exchangers in Wet Conditions; With and Without Hydrophilic Coating," Appl. Therm. Eng., **22**, pp. 267–278.
[9] Kim, G., Lee, H., and Webb, R. L., 2002, "Plasma Hydrophilic Surface Treatments for Dehumidifying Heat Exchangers," Exp. Therm. Fluid Sci., **27**, pp. 1–10.
[10] Beatty, K. O., and Katz, D. L., 1948, "Condensation of Vapors on the Outside of Finned Tubes," Chem. Eng. Prog., **44**(1), pp. 55–70.
[11] Rudy, T. M., and Webb, R. L., 1985, "An Analytical Model to Predict Condensate Retention on Horizontal Integral-Fin Tubes," ASME J. Heat Transfer, **107**, pp. 361–368.
[12] Jacobi, A. M., and Goldschmidt, V. W., 1990, "Low Reynolds Number Heat and Mass Transfer Measurements of an Overall Counterflow, Baffled, Finned-Tube, Condensing Heat Exchanger," Int. J. Heat Mass Transfer, **33**, pp. 755–765.
[13] Korte, C. M., and Jacobi, A. M., 2001, "Condensate Retention and Effects on the Performance of Plain Fin-and-Tube Heat Exchangers: Retention Data and Modeling," ASME J. Heat Transfer, **123**, pp. 926–936.
[14] El Sherbini, A. I., and Jacobi, A. M., 2004, "Liquid Drops on Vertical and Inclined Surfaces: I. An Experimental Study of Drop Geometry," J. Colloid Interface Sci., **273**, pp. 556–565.
[15] El Sherbini, A. I., and Jacobi, A. M., 2004, "Liquid Drops on Vertical and Inclined Surfaces: II. A Method for Approximating Drop Shapes," J. Colloid Interface Sci., **273**, pp. 566–575.
[16] El Sherbini, A. I., and Jacobi, A. M., 2006, "Retention Forces and Contact Angles for Critical Liquid Drops on Non-Horizontal Surfaces," J. Colloid Interface Sci., **299**, pp. 841–849.
[17] El Sherbini, A. I., and Jacobi, A. M., 2006, "A Model for Condensate Retention on Plain-Fin Heat Exchangers," ASME J. Heat Transfer, **128**, pp. 427–433.
[18] Zhong, Y., Joardar, A., Gu, Z., Park, Y.-G., and Jacobi, A. M., 2005, "Dynamic Dip Testing as a Method to Assess the Condensate Drainage Behavior From the Air-Side Surface of Compact Heat Exchangers," Exp. Therm. Fluid Sci., **29**, pp. 957–970.
[19] Threlkeld, J. L., 1970, *Thermal Environmental Engineering*, 2nd ed., Prentice-Hall, Englewood Cliffs, NJ.
[20] Incropera, F. P., and Dewitt, D. P., 1990, *Fundamentals of Heat and Mass Transfer*, 3rd ed., Wiley, New York.
[21] Hong, T. K., and Webb, R. L., 1996, "Calculation of Fin Efficiency for Wet and Dry Fins," HVAC&R Res., **2**, pp. 27–41.
[22] Kim, G. J., and Jacobi, A. M., 2000, "Condensate Accumulation Effects on the Air-Side Thermal Performance of Slit-Fin Surfaces," *CR-26, Air Conditioning and Refrigeration Center*, University of Illinois, Urbana.
[23] Wilson, E. E., 1915, "A Basis for Rational Design of Heat Transfer Apparatus," Trans. ASME, **37**, pp. 47–82.
[24] Liu, L., and Jacobi, A. M., 2006, "The Effects of Hydrophilicity on Water Drainage and Condensate Retention on Air-Conditioning Evaporators," Proceedings of the 11th International Refrigeration and Air Conditioning Conference at Purdue, West Lafayette, IN, Article No. R090.
[25] Nusselt, W., 1916, "Die Oberflachenkondensation des Wasserdampfes," Z. Ver. Dtsch. Ing., **60**, pp. 541–546.
[26] Koh, J. C. Y., Sparrow, E. M., and Hartnett, J. P., 1961, "The Two Phase Boundary Layer in Laminar Film Condensation," Int. J. Heat Mass Transfer, **2**, pp. 69–82.
[27] Koh, J. C. Y., 1962, "Film Condensation in a Forced-Convection Boundary-Layer Flow," Int. J. Heat Mass Transfer, **5**, pp. 941–954.
[28] Jacobs, H. R., 1966, "An Integral Treatment of Combined Body Force and Forced Convection in Laminar Film Condensation," Int. J. Heat Mass Transfer, **9**, pp. 637–648.
[29] Fujii, F., and Uehara, H., 1972, "Laminar Filmwise Condensation on a Vertical Surface," Int. J. Heat Mass Transfer, **15**, pp. 217–233.
[30] Mendez, F., Lizardi, J. J., and Trevino, C., 2000, "Laminar Film Condensation Along a Vertical Fin," Int. J. Heat Mass Transfer, **43**, pp. 2859–2868.
[31] Churchill, S. W., and Usagi, R., 1972, "A General Expression for the Correlation of Rates of Transfer and Other Phenomena," AIChE J., **18**(6), pp. 1121–1128.

A Simplified Model of Heat and Mass Transfer Between Air and Falling-Film Desiccant in a Parallel-Plate Dehumidifier

Anna K. Hueffed

Louay M. Chamra[1]
e-mail: chamra@me.msstate.edu

Pedro J. Mago

Department of Mechanical Engineering,
Mississippi State University,
210 Carpenter Engineering Building,
P.O. Box ME,
Mississippi State, MS 39762-5925

This paper presents a simplified model to predict the heat and mass transfer between air and falling-film liquid desiccant during dehumidification in a parallel-plate absorber. First-order, ordinary differential equations are used to estimate the heat and mass transferred, and explicit equations are derived from conservation principles to yield the exiting absorber conditions for different flow arrangements. The developed model uses a control volume approach that accounts for the change in film thickness and property values. The model results were within 5% of a more complicated parallel-flow model currently available in literature. The model was also in good agreement with existing experimental data for a counterflow absorber. [DOI: 10.1115/1.3082420]

Keywords: liquid desiccant, parallel-plate dehumidifier, modeling heat, mass transfer

1 Introduction

The cost of electricity, grid stability, and global warming have become growing concerns, which are leading to alternative sources of energy generation and a primary focus on the efficient use of energy. One such area of interest is energy use in buildings where heating, ventilating, air conditioning, humidity control, and indoor air quality are important factors that also consume a large portion of the energy supplied to the building. When compared with traditional air conditioning methods, parallel-plate liquid desiccant systems can provide improved humidity control and reduced overall energy consumption while shifting the energy use away from electricity toward renewable and cheaper fuels [1–3]. In addition, liquid desiccants have the ability to filter the air of potentially hazardous inorganic and organic contaminants allowing for better indoor air quality [3,4].

During dehumidification in the absorber, water is directly transferred from the air and absorbed into the desiccant solution because the vapor pressure of the water vapor in the air is greater than the equilibrium vapor pressure of water in the air at the air-desiccant interface [5]. This equilibrium vapor pressure is more easily referred to as the vapor pressure of the desiccant. The reverse process of removing water from the desiccant solution to allow it to be reused occurs in the regenerator, where the vapor pressure of the desiccant is higher than the air stream. This process, called regeneration, is driven by heat. While solid desiccants have to be regenerated at temperatures between 80°C and 100°C, liquid desiccants can be regenerated at lower temperatures, between 50°C and 80°C, which allows regeneration from heat sources such as solar energy [6,7]. Other heat sources include gas burners or waste exhaust heat from industrial processes, cooling, heating, and power (CHP) applications, or from the compressor of either a vapor compression cycle or an absorption cycle.

Parallel-plate absorbers utilize a film of desiccant that is distributed across a vertical plate. The absorber consists of multiple parallel-plates with the air flowing through the gaps in the plates. Parallel-plate absorbers are often internally cooled, resulting in isothermal absorption, where cool water or a refrigerant flows through the plates, which effectively removes the heat of absorption. Isothermal absorption has the potential to provide simultaneous dehumidification and cooling of the air. Adiabatic absorption occurs in the absence of internal cooling, where the temperature of the air and the desiccant will increase due to the latent heat of the absorbed water vapor requiring a higher desiccant mass flow rate for efficient dehumidification [7].

Several researchers have performed experimental and theoretical investigations on the heat and mass transferred in a parallel-plate absorber [7–14]. Some of these are Kessling et al. [7], Rahamah et al. [11], Ali et al. [12,13], and Mesquita et al. [14].

Kessling et al. [7] conducted experiments for internally cooled parallel-plates with water flowing horizontally through the plates, LiCl desiccant flowing down the plates, and air flowing upward between the plates. Variable solution mass flow rates and variable air mass flow rates were tested. In addition, a finite difference model was used to estimate the mass transfer coefficient, β, from each experiment's inlet and exiting conditions.

Numerical models for parallel-plate absorbers have been developed that utilize finite difference methods. The second-order partial differential equations that describe fluid motion for each flow stream are solved at discrete nodes using interfacial equilibrium conditions. Isothermal absorption is modeled using constant property values. In addition, the flow is assumed to be steady state. This assumption neglects the rate of water vapor absorbed into the desiccant film and results in a desiccant film of constant-thickness. Models of this nature include Rahamah et al. [11], who investigated a parallel-flow arrangement, Ali et al. [12], who compared parallel and counterflow arrangements, and Ali et al. [13], who modeled a crossflow arrangement.

Mesquita et al. [14] developed three models to investigate the parallel and counterflow arrangements for an isothermal wall. In their model, they used constant property values. The first model used a constant desiccant film. The second model used a variable desiccant film thickness and a varying desiccant mass flow rate. The final model was a simplified model that decoupled the heat and mass transfer processes resulting in two independent first-order differential equations for energy and species. The process was decoupled by neglecting the latent heat of absorption because it was immediately removed by the internal cooling. The heat transfer coefficient in the simplified model was determined from a

[1]Corresponding author.

Contributed by the Heat Transfer Division of ASME for publication in the JOURNAL OF HEAT TRANSFER. Manuscript received December 5, 2007; final manuscript received November 13, 2008; published online March 18, 2009. Review conducted by S. A. Sherif.

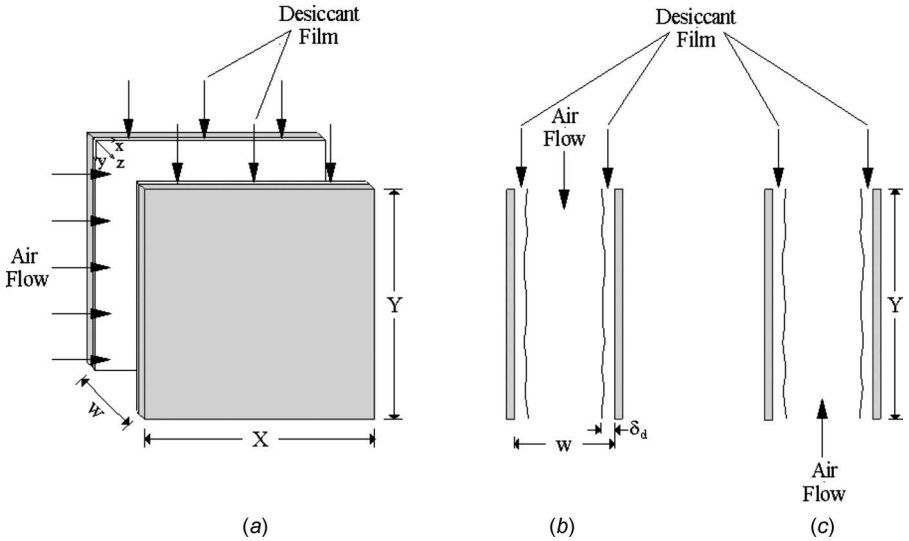

Fig. 1 Channel schematic for (*a*) crossflow, (*b*) parallel, and (*c*) counterflow arrangements

Nusselt number correlation and the mass transfer coefficient was determined from the Chilton–Colburn analogy. The constant-thickness models underpredicted the dehumidification, especially for low desiccant mass flow rates.

The objective of this paper is to develop a simplified model of desiccant dehumidification in a parallel-plate absorber that accounts for the varying thickness of the desiccant film. This simplified model would reduce simulation time, mainly because second-order partial differential equations no longer have to be solved. As a result, the application of absorbers and regenerators in complete systems could easily be modeled and evaluated. The model uses a control volume approach to determine the exiting conditions of a parallel-plate absorber based on the calculated rates of water and heat transferred from the air flow to the desiccant films. The model formulation for a control volume is developed followed by the model procedure for each flow arrangement. Results are presented and compared with available data from the open literature.

2 Analysis

This section presents the equations used to develop the model. The equations for adiabatic and isothermal absorptions, which are used to determine the exiting conditions of one control volume, are presented. This is followed by the procedure to determine the exiting conditions of the absorber from the control volumes.

2.1 Mathematical Formulation of Elemental Control Volume. In order to predict the overall performance of a parallel-plate absorber, only one channel of the absorber must be investigated, as each channel behaves independently. The schematic for one channel is presented in Fig. 1 for (a) crossflow, (b) parallel, and (c) counterflow arrangements. In every case, the desiccant solution flows down the inner side of each plate while the air flows through the channel.

To model the dehumidification process, the air flow and each desiccant film are divided into control volumes. The control volumes relative to the plate are illustrated in Fig. 2 and separated in Fig. 3 to include the rates of mass, water, and energy that cross the inlet and exit of the desiccant and air control volumes. Even though a parallel-flow arrangement is depicted, the direction of the air stream does not affect the governing equations for the control volume, but rather influences the procedure when analyzing the entire plate.

For each control volume, the inlet mass flow rate, inlet concentration of water, and inlet enthalpy, determined from the inlet temperature, are known. The inlet concentration of water in the air stream, C_a, is calculated using the molecular weight (MW) of water and dry air and the respective partial pressures according to

$$C_a = \frac{\mathrm{MW}_w P_w}{\mathrm{MW}_{\mathrm{da}}(P - P_w) + \mathrm{MW}_w P_w} \tag{1}$$

In addition, the inlet concentration of water in the air stream can be determined from the humidity ratio of the air, W_a, ($\mathrm{kg}_w/\mathrm{kg}_{\mathrm{da}}$), using the expression

$$C_a = \frac{W_a}{1 + W_a} \tag{2}$$

The inlet concentration of water in the desiccant solution, ζ_d, is related to the concentration of the desiccant in the solution, C_d, by

$$\zeta_d = 1 - C_d \tag{3}$$

Assumptions made in the formulation of the governing equations for one control volume include the following: The property values are constant and equal to the inlet value across the control volume, thermodynamic equilibrium exists at the air-desiccant interface, steady state, no heat or mass is transferred to or from the surroundings, no shear forces exists between the air and desiccant solution, no entrance length effects, and no body forces.

To determine the exiting conditions of the air and desiccant control volumes, the rates of water and heat transferred from the air to one desiccant film are first determined according to

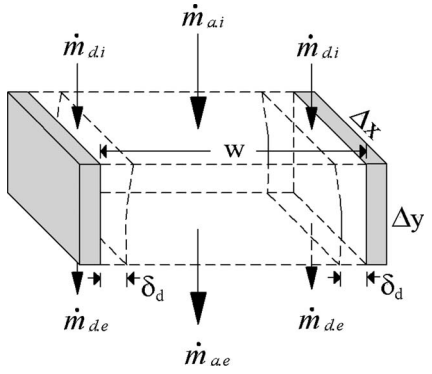

Fig. 2 Control volume relative to the plates

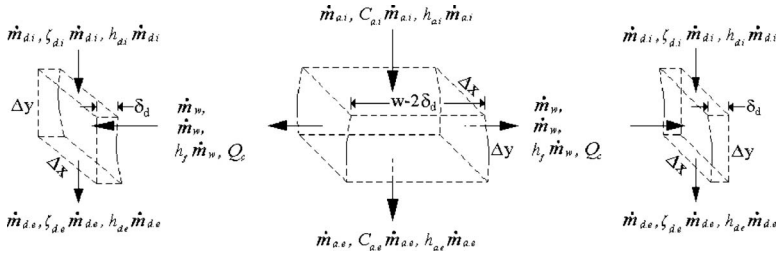

Fig. 3 Individual control volumes for the air flow and desiccant films

$$m_w = h_m \rho_a (C_a - C_{\text{int}}) \Delta x \Delta y \tag{4}$$

$$Q_c = h_h (T_a - T_d) \Delta x \Delta y \tag{5}$$

where h_m and h_h are the mass and heat transfer coefficients, respectively, and C_{int}, the equilibrium water concentration at the air-desiccant interface, is calculated by using the vapor pressure of the liquid desiccant solution instead of the water vapor pressure in Eq. (1). In Eq. (4) the vapor pressure of the liquid desiccant solution is calculated using the desiccant solution temperature since it was reported by Klausner et al. [15] that the difference between the interface temperature and the liquid temperature is negligible.

Next, conservation principles are applied across the control volume. Conservation of mass will yield the exiting mass flow rates, conservation of water will yield the exiting concentration of water, and conservation of energy will be used to determine the exiting temperatures. The conservations of mass and water for the air and desiccant solution are

$$\dot{m}_{a.e} = \dot{m}_{a.i} - 2\dot{m}_w \tag{6}$$

$$C_{a.e} = \frac{C_{a.i}\dot{m}_{a.i} - 2\dot{m}_w}{\dot{m}_{a.e}} \tag{7}$$

$$\dot{m}_{d.i} + \dot{m}_w = \dot{m}_{d.e} \tag{8}$$

$$\zeta_{d.e} = \frac{\zeta_{d.i}\dot{m}_{d.i} + \dot{m}_w}{\dot{m}_{d.e}} \tag{9}$$

2.2 Adiabatic Absorption. Dividing the air into its components of dry air and water vapor, the energy balance can be written as

$$\dot{m}_{\text{da}.i} h_{\text{da}.i} + \dot{m}_{\text{wv}.i} h_{g.i} = \dot{m}_{\text{da}.e} h_{\text{da}.e} + \dot{m}_{\text{wv}.e} h_{g.e} + 2\dot{m}_w h_{f.e} + 2Q_c \tag{10}$$

where the mass flow rates of dry air and water vapor are $\dot{m}_{\text{da}} = (1 - C_a)\dot{m}_a$ and $\dot{m}_{\text{wv}} = C_a \dot{m}_a$, respectively. Using these expressions and Eqs. (6) and (7), the exiting mass flow rate of dry air and water vapor are

$$\dot{m}_{\text{da}.e} = \dot{m}_{\text{da}.i} \tag{11}$$

$$\dot{m}_{\text{wv}.e} = \dot{m}_{\text{wv}.i} - 2\dot{m}_w \tag{12}$$

In order to determine the exiting temperature of the air flow, the enthalpy values must be represented as a function of temperature. This is done using the expressions

$$h_e - h_i = c_p (T_e - T_i) \tag{13}$$

$$h_{f.e} = c_{p.f} T_{a.e} \tag{14}$$

$$h_{g.e} = h_{g.0^\circ\text{C}} + c_{p.g} T_{a.e} \tag{15}$$

where $h_{g.0^\circ\text{C}}$ is the enthalpy of water vapor at 0 °C. Substituting Eqs. (11)–(15) into the energy balance of Eq. (10), the exiting air temperature is

$$T_{a.e} = \frac{\dot{m}_{\text{da}.i} c_{p.\text{da}} T_{a.i} + \dot{m}_{\text{wv}.i} c_{p.g} T_{a.i} + 2\dot{m}_w h_{g.0^\circ\text{C}} - 2Q_c}{\dot{m}_{\text{da}.i} c_{p.\text{da}} + \dot{m}_{\text{wv}.i} c_{p.g} - 2\dot{m}_w (c_{p.g} - c_{p.f})} \tag{16}$$

Likewise, the energy balance for a desiccant film control volume is

$$\dot{m}_{d.i} h_{d.i} + \dot{m}_w h_{f.e} + Q_c = \dot{m}_{d.e} h_{d.e} \tag{17}$$

where the enthalpy values are taken to be $h_d = c_{p.d} T_d$. The exiting desiccant temperature is then

$$T_{d.e} = \frac{\dot{m}_{d.i} c_{p.d} T_{d.i} + \dot{m}_w c_{p.f} T_{a.e} + Q_c}{\dot{m}_{d.e} c_{p.d}} \tag{18}$$

2.3 Isothermal Absorption. During isothermal absorption, each plate is internally cooled with water or a refrigerant. With an adequate flow rate of the internal fluid, the desiccant plate and, therefore, the desiccant solution will have a constant temperature equal to that of the internal fluid within a negligible distance of the absorber inlet

$$T_{d.e} = T_{\text{wall}} \tag{19}$$

Substituting the exiting mass flow rates, Eqs. (11) and (12), into Eq. (10), the energy balance can be expanded and rearranged to yield

$$0 = \dot{m}_{\text{da}.i}(h_{\text{da}.e} - h_{\text{da}.i}) + \dot{m}_{\text{wv}.i}(h_{g.e} - h_{g.i}) - 2\dot{m}_w(h_{g.e} - h_{f.e}) + 2Q_c \tag{20}$$

where the heat of absorption term $(h_{g.e} - h_{f.e})$ goes to zero for isothermal absorption. Using the same expression for the change in enthalpy, Eq. (13), the exiting air temperature reduces to

$$T_{a.e} = T_{a.i} - \frac{2Q_c}{\dot{m}_{a.i} c_{p.a}} \tag{21}$$

2.4 Determination of Transfer Coefficients. In the process of finding the exiting conditions for the air flow and desiccant film, the heat and mass transfer coefficients must be known. For laminar flow through a duct with constant surface temperature, the Nusselt number for air is 7.54 [16,17]. The heat transfer coefficient can then be obtained from the definition of Nusselt number and hydraulic diameter

$$h_h = \frac{\text{Nu}\ k_a}{D_h} \tag{22}$$

$$D_h = \frac{4A_c}{P_{\text{wetted}}} = \frac{4Y(w - 2\delta_d)}{2Y} = 2(w - 2\delta_d) \tag{23}$$

where the thickness of the desiccant film, δ_d, is [11–14]

$$\delta_d = \left(\frac{3\dot{m}_d \mu_d}{\rho_d^2 g} \right)^{1/3} \tag{24}$$

The mass transfer coefficient is determined from the Chilton–Coulburn analogy as

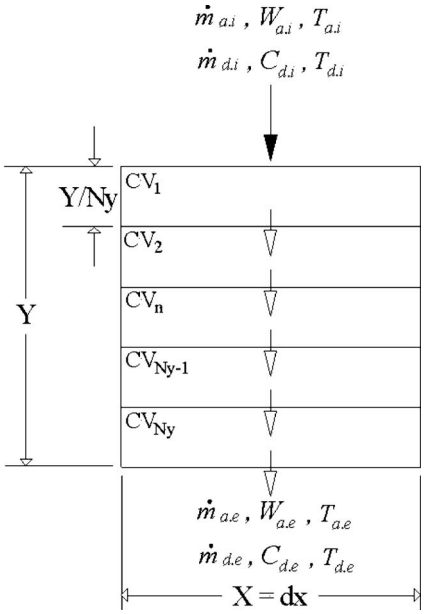

Fig. 4 Procedure illustration for parallel-flow

$$h_m = \frac{h_h}{c_{p.a}}\left(\frac{\alpha_a}{D_{a.\mathrm{wv}}}\right)^{-2/3} \tag{25}$$

For each control volume δ_d, D_h, h_h, h_m, and the physical properties are recalculated based on the inlet conditions of the control volume.

2.5 Model Procedure. For the simplest case of a parallel-flow arrangement, Fig. 1(*b*), the width of each control volume is equal to the width of the plate. The height of each control volume is the height of the plate, *Y*, divided by the number of control volumes, *Ny*, as shown in Fig. 4.

The known absorber inlet conditions for the air and desiccant solution are the inputs to the first control volume. The outputs of this control volume are determined and become the inlet conditions for the next control volume. This process is repeated until the outputs for the final control volume, the exiting conditions of the absorber, are determined.

Complexities arise in the counterflow arrangement, Fig. 1(*c*), because an iterative approach is required. Initially, for every control volume the desiccant solution is given a constant concentration and temperature equal to the inlet condition of the absorber, displayed in Fig. 5(*a*). The outlet air conditions are determined and the transfer rates of water and heat from each control volume

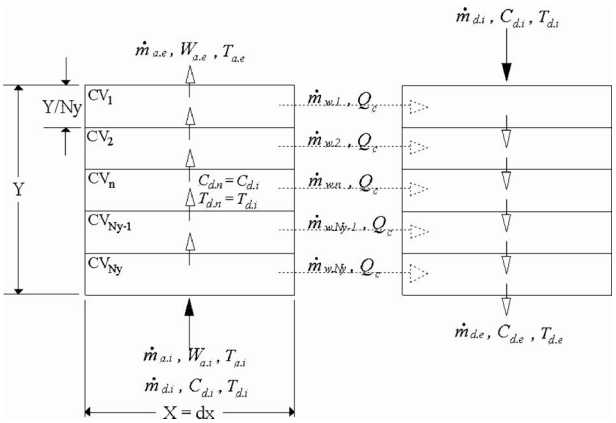

Fig. 5 Procedure illustration for counterflow

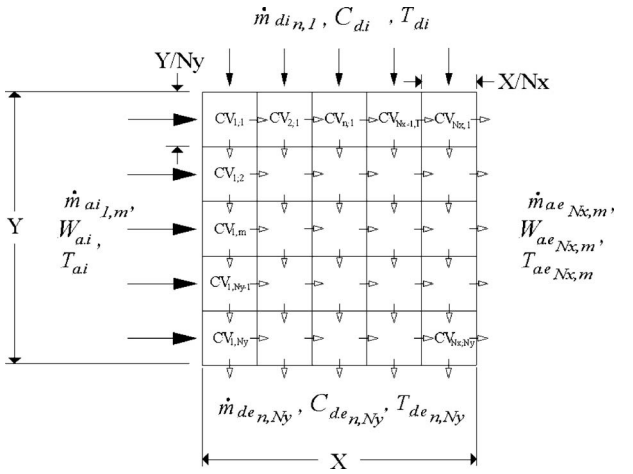

Fig. 6 Procedure illustration for crossflow

are saved. The latter information is then used to determine the exiting desiccant conditions, Fig. 5(*b*). Next, the calculated desiccant outputs for each control volume replace the previously constant desiccant values and the exiting air conditions are recalculated. This process continues until two consecutive solutions are within a specified tolerance.

In the previous two arrangements, parallel and counterflow, the program procedure was one dimensional. In the crossflow arrangement, Fig. 1(*a*), the procedure is similar but becomes two dimensional. The height of each control volume remains the height divided by the number of control volumes down the plate. The width of each control volume becomes the width of the plate, *X*, divided by the number of control volumes across the plate, *Nx*, given in Fig. 6.

An important note is that the inlet mass flow rates to the absorber must be adjusted to obtain the inlet mass flow rate for certain control volumes, and the exiting mass flow rates leaving the absorber are the sum of the individual rates leaving the last control volumes. For example, the inlet mass flow rate of air for the control volumes in the first column, $\dot{m}_{a.i_{1,m}}$ for $CV_{1,m}$, and the exiting desiccant mass flow rate of the absorber are

$$\dot{m}_{a.i_{1,m}} = \frac{\dot{m}_{a.i}}{Ny} \tag{26}$$

$$\dot{m}_{d.e} = \sum_{n=1}^{Nx} \dot{m}_{d.e_{n,Ny}} \tag{27}$$

To quantify the other exiting conditions, an average is taken of the exiting values from the control volumes on the last row or column. For example, the exiting humidity ratio of air is

$$W_{a.e} = \frac{1}{Ny}\sum_{m=1}^{Ny} W_{a.e_{Nx,m}} \tag{28}$$

3 Results and Discussion

To initially validate the results of the program, a simple mass balance was performed to verify that the amount of water lost by the air was equal to the amount of water absorbed by the two desiccant films, which is represented by

$$\dot{m}_{a.i}C_{a.i} - \dot{m}_{a.e}C_{a.e} = 2(\dot{m}_{d.e}\zeta_{d.e} - \dot{m}_{d.i}\zeta_{d.i}) \tag{29}$$

Next, the model was compared with available theoretical and experimental data in literature. The parallel-flow arrangement was compared with the variable-thickness model developed by Mesquita et al. [14], which determined the exiting air temperature and humidity ratio for a range of inlet desiccant mass flow rates. The

Table 1 Inlet conditions and absorber characteristics used to compare the present model with the variable-thickness model by Mesquita et al. [14]

Air mass flow rate $\dot{m}_a$ (kg/s)	0.01264
Air humidity ratio, W_a (kg_w/kg_a)	0.015228
Air temperature, T_a (°C)	30
Desiccant concentration, C_d (kg_d/kg_s)	0.4
Desiccant temperature, T_d (°C)	25
Wall temperature, T_{wall} (°C)	25
Plate height, Y (m)	0.5
Plate width, X (m)	1
Plate spacing, w (m)	0.005
Number of control volumes, Ny	500
Desiccant	LiCl
Flow arrangement	Parallel
Absorption process	Isothermal

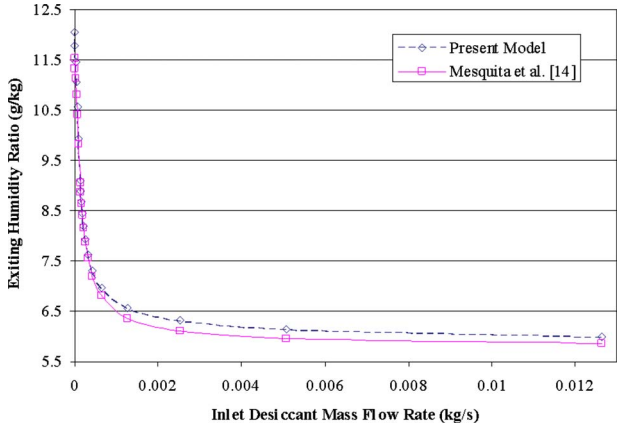

Fig. 7 Exiting humidity ratio for a range of inlet desiccant mass flow rates of the present model compared with the variable-thickness model by Mesquita et al. [7]

Table 2 Absorber characteristics from Kessling et al. [7]

Plate height, Y (m)	0.46
Plate width, X (m)	0.98
Plate spacing, w (m)	0.0055
Total pressure, P (Pa)	96000
Flow arrangement	Counterflow
Absorption process	Isothermal

inlet conditions and absorber characteristics for the model are given in Table 1. Figure 7 shows the exiting humidity ratio for a range of inlet desiccant mass flow rates. From this figure, it can be observed that the humidity ratio decreases with the increase in the inlet desiccant mass flow rate. Also, Fig. 7 illustrates that the results of the present model are in good agreement with the variable-thickness model developed by Mesquita et al. [14] with the maximum error being about 5%.

A simulation implementing a counterflow arrangement was compared with two sets of experiments conducted by Kessling et al. [7] with the absorber characteristics given in Table 2. In an additional simulation, the present model used the β values as a constant input value for the mass transfer coefficient. The experimental inlet conditions, along with the calculated β values, for variable inlet desiccant mass flow rate and variable inlet air mass flow rate experiments are given in Tables 3 and 4, respectively. The desiccant mass flow rates presented by Kessling et al. [7] were for one channel of an absorber. The desiccant mass flow rates currently reported have been adjusted to reflect the mass flow rate down a single plate. In addition, the wall temperatures currently reported are an average of the measured inlet and exiting temperatures of the internal cooling water reported by Kessling et al. [7]. The exiting humidity ratio values are plotted in Fig. 8 for the range of inlet desiccant mass flow rates and Fig. 9 presents the results for the range of inlet air mass flow rates. Figure 8 shows that the exiting humidity ratio decreases with the inlet desiccant mass flow rate, while Fig. 9 demonstrates that the exiting humidity ratio increases with the inlet air mass flow rate.

The two models follow the experimental trend for both sets of experiments. In comparison to the variable inlet desiccant mass flow rate experimental data, the present model (Nu=7.54) gave 9% error for the lowest mass flow rates, but showed large errors, up to 30%, for the highest inlet desiccant mass flow rate. When Mesquita et al. [14] compared a counterflow arrangement of the variable-thickness model to this set of experiments, the error in the exiting humidity ratio went from approximately 0% for the lowest desiccant mass flow rate to about 15% for the highest desiccant mass flow rate. The difference between the present model and the variable-thickness model by Mesquita et al. [14] could be due to the use of the constant Nusselt number along with the method used for determining the mass transfer coefficient. For variable inlet air mass flow rates, the present model predicted the exiting air conditions within 17% for the lowest air mass flow rates and 13% for the highest air mass flow rates.

When comparing to both sets of experiments, the present model consistently underpredicted the dehumidification; however, when the β values were used as the mass transfer coefficients in the

Table 3 Inlet conditions for a range of inlet desiccant mass flow rates with a constant inlet air mass flow rate of 12.64 g/s [7]

Desiccant mass flow rate, $\dot{m}_d$ g/s)	1.242	0.653	0.374	0.229	0.169	0.142	0.116
Air humidity ratio, W_a (g_w/kg_a)	14.4	14.5	14.5	14.5	14.5	14.5	14.4
Air temperature, T_a (°C)	24.5	24.8	24.6	24.4	24.4	24.1	23.9
Desiccant concentration, C_d (%)	40.2	40.2	40.2	40.2	40.2	40.2	40.2
Wall temperature, $T_{wall}=T_d$ (°C)	24.3	24.3	24.3	24.25	24.25	24.25	24.2
Mass transfer coefficient, β (mm/s)	25.9	25.2	22.6	20.8	20.3	21.5	20.7

Table 4 Inlet conditions for a range of inlet air mass flow rates with a constant inlet desiccant mass flow rate of 0.1175 g/s [7]

Air mass flow rate, $\dot{m}_a$ (g/s)	6.36	9.48	12.51	15.52	18.68	21.72	24.83
Air humidity ratio, W_a (g_w/kg_a)	14.5	14.4	14.6	14.6	14.7	14.7	14.7
Air temperature, T_a (°C)	24.7	23.4	23.6	23.4	23.3	23.5	23.8
Desiccant concentration, C_d (%)	40.2	40.2	40.2	40.2	40.2	40.2	40.2
Wall temperature, $T_{wall}=T_d$ (°C)	24.2	24.25	24.2	24.25	24.25	24.25	24.25
Mass transfer coefficient, β (mm/s)	18.7	21.5	23.5	25.4	27.7	29	30.7

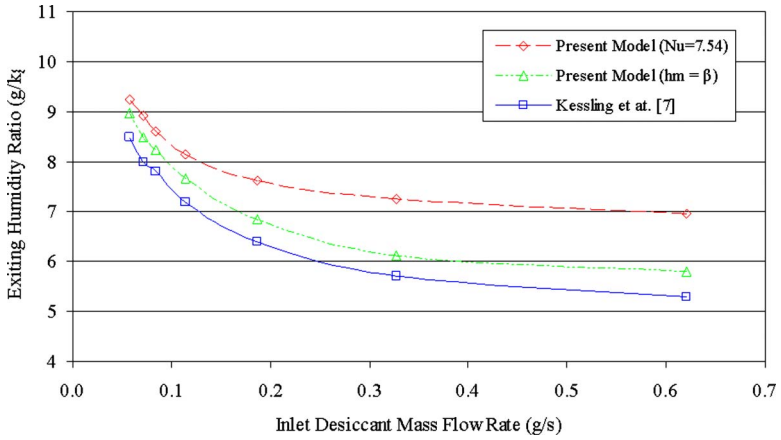

Fig. 8 Exiting humidity ratio for a range of inlet desiccant mass flow rates of the present model compared with experimental data by Kessling et al. [7]

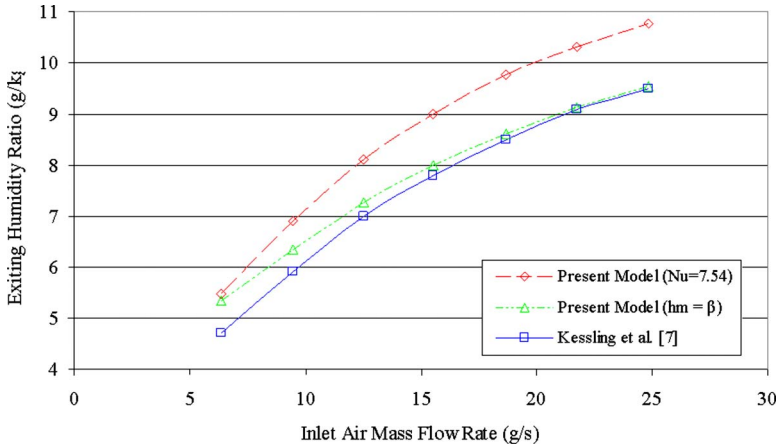

Fig. 9 Exiting humidity ratio for a range of inlet air mass flow rates of the present model compared with experimental data by Kessling et al. [7]

model, the results were significantly improved. For the variable inlet desiccant mass flow rate, the errors were about 5.5% for the lowest mass flow rate and about 9% for the highest mass flow. The variable inlet air mass flow rate resulted in errors of about 13.5% for the lowest mass flow rates to almost 0% for high mass flow rates.

The experimental data and associated uncertainties for the variable inlet desiccant mass flow rate and variable inlet air mass flow rate experiments conducted by Kessling et al. [7] were used to perform a complete uncertainty analysis. Using the β values for the mass transfer coefficient, the model uncertainty in the exiting humidity ratio has an average of 6.5%. The model uncertainty, along with the experimental data of Kessling et al. [7], was used to validate the model using the methodology described in Ref. [18]. The model was validated over the range of the input variables at the validation level of approximately 7% for the exiting air humidity ratio.

4 Conclusion

A simplified model to determine the air and desiccant exiting conditions of a parallel-plate absorber was successfully developed. Conservation of mass, water, and energy were used in a control volume approach that allowed for property variations and varying desiccant thickness. Procedures for parallel, crossflow, and counterflow were presented. Using a constant Nusselt number, the developed model was within 5% of a more complicated finite difference model for flow in a parallel arrangement. However, larger errors, between 10% and 30%, arose when the model was compared with available experimental data for a counterflow arrangement. When an experimentally determined mass transfer coefficient was used in the model, the counterflow results were within 13.5%.

Nomenclature

A_c = cross-sectional area (m^2)
C_a = concentration of water in air mixture (kg_w/kg_a)
C_d = concentration of desiccant in solution (kg_d/kg_s)
C_I = equilibrium water concentration of air at desiccant-air interface (kg_w/kg_a)
c_p = specific heat (J/kg K)
D = mass diffusivity (m^2/s)
D_h = hydraulic diameter (m)
g = acceleration due to gravity (m/s^2)
h = enthalpy (kJ/kg)
$h_{g,0°C}$ = enthalpy of saturated water vapor at 0°C (kJ/kg)
h_h = heat transfer coefficient (W/m^2 K)
h_m = mass transfer coefficient (m/s)
k = thermal conductivity (W/m K)
$\dot{m}_a$ = mass flow rate of air per channel (kg/s)
$\dot{m}_d$ = mass flow rate of desiccant per plate (kg/s)
$\dot{m}_w$ = mass flow rate of water (kg/s)

MW = molecular weight
Nu = Nusselt number
Nx = number of control volumes in the x-direction
Ny = number of control volumes in the y-direction
P = pressure (Pa)
$P_{v.d}$ = surface vapor pressure of desiccant solution (Pa)
P_w = saturation pressure of water vapor (Pa)
P_{wetted} = wetted perimeter (m)
Q_c = convective heat transfer (W)
T = temperature (°C)
W_a = humidity ratio of air ($\text{kg}_w/\text{kg}_{\text{da}}$)
w = plate spacing (m)
X = plate width (m)
x = coordinate normal to film and tangent to plate
Y = plate height (m)
y = coordinate parallel to desiccant flow
z = coordinate perpendicular to plate

Greek

α = thermal diffusivity (m^2/s)
β = mass transfer coefficient calculated by Kessling et al. [7] (m/s)
δ_d = desiccant film thickness (m)
ζ_d = concentration of water in desiccant solution (kg_w/kg_s)
ρ = density (kg/m^3)
μ = dynamic viscosity ($\text{N s}/\text{m}^2$)

Subscripts

a = air mixture of dry air and water vapor
d = desiccant
da = dry air
f = saturated liquid water
g = saturated water vapor
s = desiccant solution
w = water
wv = water vapor
i = inlet
e = exit

References

[1] Jain, S., Dhar, P. L., and Kaushik, S. C., 1994, "Evaluation of Liquid Desiccant Based Evaporative Cooling Cycles for Typical Hot and Humid Climates," Heat Recovery Syst. CHP, **14**, pp. 621–32.
[2] Waugaman, D. G., Kini, A., and Kettleborough, C. F., 1993, "A Review of Desiccant Cooling Systems," ASME J. Energy Resour. Technol., **115**, pp. 1–8.
[3] Jain, S., and Bansal, P. K., 2007, "Performance Analysis of Liquid Desiccant Dehumidification Systems," Int. J. Refrig., **30**(5), pp. 861–872.
[4] Oberg, V., and Goswami, D. Y., 1998, "Experimental Study of Heat and Mass Transfer in a Packed Bed Liquid Desiccant Air Dehumidifier," ASME J. Sol. Energy Eng., **120**, pp. 289–297.
[5] ASHRAE, 2005, *Handbook Fundamentals*, American Society of Heating, Refrigeration and Air-Conditioning Engineers, Inc., Atlanta, GA.
[6] Kessling, W., Laevemann, E., and Peltzer, M., 1998, "Energy Storage in Open Cycle Liquid Desiccant Cooling Systems," Int. J. Refrig., **21**(2), pp. 150–156.
[7] Kessling, W., Laevemann, E., and Kapfhammer, C., 1998, "Energy Storage for Desiccant Cooling Systems Component Development," Sol. Energy, **64**(4–6), pp. 209–221.
[8] Lowenstein, A., Slayzak, S., and Kozubal, E., 2006. "A Zero Carryover Liquid-Desiccant Air Conditioner for Solar Applications," 2006 National Solar Conference, Denver, CO.
[9] Park, M. S., Howell, J. R., Vliet, G. C., and Peterson, J., 1994, "Numerical and Experimental Results for Coupled Heat and Mass Transfer Between a Desiccant Film and Air in Cross-Flow," Int. J. Heat Mass Transfer, **37**, (1), pp. 395–402.
[10] Ali, A., and Vafai, K., 2004, "An Investigation of Heat and Mass Transfer Between Air and Desiccant Film in an Inclined Parallel and Counter Flow Channels," Int. J. Heat Mass Transfer, **47**, pp. 1745–1760.
[11] Rahamah, A., Elsayed, M. M., and Al-Najem, N. M., 1998, "A Numerical Solution for Cooling and Dehumidification of Air by a Falling Desiccant Film in Parallel Flow," Renewable Energy, **13**(3), pp. 305–322.
[12] Ali, A., Vafai, K., and Khaled, A.-R. A., 2003, "Comparative Study Between Parallel and Counter Flow Configurations Between Air and Falling Film Desiccant in the Presence of Nanoparticle Suspensions," Int. J. Energy Res., **27**, pp. 725–745.
[13] Ali, A., Vafai, K., and Khaled, A.-R. A., 2004, "Analysis of Heat and Mass Transfer Between Air and Falling Film in a Cross Flow Configuration," Int. J. Heat Mass Transfer, **47**, pp. 743–755.
[14] Mesquita, L. C., Harrison, S., and Thomey, D., 2006, "Modeling of Heat and Mass Transfer in Parallel Plate Liquid-Desiccant Dehumidifiers," Sol. Energy, **80**, pp. 1475–1482.
[15] Klausner, J. F., Li, Y., and Mei, R., 2006, "Evaporative Heat and Mass Transfer for the Diffusion Driven Desalination Process," Heat Mass Transfer, **42**(6), pp. 528–536.
[16] Bejan, A., 2004, *Convection Heat Transfer*, 4th ed., Wiley, Hoboken, NJ.
[17] Incropera, F. P., and DeWitt, D. P., 2002, *Fundamentals of Heat and Mass Transfer*, 5th ed., Wiley, Hoboken, NJ.
[18] Coleman, H. W., and Steele, W. G., 1999, *Experimentation and Uncertainty Analysis for Engineers*, 2nd ed., Wiley, New York.

Study on Contact Melting Inside an Elliptical Tube With Nonisothermal Wall

Yuansong Zhao
Graduate Student

Wenzhen Chen
Professor
e-mail: cwz2@21cn.com

Fengrui Sun
Professor

Faculty 301,
College of Power and Shipping,
Naval University of Engineering,
Wuhan, Hubei 430033, China

The problem of contact melting inside an elliptical tube with nonisothermal wall is investigated. A theoretical model, which the inner wall temperature of source varied with angle ϕ, is established by applying film theory. The basic equations of the melting process are solved theoretically, and a closed-form solution is obtained. Under certain cases, comparisons of results for the melting velocity with those of contact melting inside a horizontal cylindrical tube with nonisothermal wall and an elliptical tube with constant temperature are reported for the validity of the solution in this paper. Effects of aspect ratio J and inner wall temperature distribution are critically assessed. It is found that the smaller the elliptical aspect ratio J is, the greater the effect of wall temperature distribution on melting velocity, and the time to complete melting increases with the augment of coefficient c in temperature distribution. [DOI: 10.1115/1.3001018]

Keywords: contact melting, heat transfer, elliptical tube, nonisothermal wall

1 Introduction

Under the gravity or other external force, a solid phase change material (PCM) contacts with heat source, the melting occurs while the temperature of heat source is higher than the melting point of PCM, and the molten liquid at the melting interface is squeezed up through a narrow gap between the melting surface and the wall of heat source. During the melting, the solid PCM keeps contacting with the heat source all the time; this phenomenon is called ΔT-driven contact melting.

The heat transfer phenomena during the melting of PCM in a cavity attracted much attention by application in latent thermal storage systems. Due to the density change between the solid PCM and molten liquid, the solid PCM always contacted with the part wall of a cavity; therefore, this phenomenon is the so-called close-contact melting problem. Up to the present, there are a large amount of researches on melting in cavities [1]. For example, the melting of PCM in a cylindrical tube was studied by Bareiss and Beer [2] analytically. Bahrami and Wang [3] and Roy and Sengupta [4] gave the solution of contact melting in the spherical capsule. The contact melting processes inside the rectangular enclosure were investigated experimentally [5] and theoretically [6–8]. Studies [9,10] investigated the contact melting inside and around the horizontal elliptical heat source, and the role of the shape of heat source was assessed. Literatures [11–13] reported solutions of contact melting inside various capsules. Most of previous investigations focused on the contact melting under the condition of constant temperature difference. There was less research on the contact melting with varying wall temperatures. However, the inner capsule wall temperature considerably varies in the practical systems. It is significant to study the effect of temperature distribution along the wall of heat source on melting. The contact melting processes inside the spherical and horizontal cylindrical enclosures with varying temperatures were analyzed, respectively, by Saitoh and Hoshina [14] and Fomin and Saitoh [15], and the effect of temperature distribution along the wall of heat source was discussed. Halawa et al. [16] also investigated the melting characteristic of a PCM thermal storage unit (TSU) with varying wall temperatures. In the present paper, the melting of PCM inside a horizontal elliptical tube is analyzed theoretically. The influences of inner wall temperature distribution of the tube on the melting velocity and the thickness distribution of the molten layer are discussed.

2 Model and Equations

A schematic model and coordinate system used in the present analysis is illustrated in Fig. 1. An elliptical tube, with surface curve described by the equation $(x/a)^2+(y/b)^2=1$, contains the phase change material that initially is in the solid phase and entirely at melting point T_m. The wall temperature is instantly raised to temperature $T_w=T_{w0}[1+F(\phi)]$ (based on Fomin and Saitoh [15]), which is higher than T_m; as a result, the inward melting of the solid starts. The unfixed solid sinks in velocity of $\dot{H}$ because its density is higher than that of the molten liquid. The motion of the solid block is accompanied by the generation of liquid at the melting interface, and the liquid is squeezed up to the space above the solid through a narrow gap between the melting surface and the wall of the tube. Conventionally, the solid-liquid interface can be divided into two parts by the time dependent value of the polar angle ϕ_A: a bottom interface ($\phi \leq \phi_A$), which represents the close-contact melting area where the most melting occurs, and an upper interface ($\phi > \phi_A$) where much slower melting takes place. As noted investigations on melting inside a horizontal cylinder and sphere conducted by Bareiss and Beer [2] and Bahrami and Wang [3], melting at the upper surface of the solid was approximately 10–15% of total melt, and the shape of this surface did not change throughout the entire melting process. It was also discovered that the thickness of the molten layer δ in the close-contact area was considerably smaller than the characteristic size of the enclosure. On the basis of these conclusions, we apply the assumptions in the present study as follows.

(1) Melting at the upper surface of the solid block can be neglected.
(2) Since the thickness of the molten layer in the close-contact area is very small, i.e., $\delta \ll \min(a,b)$, the lubrication theory approach can be implemented for mathematical modeling of heat and mass transfer process at the bottom surface.
(3) The thermophysical properties of PCM are constant.

Contributed by the Heat Transfer Division of ASME for publication in the JOURNAL OF HEAT TRANSFER. Manuscript received April 30, 2008; final manuscript received July 14, 2008; published online March 20, 2009. Review conducted by Ali Ebadian.

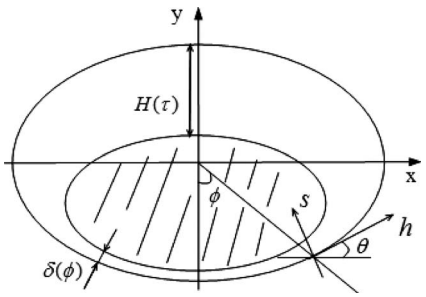

Fig. 1 Model and coordinates

(4) The process is quasisteady; the acting forces are balanced during melting.

Under the above assumptions, the momentum equation and boundary conditions can be written as follows:

$$\mu \partial^2 u/\partial s^2 = \partial P/\partial h \tag{1}$$

$$s = 0: u = v = 0, \quad T = T_w = T_{w0}[1 + F(\phi)]$$

$$s = \delta: u = 0, \quad v = -\dot{H}\cos\theta, \quad T = T_m \tag{2}$$

$$-\lambda \left.\frac{\partial T}{\partial s}\right|_{s=\delta} = \rho_s L_m \dot{H}\cos\theta \tag{3}$$

Since the molten layer is very thin, the temperature distribution inside the molten layer can be approximated by a linear distribution in s, which satisfies boundary conditions (2) and leads to

$$T = T_{w0}[1 + F(\phi)] + \frac{T_m - T_{w0}[1 + F(\phi)]}{\delta} s \tag{4}$$

Substituting Eq. (4) into Eq. (3) yields

$$\delta = \frac{\lambda[T_{w0} - T_m + T_{w0}F(\phi)]}{\rho_s \dot{H}\cos\theta} \tag{5}$$

The solution of Eq. (1) with boundary conditions (2) is

$$u = \frac{1}{2\mu}\frac{dP}{dh}(s^2 - s\delta) \tag{6}$$

The mass balance equation in the molten layer is

$$\int_0^\delta \rho_l u ds = \int_0^\phi \rho_s \dot{H}\cos\theta dh \tag{7}$$

Substituting Eq. (6) into Eq. (7), the pressure gradient in the molten layer is found to be

$$\frac{dP}{dh} = -\frac{12\mu\rho_s\dot{H}}{\rho_l\delta^3}\int_0^\phi \cos\theta dh \tag{8}$$

On the bases of the geometry relation in Fig. 1, the relations between ϕ and θ and dh and $d\phi$ are described as follows:

$$(x/a)^2 + (y/b)^2 = 1 \tag{9}$$

$$tg\theta = J^2 tg\phi \tag{10}$$

$$dh = \sqrt{\frac{1 + J^4 tg^2\phi}{1 + J^2 tg^2\phi}}\frac{b}{\cos^2\phi + J^2\sin^2\phi}d\phi = bG(\phi)d\phi \tag{11}$$

where $J(J = b/a)$ is the elliptical aspect ratio of the capsule, and

$$G(\phi) = \sqrt{\frac{1 + J^4 tg^2\phi}{1 + J^2 tg^2\phi}}\frac{1}{\cos^2\phi + J^2\sin^2\phi}$$

Substituting Eq. (11) into Eq. (8) leads to

$$\frac{dP}{d\phi} = -\frac{12\mu\rho_s\dot{H}}{\rho_l\delta^3}b^2 G(\phi)\int_0^\phi \cos\theta G(\phi)d\phi \tag{12}$$

The force balance equation is

$$2\int_0^{\phi_A} P\cos\theta dh = g(\rho_s - \rho_l)V_s \tag{13}$$

Note that

$$V_s = 2ab\left[\arccos\left(\frac{H}{2b}\right) - \left(\frac{H}{2b}\right)\sqrt{1 - \left(\frac{H}{2b}\right)^2}\right] \tag{14}$$

Combining Eqs. (12)–(14) yields

$$\int_0^{\phi_A} P\cos\theta G(\phi)d\phi = g(\rho_s - \rho_l)a\left[\arccos\left(\frac{H}{2b}\right) - \left(\frac{H}{2b}\right)\sqrt{1 - \left(\frac{H}{2b}\right)^2}\right] \tag{15}$$

The dimensionless parameters are defined as follows: $\delta^* = \delta/b$, $\rho^* = \rho_l/\rho_s$, $\dot{H}^* = \dot{H}b/(2\alpha)$, $H^* = H/(2b)$, $\mathrm{Ste} = c_p(T_{w0} - T_m)/L_m$, $\mathrm{Ste}_{w0} = c_p T_{w0}/L_m$, $P^* = P/[(\rho_s - \rho_l)gb]$, $A_r = (1 - \rho^*)gb^3/\upsilon^2$, and $\mathrm{Pr} = \upsilon/\alpha$.

Equations (5), (12), and (15) are converted to dimensionless form as follows:

$$\delta^* = \frac{\rho^*[\mathrm{Ste} + \mathrm{Ste}_{w0}F(\phi)]}{2\cdot\dot{H}^*\cos\theta} \tag{16}$$

$$\frac{dP^*}{d\phi} = \frac{-24(\dot{H}^*)^4\cos^3\theta}{\rho^{*3}\,\mathrm{Pr}\,\mathrm{Ar}\cdot[\mathrm{Ste}/2 + \mathrm{Ste}_{w0}F(\phi)/2]^3}G(\phi)\int_0^\phi \cos\theta G(\phi)d\phi \tag{17}$$

$$\int_0^{\phi_A} P^*\cos\theta\cdot G(\phi)d\phi = [\arccos(H^*) - H^*\sqrt{1 - H^{*2}}]/J \tag{18}$$

Note that

$$\cos\phi_A = \frac{H(\tau)}{2\sqrt{[H(\tau)/2]^2 + a^2\{1 - [H(\tau)/(2b)]^2\}}} = \frac{JH^*}{\sqrt{1 + (J^2 - 1)(H^*)^2}} \tag{19}$$

Equations (10) and (16)–(19) are the basic equations describing the problem in this paper. The boundary condition is $P^* = 0$ at $\phi = \phi_A$.

The time to complete melting and the melting rate can be expressed as follows:

$$\tau_f = \int_0^{2b}(\dot{H})^{-1}dH \tag{20}$$

$$V^* = 1 - V_s/(\pi ab) = 1 - 2[\arccos(H^*) - H^*\sqrt{1 - H^*}]/\pi \tag{21}$$

The variation in melting velocity $\dot{H}^*$ ($\dot{H}^* = f(H^*)$) versus drop height H^* could be obtained numerically. The result is substituted into Eq. (20), then the corresponding melting time will be solved, and the relation between the melting rate and melting time can be obtained by Eq. (21).

3 Results and Discussion

While $J = 1$, then $\theta = \phi$, the capsule is a horizontal cylindrical tube. Substituting $J = 1$ and $\theta = \phi$ into Eqs. (17) and (18) yields

$$\frac{dP^*}{d\phi} = \frac{-24(\dot{H}^*)^4\cos^3\theta\sin\theta}{\rho^{*3}\,\mathrm{Pr}\,\mathrm{Ar}\cdot[\mathrm{Ste}/2 + \mathrm{Ste}_{w0}F(\phi)/2]^3} \tag{22}$$

$$\int_0^{\phi_A} P^* \cos\phi d\phi = [\arccos(H^*) - H^*\sqrt{1-H^{*2}}] \tag{23}$$

Combining Eqs. (22) and (23), the melting velocity of solid PCM is as follows:

$$\dot{H}^* = 0.4518 \cdot [\rho^{*3}\ \mathrm{Pr}\ \mathrm{Ar}]^{1/4} \cdot \left[\frac{\arccos(H^*) - H^*\sqrt{1-H^{*2}}}{I(\mathrm{Ste}, \mathrm{Ste}_{w0}, \phi_A)}\right]^{1/4} \tag{24}$$

where

$$I(\mathrm{Ste}, \mathrm{Ste}_{w0}, \phi_A) = \int_0^{\phi_A} \frac{\cos^3\phi \sin^2\phi}{[\mathrm{Ste}/2 + \mathrm{Ste}_{w0} F(\phi)/2]^3} d\phi$$

Equation (24) is the melting velocity inside a horizontal cylindrical tube with no-isothermal wall obtained in this paper. Close-contact melting with inner wall temperature variation in a horizontal cylinder capsule was investigated by Saitoh and Hoshina [14], with an analysis model that the temperature distribution inside the molten layer is approximated by a quadratic polynomial. However, some mistakes are found in that paper. Using the same model as theirs, we analyze the melting problem again, and the corrected expression of the melting velocity is obtained as follows:

$$\dot{H}^* = 0.4518 \cdot [\rho^{*3}\ \mathrm{Pr}\ \mathrm{Ar}]^{1/4} \cdot \left[\frac{\arccos(H^*) - H^*\sqrt{1-H^*}}{I_2(\mathrm{Ste}, \phi_A)}\right]^{1/4} \tag{25}$$

where

$$I_2(\mathrm{Ste}, \phi_A) = \int_0^{\phi_A} \frac{\cos^3\phi \sin^2\phi}{[f_2(\mathrm{Ste}) + \Gamma_2(\mathrm{Ste}, \mathrm{Ste}_{w0}) F(\phi)]^3} d\phi$$

$$f_2(\mathrm{Ste}) = -\Lambda_2/8 + [\Lambda_2^2 + 160\ \mathrm{Ste}]^{1/2}/8$$

$$\Gamma_2(\mathrm{Ste}, \mathrm{Ste}_{w0}) = 10\ \mathrm{Ste}_{wo}/\Lambda_2$$

$$\Lambda_2 = 3\ \mathrm{Ste} + 10 c_p T_m (1-\rho^*)(\rho^* L) + 20$$

For small Ste (i.e., $\mathrm{Ste} < 0.1$), $f_2(\mathrm{Ste}) = \mathrm{Ste}/2$ and $\Gamma_2(\mathrm{Ste}, \mathrm{Ste}_{w0})) = \mathrm{Ste}_{w0}/2$, Eq. (25) can be simplified as Eq. (24). Therefore, under small Ste, the results obtained in this paper are also available to solve the problem of contact melting inside a horizontal cylindrical tube.

Here, *n*-octadecane is chosen as PCM, which is of most frequent use for contact melting calculation. Physical properties of this material are well documented, Prandtl number Pr is 52.53. Assuming $F(\phi) = 0$, the inner wall temperature of the capsule is constant, and the problem studied in this paper becomes contact melting under the constant wall temperature. The result of contact melting in an elliptical tube under the constant temperature difference was reported by Chen et al. [9]. The variation in melting mass versus melting time obtained in this paper is compared with that in literature [9]. As shown in Fig. 2, under the same conditions, two solutions agree well with each other.

The comparisons of contact melting under varying wall temperatures and constant wall temperatures, inside the capsules with different aspect ratios *J*, are presented in Fig. 3. In order to estimate the influence of elliptical aspect ratio on the melting, the cross-sectional areas of the capsules are taken the same. It is found that the melting velocity decreases as the melting time increases. This is caused by the decreases in pressure and the augment of molten-layer thickness during the melting. The difference between the melting under varying wall temperatures and constant wall temperatures cannot be negligible; so it is significant to study the influence of temperature distribution on the wall of the tube. It can also be seen that the melting velocity in the tube with larger elliptical aspect ratio *J* is higher than that in the tube with small *J*, and the smaller the *J* is, the greater the influence of wall temperature distribution on the melting.

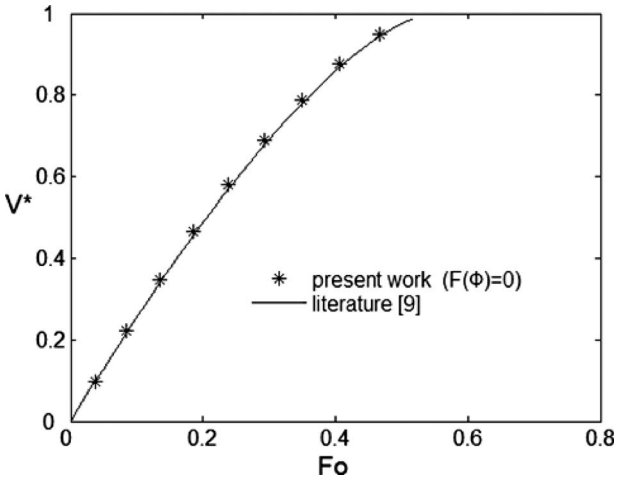

Fig. 2 Comparison of results between the present work and literature [9] for $F(\phi)=0$

In order to estimate the influence of temperature distribution along the wall, a series of calculations for different distributions are carried out, and comparison is under the condition $\overline{\mathrm{Ste}} = \int_0^{\pi/2} T_w ds / \int_0^{\pi/2} ds = 0.096$. The temperature distribution is the same as literature [15], i.e., $T_w = T_{w0}[1 + c \sin^2(\phi)]$, which is based on the experiment. It is important to study the influence of coefficient *c*. Figure 4 shows the influence of temperature distribution on contact melting. Compared with melting under the constant temperature, the melting velocity under varying temperatures drops more sharply during melting. It is also seen that the melting velocity decreases obviously with increasing coefficient *c*. The variation in dimensionless time to complete melting ($\mathrm{Fo}_f = \alpha\tau_f/b^2$) with the coefficient *c* is shown in Fig. 5. The time to complete melting is an increasing function of *c*; so more intense variation in temperature along the wall of the tube leads to lower melting velocity. It can be found that the time to complete melting increases slowly while $c < 0.2$, but it raises sharply while $c > 0.2$.

The variation in molten-layer distribution with heights of molten liquid is presented in Fig. 6 for $J = 1/2$, $T_w = T_{w0}[1 + c \sin^2(\phi)]$, and $\overline{\mathrm{Ste}} = 0.096$. It can be seen that the thickness of the molten layer increases along the wall of the tube, which in-

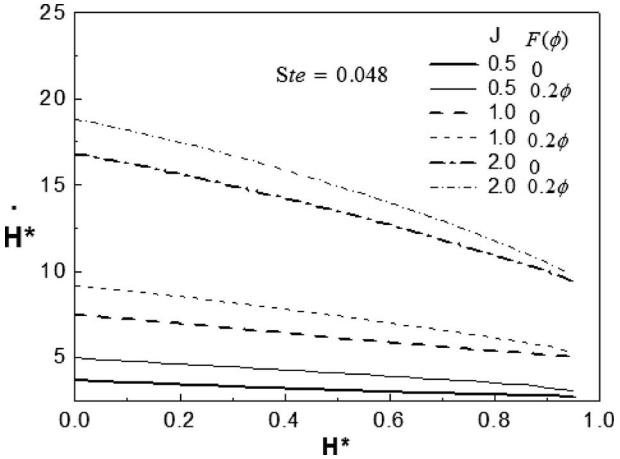

Fig. 3 Variation in melting velocity H^* with height of liquid H^* for $T_w = T_{w0}[1 + F(\phi)]$

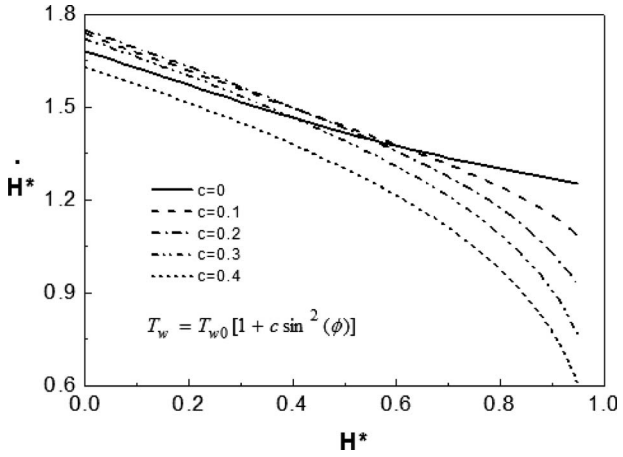

Fig. 4 Influence of temperature distribution on melting

creases gradually during the melting process. This is caused by the reduction in the height of solid and the falling of pressure in the molten layer. From Fig. 6 it can also be found that the variation in the molten layer along the wall of the tube gets more intense with the increase in coefficient c.

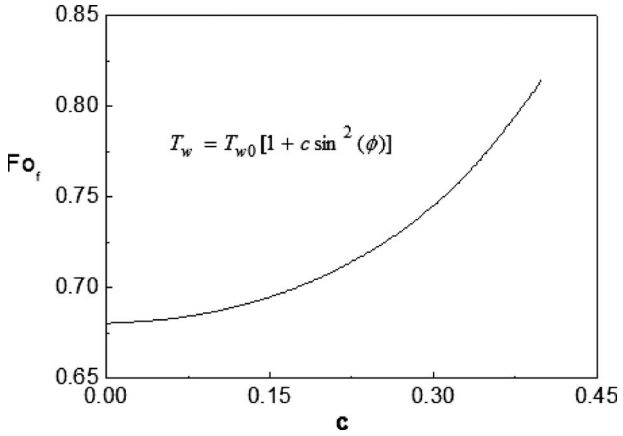

Fig. 5 Variation in dimensionless time to complete melting with c for Ste=0.096

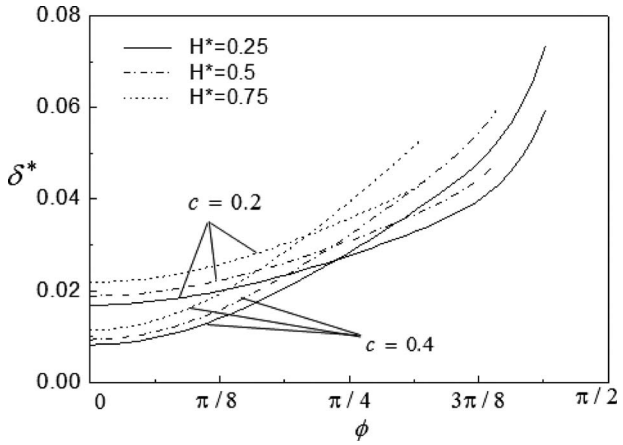

Fig. 6 Thickness distribution of the molten layer with different heights of molten liquid for $T_w = T_{w0}[1 + c\sin^2(\phi)]$

4 Conclusions

The contact melting of PCM in an elliptical tube with no-isothermal inner wall temperature is studied. The basic equations to describe the melting process are obtained. To correct errors in literature [14], the contact melting in the cylindrical tube with no-isothermal inner wall temperature is analyzed again, and corrected expression of the melting velocity is obtained. The conclusions are drawn as follows.

(1) The results in this paper can solve the problem of contact melting in the cylindrical tube while aspect ratio $J=1$ and agree with those of melting in an elliptical tube with the constant temperature obtained in literature [9].
(2) The melting velocity drops during melting. Compared with melting under the condition of constant temperature, the melting velocity under the condition of varying temperatures drops more sharply.
(3) Under the same Ste, the time to complete melting increases with the increase in coefficient c in temperature distribution $T_w = T_{w0}[1 + c\sin^2(\phi)]$, and the variation is smooth while $c < 0.2$, but becomes intense while $c > 0.2$.

Acknowledgment

This research was supported by the National Natural Science Foundation of China (Project No. 50376074).

Nomenclature

J = aspect ratio of the ellipse $J=b/a$
u = tangential velocity
v = normal velocity
H = height of the molten liquid
$\dot{H}$ = melting velocity $\dot{H}=dH/d\tau$
V = molten volume
V_s = volume of solid PCM
T_w = inner wall temperature of the tube
T_{w0} = reference wall temperature
T_m = melting point
c = coefficient in temperature function
L_m = latent heat of fusion
c_p = liquid specific heat capacity
Ar = Archimedes number $A_r=(1-\rho^*)gb^3/\nu^2$
Pr = Prandtl number $\mathrm{Pr}=\nu/\alpha$
Ste = Stefan number, $\mathrm{Ste}=c_p(T_{w0}-T_m)/L_m$
Fo = Fourier number, $\mathrm{Fo}=\alpha\tau/b^2$
s = distance normal to the heat source
h = distance tangential to the heat source

Greek Symbols

μ = dynamic viscosity of the liquid
ν = kinematic viscosity of the liquid
ρ_s = density of solid PCM
ρ_l = density of the molten liquid
α = liquid thermal diffusivity
δ = molten layer thickness
τ = melting time
ϕ = polar angle, see Fig. 1
ϕ_A = polar angle that indicates the contact melting area
θ = angle between the horizontal axis and tangent to the tube wall, see Fig. 1

Superscript

$*$ = dimensionless quantity

Subscripts

l = liquid
s = solid
w = wall of the tube

References

[1] Bejan, A., 1994, "Contact Melting Heat Transfer and Lubrication," Adv. Heat Transfer, **24**, pp. 1–38.

[2] Bareiss, M., and Beer, H., 1984, "An Analytical Solution of the Heat Transfer Process During Melting of an Unfixed Solid Phase Change Material Inside a Horizontal Tube," Int. J. Heat Mass Transfer, **27**(5), pp. 739–746.

[3] Bahrami, P. T., and Wang, T. G., 1987, "Analysis of Gravity and Conduction-Driven Melting in a Sphere," ASME J. Heat Transfer, **19**, pp. 806–809.

[4] Roy, S. K., and Sengupta, S., 1987, "The Melting Process Within Spherical Enclosures," ASME J. Heat Transfer, **109**, pp. 460–462.

[5] Dong, Z. F., Chen, Z. Q., Wang, Q. J., and Ebadian, M. A., 1991, "Experimental and Analytical Study of Contact Melting in a Rectangular Cavity," J. Thermophys. Heat Transfer, **5**(3), pp. 347–354.

[6] Chen, W. Z., Cheng, S. M., and Luo, Z., 1995, "Analysis of Contact Melting of Phase Change Materials Inside a Heated Rectangular Capsule," Int. J. Energy Res., **19**(4), pp. 337–345.

[7] Lacroix, M., 2001, "Contact Melting of Phase Change Material Inside a Heated Parallelepedic Capsule," Energy Convers. Manage., **42**(1), pp. 35–47.

[8] Hirata, T., Makino, Y., and Kneko, Y., 1991, "Analysis of Close-Contact Melting for Octadecane and Ice Inside Isothermally Heated Horizontal Rectangular Capsule," Int. J. Heat Mass Transfer, **34**(12), pp. 3097–3105.

[9] Chen, W. Z., Yang, Q. S., Dai, M. Q., and Chen, S. M., 1998, "An Analytical Solution of the Heat Transfer Process During Contact Melting of Phase Change Material Inside a Horizontal Elliptical Tube," Int. J. Energy Res., **22**(2), pp. 131–140.

[10] Chen, W. Z., Zhao, Y. S., Sun, F. R., Chen, Z. Y., and Gong, M., 2008, "Analysis of ΔT-Driven Contact Melting of Phase Change Material Around Horizontal Cylinder," Energy Convers. Manage., **49**(5), pp. 1002–1007.

[11] Roy, S. K., and Sengupta, S., 1990, "A Generalized Model for Gravity-Assisted Melting in Enclosures," J. Heat Transfer, **112**, pp. 804–808.

[12] Bejan, A., 1992, "Single Correlation for Theoretical Contact Melting Results in Various Geometries," Int. Commun. Heat Mass Transfer, **19**, pp. 473–483.

[13] Chen, W. Z., Zhao, Y. S., Luo, L., and Sun, F. R., 2008, "The Unified Formulation for Contact Melting Inside a Symmetric Enclosure," AIAA J., **22**(2), pp. 227–233.

[14] Saitoh, T. S., and Hoshina, H., 1997, "Analysis of Close-Contact Melting With Inner Wall Temperature Variation in a Horizontal Cylindrical Capsule," *Proceedings of 32nd International Energy Conversion Engineering Conference*, Honolulu, HI, pp. 1641–1645.

[15] Fomin, S. A., and Saitoh, T. S., 1999, "Melting of Unfixed Material in Spherical Capsule With Non-Isothermal Wall," Int. J. Heat Mass Transfer, **42**, pp. 4197–4205.

[16] Halawa, E., Bruno, F., and Saman, W., 2005, "Numerical Analysis of a PCM Thermal Storage System With Varying Wall Temperature," Energy Convers. Manage., **46**, pp. 2592–2604.

A Micro-Insulation Concept for MEMS Applications

Rui Yao

James Blanchard
e-mail: blanchard@engr.wisc.edu

Department of Engineering Physics,
University of Wisconsin-Madison,
1500 Engineering Drive,
Madison, WI 53706

Small scale, thermally driven power sources will require appropriate insulation to achieve sufficiently high thermal conversion efficiencies. This paper presents a micro-insulation design, which was developed for a thermionic microbattery, which converts the decay heat from radioactive isotopes directly to electricity using a vacuum thermionic diode. The insulation concept, which is suitable for any small scale application, separates two planar surfaces with thin, semicircular posts, thus reducing conduction heat transfer and increasing the relative radiation heat transfer. In this case, the surfaces are silicon wafers and the columns are SU-8, a photoresist material. The experimental results indicate that this design is adequate for a practical power source concept, and they are supported by a numerical model for the effective thermal conductivity of the structure. The results show that a typical design of 20 columns/cm^2 with a 200 μm diameter and a 10 μm wall thickness has an apparent thermal conductivity on the order of 10^{-4} W/m K at a pressure of 1 Pa. System models of a thermionic power source indicate that this is sufficiently low to provide practical efficiency. [DOI: 10.1115/1.3084121]

Keywords: micro-insulation, MEMS, microscale

1 Introduction

Numerous studies have been carried out regarding technologies for providing electrical power to MEMS devices. The electrical power can be converted from various energy sources, such as chemical, solar, and radioisotopes, using a variety of conversion technologies. One example is a radioisotope powered thermionic microbattery [1,2]. The microbattery converts the radioisotope decay heat directly to electricity using a vacuum thermionic diode. At MEMS scales, due to the relatively large surface to volume ratio, the heat losses become significant. Thus a small scale thermionic device requires an appropriate thermal insulation to maintain high radioisotope source temperature and achieve high conversion efficiency. There are currently no available insulation concepts suitable for MEMS-scale applications, but there are some similar concepts used for other applications. One example is the MULTI-FOIL™ insulation developed by Thermo Electron Technologies Corporation[1] (TTC) [3,4] or the products from Actis (Limoux France). These concepts consist of evacuated layers of thin metal foils spaced by oxide particles. These structures have an apparent thermal conductivity as low as 0.001 W/m K when the cold-side temperature is 294 K [5]. The oxide particles are selected on the basis of their low thermal conductivity and compatibility with the foil chosen for the application (usually dependent on temperature). Unfortunately, the layer separation in these materials is at least a few millimeters, so it is difficult to use them at MEMS scales. An alternative is aerogel insulation, but the concept proposed here has the potential for a lower apparent thermal conductivity than a silica aerogel, which has an apparent thermal conductivity of 0.03 W/m K when the cold-side temperature is 294 K [5].

A microscale insulation concept has been proposed by Sandia National Laboratory [6]. In this approach, small conical structures, <10 μm in length, are used to separate layers of silicon, providing an analog to multifoil insulation that is suitable for MEMS applications. To date there are no published measurements of the performance of the Sandia concept. Hence, this paper presents a new concept, based on the Sandia concept, for micro-insulation suitable for MEMS and compares the measured performance to a model for heat transfer through the insulation. This micro-insulation can be designed and fabricated by semiconductor and MEMS fabrication techniques so as to be integrated easily with the other parts of a microbattery.

2 Proposed Micro-Insulation Concept

Figure 1 shows a schematic of the proposed micro-insulation concept. An array of thin-walled, half-circular columns separates the top and bottom layers, creating a gap that is evacuated to reduce gas conduction. The columns have thin walls and are fabricated from a low thermal conductivity material, such as SU-8, to minimize the solid conduction. The downward-facing surface of the top layer is coated by a low emissivity material, such as gold or silver, to reduce radiation heat transfer between the top and bottom layers. A single insulation layer fabricated in this way can also be stacked on top of another and bonded together to make a multileveled assembly. The radiation heat transfer can be reduced further by employing multiple reflecting layers.

SU-8 is a negative, epoxy-type, near-UV (350–400 nm) photoresist. It is based on the EPON® Resin SU-8 from Shell Chemical (www.shell.com/chemicals). This photoresist allows the fabrication of high aspect ratio microstructures and a broad range of thicknesses, which can be obtained in one step. Structures of up to 2 mm in height can be produced by using multiple coats. SU-8 was originally developed and patented by IBM-Watson Research Center (www.watson.ibm.com) and has been adapted for MEMS applications [7]. The thermal conductivity of this material was taken to be 0.2 W/m K [8].

This micro-insulation can be fabricated by standard lithography processes. Figure 2 illustrates the cross-sectional views of the fabrication process of a single micro-insulation. By applying appreciable pressure and temperature, the various layers of the insulation can be bonded together. Nordström et al. [9] investigated the bonding strength between SU-8 and gold. Without any adhesion promoter they found bond strengths of 4.8 ± 1.2 MPa for a 7.5 μm layer of SU-8. The value of the bond strength can be increased additionally by up to 75% using an adhesion promoter

By using OmniCoat™ and fully optimizing the processing conditions of the SU-8, Pan et al. [10] developed a silicon wafer

[1] http://www.insulation-actis.com/

Contributed by the Heat Transfer Division of ASME for publication in the JOURNAL OF HEAT TRANSFER. Manuscript received August 24, 2007; final manuscript received November 18, 2008; published online March 16, 2009. Review conducted by Roger Schmidt.

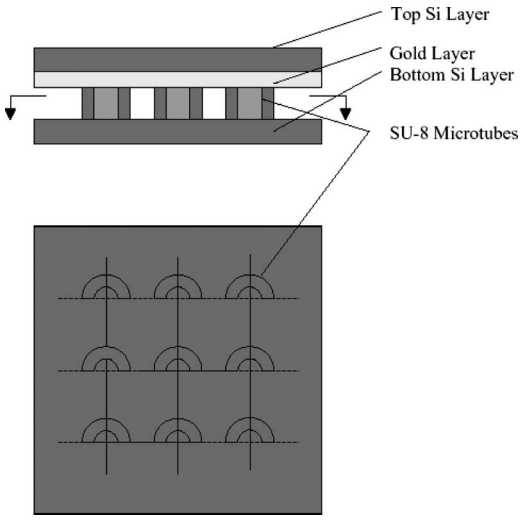

Fig. 1 Schematic of micro-insulation design (not to scale)

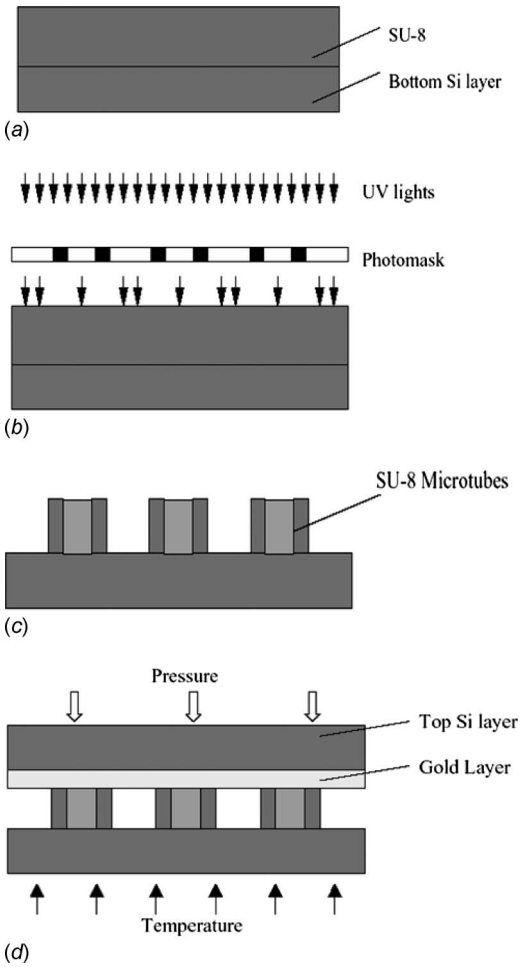

Fig. 2 (*a*) An SU-8 photoresist layer has been deposited on top of the bottom silicon substrate and soft-baked to evaporate the solvent and densify the film before exposure. (*b*) The SU-8 layer is exposed under UV lights through a photomask and baked to selectively cross-link the exposed portions of the film. (*c*) The exposed SU-8 is developed using MicroChem's SU-8 developer to form the designed structure. (*d*) The top silicon layer with gold deposited on the downward surface is placed on top of the patterned SU-8 structure.

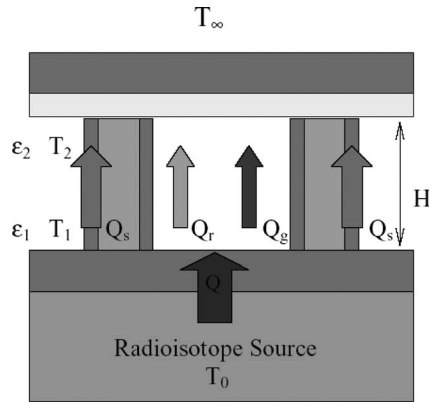

Fig. 3 Heat transfer modeling through micro-insulation. Note that Q_s represents the total heat conduction through all columns.

bonding technique and tested several patternable materials. The results indicated that SU-8 is the best material with a bonding strength of up to 20.6 MPa.

For the applications with temperatures higher than 400°C, SU-8 has to be replaced with other materials such as GaAs or SiO_2 and the fabrication processes are different from those described above.

3 Thermal Modeling

To investigate the feasibility of this concept, a computational model has been built to study the heat transfer through the layers. The schematic of the heat transfer model is shown in Fig. 3. This steady state, one-dimensional model includes several heat transfer modes, including solid conduction through the walls of the columns and gas conduction and radiation through the gap between the top and bottom layers. Free convection is not considered because the two layers are too close to allow development of convection cells even for micro-insulation at atmospheric pressure. Nonetheless, the model is most accurate at low air pressures. The Rayleigh number (the product of the Prandtl and Grashof numbers) is used to justify the decision to ignore convection [11].

In the model, Q is the total heat passing through the insulation; Q_s, Q_g, and Q_r are the heat flows through the columns, gas, and radiation, respectively; T_2 and T_∞ are the cold-side and environment temperatures and are assumed constant and identical; T_1 and T_0 are the hot-side and radioisotope source temperatures, respectively, and are assumed to be identical; ε_1 and ε_2 are the emissivities of the top and bottom layers, respectively; and H is the height of the columns. The model assumes that there are no heat losses laterally, which means all heat fluxes are parallel to the axial direction of the columns and that all surfaces are gray surfaces so that their emissivities are independent of the wavelength of the radiation.

For the problems involving combined radiation and conduction, a simple approach is to assume that both heat transfer modes are uncoupled and the desired temperatures and heat fluxes can be found by adding separate solutions. Unfortunately, uncoupled problems are not as common as coupled problems, especially when the total energy flux is specified, so the entire problem typically must be treated simultaneously because of the nonlinear coupling of the unknown temperatures [12].

The energy balance equation is

$$Q = Q_S + Q_r + Q_g = Q \cdot (\eta_S + \eta_r + \eta_g) \tag{1}$$

where η_S, η_r, and η_g represent the fractions of total heat flows by solid conduction, radiation, and gas conduction, respectively, and Q is the total heat flow.

The heat flow by conduction through the columns is given by

$$Q_s = Q \cdot \eta_S = \frac{k_s A_s}{H}(T_1 - T_2) \tag{2}$$

where k_s is the thermal conductivity of the column material and A_s is the total cross-sectional area of the columns.

The heat flow by radiation from the bottom layer to the top layer is given by

$$Q_r = Q \cdot \eta_r = \frac{\sigma \cdot A_r \cdot (T_1^4 - T_2^4)}{\left(\frac{1}{\varepsilon_1} + \frac{1}{\varepsilon_2} - 1\right)} \tag{3}$$

where σ is the Stefan–Boltzmann constant, ε_1 and ε_2 are the emissivities of the top and bottom layer surfaces, and A_r is the total radiation cross-sectional area.

Heat conduction in gases is normally divided into four separate molecular regimes: free-molecule (Kn$>$10), transition (10$>$Kn$>$0.1), temperature-jump (slip) (0.1$>$Kn$>$0.01), and continuum (Kn$<$0.01), where Kn is the Knudsen number (Kn$=\lambda/H$, where λ is the mean free path of the gaseous molecules and H is the characteristic length of the gas layer). Based on the Maxwell–Boltzmann distribution of velocities, the mean free path of gaseous molecules in an infinite space is given by

$$\lambda = \frac{1}{\sqrt{2}\pi \cdot d^2 n} = \frac{k_B T}{\sqrt{2}\pi \cdot d^2 P} \tag{4}$$

where d is the diameter of air molecules, n is the number of molecules per unit volume, k_B is the Boltzmann constant, T is the temperature, and P is the pressure. For example, assuming an air molecule diameter of 3 Å at a temperature of 400 K and pressure of 1 Pa, we find $\lambda = 13.8$ mm. Since the mean free path is much larger than the characteristic length of the micro-insulation, the effective mean free path is constrained by the height of the columns.

The heat flux through the gas is given by [13]

$$Q''_{\mathrm{FM}} = \frac{1}{2}(\gamma + 1)c_V \frac{P}{\sqrt{2\pi RT}} \cdot \frac{\alpha_1 \alpha_2}{\alpha_1 + \alpha_2 - \alpha_1 \alpha_2}(T_1 - T_2) \tag{5}$$

and the gas thermal conductivity is

$$k_{\mathrm{gas}} = \frac{1}{2}(\gamma + 1)c_v \frac{P}{\sqrt{2\pi RT}} H \tag{6}$$

where γ is the ratio of the heat capacity at constant pressure to that at constant volume, c_v is the heat capacity at constant volume, T_1 and T_2 are the temperatures at the two boundaries, T is the mean temperature of T_1 and T_2, R is the universal gas constant, P is the gas pressure at T, and α_1 and α_2 are the accommodation coefficients of the gaseous molecules on the two boundaries. The accommodation coefficient is a measure of the efficiency of thermal energy interchange that occurs when a gas molecule collides with the surface. It varies between 1 (complete accommodation and diffuse re-emission) and 0 (specular re-emission). Its exact value depends on the kind of gas molecule, the surface temperature, and, most importantly, the surface condition.

When the vacuum is from approximately 1 Torr to atmospheric pressure (760 Torr), the heat transfer falls into the transition regime (10$>$Kn$>$0.1). Gas conduction in this regime is rather complicated. For practical calculations, the following simple interpolation formula is suggested by Sherman [14]:

$$\frac{Q''}{Q''_{\mathrm{FM}}} = \frac{1}{1 + \frac{Q''_{\mathrm{FM}}}{Q''_C}} \tag{7}$$

where Q'' is the transition heat flux, Q''_{FM} is the free-molecule heat flux given in Eq. (5), and Q''_C is the continuum heat flux. For a plane layer, Q''_C can be written from the simple kinetic theory as

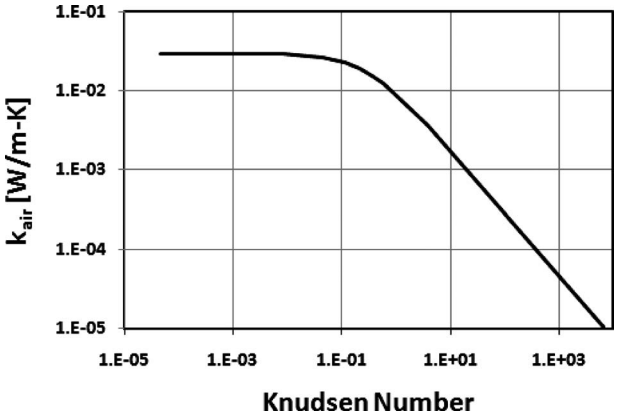

Fig. 4 Thermal conductivity of air at 400 K as a function of Knudsen number

$$Q''_C = \frac{k_{\mathrm{gas},C}(T_1 - T_2)}{H} = \frac{9\gamma - 5}{4}\mu \cdot c_v \frac{T_1 - T_2}{H} \tag{8}$$

where c_v is the constant volume specific heat and μ is the dynamic viscosity.

Figure 4 shows the air thermal conductivity as a function of Knudsen number for a given air gap (therefore also a function of pressure) at 400 K. Although the free-molecule conduction is the most efficient conduction mode, the air thermal conductivity decreases linearly with pressure because of the decreasing number of air molecules involved. In the transition regime, energy is transported less efficiently due to the collisions between air molecules, but the higher molecule density makes the thermal conductivities increase. In the continuum regime, the gas particles and mean free path are directly and indirectly proportional to the gas pressure and the gas thermal conductivity is independent of pressure. From Fig. 4 we can also estimate that for this micro-insulation design, to obtain a thermal conductivity on the order of 10^{-4} W/m K, the Knudsen number should be at least 500.

In the micro-insulation design described in this paper, the two layers are so close that the gas conduction between them is in the free-molecule regime. Thus the heat flow by conduction through the gas is

$$Q_g = Q \cdot \eta_g = k_{\mathrm{gas}} \cdot A_g \cdot (T_1 - T_2) \tag{9}$$

where A_g is the gas conduction cross-sectional area, assumed to be identical to A_r, and k_{gas} is the gas thermal conductivity at the mean temperature of T_1 and T_2.

By solving Eqs. (1)–(9), the thermal transmittance of the micro-insulation can be obtained as

$$C = \frac{Q}{(T_1 - T_2)A} \tag{10}$$

where A is the cross-sectional area of the top and bottom layers.

The apparent thermal conductivity of the micro-insulation, which is convenient for comparison to conduction through suitable solid materials, is defined as

$$k_{\mathrm{app}} = C \cdot H \tag{11}$$

The conceptual design parameters used in this model are given in Table 1.

4 Experimental Results

To test the ability of the proposed micro-insulation to provide the characteristics needed for a small scale application, a representative sample was fabricated for testing. This sample consisted of two silicon wafers (10 cm in diameter) separated by semicircular, SU-8 columns with a wall thickness of 10 μm and height of 45 μm. The column density is 20 columns/cm^2. The apparatus

Table 1 Design parameters of a typical micro-insulation concept

Parameters	Values
Top and bottom layers' cross-sectional area, A	1×1 cm^2
Heights of columns, H	10 μm
Vacuum between the two layers, P	1 Pa
Diameter of columns (outer), D	200 μm
Wall thickness of columns, δ	10 μm
Cold-side temperature, T_2	300 K
Total heat applied on the micro-insulation, Q	1 W
Top and bottom layers' surface emissivities, ε_1 and ε_2	0.05 and 0.5
Thermal conductivity of SU-8, k_s	0.2 W/m K
Top and bottom layers' accommodation coefficients, α_1 and α_2	0.9 and 0.9
No. of columns	20

for measuring the micro-insulation's apparent thermal conductivity is shown schematically in Fig. 5. The apparatus is intended to establish one-dimensional heat flow through a micro-insulation specimen sandwiched by two parallel heat flux transducers. An infrared lamp, producing 3 W, was used to generate an appropriate input heat flux from one side. The entire experiment was carried out in a small vacuum chamber. This approach eliminated the need to seal the insulation itself, so the feasibility of sealing the insulation for practical applications is an open question that requires further research. The ratio of the sample diameter to the entire insulation thickness is chosen to be 100 in order to reduce the side losses.

Two BF-02 heat flux transducers from Vatell Corporation (www.vatell.com) are used to measure the heat flux and temperature at both sides of the micro-insulation. The heat flux transducer is also associated with a T type thermocouple. The thermal conductivity of the BF-02 is 0.25 W/m K and the thickness is 0.25 mm, with several thermocouples through the thickness. Hence, so the temperature drop through the surface thermocouple is small and can be neglected. Similarly, the sensor is attached to the insulation surface with a thin (0.127 mm), high conductivity tape, providing good thermal contact with negligible impact on the measured surface temperature.

By measuring the hot-side and cold-side heat fluxes q_h'' and q_c'', the hot and cold temperatures T_h and T_c, and the average height of the columns H, the apparent thermal conductivity can be obtained by

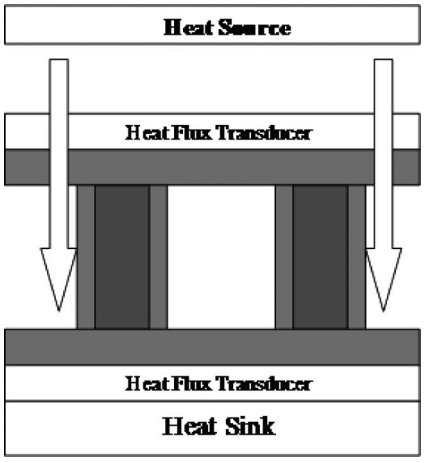

Fig. 5 The apparatus for thermal conductivity measurement

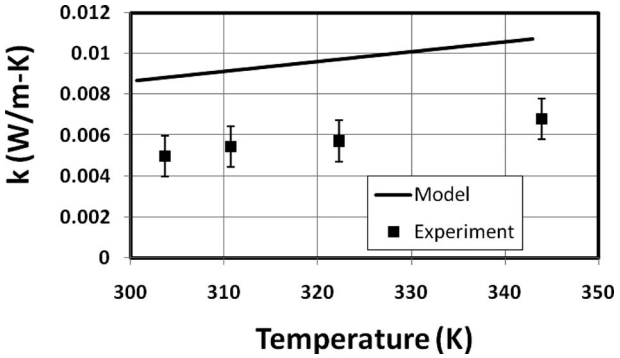

Fig. 6 Apparent thermal conductivity of micro-insulation at atmospheric pressure as a function of hot-side temperature

$$k_{\exp} = \frac{(q_h'' + q_c'')H}{2(T_h - T_c)} \tag{12}$$

The average of the hot-side and cold-side heat fluxes has been used here because it provides a conservative estimate of the apparent thermal conductivity of the micro-insulation. The two heat fluxes differ because some heat entering the hot-side sensor conducts laterally and radiates away from the top surface of the hot-side wafer, thus reducing the heat transferred through the micro-insulation. Hence, the cold-side sensor provides a better estimate of the heat flux transporting through the insulation, but there is some chance that lateral losses are also an issue. Hence, the average is used to be conservative.

Figure 6 shows that at atmospheric pressure, the measured apparent thermal conductivities of the micro-insulation are lower than the theoretical values. The reason for this disagreement is that the heat losses from the edge of the micro-insulation and from the top silicon wafer are not taken into account in the model. When the pressure is reduced, these losses are significantly reduced and the agreement between the experiment and the model is improved. This is shown in Fig. 7, which shows the comparison at a pressure of 6.5 Pa (50 mTorr). Figure 8 shows a comparison of the measured and theoretical apparent thermal conductivities at pressures ranging from 2 Pa to 120 Pa. In all cases, the cold-side temperature was approximately 50°C and the hot-side temperature varied according to the apparent thermal conductivity.

5 Discussion

To further assess the ability of the proposed micro-insulation to provide adequate performance in a MEMS application, parametric studies have been carried out to assess the impact in design varia-

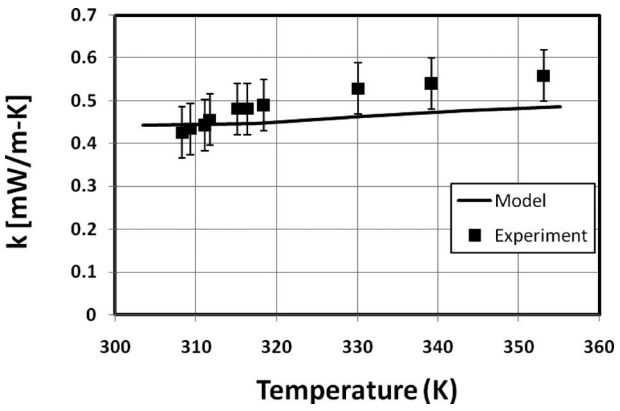

Fig. 7 Apparent thermal conductivity of micro-insulation at 6.5 Pa as a function of hot-side temperature

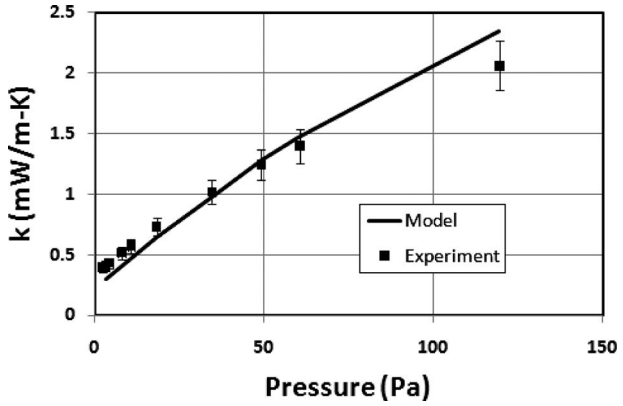

Fig. 8 Apparent thermal conductivity as a function of pressure. The cold-side temperature began at room temperature and reached a steady state temperature of approximately 50°C before the apparent thermal conductivity was determined.

tions around the nominal specifications used in the experiments described in Sec. 4. Figure 9 shows the variation of the apparent conductivity and hot-side temperature as a function of pressure, demonstrating that below pressures on the order of a few pascals the micro-insulation can achieve apparent conductivities of approximately 1.5×10^{-4} W/m K. This indicates that such a design can achieve an apparent thermal conductivity, which is two orders of magnitude below a typical silica aerogel and on the same order of commercial MULTI-FOIL insulation. From Fig. 4 we conclude that in the transition regime, the air thermal conductivity decreases very slowly with vacuum, which results in a situation in which gas conduction dominates the heat transfer when the pressure is higher than 5 Pa (Fig. 10). Furthermore, for a certain design of this micro-insulation, there exists a pressure limit, beyond which lowering the pressure will not improve the heat transfer performance significantly.

At higher vacuum (pressures less than 1 Pa), conduction through the column wall becomes important. Decreasing the number or wall thickness of the columns would reduce the heat conduction cross-sectional area between the top and bottom layers. Thus a lower thermal conductivity can be obtained (Fig. 11). On the other hand, very thin wall thicknesses and inadequate numbers of columns can result in a mechanical instability of the micro-insulation structure, so there is a limit to the allowed spacing between tubes.

A low emissivity coating on the downward surface of the top layer can reduce radiation loss through the micro-insulation. Figure 12 shows that compared with a silicon layer without a coating (assuming emissivity of 0.5), a gold coating (emissivity of 0.05) can reduce the apparent thermal conductivity by about 40%. A gold coating on the upward surface of the bottom layer can reduce the radiation loss further.

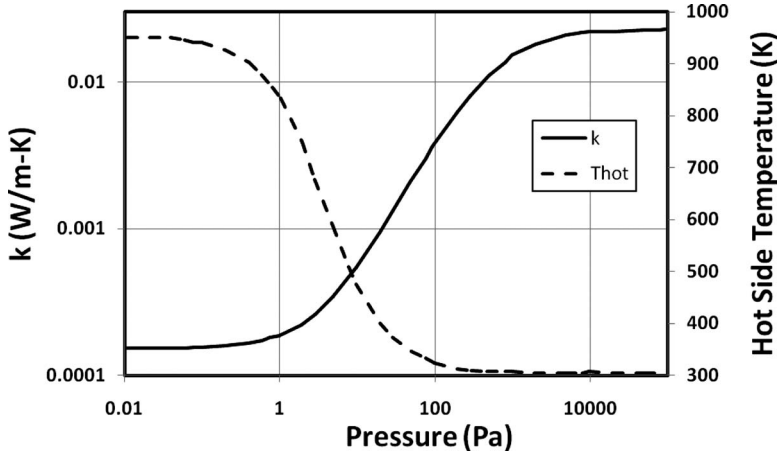

Fig. 9 The apparent thermal conductivity and hot-side temperature as a function of pressure

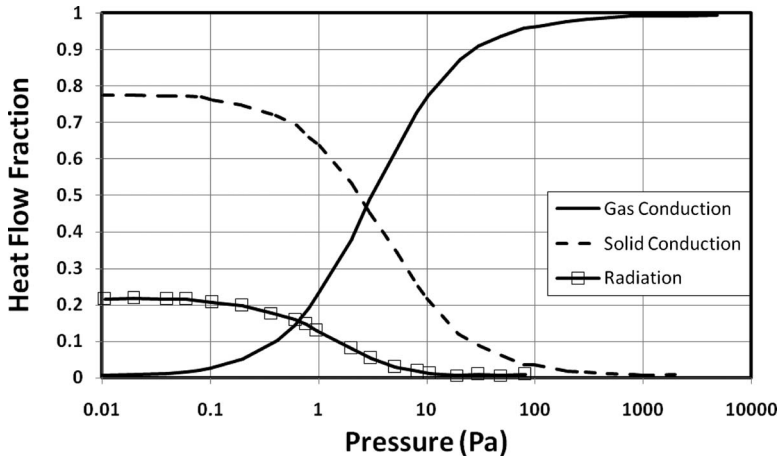

Fig. 10 The fraction of heat flow contribution from radiation, gas conduction, or solid conduction as a function of pressure

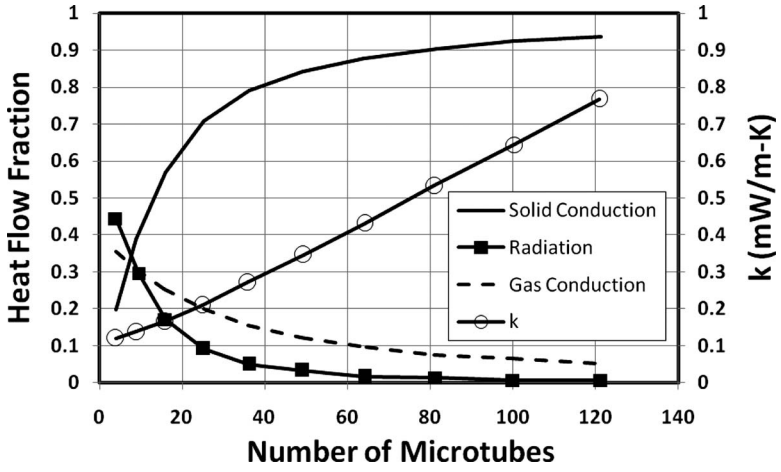

Fig. 11 The apparent thermal conductivity and heat flow contributions as a function of the number of columns at a pressure of 1 Pa

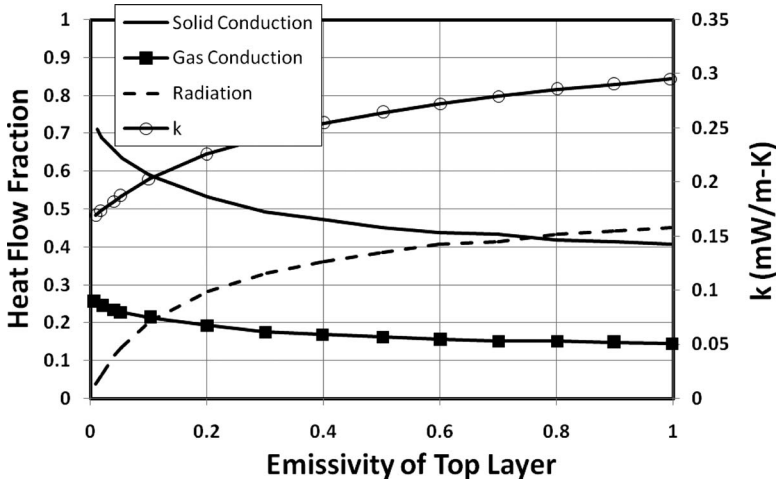

Fig. 12 The apparent thermal conductivity and heat flow contributions as a function of the top layer emissivity at a pressure of 1 Pa

6 Conclusions

This paper has demonstrated that effective micro-insulation can be fabricated using silicon layers separated by SU-8 columns. At pressures below about 1 Pa, gas conduction is minimized and the heat transfer is dominated by solid conduction through the columns and radiation. For a design that consists of 20 columns/cm^2 with a 200 μm diameter and a 10 μm wall thickness, experiments and modeling indicate an apparent thermal conductivity on the order of 10^{-4} W/m K at a device pressure of 1 Pa. Better results can be achieved by decreasing the areal density of the columns, further reducing the pressure (though this has minimal return below 1 Pa), decreasing the thermal conductivity of the column material, or reducing the emissivity of the surfaces of the micro-insulation. These results indicate the feasibility of using this micro-insulation concept in a practical, thermally driven power source. To truly demonstrate viability, the design must include a concept for sealing the device without creating a thermal shunt. This requires further work.

Acknowledgment

This work was supported by the Department of Energy, through the NEER program.

Nomenclature

A = heat transfer cross-sectional area, m^2
C = thermal transmittance, W/m^2 K
c_v = constant volume specific heat, J/kg K
d = diameter of air molecules, m
H = height of columns, m
k = thermal conductivity, W/m K
k_B = Boltzmann constant, 1.38×10^{-23} J/K
Kn = Knudsen number
n = number of molecules per unit volume
P = pressure between the two silicon layers, Pa
Q = heat flow, W
R = universal gas constant, 8.31 J/mol K
T = temperature, K
α = accommodation coefficient
γ = the ratio of the heat capacity at constant pressure to that at constant volume
δ = wall thickness of columns, m
ε = emissivity
η = fraction of heat flows through the micro-insulation
λ = mean free path, m
μ = dynamic viscosity, kg/s m

σ = Stefan–Boltzmann constant, 5.67×10^{-8} W/m^2 K^4
σ_{cr} = local buckling critical stress, Pa

Subscripts

1 = top (hot) layer
2 = bottom (cold) layer
c = continuum conduction
FM = free-molecule conduction
g = gaseous phase conduction
r = radiation heat transfer
s = solid phase conduction

References

[1] Hernqvist, K. G., 1960, "Thermionic Power Conversion and Its Possibilities in the Nuclear Field," *Direct Conversion of Heat to Electricity*, J. Kaye and J. A. Welsh, eds., Wiley, New York, Chap. 9.

[2] King, D. B., Sadwick, L. P., and Wernsman, B. R., 2001, "Microminiature Thermionic Converters," U.S. Patent No. 6,294,858.

[3] Dunlay, J. B., 1967, "The Development of Foil Thermal Insulation of High Temperature Heat Sources," *Proceedings of the Second Intersociety Energy Conversion Engineering Conference*, ASME, New York.

[4] Paquin, M. L., 1969, "The MULTI-FOIL Thermal Insulation Development Program," *Proceedings of the Fourth Intersociety Energy Conversion Engineering Conference*, ASCE, New York.

[5] Kreith, F., 2000, *The CRC Handbook of Thermal Engineering*, CRC, Boca Raton, FL, pp. 4–194.

[6] Marshall, A., Kravitz, S., Tigges, C., and Vawter, G., 2004, "Methods for Fabricating a Micro Heat Barrier," U.S. Patent No. 6673254.

[7] Lorenz, H., Despont, M., Fahrni, N., LaBianca, N., Prenaud, P., and Vettiger, P., 1997, "SU-8: A Low-Cost Negative Resist for MEMS," J. Micromech. Microeng., **7**, pp. 121–124.

[8] Chang, S., Warren, J., Hong, D., and Chiang, F., 2002, "Testing Mechanical Properties of EPON SU-8 With SIEM," 2002 SEM Annual Conference and Exposition on Experimental and Applied Mechanics, Milwaukee, WI, p. 2002.

[9] Nordström, M., Johansson, A., Nogueron, S., Clausen, B., Calleja, M., and Boisen, A., 2005, "Investigation of the Bond Strength Between the Photo-Sensitive Polymer SU-8 and Gold," Microelectron. Eng., **78–79**, pp. 152–157.

[10] Pan, C.-T., Yang, H., Shen, S.-C., Chou, M.-C., and Chou, H.-P., 2002, "A Low-Temperature Wafer Bonding Technique Using Patternable Materials," J. Micromech. Microeng., **12**, pp. 611–615.

[11] Incropera, F. P., and Dewitt, D. P., 2002, *Fundamentals of Heat and Mass Transfer*, Wiley, New York.

[12] Siegel, R., and Howell, J. R., 1992, *Thermal Radiation Heat Transfer*, Hemisphere, New York.

[13] Devienne, F. M., 2002, "Low Density Heat Transfer," *Advances in Heat Transfer*, Vol. 2, Academic, New York.

[14] Sherman, F. S., 1963, "A Survey of Experimental Results and Methods for the Transition Regime of Rarefied Gas Dynamics," *Rarefied Gas Dynamics*, Vol. II, J. A. Lauermann, ed., Academic, New York, pp. 228–260.

Convective Performance of Nanofluids in a Laminar Thermally Developing Tube Flow

Babajide Kolade

Kenneth E. Goodson

John K. Eaton

Department of Mechanical Engineering,
Stanford University,
Stanford, CA 94305-3030

While many of the published papers on nanofluids focus on measuring the increased thermal conductivity of the suspension under static conditions, the convective performance of these fluids has received relatively little attention. The present work measures the effective thermal conductivity of nanofluids under developing convective boundary layer conditions in tubes of diameter 5 mm. The experiments use a hydrodynamically fully developed laminar tube flow in the range $500 \leq Re \leq 1600$ *with constant wall heat flux. The experiments were validated through measurements on pure de-ionized (DI) water, which results in a thermal conductivity value that agrees within 0.4% of handbook value. The increase in effective thermal conductivity for DI-water/*Al_2O_3 *nanofluids is 6% for 2% volume concentration of* Al_2O_3*, which is consistent with the previously reported conductivity values for this sample. For a suspension of multiwall carbon nanotubes in silicone oil, the thermal conductivity is increased by 10% over that of the base fluid for a concentration of 0.2% by volume. Scanning electron microscopy was utilized to examine the structure of the dry state of the nanotubes and elucidate the performance differences of carbon nanomaterials.* [DOI: 10.1115/1.3013831]

Keywords: nanofluids, thermal conductivity, convective heat transfer, laminar flow, conjugate heat transfer, nanotube structure

1 Introduction

The term nanofluid is used to describe a suspension of nanosized particles in a base fluid. Metals and crystalline solids have thermal conductivities that are orders of magnitude larger than those of liquids. Suspensions of particles of such materials are expected to have higher thermal conductivity than those of the base liquid. Suspensions with micron-/millimeter-sized particles exhibit enhanced thermal characteristics [1]. However, these slurries have drawbacks such as clogging and abrasion. The level of enhancement brought about by the inclusion of micron-/millimeter-sized particles is not as significant as suspensions with nanoparticles. It has been reported that the addition of small quantities of nanosized (10–300 nm) metals, metallic oxides, and carbon nanotubes significantly increases the thermal conductivity of the base fluid. For example, Eastman et al. [2] reported an increase of 40% in the thermal conductivity of ethylene glycol with the suspension of 0.3% by volume of 10 nm copper (Cu) particles. Such a marked increase has been attributed to the large surface area to volume ratio of nanoparticles [3] or the layering of fluid particles at the interface of included solid particles [4]. With these enhanced thermal characteristics and diminutive dimensions of the suspended particles, nanofluids are viable options as working fluids in such fields as microelectromechanical system (MEMS) technology, automotive cooling, high-speed computing, laser technology, and other energy intensive applications.

The majority of the published research works on nanofluids have focused on measuring the increased thermal conductivity of the suspension under stationary conditions. The conventional methods utilized for this purpose are the transient hot-wire (THW) method [2–7], the 3-ω method [8], and the parallel plate method [9].

There is considerable scatter in reported values of thermal conductivity enhancement [10]. For example, Choi et al. [4] measured an increase of 160% in thermal conductivity of a synthetic oil, poly (α-olefin), with the addition of 1% by volume of multiwall carbon nanotubes (MWCNTs) using the THW method. Xie et al. [6], also using the THW method, measured an increase of only 19.6% with the addition of 1% by volume of MWCNT to decene (also an olefin), which has a base thermal conductivity of 0.14 W/m K. The THW technique and similar methods are susceptible to measurement errors; this may be due to the development of convection cells around the heater probe [11] or due to the temperature inhomogeneity in the sample caused by successive measurements [7].

Experimental work on the effect of nanoparticles in convective heat transfer has not been extensively or rigorously conducted. Xuan and Li [12] measured an increase of 39% in the Nusselt number in a turbulent fully developed flow in a tube, with constant heat flux, with the addition of 2% by volume of Cu nanoparticles (diameter <100 nm). Wen and Ding [13] studied the entrance region of a tube flow under laminar flow conditions, with constant heat flux. Their results showed an increase of over 40% in the convective heat transfer coefficient at an x/D location of 63 for the addition of 1.6% by volume of 27–56 nm Al_2O_3 particles to de-ionized water. However, there were significant errors in their baseline measurement of the thermal conductivity of water, casting doubt on the validity of the measurement. Similarly, Heris et al. [14] measured the effect of the addition of 20 nm aluminum oxide (Al_2O_3) particles to water in a constant wall temperature laminar tube flow. The tube inner diameter was 5 mm and the test section was 1 m long. They measured an increase of 10–30% in the convective heat transfer coefficient for a Péclet number ranging from 2500–6000 at 2% by volume concentration of Al_2O_3. There is concern about the accuracy of their measurements of the sensible energy increase because they reported that the exiting flow temperature was measured using a thermocouple (TC) inserted directly into the flow line. For the Péclet number range they considered, the flow is not thermally fully developed and therefore a one-point measurement of the flow temperature within the test section is not representative of the mixed-mean temperature.

Contributed by the Heat Transfer Division of ASME for publication in the JOURNAL OF HEAT TRANSFER. Manuscript received February 11, 2008; final manuscript received October 7, 2008; published online March 19, 2009. Review conducted by Patrick E. Phelan.

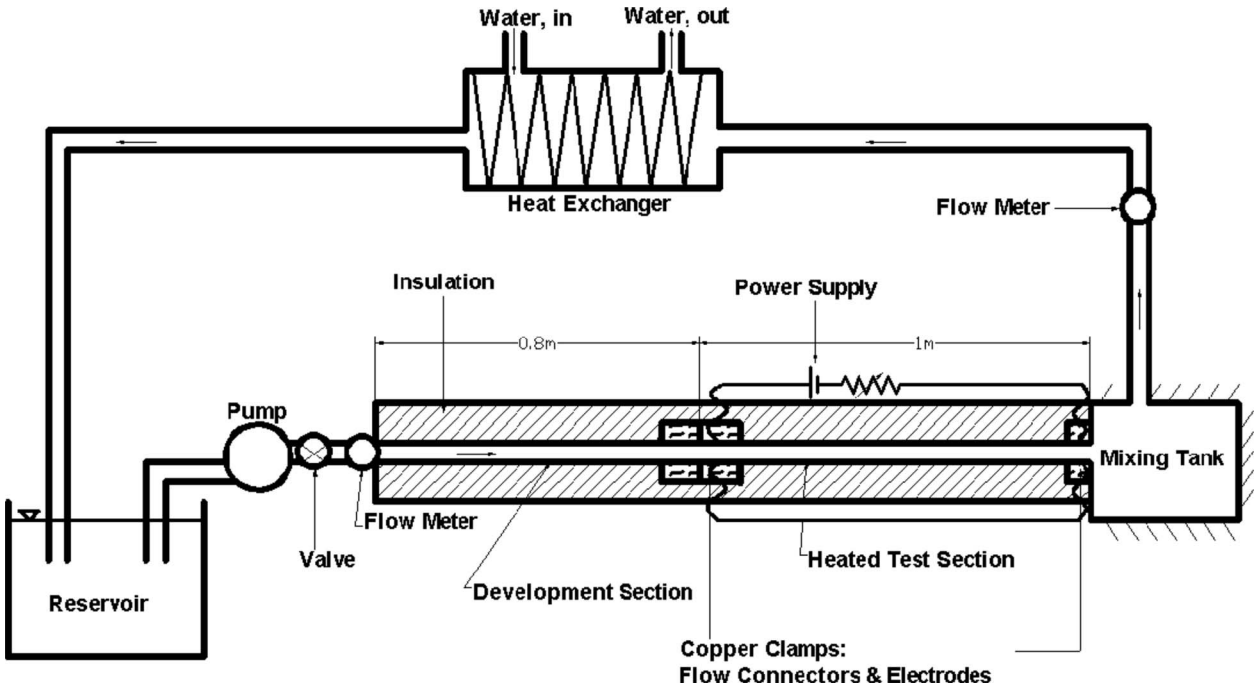

Fig. 1 Schematic of experimental setup

The main objective of the present work is to quantify the augmentation of the thermal conductivity of a liquid by the addition of nanoparticles in a convective environment. This experiment is conducted in a macroscale heat transfer apparatus; it is based on a laminar hydrodynamically fully developed flow in a tube, with constant heat flux. The heat transfer behavior in this simple flow is well understood, and the fluid conductivity can be extracted using only wall temperature measurements. Furthermore, the accuracy of the apparatus can be assessed by direct measurement of pure fluids for which the thermal conductivity is well known. Thus, the goal is to measure the effective thermal conductivity of a nanofluid in a convection application with a documented uncertainty of less than 0.04 W/m K.

2 Experimental Facility

A schematic of the experimental setup is shown in Fig. 1. The system is a closed recirculatory system. Fluid is pumped from the actively cooled reservoir, through a ball valve and a flow meter before entering a continuous stainless steel tube, comprising the development and test sections. The flow meter is a Micro Motion ELITE CMF025 Coriolis-type mass flow rate meter. This meter has the additional capability of measuring the density of the fluid. The flow exiting the test section passes into a mixing tank for the measurement of the mixed-mean temperature, through a heat exchanger, and then back to the reservoir.

The tube is thin walled and seamless, and it is made out of 316L stainless steel. It is 1.8 m long, with an inner diameter of 5.3 mm, and a wall thickness of 0.5 mm. The tube is partitioned into two sections: the development section, which is 0.8 m long, and the test section, which is 1 m long. The flow is allowed to develop hydrodynamically in the development section.

The inlet fluid temperature into the development section is measured by a sheathed, 0.8-mm-diameter, K-type thermocouple inserted into the flow at a location 2.5 mm from the entrance of the tube. Beaded, 36-gauge, K-type thermocouples are mounted on the external tube wall at three axial locations along the development section. In the test section, beaded K-type thermocouples made out of 0.13-mm-diameter (36-gauge) wires are mounted on the external wall of the tube at 19 axial locations. The thermocouples are attached using Omegabond® 101, a thermally conductive electrically insulating epoxy adhesive. Data from thermocouples used in this experiment were transferred to a zone box and recorded using an HP3497A multiplexer and a Fluke 8842A digital multimeter (DMM), at a sampling rate of 2.5 Hz. The mean and standard deviation are calculated for a sample size of 50 in the DI-water experiments and a sample size of 30 in the silicone oil experiments.

Constant heat flux is applied to the flow by means of Joule heating. Press-fit pairs of electrodes, made of electronic-grade copper, are mounted on the opposite ends of the test section at $x=0.8$ m and $x=1.8$ m. These electrodes serve as junctions to the power supply, as well as ports for four-wire electrical measurements. An Agilent 6651 A dc power supply delivers current to the test section. This power supply is capable of delivering a maximum current of 50 A at 8 V and also measures the current flow. The voltage drop across the test section is measured using a Fluke 8842A digital multimeter and the current is measured by a Pace Scientific Model DC50A Hall-effect current sensor. The current measurement from the Hall-effect current sensor is compared with the measurement value provided by the power supply. The two values agree within 0.6% across the entire range of power input into the system. The resistance of the test section (0.085 Ω), calculated from the voltage and current measurement acquired when the power supply is online, is corroborated by a four-point resistance measurement, acquired with the power supply off-line. These measurements agree within 0.5%. The maximum field strength applied axially for Joule heating in the experiments was 4 V/m. Because of the low value of the field strength and the low electrical conductivity of the nanofluid as compared with the tube, we assume that the Joule heating in the stainless steel tube will have negligible effect on the nanofluid heat transfer.

The entire tube is insulated in layers of polyethylene foam rubber insulation. The overall thermal resistance of the insulation is 12.3 K/W. The mixed-mean temperature of the flow exiting the test section is measured in an insulated mixing tank, using a sheathed K-type thermocouple. From the measurement of the mass flow rate and the inlet and exit flow bulk temperatures, the thermal energy conservation of the rig can be assessed. Since the

test section is well insulated, over 97% of the energy supplied by the power supply shows up as an increase in sensible energy of the test fluid.

3 Data Analysis and Rig Validation

The experimental measurements include mass flow rate, the applied electrical power, the mixed-mean temperature into and out of the tube, and the wall temperature at three points in the development section and 19 points in the heated section (test section). The goal of the analysis is to extract the fluid specific heat and the thermal conductivity. The accuracy of the measurement and data analysis procedures are verified by measuring the properties of pure fluids, as described in this section.

The specific heat is determined by a straightforward application of the conservation of energy as

$$C_p = \frac{P_E}{\dot{m}(T_{m,\text{out}} - T_{m,\text{in}})} \tag{1}$$

where P_E is the electrical power dissipated in the tube, and $T_{m,\text{out}}$ and $T_{m,\text{in}}$ are the mixed-mean temperature out and in of the tube, respectively. Note that there is no correction made for losses because the system is well insulated. To qualify the system, specific heat capacity was measured for pure de-ionized water at an average inlet temperature of 13 °C and an average rise in bulk temperature of 4 °C. All the measured values of specific heat were within 2.5% of the tabulated values. These qualification data show that the losses from the apparatus are small and that the specific heat can be measured with an uncertainty of 2.5% in the range of interest.

The experiment is modeled after a classic convective heat transfer problem, namely, the thermal entry region of laminar hydrodynamically fully developed round tube flow with constant heat flux. The analysis is complicated by the finite wall thickness of the tube, even though the tube wall thickness is small and the thermal conductivity of stainless steel is small relative to other metal tube materials. The product of the tube cross-sectional area and the stainless steel thermal conductivity was 1.6×10^{-4} W m/K. However, axial conduction through the tube wall was included in the data analysis procedure. The solution of the wall temperature rise in the stainless steel tube is derived from a conjugate heat transfer model of the experiment: Volumetric heat generation in the tube wall due to the Joule heating is balanced by convective heat transfer to the fluid, axial conduction, and losses through the insulation to the ambient.

The tube wall temperature profile was calculated using a finite volume scheme. The flow and the tube wall were discretized into unit cells. The energy balance for the fluid cell is as follows:

$$\dot{m}C_p(T_f^i - T_f^{i-1}) = (hA)^i(T_w^i - T_f^i) \tag{2}$$

In this equation, superscript i represents the ith cell in the discretization scheme; subscripts f and w denote the fluid and wall cells, respectively. An energy balance for a tube wall element is written as

$$q'''V_w + \frac{k_wA_w}{\Delta x}(T_w^{i+1} - T_w^i) = (hA)^i(T_w^i - T_f^i) + \frac{k_wA_w}{\Delta x}(T_w^i - T_w^{i-1}) + \frac{T_w^i - T_\infty}{R_{t,\text{ins}} + R_{t,\text{amb}}} \tag{3}$$

The terms representing the electrical heating generated in the wall and the axial conduction from the downstream wall element (on the left hand side of the equation) are balanced by the terms representing the transfer of thermal energy to the fluid, the axial conduction to the upstream wall cell, and the thermal energy loss through the insulation to the ambient. Variables q''', V_w, k_w, A_w, and Δx represent the volumetric heat generation, the volume of the cell wall, the thermal conductivity of the tube wall, the cross-sectional area of the wall, and the discretization step length, respectively. The variables $R_{t,\text{ins}}$ and $R_{t,\text{amb}}$ represent the thermal resistance of the insulation and the convective resistance from the insulation to ambient. These terms are defined as follows:

$$R_{t,\text{ins}} = \frac{\log[1 + t_{\text{ins}}/(r_o + t_w)]}{2\cdot\pi\cdot\Delta x\cdot k_{\text{ins}}} \tag{4}$$

$$R_{t,\text{amb}} = [2\cdot\pi\cdot(r_o + t_w + t_{\text{ins}})\cdot\Delta x\cdot h_\infty]^{-1} \tag{5}$$

The variables r_o, t_w, t_{ins}, k_{ins}, and h_∞ represent the internal radius of the tube, the thickness of the tube wall, the thickness of the insulation, the thermal conductivity of the insulation, and the ambient convective heat transfer coefficient, respectively. A value of 5 W/m^2 K, estimated from empirical correlations [15], was used for the ambient convective heat transfer coefficient. Note that the modeling results are not sensitive to the assumed natural convective heat transfer coefficient within the range of 1–20 W/m^2 K. Apart from the heat transfer coefficient h, all the variables necessary for the conjugate analysis (solving Eqs. (2) and (3)) are known from the operating conditions or from geometrical parameters in the experiment.

In the case in which the temperature variation is small and the thermal properties of the fluid can be assumed constant, there is an infinite-series solution for the local Nusselt number [16].

$$\text{Nu}_x = \left[\frac{1}{\text{Nu}_\infty} - \frac{1}{2}\sum_{m=1}^{\infty}\frac{\exp(-\gamma_m^2x^+)}{A_m\gamma_m^4}\right]^{-1} \tag{6}$$

The variable Nu_∞ is the asymptotic Nusselt number for a laminar constant heat flux problem and has a value of 4.364; x^+ is a nondimensional axial location defined as $x/r_o/\text{RePr}$, where Re and Pr are the Reynolds number and Prandtl number of the flow, respectively. The eigenvalues and constants required for evaluating the expression may be found in Ref. [16]. For a known value of fluid thermal conductivity, Eqs. (2)–(6) can be combined to calculate a wall temperature distribution.

To facilitate the implementation of a numerical scheme, Eqs. (2) and (3) are rewritten, respectively, in the following form:

$$T_f^{i-1}(-X^i) + T_f^i(1 + X^i) + T_w^i(-1) = 0$$

$$T_w^{i-1}(Y^i) + T_f^i(1) + T_w^i(-1 - 2Y^i - Z^i) + T_w^{i+1}(Y^i) = -T_\infty(Z^i + Q^i)$$

where

$$X^i = \dot{m}C_p/(hA)^i, \quad Y^i = (k_wA_w/\Delta x)/(hA)^i$$

$$Z^i = [(R_{t,\text{ins}} + R_{t,\text{amb}})\cdot(hA)^i]^{-1} \quad \text{and} \quad Q^i = q'''V_w/[(hA)^i\cdot T_\infty]$$

The tube is discretized into 100 cells. Forms of Eqs. (2) and (3) are written for each cell with appropriate boundary conditions. These equations are assembled into a matrix-vector form and the temperature profiles of the fluid and wall cells are solved for using MATLAB.

To validate the experimental setup, DI water with a known thermal conductivity of 0.6 W/m K is utilized as the working fluid in the experiment. Measured tube wall temperature values are compared with the temperature values calculated using the methodology described above. The comparisons for two operating conditions are shown in Figs. 2 and 3. Agreement between the measurement and theory is excellent, and within the estimated temperature uncertainty of 0.2 °C.

4 Nanofluid Experiments

The augmentation in thermal conductivity is evaluated by comparing the tube wall temperature profile, at the same operating conditions, before and after the addition of nanoparticles to the base fluid. Two sets of base fluid/nanoparticles were investigated: a suspension of DI-water and 2% by volume of aluminum oxide (Al_2O_3) particles and a suspension of silicone oil (Dow Corning 200® Fluid, 10 cS) and 0.2% by volume of MWCNTs. The characteristic viscosity of the silicone oil is 10 cS. The

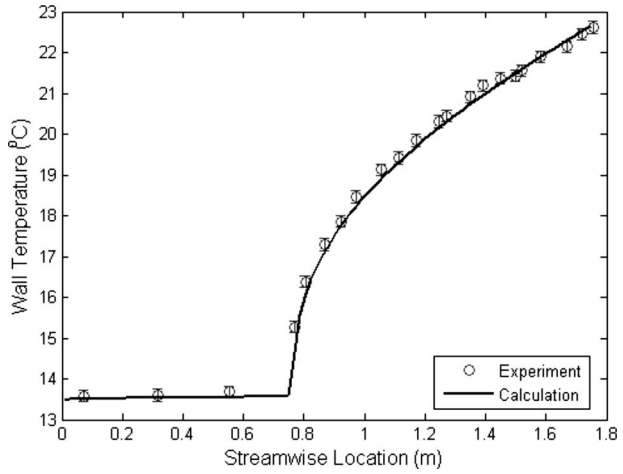

Fig. 2 Comparison of the measured and calculated temperature profiles in tube for nominal Re=800 and power output of 50 W

DI-water/Al_2O_3 experiments were conducted for three conditions: three flow conditions (Reynolds numbers of 800, 1200, and 1600) at a power input of 50 W. The silicone oil/MWCNT experiments were conducted for four power settings (50 W, 100 W, 150 W, and 200 W) and two flow conditions (Reynolds number of 500 and 750). The values of kinematic viscosities of 1.0×10^{-6} m^2/s and 1.0×10^{-5} m^2/s were used to calculate nominal Reynolds number for the flow conditions in the DI-water/Al_2O_3 and silicone oil/MWCNT experiments, respectively. Viscosity measurements were not performed for the nanofluids.

4.1 DI-Water/Al_2O_3 Nanofluid Synthesis and Characterization. Spherical aluminum oxide particles, purchased from Alfa Aesar Corporation (Ward Hill, MA), were suspended in DI-water to produce the nanofluid. The Al_2O_3 particles were quoted to have a diameter of 40–50 nm. The particles had a purity of 99.5% and a specific gravity of 3.97 g/cm. The as-produced particles were dispersed in water with the aid of a Hielscher UP400S titanium probe ultrasonic processor. Agglomerates created by interparticle bonding forces are disintegrated by jet streams emanating from ultrasonic cavitation created by the oscillation of the processor tip. The time necessary for the deagglomeration process was determined by fixing the intensive energy deposited into the suspension. The intensive energy was fixed at 2.0×10^9 J/m^3. Pohl and Schubert [17] reported that the deagglomeration process is independent of the particle loading concentration, up to 50% by volume particle loading.

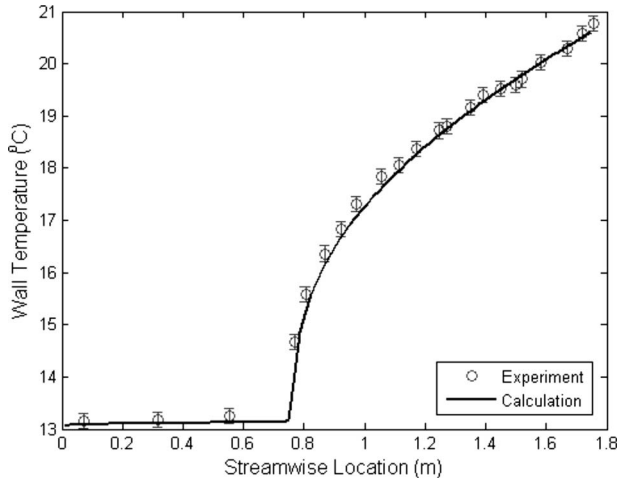

Fig. 3 Comparison of the measured and calculated temperature profiles in tube for nominal Re=1200 and power output of 50 W

According to the Derjaguin–Landau–Verweym–Overbeek (DLVO) theory, there is a balance between the attractive van der Waals forces and the electrostatic repulsion force, core repulsion force, and osmotic repulsion force [18]. This balance results in agglomerate sizes that differ from the particle size range quoted by the particle manufacturer. The particle size distribution in suspension was measured using a Brookhaven 90Plus Nanoparticle Size Analyzer, which employs the dynamic light scattering (DLS) technique.

In the DLS scheme, a laser beam incident on a volume in the colloidal sample is scattered in all directions. The colloidal sample is diluted so that single photon scattering is probable. The scattered beam is collected by a photomultiplier detector. In the case of the equipment used, the detector is static and is at a 90 deg angle from the incident beam. The photomultiplier collects the time autocorrelation of the light intensity, and the signal processing system determines the characteristic time delay for the scattered light to become random. Smaller particles diffuse faster within the scattering volume due to the Brownian motion, so the time autocorrelation is shorter for smaller particles. The time autocorrelation directly yields information about the diffusion coefficient of the particles. Given the diffusion coefficient and the viscosity of the base solvent, one may use the Stokes–Einstein equation to calculate the diameter of spherical particles.

The measured mean effective diameter of the particles in solution is 160 nm with a polydispersity of 0.14 (equivalent to a standard deviation of 57 nm), even though the manufacturer quoted a nominal particle size of 40–50 nm. Other researchers have also measured Al_2O_3/DI-water nanofluid particle sizes larger than sizes quoted by the manufacturer. Ju et al. [7] measured an average particle size of 120 nm for Al_2O_3 particles that were quoted to be 30 nm. Lee et al. [19] studied the effect of different techniques on the dispersion of Al_2O_3 particles in water, using the same batch of particles as was used in the present work. The methods they employed included the modulation of the pH of the suspension, dispersion of the particles using both probe-type and bath-type ultrasonicators for varying periods of time, and the use of surfactants. They measured a mean effective diameter of the particles ranging from 140 nm to 230 nm, with a pH of 4 or lower resulting in the lower bound of mean effective diameter.

4.2 Silicone Oil/MWCNT Nanofluid Synthesis. The silicone oil used in the oil/MWCNT experiments has a nominal thermal conductivity of 0.15 W/m K, a kinematic viscosity of 10 cS, a density of 940 kg/m^3, a specific heat capacity of 1600 J/kg K, and a Prandtl number of 100. The silicone oil selected for the experiment has thermal characteristics, at room temperature, similar to the thermal characteristics of engine oil at its operating conditions ($\sim130°C$). The results of the experiments may have direct applicability to engine cooling technologies. The MWCNT purchased from Sigma-Aldrich Inc. (St. Louis, MO) had quoted inside diameters of 5–10 nm, outside diameters of 10–30 nm, length of 0.5–500 μm, and a purity level of 95+%. The ultrasonic processor was used to deagglomerate the tubes in suspension. The intensive energy used in the deagglomeration process was 2.0×10^8 J/m^3. The intensive energy used in this silicone oil/MWCNT synthesis is lower than in the DI-water/Al_2O_3 because higher deagglomeration time, in the case of carbon nanotubes, seemed to have only marginal effects on the dispersion of the nanotubes in oil. The extent to which the nanotubes bundles were disentangled was not established. Dispersion of the nanoparticles was characterized using the DLS technique for the DI-water/Al_2O_3 nanofluid experiments. In the silicone oil/MWCNT nanofluid experiments, dispersion was qualified by the settling time of the particles in suspension. The issue of the col-

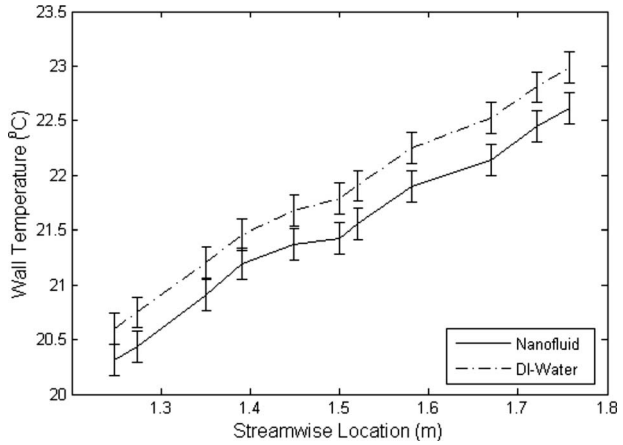

Fig. 4 Comparison of temperature rise in stainless steel tube for water and Al_2O_3 nanofluid at nominal Re = 800 and power input of 50 W

loidal stability is mitigated because the experimental setup is a recirculatory system. Experimental data taken a month apart, without draining and refilling the system, were identical.

5 Results and Discussion

Figure 4 shows a representative comparison of temperature rise in the wall of the stainless steel tube (test section) for the case of DI-water/Al_2O_3 nanofluid for a Reynolds number of 800 and power input of 50 W. The wall temperature values for the experiments using water were 0.4°C higher than that of experiments using the nanofluid. This difference in temperature is a reflection of the slight increase in the thermal conductivity of the working fluid.

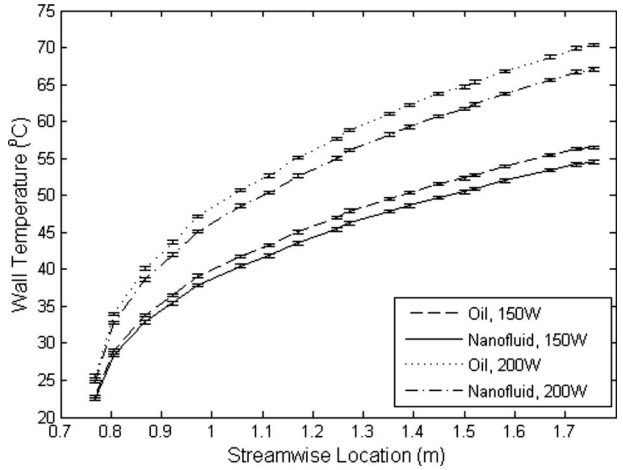

Fig. 5 Temperature rise in stainless steel tube for silicone oil and oil/MWCNT nanofluid at nominal Re = 500 and power input of 150 W and 200 W

Figure 5 shows comparisons between the wall temperature profiles in the test section for experiments run with silicone oil and silicone oil/MWCNT nanofluid. The Reynolds number of the flow is 500. The power inputs into the flow are 150 W and 200 W. There is a drop in the maximum wall temperature from the silicone oil cases to the nanofluid cases: 2°C for 150 W power input and 3.2°C for 200 W power input case. This temperature drop is indicative of the increase in thermal conductivity of the working fluid. The drop is more significant than that observed for the DI-water/Al_2O_3 nanofluid. This suggests that the increase in thermal conductivity by suspending MWCNT in silicone oil is more significant than the increase in thermal conductivity by suspending Al_2O_3 in water, especially since only 0.2% by volume of MWCNT was suspended in the silicone oil.

5.1 Effective Thermal Conductivity. The heat input into the flow and wall temperatures are measured quantities in the experiment. For a constant heat flux experiment, the bulk temperature varies linearly with the axial position. Thus, the convective heat transfer coefficient may be directly calculated as $h=q''/(T_w-T_f)$. For constant properties and hydrodynamically fully developed flow, there is an infinite-series solution for the Nusselt number [16]. The Nusselt number is a function of the nondimensional axial location x^+, which is a function of the thermal conductivity: $x^+=k/\rho\cdot C_p\cdot\bar{U}\cdot D$. The thermal conductivity may be calculated from the heat transfer coefficient and the Nusselt number: $k=h\cdot D/\mathrm{Nu}$. Using this model for the Nusselt number, one can iteratively calculate the effective thermal conductivity of the fluid.

Single-sample uncertainty analysis is used in this work to quantify the uncertainties in the experimental results. This methodology was put forth by Kline and McClintock [20] and expanded on by Moffat [21]. Uncertainties in the wall temperature measurement, bulk temperature measurement, mass flow rate, and axial location of thermocouples were estimated. Uncertainties in the power input into the flow are accounted for by uncertainties in the change in the sensible energy of the liquid. These uncertainty values were propagated to the calculation of the effective thermal conductivity, using a 95% confidence interval.

The sources of uncertainties that were considered for the estimation of the uncertainty in the temperature measurements are thermocouple accuracy and resolution, digital multimeter accuracy and resolution, NIST K-type thermocouple conversion polynomial, and the standard deviation of the data set. The accuracy and resolution of the Coriolis meter and the standard deviation of the data set were considered as factors contributing to the uncertainty in the mass flow rate measurement. These sources of uncertainties and their associated numerical values are listed in Table 1.

Individual uncertainty estimates were calculated for each data point. The typical uncertainty in measuring thermal conductivity

Table 1 Uncertainty sources considered in uncertainty calculations

Device	Uncertainty source	Value
K-type thermocouples	NIST maximum voltage-to-temperature conversion error	$6.0(10)^{-2}$ °C
K-type thermocouples	Accuracy of location of thermocouple (TC) beads	$1.6(10)^{-3}$ m
Digital multimeter (DMM)	DMM resolution for TC sampling	$1.0(10)^{-6}$ V
Digital multimeter	DMM accuracy in TC sampling	$2.0(10)^{-8}$ V
Current sensor	Fractional accuracy of measurement of power supply current	$6.0(10)^{-3}$
Digital multimeter	DMM resolution in measuring power supply voltage	$1.0(10)^{-4}$ V
Digital multimeter	DMM accuracy in measuring power supply voltage	$1.2(10)^{-3}$ V
Coriolis meter	Fractional accuracy of mass flow rate measurement	$3.0(10)^{-4}$
Coriolis meter	Resolution of Coriolis meter mass flow rate measurement	$2.1(10)^{-5}$ kg/s
Coriolis meter	Accuracy of density measurement	$2.0(10)^{-1}$ kg/m^3

Table 2 Uncertainty estimates for measured quantities

Quantity	Uncertainty
Wall temperature	$2.0(10)^{-1}$ °C
Inlet flow temperature	$4.2(10)^{-2}$ °C
Outlet flow temperature	$4.9(10)^{-2}$ °C
Flow temperature rise	$6.5(10)^{-2}$ °C
Mass flow rate	$5.7(10)^{-5}$ kg/s
Effective thermal conductivity (water-based experiments)	$3.0(10)^{-2}$ W/m K
Effective thermal conductivity (oil-based experiments)	$1.5(10)^{-2}$ W/m K

using this experimental methodology is 0.03 W/m K for water-based experiments and 0.015 W/m K for silicone oil-based experiments. The uncertainty estimates for the measured quantities are listed in Table 2.

Comparisons of the effective thermal conductivity calculated for DI-water-DI-water/Al_2O_3 nanofluid and for silicone oil-oil/MWCNT nanofluid are shown in Figs. 6 and 7, respectively. Figure 6 shows an average thermal conductivity of water as 0.59 W/m K. This value compares well to the handbook value of 0.592 W/m K [16] at the average temperature of 15.3 °C. The

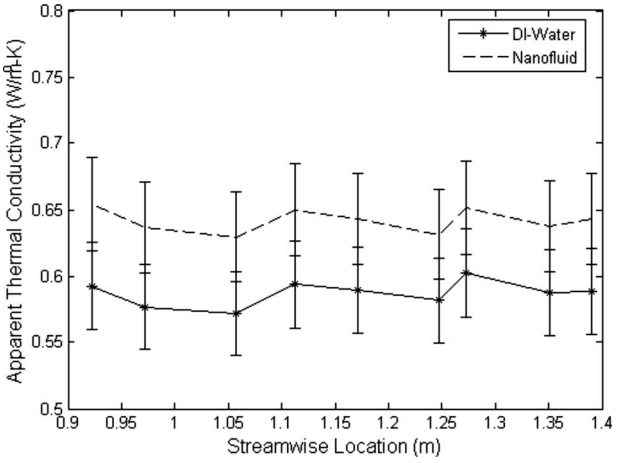

Fig. 6 Effective thermal conductivity for DI-water and DI-water/Al_2O_3 nanofluid at nominal Re = 800 and power input of 50 W

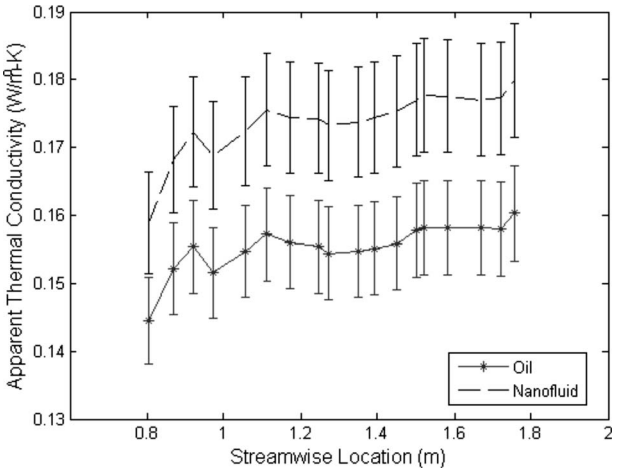

Fig. 7 Effective thermal conductivity of silicone oil and oil/MWCNT nanofluid at nominal Re = 500 and power input of 200 W

Table 3 Base fluid thermal conductivity of DI-water and augmentation of effective thermal conductivity by the addition of 2% by volume of Al_2O_3

Re	Power (W)	Base fluid thermal cond. (W/m^2 K)	Nanofluid eff. thermal cond. (W/m^2 K)
800	50	0.59	0.64
1200	50	0.61	0.64
1600	50	0.62	0.64

figure also shows an augmentation of about 8% in the thermal conductivity of DI-water by the addition of Al_2O_3 nanoparticles, at this operating condition. This increase in effective thermal conductivity is reflected by the decrease in measured wall temperatures for the DI-water/Al_2O_3 nanofluid experiment, as shown in Fig. 4. Figure 7 shows an average thermal conductivity of silicone oil of 0.16 W/m K and an augmentation of around 12% by the addition of MWCNT, at that operating condition.

Similar experiments to those illustrated in Figs. 4–7 were run for a range of power settings and Reynolds numbers. The averaged values of measured thermal conductivities for DI-water and silicone oil are shown in Tables 3 and 4, respectively. Table 3 lists the measured values of thermal conductivity of water ranging from 0.59 W/m K to 0.62 W/m K. The handbook values of thermal conductivity are within the uncertainty range of the measured values. Table 4 lists the measured values of thermal conductivity of silicone oil ranging from 0.14 W/m K to 0.16 W/m K and the thermal conductivity of the silicone oil/MWCNT nanofluid ranging from 0.16 W/m K to 0.18 W/m K.

The intensive augmentation factor is defined as the percentage increase in thermal conductivity per percentage of volume of particles suspended. Averaged across the range of operating conditions, the addition of 2% by volume of Al_2O_3 nanoparticles to DI-water increased the thermal conductivity of water by 5.6%. Thus, the intensive augmentation factor for the DI-water/Al_2O_3 nanofluid is 2.8. The addition of 0.2% by volume of MWCNT to silicone oil increased the thermal conductivity of the oil by 10.3%, averaged across the range of operating conditions; the thermal conductivity increased from a nominal value of 0.154 W/m K to a nominal value of 0.170 W/m K. The intensive augmentation factor of the oil/MWNCT nanofluid is 52.

Samples of the silicone oil and oil/MWCNT nanofluid that were used in this experiment were independently analyzed by Gharagozloo et al. [22]. They used a parallel plate method to measure the thermal conductivity of the oil and oil/MWCNT nanofluid under stationary conditions. Their experimental configuration was designed to minimize the development of convection cells. They measured a thermal conductivity of 0.151 W/m K for the silicone oil and a thermal conductivity of the 0.175 W/m K for the oil/MWCNT nanofluid. A representative plot of their mea-

Table 4 Increase in effective thermal conductivity of silicone oil by the addition of 0.2% by volume MWCNT

Re	Power (W)	Base fluid thermal cond. (W/m^2 K)	Nanofluid eff. thermal cond. (W/m^2 K)
500	50	0.15	0.16
500	100	0.15	0.16
500	150	0.16	0.17
500	200	0.16	0.18
750	50	0.14	0.16
750	100	0.16	0.17
750	150	0.16	0.18
750	200	0.16	0.18

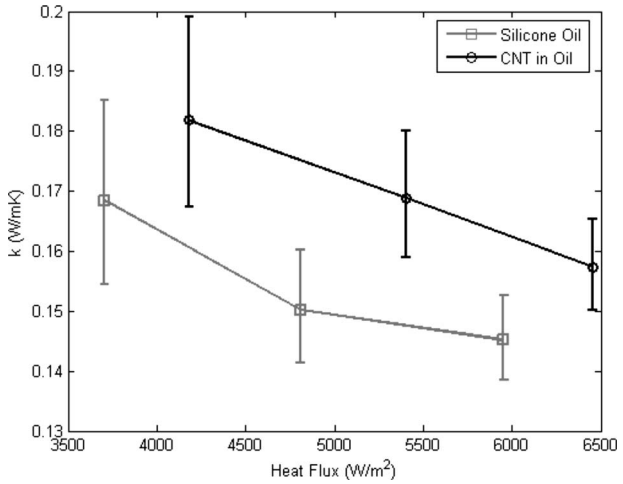

Fig. 8 Measurement of effective thermal conductivity of silicone oil and oil/MWCNT using parallel plate method [22]

surement is shown in Fig. 8. This measurement confirms the nominal value of the thermal conductivity of the pure silicone oil and indicates a 16% increase with the addition of 0.2% by volume of MWCNT. Therefore, both the convection and static experiments indicate an augmentation in thermal conductivity in excess of 10%.

5.2 Electron Microscopy Characterization. A different set of carbon nanomaterial, purchased from NanoCraft Inc. (Renton, WA). (Product: MWNT-A, No. 25921966870), was used to prepare nanofluid in the same procedure described above. Experiments with this batch of nanofluid did not indicate any increase in the thermal conductivity of the fluid. The wall temperature profiles in the test section in experiments utilizing this nanofluid were similar to wall temperature profiles in experiments utilizing only the base liquid. Figure 9 shows a comparison of the effective thermal conductivity of base fluid, the original nanofluid, and the new nanofluid, at a Reynolds number of 500 and a power input of 200 W. This plot demonstrates the repeatability of the methodology for calculating the augmentation in thermal conductivity and also shows the lack of the performance of the alternate nanomaterial.

The difference in the performance of the nanoparticles is attributed to the difference in the geometrical structure of the two sets

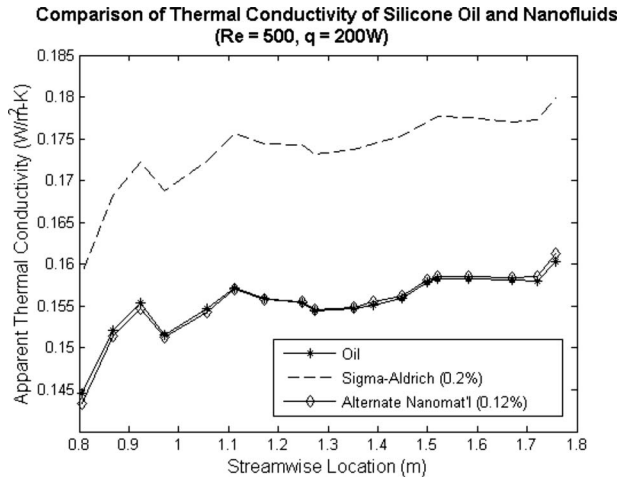

Fig. 9 Comparison of effective thermal conductivity of different nanofluids and silicone oil

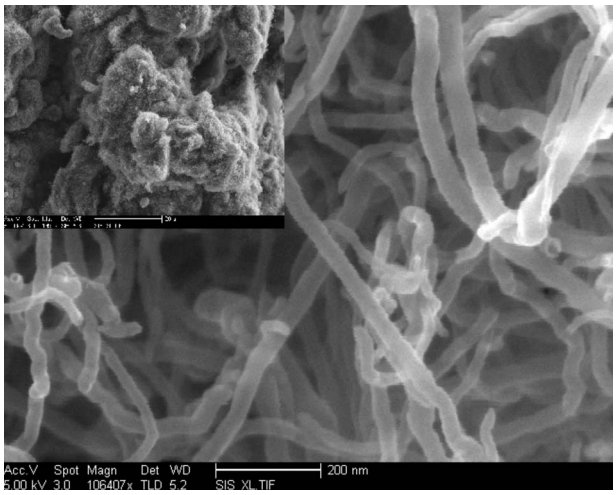

Fig. 10 SEM imaging of Sigma-Aldrich nanoparticles at a magnification of 100,000×. The inset is a 1500× magnification of the same sample.

of nanomaterials. Although they appear quite similar to the eye, the two materials show stark differences under magnification. Scanning electron microscopy (SEM) was utilized to examine the structure of the dry state of the nanotubes. The equipment used for SEM imaging is an FEI XL30 Sirion SEM, with FEG source and EDX detector. Figure 10 shows a sample of the Sigma-Aldrich nanotube under a 100,000× magnification; the inset in the picture is the same sample under a 1500× magnification. Figure 11 shows a similar size sample of the alternate nanomaterial under a 90,000× magnification; the inset in the picture is the alternate sample under 1500× magnification. The differences that start to become obvious in the 1500× magnification are glaring in the 90,000× / 100,000× magnification. Figure 10 shows an entangled bundle of nanotubes, whereas the material imaged in Fig. 11 has a semicrystalline nature. These differences in the material structure and aspect ratio are probably responsible for the thermal performance of the nanofluids.

6 Conclusions

The convective heat transfer performance of nanofluid in a hydrodynamically fully developed, thermally developing, laminar

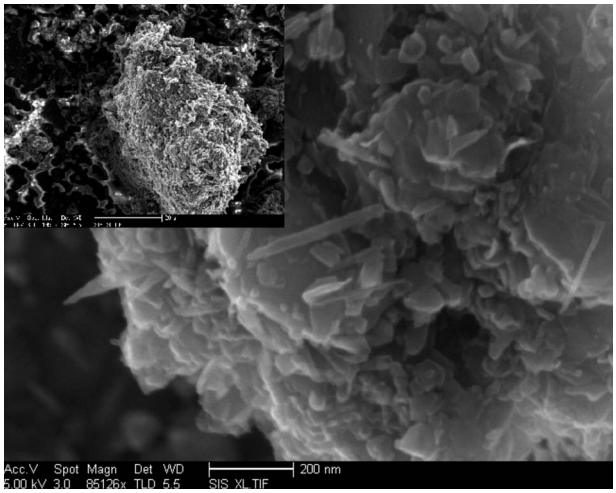

Fig. 11 SEM imaging of alternate carbon nanomaterial at a magnification of 90,000×. The inset is a 1500× magnification of the same sample.

tube flow, with constant heat flux, has been investigated. The experimental setup was first validated before the rig was used to measure the thermal conductivity of nanofluid. The validation methodology utilized standard heat transfer theory and conjugate heat transfer techniques to validate the experimental setup. DI-water/Al_2O_3 nanofluid showed an intensive augmentation factor of about 3. This augmentation factor is more modest than what was earlier reported for some static measurements. Dynamic light scattering showed that the particle size in suspension was substantially larger than the size quoted by the supplier.

Oil/MWCNT nanofluid had an intensive augmentation factor of above 50. The thermal conductivity of the base liquid and the increase in thermal conductivity were corroborated by stationary parallel plate measurements. SEM imaging was used to visualize the dry state of the carbon nanotubes. The results of the carbon nanotube experiments suggest that the structure of the nanomaterial is an important factor in the augmentation of thermal conductivity of a liquid by the means of nanoparticles.

Acknowledgment

The authors would like to thank the Office of Naval Research Thermal Management Program, and Stanford University's School of Engineering Course Assistantship program for financial support. The authors would also like to acknowledge Anthony Burdi for his assistance in the development of the graphical interface for the data acquisition system and Andrew Lee for his assistance with SEM imaging.

Nomenclature

Δx = discretization length, m
A_w = cross-sectional area of tube wall, m^2
C_p = specific heat capacity of fluid, J/kg K
h_∞ = ambient convective heat transfer, W/m^2 K
$(hA)^i$ = thermal conductance of ith fluid cell, W/K
k_{ins} = thermal conductivity of insulation, W/m K
k_w = thermal conductivity of tube wall, W/m K
$\dot{m}$ = mass flow rate of fluid, kg/s
Nu_x = Nusselt number based on axial location
Pr = Prandtl number of fluid
q''' = volumetric heat generation, W/m^3
r_o = radius of tube, m
$R_{t,\text{amb}}$ = thermal resistance of the ambient, K/W
$R_{t,\text{ins}}$ = thermal resistance of insulation, K/W
Re = Reynolds number based on tube diameter
t_{ins} = thickness of insulation, m
t_w = thickness of tube wall, m
T_∞ = ambient temperature, K
T_f^0 = temperature of incoming fluid, K
T_f^i = temperature of ith fluid cell, K
T_w^i = temperature of ith wall cell, K
x = dimensional axial location, m
x^+ = nondimensional axial location
V_w = tube wall volume of a cell, m^3

References

[1] Ahuja, A. S., 1975, "Augmentation of Heat Transport in Laminar Flow of Polystyrene Suspensions," J. Appl. Phys., **46**(8), pp. 3408–3425.
[2] Eastman, J. A., Choi, S. U. S., Li, S., Yu, W., and Thompson, L. J., 2001, "Anomalously Increased Effective Thermal Conductivities of Ethylene Glycol-Based Nanofluids Containing Copper Particles," Appl. Phys. Lett., **78**(6), pp. 718–720.
[3] Lee, S., Choi, S. U.-S., Li, S., and Eastman, J. A., 1999, "Measuring Thermal Conductivity of Fluids Containing Oxide Nanoparticles," ASME J. Heat Transfer, **121**, pp. 280–289.
[4] Choi, S. U. S., Zhang, Z. G., Yu, W., Lockwood, F. E., and Grulke, E. A., 2001, "Anomalous Thermal Conductivity Enhancement in Nanotube Suspensions," Appl. Phys. Lett., **79**(14), pp. 2252–2254.
[5] Eastman, J. A., Choi, U. S., Li, S., Thompson, L. J., and Lee, S., 1997, "Enhanced Thermal Conductivity Through the Development of Nanofluids," Mater. Res. Soc. Symp. Proc., **457**, pp. 3–11.
[6] Xie, H., Lee, H., Youn, W., and Choi, M., 2003, "Nanofluids Containing Multiwalled Carbon Nanotubes and Their Enhanced Thermal Conductivities," J. Appl. Phys., **94**(8), pp. 4967–4971.
[7] Ju, Y. S., Kim, J., and Hung, M.-T., 2008, "Experimental Study of Heat Conduction in Aqueous Suspensions of Aluminum Oxide Nanoparticles," ASME J. Heat Transfer, **130**, pp. 092403.
[8] Das, S. K., Putra, S., Thiesen, P., and Roetzel, W., 2003, "Temperature Dependence of Thermal Conductivity Enhancement for Nanofluids," ASME J. Heat Transfer, **125**, pp. 567–574.
[9] Wang, X., Xu, X., and Choi, S. U. S., 1999, "Thermal Conductivity of Nanoparticle-Fluid Mixture," J. Thermophys. Heat Transfer, **13**(4), pp. 474–480.
[10] Eastman, J. A., Phillpot, S. R., Choi, S. U. S., and Keblinski, P., 2004, "Thermal Transport in Nanofluids," Annu. Rev. Mater. Res., **34**, pp. 219–246.
[11] Ju, Y. S., and Kim, J., 2007, "Experimental Study of Heat Conduction in Aqueous Suspensions of Aluminum Oxide Nanoparticles," *Proceedings of IPACK2007*, ASME InterPACK '07, Vancouver, BC, Canada, Paper No. IPACK2007-32689.
[12] Xuan, Y., and Li, Q., 2003, "Investigation on Convective Heat Transfer and Flow Features of Nanofluids," ASME J. Heat Transfer, **125**, pp. 151–155.
[13] Wen, D., and Ding, Y., 2004, "Experimental Investigation Into Convective Heat Transfer of Nanofluids at the Entrance Region Under Laminar Flow Conditions," Int. J. Heat Mass Transfer, **47**, pp. 5181–5188.
[14] Heris, S. Z., Esfahany, M. N., and Etemad, S. Gh., 2006, "Experimental Investigation of Convective Heat Transfer of Al_2O_3/Water Nanofluid in Circular Tube," Int. J. Heat Fluid Flow, **28**, pp. 203–210.
[15] Incropera, F. P., and DeWitt, D. P., 1996, *Fundamentals of Heat and Mass Transfer*, Wiley, New York, Chap. 9.
[16] Kays, W. M., and Crawford, M. E., 1993, *Convective Heat and Mass Transfer*, McGraw-Hill, New York, Chap. 9.
[17] Pohl, M., and Schubert, H., 2004, "Dispersion and Deagglomeration of Nanoparticles in Aqueous Solutions," PARTEC, pp. 1–4.
[18] Stokes, R. J., and Evans, D. F., 1997, *Fundamentals of Interfacial Engineering*, Wiley-VCH, New York, Chap. 4.
[19] Lee, J., Flynn, R. D., Goodson, K. E., and Eaton, J. K., 2007, "Convective Heat Transfer of Nanofluids (DI Water-Al_2O_3) in Microchannels," *Proceedings of HT2007*, ASME-JSME Thermal Engineering Summer Heat Transfer Conference, Vancouver, BC, Canada, Paper No. HT2007-32630.
[20] Kline, S. J., and McClintock, F. A., 1953, "Describing Uncertainties in Single-Sample Experiments," Mech. Eng., **75**, pp. 3–8.
[21] Moffat, R. J., 1982, "Contributions to the Theory of Single-Sample Uncertainty Analysis," ASME J. Fluids Eng., **104**, pp. 250–260.
[22] Gharagozloo, P. E., Goodson, K. E., and Eaton, J. K., 2007, "Impact of Thermodiffusion on Temperature Fields in Stationary Nanofluids," *Proceedings of IPACK2007*, ASME InterPACK '07, Vancouver, BC, Canada, Paper No. IPACK2007–33293.

The Effect of the Top Wall Temperature on the Laminar Natural Convection in Rectangular Cavities With Different Aspect Ratios

Wenjiang Wu
Graduate Student
e-mail: wuw6@mcmaster.ca

Chan Y. Ching
Associate Professor
e-mail: chingcy@mcmaster.ca

Department of Mechanical Engineering,
McMaster University,
1280 Main Street West,
Hamilton, ON, L8S 4L7, Canada

The effect of the top wall temperature on the laminar natural convection in air-filled rectangular cavities driven by a temperature difference across the vertical walls was investigated for three different aspect ratios of 0.5, 1.0, and 2.0. The temperature distributions along the heated vertical wall were measured, and the flow patterns in the cavities were visualized. The experiments were performed for a global Grashof number of approximately 1.8×10^8 and nondimensional top wall temperatures from 0.52 (insulated) to 1.42. As the top wall was heated, the flow separated from the top wall with an undulating flow region in the corner of the cavity, which resulted in a nonuniformity in the temperature profiles in this region. The location and extent of the undulation in the flow are primarily determined by the top wall temperature and nearly independent of the aspect ratio of the cavity. The local Nusselt number was correlated with the local Rayleigh number for all three cavities in the form of $Nu=C\cdot Ra^n$, but the values of the constants C and n changed with the aspect ratio. [DOI: 10.1115/1.2993138]

Keywords: natural convection, rectangular cavities, aspect ratio

1 Introduction

The importance of natural convection in enclosures can be found in many engineering applications such as energy transfer in rooms and buildings, nuclear reactors, electronic packaging, and solar collectors. There have been numerous experimental [1–4] and numerical [5,6] investigations of the natural convection that occurs in a rectangular enclosure driven by a temperature difference across the vertical walls. Most of the early studies focused on the natural convection in a rectangular cavity with insulated or adiabatic horizontal walls. Ostrach [7] showed that the natural convection is extremely sensitive to the thermal boundary conditions and the cavity geometry. For example, Ostrach and Raghavan [8] and Shiralkar and Tien [9] observed that the temperature of the top and bottom walls of a cavity had a significant effect on the stratification inside the cavity that, in turn, affected the flow pattern and the heat transfer characteristics. Ravi et al. [10] and Wu et al. [11] found that an increase in the top wall temperature resulted in a significant change in the flow pattern in the cavity. When the temperature of the top wall was close to or larger than that of the heated vertical wall, the flow separated from the top wall near the upper corner between the heated vertical wall and the top wall due to the formation of a negatively buoyant plume. Recently, Wu et al. [12] found that when the top wall temperature was much larger than the heated vertical wall, the upward natural convection flow on the heated vertical wall separated from the wall before reaching the top wall. As a result, a highly stratified region occurred above the natural convection plume after it had separated from the vertical wall. The highly stratified region became larger and more stable with an increase in the top wall temperature.

The effect of the cavity configuration on the natural convection in a rectangular cavity has also been numerically and experimentally investigated [13–18]. Emery and Chu [13] and MacGregor and Emery [14] showed that the aspect ratio of a rectangular cavity had a significant effect on the natural convection heat transfer. As the aspect ratio was increased, secondary flow cells formed in the core region with an increase in the Rayleigh number [15–18]. Cormack et al. [5] simulated natural convection flows in a cavity with aspect ratio varying from 0.05 to 1. They observed that the

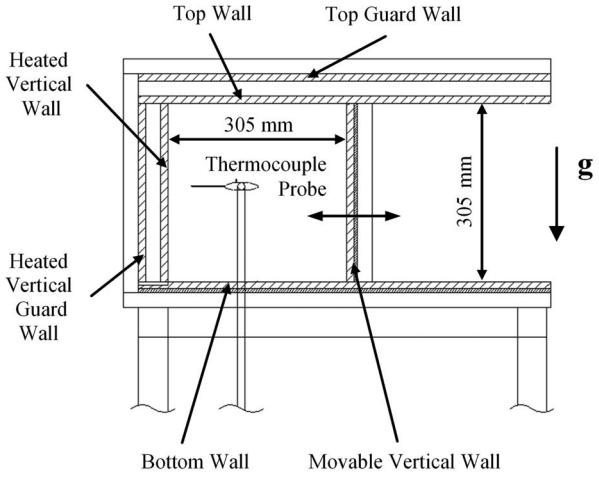

Fig. 1 Schematic of the enclosure with an adjustable aspect ratio

Contributed by the Heat Transfer Division of ASME for publication in the JOURNAL OF HEAT TRANSFER. Manuscript received June 27, 2007, final manuscript received July 29, 2008; published online March 16, 2009. Review conducted by Yogendra Joshi. Paper presented at the 2007 ASME-JSME Thermal Engineering Conference and Summer Heat Transfer Conference (HT2007), Vancouver, BC, Canada, July 8–12, 2007.

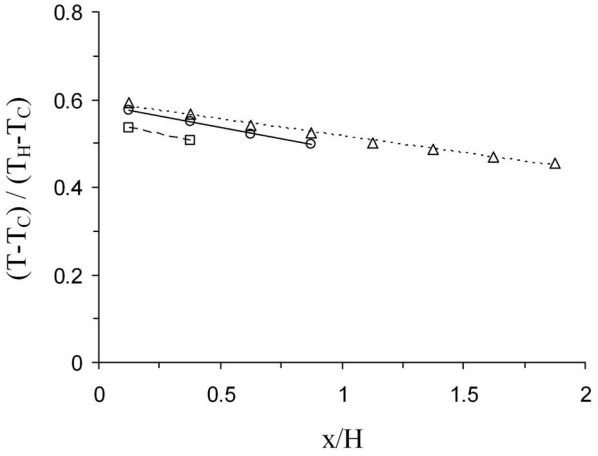

Fig. 2 Nondimensional temperature distributions on the insulated top wall with aspect ratio of (△) 0.5, (◯) 1.0, and (□) 2.0

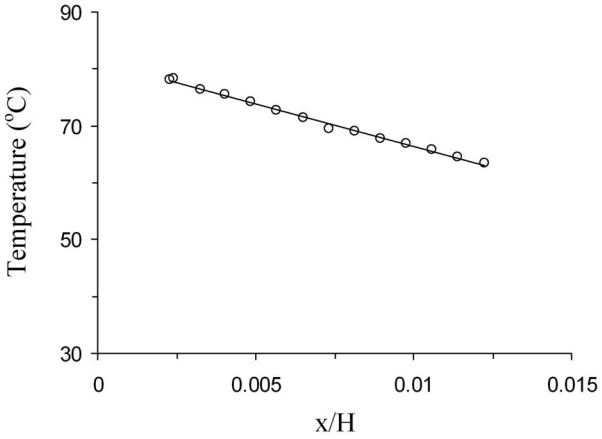

Fig. 3 Best linear fit used to determine the slope of the temperature profile at the nondimensional height y/H=0.6 of the square cavity with the top wall temperature of 109°C

natural convection flow in the cavity was reduced as the aspect ratio of the cavity decreased and the viscous force on the top and bottom walls became more prevalent.

Most previous investigations have mainly focused on the natural convection in a rectangular cavity with insulated horizontal walls and aspect ratio either very much less or larger than unity. In these cases, the heat transfer characteristics were significantly changed due to the change in the flow pattern, particularly in the core region of the cavity. The objective of this investigation was to experimentally characterize the effect of the top wall temperature on the laminar natural convection in rectangular cavities with relatively modest aspect ratios. The measurements were performed for three rectangular cavities with aspect ratios of 0.5, 1.0, and 2.0 for cases where the top wall of the cavity was heated and the bottom wall cooled. The experimental facility and experimental procedure are outlined in Sec. 2. The results of the experiments are given in Sec. 3, followed by the conclusions of this study.

2 Experimental Methodology

The experiments were performed in an air-filled rectangular cavity with an adjustable aspect ratio shown schematically in Fig. 1, which was also used by Wu et al. [11,12]. The cavity had a height of 305 mm (12 in.) and a width that could be adjusted from 100 mm to 610 mm (3.9–24 in.) by moving one vertical wall. The width of the cavity for the current investigation was set to 152.5 mm, 305 mm, and 610 mm (6 in., 12 in., and 24 in.), corresponding to aspect ratios of 2, 1, and 0.5. The depth of the cavity was 914 mm (36 in.), which was three times the height, so that the flow should be approximately two-dimensional, as suggested in a

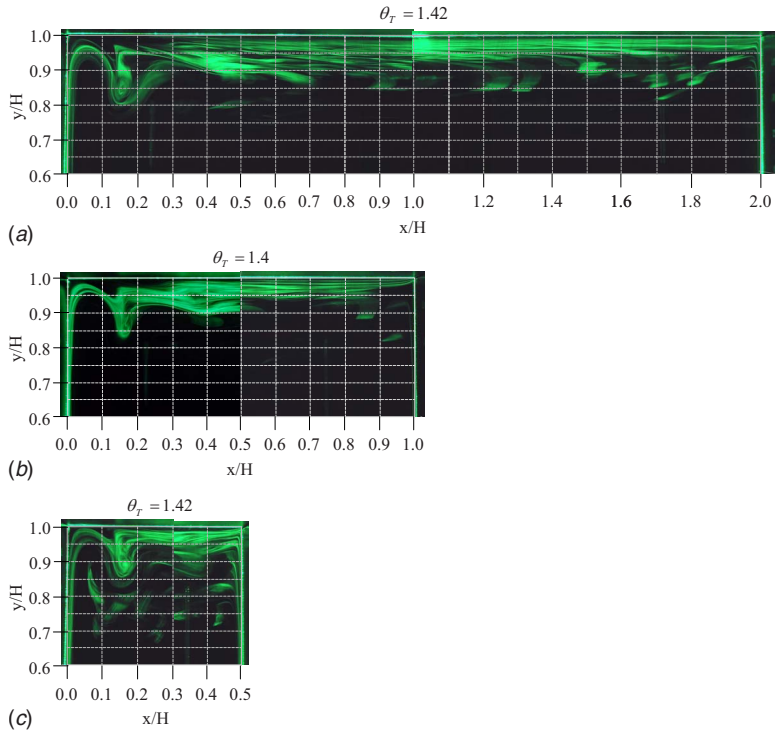

Fig. 4 Flow patterns in the upper left region of the rectangular cavities with the aspect ratios of (*a*) 0.5, (*b*) 1.0, and (*c*) 2.0 for nondimensional top wall temperatures of approximately 1.42

number of previous studies [3,8]. The walls of the cavity were designed so that one of the vertical walls and the top wall could be heated independently, while the other vertical wall and the bottom wall could be cooled. The ends of the cavity were sealed using walls with large glass windows so the flow in the cavity could be visualized.

The top wall and the heated vertical wall were constructed using 12.7 mm (0.5 in.) thick aluminum plates. The heated vertical wall had three silicone rubber heaters, with a maximum capacity of 180 W, while the top wall had four heaters, which were attached on the outside surface of these plates. Each heater was independently controlled using a multichannel variable duty controller. To minimize heat losses from the heated walls to the ambient, the walls were insulated using aluminum guard heater walls constructed similar to the heated walls. The walls were separated by a 25 mm thick layer of insulation, with an additional layer outside of the guard walls. The heat transfer between the heated vertical wall and its guard wall was less than 3 W, corresponding to approximately 15% of the heat transfer into the cavity from the heated vertical wall. This heat loss was estimated from the temperature difference between the heated vertical wall and its guard wall, and knowing the thermal conductivity of the insulation. The surface radiation effects from the cavity walls were estimated using an emissivity value of 0.4 for the aluminum plates and were found to be negligible compared with the natural convection heat transfer along the heated vertical wall.

The bottom wall and the cooled vertical wall were also constructed from 12.7 mm (0.5 in.) thick aluminum plates that contained serpentine cooling channels. The channels were closed using 6.4 mm (0.25 in.) thick outer aluminum plates that were insulated from the outside using a 25 mm (1 in.) thick layer of insulation. Municipal water was circulated through the channels to remove the heat from these two plates. The temperature of these walls in this case was kept approximately uniform by maintaining the cooling water flow rate relatively high at approximately 0.9 L/min. This was facilitated by the fact that the heat flux through the walls was relatively low, approximately less than 480 W/m^2 in the current investigation. The heated walls were also maintained at a uniform temperature by independently controlling the power to the individual heaters. In all cases, the maximum discrepancy, which occurred near the corner regions, between the local temperature and the average wall temperature was less than $\pm 4\%$. When the heaters on the top and guard wall were turned off, only the two layers of insulation reduce the heat transfer from the top wall to the ambient. This thermal boundary condition is defined as "insulated" here. The typical top wall temperature distributions under this thermal boundary condition are shown in Fig. 2, and the mean temperature of the top wall is used in the analysis for this case.

The temperature difference between the walls will result in a singularity in temperature at the junctions, which has been studied by Nansteel et al. [19]. In order to minimize the heat transfer between the heated vertical wall and the top wall, the junction between the walls was insulated using a thin layer of mineral fiber paper. The maximum temperature difference across the mineral fiber paper was approximately 24°C. The maximum temperature gradient in the vicinity of the junction on the heated vertical wall and the top wall, estimated from the temperature measurements, were approximately 0.11°C/cm and 0.17°C/cm, respectively. The heated vertical wall was isolated from the bottom wall by supporting its guard wall on four small Delrin blocks so that an air gap of approximately 1 mm high was present. The temperature on the walls of the cavity was measured using 0.25 mm (0.010 in.) T-type thermocouples that were embedded in the plates. The thermocouples were placed in holes that were drilled from the rear surface to a depth of 11.1 mm (04375 in.), and held in place using a high thermal conductivity paste. There were, respectively, 18, 11, 12, and 11 thermocouples embedded in the heated vertical wall, cooled vertical wall, top wall, and bottom wall. Among them, 6, 3, 4, and 3 thermocouples were embedded along the centerlines to continuously monitor the changes in the tempera-

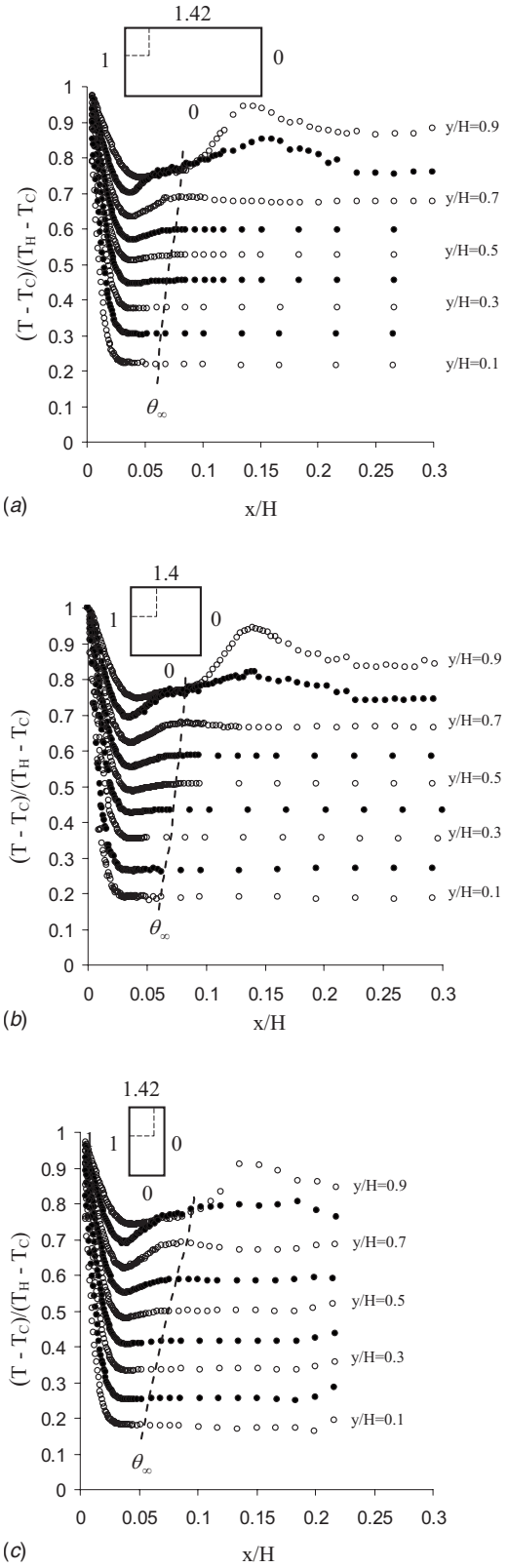

Fig. 5 Nondimensional temperature profiles in cavities with aspect ratios of (*a*) 0.5, (*b*) 1.0, and (*c*) 2.0 for nondimensional top wall temperatures of approximately 1.42. Here, the open and filled symbols were used to distinguish the temperature distributions at the different heights.

Table 1 Summary of the wall temperatures, Grashof numbers, and parameters in the correlation $Nu = C \cdot Ra^n$ for cases studied here

AR	Case	T_H (°C)	T_C (°C)	T_T (°C)	T_B (°C)	θ_H	θ_C	θ_T	θ_B	$Gr \times 10^{-8}$	n	C
0.5	1	81	15	109	15	1	0	1.42	0	1.82	0.36	0.089
	2	84	20	93	20	1	0	1.14	0	1.67	0.36	0.085
	3	81	16	81	16	1	0	1	0	1.78	0.36	0.082
	4	81	16	70	16	1	0	0.83	0	1.78	0.36	0.08
	5	81	14	49 (insulated)	14	1	0	0.52	0	1.86	0.36	0.071
1.0	1	82	14	109	14	1	0	1.4	0	1.87	0.32	0.19
	2	80	13	89	13	1	0	1.13	0	1.88	0.32	0.185
	3	80	13	79	13	1	0	0.99	0	1.88	0.32	0.165
	4	83	13	71	12	1	0	0.83	0	1.93	0.32	0.16
	5	83	16	52 (insulated)	16	1	0	0.54	0	1.81	0.32	0.15
2.0	1	84	17	112	17	1	0	1.42	0	1.78	0.37	0.074
	2	84	16	94	16	1	0	1.15	0	1.82	0.37	0.074
	3	83	17	83	17	1	0	1	0	1.77	0.37	0.076
	4	87	19	75	19	1	0	0.82	0	1.75	0.37	0.074
	5	90	21	57 (insulated)	21	1	0	0.52	0	1.71	0.37	0.072

tures so that the average wall temperatures reported here can be calculated.

The temperature distribution of the air in the cavity was measured using a 0.051 mm (0.002 in.) diameter T-type thermocouple mounted between two 1.5 mm diameter tubes that were 57 mm long and 29 mm apart. The thermocouple probe unit was mounted on a two-dimensional traverse that could be moved in both the horizontal and vertical directions. The position of the thermocouple relative to the walls was determined using positioning rods installed in the probe holder that closed an electrical circuit when they touched the wall. The first measurement location was 0.7 mm from the heated vertical wall. Due to the relatively large change in temperature of the air near the heated vertical wall, the temperature measurements were made at 0.25 mm intervals for the first 7.2 mm from the wall. The distance between consecutive measurement locations was subsequently increased from 0.5 mm to 30 mm as the distance from the wall was increased. For the step size of 0.25 mm, the accuracy of the location of the probe is approximately 0.02–0.03 mm. The uncertainty of the temperature measured by the thermocouple probe is $\pm 1\,^{\circ}C$ resulting in an uncertainty in the temperature gradient of approximately $\pm 5\%$.

In each experiment, the desired wall temperatures were reached by adjusting the power to the heaters and the cooling water flow rates. Measurements were started after the wall temperatures fluctuated less than $\pm 0.5\,^{\circ}C$ for over 1 h. The temperature distributions near the heated vertical wall for the different aspect ratios were measured at nine heights that were 25 mm (1 in.) apart. The instantaneous temperature measurements from the thermocouple probes were averaged for 20 s at each measurement location. The local heat flux from the heated vertical wall into the rectangular cavity was estimated from the slope of the temperature profile in the near-wall region of the boundary layer as described by Wu et al. [11], where conduction is the dominant mode of heat transfer. In all cases, at least seven measurement points existed in this region, as shown in Fig. 3. The accuracy of the local heat flux computed from the temperature profiles were checked by applying an energy balance for the heated vertical wall following the procedure presented in Ref. [20]. This was done only in the central area of the heated vertical wall since it was difficult to estimate the heat losses at the edges of the wall. The energy input was estimated from the heater input parameters, while the energy output was calculated by integrating the heat convected to the upward boundary layer over this area. The conduction heat transfer from the adjacent areas including the guard wall was considered in the energy balance as well. The discrepancy in the energy balance was within 15–25% in this central area. An energy balance was also performed for the entire system [20] and was found to be within 5–15% for all cases. The uncertainty in the temperatures measured by the T-type thermocouple probe was $\pm 1\,^{\circ}C$ so that the uncertainty in the local heat flux was 3–5% and the uncertainty in the local Nusselt number obtained here was estimated to be 5–8% using the approach outlined by Coleman and Steele [21].

The flow in the upper corner of the cavity was visualized using incense smoke that was illuminated by a laser light sheet. The smoke was generated by slowly moving air over burning incense. The smoke was cooled to approximately room temperature before it was injected into the cavity through one of the two slots machined in the bottom wall of the cavity for the traverse. Care was taken to ensure the injection of the smoke was slow enough to allow it to follow the flow streamlines in the cavity. The flow images were recorded using a digital camera positioned outside the window of the sidewall of the cavity. The resolution of these pictures is 2592×1944 pixels that covered an area of 595 cm^2 with an exposure time of 1 s.

3 Results and Discussion

The effect of the top wall temperature on the laminar natural convection flow in the three cavities was initially investigated by maintaining the vertical walls at approximately $82\,^{\circ}C$ and $15\,^{\circ}C$, respectively, so the global Grashof number based on the height of the cavities was approximately 1.8×10^8. The bottom wall temperature for all three cases was maintained at approximately $15\,^{\circ}C$, and the top wall was heated up to about $110\,^{\circ}C$, corresponding to a nondimensional temperature of approximately 1.42. The flow patterns in the upper section for the three cavities at a nondimensional top wall temperature of about 1.4 are shown in Fig. 4. In this case, the natural convection boundary layer along the heated vertical wall separated before reaching the top wall for all three cavities. This results in a secondary flow between the separated flow and the boundary layer on the heated vertical wall, similar to that of Wu et al. [12]. The natural convection flow reattached to the top wall after turning over and undulating in the vertical direction. The location and size of the undulating flow region is approximately the same for the three cavities. The present results also show that the distance from the top wall to the location where the upward flow along the heated vertical wall turned over decreased slightly as the aspect ratio (AR) was increased from 0.5 to 2.0.

The nondimensional temperature profiles along the heated vertical wall in the three cavities are shown in Fig. 5. There is a thin thermal boundary layer along the heated vertical wall and the temperature in the region far from the heated vertical wall increases with height so most of the air in the cavity was stably

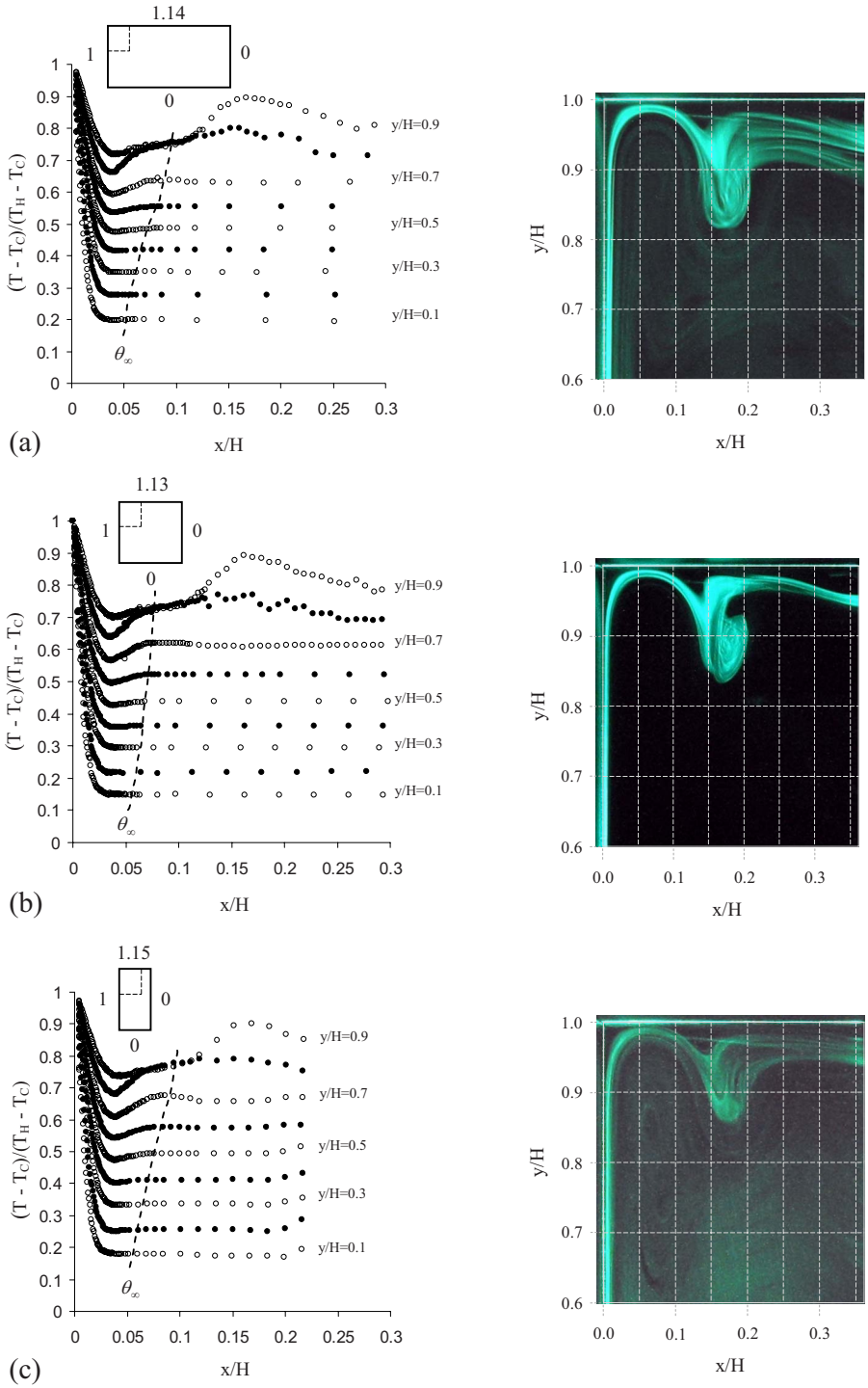

Fig. 6 Nondimensional temperature profiles in cavities (left) and flow patterns in the upper corner region (right) for cases with aspect ratios of (*a*) 0.5, (*b*) 1.0, and (*c*) 2.0 for nondimensional top wall temperatures of approximately 1.14. Here, open and filled symbols were used to distinguish the temperature distributions at the different heights.

stratified. The temperature of the air outside the boundary layer near the top wall was not uniform and corresponds to the region where the undulation in the flow was observed (Fig. 4).

Additional experiments were performed for nondimensional top wall temperatures from around 1.14 to 0.52 (insulated), while maintaining the nondimensional temperatures of the vertical walls and the bottom wall so that the global Grashof numbers in these cases were approximately the same as before, indicating that the thermal boundary conditions of the vertical walls in the different cases were approximately the same. The experimental conditions are summarized in Table 1, and the temperature profiles along the heated vertical wall with the corresponding flow images in the top corner are presented in Fig. 6–9. When the nondimensional top wall temperature was decreased to 1.14 (Fig. 6), the natural convection flow moved a short distance along the top wall before separating from the top wall. As the top wall temperature was further decreased, the separation occurred further away from the heated vertical wall, and no separation was observed for the case

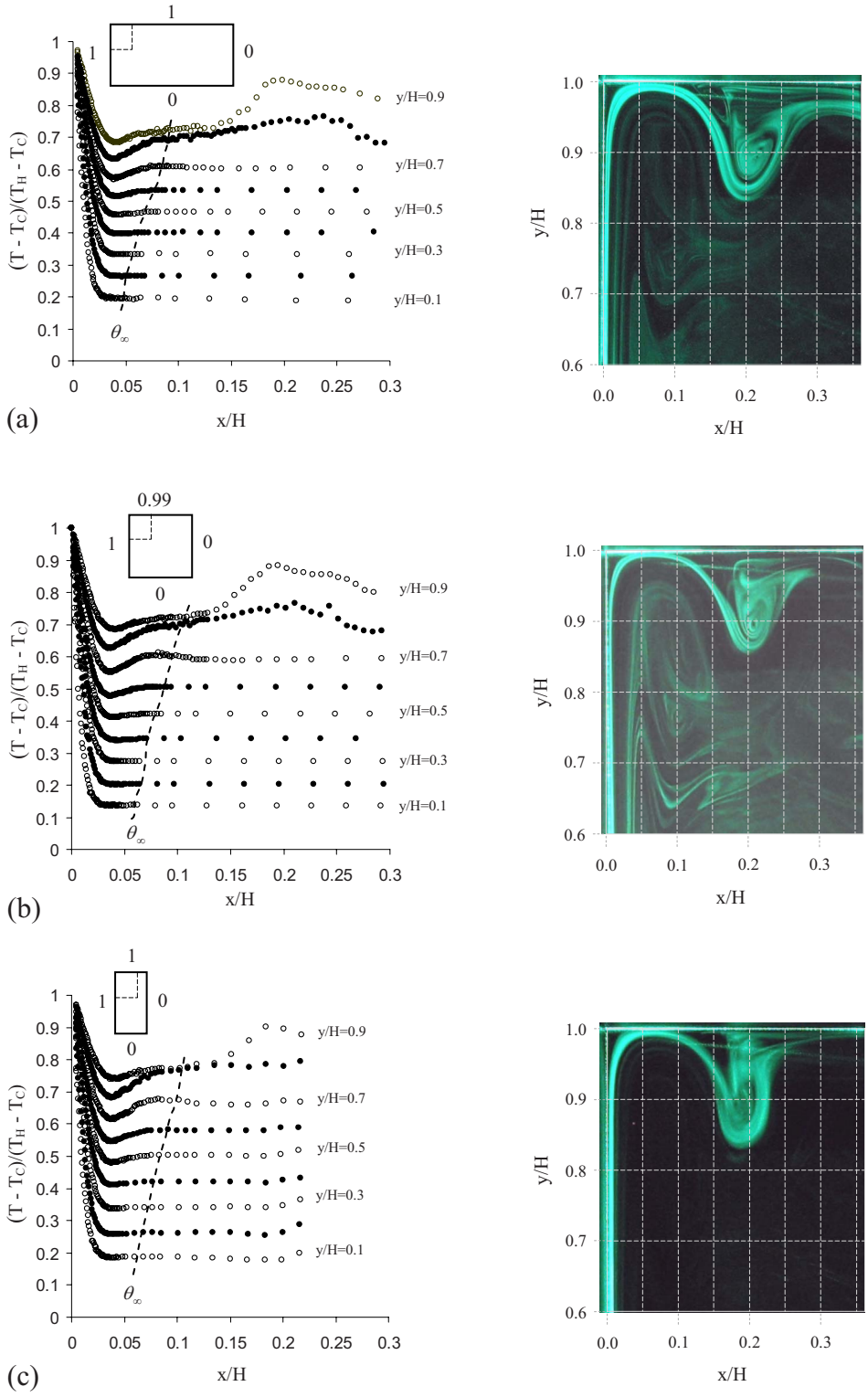

Fig. 7 Nondimensional temperature profiles in cavities (left) and flow patterns in the upper corner region (right) for cases with aspect ratios of (*a*) 0.5, (*b*) 1.0, and (*c*) 2.0 for nondimensional top wall temperatures of approximately 1. Here, open and filled symbols were used to distinguish the temperature distributions at the different heights.

when the nondimensional top wall temperature was around 0.52 (Fig. 9). For a given top wall temperature, the location of the undulation in the flow was approximately the same for all three cavities. The regions where the temperature is nonuniform closely corresponds to the regions of the flow undulation. This strongly suggests that the temperature nonuniformity is a direct result of the flow field.

At a given height, the nondimensional temperature distribution

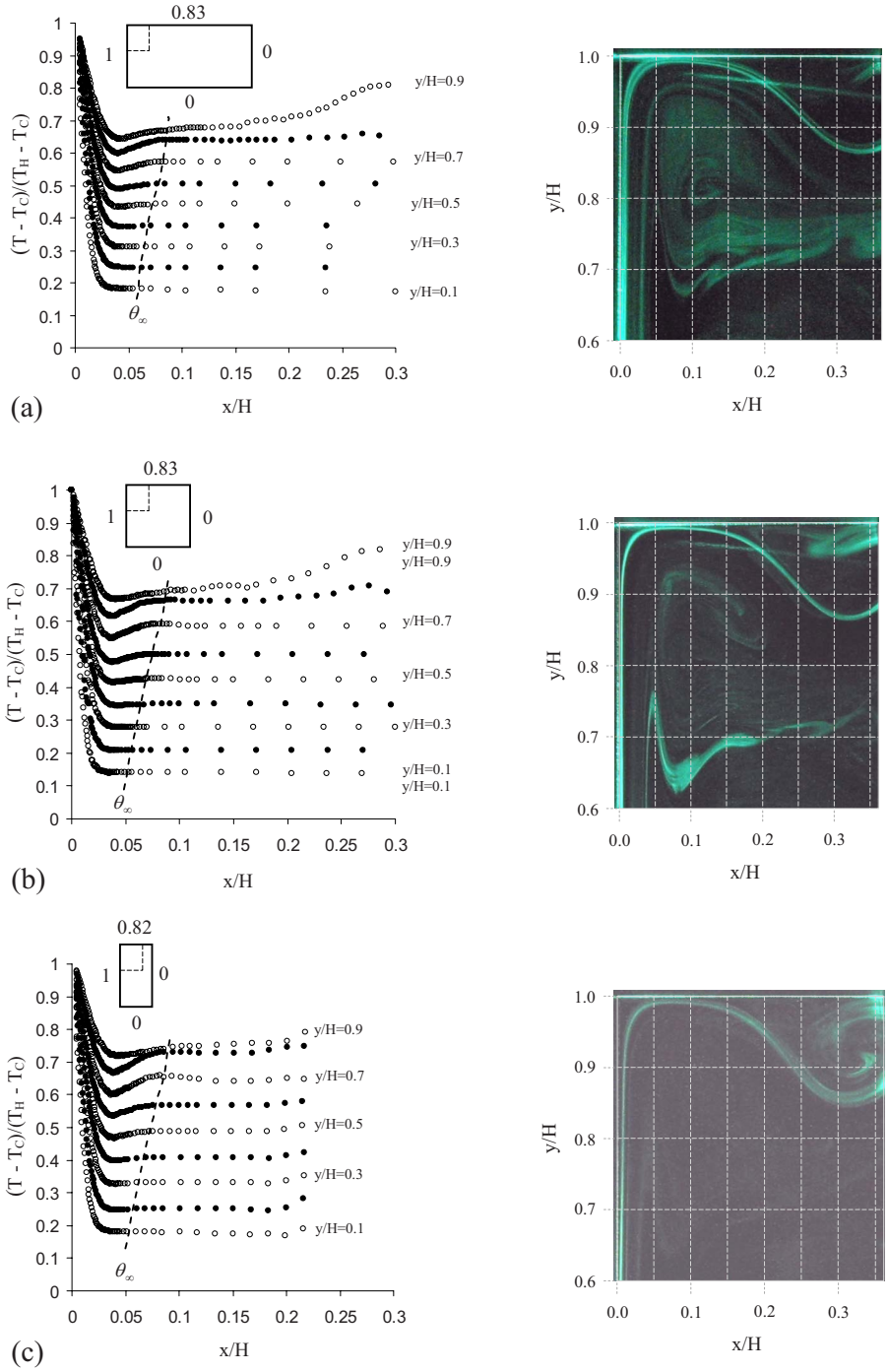

Fig. 8 Nondimensional temperature profiles in cavities (left) and flow patterns in the upper corner region (right) for cases with aspect ratios of (*a*) 0.5, (*b*) 1.0, and (*c*) 2.0 for nondimensional top wall temperatures of approximately 0.83. Here, open and filled symbols were used to distinguish the temperature distributions at the different heights.

outside the boundary layer generally increased with an increase in the aspect ratio, particularly in the region $y/H > 0.5$. For the case where the top wall was insulated, the temperature of the convection flow moving along the top wall was larger than the top wall temperature, so the heat flux was into the top wall from the flow. With an increase in the aspect ratio, the area of the top wall becomes smaller, resulting in less heat transfer into the wall. Thus, for a given height, the temperature distributions in the core region of the cavity were larger for the larger aspect ratio cavity compared with the smaller aspect ratio cavity.

Variation in the nondimensional temperature just outside the boundary layer with height for the different top wall temperatures are shown in Fig. 10. Following the definition of Wu et al. [11], the temperature just beyond the undershoot in the temperature profiles shown in Figs. 5–9 was used as a measure of the local ambient temperature outside the boundary layer, shown as a dashed line in these figures. In all three cavities, the temperature outside the boundary layer increased approximately linearly with the height over the most of the cavity. For $y/H > 0.8$, there is no significant change in the temperature outside the boundary layer.

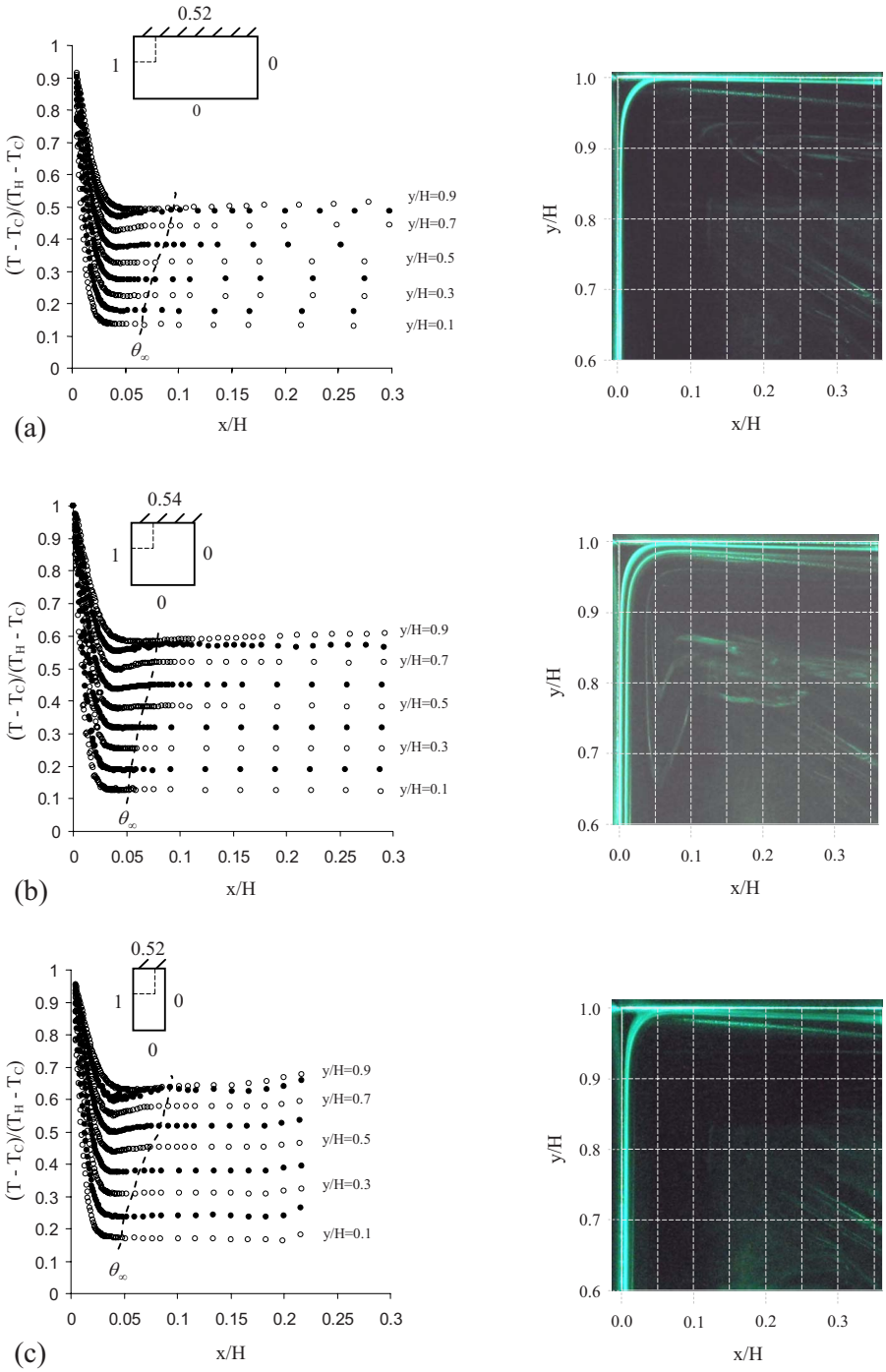

Fig. 9 Nondimensional temperature profiles in cavities (left) and flow patterns in the upper corner region (right) for cases with aspect ratios of (*a*) 0.5, (*b*) 1.0, and (*c*) 2.0 for nondimensional top wall temperatures of approximately 0.52 (insulated). Here, open and filled symbols were used to distinguish the temperature distributions at the different heights.

This is likely due to the mixing caused by the secondary flow in the region between the upward flow along the heated vertical wall and the undulating flow, as shown in the flow visualizations. With an increase in the top wall temperature, the local temperature outside the boundary layer increased as expected.

The change in the temperature gradient $d\theta_\infty/d(y/H)$, from a linear fit to the data between $y/H=0.1$ and 0.7, with the change in the top wall temperature, is shown in Fig. 11. For all three cavities, the temperature gradient increased linearly with an increase in the top wall temperature. The exception was for the case with the insulated top wall since the flow pattern in this case was different from the other cases, with no flow separation from the top wall. The increase in the temperature gradient $d\theta_\infty/d(y/H)$ was more significant for the smaller aspect ratio. This difference may be due to the change in the ratio of the size of the undulating flow region to the cavity width for the different aspect ratios. For the 0.5 aspect ratio cavity, this ratio is approximately 0.1, so the local ambient temperature outside the boundary layer is significantly affected by the convection flow moving along the top wall, which is sensitive to the change in the top wall temperature. However,

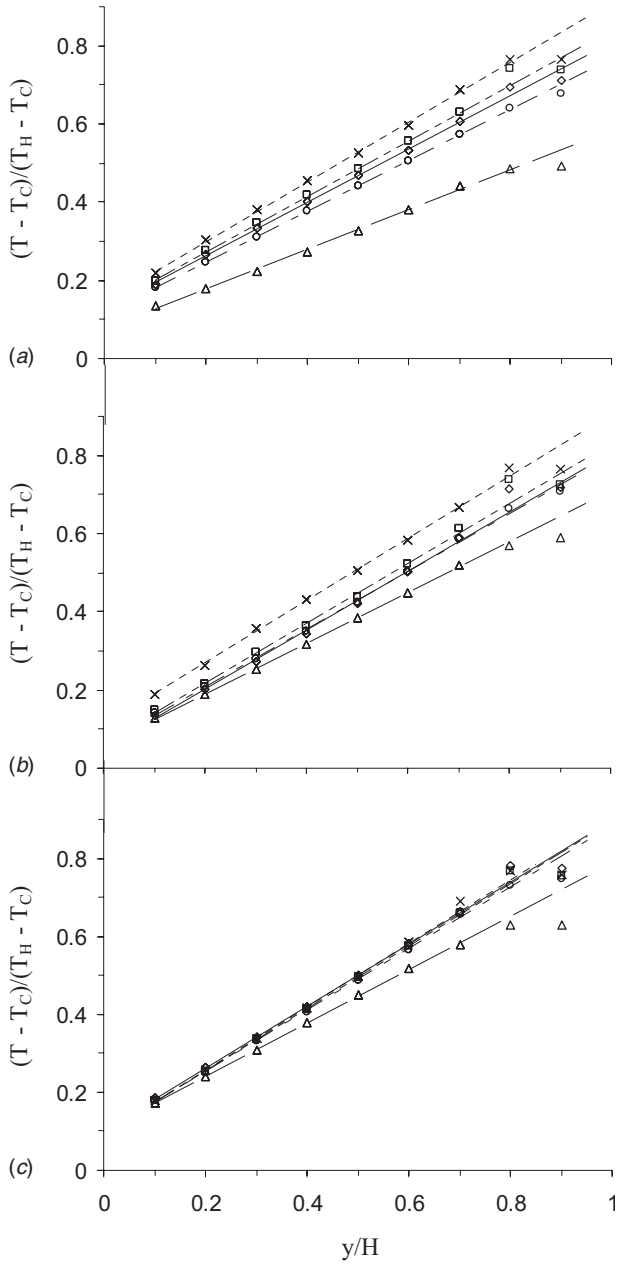

Fig. 10 Comparison of the nondimensional temperature outside of the boundary layer for cases with aspect ratios of (*a*) 0.5, (*b*) 1.0, and (*c*) 2.0. Here the nondimensional bop wall temperatures were (△) 0.52 (insulated), (◯) 0.83, (◇) 1, (□) 1.14, and (×) 1.42.

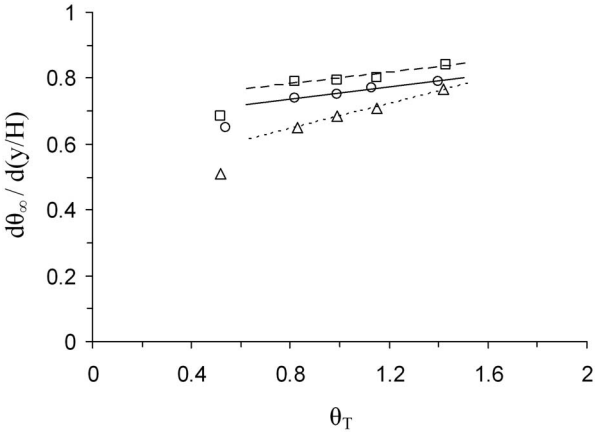

Fig. 11 Change in the vertical gradient of the temperature outside the boundary layer on the heated vertical wall with the change in the top wall temperature for cases with aspect ratios of (△) 0.5, (◯) 1.0, and (□) 2.0

for the higher aspect ratio cavity, the ratio of the size of the undulated flow region to the cavity width increased to around 0.4. In this case, the local ambient temperature outside the boundary layer is, to a large extent, determined by the temperature of the undulating flow, which is more sensitive to the heated vertical wall temperature than the top wall temperature.

The local heat flux from the heated vertical wall, q'' (determined from the temperature profiles) for the three cavities under the different top wall temperatures is shown in Fig. 12. As expected, the local heat flux into the cavity from the heated vertical wall decreased as the flow developed along the wall. The change in the top wall temperature had an obvious effect on the local heat transfer near the top of the heated vertical wall. As the nondimensional top wall temperature was increased, the local heat flux near the top of the heated vertical wall decreased due to the change in the flow pattern in this region. The change in the local heat flux with the top wall temperature was dependant on the aspect ratio. For example, when the nondimensional top wall temperature was increased from 0.83 to 1.42, the local heat flux near the top of the heated vertical wall decreased by approximately 36% in the 0.5 aspect ratio cavity, while it decreased by approximately 18% in the 2.0 aspect ratio cavity. This can be attributed to the effect of the undulating flow on the local ambient temperatures outside the boundary layer, which increased with an increase in the aspect ratio.

The change in the local Nusselt number with the local Rayleigh number for the three cavities is shown in Fig. 13. The local Rayleigh numbers along the heated vertical walls of the cavities for nondimensional heights from $y/H=0.1$ to 0.9 varied from 8.6×10^4 to 3.8×10^7. These are well below the critical value for transition from laminar to turbulent flow, suggesting that the flow is laminar. This was supported by flow visualizations, which clearly showed a laminar boundary layer along the heated vertical wall. It was found that the data over most of the heated vertical wall could be correlated by $\mathrm{Nu}=C\cdot\mathrm{Ra}^n$, except for $y/H\geq0.8$ due to the secondary flow in this region and $y/H\leq0.1$. The values of the constant C and the index n were different for the different aspect ratios and are given in Table 1. For the cavities with aspect ratios of 0.5 and 1.0, the value of C increased with an increase in the top wall temperature, while there was no significant change in C with the top wall temperature for the 2.0 aspect ratio cavity.

The local Nusselt numbers are plotted against the local Rayleigh numbers along the heated vertical wall from $y/H=0.2$ to 0.7 for all cases in Fig. 14. The data were correlated by

$$\mathrm{Nu}=0.0951\cdot\mathrm{Ra}^{0.3545} \tag{1}$$

with a coefficient of determination of 0.91 for the local Rayleigh number in the range $6\times10^5-2\times10^7$.

4 Conclusions

An experimental investigation was performed to characterize the effect of the top wall temperature on the laminar natural convection flow in air-filled rectangular cavities with aspect ratios of 0.5, 1.0, and 2.0. The natural convection flow in these cavities was driven by a temperature difference between the vertical walls. The experiments were performed for a global Grashof number based on the height of the cavities of approximately 1.8×10^8, and nondimensional top wall temperatures in the range 0.52–1.42. Flow visualizations and temperature measurements showed that the flow pattern and temperature profiles near the top wall were significantly changed as the top wall of the cavity was heated. As the

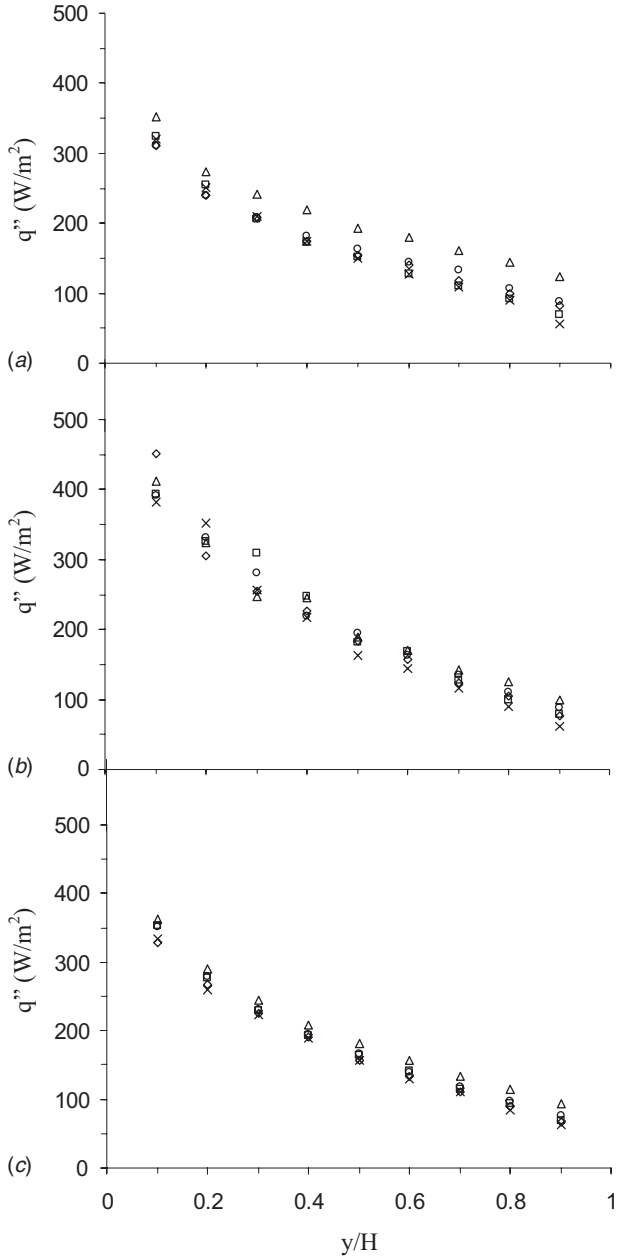

Fig. 12 Comparison of the local heat flux along the heated vertical wall of cavities with aspect ratios of (*a*) 0.5, (*b*) 1.0, and (*c*) 2.0. The symbols are the same as in Fig. 10.

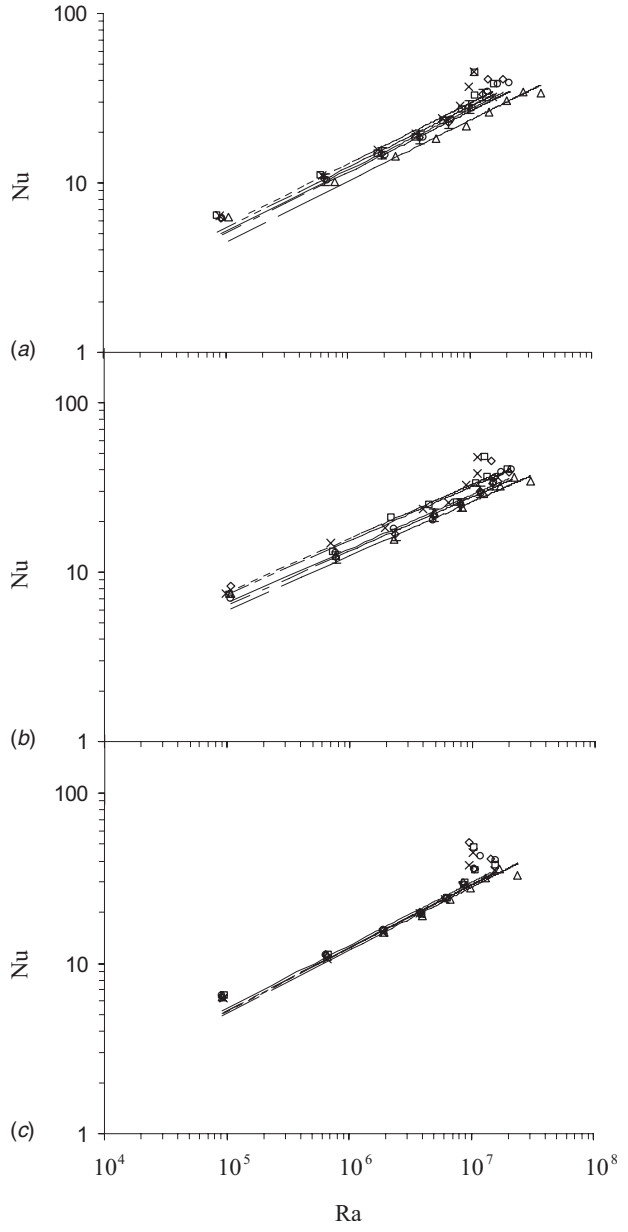

Fig. 13 Change in the local Nusselt number with the local Rayleigh number for cases with aspect ratios of (*a*) 0.5, (*b*) 1.0, and (*c*) 2.0. The symbols are the same as in Fig. 10. Here error bars with ±8% were added to the data in the cases with nondimensional top wall temperature of approximately 1.

top wall was heated, the natural convection boundary layer along the heated wall separated before reaching the top wall. This results in an undulating flow region in the left upper corner of the cavity causing a nonuniformity in the temperature profiles in this region. The location of the undulation in the flow changed with the top wall temperature but was nearly independent of the aspect ratio. The ratio of the size of the undulating flow region to the cavity width increased with an increase in the aspect ratio, which resulted in different temperature fields within the cavities. The effect of the top wall temperature on the temperature gradient $d\theta_\infty/d(y/H)$ became larger when the aspect ratio of the cavity was decreased. This results in a more significant decrease in the local heat flux near the top of the heated vertical wall for the smaller aspect ratio cavity with an increase in the top wall temperature. The local Nusselt number was correlated with the local Rayleigh number in the form $\mathrm{Nu}=C\cdot\mathrm{Ra}^n$. However, the values of the constant C and the index n changed with the aspect ratio of the cavity.

Acknowledgment

The support of the Natural Sciences and Engineering Research Council (NSERC) of Canada is gratefully acknowledged.

Nomenclature

- AR = aspect ratio of the cavity, $\mathrm{AR}=H/L$
- C = constant in the Nusselt–Rayleigh number correlation, $\mathrm{Nu}=C\cdot\mathrm{Ra}^n$
- g = gravity constant, $\mathrm{m/s^2}$
- Gr = global Grashof number based on the height of the cavity, $\mathrm{Gr}=(g\beta(T_H-T_C)H^3/\nu^2)$
- h = local heat transfer coefficient, $\mathrm{W/m^2\ ^\circ C}$
- H = height of the cavity, m
- k = thermal conductivity of the air, $\mathrm{W/m\ ^\circ C}$
- L = width of the cavity, m

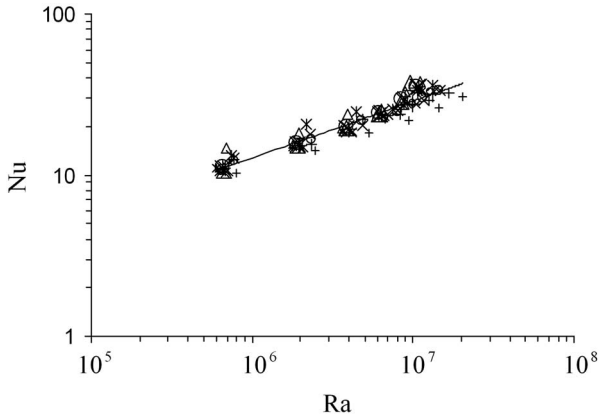

Fig. 14 Change in the local Nusselt number with the local Rayleigh number along the heated vertical wall from $y/H=0.2$ to 0.7 for cases with aspect ratios of 0.5 (small size symbols), 1.0 (midsize symbols), and 2.0 (large size symbols) under the nondimensional top wall temperatures of (+) 0.52 (insulated), (×) 0.83, (◯) 1, (∗) 1.14, and (△) 1.42

n = exponent in the Nusselt Rayleigh number correlation, $\mathrm{Nu}=C\cdot\mathrm{Ra}^n$
Nu = local Nusselt number, $\mathrm{Nu}=(hy/k)$
q'' = local heat flux, $\mathrm{W/m^2}$
Ra = local Rayleigh number, $\mathrm{Ra}=(g\beta(T_H-T_\infty)y^3/\alpha\nu)$
T_B = average temperature of the bottom wall in the cavity, °C
T_C = average temperature of the cooled vertical wall in the cavity, °C
T_H = average temperature of the heated vertical wall in the cavity, °C
T_T = average temperature of the top wall in the cavity, °C
T_∞ = local ambient temperature outside of the boundary layer, °C
X = distance from the heated vertical wall, m
Y = height above the bottom wall, m

Greek Symbols

α = thermal diffusivity, $\mathrm{m^2/s}$
β = volume expansion coefficient at constant pressure, $\mathrm{K^{-1}}$
ν = kinematic viscosity, $\mathrm{m^2/s}$
ρ_∞ = density of the ambient air, $\mathrm{kg/m^3}$
θ_B = nondimensional temperature of the bottom wall in the cavity, $\theta_B=(T_B-T_C)/(T_H-T_C)$
θ_C = nondimensional temperature of the cooled vertical wall in the cavity, $\theta_C=(T_C-T_C)/(T_H-T_C)$
θ_H = nondimensional temperature of the heated vertical wall in the cavity, $\theta_H=(T_H-T_C)/(T_H-T_C)$
θ_T = nondimensional temperature of the top wall temperature in the cavity, $\theta_T=(T_T-T_C)/(T_H-T_C)$
θ_∞ = nondimensional local ambient temperature outside the boundary layer, $\theta_\infty=(T_\infty-T_C)/(T_H-T_C)$
$(d\theta_\infty/d(y/H))$ = vertical gradient of the nondimensional temperature outside the boundary layer on the heated vertical wall

Subscripts

B = bottom wall of the cavity
C = cooled vertical wall of the cavity
H = heated vertical wall of the cavity
T = top wall of the cavity

References

[1] Eckert, E. R. G., and Carlson, W. O., 1961, "Natural Convection in an Air Layer Enclosed Between Two Vertical Plates With Different Temperatures," Int. J. Heat Mass Transfer, **2**, pp. 106–120.
[2] Yin, S. H., Wung, T. Y., and Chen, K., 1978, "Natural Convection in an Air Layer Enclosed Within Rectangular Cavities," Int. J. Heat Mass Transfer, **21**, pp. 307–315.
[3] Tian, Y. S., and Karayiannis, T. G., 2000, "Low Turbulence Natural Convection in an Air Filled Square Cavity, Part I: The Thermal and Fluid Flow Fields," Int. J. Heat Mass Transfer, **43**, pp. 849–866.
[4] Seki, N., Fukusako, S., and Inaba, H., 1978, "Visual Observation of Natural Convection Flow in a Narrow Vertical Cavity," J. Fluid Mech., **84**, pp. 695–704.
[5] Cormack, D. E., Leal, L. G., and Seinfeld, J. H., 1974, "Natural Convection in a Shallow Cavity With Differentially Heated End Walls: Part II. Numerical Solutions," J. Fluid Mech., **65**, pp. 231–246.
[6] Newell, M. E., and Schmidt, F. W., 1970, "Heat Transfer By Laminar Natural Convection Within Rectangular Enclosures," ASME J. Heat Transfer, **92**, pp. 159–168.
[7] Ostrach, S., 1988, "Natural Convection in Enclosures," ASME J. Heat Transfer, **110**, pp. 1175–1190.
[8] Ostrach, S., and Raghavan, C., 1979, "Effect of Stabilizing Thermal Gradients on Natural Convection in Rectangular Enclosures," ASME J. Heat Transfer, **101**, pp. 238–243.
[9] Shiralkar, G. S., and Tien, C. L., 1982, "A Numerical Study of the Effect of a Vertical Temperature Difference Imposed on a Horizontal Enclosure," Numer. Heat Transfer, **5**, pp. 185–197.
[10] Ravi, M. R., Henkes, R. A. W. M., and Hoogendoorn, C. J., 1994, "On The High-Rayleigh-Number Structure of Steady Laminar Natural-Convection Flow in a Square Enclosure," J. Fluid Mech., **262**, pp. 325–351.
[11] Wu, W., Ewing, D., and Ching, C. Y., 2006, "The Effect of the Top and Bottom Wall Temperatures on the Laminar Natural Convection in an Air-Filled Square Cavity," Int. J. Heat Mass Transfer, **49**, pp. 1999–2008.
[12] Wu, W., Ewing, D., and Ching, C. Y., 2008, "Investigation of a Large Top Wall Temperature on the Natural Convection Plume Along a Heated Vertical Wall in a Square Cavity," Int. J. Heat Mass Transfer, **51**, pp. 1551–1561.
[13] Emery, A., and Chu, N. C., 1965, "Heat Transfer Across Vertical Layers," ASME J. Heat Transfer, **87**, pp. 110–114.
[14] MacGregor, R. K., and Emery, A. F., 1969, "Free Convection Through Vertical Plane Layers—Moderate and High Prandtl Number Fluids," ASME J. Heat Transfer, **91**, pp. 391–403.
[15] Elder, J. W., 1965, "Laminar Free Convection in a Vertical Slot," J. Fluid Mech., **23**, pp. 77–98.
[16] Wakitani, S., 1998, "Flow Patterns of Natural Convection in an Air-Filled Vertical Cavity," Phys. Fluids, **10**, pp. 1924–1928.
[17] Lartigue, B., Lorente, S., and Bourret, B., 2000, "Multicellular Natural Convection in a High Aspect Ratio Cavity: Experimental and Numerical Results," Int. J. Heat Mass Transfer, **43**, pp. 3157–3170.
[18] Drummond, J., and Korpela, S. A., 1987, "Natural Convection in a Shallow Cavity," J. Fluid Mech., **182**, pp. 543–564.
[19] Nansteel, M. W., Sadhal, S. S., and Ayyaswamy, P. S., 1986, "Discontinuous Boundary Temperatures in Heat Transfer Theory," HTD (Am. Soc. Mech. Eng.), **60**, pp. 123–126.
[20] Wu, W., 2004, "The Effect of Stable Stratification on the Natural Convection in a Square Cavity Caused By a Horizontal Temperature Difference," M.S. thesis, McMaster University, Hamilton, ON, Canada.
[21] Coleman, H. W., and Steele, W. G., 1999, *Experimentation and Uncertainty Analysis for Engineers*, 2nd ed., Wiley, New York.

Transient Double-Diffusive Convection of Water Around 4 °C in a Porous Cavity

M. Eswaramurthi

P. Kandaswamy
e-mail: pgkswamy@yahoo.co.in

UGC DRS Centre for Fluid Dynamics,
Bharathiar University,
Coimbatore-641 046, India

The buoyancy-driven transient double-diffusive convection in a square cavity filled with water-saturated porous medium is studied numerically. While the right and left side wall temperatures vary linearly from θ_a to θ_o and θ_o to θ_b, respectively, with height, the top and bottom walls of the cavity are thermally insulated. The species concentration levels at the right and left walls are c_1 and c_2, respectively, with $c_1 > c_2$. The Brinkman–Forchheimer extended Darcy model is considered to investigate the average heat and mass transfer rates and to study the effects of maximum density, the Grashof number, the Schmidt number, porosity, and the Darcy number on buoyancy-induced flow and heat transfer. The finite volume method with power law scheme for convection and diffusion terms is used to discretize the governing equations for momentum, energy, and concentration, which are solved by Gauss–Seidel and successive over-relaxation methods. The heat and mass transfer in the steady-state are discussed for various physical conditions. For the first time in the literature, the study of transition from stationary to steady-state shows the existence of an overshooting between the two cells and in the average Nusselt number. The results obtained in the steady-state regime are presented in the form of streamlines, isotherms, and isoconcentration lines for various values of Grashof number, Schmidt number, porosity and Darcy number, and midheight velocity profiles. It is found that the effect of maximum density is to slow down the natural convection and reduce the average heat transfer and species diffusion. The strength of convection and heat transfer rate becomes weak due to more flow restriction in the porous medium for small porosity. [DOI: 10.1115/1.3000608]

Keywords: double-diffusive convection, maximum density, porosity

1 Introduction

Double-diffusive natural convection exists in fluids containing two different constituents, which influence its buoyancy. The buoyancy forces are induced by combined temperature and concentration gradients, and the convective flow occurs in the fluid contained in enclosures with nonvanishing thermal/concentration gradients. The problem of double-diffusive natural convection through porous media is encountered in different natural and engineering applications such as oil recovery, underground water flow, high-performance insulation for building and cryogenic containers particularly in the field of large storage system of agricultural products, the migration of moisture through air contained in fibrous insulations and the dispersion of chemical contaminants through water saturated soil, oceanography, and solar energy system. Furthermore, in many applications such as bioengineering and chemical engineering, it is important to observe the evolution of the fluid motion and subsequent heat and mass transfer with time. The buoyancy-driven double-diffusive convection arises in a fluid due to the density variations caused by the temperature differences and concentration variations in the system.

Several studies on double-diffusive natural convection of water in porous media have been reported for different physical formulations and geometric models with various boundary conditions. The model commonly used consists of a porous cavity with either both the vertical walls maintained at constant temperature or one vertical wall subject to a constant heat flux and the other isothermal, while the horizontal walls are adiabatic. A linear temperature-density relationship has been considered. The density of water varies nonlinearly with temperature, having its maximum around 4 °C.

The present study aims at throwing light on the effect of the maximum density of water and varied parameters of the porous medium on transient heat and mass transfer in a square porous cavity with linearly varying side wall temperatures. The flow associated with the mechanism of double-diffusive buoyancy-driven convection has been extensively studied by many authors. A few closely related studies—needed to follow the present work—are reviewed in this section.

Han and Kuehn [1] studied numerically double-diffusive natural convection flow in a vertical rectangular cavity. They found that double-diffusive multicellular flow structures observed in experiments are successfully simulated in numerical study. Steady-state thermosolutal convection in a square cavity filled with air, subjected to horizontal temperature and concentration gradients, was studied numerically by Beghein et al. [2]. They have shown that the concentration boundary layer is thick and hence the cavity is filled with a high diffusion pollutant for the Lewis number less than unity. Nithiarasu et al. [3] investigated double-diffusive natural convection in a fluid saturated porous cavity with a freely convecting wall and showed that the flow, heat, and mass transfer become sensitive to applied mass transfer coefficient in both the Darcy and non-Darcy flow regimes.

Kandaswamy and Kumar [4] studied numerically the effect of a magnetic field on the buoyancy-driven flow of water inside a square cavity with differentially heated side walls. Their study reveals that the average heat transfer rate decreases with an increase in the Hartmann number. Sundaravadivelu and Kandaswamy [5] used a fourth order polynomial approximation for the temperature-density relation to study double-diffusive nonlinear convection in a square cavity. They found that the average

Contributed by the Heat Transfer Division of ASME for publication in the JOURNAL OF HEAT TRANSFER. Manuscript received November 6, 2007; final manuscript received September 13, 2008; published online March 17, 2009. Review conducted by Cholik Chan.

heat and mass transfer rates depend nonlinearly on the temperature gradient in the cavity. Khanafer and Vafai [6] through an investigation on double-diffusive mixed convection in a lid-driven enclosure filled with a fluid saturated porous medium showed that the buoyancy ratio, Darcy number, Lewis number, and Richardson number have profound effects on the double-diffusive phenomenon.

Saeid and Pop [7] conducted a numerical study on the effects of maximum density on natural convection from a discrete heater in a cavity filled with porous medium. They have demonstrated the existence of buoyancy force reversal resulting from the maximum density effect leading to a reduction in the convective flow and average heat transfer rate. Very few studies using extended Darcy models are reported on double-diffusive convection. Those relevant to the present study are reviewed below. Sezai and Mohamad [8] used a three-dimensional mathematical model based on the Brinkman extended Darcy equation to study double-diffusive natural convection in a fluid saturated porous cubic enclosure subject to opposing and horizontal gradients of temperature and concentration. Sezai and Mohamad [9] performed a three-dimensional numerical study on double-diffusive natural convection in a cubic enclosure subject to opposing and horizontal gradients of heat and solute. Both of these studies reported that the double-diffusive flow in enclosures with opposing buoyancy forces is three-dimensional for a certain range of parameters.

Mohamad et al. [10] numerically investigated the three-dimensional double-diffusive natural convection in a rectangular enclosure filled with binary fluid saturating porous media. The study indicated that two-dimensional double-diffusion results should be treated carefully because the three dimensionality of the problem may affect the flow pattern and the rate of heat and mass transfer. Mohamad and Bennacer [11] investigated double-diffusive natural convection in an enclosure filled with saturated porous medium and subjected to cross gradients. Vafai [12] gave deep insight into convective heat transfer in porous media. Nield and Bejan [13] provided a comprehensive literature survey on natural convection in porous media.

The limitations of most of the existing studies in a porous cavity are (i) using linear density-temperature relation and (ii) uniform heating of vertical side walls of the cavity. The most industrial and natural flows through porous structures cannot be truly represented by a Darcy model. Density-temperature relation is not a linear function for natural fluids (water) and industrial fluids (glycerin-water mixture). Hence in this study, the Brinkman–Forchheimer extended Darcy model is used to investigate the effects of maximum density, the Grashof number, the Schmidt number, the Darcy number, and porosity on heat and mass transfer rates inside a square cavity filled with water saturated porous medium. A fourth order polynomial approximation of the temperature-density relation for water is considered. Furthermore, the wall temperatures are allowed to vary linearly with height.

2 Mathematical Formulation and Method of Solution

A two-dimensional square cavity of side L with water saturated porous medium is considered. The right wall temperature (θ_R) varies linearly from $\theta_a(=0\,^\circ\mathrm{C})$ at the bottom to $\theta_o=(\theta_a+\theta_b)/2$ at the top. The left wall temperature (θ_L) varies linearly from θ_o at the bottom to θ_b at the top such that $\theta_b>\theta_a$ with horizontal adiabatic walls. The concentration levels at the right and left walls are c_1 and c_2, respectively, with $c_1>c_2$. The gravity acts in the downward direction. The velocity components u and v are taken in the x and y directions, respectively. The isotropic homogeneous porous medium is in thermodynamic equilibrium with water having density $\rho=\rho_o[1-\Sigma_{i=1}^{4}(-1)^i\beta_i(\theta-\theta_a)^i+\beta_5(c-c_0)]$ (see Refs. [4,5])

The governing equations for the system in the left-hand coordinate system with the x-axis in the opposite direction of the gravity vector and y-axis in the horizontal with u and v as velocity components (see Ref. [6]) in the vorticity-stream function formulation takes the form

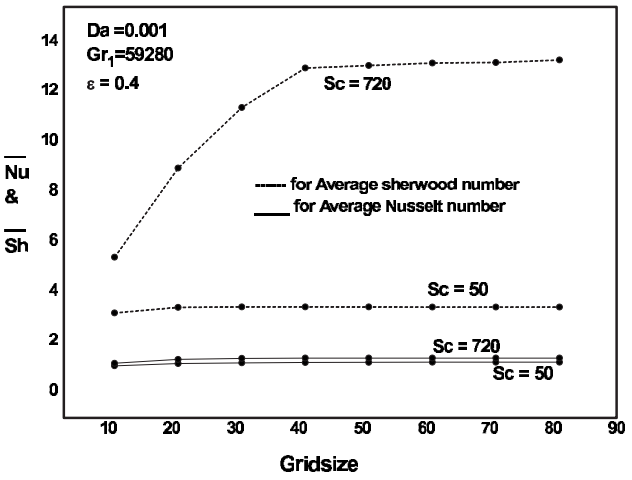

Fig. 1 Average Nusselt number and Sherwood number for different grid systems with $Gr_1=59{,}280$, $Da=0.001$, $\epsilon=0.4$, $Sc=50$, and $Sc=720$ in the steady-state regime

$$\frac{1}{\epsilon}\frac{\partial\zeta}{\partial\tau}+\frac{1}{\epsilon^2}\left[\frac{\partial\Psi}{\partial Y}\frac{\partial\zeta}{\partial X}-\frac{\partial\Psi}{\partial X}\frac{\partial\zeta}{\partial Y}\right]=\frac{1}{\epsilon}\nabla^2\zeta-\frac{1}{\mathrm{Da}}\zeta-\frac{F_c\zeta}{\sqrt{\mathrm{Da}}}-\frac{F_c}{\sqrt{\mathrm{Da}}|\mathbf{v}|}\left[\frac{\partial\Psi}{\partial Y}\frac{\partial|\mathbf{v}|}{\partial Y}+\frac{\partial\Psi}{\partial X}\frac{\partial|\mathbf{v}|}{\partial X}\right]-\sum_{i=1}^{4}i(-1)^i\mathrm{Gr}_iT^{(i-1)}\frac{\partial T}{\partial Y}-\mathrm{Gr}_5\frac{\partial C}{\partial Y} \tag{1}$$

$$\nabla^2\Psi=-\zeta \tag{2}$$

$$U=\frac{\partial\Psi}{\partial Y},\quad V=-\frac{\partial\Psi}{\partial X},\quad \zeta=\frac{\partial V}{\partial X}-\frac{\partial U}{\partial Y} \tag{3}$$

$$\sigma\frac{\partial T}{\partial\tau}+\frac{\partial\Psi}{\partial Y}\frac{\partial T}{\partial X}-\frac{\partial\Psi}{\partial X}\frac{\partial T}{\partial Y}=\frac{1}{\mathrm{Pr}}\nabla^2T \tag{4}$$

$$\epsilon\frac{\partial C}{\partial\tau}+\frac{\partial\Psi}{\partial Y}\frac{\partial C}{\partial X}-\frac{\partial\Psi}{\partial X}\frac{\partial C}{\partial Y}=\frac{1}{\mathrm{Sc}}\nabla^2C \tag{5}$$

The initial conditions are when $\tau=0$ and $U=V=\zeta=\Psi=T=C=0$ for all X and Y. The no-slip velocity boundary conditions are used at all four walls of the cavity where ζ is the vorticity, Ψ is the stream function, τ is the nondimensional time, T is the dimensionless temperature, and C is the dimensionless species concentration. The nondimensional parameters that appear in the equations are $\mathrm{Da}=K/L^2$, the Darcy number; $\mathrm{Gr}_i=g\beta_i(\theta_L-\theta_R)^iL^3/\nu^2$, $i=1,2,3,4$, where $\theta_0\le\theta_L\le\theta_b$ and $\theta_a\le\theta_R\le\theta_0$, the thermal Grashof numbers; $\mathrm{Gr}_5=g\beta_5(c_1-c_2)L^3/\nu^2$, the species Grashof number; $\mathrm{Pr}=\nu/\alpha$, the Prandtl number; and $\mathrm{Sc}=\nu/(\epsilon D)$, the Schmidt number. The function of ϵ in $F_c=1.75|\mathbf{V}|/\sqrt{150}\times\epsilon^{3/2}$ is the porous medium inertia coefficient as described by Khanafer and Vafai [6]. The local Nusselt number is defined by $\underline{\mathrm{Nu}}=\partial T/\partial Y|_{Y=0}$ and the average Nusselt Number is given by $\mathrm{Nu}=\int_0^1\mathrm{Nu}\,dX$. The local Sherwood number is defined by $\underline{\mathrm{Sh}}=\partial C/\partial Y|_{Y=1}$ and the average Sherwood number is given by $\overline{\mathrm{Sh}}=\int_0^1\mathrm{Sh}\,dX$. The nondimensional governing equations are discretized by finite volume method of Patankar [14] and are solved iteratively. Figure 1 shows that a 41×41 uniform grid is enough to investigate the problem. The boundary conditions of Rudraiah

Table 1 Comparison of the results of the present work with those of Refs. [4,5]

	$\overline{\text{Nu}}$		
T (K)	Ref. 4	Ref. 5	Present
277	1.1214	1.0804	1.0606
280	1.0484	1.0288	1.0158
281	1.0140	1.0068	1.0049
282	1.0178	1.0169	1.0204
285	1.3318	1.2828	1.2725

et al. [15] for ζ are used. The standard convergence criteria for field variables with 10^{-6} bound is used in this study.

3 Results and Discussion

The convective flow of water at temperatures around the maximum density temperature is studied in the presence of solute transfer. Tables 1 and 2 provide a comparison of the results of the present work for constant wall temperature with those of Kandaswamy and Kumar [4] and Sundarvadivelu and Kandaswamy [5] for code validation, and they agree well.

3.1 Evolution of Flow Field in Transient State Regime. At time $\tau=0$, the fluid contained in the entire cavity is pure and is at 0 °C. For $\tau>0$, the wall temperatures are changed to θ_L (left wall) and θ_R (right wall) simultaneously. Since the temperatures of both the walls are higher than that of the fluid inside the cavity, the walls transmit heat to the fluid by conduction and raise the temperature of fluid particles adjoining the walls. As the temperature of fluid increases from 0 °C to a temperature less than 4 °C, the density of the fluid also increases, making them fall along both walls. This introduces a bicellular fluid motion with a counterclockwise rotating cell close to the left hot wall and a clockwise rotating cell close to the right cold wall.

Figures 2(*a*)–2(*f*) are presented to show the evolution of fluid motion and subsequent distribution of heat and concentration across the porous cavity as time evolves ($100 \leq \tau \leq 126{,}900$). The results for the transient state regime are presented for thermal Grashof number $\text{Gr}_1=53{,}634$ and solute Grashof number $\text{Gr}_5=8372$ with porosity $\epsilon=0.4$, Darcy number $\text{Da}=10^{-3}$, and $\text{Sc}=50$ as a representative case. Figure 2(*a*) shows the evolution of the fluid motion and the distribution of heat and concentration at $\tau=100$. It is observed that the fluid particles adjoining both walls receive heat from the walls and increase temperature and density. When the density increases, the fluid starts falling along the walls creating a counterclockwise rotating cell near the left wall and clockwise rotating cell near the right wall, resulting in the formation of two small cells rotating in opposite directions near the vertical walls. The corresponding isotherms are parallel to the vertical walls, indicating that the heat is initially transferred from the walls to the fluid only by conduction. Since the left wall is hot, it introduces a stronger thermal gradient between the left wall and the fluid than the right cold wall as time progresses ($\tau=1000$). The counterclockwise rotating cell grows faster than the clockwise rotating cell and starts occupying a major portion of the cavity.

Table 2 Comparison of the results of the present work with those of Ref. [5]

	$\overline{\text{Nu}}$		$\overline{\text{Sh}}$	
T (K)	Ref. 5	Present study	Ref. 5	Present
277	4.466	4.047	2.628	2.452
282	3.193	2.902	2.028	1.929
283	2.926	2.478	2.021	1.551
284	3.140	3.160	1.800	1.799
285	3.784	3.730	2.082	2.073
288	5.302	4.988	2.888	2.911

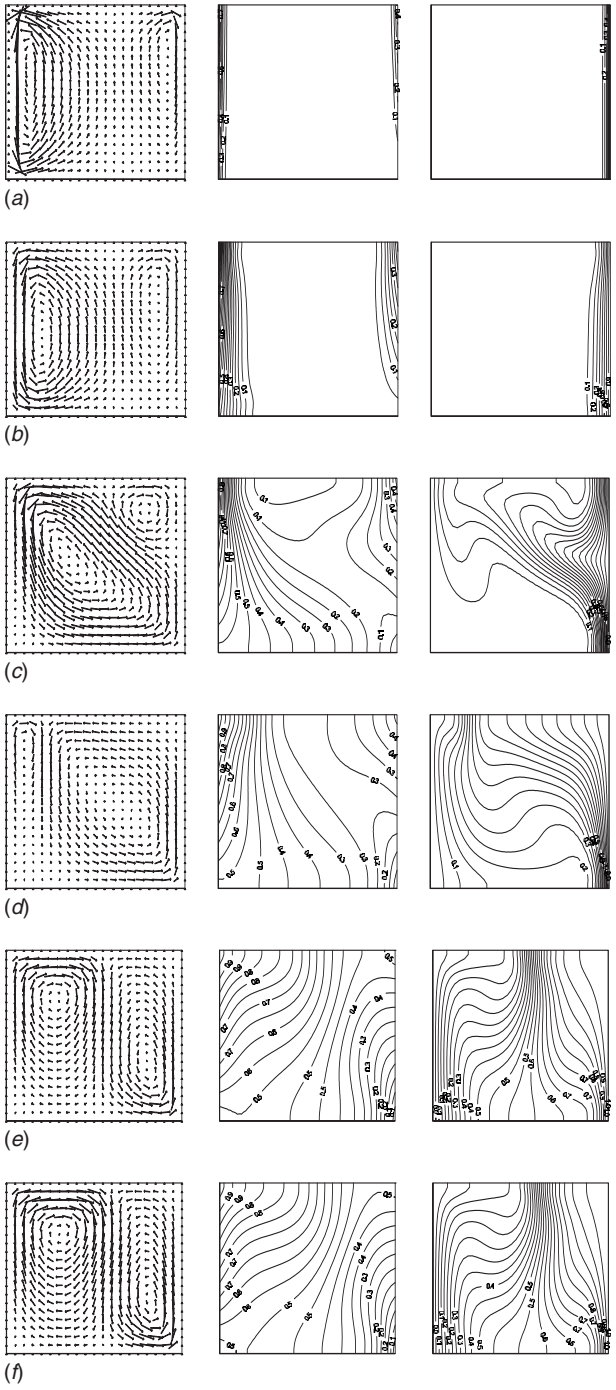

Fig. 2 (*a*) Velocity vector, isotherms, and isoconcentrations at $\tau=100$ for $\text{Gr}_1=53{,}634$, $\epsilon=0.4$, $\text{Sc}=50$, and $\text{Da}=0.001$ in the transient state regime; (*b*) velocity vector, isotherms, and isoconcentrations at $\tau=1000$ for $\text{Gr}_1=53{,}634$, $\epsilon=0.4$, $\text{Sc}=50$, and $\text{Da}=0.001$ in the transient state regime; (*c*) velocity vector, isotherms, and isoconcentrations at $\tau=10{,}000$ for $\text{Gr}_1=53{,}634$, $\epsilon=0.4$, $\text{Sc}=50$, and $\text{Da}=0.001$ in the transient state regime; (*d*) velocity vector, isotherms, and isoconcentrations at $\tau=25{,}000$ for $\text{Gr}_1=53{,}634$, $\epsilon=0.4$, $\text{Sc}=50$, and $\text{Da}=0.001$ in the transient state regime; (*e*) velocity vector, isotherms, and isoconcentrations at $\tau=100{,}000$ for $\text{Gr}_1=53{,}634$, $\epsilon=0.4$, $\text{Sc}=50$, and $\text{Da}=0.001$ in the transient state regime; and, (*f*) velocity vector, isotherms, and isoconcentrations at $\tau=126{,}900$ for $\text{Gr}_1=53{,}634$, $\epsilon=0.4$, $\text{Sc}=50$, and $\text{Da}=0.001$ in the transient state regime

When $\tau=1000$, the fluid motion gains momentum and the convective mode of heat transfer sets in the porous cavity, as shown in Fig. 2(*b*).

Further progress in time makes the counterclockwise rotating cell moving closer to the left wall and receiving more heat and growing stronger in strength and starts suppressing the clockwise rotating cell close to the right wall, thus reducing the volume of fluid associated with the clockwise rotating cell. As the volume of the fluid involved with clockwise rotating cell gets reduced, the heat received from the adjoining wall makes it gain strength and starts suppressing the counterclockwise rotating cell. A further progress in time $\tau=10{,}000$ extends this progress and pushes the cell close to the right corner, making the fluid volume associated with the clockwise rotating cell to a minimum. Figures 2(*c*) presented for time $\tau=10{,}000$ shows that the cell near the left wall grows in size and pushes another cell upwards to the top right corner of the cavity. The corresponding isotherms and isoconcentration lines indicate that convective mode of heat and mass transfer improves further. With further progress in time, the clockwise rotating cell gets reduced to a small one with the fluid volume involved getting reduced to a minimum. The fluid mass associated with clockwise rotating cell is very less and receives the same amount of heat from the adjoining right wall, which grows in strength and starts to dominate the counter clockwise rotating cell.

As time progresses, the growing cell emerges as the single largest one, rotating in counterclockwise direction, while the smaller cell at the right top corner vanishes. As the fluid falls along the left wall and rises along the right wall, it is clear that the temperature of the maximum density of water exists along the left wall. It is observed from the corresponding isotherms and isoconcentration lines that the transfer of heat and mass takes place by means of convection and the clockwise rotating cell dominates its counterpart, making the fluid mass associated with this to its minimum. When time $\tau=25{,}000$, the maximum density plane moves farther away from the left wall and as such, a small cell rotating in the clockwise direction appears near the left wall, as shown in Fig. 2(*d*). The release of heat due to the strong thermal gradient between the left hot wall and the adjoining fluid particles makes the cell quickly gain strength and push the clockwise rotating cell toward the right cold wall ($\tau=25{,}000$). The clockwise rotating cell receives heat from the adjoining wall and grows in volume and strength and starts to suppress the counter clockwise rotating cell. Further progress in time makes the clockwise rotating cell strong, pushing the counterclockwise rotating cell close to the left wall.

As time τ progresses to 100,000, the clockwise rotating cell grows in size and pushes the counterclockwise rotating cell farther toward the right wall, resulting in the formation of dual cell structure, as shown in Figs. 2(*e*) with the corresponding isotherms and isoconcentration lines. This is due to the fact that the temperature of the maximum density of water exists in the middle of the cavity, where the fluid falls and rises along both the vertical walls. This overshooting of one cell over the other continues for some time and finally settles down when $\tau=126{,}900$ with the two cells, as shown in Fig. 2(*f*). During this process, the cells continue to be separated by the maximum density curve. This curve during the transition from stationary state to steady-state overshoots the midplane of the cavity. This overshooting during transition from stationary state to steady-state is also noticed in the Nusselt number at the midplane of the cavity, as seen in Fig. 3. This phenomenon is observed for the first time and no earlier study has reported such overshooting. This feature is unique to the maximum density fluids and is observed for the first time in this study.

Figure 3 shows the time history of average Nusselt number and average Sherwood number calculated at $Y=1/2$ for various values of the Grashof number corresponding to the temperature around the maximum density temperature with $\epsilon=0.4$, Sc=50, and Da $=0.001$. The Nusselt number, which is a measure of the heat transfer calculated at the midplane of the cavity presented in Fig. 3, also exhibits overshooting of cells.

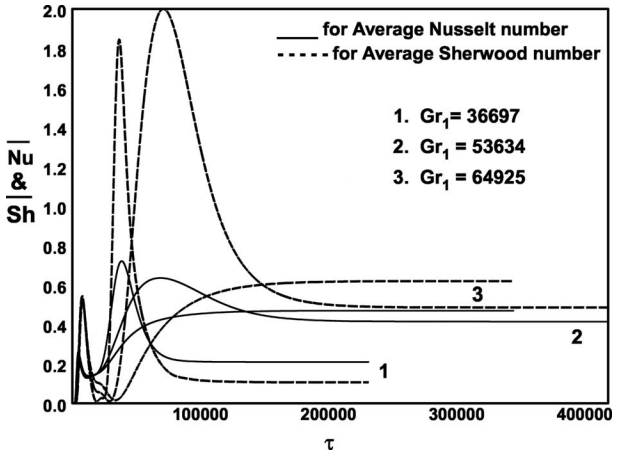

Fig. 3 Time history of the average Nusselt and Sherwood numbers for various values of Grashof number with $\epsilon=0.4$, Da $=0.001$, and Sc=50 at $Y=(1/2)$

3.2 Flow Field in Steady-State Regime. Figures 4(*a*)–4(*d*) show the velocity vector for the fluid motion and the resulting temperature and concentration distribution for different varying side wall temperatures with porosity $\epsilon=0.4$, Darcy number Da $=10^{-3}$, and Sc=50. When the left wall is maintained at a temperature that corresponds to $Gr_1=22{,}582$ and a concentration that corresponds to $Gr_5=4961$, the flow pattern consists of a single major cell rotating in the counterclockwise direction, as seen in Fig. 4(*a*). The maximum density temperature of water, which is at the left wall, makes the density of the fluid monotonically increase from left to right, introducing a single counterclockwise rotating cell. In the case of $Gr_1=22{,}582$, the line of maximum density temperature of water is moved away near the left wall. Hence, the water falls close to the left wall and rises near the opposite wall, leading to a single cell formation. This is due to the absence of density inversion of water with temperature inside the cavity. The single cell occupies the entire cavity with boundary layers being formed along the vertical walls. The corresponding isotherms appear crowded near the upper left corner of the left wall as well as near the lower right corner of the right wall of the cavity. The isotherms in the core region are nearly parallel in vertical direction, indicating that most of the heat transfer is carried out by conduction. On the other hand, the isoconcentration field indicates that the concentration boundary layers are formed along the vertical walls. The isoconcentration lines on the core of the cavity are almost uniform.

Figure 4(*b*) shows the flow structure and the corresponding isotherms and isoconcentration lines for $Gr_1=50{,}811$ and $Gr_5=8062$ with $\epsilon=0.4$, Darcy number Da$=10^{-3}$, and Sc=50. A secondary cell grows in size and pushes the primary cell toward the right wall of the cavity. When the Grashof number increases to $Gr_1=50{,}811$, which corresponds to a temperature above the maximum density temperature of water allowing the maximum density temperature to lie inside the cavity, the flow changes gradually, as seen in Fig. 4(*b*). As the left wall temperature is above the maximum density temperature of water for the case $Gr_1=50{,}811$, the maximum density line moves from the left wall into the cavity. Since the maximum density line lies between the walls of the cavity as one moves into the cavity from either wall, the density of water near the walls decreases, introducing a bicellular flow pattern with a clockwise rotating cell near the left wall and an anticlockwise rotating cell near the right wall. These two cells are separated by the maximum density temperature line along which the fluid always moves from top to bottom of the cavity. As such, the fluid rises along the vertical walls and falls inside the cavity where the temperature of maximum density prevails. A deformation in the corresponding isotherms is observed near the boundary.

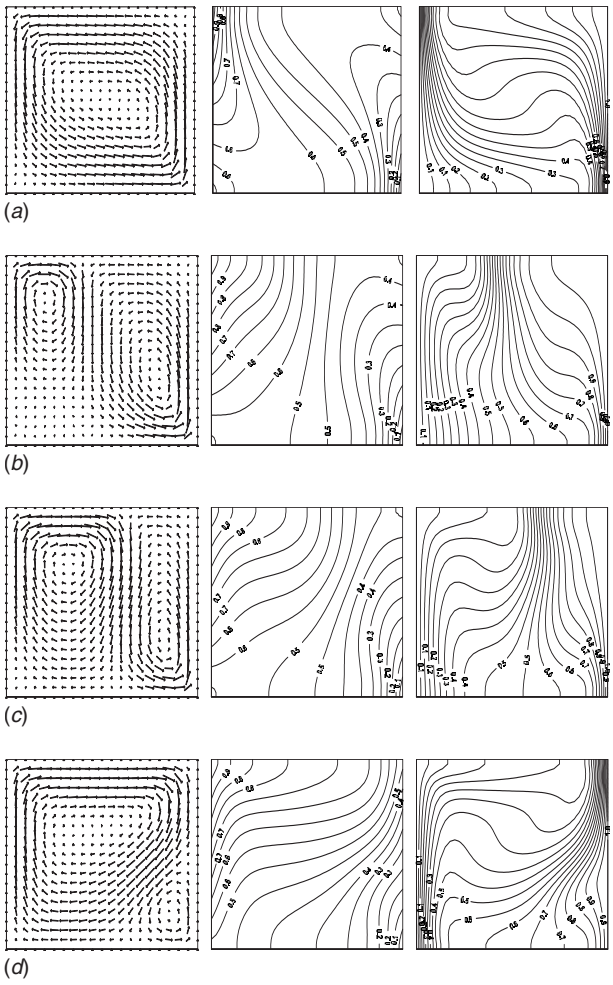

Fig. 4 (*a*) Velocity vector, isotherms, and isoconcentrations for $Gr_1=22{,}582$, $\epsilon=0.4$, Sc=50, and Da=0.001 in the steady-state regime; (*b*) velocity vector, isotherms, and isoconcentrations for $Gr_1=50{,}811$, $\epsilon=0.4$, Sc=50, and Da=0.001 in the steady-state regime; (*c*) velocity vector, isotherms, and isoconcentrations for $Gr_1=53{,}634$, $\epsilon=0.4$, Sc=50, and Da=0.001 in the steady-state regime; and (*d*) velocity vector, isotherms, and isoconcentrations for $Gr_1=64{,}925$, $\epsilon=0.4$, Sc=50, and Da=0.001 in the steady-state regime

The solute boundary layer thickness decreases and consequently enhances thermosolutal activities in the cavity. In this case, the maximum density temperature of water prevails in the middle of the cavity. Hence, the density of water increases from the walls as one moves from either side of the vertical walls. The density attains a maximum level in between the walls, where the fluid falls, thus forming the bicellular flow structure. This bicellular formation in the flow structure has significant effect on the thermal and concentration fields.

In the bicellular pattern, there appear two counter-rotating cells, one independent of the other. Convective heat transfer is restricted by the dual cell structure. As the fluid particles of a cell do not mix up with those of another cell, temperature distribution takes place only by conduction in the middle of the cavity. The isotherms are substantially linear in the bulk of the interior region. Thus, the overall heat transfer is mostly by conduction in the middle and bottom parts of the cavity except in a relatively small region close to the top left corner of the cavity, where the induced convective activities are appreciable. The corresponding convective field shows that the solutal boundary layer thickness becomes thinner, and solutal convection is gradually enhanced as the Grashof number increases. The heat and mass transfer processes

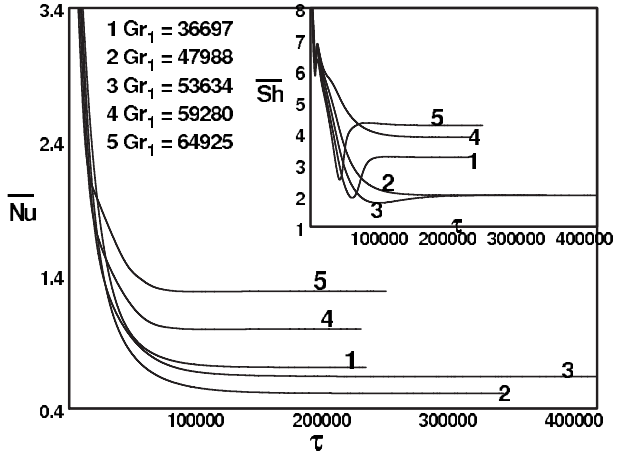

Fig. 5 Time history of the average Nusselt and Sherwood numbers for various values of Grashof number with $\epsilon=0.4$, Da =0.001, and Sc=50

are found to be disturbed due to the resulting bicellular flow structure. Hence the there is a sharp fall in the average Nusselt number and Sherwood number. This nonlinear behavior of the average Nusselt and Sherwood numbers is due to the effect of maximum density of water in the cavity.

Figures 4(*c*) and 4(*d*) are presented to show the flow pattern and the resulting isotherms and isoconcentration lines for thermal Grashof number $Gr_1=53{,}634$ with solute Grashof number $Gr_5=8372$, and thermal Grashof number $Gr_1=64{,}925$ with solute Grashof number $Gr_5=9613$, respectively. The secondary cell grows in size and flow strength, pushing the primary cell closer to the right wall. In this case, the density of water increases from left wall to right wall, and the density of water is at maximum along the left wall. Hence, the fluid falls along right wall, resulting in a single cell rotating in the clockwise direction. The corresponding isotherms are extended to almost the entire cross section except the bottom most part of the cavity. The isotherms are almost parallel to the horizontal wall for higher Grashof numbers, indicating that most of the heat transfer is carried out by convection. Further increase in the Grashof number continues to improve the double-diffusive convective heat and mass transfer rates.

Figure 5 shows the time history of the average Nusselt number and the average Sherwood number calculated at the left vertical wall for various values of the Grashof number with $\epsilon=0.4$, Sc =50, and Da=0.001. The average heat and mass transfer rates go down initially as the Grashof number increases and attain steady-state condition. This is because, heat is initially transferred from the left wall to the fluid inside the cavity by conduction. As time evolves, the convective activities dominate in the cavity.

3.3 Effects of Porosity, the Darcy Number, and Schmidt Number in Steady-State Regime. Figure 6 shows how the porosity of the medium affects the average heat and mass transfer rates. As the porosity, being the fraction of the total volume that is occupied by void space, increases, the heat and mass transfer rates also increase. The higher porosity leads to higher heat and mass transfer rates. This is because of the fluid motion at a higher velocity due to larger porosity. The nonlinear behavior of heat and mass transfer seen in Fig. 6 is due to the effect of maximum density-temperature of water inside the cavity.

Figure 7 exhibits the impact of the Darcy numbers on the average heat and mass transfer rates for different values of the Grashof number with $\epsilon=0.4$ and Sc=50. The Darcy number, which depends on the permeability of porous medium, leaves strong effects on convection in porous cavity. It is observed that an increase in Darcy number enhances the average heat and mass transfer rates. The flow of fluid is restricted largely in the case of

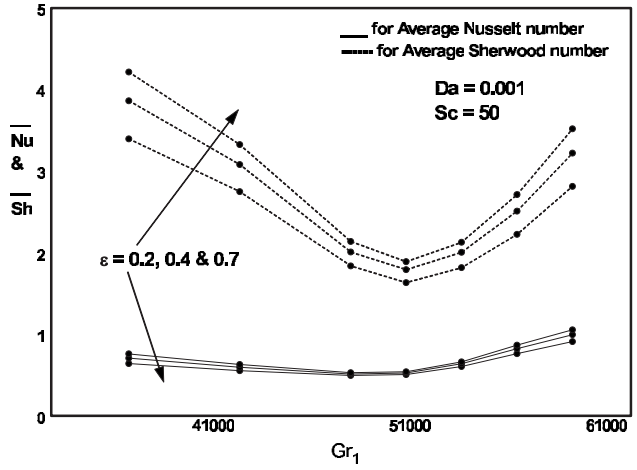

Fig. 6 The average Nusselt and Sherwood numbers for various values of porosity and Grashof number with Da=0.001 and Sc=50 in the steady-state regime

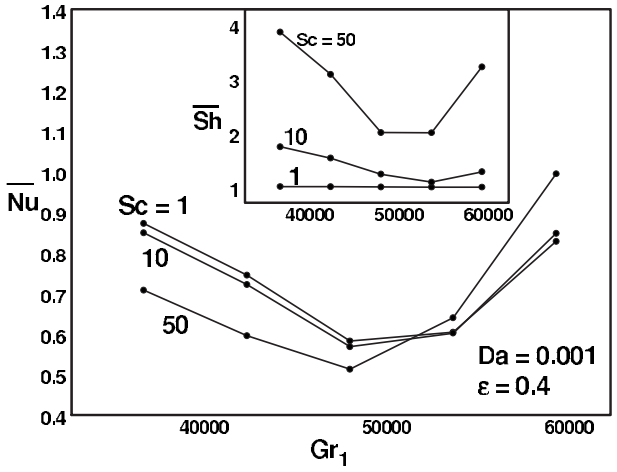

Fig. 8 The average Nusselt and Sherwood numbers for various low values of Schmidt number and Grashof number with ϵ=0.4 and Da=0.001 in the steady-state regime

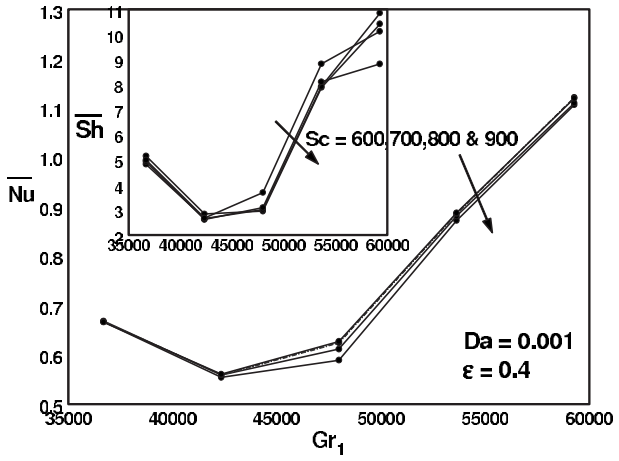

Fig. 9 The average Nusselt and Sherwood numbers for various higher values of Schmidt number and Grashof number with ϵ=0.4 and Da=0.001 in the steady-state regime

smaller values of Darcy number. It is observed that the velocity of the fluid particles is restricted for very low values of the Darcy number. As the Darcy number decreases, the increase in the drag force suppresses the buoyancy force and consequently decreases the average heat and mass transfer rates.

Figure 8 shows the effect of the Schmidt number on the average Nusselt and Sherwood numbers, which give a measure of the dimensionless heat and mass transfer rates. These numbers are found to depend strongly on double-diffusive effects caused by the difference in the diffusivity of heat and mass. It is observed that the average Nusselt number decreases and the Sherwood number increases with increasing Schmidt number. For all values of Schmidt number, it is noticed that both Nusselt number and Sherwood number behave nonlinearly with Grashof number. This nonlinear behavior is associated with the maximum density temperature of water inside the cavity. Figure 9 for the water-NaCl solution (Schmidt number 600–900) also demonstrates similar behavior with solutions having the Schmidt number range 1–50. Hence it may be observed for a wide range of Schmidt number that the behavior of heat and mass transfer is similar.

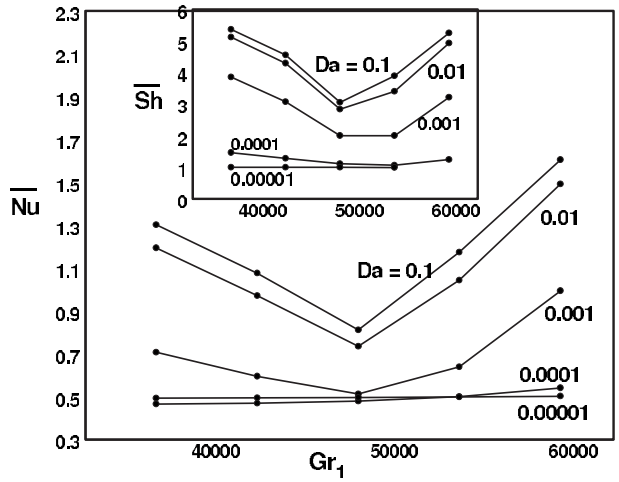

Fig. 7 The average Nusselt and Sherwood numbers for various values of Darcy number and Grashof number with ϵ=0.4 and Sc=50 in the steady-state regime

4 Conclusion

The effects of water maximum density on the heat and mass transfer in a porous cavity with variable side wall temperatures have been studied numerically for various values of porosity, Grashof number, and Schmidt and Darcy numbers. It is shown that the maximum density surface executes an overshooting with time about the midplane of the cavity. This overshooting is also observed in the heat transfer rate across the midplane of the cavity. It is for the first time that this behavior is noticed, and it is due to the maximum density temperature of water. Such behavior is not noticed in fluids where the density is a monotonic function of temperature. It is also observed that the temperature of maximum density leaves strong effects on the heat and mass transfer due to the formation of bicellular fluid flow. The nonlinear behavior of the heat and mass transfer rates is also the maximum density effects. The results show that higher heat and mass transfer rates can be achieved in a water saturated porous medium in the presence of high porosity, Schmidt number, and Darcy number.

References

[1] Han, H., and Kuehn, T. H., 1991, "Double-Diffusive Natural Convection in a Vertical Rectangular Enclosure-II: Numerical Study," Int. J. Heat Mass Transfer, **34**, pp. 461–471.

[2] Beghein, C., Haghighat, F., and Allard, F., 1992, "Numerical Study of Double-

Diffusive Natural Convection in a Square Cavity," Int. J. Heat Mass Transfer, **35**, pp. 833–846.
[3] Nithiarasu, P., Sundararajan, T., and Seetharamu, K. N., 1997, "Double-Diffusive Natural Convection in a Fluid Saturated Porous Cavity With a Freely Convecting Wall," Int. Commun. Heat Mass Transfer, **24**(8), pp. 1121–1130.
[4] Kandaswamy, P., and Kumar, K., 1999, "Buoyancy-Driven Nonlinear Convection in a Square Cavity in the Presence of a Magnetic Field," Acta Mech., **136**, pp. 29–39.
[5] Sundaravadivelu, K., and Kandaswamy, P., 2000, "Double Diffusive Nonlinear Convection in a Square Cavity," Fluid Dyn. Res., **27**, pp. 291–303.
[6] Khanafer, K., and Vafai, K., 2002, "Double-Diffusive Mixed Convection in a Lid-Driven Enclosure Filled With a Fluid Saturated Porous Medium," Numer. Heat Transfer, Part A, **42**, pp. 465–486.
[7] Saeid, N. H., and Pop, I., 2004, "Maximum Density Effects on Natural Convection From a Discrete Heater in a Cavity Filled With a Porous Medium," Acta Mech., **171**, pp. 203–212.
[8] Sezai, I., and Mohamad, A. A., 1999, "Three Dimensional Double Diffusive Convection in a Porous Cubic Enclosure Due to Opposing Gradients of Temperature and Concentration," J. Fluid Mech., **400**, pp. 333–353.
[9] Sezai, I., and Mohamad, A. A., 2000, "Double Diffusive Convection in a Cubic Enclosure With Opposing Temperature and Concentration Gradients," Phys. Fluids, **12**(9), pp. 2210–2223.
[10] Mohamad, A. A., Bennacer, R., and Azaiez, J., 2004, "Double Diffusion Natural Convection in a Rectangular Enclosure Filled With Binary Saturated Porous Media: The Effect of Lateral Aspect Ratio," Phys. Fluids, **16**(1), pp. 184–199.
[11] Mohamad, A. A., and Bennacer, R., 2002, "Double Diffusion Natural Convection in an Enclosure Filled With Saturated Porous Medium and Subjected to Cross Gradients: Stably Stratified Fluid," Int. J. Heat Mass Transfer, **45**, pp. 3725–3740.
[12] Vafai, K., 2005, *Handbook of Porous Media*, 2nd ed., Dekker, New York.
[13] Nield, D. A., and Bejan, A., 2006, *Convection in Porous Media*, 3rd ed., Springer, New York.
[14] Patankar, S. V., 1980, *Numerical Heat Transfer and Fluid Flow*, Hemisphere, Washington, DC.
[15] Rudraiah, N., Barron, R. M., Venkatachalappa, M., and Subbaraya, C. K., 1995, "Effect of a Magnetic Field on Free Convection in a Rectangular Enclosure," Int. J. Eng. Sci., **33**(8), pp. 1075–1084.

Numerical Modeling of Multidirectional Flow and Heat Transfer in Graphitic Foams

S. A. Mohsen Karimian
Postdoctoral Scientist
Mem. ASME
Flow Simulation and Analysis Group,
George Washington University,
Washington, DC 20052
e-mail: karimian@gwu.edu

Anthony G. Straatman[1]
Assoc. Professor
Mem. ASME
Department of Mechanical and Materials Engineering,
The University of Western Ontario,
London, ON, N6A 5B9, Canada
e-mail: astraatman@eng.uwo.ca

To investigate the feasibility of the use of foams with an interconnected spherical pore structure in heat transfer applications, models for heat transfer and pressure drop for this type of porous materials are developed. Numerical simulations are carried out for laminar multidirectional thermofluid flow in an idealized pore geometry of foams with a wide range of geometry parameters. Semiheuristic models for pressure drop and heat transfer are developed from the results of simulations. A simplified solid-body drag equation with an extended high inertia term is used to develop the hydraulic model. A heat transfer model with a nonzero asymptotic term for very low Reynolds numbers is also developed. To provide hydraulic and heat transfer models suitable for a wide range of porosity, only a general form of the length-scale as a function of pore structure is defined a priori, where the parameters of the function were determined as part of the modeling process. The proposed ideal models are compared to the available experimental results, and the source of differences between experimental results and the ideal models is recognized and then calibrated for real graphitic foam. The thermal model is used together with volume-averaged energy equations to calculate the thermal dispersion in graphitic foam. The results of the calculations show that the linear models for thermal dispersion available in literature are oversimplified for predicting thermal dispersion in this type of porous material. [DOI: 10.1115/1.3084122]

Keywords: convective heat transfer, hydraulic loss, thermal dispersion, porous media, metallic foam, graphitic foam

1 Introduction

In recent years, there has been an increasing number of works on the hydraulic and thermal characterization of graphitic foam (GF) for heat transfer applications. GF is a relatively new type of porous material, which is produced by a process of foaming and heat treatment of a carbon precursor [1,2]. Graphitic foam has an open interconnected spherical void structure and an extremely high effective conductivity (40–180 W/m K) [1] due to its high solid-phase conductivity (k=800–1900 W/m K), which enables heat to penetrate deeply into the solid structure of the foam, thereby increasing thermal nonequilibrium between the solid and fluid phases and increasing convective heat transfer under forced-flow conditions.

Gallego and Klett [2] investigated the use of GF in electronic cooling applications and studied the effect of various macroscopic geometry configurations on the pressure loss and heat transfer. Yu et al. [3] proposed a spherical-void-phase (SVP) unit-cube geometry model to approximate the geometric properties of GF, such as internal surface area and surface roughness, as functions of pore diameter and porosity. To study the convective enhancement obtained using GF in cooling applications, Straatman et al. [4] measured convection in parallel air flow and observed convective enhancements of 30–10% over that obtained from a flat plate for the range of Reynolds numbers of 150,000–500,000. Recently, Straatman et al. [5] carried out experimental measurements of pressure loss and heat transfer for forced flow through various GFs and showed that the pressure loss and heat transfer are strong functions of the internal structure of the foam and that the more *open* foams had the best balance of pressure drop and heat transfer.

The data obtained in Straatman et al. [5] were also used to calibrate a finite-volume computational fluid dynamics (CFD) code [6] that solved the volume-averaged transport equations for mass, momentum, and energy in three-dimensional domains. The CFD code was developed specifically to explore high-conductivity porous metals in a local thermal nonequilibrium framework, and thus coupled energy equations were solved for the fluid and solid constituents of the porous domain. A model for the local interstitial heat transfer was obtained from Calmidi and Mahajan [7] and was calibrated using data from the GF experiments. Thermal dispersion was modeled using an expression derived for reticulated aluminum foams [8]. While the resulting computations gave reasonable predictions of the overall heat transfer, it is not known whether the interstitial exchange and thermal dispersion models led to accurate predictions of the temperature distributions in the porous GF domain; i.e., it is questionable whether the same thermal dispersion model can be used for both reticulated foams and spherical-void-phase foams since dispersion is highly dependent on internal hydrodynamics and, thus, internal geometry of the foam. To date, models for interstitial exchange and thermal dispersion in volume-averaged calculations have been formulated based on simple expressions and then calibrated using available experimental data. While this approach is reasonable, the resulting models have a narrow range of applicability, and parametric studies on the foam structure itself are not possible. From a scientific perspective, it is of great interest to understand the pore-level flow and energy transfer, first to observe the impact of porosity and pore diameter and second to serve as the basis for formulating more accurate model expressions for volume-averaged calculations. Since experimental studies of the flow structure at the pore level are practically impossible, direct numerical simulations of the flow and energy transport inside an idealized representation of the SVP foam serve as a useful alternative and could provide information useful for both physical insight and the development

[1]Corresponding author.

Contributed by the Heat Transfer Division of ASME for publication in the JOURNAL OF HEAT TRANSFER. Manuscript received December 7, 2007; final manuscript received December 4, 2008; published online March 18, 2009. Review conducted by Jamal Seyed-Yagoobi.

of models. To this end, Karimian and Straatman [9] and Karimian [10] used the unit-cube cell geometry model as the idealized internal structure of GF and simulated periodic thermofluid flow at the pore level for a range of porosities (75%–90%) and pore diameters (300–600 μm) to investigate the dependence of pressure loss and heat transfer on the microscopic properties of the foam. In their simulations, the flow direction was normal to the pore windows, and the resulting flow field was very similar to a fully developed pipe flow at high flow rates, resulting in the asymptotic behavior of hydraulic loss and convective heat transfer. While the results of the simulations were useful for gaining insight into the physics of unidirectional flow in the idealized geometry, the trends observed were not similar to those measured in experiments on real graphitic foam. Therefore, to develop hydraulic and thermal models for GF, it is necessary to explore more generic forms of flow fields such as multidirectional periodic flow at the pore level of the idealized SVP foam.

In the present work, the parallel finite-volume code PARTISUN [11] is used to solve multidirectional periodic thermofluid flow at the pore level of an idealized geometry based on the unit-cube geometry model of Yu et al. [3] for a wide range of Reynolds numbers and porosities, and suitable general forms of engineering models are proposed for pressure loss, convective (interstitial) heat transfer, and thermal dispersion based on the results of the simulations. The proposed ideal models are compared to the experimental results of Straatman et al. [5], and the source of differences between experimental results and the ideal models is recognized and then calibrated for real graphitic foam. The following sections of this paper present the computational domain, the numerical formulation, results of the simulations, and models for the pressure loss, heat transfer, and thermal dispersion.

2 Computational Domain

In this study, we consider the flow and heat transfer inside a generic section of an idealized GF foam block, which is ideally composed of hundreds of identical cells in each direction. It is reasonable to assume that the flow in a generic section inside the foam is periodic in nature, and thus, only a representative portion of the domain requires modeling.

To approximate the internal structure of graphitic foam in this work, we use the unit-cube cell geometry model proposed by Yu et al. [3]. The model is based on interconnected sphere-centered cubes, where the interconnected spheres represent the void phase of the porous media. Each cube is called a unit-cube cell or simply a cell. Figure 1(*a*) shows a three-dimensional CAD image of a unit-cube cell with its detailed dimensions. Here, D_p is the pore diameter, H is the cell size, and D_w is the interconnected pore-window diameter. This idealized geometry is assumed as the building block of the porous media. A unit-cube cell in this model is defined by the porosity, ε, of the represented graphitic foam and the pore diameter D_p. It can be shown [10] that for a given porosity, the cell size and the pore-window diameter vary proportionally to the pore diameter,

$$\eta = \frac{H}{D_p} = f(\varepsilon) \tag{1}$$

$$D_w = (1 - \eta^2)^{0.5} D_p \tag{2}$$

Here, η is the cell ratio and is only a function of porosity. Therefore, the pore-level thermofluid flow structure can be scaled using pore diameter or one of its products, e.g., cell size or pore-window diameter, as a pore-level length-scale, and hence all dimensionless quantities are solely functions of porosity.

Comparing the results of the direct numerical simulations in Ref. [9] with the experimental measurements of Straatman et al. [4] indicates that pressure drop and convective heat transfer of a periodic unidirectional flow inside the idealized foam have a different dependence on the Reynolds number compared to those of a flow through a real block of graphitic foam. This is mainly because the direction of the flow in a real block of foam is fairly random and not necessarily normal to the pore windows. Therefore, a multidirectional periodic flow can better represent the flow in a real foam. To simulate the most generic multidirectional periodic flow, a domain consisting of a cluster of idealized cells was (mathematically) constructed such that a spatially periodic flow could be simulated where the incoming velocity has equal components in all directions with respect to the pore-window planes. It is felt that such velocity direction represents the "average" orientation of the windows with respect to the incoming flow. This procedure generates a computational domain comprised of two consecutive interconnected cells in each direction of X, Y, and Z with three pore windows as periodic sections in each direction (see Fig. 1(*b*)).

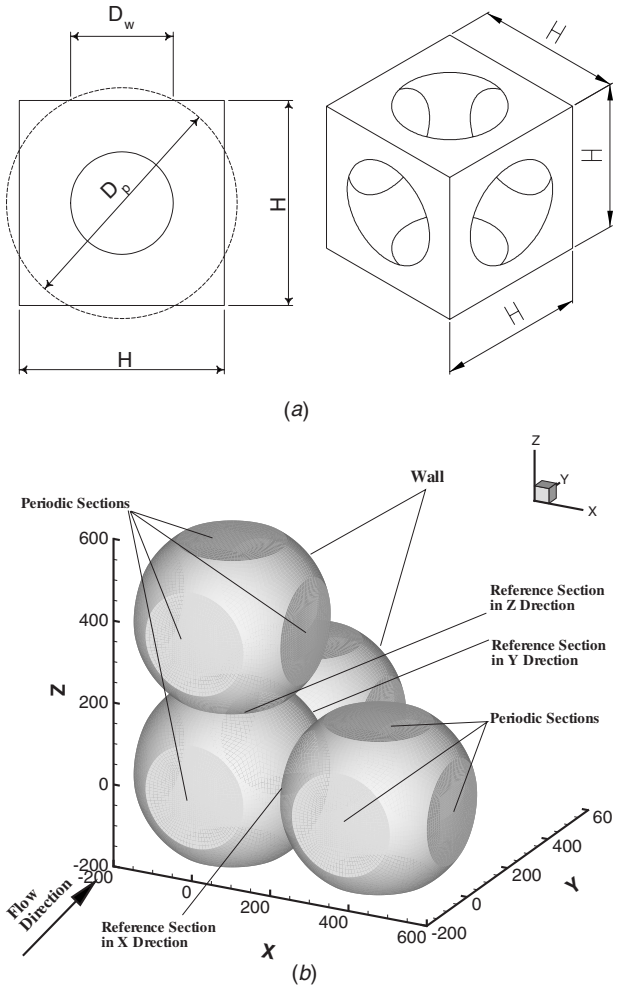

Fig. 1 (*a*) CAD images showing the unit-cube model [3]; detailed dimensions of the unit-cube cell geometry. (*b*) Computational domain for an idealized SVP foam with $\varepsilon = 0.80$.

3 Governing Equations and Numerical Method Setup

3.1 Governing Equations and Discretization Method. The integral form of the conservation equations for mass, momentum, and energy for an arbitrary fixed control volume $\Omega \subset \mathbb{R}^3$, of volume V bounded by a piecewise smooth boundary $\partial\Omega$, with unit normal vector $\hat{n}$ pointing outward, occupied by an incompressible Newtonian fluid are, respectively, given by

$$\int_{\partial\Omega} \boldsymbol{V} \cdot \hat{n} dS = 0 \tag{3}$$

$$\int_{\Omega} \rho \partial_t \boldsymbol{V} dV + \int_{\partial\Omega} \{\rho(\boldsymbol{VV}) - \mu[(\nabla \boldsymbol{V}) + (\nabla \boldsymbol{V})^T]\} \cdot \hat{n} dS = -\int_{\partial\Omega} P \hat{n} dS \tag{4}$$

$$\int_{\Omega} \rho \partial_t T dV + \int_{\partial\Omega} (\rho \boldsymbol{V} T) \cdot \hat{n} dS - \int_{\partial\Omega} \hat{n} \cdot \left(\frac{k}{C_p} \nabla T \right) dS = 0 \tag{5}$$

where ρ is the density, μ is the viscosity, k is the heat diffusion coefficient (conductivity), C_p is the specific heat, P is the relative pressure, $\boldsymbol{V}$ is the velocity vector, T is the absolute temperature, dS is the surface differential, and dV is the volume differential. Please note that for an incompressible flow, the cross-diffusion term is zero by virtue of continuity,

$$\int_{\partial\Omega} (\nabla \boldsymbol{V})^T \cdot \hat{n} dS = \int_{\Omega} \nabla^T (\nabla \cdot \boldsymbol{V}) dV = 0 \tag{6}$$

since in the finite-volume method, mass is conserved for each control volume Ω. To conserve mass strongly, the cross-diffusion term is enforced to zero when solving the integral equations numerically.

Equations (3)–(5) are solved using an in-house parallel code (PARTISUN) [11]. PARTISUN is developed using an implicit, coupled, unstructured finite-volume method and is based on a single-instruction-multiple-data (SIMD) parallelization model (within the PETSC framework [12]) to exploit the maximum capability of a cluster of distributed-memory machines. An inexact Jacobian Newton–Krylov (iJNK) method was used in conjunction with the nonlinear iterations to accelerate the nonlinear convergence in each time step. The convection term is implicitly modeled using a first-order upstream difference scheme (UDS) and explicitly corrected to higher order using a deferred-correction technique [13]. In this work, a second-order central difference scheme is selected as the higher-order scheme. The details of the discretization method, parallel implementation, and iJNK technique may be found in Ref. [11] and are omitted here for brevity.

3.2 Boundary Conditions. All boundary conditions are imposed implicitly [11]. A no-slip boundary condition is applied at all walls, i.e., $\boldsymbol{V}=0$, and pressure is extrapolated from inside the domain. A constant wall-temperature condition is imposed on the temperature field.

A flow specified periodic boundary condition method similar to that proposed in Ref. [14] is implemented at the periodic inflow and outflow windows in each direction, using the velocity vector at the reference section in that direction as a reference (see Fig. 1(*b*)),

$$\boldsymbol{V}_{i,\mathrm{in}_j} = \boldsymbol{V}_{i,r_j} - (U_{b,\mathrm{in}_j} - U_{b,r_j}) \hat{n}_j \tag{7}$$

Here index i loops over the control surfaces at the inflow section in_j and their counterparts at the reference section r_j, index j indicates the normal window directions, here X, Y, and Z, $\hat{n}$ is the unit normal vector of the section pointing outward, U_{b,in_j} is the normal component of the bulk inflow velocity that satisfies the mass flow rate at the windows in the jth direction, and U_{b,r_j} is the normal component of the bulk velocity at the reference section in the jth direction. Note that due to the direction of the normal vectors at the inflow and reference sections, a negative sign appears between the first and second terms on the right-hand side of Eq. (7). This method automatically preserves a multidirectional flow condition at each inflow window by conserving the size of the velocity components parallel to that window, copied from the reference section. For more information, the reader is referred to Ref. [14].

Using Eq. (7), only the normal component of the bulk inflow velocity is required to impose the boundary condition at the inflow section. The normal component of the bulk inflow velocity vector at each inflow window is calculated by solving a conservation of mass equation for a unit-cube cell,

$$U_{b,\mathrm{in}_j} = \frac{A_b}{A_w} \boldsymbol{V}_{\mathrm{ext}} \cdot \hat{n}_j = \frac{4\eta^2}{(1-\eta^2)\pi} \boldsymbol{V}_{\mathrm{ext}} \cdot \hat{n}_j \tag{8}$$

where $\boldsymbol{V}_{\mathrm{ext}} = \varepsilon \times \boldsymbol{V}_{\mathrm{int}}$ is the extrinsic velocity, A_b is the blockage area, A_w is the pore-window area, and η is the cell ratio (see Eq. (1)). The intrinsic velocity $\boldsymbol{V}_{\mathrm{int}}$ in Eq. (8) is determined from the following equation by setting the cell-based Reynolds number Re_H:

$$\mathrm{Re}_H = \frac{\rho V_{\mathrm{int}} H}{\mu} \tag{9}$$

where V_{int} is the magnitude of the intrinsic velocity vector $\boldsymbol{V}_{\mathrm{int}}$. In this study, a flow with equal velocity components in each direction is of interest, i.e.,

$$\boldsymbol{V}_{\mathrm{int}} = \frac{\mu \mathrm{Re}_H}{\rho H} \times \frac{\sqrt{3}}{3} (\hat{i} + \hat{j} + \hat{k}) \tag{10}$$

A constant wall temperature of $T_{\mathrm{sf}}=450$ K and a bulk inflow temperature of $T_{b,\mathrm{in}}=300$ K are imposed in all simulations. The fully developed temperature field does not periodically repeat in each cell. However, a constant wall temperature, combined with a fully developed flow, implies periodic behavior in the thermal process. This periodic behavior is the basis of a thermal periodic boundary condition developed by Karimian and Straatman [14] and implemented in this work. Implementation details of the periodic boundary conditions can be found in Ref. [14].

4 The Simulations

Simulations are carried out for a wide range of internal geometries, pore-level flow regimes, and fluid types. In order to have the optimum number of simulations with affordable computational cost, a proper selection of parameters as well as their variation range is necessary.

The internal structure of an idealized SVP foam is characterized by a length-scale, usually pore diameter D_p, and the porosity of the foam [10]. The pore diameter in a real graphitic foam can range from 150 μm to 800 μm, and the porosity in the real foam ranges $75\% \leq \varepsilon \leq 90\%$ [4]. In this study the pore diameter of the unit-cube cell is fixed to 450 μm, and grids for various internal structures are generated for porosities of $\varepsilon=0.75$, 0.80, 0.85, and 0.90.

A cell-based (pore-level) Reynolds number is defined herein based on the cell size H and is expressed by Eq. (9). Flow regimes ranging from creeping flow up to strong inertia flow are of interest in this study. The upper limit of the cell-based Reynolds number is determined by continuing the simulations for each porosity by increasing the cell-based Reynolds number until instability occurs in the flow field. The results of the simulations show that $0.1 \leq \mathrm{Re}_H \leq 95$ is a suitable range for the porosities considered. Three different fluid types, air, Freon-12, and water, are used in the simulations to cover a range of Prandtl numbers of $0.706 \leq \mathrm{Pr} \leq 5.83$ for the heat transfer models.

To ensure that the solutions were grid independent, simulations were conducted in computational domains with 340,000 and 790,000 control volumes at Reynolds number of 95. The results showed changes in the average Nusselt number of less than 1% and changes in the overall pressure drop of less than 2%. As such, all subsequent computations were run on a grid of 340,000 cells. This grid has a wall-grid size of $\Delta_w / D_p = 4/450$ and smooth variations across the computational domain with a maximum-to-minimum edge size ratio of $\Delta_{\max}/\Delta_w \leq 3$. To achieve a fully developed periodic flow field, a time-marching iteration was performed in each simulation until a maximum steady-state residual of $\xi_{\mathrm{st}}=10^{-5}$ was reached. At each time step, a nonlinear iteration was performed until a maximum nonlinear iteration of $n_{\max}=10$ or a maximum nonlinear residual of $\xi=10^{-4}$ was reached.

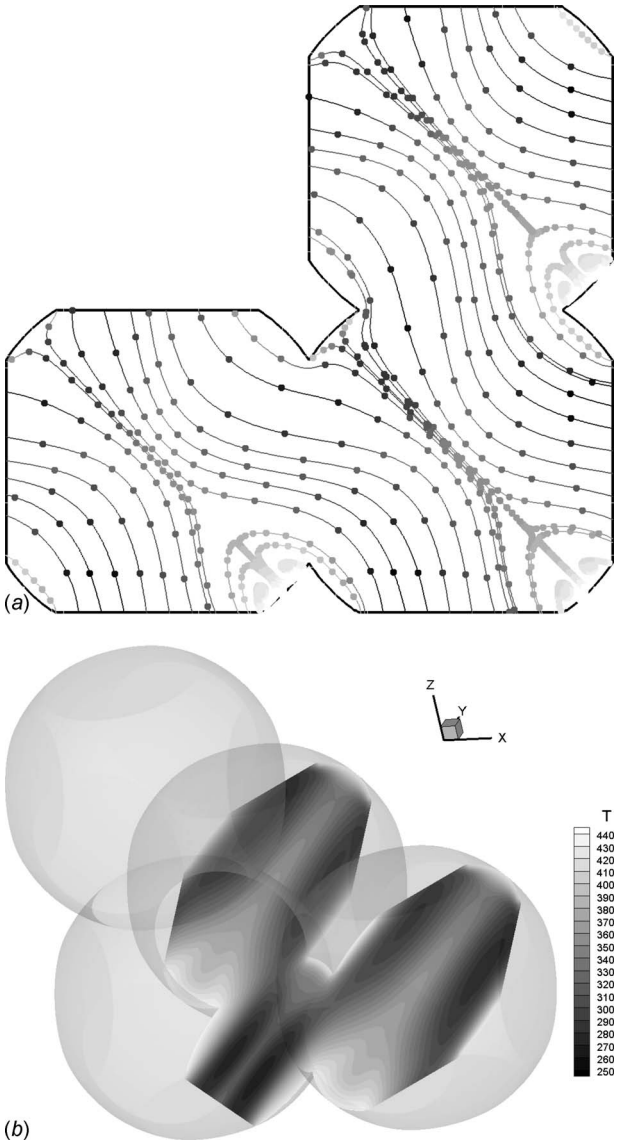

Fig. 2 The results of the simulations for the case of $\varepsilon=0.80$, with Re=40: (*a*) two-dimensional streamlines in an *X-Y* plane. Colors of the markers indicate the local flow temperature. (*b*) Temperature field in a plane parallel to the flow direction.

288 simulations were performed for a combination of the above-mentioned parameters. All simulations were performed using 32 or 48 processors on a cluster of distributed-memory machines [15], with 32 nodes interconnected by a low latency Myrinet G2 network. Each node is a Quad-Processor machine of AMD Opteron 2.20 GHz with 8 Gbytes of random access memory (RAM).

Figure 2(*a*) shows the streamlines in an *X-Y* plane for Re=40 in the pores of a foam with a porosity of $\varepsilon=0.80$. The colors of the markers indicate the variation in the temperature field. Figure 2(*b*) shows the temperature field on a plane parallel to the flow direction. The periodicity of the flow and temperature field is clearly observed in these figures. It can be seen that while the flow absorbs heat from the walls and the bulk temperature in the cells downstream is increased, a periodic condition prevails in the temperature field.

5 Hydraulic Model

For a multidirectional periodic flow with equal velocity components in a homogeneous periodic pore structure, where the flow is assumed to be steady at the pore level, the macroscopic pressure gradient is expected to be comprised of identical components in all directions,

$$\nabla P = -\frac{\Delta P}{H}(\hat{i}+\hat{j}+\hat{k}) \tag{11}$$

where ∇P is the macroscopic pressure gradient, ΔP is the pressure drop between the inflow and outflow windows of a unit-cube cell in one direction, and H is the unit-cube cell size. The maximum difference in the value of the cell-based pressure drop, ΔP, obtained from the results of the simulations for all four unit-cube cells in all three directions (X,Y,Z) at each Reynolds number is less that 4%. An average of the 12 values (in three directions of four cells) is selected for ΔP at each Reynolds number.

In the case of multidirectional flow in a spherical-void-phase foam, the solid phase is similar to a network of obstacles in a flow field. Therefore, a hydraulic model based on drag forces is deemed to be suitable for this type of porous media. It is worth mentioning that while drag models are not new concepts [16], they have only recently become of interest due to their application in modeling high-porosity open cell metal foams (see, for example, Ref. [17]). In this work, a hydraulic model is developed based on the analogy of bluff body drag forces.

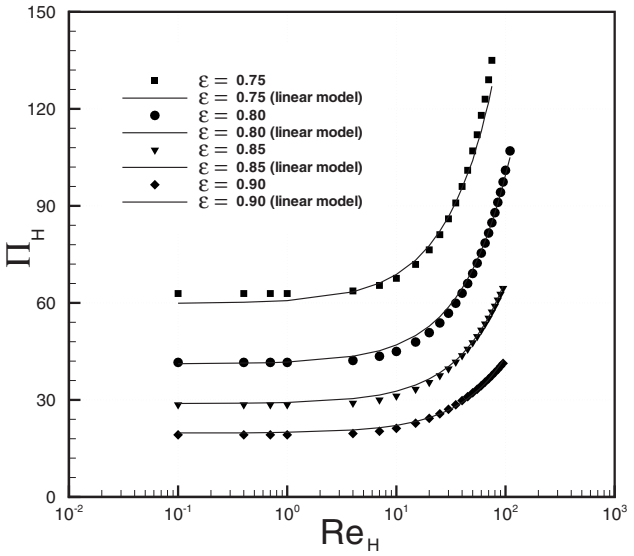

Fig. 3 Normalized pressure drop Π_H versus cell-based Reynolds number Re_H for the range of $0.75 \le \varepsilon \le 0.90$

5.1 Solid-Body Drag Model. The cell-based pressure drop ΔP between two consecutive pore windows (sections) of a cell in one direction (see Fig. 1(*b*)) can be normalized using the unit-cube cell size H and the extrinsic velocity V_{ext},

$$\Pi_H = -\frac{\Delta P}{H}\frac{H^2}{\mu V_{\text{ext}}} \tag{12}$$

Figure 3 shows the normalized pressure drop calculated from the results of the simulations as a function of the cell-based Reynolds number Re_H defined by Eq. (9) for the range of porosities considered in this work. The normalized pressure drop can be modeled using an extended permeability model in the form of

$$\Pi_H = a(\varepsilon) + b(\varepsilon)\text{Re}_H \tag{13}$$

The solid lines in Fig. 3 show the linear models for each porosity. It is our goal in this work to determine a generic form for the functions $a(\varepsilon)$ and $b(\varepsilon)$ for a range of $0.75 \le \varepsilon \le 0.90$. For a multidirectional flow in an idealized SVP foam with a velocity vector similar to that expressed by Eq. (10), the internal structure of the foam can be imagined as a network of interconnected solid bodies

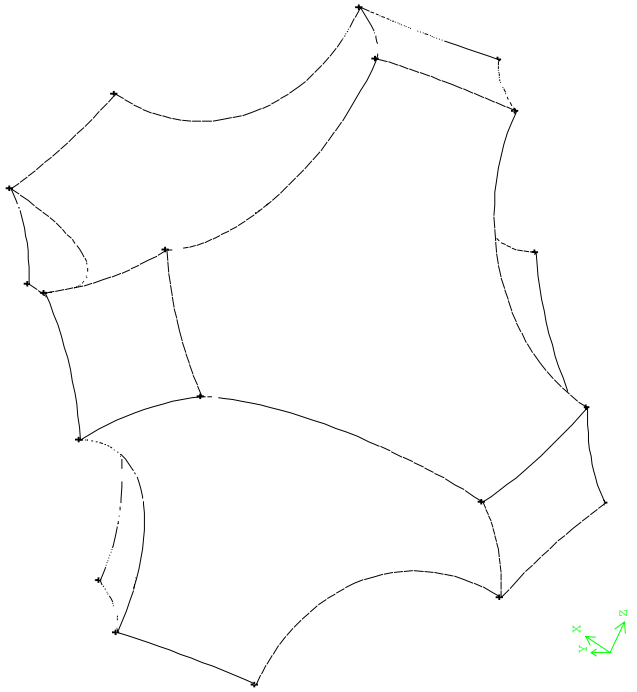

Fig. 4 A unit solid body of an idealized SVP foam with $\varepsilon = 0.80$

of diamond shape (see Fig. 4). To calculate drag forces, a simple drag model is used herein,

$$C_D = \frac{|\boldsymbol{F}|}{0.5\rho V_{\text{int}}^2 A_{\text{fs}}} = A\text{Re}_d^{-1} + B \tag{14}$$

where C_D is the drag coefficient, $\boldsymbol{F}$ is the total drag force exerted by fluid flow on the unit solid body, Re_d is the pore-level Reynolds number based on the unit solid-body length-scale d, which is the model length-scale herein, A and B are model constants, and A_{fs} is the fluid-solid interface area [3],

$$A_{\text{fs}} = \pi D_p^2(3\eta - 2) \tag{15}$$

Here, η is the cell ratio as defined by Eq. (1). The total drag force $\boldsymbol{F}$ can be calculated by solving the momentum equations for a periodic cubic shape control volume surrounding the unit solid body. Note that due to the periodicity of the flow and the solid structure, the drag force exerted on a unit solid body is equal to the drag force exerted on the walls of a unit-cube cell. Therefore,

$$\boldsymbol{F} = -(\Delta P A_w)(\hat{i} + \hat{j} + \hat{k}) \quad \text{or} \quad |\boldsymbol{F}| = -\sqrt{3}\Delta P A_w \tag{16}$$

Here, ΔP is the cell-based pressure drop and A_w is the pore-window area, which, using Eq. (2), can be determined by the relation

$$A_w = \frac{\pi D_w^2}{4} = \frac{\pi}{4} D_p^2(1 - \eta^2) \tag{17}$$

Due to the complex geometry of the unit solid body (Fig. 4), the definition of the model length-scale d is not clear. For the sake of the generality of the model, d is left as an unknown that is to be determined as a result of the modeling. Using Eqs. (15)–(17), Eq. (14) can be rewritten as

$$-\frac{\Delta P(1 - \eta^2)}{\rho V_{\text{int}}^2(3\eta - 2)} = A\frac{\mu}{\rho V_{\text{int}} d} + B \tag{18}$$

If we define the model normalized length-scale D as

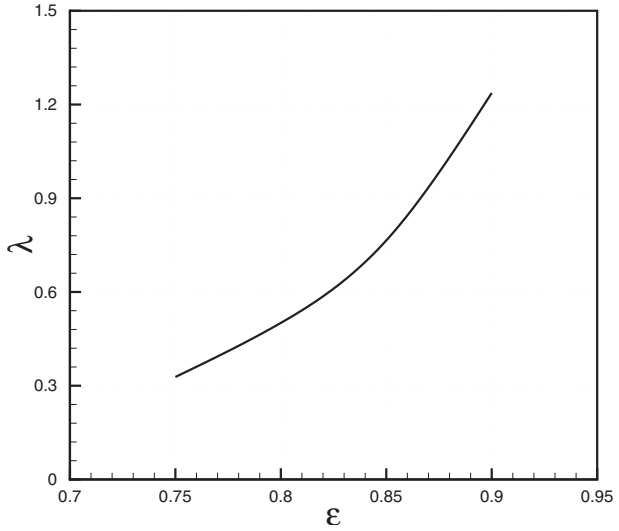

Fig. 5 Variation in the cell passability versus porosity

$$D = \frac{d}{D_p} \tag{19}$$

and the cell passability factor λ as

$$\lambda = \frac{(1 - \eta^2)\varepsilon}{3\eta - 2} \tag{20}$$

we can rewrite Eq. (18) using the definition of the normalized pressure drop (Eq. (12)) to have

$$\Pi_H = \lambda^{-1}\eta A D^{-1} + \lambda^{-1} B\text{Re}_H \tag{21}$$

Therefore,

$$a = \lambda^{-1}\eta A D^{-1} \quad \text{and} \quad b = \lambda^{-1} B \tag{22}$$

Note that the cell passability is a ratio of the pore-window surface area to the fluid-solid interface area of a cell times porosity. As shown in Fig. 5, this factor increases significantly with porosity and thus is directly related to the permeability of the foam. The variation in the inertia coefficient b versus λ^{-1} in Fig. 6(*a*) indicates that B in Eq. (21), the hydraulic model, is in fact a constant with a value of $B = 0.293$.

To complete the hydraulic model, the value of A in Eq. (21) and a closure form for the model normalized length-scale D must still be determined. It is assumed herein that the model normalized length-scale D is a function of the normalized equivalent particle diameter D_E defined as

$$D_E = \frac{6V_s}{D_p A_{\text{fs}}} = \frac{6(1 - \varepsilon)\eta^3}{\pi(3\eta - 2)} \tag{23}$$

Here, V_s is the volume of the unit solid body or the solid-phase volume of the unit-cube cell. The value of $a\lambda\eta^{-1}$ (see Eq. (22)) is plotted versus the normalized equivalent particle diameter D_E in Fig. 6(*b*). A curve fitting process shows that

$$\frac{a\lambda}{\eta} = AD^{-1} = 17.8(D_E)^{-0.44} \tag{24}$$

and therefore,

$$A = 17.8 \quad \text{and} \quad D = (D_E)^{0.44} \tag{25}$$

This equation is a closure for the hydraulic model,

$$\Pi_H = \frac{17.8\eta}{\lambda}(D_E)^{-0.44} + \frac{0.293}{\lambda}\text{Re}_H \tag{26}$$

The predicted pressure loss by this model is within 7% of the pressure loss computed by the numerical solution.

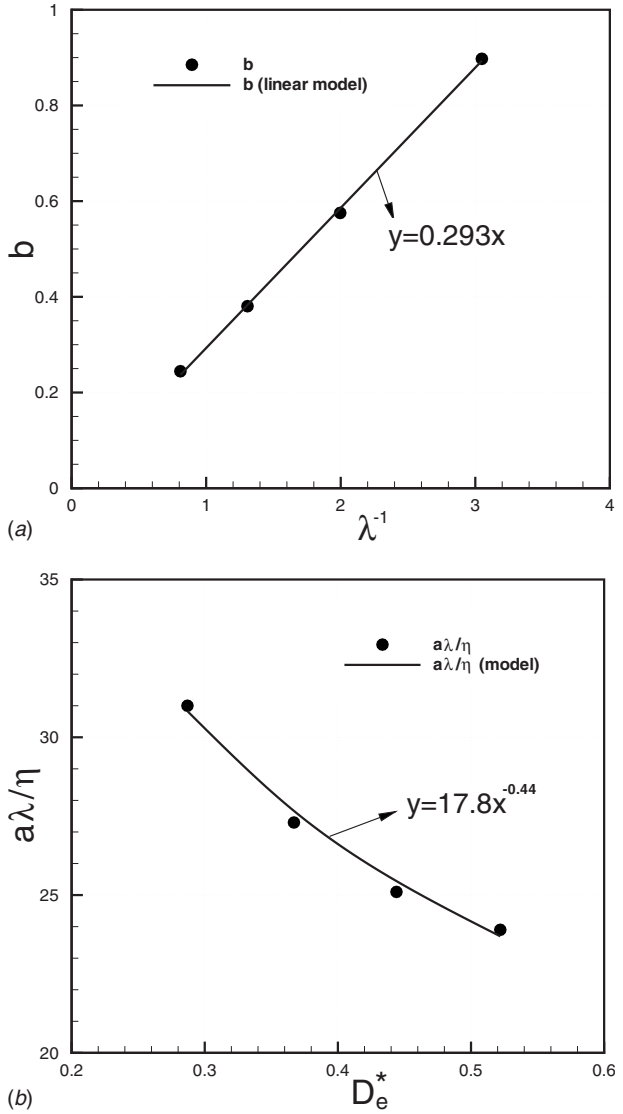

Fig. 6 (*a*) Inertia coefficient and (*b*) the Darcy term for the range of $0.75 \leq \varepsilon \leq 0.90$

5.2 Real Foam Calibrations. Straatman et al. [5] performed experimental measurements of hydraulic loss and convective heat transfer in four different graphitic foam specimens. Table 1 shows the physical properties of the foams tested in Ref. [5]. A higher pressure loss, with a similar trend, compared to that of the numerical simulations performed herein is observed in their measurements. We suggest that it is the effect of the deviations in the internal structure of the real foam from the idealized geometry that is mainly responsible for such higher pressure loss in the real foam. The internal structure of the real foam is not as homogeneous, and the cell windows in the real foam are not as perfectly open as those in idealized SVP foam. To calibrate the idealized hydraulic model, Eq. (26), for a real foam, two calibration parameters are introduced herein: blockage ratio r_β, which reflects the effect of size of the interconnect windows in the real foam, and the size factor δ, which reflects the effect of the inhomogeneity of the real foam on the hydraulic behavior.

Table 1 Summary of properties for the graphitic foam specimens tested in Ref. [5]

Specimen	Porosity (%)	Average pore diameter (μm)
219-3	86	350
219-3-3	88	400
218-3	88	400
POCO™	82	500

For a fixed extrinsic velocity, the pore-level flow rate changes as the pore-window diameter D_w and the cell size H vary (see Eq. (8)). In other words, the pore-level flow "sees" the world outside through the interconnected pore windows. As opposed to the idealized SVP foam, for a given porosity and pore diameter, pores in a real foam can have various pore-window diameters. A smaller pore-window diameter will cause a higher pore-window velocity and thus a higher local shear stress. This effect can be more significant at higher flow rates.

In a flow with an extrinsic velocity of V_{ext}, the average pore-window velocity $\bar{u}_w$ for a real foam with an average pore-window diameter of $\bar{D}_w$ is

$$\bar{u}_w = \frac{4V_{\text{ext}}H^2}{\pi \bar{D}_w^2} \tag{27}$$

If instead of the average pore-window diameter $\bar{D}_w$, the pore-window diameter of an idealized geometry D_w with a similar porosity and pore diameter is used,

$$\bar{u}_w = \frac{4V_{\text{ext},a}H^2}{\pi D_w^2} \tag{28}$$

Here, $V_{\text{ext},a}$ is the artificial extrinsic velocity, i.e., the extrinsic velocity that the pore-level flow in a real foam sees in the framework of the idealized hydraulic model. Hence, this is the extrinsic velocity that must be used in the idealized hydraulic model to predict the hydraulic loss in a real foam. If we define the foam blockage ratio r_β such that

$$1 - r_\beta = \frac{\bar{D}_w}{D_w} \tag{29}$$

using Eqs. (27) and (28),

$$V_{\text{ext},a} = \frac{V_{\text{ext}}}{(1 - r_\beta)^2} \tag{30}$$

$$V_{\text{int},a} = \frac{V_{\text{int}}}{(1 - r_\beta)^2} \tag{31}$$

where $V_{\text{int},a}$ is the artificial intrinsic velocity that must be used in the idealized hydraulic model for a real foam. From Eqs. (30) and (31), we can find the artificial Reynolds number $\text{Re}_{H,a}$ and the artificial normalized pressure drop $\Pi_{H,a}$ as

$$\text{Re}_{H,a} = \frac{\text{Re}_H}{(1 - r_\beta)^2} \tag{32}$$

$$\Pi_{H,a} = \frac{\Pi_H}{(1 - r_\beta)^2} \tag{33}$$

respectively.

For an inhomogeneous foam that has a wide range of pore-window shapes, the shape and the length-scale of the unit solid body are different from those of the idealized SVP foam. Therefore, it is the average solid-body length-scale $\bar{D}$ that must be used in the idealized hydraulic model for a real foam. If we define the foam solid-phase size factor δ as

$$\delta = \frac{\bar{D}}{D} \tag{34}$$

and substitute Eqs. (32)–(34) into Eq. (26), we will have the calibrated hydraulic model for the real foam,

Table 2 Hydraulic model calibration factors calculated for the graphitic foam specimens tested in Ref. [5]

Specimen	Blockage ratio r_β	Solid-phase size factor δ
219-3	60%	0.50
219-3-3	62%	0.53
218-3	52%	0.44
POCO™	49%	0.56

$$\Pi_H = \frac{17.8\,\eta}{\lambda\,\delta(1-r_\beta)^2}(D_E)^{-0.44} + \frac{0.293}{\lambda(1-r_\beta)^4}\mathrm{Re}_H \tag{35}$$

The two calibration factors, i.e., foam blockage ratio r_β and foam solid-phase size factor δ, vary for different graphitic foams. These two factors indicate how close the internal structure of a GF is to that of the idealized SVP foam. For an idealized geometry, $r_\beta=0.0$ and $\delta=1.0$. Table 2 shows the calibration factors calculated for the foams tested in Ref. [5]. Graphitic foams with a larger pore diameter and porosity have a slightly smaller blockage ratio and a closer solid-phase length-scale to that of the idealized SVP foam. Figure 7 compares the pressure drop predicted by calibrated models to the experimental measurements of Straatman et al. [5]. The predicted pressure drops are within 10% of that of the experimental measurement. The largest deviations appear in very low Reynolds numbers, where the uncertainty of both experimental measurements and numerical calculations could be relatively high.

While higher pressure drop, as seen in real foams, would seem to indicate a larger solid-phase length-scale, in reality, the solid-phase size factor δ appears to be smaller than 1. This is basically because a smaller pore window indicates thicker ligaments, more uniform local mass distribution, and less mass concentration where the ligaments interconnect, whereas the unit solid-body geometry shown in Fig. 4 can be characterized by ligaments with less thickness in the middle and more mass concentration at the two ends. A more uniform mass distribution in real foams, on one hand, means a smaller size of concentrated mass (solid body) and, therefore, a smaller length-scale in the framework of a solid-body drag model, which can be interpreted to a smaller solid-phase size factor. On the other hand, it indicates smaller openings in the internal structure of the foam, which is predicted by a larger blockage ratio.

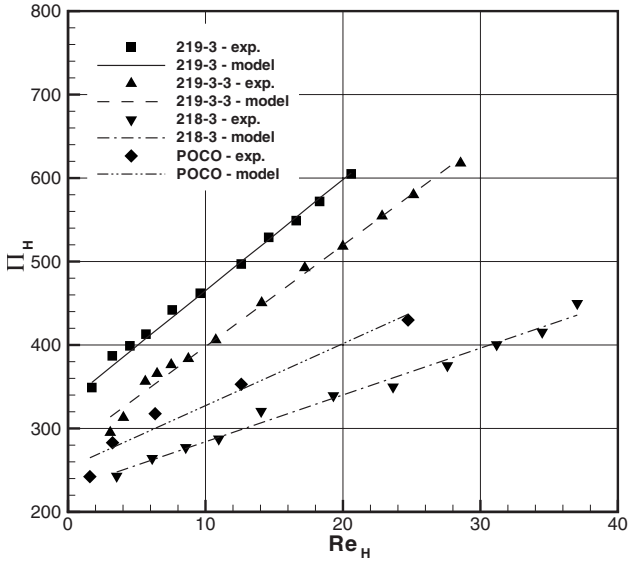

Fig. 7 Normalized pressure drop Π_H versus cell-based Reynolds number Re_H for real foams: experimental measurements compared to the calibrated model

6 Convective Heat Transfer Model

For fully developed flow in a homogeneous porous media, the value of the pore-level convective heat transfer coefficient is independent of the size of the porous medium [9]. The cell-based convective heat transfer coefficient for periodic flow in a cell, $\bar{h}_c$, is calculated herein based on the logarithmic temperature difference [18]. This coefficient is calculated under thermal nonequilibrium conditions [9] and, as defined in Ref. [14], for a constant wall-temperature condition. For the thermal nonequilibrium condition to prevail, only the results of the simulations for flow with high Peclet numbers ($\mathrm{Pe}\gg 1$) are considered. Moreover, the model has an asymptotic term that provides more flexibility to the model in order to cover a wider range of geometry and flow parameters.

6.1 Nonzero Asymptotic Heat Transfer Model. Similar to the model length-scale d described in Sec. 5, it is assumed here that the model length-scale d is an unknown that is to be determined as a result of modeling. Therefore, the pore-level Nusselt number Nu_d is defined as

$$\mathrm{Nu}_d = \frac{\bar{h}_c d}{k} = \mathrm{Nu}_H \frac{D}{\eta} \tag{36}$$

where k is the heat diffusion coefficient of the fluid and $D = d/D_p$. Similarly, the pore-level Reynolds number Re_d is defined as

$$\mathrm{Re}_d = \mathrm{Re}_H \frac{D}{\eta} \tag{37}$$

where Re_H is the cell-based Reynolds number defined by Eq. (9). A general form of the Nusselt number as a function of the Prandtl number, the Reynolds number, and the pore structure can be defined as

$$\mathrm{Nu}_d = \mathrm{Pr}^m[a + b\mathrm{Pr}^n\mathrm{Re}_d^s] \tag{38}$$

Here, Pr is the fluid Prandtl number, a and b are model constants, m and n describe the exponential dependence of the model to the fluid type, and s indicates the exponential dependence of the model to the flow regime. The first term in the right-hand side of the model shows the asymptotic behavior of the model at very low Peclet numbers and covers the molecular diffusion at the pore level. Substituting Eqs. (36) and (37) into Eq. (38) results in the general form of the model,

$$\mathrm{Nu}_H = a\left(\frac{D}{\eta}\right)^{-1}\mathrm{Pr}^m\left[1 + \frac{b}{a}\left(\frac{D}{\eta}\right)^s \mathrm{Pr}^n\mathrm{Re}_H^s\right] \tag{39}$$

It is our goal herein to determine the constants a and b, the exponents m, n, and s, as well as the form of the function for the model normalized length-scale $D(\varepsilon)$ in the above model.

In Fig. 8, the variation in the cell-based Nusselt number Nu_H with the cell-based Reynolds number Re_H is shown for the case of Freon-12 and the range of porosities $0.75 \le \varepsilon \le 0.90$. A curve fitting process on the resulting data for the three fluids of air, Freon-12, and water shows that a model with parameters $m=0.130$, $n=0.114$, and $s=0.6$ is an optimum selection with a maximum deviation of 6.08% from the simulation data.

In order to determine the values for the constants a and b and the form of the model normalized length-scale function $D(\varepsilon)$, let us assume a general form for the normalized length-scale D based on the normalized equivalent particle diameter D_E,

$$D = D_E^t \tag{40}$$

Moreover, let us define model parameters $X(\varepsilon)$ and $Y(\varepsilon)$ as

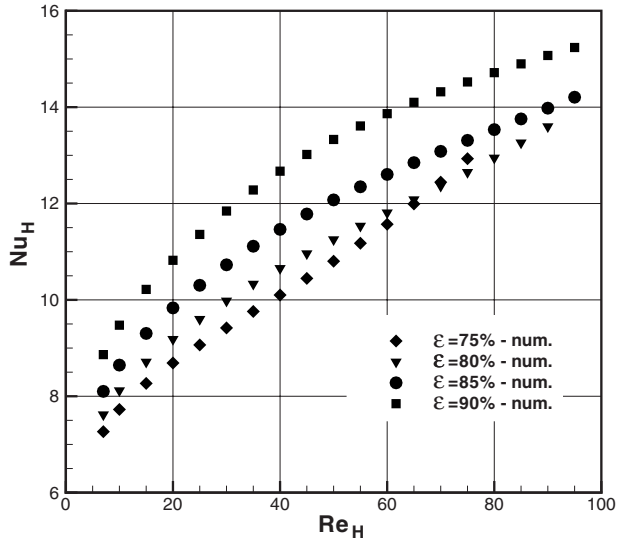

Fig. 8 Variation in the cell-based Nusselt number Nu_H versus cell-based Reynolds number Re_H for the range of $0.75 \leq \varepsilon \leq 0.90$

$$X(\varepsilon) = a\left(\frac{D}{\eta}\right)^{-1} = a\,\eta D_E^{-t} \tag{41}$$

and

$$Y(\varepsilon) = \frac{b}{a}\left(\frac{D}{\eta}\right)^{s} = \frac{b}{a}\,\eta^{-0.6} D_E^{0.6t} \tag{42}$$

respectively. Curve fittings shown in Figs. 9(*a*) and 9(*b*) indicate that $a=3.23$, $b=0.282$, and $t=0.716$. This closes the convective heat transfer model,

$$\mathrm{Nu}_H = 3.23\,\eta D^{-1}\mathrm{Pr}^{0.130} + 0.282\,\eta^{0.4} D^{-0.4}\mathrm{Pr}^{0.244}\mathrm{Re}_H^{0.6} \tag{43}$$

where $D=D_E^{0.716}$. In Fig. 10, the above model (solid line) is compared to the simulation data for the case of Freon-12.

6.2 Real Foam Calibrations. Similar methodology used in Sec. 5.2 can be implemented here to calibrate the idealized heat transfer model for a real foam. In addition to the parameters introduced in Sec. 5.2, it is necessary to introduce a new parameter to characterize the accessibility of the internal surface of the real foam compared to that of the idealized geometry. Due to the variation in pore-window diameter in real foams, the fluid-solid interface of the pores are not uniformly and equally accessible to the fluid flow. In many cases, a large portion of the internal surface of a real foam is not accessible to the fluid flow. This deficiency has a significant effect on the size of the pore-level length-scale. If the actual accessible internal surface area of a real $\bar{A}_{\mathrm{fs}}$ is used in the definition of the cell-based Nusselt number, we will have the average Nusselt number of the foam $\overline{\mathrm{Nu}}_H$. The average Nusselt number of the foam in the framework of the idealized geometry can be viewed as

$$\overline{\mathrm{Nu}}_H = \alpha^{-1}\mathrm{Nu}_H \tag{44}$$

where the foam accessibility factor α is defined as

$$\alpha = \frac{\bar{A}_{\mathrm{fs}}}{A_{\mathrm{fs}}} \tag{45}$$

The accessibility factor of a foam indicates the accessibility of the internal surface area of the foam to the fluid flow and its effectiveness in exchanging heat between the solid and fluid phases compared to the idealized SVP foam. For a real foam, it is the average Nusselt number $\overline{\mathrm{Nu}}_H$ that must be used together with

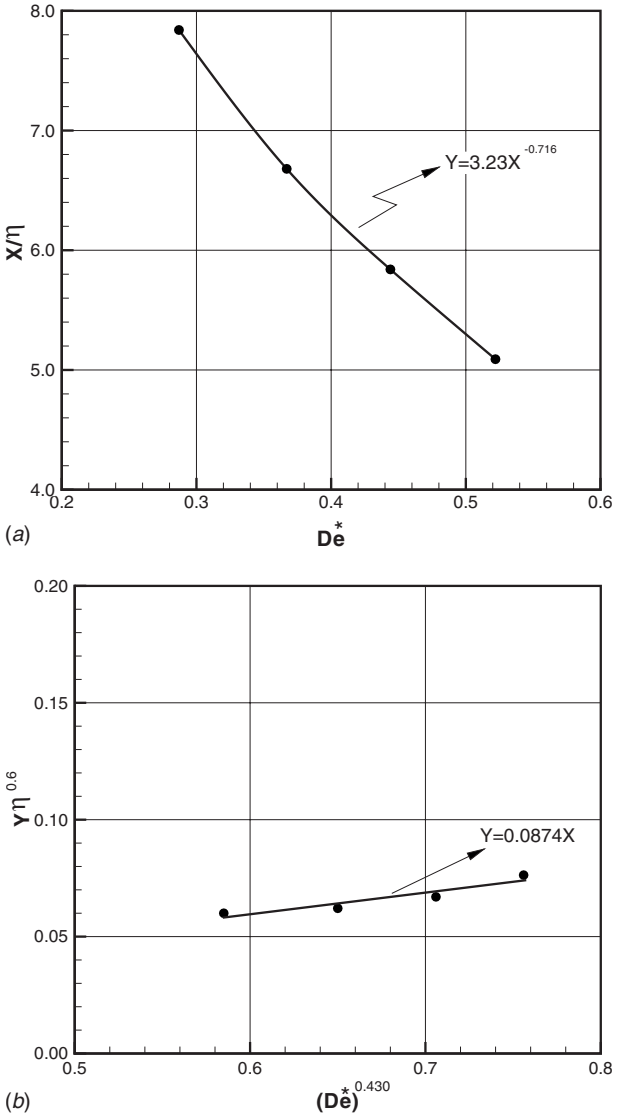

Fig. 9 Plot of heat transfer model parameters, (*a*) $X(\varepsilon)$ and (*b*) $Y(\varepsilon)$, versus the normalized equivalent particle diameter D_E

the average normalized length-scale $\bar{D}$ and the artificial Reynolds number $\mathrm{Re}_{H,a}$ in the heat transfer model of Eq. (43),

$$\overline{\mathrm{Nu}}_H = 3.23\,\eta\bar{D}^{(-1)}\mathrm{Pr}^{0.130} + 0.282\,\eta^{0.4}\bar{D}^{(-0.4)}\mathrm{Pr}^{0.244}\mathrm{Re}_{H,a}^{0.6} \tag{46}$$

By substituting Eqs. (32), (34), and (44) in Eq. (46), the heat transfer model for the real foam, in the framework of the idealized geometry, is obtained,

$$\mathrm{Nu}_H = 3.23\alpha\eta(\delta D)^{(-1)}\mathrm{Pr}^{0.130} + 0.282\alpha\eta^{0.4}(\delta D)^{(-0.4)}\mathrm{Pr}^{0.244}\left[\frac{\mathrm{Re}_H}{(1-r_\beta)^2}\right]^{0.6} \tag{47}$$

where $D=D_E^{0.716}$. The blockage ratio r_β of a foam is a 0 structural property that does not vary from the hydraulic model to the heat transfer model. The solid-phase size factor δ, on the other hand, is a parameter that varies with the length-scale of the model. Therefore, it is different in the hydraulic and heat transfer models.

Table 3 shows the solid-phase size factor δ and the accessibility factor α of the graphitic foams, determined using a curve fitting shown in Fig. 11 on the experimental measurements of Straatman et al. [5]. One of the factors contributing to the significant difference between experimental measurements and the idealized heat

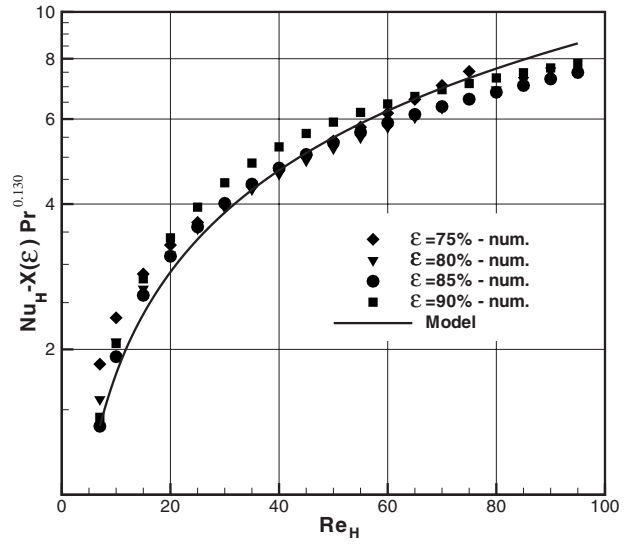

Fig. 10 Convective heat transfer model compared to the results of simulations for the case of Freon-12 and the range of porosity $0.75 \leq \varepsilon \leq 0.90$

transfer model, leading to relatively large solid-phase size factors and extremely low accessibility, is the fact that the experimental measurements are performed in relatively low Reynolds number flow regimes ($1.6 < \mathrm{Re}_H < 33.5$). As mentioned in Ref. [9], the uncertainty of experimental measurements, as well as the numerical computations, of heat transfer increases as the Reynolds number decreases. Moreover, the accuracy of the idealized model in low Reynolds numbers depends highly on the accuracy of the extrapolated asymptotic term. This also contributes to the high uncertainty.

Table 3 Heat transfer model calibration factors calculated for the graphitic foam specimens tested in Ref. [5]

Specimen	Solid-phase size factor δ	Accessibility factor α
219-3	17.5	4.9%
219-3-3	6.74	4.5%
218-3	13.7	3.9%
POCO™	4.75	3.0%

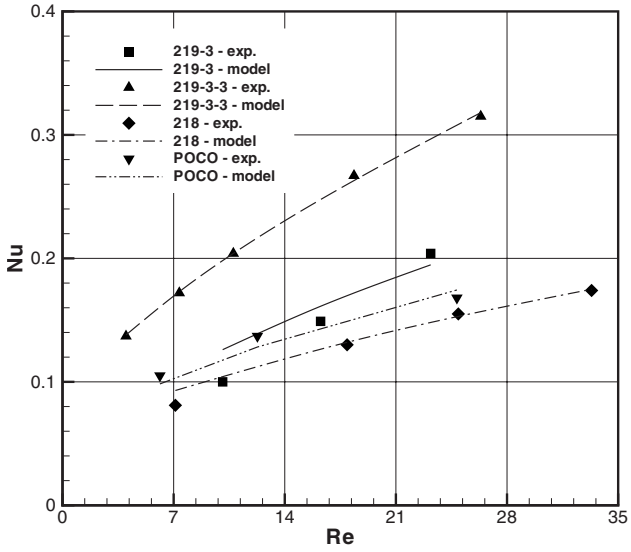

Fig. 11 Cell-based Nusselt number Nu_H versus cell-based Reynolds number Re_H for real foams: experimental measurements compared to the calibrated model

Nevertheless, a large size factor in real foams indicates that the internal surface of several large portions of the real foam is not effectively accessible to the thermofluid flow, and, therefore, these portions of the foam are "seen" as a solid lump by the thermofluid flow. This is consistent with a very low accessibility in the real foam. While an extremely low accessibility means that a significant portion of the internal surface of the foam is not "effectively" accessible to the flow, it should not necessarily be interpreted as an extremely large amount of physically inaccessible internal surface of the foam. There are many other factors in the real foam that can cause low accessibility, such as the distance of the accessible internal surface from the heat source/sink and the local effective conductivity of the foam. In other words, when a physical irregularity appears in a real foam, it can cause many forms of deficiency: closed interconnect pore windows, large hollow volumes inaccessible to the flow that can act as an insulator with nearly zero local effective conductivity, etc. Moreover, the distance of such irregularities to the heat source/sink can have a significant impact on the accuracy of the model used for equivalent microfin efficiency (see Ref. [5] for more details on this factor). In such cases, heat is forced to travel a much longer path to be removed by the fluid flow. Therefore, a relatively small local physical irregularity can have a much larger influence on the heat transfer process, which is reflected by the accessibility factor.

7 Thermal Dispersion

As a part of thermal closure model, thermal dispersion is often used as an augmentation to the macroscopic, convective, and/or conductive heat transfer. Thermal dispersion is a numerical artifact that results from performing the volume averaging operation over the conservation equations. Using the dispersion-particle-based model [16], the steady-state volume-averaged energy equations for solid and liquid phases in a periodic geometry can be written as

$$\boldsymbol{u}_{\mathrm{int}} \cdot \nabla \langle T \rangle^f = (\vec{\vec{D}}_f + \alpha \vec{\vec{I}}) : \nabla\nabla \langle T \rangle^f + \frac{A_{\mathrm{fs}} h_{\mathrm{sf}}}{\rho C_p \forall_f} (T_{\mathrm{sf}} - \langle T \rangle^f) \quad (48)$$

$$0 = \alpha_s \nabla^2 T_s \quad (49)$$

$$-k_s \nabla T_s = h_{\mathrm{sf}} (T_{\mathrm{sf}} - \langle T \rangle^f) \quad \text{on} \quad A_{\mathrm{fs}} \quad (50)$$

Here $\boldsymbol{u}_{\mathrm{int}}$ is the intrinsic velocity vector,

$$\vec{u}_{\mathrm{int}} = \frac{\sqrt{3}}{3} V_{\mathrm{int}} \hat{i} + \frac{\sqrt{3}}{3} V_{\mathrm{int}} \hat{j} + \frac{\sqrt{3}}{3} V_{\mathrm{int}} \hat{k} \quad (51)$$

and V_{int} is the intrinsic velocity, $\langle T \rangle^f$ is the fluid volume-averaged temperature, $\vec{\vec{D}}_f$ is the flow thermal dispersion, A_{fs} is the internal surface area, h_{sf} is the interstitial heat transfer coefficient, which is determined by the convective heat transfer model (Eq. (43)), $\forall_f$ is the unit-cell fluid volume, $\forall_f = \varepsilon H^3$, T_{sf} is the wall temperature, α_s is the solid-phase diffusivity, k_s is the solid-phase conductivity, T_s is the solid-phase temperature, and $\nabla \langle T \rangle^f$ is determined by [16]

$$\nabla \langle T \rangle^f = \int_{A_e} T \hat{n} dS \quad (52)$$

where the integral is over the inflow and outflow windows of a unit-cube cell (A_e), $\hat{n}$ is the surface unit normal vector, and dS is the surface differential.

For a unit-cube cell of a size of hundreds of micrometers, with high solid-phase conductivity, it is suitable to assume that the variation in temperature in the solid phase is insignificant compared to that in the fluid phase,

$$\nabla T_s \ll \nabla T_f \tag{53}$$

Therefore, for periodic thermofluid flow in a unit-cube cell, the energy equations can be reduced to

$$\boldsymbol{u}_{\text{int}} \cdot \nabla \langle T \rangle^f = (\overleftrightarrow{D}_f + \alpha \overleftrightarrow{I}) : \nabla\nabla \langle T \rangle^f + \frac{A_{\text{fs}} h_{\text{sf}}}{\rho C_p \forall_f} (T_{\text{sf}} - \langle T \rangle^f) \tag{54}$$

$$T_s = T_{\text{sf}} \tag{55}$$

For a periodic flow with equal velocity components in all directions,

$$\nabla \langle T \rangle^f = \begin{bmatrix} \acute{\text{T}} \\ \acute{\text{T}} \\ \acute{\text{T}} \end{bmatrix} \quad \text{and} \quad \nabla\nabla \langle T \rangle^f = \begin{bmatrix} \acute{\acute{\text{T}}} & \acute{\acute{\text{T}}} & \acute{\acute{\text{T}}} \\ \acute{\acute{\text{T}}} & \acute{\acute{\text{T}}} & \acute{\acute{\text{T}}} \\ \acute{\acute{\text{T}}} & \acute{\acute{\text{T}}} & \acute{\acute{\text{T}}} \end{bmatrix} \tag{56}$$

It is customary, however, to select a coordinate system with its X axis along the flow direction. The following transformation matrix is used to transform the volume-averaged variables into a coordinate system of a unidirectional flow field:

$$\begin{bmatrix} \frac{\sqrt{3}}{3} & \frac{\sqrt{3}}{3} & \frac{\sqrt{3}}{3} \\ \frac{\sqrt{12}+6}{12} & \frac{\sqrt{12}-6}{12} & -\frac{2\sqrt{12}}{12} \\ -\frac{\sqrt{12}+6}{12} & -\frac{\sqrt{12}-6}{12} & \frac{2\sqrt{12}}{12} \end{bmatrix} \tag{57}$$

We also assume that in a coordinate system with its X axis parallel to the flow direction, the thermal dispersion tensor is diagonal, i.e., $\overleftrightarrow{D}_f = D_{\parallel} \overleftrightarrow{I}$. The velocity field in this coordinate system is

$$\vec{u}_{\text{int}} = V_{\text{int}} \hat{i} \tag{58}$$

and the gradient and Hessian of the volume-averaged temperature for a unit-cube cell are expressed as

$$\nabla \langle T \rangle^f = \sqrt{3} \acute{\text{T}} \hat{i} \tag{59}$$

$$\nabla\nabla \langle T \rangle^f = \sqrt{3} \acute{\acute{\text{T}}} (\hat{i}\hat{i} + \hat{i}\hat{j} + \hat{i}\hat{k}) \tag{60}$$

In the new coordinate system, the volume-averaged energy equation is

$$V_{\text{int}} \partial_x \langle T \rangle^f = (D_{\parallel} + \alpha_f) \partial_x \partial_x \langle T \rangle^f + \frac{A_{\text{fs}} h_{\text{sf}}}{\rho C_p \forall_f} (T_{\text{sf}} - \langle T \rangle^f) \tag{61}$$

The goal herein is to solve Eq. (61) for $D_{\parallel}$ using the results of simulations.

The results of the simulation for the range of porosities $0.75 \leq \varepsilon \leq 0.90$ and for two fluids of water and Freon-12 are used to study the effect of the fluid type and pore-level structure of thermal dispersion. Having $\langle T \rangle^f$, $\nabla \langle T \rangle^f$, and $\nabla\nabla \langle T \rangle^f$ for a unit-cube cell, Eq. (61) is solved for $D_{\parallel}$. Figure 12 illustrates the variation in normalized thermal dispersion $D_{\parallel}/\alpha_f$ with pore-level Reynolds number for the upper and lower limits of porosity.

In most works, such as that of Calmidi and Mahajan [8], the thermal dispersion is modeled as a linear function of the Peclet number. However, it can be seen in Fig. 12 that starting from a model for the interstitial heat transfer for SVP foams based on the log-mean temperature [9,14], a linear function is not a suitable approximation for GF with low porosity. Furthermore, Fig. 12(*b*) indicates that a linear model, as suggested for reticulated metals by Calmidi and Mahajan [7,8], can predict the thermal dispersion in high-porosity GF, where the structure of the foam is more similar to that of low-porosity reticulated metals. For lower-porosity foams, it may be necessary to adopt the approach of Nakayama et al. [19], wherein an additional transport equation is solved for a dynamic coefficient relating the local fluctuating temperature to the volume-averaged temperature gradient.

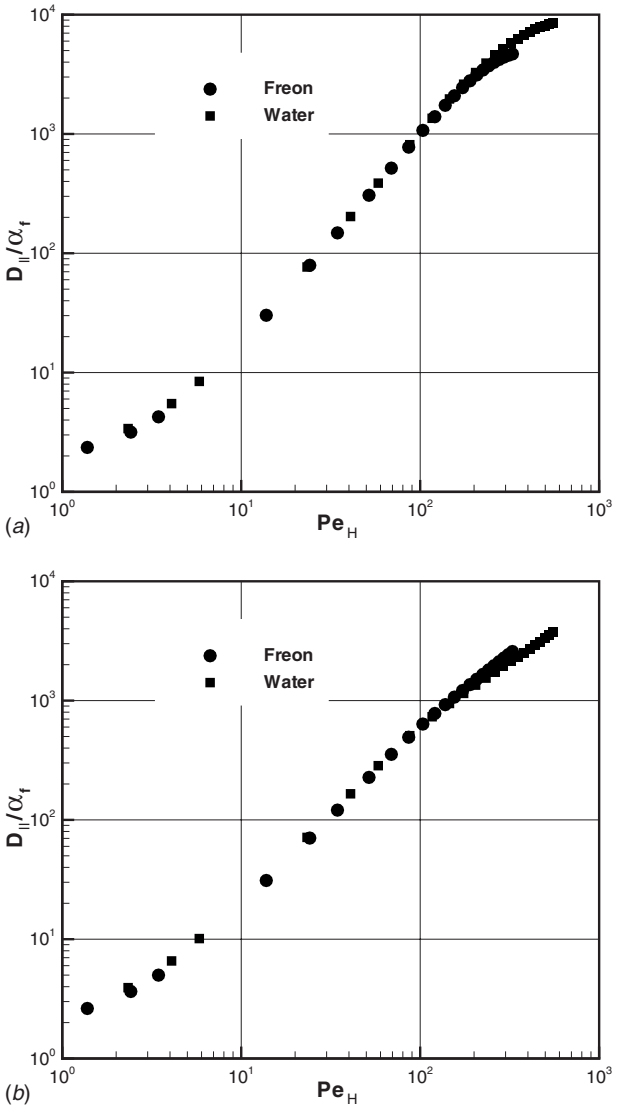

Fig. 12 Normalized thermal dispersion $D_{\parallel}/\alpha_f$ versus pore-level Reynolds number Re_H: (*a*) $\varepsilon = 0.75$ and (*b*) $\varepsilon = 0.90$

8 Summary

A set of simulations of the multidirectional pore-level thermofluid flow in spherical-void-phase porous media has been carried out to better understand the hydraulic and thermal behavior of the flow. A flow field with equal intrinsic velocity components in all directions is assumed in the simulations to represent a statistically average orientation of the flow with respect to the pore windows in a real foam.

A permeability model was developed for the interconnected spherical void geometry based on a solid-body drag formulation, and a nonlinear extension was added to the model for high inertia flow regimes. The resulting model is within 7% of the measurements of the numerical simulations. By introducing two calibration factors, the foam blockage ratio r_β and the solid-phase size factor δ, the hydraulic model was calibrated using the available experimental data of graphitic foams [5].

The pore-level Nusselt number for a cell was calculated based on the log-mean temperature difference. A nonzero asymptotic convective heat transfer model was developed, where the nonzero

asymptote represents the conduction heat transfer at very low speed flow regimes. The resulting model is within 6.5% of the numerical measurements for the range of fluid flow parameters and porosity considered. An additional calibration parameter, the foam accessibility factor α, was introduced to calibrate the model for real foams. The calibration process showed that real GF has extremely low accessibility and large solid-phase size factor compared to the ideal geometry model, which is likely due to the presence of inaccessible chunks of foam near the heat source/sink in the measured specimens.

The results of the simulations were also used to determine a thermal dispersion matrix based on the volume-averaged energy equation for the consecutive cells in each direction. A complex behavior was observed for the thermal dispersion in SVP foams. This suggests that a simple linear model based on the Peclet number, as proposed by others for highly porous metal foams (e.g., see Ref. [8]), cannot accurately predict the thermal dispersion behavior in SVP foams.

Acknowledgment

The authors gratefully acknowledge the financial support from the Natural Sciences and Engineering Research Council of Canada (NSERC) and from SHARCNET. The authors would like to thank Lee Betchen for his helpful discussions in thermal dispersion.

References

[1] Klett, W., Hardy, R., Romine, E., Walls, C., and Burchell, T., 2000, "High-Thermal Conductivity, Mesophase-Pitch-Derived Carbon Foam: Effect of Precursor on Structure and Properties," Carbon, **38**, pp. 953–973.

[2] Gallego, C., and Klett, W., 2003, "Carbon Foams for Thermal Managements," Carbon, **41**, pp. 1461–1466.

[3] Yu, Q., Thompson, B. E., and Straatman, A. G., 2006, "A Unit Cube-Based Model for Heat Transfer and Fluid Flow in Porous Carbon Foam," ASME J. Heat Transfer, **128**, pp. 352–360.

[4] Straatman, A. G., Gallego, N. C., Thompson, B. E., and Hangan, H., 2006, "Thermal Characterization of Porous Carbon Foam—Convection in Parallel Flow," Int. J. Heat Mass Transfer, **49**, pp. 1991–1998.

[5] Straatman, A. G., Gallego, N. C., Yu, Q., Betchen, L., and Thompson, B. E., 2007, "Forced Convection Heat Transfer and Hydraulic Losses in Graphitic Foam," ASME J. Heat Transfer, **129**(9), pp. 1237–1245.

[6] Betchen, L., Straatman, A. G., and Thompson, B. E., 2006, "A Nonequilibrium Finite-Volume Model for Conjugate Fluid/Porous/Solid Domains," Numer. Heat Transfer, Part A, **49**, pp. 543–565.

[7] Calmidi, V., and Mahajan, R., 1999, "The Effective Thermal Conductivity of High Porosity Fibrous Metal Foam," ASME J. Heat Transfer, **121**, pp. 466–471.

[8] Calmidi, V., and Mahajan, R., 2000, "Forced Convection in High Porosity Metal Foams," ASME J. Heat Transfer, **122**, pp. 557–565.

[9] Karimian, S. A. M., and Straatman, A. G., 2008, "CFD Study of the Hydraulic and Thermal Behavior of Spherical-Void-Phase Porous Materials," Int. J. Heat Fluid Flow, **29**(1), pp. 292–305.

[10] Karimian, S. A. M., 2006. "Computational Modeling of the Flow and Heat Transfer in an Idealized Porous Metal," Ph.D. thesis, The University of Western Ontario, London, ON, Canada.

[11] Karimian, S. A. M., and Straatman, A. G., 2006, "Discretization and Parallel Performance of an Unstructured Finite Volume Navier–Stokes Solver," Int. J. Numer. Methods Fluids, **52**(6), pp. 591–615.

[12] Balay, S., Buschelman, K., Eijkhout, V., Gropp, W. D., Kaushik, D., Knepley, M. G., McInnes, L. C., Smith, B. F., and Zhang, H., 2004, PETSc Users Manual, Revision 2.1.5, Argonne National Laboratory, Technical Report No. ANL-95/11.

[13] Khosla, P. K., and Rubin, S. G., 1974, "A Diagonally Dominant Second-Order Accurate Implicit Scheme," Comput. Fluids, **2**, pp. 207–209.

[14] Karimian, S. A. M., and Straatman, A. G., 2007, "A Thermal Periodic Boundary Condition for Heating and Cooling Processes," Int. J. Heat Fluid Flow, **28**, pp. 329–339.

[15] SHARCNET, 2006, http://www.sharcnet.ca

[16] Kaviany, M., 1999, *Principles of Heat Transfer in Porous Media*, 2nd ed., Springer, New York.

[17] Fourie, J. G., and Du Plessis, J. P., 2002, "Pressure Drop Modeling in Cellular Metallic Foams," Chem. Eng. Sci., **57**, pp. 2781–2789.

[18] Incropera, F. P., and DeWitt, D. P., 2002, *Fundamentals of Heat and Mass Transfer*, 5th ed., Wiley, New York.

[19] Nakayama, A., Kuwahara, F., and Kodama, Y., 2006, "An Equation for Thermal Dispersion Flux Transport and Its Mathematical Modeling for Heat and Fluid Flow in a Porous Medium," J. Fluid Mech., **563**, pp. 81–96.

Zhenjin Zhu
Department of Mechanical & Industrial Engineering,
University of Toronto,
Toronto, ON, M5S 3G8, Canada
e-mail: zjzhu@mie.utoronto.ca

Jin Ho Zong
Department of Materials, Mechanical & Automation Engineering,
Yanbian University of Science & Technology,
Yanji, Jilin, P. R. China 133000
e-mail: zongyust@gmail.com

Chul B. Park[1]
Department of Mechanical & Industrial Engineering,
University of Toronto,
Toronto, ON, M5S 3G8, Canada
e-mail: park@mie.utoronto.ca

Manoj Choudhary
Owens Corning,
2790 Columbus Road,
Route 16,
Granville, OH 43023
e-mail: manoj.choudhary@owenscorning.com

Effect of Loss of Blowing Agents on Thermal Insulation Properties of Polystyrene Foams

This paper presents a numerical study to characterize the effect of loss of blowing agents on the thermal insulation properties of polystyrene foams. In this study, a transient cell-to-cell diffusion model is developed to predict the loss of the blowing agents. The Mie theory is used to quantify the radiative conductivity. A cubic-series-parallel approach in analogy with electric circuits is employed to acquire the thermal conductivity of the gas-polymer matrix. The effects of foam morphology and blowing agent type on the loss of blowing agents and the resulting thermal insulation properties of polystyrene foams are examined. [DOI: 10.1115/1.3013830]

Keywords: thermal insulation properties, polystyrene foams, loss of blowing agents, radiative conductivity, cell-to-cell diffusion

1 Introduction

Polymeric foams are often used for thermal insulation [1]. The blowing agent with high insulating property can be well retained in the insulation foam through controlling the melt and die temperature properly during the manufacturing process [2–4]. Nevertheless, over time, the blowing agent initially retained in the voids will effuse whereas the surrounding gas will infuse. Apparently, the loss of blowing agent with lower thermal conductivity will diminish the thermal insulation capacity of the polymeric foams and furthermore, may contribute to stratospheric ozone depletion. To reduce insulation costs and improve energy efficiency, it is essential to understand the variation in thermal insulation properties of polymeric foams as the blowing agent decays. Therefore, this paper conducts a numerical study to elucidate the loss of blowing agents in polystyrene foams and then estimates the resulting thermal insulation properties. The estimated data are compared to the published experimental data [5].

Skochdopole demonstrated that the effect of free convection within cells was negligible for cells under 4 mm in diameter [6]. Hence, the thermal conductivity of fine-celled foams consists mainly of conduction through the polymer matrix and conduction through the gas inside the cells and thermal radiation. The gaseous conductivity depends on the composition of the trapped gas, which varies with time due to the infusion of atmospheric gases and effusion of the blowing agent. The solid and radiative conductivities depend on the cellular structure of the foam. Consequently, both the gas components in each cell and the cell morphology govern the thermal insulation properties of the foam.

Thermal transport inside polymeric foams was studied by Vo and Paquet [5], Booth [7], Biedermann et al. [8], Wu et al. [9], Ostrogorsky et al. [10], Leach [11], Caps et al. [12], Tseng et al. [13], Wong and Hung [14], and Coquard and Baillis [15]. The radiative transfer of polymeric foams was investigated by Glicksman et al. [16], Kuhn et al. [17], and Doermann and Sacadura [18]. Effusion of blowing agents from polymeric foams was researched by Yang and Lee [19], Pilon et al. [20], Briscoe and Savvas [21], Alsoy [22], Booth et al. [23], Bhattacharjee et al. [24], Shankland [25], Tant and Wilkes [26], Ruiz-Herrero et al. [27], Quoc et al. [28], Griffiths et al. [29], Takeno et al. [30], Hanssen [31], and Gandel'sman et al. [32]. In addition, relevant research in metallic foams and glass foams has been conducted by Varady and Fedorov [33], Krishnan et al. [34], Ghosh [35], Chen and Jaluria [36], Liu and Liu [37], and An et al. [38]. Nevertheless, few publications have synthesized these three topics by predicting the thermal insulation properties of polymeric foams with the loss of blowing agents.

In this paper, a theoretical model is developed to characterize the thermal insulation performance of polystyrene foams with loss of physical foaming agents. For the determination of radiative conductivity, each cell is considered to be a pentagonal dodecahedron consisting of plateau borders and cell walls. The Mie theory is used to quantify the extinction and scattering of each single plateau border and cell wall, and then the results are extended to the entire foam morphology. To determine the loss of blowing agents, a transient cell-to-cell diffusion model is developed, which assumes that the polymeric foams are made up of stacked and juxtaposed cubic unit cells. A cubic-series-parallel approach in analogy with electric circuits is applied to estimate the thermal conductivity of gas-polymer matrix. As a result, the thermal insulation properties of the polymeric foams with the loss of blowing agent can be understood.

2 Modeling and Methodology

Based on the law of conservation of energy, the total heat flux through the polymeric foam is equal to the sum of the radiative heat flux and conductive heat flux. Radiative heat flux can be

[1]Corresponding author.

Contributed by the Heat Transfer Division of ASME for publication in the JOURNAL OF HEAT TRANSFER. Manuscript received February 8, 2008; final manuscript received September 22, 2008; published online March 19, 2009. Review conducted by Jamal Seyed-Yagoobi.

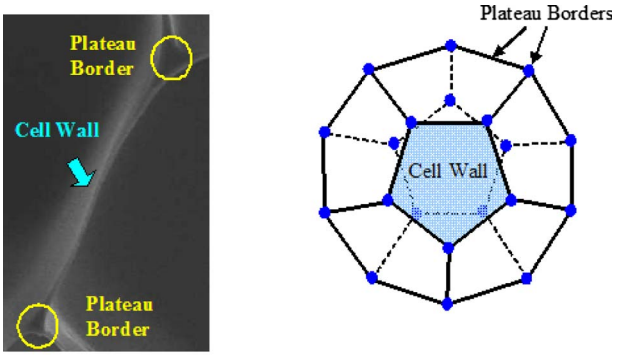

(*a*) (*b*)

Fig. 1 Plateau borders and cell walls. (*a*) SEM picture and (*b*) a pentagonal, dodecahedral cell.

described by an integrodifferential equation, which reduces to a diffusive equation for optically thick media [39]. The conductive heat flux can be determined by using Fourier's law. Thus, the total thermal conductivity of the polymeric foam is equal to the radiative conductivity plus the thermal conductivity of gas-polymer matrix.

2.1 Radiative Conductivity of Polymeric Foam. The radiative conductivity is approximated using the Rosseland equation. The Rosseland mean extinction coefficient $K_{e,R}$ is given by

$$\frac{1}{K_{e,R}} = \int_0^\infty \frac{1}{K_{e,\lambda}} \frac{\partial e_{b,\lambda}}{\partial e_b} d\lambda \tag{1}$$

where $e_{b,\lambda}$ is the spectral blackbody emissive power, e_b is the blackbody emissive power, and $K_{e,\lambda}$ is the spectral extinction coefficient. The spectral blackbody emissive power is determined using Planck's law, and the blackbody emissive power is calculated from the Stefan–Boltzmann equation [40].

The solid polymer matrix in the foam is composed of cell walls and plateau borders. As demonstrated in Fig. 1(*a*), the plateau borders, i.e., the junction parts among multiple cells, present a triangular shape. Therefore, the real 3D plateau borders could be either tetrahedral or prismatic, depending on the number of surrounding cells. To determine the spectral extinction coefficient using the Mie theory, this paper approximated each tetrahedral border to be a sphere. Moreover, each prismatic border was first divided into three parts, and then the separated parts were integrated with the neighboring cell walls. The contribution of the prismatic borders on thermal radiation would be included in the cell walls. That is, the polymer matrix was simplified to consist of cell walls and spherical borders, which are schematically diagrammed in Fig. 1(*b*). Hence, the spectral extinction coefficient of the foam can be obtained by combining the effects of the two geometrical structures weighted using the border fraction. Namely,

$$K_{e,\lambda} = f_b K_{\text{borders},\lambda} + (1 - f_b) K_{\text{walls},\lambda} \tag{2}$$

where $k_{\text{border},\lambda}$ symbolizes the weighted border extinction coefficient, $k_{\text{walls},\lambda}$ represents the weighted wall extinction coefficient, and f_b signifies the border volumetric fraction. Assuming each cell to be a pentagonal dodecahedron, the cell geometry including the volume of a single cell, the volume of plateau borders, the cell wall thickness, and the volume of the cell-wall could be characterized [41].

For foam made of randomly oriented plateau borders only, the border weighted extinction coefficient is defined as [41]

$$K_{\text{borders},\lambda} = \frac{4\rho_f}{\pi \Phi_b \rho_0} \times \int_0^{\pi/2} [Q_{e,\lambda}(\Phi_b, m) - Q_{s,\lambda}(\Phi_b, m)\sin^2\varphi - g(\Phi_b, m) Q_{e,\lambda}(\Phi_b, m)\cos^2\varphi]\cos\varphi d\varphi \tag{3}$$

where m is the effective refraction index; $Q_{e,\lambda}$ is the efficiency factor for extinction; $Q_{s,\lambda}$ is the efficiency factor for scattering; g is the anisotropy factor of a plateau border; and φ, Φ_b, ρ_0, and ρ_f correspond to the angle, diameter, bulk density, and foam density, respectively. The extinction and scattering efficiencies are given by the following equations [42,43]:

$$Q_{e,\lambda} = \frac{\lambda^2}{2\pi^2 \Phi_b^2} \sum_{n=1}^{\infty} (2n+1)\text{Re}(a_n + b_n) \tag{4}$$

$$Q_{s,\lambda} = \frac{\lambda^2}{2\pi^2 \Phi_b^2} \sum_{n=1}^{\infty} (2n+1)(\|a_n\|^2 + \|b_n\|^2) \tag{5}$$

where a_n and b_n are the scattering coefficients. In addition, the anisotropic factor in Eq. (3) is determined by using an approximation derived by Bashkatovia et al. [44].

In general, the thickness of the cell-wall is much smaller than the other two dimensions. For foam consisting of only randomly oriented cell-walls, the wall-weighted extinction coefficient is formulated as follows [41]:

$$K_{\text{walls},\lambda} = \frac{\rho_f}{2h\rho_0} \int_0^{\pi/2} [R(\varphi, m)\cos(2\varphi) + 1 - T(\varphi, m)]\sin(2\varphi) d\varphi \tag{6}$$

where R represents the reflection, T is the transmission of a thin slab, and h represents the thickness of the cell-wall. The reflection and transmission of a cell-wall are given by [45,46]

$$R = R_F + \frac{R_F T_F^2 \exp(-2\alpha h)}{1 - R_F \exp(-2\alpha h)} \tag{7}$$

$$T = \frac{T_F^2 \exp(-\alpha h)}{1 - R_F \exp(-2\alpha h)} \tag{8}$$

where R_F and T_F represent the intensity of reflection and transmission coefficients, respectively, and α stands for the absorption coefficient of the foam board.

Considering that the polystyrene foam is used at intermediate temperatures (200–500 K), most thermal energy radiates in an approximate spectral range of 2–40 μm. During this spectrum, the complex refractive index of polystyrene is reported in Ref. [17]. Therefore, both the border and wall-weighted extinction coefficients can be obtained.

2.2 Thermal Conductivity of the Gas-Polymer Matrix. The thermal conduction of the gaseous and polymer components of the foam represents the amount of heat flowing across one unit area in one unit time, as induced by a temperature gradient. Assuming that the foam is composed of stacked and juxtaposed cubic unit cells, the total thermal resistance of the foam will be a sum of the thermal resistances of each cell in series. To determine the thermal resistance of each cell, a cubic-series-parallel approach was applied [11]. As illustrated in Fig. 2, the thermal resistance of each element is composed of three parts in series: the front wall, compound, and rear wall. The compound material consists of the four side walls and the gas inside the cell in parallel. And the four side walls which include the struts are divided for equal cross-sectional areas. In analogy with electric circuits, the thermal resistance of the *i*th cell can be described with the following equation:

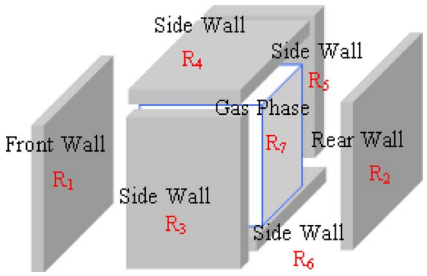

Fig. 2 Thermal resistance of a unit cell using a cubic-series-parallel approach

$$R_i = R_1 + \frac{1}{\frac{1}{R_3}+\frac{1}{R_4}+\frac{1}{R_5}+\frac{1}{R_6}+\frac{1}{R_7}} + R_2 \tag{9}$$

where $R_{1-2}=\delta/(2\lambda_p(l+\delta)^2)$ are the resistances of the front and rear walls, $R_{3-6}=4l/(\lambda_p(2l+\delta)\delta)$ are the resistances of the four side walls, and $R_7=l/(\lambda_g l^2+(\lambda_p-\lambda_g)\pi R_{\text{border}}^2)$ is the resistance of the central cube, including the borders along the cell corners. In turn, λ_p, λ_g l, δ, and R_{border} represent the thermal conductivity of the polymer phase, thermal conductivity of the gas phase, cell size, cell-wall thickness, and border radius, respectively.

The gaseous phase inside each cell consists of two components: the blowing agent and air. The gaseous thermal conductivity is calculated based on the Wassiljewa equation [47]; that is,

$$\lambda_g = \frac{y_1\lambda_1}{y_1\cdot A_{11}+y_2\cdot A_{12}} + \frac{y_2\lambda_2}{y_1\cdot A_{21}+y_2\cdot A_{22}} \tag{10}$$

where the subscripts 1 and 2 correspond to the air and blowing agent, respectively, y denotes the mole fraction of each component, and A_{ij} represents the gas interaction parameter. In this study, the total gas pressure inside each cell is presumed to be atmospheric pressure. The mole fraction of each component in the cell was obtained once the effusion of the blowing agent was simulated. The gas interaction parameters are found using the Mason and Saxena equation [48].

2.3 Cell-to-cell Diffusion of Blowing Agent. Figure 3 depicts a schematic of a row of cells in a half-slab of polymeric foam. Since the blowing agent in the foam diffuses from a higher concentration site to a lower one, the blowing agent from the cells closest to the foam skin will be the first to emit into the ambient surroundings. As the concentration of blowing agent in the outer cells decreases, the blowing agent in the upstream neighboring cells will effuse into these cells, and so on. Based on this concept, a cell-to-cell diffusion model was established to estimate the loss of blowing agent.

In this model, the time-dependent distribution of gas concentration within the polymer matrix is calculated by solving Fick's second law:

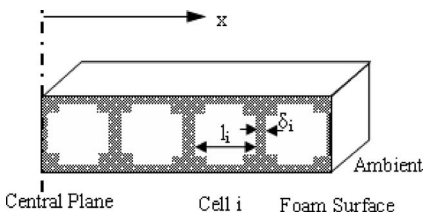

Fig. 3 Cell-to-cell diffusion model

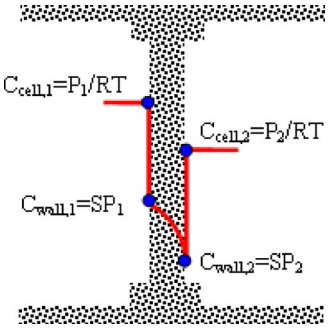

Fig. 4 Concentration profile of blowing agent within a cell-wall

$$\frac{\partial C}{\partial t} = D\cdot\nabla^2 C \tag{11}$$

where C represents the concentration of blowing agent in the polymer matrix, and D denotes the diffusion coefficient of the blowing agent in the polymer matrix. The amount of blowing agent diffusing into/out of each cell is solved using Fick's first law:

$$\dot{m} = -D\cdot\nabla C \tag{12}$$

where $\dot{m}$ symbolizes the flux of the blowing agent across the cell-wall of the unit area. After the amount of the blowing agent inside each cell was obtained, the partial pressure of the blowing agent at the ith cell $P_{g,i}$ was determined using the ideal gas law. As illustrated in Fig. 4, the concentration of the blowing agent at the polymer-gas interface is linearly related to the partial pressure of blowing agent in the cell [49]. Initially, the concentration of the blowing agent in each cell is assigned using atmospheric pressure. Furthermore, a zero-gradient of gas concentration and a zero-gas concentration are applied at the foam center and skin, respectively.

3 Numerical Simulation Procedure

The algorithm used by the numerical simulations is as follows.

1. Physical properties of the polymer-gas system as well as the initial and boundary concentrations were assigned.
2. The radiative conductivity was calculated using the Mie theory.
3. The finite difference method with an explicit scheme was applied to solve the governing diffusion equation.
4. The mole fraction of the blowing agent in each cell was obtained, and the thermal conductivity of the gas mixture in each cell was achieved.
5. The thermal resistance of each cell was acquired.
6. The thermal conductivity of the foam board was determined.

4 Results and Analysis

First, the theoretical model was experimentally verified using STYROFOAM™ ROORMATE™ brand XPS foam samples blown with HFC-134a [5]. The average cell-wall thickness was determined based on the scanning electron microscope (SEM) pictures as well as the information in Ref. [5]. The results shown in Fig. 5 indicate that the simulated thermal conductivity of the foam agreed with the long-term experimental results.

Nevertheless, in the early stages, the experimental curve rises much faster than the numerical curve, for the following reasons. First, the numerical simulations assume isothermal conditions, and the diffusivity of blowing agent in the polymer matrix is calculated at room temperature. However, in the experiments, the initial temperature might be higher than room temperature, resulting in a higher gas diffusion coefficient. Prior to the loss of blowing agent, an initial higher gas concentration within the polymer will also increase the gas diffusivity. Secondly, the simulations

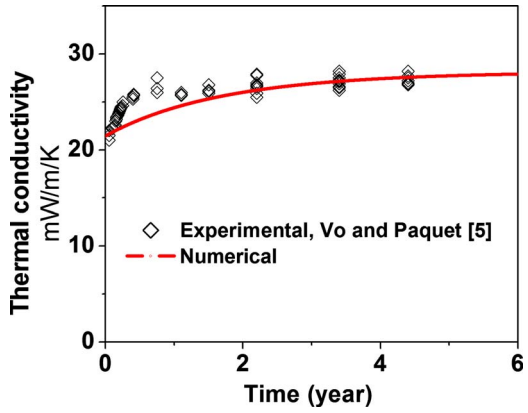

Fig. 5 Verification in theoretical modeling

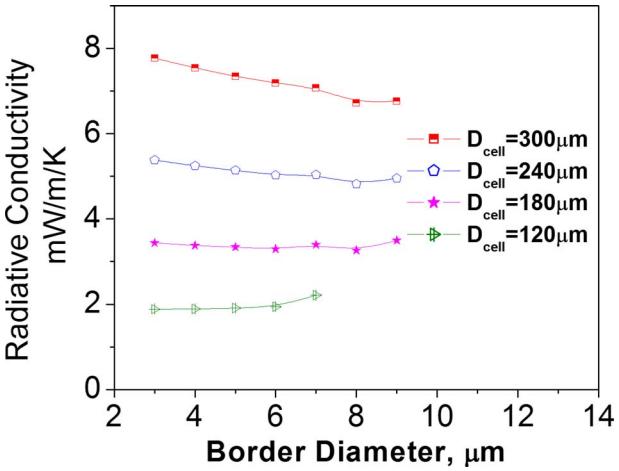

Fig. 7 Effect of border diameter on radiative conductivity

assume that all cells in the foam are closed. However, some cells in the experimental foam may have been open, leading to gas flow, rather than gas diffusion through the cell walls. This assumption can cause a low estimate of the loss of blowing agent. Thirdly, the assumption of a cubic cell model with an average wall thickness will tend to underestimate the loss of blowing agent compared to the real cell-wall.

4.1 Radiative Conductivity of Polystyrene Foams

4.1.1 Effect of Foam Temperature on Radiative Conductivity. In this context, the foam geometry is as follows: bulk density of 1050 kg/m^3, foam density of 25 kg/m^3, average cell diameter of 300 μm, border diameter of 6 μm, and wall thickness of 1.27 μm. The average temperature of the foam board ranged from 300 K to 373 K. As expected, the results show that the radiative conductivity goes up as the mean foam temperature increases.

4.1.2 Effect of Cell Morphology on Radiative Conductivity. To understand the effects of cell morphology on radiative conductivity, the bulk density and foam density were fixed at 1050 kg/m^3 and 25 kg/m^3, respectively, and the mean foam temperature was maintained at 300 K. The cell size varied from 120 μm to 300 μm, and the border diameter ranged from 3 μm to 9 μm. Figure 6 plots the radiative conductivities with respect to the cell size and border size, demonstrating that regardless of the border diameter, the radiative conductivity increases as the cell size increases. The reason is that transmission of radiative waves through gaseous parts is increased. As illustrated in Fig. 7, it is interesting to note that with large cells, the radiative conductivity decreases as the border diameter increases. However, with small cells, the radiative conductivity increases slightly as the border size increases. These could be explained as follows: With large cells, the increase in border diameter does not change the cell-wall thickness too much due to a large surface area as well as a thick cell-wall. An increase in border diameter will increase the reflection and absorption of radiative waves, leading to a decrease in radiative conductivity. However, with a small cell size and a fixed foam density, the cell-wall thickness is small and will be decreased as the border diameter increases. The decrease in cell-wall thickness will increase radiative conductivity.

4.1.3 Effect of Cell Density on Radiative Conductivity. Here, cell density is defined as the cell number in a unit of unfoamed polymer whereas volume expansion ratio is defined as the ratio between the foam volume and the polymer occupied volume. In this case, the volume expansion ratio of the foam is fixed at 42, and the foam density at 25 kg/m^3. Figure 8 illustrates the effects of changing cell density on radiative conductivity, revealing that an elevated cell density leads to a weak radiative conductivity. This may be due to an increased reflection of radiative waves in polymer phase and a decreased transmission of radiative waves in gaseous phase with an elevated cell density.

Meanwhile, as illustrated in Fig. 8, with a high cell density, border volumetric fraction does not significantly affect the radiative conductivity. However, with a low cell density, the radiative conductivity tends to decrease as the border volumetric fraction

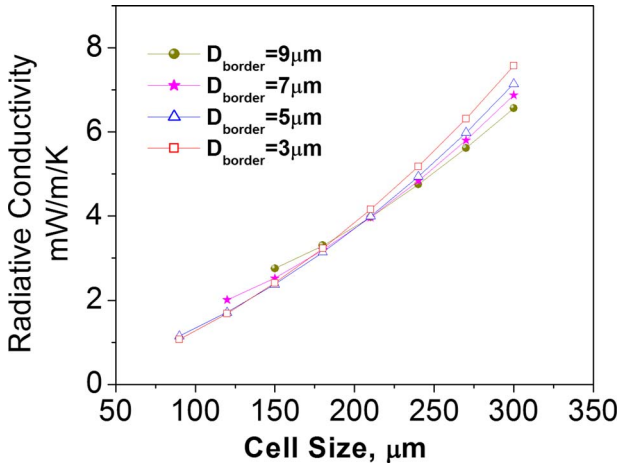

Fig. 6 Effect of cell size on radiative conductivity

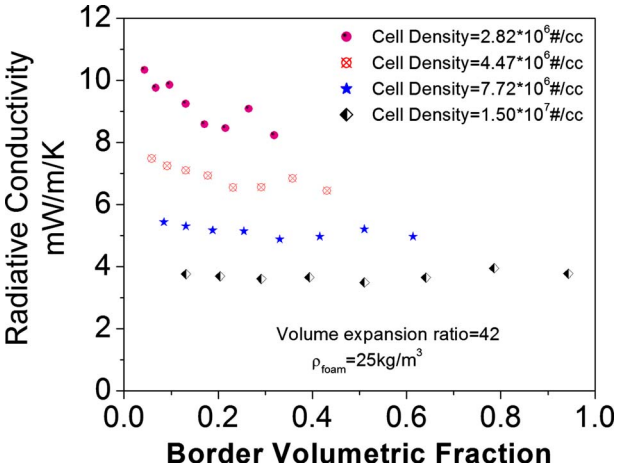

Fig. 8 Effect of cell density on radiative conductivity

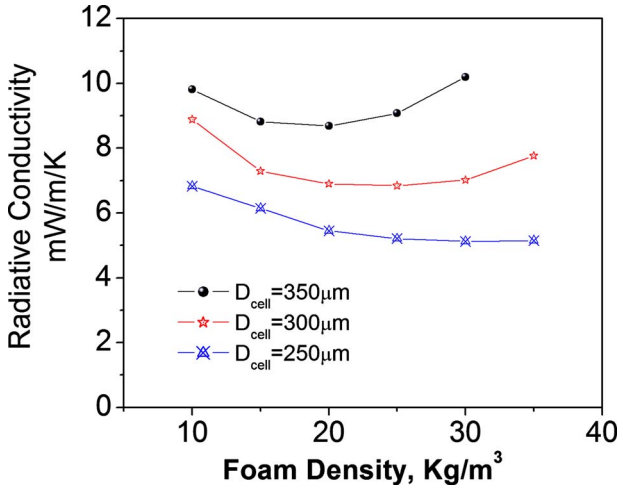

Fig. 9 Effect of foam density on radiative conductivity

increases. The phenomena could be explained as the following. A high cell density has a small cell diameter as well as a thin cell-wall. Increasing the border volumetric fraction will increase the border size and decrease the cell-wall thickness. The synthesized effects of increased border size and decreased cell-wall thickness will not change the radiative conductivity too much. However, with a low cell density, the foam has a thick cell-wall and a large cell size. An increase in the border volumetric fraction will enlarge the border size. In this case, variation in the contribution of cell-wall thickness on radiative conductivity will not change too much because of a thick cell-wall. As a consequence, an increased border size results in a decreased radiative conductivity.

4.1.4 Effect of Foam Density. Figure 9 displays the effect of changing foam density on radiative conductivity with cell diameters of 350 μm, 300 μm, and 250 μm. The figure indicates that when the foam density varies from 10 kg/m^3 to 25 kg/m^3, a minimum radiative conductivity is obtained at an optimal foam density, which tends to shift lower with increasing cell size.

Under the assumption of each cell to be a pentagonal dodecahedron, the geometrical relationship can be reduced to the following equation [41]:

$$\frac{\rho_{\text{foam}}}{\rho_{\text{bulk}}} = \frac{1}{\text{VER}} = 3.775\frac{h}{\Phi_c} \tag{13}$$

where h represents cell-wall thickness and Φ_c stands for cell diameter. It reveals that with a fixed cell diameter, the cell-wall thickness increases as the foam density increases and vice versa. Based on the results in Ref. [41] and this study, it is known that the Rosseland extinction coefficient versus the cell-wall thickness has a maximum value at a mean cell-wall thickness. With a mean cell diameter, this generates a minimum radiative conductivity. Thus, with a fixed cell diameter, an increase in foam density will increase cell-wall thickness, leading to a maximum Rosseland extinction coefficient and therefore a minimum radiative conductivity. Nevertheless, when the cell diameter is small, the cell-wall thickness is so thin that the Rosseland extinction coefficient cannot reach its peak, resulting in a decreasing radiative conductivity shown in Figure 9. As foam density increases, an increase in cell diameter will increase cell-wall thickness significantly. In other words, with a large cell size, an increase in foam density makes the peak of the Rosseland extinction coefficient occur early, leading to a shift of minimum radiative conductivity to the left, as demonstrated in Fig. 9.

Table 1 Geometric parameters of polystyrene foam

Parameter	Value
Half-thickness	1.27 cm
Cell size	369.5 μm
Cell wall thickness	4.2 μm
Border diameter	8.4 μm
Cell layer number	34
Cell density	5.747×10^5 #/cm^3
Volume expansion ratio	30

4.2 Loss of Blowing Agent in Polystyrene Foams

4.2.1 Loss of HFC134a in Polystyrene Foam. Table 1 tabulates the geometric parameters of polystyrene foam blown with HFC134a. Figure 10 illustrates the decay of HFC134a within the foam at atmospheric pressure and room temperature. It is observed that, at early stages, the blowing agent is lost quickly from the cells close to the foam skin and more slowly from inside the foam. It takes a long time for HFC134a to effuse completely from a 1 in.-thickness foam board.

Figure 11 illustrates variation in gaseous conductivity in the foam. It is indicated that the gaseous conductivity in cells close to the skin will increase significantly. On the contrary, the gaseous conductivity at the foam center increases gradually. Furthermore, the profile of average conductivity of the gas phase in the foam shows that decay of blowing agent takes a remarkable effect on the gaseous conductivity. To quantify the loss of blowing agent, the notion of the residual concentration of blowing agent in the

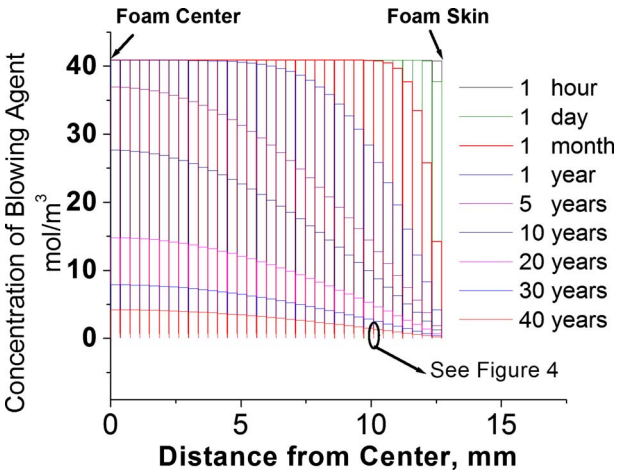

Fig. 10 Concentration profiles of HFC134a in 1 in. PS foam

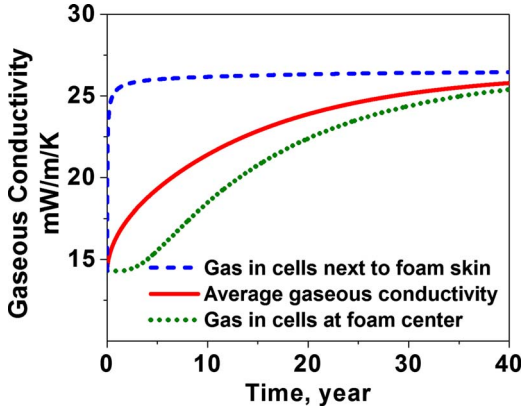

Fig. 11 Variation in gaseous conductivity

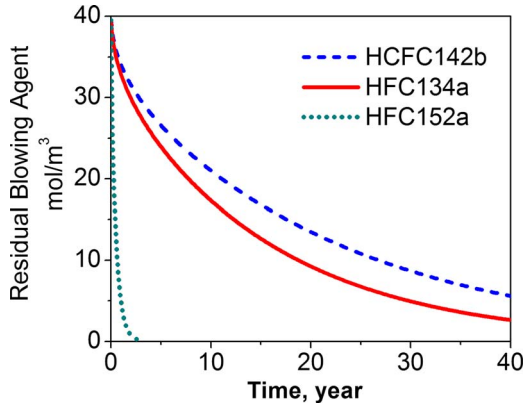

Fig. 12 The decay of HFC134a, HCFC142b, and HFC152a in PS foam

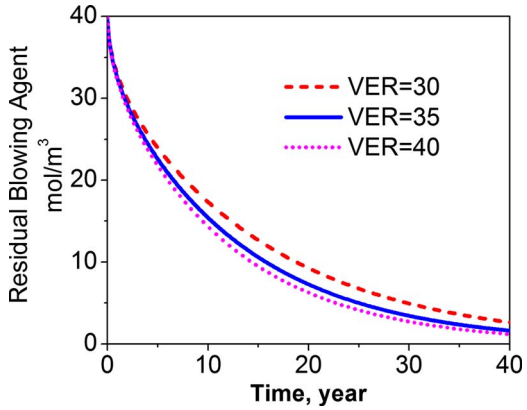

Fig. 13 Effect of volume expansion ratio on the decay of HFC134a

foam board is applied. Figure 12 plots the residual HFC134a in the foam against aging time, revealing that the loss of blowing agent does not vary linearly with foam age. Initially, the decay of blowing agent trapped in voids is rapid but slows down over time.

4.2.2 Effect of Blowing Agent Type on Loss of Blowing Agent. Here, three typical blowing agents HCFC142b, HFC134a, and HFC152a are selected [50–52]. The physical properties of these blowing agents are listed in Table 2. The foam morphology of these cases is identical to the case described in Table 1. Figure 12 diagrams the decay profiles of the three different blowing agents, showing that HCFC142b and HFC134a decay slowly in comparison to HFC152a.

4.2.3 Effect of Cell Morphology on Loss of Blowing Agents. To inspect the effects of cell morphology on the loss of blowing agents, polystyrene foams with a variety of cell densities and volume expansion ratios were designed. The properties are listed in Table 3. All use HFC134a as the blowing agent.

Figure 13 depicts the effects of changing the volume expansion ratio on the decay of HFC134a. It is seen that a low volume expansion ratio makes the gas loss more gradual. In addition, the results show that cell density does not influence the decay of HFC134a under a certain volume expansion ratio and a fixed total cell-wall thickness.

4.2.4 Effect of Foam Thickness on Loss of Blowing Agents. To predict the effects of foam thickness on the loss of blowing agent, three foams with different thicknesses were chosen, i.e., half-thicknesses were 0.5 in., 1 in., and 1.5 in., respectively. Other geometric parameters maintain the same values demonstrated in Table 1. As expected, the results show that the thick foam attenuates the decay of blowing agent remarkably well.

4.3 Effect of Loss of Blowing Agents on Thermal Insulation Property. To estimate the thermal insulation properties of the polymeric foams, the same cases have been used as those employed for the studies of decay of blowing agents. Figure 14 charts the effects of the blowing agent type on thermal insulation properties, indicating that different blowing agents lead to dissimilar long-term thermal insulation performance. That is, even with identical geometries, foam boards blown with different blowing agents generate totally different thermal insulation characteristics. As well, it is noted that both HFC134a and HCFC142b generate foam with good long-term thermal insulation properties, whereas HFC152a makes foam with poor long-term insulation property.

Figure 15 demonstrates thermal conductivity as a function of cell density, indicating that a low cell density leads to a high thermal conductivity due to the large radiative conductivity. Figure 16 shows the change in thermal insulation capacity with respect to volume expansion ratio and reveals that a high volume

Table 2 Physical properties of blowing agents and polystyrene in foams

Blowing agent	Molecular weight (g/mol)	Thermal conductivity (m W/m/K)	Diffusivity (cm^2/s)	Permeability (cm^3 cm /cm^3 cmHgs)	Critical pressure (MPa)	Critical temperature (K)
HCFC142b	100.5	9.8	5.95×10^{-10}	1.26×10^{-13}	4.04	137.1
HFC134a	102.0	14.3	8.50×10^{-10}	1.80×10^{-13}	4.06	101.1
HFC152a	66.0	13.8	2.55×10^{-8}	5.40×10^{-12}	4.51	113.3

Table 3 Foam structure with respect to cell density and volume expansion ratio

Blowing agent	Half-foam thickness (cm)	Cell layer	Cell size (μm)	Cell wall thickness (μm)	Border diameter (μm)	Cell density (#/cc)	Volume expansion ratio (VER)
HFC134a	1.27	34	369.5	4.20	8.40	5.7×10^5	30
HFC134a	1.27	55	226.4	2.57	5.15	2.5×10^6	30
HFC134a	1.27	88	142.6	1.62	3.24	1.0×10^7	30
HFC134a	1.27	32	393.0	3.72	7.44	5.7×10^5	35
HFC134a	1.27	31	407.9	3.46	6.92	5.7×10^5	40

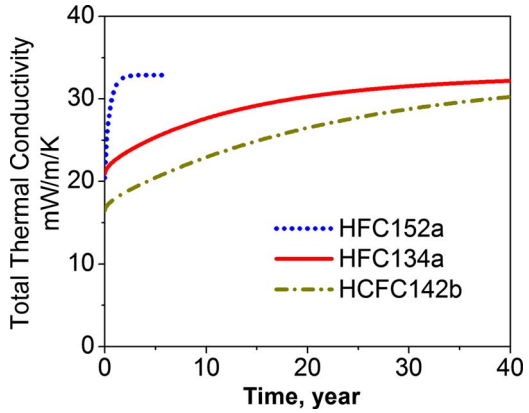

Fig. 14 Effect of blowing agent type on thermal insulation capacity

expansion ratio results in a high thermal conductivity. Furthermore, a thick foam board leads to low thermal conductivity, thus effectively improving the stability of thermal insulation.

5 Concluding Remarks

This paper describes a mathematical model for estimating the change in thermal insulation properties of polystyrene foams with the loss of blowing agents. The model allows for thermal conductivity of polymer, thermal conductivity of blowing agent-air mixture and thermal radiation. It solves the transient diffusion equation to calculate the composition of the gas mixture in the foam. The Mie theory is used to estimate the absorption and scattering extinction of the each cell-wall and border. The total extinction coefficient of the foam is obtained by combining the two contributions through the use of the fraction border in the cell morphology under the assumption that each cell is dodecahedral.

The model is used to investigate the effect of cellular morphology and other important variables such as the foam density and foam thickness on the conductivity of the polystyrene foam and its change with time due to the effusion of the blowing agent from the foam. The study shows that a minimum in radiative conductivity can be generated by optimizing the foam geometry, and the diffusing out of blowing agents significantly influences long-term thermal insulation performance. The foams with low-diffusivity blowing agents, low volume expansion ratios, high cell density, and large thickness attenuate the loss of blowing agent, thus better maintaining the foam's thermal insulation capacity.

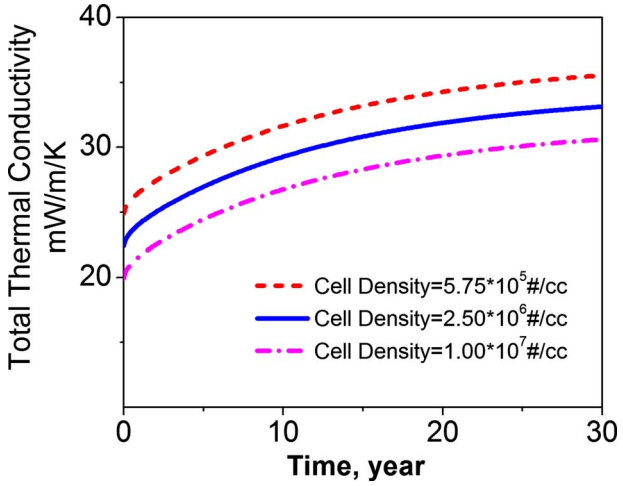

Fig. 15 Effect of cell density on thermal insulation capacity

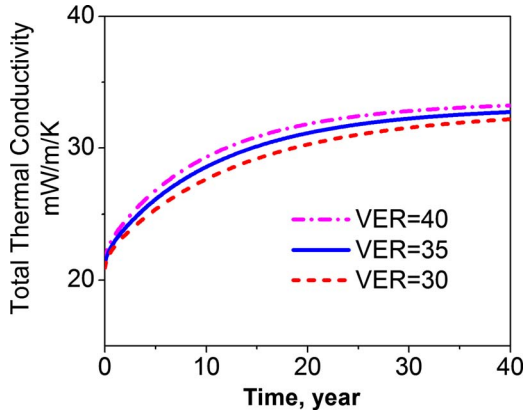

Fig. 16 Effect of volume expansion ratio on thermal conductivity capacity

Acknowledgment

We would like to thank the Consortium for Cellular and Microcellular Plastics (CCMCP) for their financial support of this project.

Nomenclature

A_{ij} = gas interaction parameter
a_n = scattering coefficient
b_n = scattering coefficient
C = gas concentration (mol/m^3)
D = diffusivity (m^2/s)
e_b = black body emissive power (W/m^2)
$e_{b,\lambda}$ = spectral black body emissive power (W/m^2)
f_b = border volume fraction
g = anisotropy factor
h = thickness of cell-wall (m)
$K_{\text{borders},\lambda}$ = weighted border extinction coefficient
$K_{e,R}$ = Rosseland mean extinction coefficient (1/m)
$K_{e,\lambda}$ = spectral extinction coefficient
$K_{\text{walls},\lambda}$ = weighted wall extinction coefficient
l = length of a cubic cell (m)
m = effective refraction index
M = molecular weight, (g/mol)
$\dot{m}$ = flux of the blowing agent (mol/m^2/s)
n = real part of the complex refractive index
$Q_{e,\lambda}$ = efficiency factor for extinction
$Q_{s,\lambda}$ = efficiency factor for scattering
$R_{1,2}$ = thermal resistance of the front and rear wall (°C/W)
R_{3-6} = thermal resistance of each side wall (°C/W)
R_7 = thermal resistance of the central cube including borders (°C/W)
R = reflection of cell-wall
R_F = the intensity of reflection coefficient
R_i = thermal resistance of the ith cell (°C/W)
T = transmission of cell-wall
T_F = intensity of transmittance coefficient
t = time (s)
VER = volume expansion ratio
y = mole fraction of each component

Greek

α = absorption coefficient of the foam
δ = thickness of cell-wall (m)
Φ_b = border diameter (m)
Φ_c = cell diameter (m)
φ = angle (rad)

λ = wavelength (m)
λ_g = thermal conductivity of gas phase (W/m/K)
λ_p = thermal conductivity of polymer phase (W/m/K)
ρ = density (kg/m^3)
ρ_f = foam density (kg/m^3)
ρ_0 = bulk density (kg/m^3)

Subscripts

1 = air
2 = blowing agent

References

[1] Suh, K. W., 2006, "Blowing Agent," *Encyclopedia of Chemical Processing*, Vol. 1, S. Lee, ed., CRC Press, Boca Raton, FL, pp. 237–250.
[2] Park, C. B., Behravesh, A. H., and Venter, R. D., 1998, "Low-Density, Microcellular Foam Processing in Extrusion Using CO_2," Polym. Eng. Sci., **38**(11), pp. 1812–1823.
[3] Naguib, H. E., Park, C. B., and Reichelt, N., 2004, "Fundamental Foaming Mechanisms Governing Volume Expansion of Extruded PP Foams," J. Appl. Polym. Sci., **91**(4), pp. 2661–2668.
[4] Xu, X., Park, C. B., Xu, D., and Pop-Iliev, R., 2003, "Effect of the Die Geometry on Cell Nucleation of PS Foams Blown With CO_2," Polym. Eng. Sci., **43**(7), pp. 1378–1390.
[5] Vo, C. V., and Paquet, A. N., 2004, "An Evaluation of the Thermal Conductivity of Extruded Polystyrene Foam Blown with HFC-134a or HCFC-142b," J. Cell. Plast., **40**(3), pp. 205–228.
[6] Skochdopole, R. E., 1961, "The Thermal Conductivity of Foamed Plastics," Chem. Eng. Prog., **57**, pp. 55–59.
[7] Booth, J. R., 1993, "An Evaluation of the Dow Thermal Performance Prediction Model for a Database of XPS/CFC-12 Aged Resistivity and Physical Properties," J. Thermal Insul., Bldg. Envelops, **17**, pp. 154–170.
[8] Biedermann, A., Kudoke, C., and Merten, A., 2001, "Analysis of Heat Transfer Mechanisms in Polyurethane Rigid Foam," J. Cell. Plast., **37**(6), pp. 467–483.
[9] Wu, J. W., Sung, W. F., and Chu, H. S., 1999, "Thermal Conductivity of Polyurethane Foams," Int. J. Heat Mass Transfer, **42**, pp. 2211–2217.
[10] Ostrogorsky, A. G., Glicksman, L. R., and Reitz, D. W., 1986, "Aging of Polyurethane Foams," Int. J. Heat Mass Transfer, **29**(8), pp. 1169–1176.
[11] Leach, A. G., 1993, "The Thermal Conductivity of Foams I: Models for Heat Transfer," J. Phys. D: Appl. Phys., **26**, pp. 733–739.
[12] Caps, R., Heinemann, U., Fricke, J., and Keller, K., 1997, "Thermal Conductivity of Polyamide Foams," Int. J. Heat Mass Transfer, **40**(2), pp. 269–280.
[13] Tseng, C. J., Ramaguch, M., and Ohmori, T., 1997, "Thermal Conductivity of Polyurethane Foams From Room Temperature to 20K," Cryogenics, **37**(6), pp. 305–312.
[14] Wong, C. M., and Hung, M. L., 2008, "Polystyrene Foams as Core Materials Used in Vacuum Insulation Panel," J. Cell. Plast., **44**(3), pp. 239–259.
[15] Coquard, R., and Baillis, D., 2006, "Modeling of Heat Transfer in Low-density EPS Foams," ASME J. Heat Transfer, **128**(6), pp. 538–549.
[16] Glicksman, L. R., Schuetz, M., and Sinofsky, M., 1987, "Radiation Heat Transfer in Foam Insulation," Int. J. Heat Mass Transfer, **30**(1), pp. 187–197.
[17] Kuhn, J., Ebert, H. P., Arduini-schuster, M. C., Buttner, D., and Fricke, J., 1992, "Thermal Transport in Polystyrene and Polyurethane Foam Insulations," Int. J. Heat Mass Transfer, **35**(7), pp. 1795–1801.
[18] Doermann, D., and Sacadura, J. F., 1996, "Heat Transfer in Open Cell Foam Insulation," ASME J. Heat Transfer, **118**(1), pp. 88–93.
[19] Yang, C. T., and Lee, S. T., 2003, "Dimensional Stability Analysis of Foams Based on LDPE and Ethylene-styrene Interpolymer Blends," J. Cell. Plast., **39**(1), pp. 59–69.
[20] Pilon, L., Fedorov, A. G., and Viskanta, R., 2000, "Gas Diffusion in Closed Foams," J. Cell. Plast., **36**(6), pp. 451–474.
[21] Briscoe, B. J., and Savvas, T., 1998, "Gas Diffusion in Dense Poly(ethylene) Foams," Adv. Polym. Technol., **17**, pp. 87–106.
[22] Alsoy, S., 1999, "Modeling of Diffusion in Closed Cell Polymeric Foams," J. Cell. Plast., **35**(3), pp. 247–271.
[23] Booth, J. R., Graves, R. S., and Yarbrough, D. W., 1995, "Aging of Thin-slices of PIR Foams Manufactured With Alternative Blowing Agents," J. Thermal Insul., Bldg. Envelops, **19**(2), pp. 118–131.
[24] Bhattacharjee, D., Irwin, P. W., Booth, J. R., and Grimes, J. T., 1994, "The Acceleration of Foam Aging by Thin Slicing—Some Interpretations and Limitations," J. Thermal Insul., Bldg. Envelops, **17**(3), pp. 219–237.
[25] Shankland, I. R., 1995, "Blowing Agent Emission Calculations for a Refrigerator," J. Cell. Plast., **31**(3), pp. 227–243.
[26] Tant, M. R., and Wilkes, G. L., 1981, "Physical Aging Studies of Semicrystalline Poly (ethylene Terephthalate)," J. Appl. Polym. Sci., **26**, pp. 2813–2825.
[27] Ruiz-Herrero, J. L., Rodríguez-pérez, M. A., and de Saja, J. A., 2005, "Effective Diffusion Coefficient for the Gas Contained in Closed Cell Polyethylene-Based Foams, Subjected to Compressive Creep Tests," Polymer, **46**, pp. 3105–3110.
[28] Quoc, P. N., Zitha, P. L. J., and Currie, P. K., 2002, "Effect of Foam Films on Gas Diffusion," J. Colloid Interface Sci., **248**(2), pp. 467–476.
[29] Griffiths, P. C., Tipples, C. N., Stilbs, P., and McCormick, B. H., 1998, "Restricted Diffusion of a "Gas" in a Solid Foam," Langmuir, **14**(22), pp. 6603–6605.
[30] Takeno, K., Ichinose, T., and Tokuda, K., 1996, "Effects of High Expansion Foam Dispersed onto Leaked LNG on the Atmospheric Diffusion of Vaporized Gas," J. Loss Prev. Process Ind., **9**(2), pp. 125–133.
[31] Hanssen, J. E., 1993, "Foam as a Gas-Blocking Agent in Petroleum Reservoirs II: Mechanisms of Gas Blockage by Foam," J. Pet. Sci. Eng., **10**(2), pp. 135–156.
[32] Gandel'sman, M. I., Matveyenko, R. V., and Budtov, V. P., 1987, "Diffusion in Porous Strained Polymer Media," Polym. Sci. U.S.S.R., **29**(6), pp. 1212–1218.
[33] Varady, M. J., and Fedorov, A. G., 2002, "Combined Radiation and Conduction in Glass Foams," ASME J. Heat Transfer, **124**(6), pp. 1103–1109.
[34] Krishnan, S., Murthy, J. Y., and Garimella, S. V., 2006, "Direct Simulation of Transport in Open-cell Metal Foam," ASME J. Heat Transfer, **128**(8), pp. 793–799.
[35] Ghosh, I., 2008, "Heat-Transfer Analysis of High Porosity Open-Cell Metal Foam," ASME J. Heat Transfer, **130**(3), p. 034501.
[36] Chen, C. and Jaluria, Y., 2007, "Modeling of Radiation Heat Transfer in the Drawing of an Optical Fiber With Multilayer Structure," ASME J. Heat Transfer, **129**(3), pp. 342–352.
[37] Liu, L. H., and Liu, L. J., 2007, "Discontinuous Finite Element Approach for Transient Radiative Transfer Equation," ASME J. Heat Transfer, **129**(8), pp. 1069–1074.
[38] An, W., Ruan, L. M., Tan, H. P., and Qi, H., 2006, "Least-Squares Finite Element Analysis for Transient Radiative Transfer in Absorbing and Scattering Media," ASME J. Heat Transfer, **128**(5), pp. 499–503.
[39] Giaretto, V., Miraldi, E., and Ruscica, G., 1995/1996, "Simultaneous Estimations of Radiative and Conductive Properties in Lightweight Insulation Materials," High Temp. - High Press., **27/28**, pp. 191–204.
[40] Çengel, Y. A., 1977, *Heat Transfer-a Practical Approach*, 2nd ed., McGraw-Hill, New York.
[41] Placido, E., Arduini-Schuster, M. C., and Kuhn, J., 2005, "Thermal Properties Predictive Model for Insulating Foams," Infrared Phys. Technol., **46**, pp. 219–231.
[42] Kerker, M., 1969, *The Scattering of Light and Other Electromagnetic Radiation*, Academic, New York.
[43] van de Hulst, H. C., 1981, *Light Scattering by Small Particles*, Dover, New York.
[44] Bashkatova, T. A., Bashkatov, A. N., Kochubey, V. I., and Tuchin, V. V., 2001, "Light Scattering Properties for Spherical and Cylindrical Particles: A Simple Approximation Derived From Mie Calculations," Proc. SPIE, **4241**, pp. 247–259.
[45] Nichelatti, E., 2002, "Complex Refractive Index of a Slab From Reflectance and Transmittance: Analytical Solution," J. Opt. A, Pure Appl. Opt., **4**, pp. 400–403.
[46] Ho, W., and Ma, C. M., 1998, "Diffuse Reflectance and Transmittance of IR Absorbing Polymer Film," Polym. Eng. Sci., **38**(10), pp. 1666–1674.
[47] Wassiljewa, A., 1904, "Wärmeleitung in Gasgemischen," Phys. Z., **5**, pp. 737–742.
[48] Mason, E. A., and Saxena, S. C., 1958, "Approximate Formula for the Thermal Conductivity of Gas Mixtures," Phys. Fluids, **1**(5), pp. 361–369.
[49] Basmadjian, D., 2004, *Mass Transfer: Principles and Applications*, CRC LLC, Boca Raton, FL.
[50] Seifert, H., Biedermann, A., and Giesker, C., 2003, "Can HFC245fa or Cyclopentane Blown Foams Match the Performance of HFC-Foams?" J. Cell. Plast., **39**(5), pp. 417–426.
[51] Zipfel, L., Krücke, W., Börner, K., Barthélemy, P., and Dournel, P., 1998, "HFC 365mfc and HFC-245fa Progress in Application of New HFC Blowing Agents," J. Cell. Plast., **34**(6), pp. 511–525.
[52] Willams, D. J., Bogdan, M. C., Parker, R. C., and Knopech, G. M., 1997, "Update on the Development of HFC-245fa as a Liquid HFC Blowing Agent," J. Cell. Plast., **33**(3), pp. 238–263.

Analytical Characterization and Production of an Isothermal Surface for Biological and Electronic Applications

Shadi Mahjoob

Kambiz Vafai[1]
e-mail: vafai@engr.ucr.edu

Mechanical Engineering Department,
University of California,
Riverside, CA 92521

Characterization and regulation of isothermal surfaces are key issues in a number of thermal management devices. The surface temperature uniformity can be controlled utilizing a variable area channel heat exchanger filled with a porous medium. A comprehensive analytical investigation of forced convection through a generic variable area channel is carried out to design a compact heat exchanger in producing an isothermal surface subject to a constant heat flux, which may be required in the biological, electronics, optical, laser, manufacturing, and solidification applications. Exact solutions for the fluid and solid phases and the wall surface temperature distributions as well as the Nusselt number correlations are established while incorporating local thermal nonequilibrium and transverse conduction contributions. The channel temperature field is adjusted utilizing either an adiabatic or a constant temperature on the inclined surface. The effects of the pertinent physical parameters, such as channel inlet/outlet thickness, inclination angle, Biot number, ratio of fluid and matrix thermal conductivities, working fluid properties, and imposed heat flux, on the fluid and solid temperature fields and the isothermal surface are thoroughly investigated. The results indicate that utilizing proper pertinent parameters, an isothermal surface is achieved. The validity of the utilization of the local thermal equilibrium model is also investigated and error maps are presented.
[DOI: 10.1115/1.2995690]

Keywords: isothermal surface production, porous media, analytical, PCR

1 Introduction

Porous inserts are quite effective in heat transfer augmentation and thermal control. A porous medium provides an extensive surface area for a given volume between a solid and fluid, which enhances the interstitial heat transfer. As such, porous inserts are an attractive choice for a variety of applications such as solar receiver devices, electronics equipments, building thermal insulation, energy storage units, flat-shaped heat pipes [1,2], catalytic reactors, jet impingement and microchannel cooling technology [3–5], bioheat transfer modeling [6], and recently in biomicrofluidic thermal cyclers [7]. A key issue in a number of heat management devices is the production and regulation of isothermal surfaces by maintaining a relatively constant temperature equal or below a maximum operating temperature for electronic equipment subject to a high heat flux [8,9] such as processors, memory and graphics chips, telecom switches, and high powered military equipments and laser devices, as well as imposing a uniform temperature throughout a biomicrofluidic chip for thermal cycling applications such as polymerase chain reaction (PCR) for nucleic acid (e.g., DNA and RNA) amplification [7,10]. Production of an isothermal surface is also an important issue in thermal therapies (e.g., hyperthermia treatment for cancer tumors [11]), laser light emitting diodes with similar wavelength light, solidification processing [12], single crystal growth [13], turbine blade manufacturing utilizing directional solidification processes [14–17], telescope meniscus mirrors [18], and optical systems [19]. The temperature uniformity can be controlled using a proper utilization of a variable area channel filled with a porous medium. The variation of the channel area can be controlled by the inlet/outlet channel thickness or the angle of the longitudinal direction with respect to the channel upper wall, the so called inclination angle. The velocity and temperature of the working fluid passing through the channel along with its properties (e.g., density, specific heat, and thermal conductivity) are some of the other effective parameters that affect the heat transport augmentation in these types of devices.

Two approaches can be pursued in investigating heat transport through a porous medium utilizing a volume averaging technique: averaging over a representative elementary volume containing both the fluid and the solid phases, and averaging separately over each of the phases, resulting in energy equations for each individual phase [20–24]. These two models are referred to as the one equation model (utilizing local thermal equilibrium assumption) and the two equation model (incorporating the local thermal nonequilibrium condition), respectively [25–29]. The assumption of local thermal equilibrium has been widely used in analyzing transport processes through porous media [28–32]. However, this assumption is not valid for applications where a substantial temperature difference exists between the solid and the fluid phases such as high porosity fibrous materials [25–29,33–35]. Mahjoob and Vafai [33] presented a synthesis of fluid and thermal transport models for metal foams and considered the validity of local thermal equilibrium assumption for foam metal modeling. They also indicated the substantial advantages of utilizing metal foams to improve the performance of heat exchangers considering both heat transfer and pressure drop issues.

Heat transport characteristics in porous media are quite complicated [36–40]. Utilizing the Darcy model and accounting for local thermal nonequilibrium, Lee and Vafai [28] established an exact solution for normalized fluid and solid temperature profiles and the Nusselt number for forced convective flow through a channel filled with a porous medium subject to a constant heat flux. Marafie and Vafai [29] developed an analytical solution utilizing

[1]Corresponding author.

Contributed by the Heat Transfer Division of ASME for publication in the JOURNAL OF HEAT TRANSFER. Manuscript received March 12, 2008; final manuscript received July 9, 2008; published online March 19, 2009. Review conducted by Yogesh Jaluria.

Darcy–Forchheimer–Brinkman model and local thermal nonequilibrium energy transport model and established the temperature profiles and heat transfer correlations. Amiri and Vafai [25,26] employed the generalized model for the momentum equation and local thermal nonequilibrium model for the energy equation, including axial and transverse thermal dispersions to investigate forced convection, and validated their numerical findings utilizing an experimental investigation. They presented detailed error maps for assessing the importance of various simplifying assumptions. Alazmi and Vafai [27] investigated the proper form of boundary conditions for a constant wall heat flux imposed on a porous medium under local thermal nonequilibrium conditions. Effects of variable porosity and thermal dispersion were also analyzed.

In this work, analytical characterizations and production of an isothermal surface for biological (such as in DNA amplification utilizing PCR), electronic, optical, laser, manufacturing, and solidification applications are considered while incorporating the local thermal nonequilibrium conditions. Exact solutions for fluid and solid temperature distributions are presented as well as analytical surface temperature distribution and heat transfer correlations for a generic variable cross sectional area channel filled with a porous medium. Pertinent design parameters affecting the isothermal surface production such as channel inlet/outlet thickness, inclination angle, Biot number, ratio of the fluid and solid thermal conductivities and specific surface area are analytically characterized, and investigated.

2 Modeling and Formulation

2.1 Problem Description. Analysis and design of a highly efficient and compact device for isothermal surface production, when subject to a constant heat flux, are presented in this work. The variable cross sectional area channel heat exchanger is filled with a porous medium, which is attached to a target surface, as shown in Fig. 1. The top part of the channel can be either a constant temperature or an adiabatic surface to minimize losses and control the heat transfer through the channel. The height of the channel inlet is H and the top surface angle relative to the longitudinal direction, the so called inclination angle, is α. Flow is assumed to be hydraulically and thermally fully developed. Natural convection and radiation are assumed to be negligible and all thermodynamic properties of the solid and fluid are considered to be temperature independent. The porous medium is assumed to be homogenous and isotropic.

2.2 Governing Equations. The governing energy equations for the solid and fluid phases incorporating local thermal nonequilibrium conditions are as follows [25,27].

In fluid phase,

$$k_{f,\text{eff}}\nabla_y^2\langle T_f\rangle^f + h_{sf}a_{sf}(\langle T_s\rangle^s - \langle T_f\rangle^f) = \rho c_P\langle u\rangle\frac{\partial\langle T_f\rangle^f}{\partial x} \tag{1}$$

In solid phase,

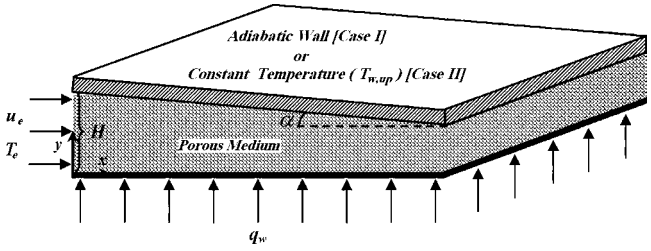

Fig. 1 Schematic of a channel filled with a porous medium subject to a constant heat flux; Case I: adiabatic boundary condition at the upper wall, Case II: constant surface temperature boundary condition at the upper wall

$$k_{s,\text{eff}}\nabla_y^2\langle T_s\rangle^s - h_{sf}a_{sf}(\langle T_s\rangle^s - \langle T_f\rangle^f) = 0 \tag{2}$$

where $k_{f,\text{eff}}$ and $k_{s,\text{eff}}$ are the effective fluid and solid thermal conductivities, ρ is the density, c_p is the specific heat of the fluid, $\langle u\rangle$ is the locally volume averaged fluid velocity, $\langle T_f\rangle^f$ and $\langle T_s\rangle^s$ are the intrinsic phase average fluid and solid temperatures, and h_{sf} and a_{sf} are the interfacial heat transfer coefficient and specific surface area, respectively.

2.3 Boundary Conditions. Based on the work of Amiri et al. [26], Lee and Vafai [28], and Marafie and Vafai [29], the imposed constant heat flux boundary condition under local thermal nonequilibrium conditions can be represented as

$$q_w = -k_{f,\text{eff}}\left.\frac{\partial\langle T_f\rangle^f}{\partial y}\right|_{y=0} - k_{s,\text{eff}}\left.\frac{\partial\langle T_s\rangle^s}{\partial y}\right|_{y=0} \tag{3}$$

In most cases, a solid substrate of finite thickness is attached to the porous medium and the heat flux is applied to the outer wall of the substrate. The heat will then be transferred to the porous medium through the substrate. The temperature at the interface of the porous medium and the solid substrate is likely to be uniform regardless of whether it contacts the solid or fluid. As such, the temperature of the solid and the fluid at the wall interface will be the same [26–28]:

$$\langle T_f\rangle^f|_{y=0} \approx \langle T_s\rangle^s|_{y=0} \approx T_w \tag{4}$$

For the upper wall of the channel, two general thermal boundary conditions are investigated: adiabatic and constant temperature ($T_{w,\text{up}}$) conditions. These are represented as follows.

Case I: Adiabatic boundary condition

$$\left.\frac{\partial\langle T_f\rangle^f}{\partial y}\right|_{y=H-x\tan\alpha} = \left.\frac{\partial\langle T_s\rangle^s}{\partial y}\right|_{y=H-x\tan\alpha} = 0 \tag{5}$$

Case II: Constant wall temperature boundary condition

$$\langle T_f\rangle^f|_{y=H-x\tan\alpha} \approx \langle T_s\rangle^s|_{y=H-x\tan\alpha} \approx T_{w,\text{up}} \tag{6}$$

2.4 Normalization. The governing equations are normalized utilizing the following nondimensional variables:

$$Y = \frac{y}{H - x\tan\alpha}, \quad \psi = \frac{(H - x\tan\alpha)^2}{H^2}, \quad \kappa = \frac{k_{f,\text{eff}}}{k_{s,\text{eff}}},$$
$$\bar{u} = \frac{\langle u\rangle}{u_e H/(H - x\tan\alpha)}, \quad \text{Bi} = \frac{h_{sf}a_{sf}H^2}{k_{s,\text{eff}}} \tag{7}$$

where the parameter ψ is the upper wall shape factor and the parameter κ represents the ratio of fluid to solid thermal conductivities. The parameter Bi is an equivalent Biot number representing the ratio of the conduction resistance within the solid matrix to the thermal resistance associated with the internal convective heat exchange between the matrix and the fluid phase. The temperature is normalized utilizing the above nondimensionalization and considering the two general upper boundary conditions given by the adiabatic and constant wall temperature boundary conditions, respectively, as follows.

Case I: Adiabatic boundary condition

$$\theta = \frac{k_{s,\text{eff}}(\langle T\rangle - T_w)}{Hq_w\sqrt{\psi}} \tag{8}$$

Case II: Constant wall temperature boundary condition

$$\theta = \frac{k_{s,\text{eff}}(\langle T\rangle - T_w)}{Hq_w\sqrt{\psi} + k_{s,\text{eff}}(1+\kappa)(T_{w,\text{up}} - T_w)} \tag{9}$$

Utilizing Eqs. (7)–(9), the governing equations (1) and (2) can be casted as

$$\kappa\frac{\partial^4\theta_f}{\partial Y^4} - (1+\kappa)\text{Bi}\cdot\psi\left(\frac{\partial^2\theta_f}{\partial Y^2}\right) = -\text{Bi}\cdot\psi \tag{10}$$

$$\kappa\frac{\partial^4\theta_s}{\partial Y^4}-(1+\kappa)\mathrm{Bi}\cdot\psi\left(\frac{\partial^2\theta_s}{\partial Y^2}\right)=-\mathrm{Bi}\cdot\psi \tag{11}$$

along with the following boundary conditions for the lower boundary:

$$\theta_f|_{Y=0}=\theta_s|_{Y=0}=0 \tag{12}$$

and the upper boundary as follows.

Case I: Adiabatic boundary condition

$$\left.\frac{\partial\theta_f}{\partial Y}\right|_{Y=1}=\left.\frac{\partial\theta_s}{\partial Y}\right|_{Y=1}=0 \tag{13}$$

Case II: Constant wall temperature boundary condition

$$\theta_f|_{Y=1}=\theta_s|_{Y=1}=\theta_{w,\mathrm{up}} \tag{14}$$

where

$$\theta_{w,\mathrm{up}}=\frac{k_{s,\mathrm{eff}}(T_{w,\mathrm{up}}-T_w)}{Hq_w\sqrt{\psi}+k_{s,\mathrm{eff}}(1+\kappa)(T_{w,\mathrm{up}}-T_w)} \tag{15}$$

Additional boundary conditions can be obtained by evaluating the second derivatives of θ_f and θ_s at the wall, which results in

$$\left.\frac{\partial^2\theta_f}{\partial Y^2}\right|_{Y=0}=1/\kappa,\qquad\left.\frac{\partial^2\theta_s}{\partial Y^2}\right|_{Y=0}=0 \tag{16}$$

A set of extra boundary conditions is obtained utilizing the governing equations and evaluating them at $Y=1$ along with Eq. (13) or (14) for the upper boundary for adiabatic and constant wall temperature cases, respectively. This results in the fourth set of required boundary conditions given by the following.

Case I: Adiabatic boundary condition

$$\left.\frac{\partial^3\theta_f}{\partial Y^3}\right|_{Y=1}=\left.\frac{\partial^3\theta_s}{\partial Y^3}\right|_{Y=1}=0 \tag{17}$$

Case II: Constant wall temperature boundary condition

$$\left.\frac{\partial^2\theta_f}{\partial Y^2}\right|_{Y=1}=1/\kappa,\qquad\left.\frac{\partial^2\theta_s}{\partial Y^2}\right|_{Y=1}=0 \tag{18}$$

2.5 Fluid, Solid, and Wall Temperature Fields. The fluid and solid phase temperature distributions can be obtained by solving the governing equations and boundary conditions given by Eqs. (10)–(12) and (16), and additional boundary conditions given by Eqs. (13) and (17) for an adiabatic and Eqs. (14) and (18) for a constant temperature upper wall boundary, respectively. Differential equations (10) and (11) are solved and modified using the appropriate Neumann and Dirichlet boundary conditions obtained earlier. After considerable analysis, this results in the following results for fluid, solid, fluid bulk-mean, and wall temperature profiles.

Case I: Adiabatic boundary condition

$$\theta_f=\frac{1}{1+\kappa}\left(Y\left(\frac{Y}{2}-1\right)-\frac{1}{(1+\kappa)\mathrm{Bi}\psi}\left\{1-\frac{e^{\lambda Y}+e^{\lambda(2-Y)}}{1+e^{2\lambda}}\right\}\right) \tag{19}$$

$$\theta_s=\frac{1}{1+\kappa}\left(Y\left(\frac{Y}{2}-1\right)+\frac{\kappa}{(1+\kappa)\mathrm{Bi}\psi}\left\{1-\frac{e^{\lambda Y}+e^{\lambda(2-Y)}}{1+e^{2\lambda}}\right\}\right) \tag{20}$$

where

$$\lambda=\sqrt{\mathrm{Bi}\psi(1+\kappa)/\kappa} \tag{21}$$

and

$$\Delta\theta=\theta_s-\theta_f=\frac{1}{(1+\kappa)\mathrm{Bi}\psi}\left(1-\frac{e^{\lambda Y}+e^{\lambda(2-Y)}}{1+e^{2\lambda}}\right) \tag{22}$$

$$\theta_{f,b}=\frac{-1}{1+\kappa}\left(\frac{1}{3}+\frac{1}{(1+\kappa)\mathrm{Bi}\psi}\left\{1-\frac{1}{\lambda}\frac{e^{2\lambda}-1}{e^{2\lambda}+1}\right\}\right) \tag{23}$$

$$T_w=\frac{q_w}{\rho c_pHu_e}x+T_e+\frac{q_w(H-x\tan\alpha)}{k_{s,\mathrm{eff}}(1+\kappa)}\left(\frac{1}{3}+\frac{1}{(1+\kappa)\mathrm{Bi}\psi}\times\left\{1-\frac{1}{\lambda}\frac{e^{2\lambda}-1}{e^{2\lambda}+1}\right\}\right) \tag{24}$$

Case II: Constant wall temperature boundary condition

$$\theta_f=\frac{1}{1+\kappa}\left(Y\left(\frac{Y}{2}+(1+\kappa)\theta_{w,\mathrm{up}}-\frac{1}{2}\right)-\frac{1}{(1+\kappa)\mathrm{Bi}\psi}\left\{1-\frac{e^{\lambda Y}+e^{\lambda(1-Y)}}{1+e^{\lambda}}\right\}\right) \tag{25}$$

$$\theta_s=\frac{1}{1+\kappa}\left(Y\left(\frac{Y}{2}+(1+\kappa)\theta_{w,\mathrm{up}}-\frac{1}{2}\right)+\frac{\kappa}{(1+\kappa)\mathrm{Bi}\psi}\left\{1-\frac{e^{\lambda Y}+e^{\lambda(1-Y)}}{1+e^{\lambda}}\right\}\right) \tag{26}$$

where

$$\lambda=\sqrt{\mathrm{Bi}\psi(1+\kappa)/\kappa}$$

and

$$\Delta\theta=\theta_s-\theta_f=\frac{1}{(1+\kappa)\mathrm{Bi}\psi}\left(1-\frac{e^{\lambda Y}+e^{\lambda(1-Y)}}{1+e^{\lambda}}\right) \tag{27}$$

$$\theta_{f,b}=\frac{-1}{1+\kappa}\left(\frac{1}{12}-\frac{(1+\kappa)\theta_{w,\mathrm{up}}}{2}+\frac{1}{(1+\kappa)\mathrm{Bi}\psi}\left\{1-\frac{2}{\lambda}\frac{e^{\lambda}-1}{e^{\lambda}+1}\right\}\right) \tag{28}$$

$$T_{f,b}=\left(T_e-T_{w,\mathrm{up}}-\frac{q_wH}{2k_{s,\mathrm{eff}}(1+\kappa)}\right)\exp\left[\frac{-12\mathrm{Bi}k_{s,\mathrm{eff}}(1+\kappa)^2x}{\rho c_pu_eH^2\left(7\mathrm{Bi}(1+\kappa)+12\left(1-\frac{2(e^{\lambda}-1)}{\lambda(e^{\lambda}+1)}\right)\right)}\right]+T_{w,\mathrm{up}}+\frac{q_wH}{2k_{s,\mathrm{eff}}(1+\kappa)}\quad\text{for }\alpha=0 \tag{29a}$$

$$T_{f,b}=\frac{1}{2}(T_w+T_{w,\mathrm{up}})+\left[\frac{1}{12}+\frac{1}{\mathrm{Bi}\psi(1+\kappa)}\left(1-\frac{2(e^{\lambda}-1)}{\lambda(e^{\lambda}+1)}\right)\right]\left(T_w-T_{w,\mathrm{up}}-\frac{q_w(H-x\tan(\alpha))}{k_{s,\mathrm{eff}}(1+\kappa)}\right)\quad\text{for }\alpha\neq0 \tag{29b}$$

$$T_w(x)=\left(T_{w,x=0}-T_{w,\mathrm{up}}-\frac{q_wH}{k_{s,\mathrm{eff}}(1+\kappa)}\right)\exp\left[\frac{-12\mathrm{Bi}k_{s,\mathrm{eff}}(1+\kappa)^2x}{\rho c_pu_eH^2\left(7\mathrm{Bi}(1+\kappa)+12\left(1-\frac{2(e^{\lambda}-1)}{\lambda(e^{\lambda}+1)}\right)\right)}\right]+\frac{q_wH}{k_{s,\mathrm{eff}}(1+\kappa)}+T_{w,\mathrm{up}}\quad\text{for }\alpha=0 \tag{30a}$$

$$T_w(x) = \exp\left(-\int_0^x A(\xi)d\xi\right)\left[\int_0^x \exp\left(\int_0^\xi A(\xi)d\xi\right)B(\xi)d\xi + T_{w,x=0}\right] \quad \text{for } \alpha \neq 0 \tag{30b}$$

where

$$A(\xi) = \frac{\dfrac{k_{s,\text{eff}}(1+\kappa)}{\rho c_p u_e H^2 \psi_1^{1/2}} + \dfrac{2\tan(\alpha)}{H\text{Bi}(1+\kappa)\psi_1^{3/2}}\left(\dfrac{(\lambda_1-3)e^{2\lambda_1}+4\lambda_1 e^{\lambda_1}+\lambda_1+3}{\lambda_1(e^{\lambda_1}+1)^2}\right)}{\dfrac{7}{12}+\dfrac{1}{\text{Bi}\psi_1(1+\kappa)}\left(1-\dfrac{2(e^{\lambda_1}-1)}{\lambda_1(e^{\lambda_1}+1)}\right)} \tag{30c}$$

$$B(\xi) = \frac{\left\{\begin{array}{l}\left[\dfrac{k_{s,\text{eff}}(1+\kappa)}{\rho c_p u_e H^2 \psi_1^{1/2}} + \dfrac{2\tan(\alpha)}{H\text{Bi}(1+\kappa)\psi_1^{3/2}}\left(\dfrac{(\lambda_1-3)e^{2\lambda_1}+4\lambda_1 e^{\lambda_1}+\lambda_1+3}{\lambda_1(e^{\lambda_1}+1)^2}\right)\right]T_{w,\text{up}} \\ +\dfrac{q_w\tan(\alpha)}{k_{s,\text{eff}}(1+\kappa)^2\text{Bi}\psi_1}\left[\dfrac{-(1+\kappa)\text{Bi}\psi_1}{12}+\dfrac{2(e^{\lambda_1}(\lambda_1+1)-1)}{\lambda_1(e^{\lambda_1}+1)}+\dfrac{2(-3(e^{\lambda_1}+1)-\lambda_1 e^{\lambda_1})(e^{\lambda_1}-1)}{\lambda_1(e^{\lambda_1}+1)^2}+1\right]+\dfrac{q_w}{\rho c_p u_e H}\end{array}\right\}}{\dfrac{7}{12}+\dfrac{1}{\text{Bi}\psi_1(1+\kappa)}\left(1-\dfrac{2(e^{\lambda_1}-1)}{\lambda_1(e^{\lambda_1}+1)}\right)} \tag{30d}$$

$$\psi_1 = \frac{(H-\xi\tan\alpha)^2}{H^2} \tag{30e}$$

$$\lambda_1 = \frac{\sqrt{\text{Bi}(1+\kappa)/\kappa}}{H}(H-\xi\tan\alpha) \tag{30f}$$

and

$$T_{w,x=0} = \frac{\dfrac{q_w H + k_{s,\text{eff}}(1+\kappa)T_{w,\text{up}}}{k_{s,\text{eff}}\text{Bi}(1+\kappa)^2}\left(1-\dfrac{2(e^{\Delta}-1)}{\Delta(e^{\Delta}+1)}\right)+\dfrac{q_w H}{12k_{s,\text{eff}}(1+\kappa)}-\dfrac{5}{12}T_{w,\text{up}}+T_e}{\dfrac{7}{12}+\dfrac{1}{\text{Bi}(1+\kappa)}\left(1-\dfrac{2(e^{\Delta}-1)}{\Delta(e^{\Delta}+1)}\right)} \tag{31}$$

where

$$\Delta = \sqrt{\text{Bi}(1+\kappa)/\kappa} \tag{32}$$

A simplified solution for the wall and fluid bulk-mean temperature distributions at nonzero inclination angle for Case II can be obtained when $x\tan\alpha$ is significantly smaller than the inlet of the channel.

$$T_w(x) = \Lambda + (T_{w,x=0}-\Lambda)\exp\left[\frac{-12\text{Bi}\psi k_{s,\text{eff}}(1+\kappa)^2 - 24\rho c_p u_e H\tan(\alpha)\left(\dfrac{(\lambda-3)e^{2\lambda}+4\lambda e^{\lambda}+\lambda+3}{\lambda(e^{\lambda}+1)^2}\right)}{\rho c_p u_e H^2\left\{7\text{Bi}\psi^{3/2}(1+\kappa)+12\psi^{1/2}\left(1-\dfrac{2(e^{\lambda}-1)}{\lambda(e^{\lambda}+1)}\right)\right\}}x\right] \quad \text{for } \alpha \neq 0 \tag{33}$$

$$\begin{aligned}T_{f,b} = {} & \left[\frac{7}{12}+\frac{1}{\text{Bi}\psi(1+\kappa)}\left(1-\frac{2(e^{\lambda}-1)}{\lambda(e^{\lambda}+1)}\right)\right] \\ & \times\left\{\Lambda+(T_{w,x=0}-\Lambda)\exp\left[\frac{-12\text{Bi}\psi k_{s,\text{eff}}(1+\kappa)^2 - 24\rho c_p u_e H\tan(\alpha)\left(\dfrac{(\lambda-3)e^{2\lambda}+4\lambda e^{\lambda}+\lambda+3}{\lambda(e^{\lambda}+1)^2}\right)}{\rho c_p u_e H^2\left\{7\text{Bi}\psi^{3/2}(1+\kappa)+12\psi^{1/2}\left(1-\dfrac{2(e^{\lambda}-1)}{\lambda(e^{\lambda}+1)}\right)\right\}}x\right]\right\} \\ & +\frac{T_{w,\text{up}}}{2}-\left[\frac{1}{12}+\frac{1}{\text{Bi}\psi(1+\kappa)}\left(1-\frac{2(e^{\lambda}-1)}{\lambda(e^{\lambda}+1)}\right)\right]\left(T_{w,\text{up}}+\frac{q_w(H-x\tan(\alpha))}{k_{s,\text{eff}}(1+\kappa)}\right) \quad \text{for } \alpha \neq 0\end{aligned} \tag{34}$$

where

$$\Lambda = T_{w,\mathrm{up}} + \frac{\rho c_p u_e H^2 q_w \tan(\alpha)\psi^{1/2}\left[-\frac{(1+\kappa)\mathrm{Bi}\psi}{12} + \frac{2(e^{\lambda}(\lambda+1)-1)}{\lambda(e^{\lambda}+1)} + \frac{2(-3(e^{\lambda}+1)-\lambda e^{\lambda})(e^{\lambda}-1)}{\lambda(e^{\lambda}+1)^2} + 1\right] + q_w H k_{s,\mathrm{eff}}(1+\kappa)^2\mathrm{Bi}\psi^{3/2}}{k_{s,\mathrm{eff}}(1+\kappa)\left\{k_{s,\mathrm{eff}}(1+\kappa)^2\mathrm{Bi}\psi + 2H\rho c_p u_e \tan(\alpha)\left(\frac{(\lambda-3)e^{2\lambda}+4\lambda e^{\lambda}+\lambda+3}{\lambda(e^{\lambda}+1)^2}\right)\right\}} \tag{35}$$

2.6 Heat Transfer Correlations. The wall heat transfer coefficient for the local thermal nonequilibrium model is obtained from

$$h_{w,\mathrm{nonequil}} = \frac{q_w}{T_w - T_{f,b}} \tag{36}$$

Case I: Adiabatic boundary condition

The Nusselt number at the channel wall subject to a constant heat flux can be represented as

$$\mathrm{Nu}_{w,\mathrm{nonequil}} = \frac{h_{w,\mathrm{nonequil}} D_h}{k_{f,\mathrm{eff}}} = \frac{-2}{\kappa\sqrt{\psi}\theta_{f,b}} \tag{37}$$

Utilizing Eq. (23) and after some manipulation,

$$\mathrm{Nu}_{w,\mathrm{nonequil}} = 6\frac{1+\kappa}{\kappa\sqrt{\psi}}\frac{1}{1+\frac{3}{(1+\kappa)\mathrm{Bi}\psi}\left(1-\frac{1}{\lambda}\frac{e^{2\lambda}-1}{e^{2\lambda}+1}\right)} \tag{38}$$

Case II: Constant wall temperature boundary condition

Using Eq. (9), the Nusselt number at the channel wall subject to a constant heat flux can be represented as

$$\mathrm{Nu}_{w,\mathrm{nonequil}} = \frac{h_{w,\mathrm{nonequil}} D_h}{k_{f,\mathrm{eff}}} = \frac{-2}{\kappa\theta_{f,b}\left(\sqrt{\psi} + \frac{k_{s,\mathrm{eff}}(1+\kappa)}{q_w H}(T_{w,\mathrm{up}} - T_w)\right)} \tag{39}$$

Utilizing Eq. (28) and after some manipulation, the Nusselt number can be represented as

$$\mathrm{Nu}_{w,\mathrm{nonequil}} = \frac{24\frac{1+\kappa}{\kappa}}{6+\left\{-5+\frac{12\left(1-\frac{2}{\lambda}\frac{e^{\lambda}-1}{e^{\lambda}+1}\right)}{(1+\kappa)\mathrm{Bi}}\right\}\times\left[\frac{k_{s,\mathrm{eff}}(1+\kappa)}{q_w H}(T_{w,\mathrm{up}} - T_{w,x=0}) + 1\right]\exp\left[\frac{-12\mathrm{Bi}k_{s,\mathrm{eff}}(1+\kappa)^2 x}{\rho c_p u_e H^2\left(7\mathrm{Bi}(1+\kappa) + 12\left(1-\frac{2(e^{\lambda}-1)}{\lambda(e^{\lambda}+1)}\right)\right)}\right]} \quad \text{for } \alpha = 0 \tag{40a}$$

$$\mathrm{Nu}_{w,\mathrm{nonequil}} = \frac{24\frac{1+\kappa}{\kappa\sqrt{\psi}}}{1+\frac{12}{\mathrm{Bi}\psi(1+\kappa)}\left(1-\frac{2}{\lambda}\frac{e^{\lambda}-1}{e^{\lambda}+1}\right)+\frac{k_{s,\mathrm{eff}}(1+\kappa)}{q_w H\sqrt{\psi}}(T_{w,\mathrm{up}} - T_w)\left\{-5+\frac{12}{\mathrm{Bi}\psi(1+\kappa)}\left(1-\frac{2}{\lambda}\frac{e^{\lambda}-1}{e^{\lambda}+1}\right)\right\}} \quad \text{for } \alpha \neq 0 \tag{40b}$$

2.7 Local Thermal Equilibrium Model. The energy equation for the one equation model can be obtained by adding Eqs. (1) and (2) assuming thermal equilibrium between the fluid and solid phases with the following boundary conditions:

$$\theta|_{Y=0} = 0 \tag{41}$$

and

$$\left.\frac{\partial\theta}{\partial Y}\right|_{Y=1} = 0 \quad \text{for Case I: Adiabatic boundary condition} \tag{42}$$

$$\theta|_{Y=1} = \theta_{w,\mathrm{up}} \quad \text{for Case II: Constant wall temperature boundary condition} \tag{43}$$

where $\theta_{w,\mathrm{up}}$ is defined in Eq. (15).

Based on the local thermal equilibrium model, the following results for the wall, the temperature field, and the Nusselt number are obtained.

Case I: Adiabatic boundary condition

$$\theta = \frac{Y}{1+\kappa}\left(\frac{Y}{2} - 1\right) \tag{44}$$

$$T_w = \left(\frac{1}{\rho c_p H u_e} - \frac{\tan(\alpha)}{3(k_{f,\mathrm{eff}} + k_{s,\mathrm{eff}})}\right)q_w x + T_e + \frac{q_w H}{3(k_{f,\mathrm{eff}} + k_{s,\mathrm{eff}})} \tag{45}$$

$$\mathrm{Nu}_{w,\mathrm{equil}} = 6[(1+\kappa)/\kappa\sqrt{\psi}] \tag{46}$$

Case II: Constant wall temperature boundary condition

$$\theta = \frac{Y}{1+\kappa}\left(\frac{Y}{2} + (1+\kappa)\theta_{w,\mathrm{up}} - \frac{1}{2}\right) \tag{47}$$

$$T_w(x) = \left(T_{w,x=0} - T_{w,\mathrm{up}} - \frac{q_w H}{k_{s,\mathrm{eff}}(1+\kappa)}\right)\exp\left[\frac{-12k_{s,\mathrm{eff}}(1+\kappa)x}{7\rho c_p u_e H^2}\right] + \frac{q_w H}{k_{s,\mathrm{eff}}(1+\kappa)} + T_{w,\mathrm{up}} \quad \text{for } \alpha = 0 \tag{48a}$$

$$T_w(x) = T_{w,\mathrm{up}} + \frac{q_w(H - x\tan(\alpha))}{1 - \dfrac{12k_{s,\mathrm{eff}}(1+\kappa)}{7\rho c_p u_e H\tan(\alpha)}}\left(\frac{1}{7k_{s,\mathrm{eff}}(1+\kappa)} - \frac{12}{7\rho c_p u_e H\tan(\alpha)}\right) + \left[T_{w,x=0} - T_{w,\mathrm{up}} - \frac{q_w H}{1 - \dfrac{12k_{s,\mathrm{eff}}(1+\kappa)}{7\rho c_p u_e H\tan(\alpha)}}\left(\frac{1}{7k_{s,\mathrm{eff}}(1+\kappa)} - \frac{12}{7\rho c_p u_e H\tan(\alpha)}\right)\right]\left(\frac{H - x\tan(\alpha)}{H}\right)^{12k_{s,\mathrm{eff}}(1+\kappa)/7\rho c_p u_e H\tan(\alpha)} \quad \text{for } \alpha \neq 0 \tag{48b}$$

$$\mathrm{Nu}_{w,\mathrm{equil}} = \frac{24\dfrac{1+\kappa}{\kappa}}{6 - 5\left(\dfrac{k_{s,\mathrm{eff}}(1+\kappa)}{q_w H}(T_{w,\mathrm{up}} - T_{w,x=0}) + 1\right)\exp\left[\dfrac{-12k_{s,\mathrm{eff}}(1+\kappa)x}{7\rho c_p u_e H^2}\right]} \quad \text{for } \alpha = 0 \tag{49a}$$

$$\mathrm{Nu}_{w,\mathrm{equil.}} = \frac{24\dfrac{1+\kappa}{\kappa\sqrt{\psi}}}{1 + \dfrac{5k_{s,\mathrm{eff}}(1+\kappa)}{1 - \dfrac{12k_{s,\mathrm{eff}}(1+\kappa)}{7\rho c_p u_e H\tan(\alpha)}}\left[\dfrac{\dfrac{1}{7k_{s,\mathrm{eff}}(1+\kappa)} - }{\dfrac{12}{7\rho c_p u_e H\tan(\alpha)}}\right] - 5\times\left[\begin{array}{l}\dfrac{k_{s,\mathrm{eff}}(1+\kappa)}{q_w H}\left(T_{w,up} - T_{w,x=0}\right) + \\ \dfrac{k_{s,\mathrm{eff}}(1+\kappa)}{\left(1 - \dfrac{12k_{s,\mathrm{eff}}(1+\kappa)}{7\rho c_p u_e H\tan(\alpha)}\right)}\times \\ \left(\dfrac{1}{7k_{s,\mathrm{eff}}(1+\kappa)} - \dfrac{12}{7\rho c_p u_e H\tan(\alpha)}\right)\end{array}\right]\times\psi^{\left(\frac{6k_{s,\mathrm{eff}}(1+\kappa)}{7\rho c_p u_e H\tan(\alpha)} - \frac{1}{2}\right)}}$$

$$\text{for} \quad \alpha \neq 0 \tag{49b}$$

where

$$T_{w,x=0} = \frac{q_w H}{7k_{s,\mathrm{eff}}(1+\kappa)} - \frac{5}{7}T_{w,\mathrm{up}} + \frac{12}{7}T_e \tag{50}$$

The error in utilization of the local thermal equilibrium is established based on Nusselt number expressions derived for the local thermal equilibrium and nonequilibrium models:

$$E = \frac{\mathrm{Nu}_{w,\mathrm{equil}} - \mathrm{Nu}_{w,\mathrm{nonequil}}}{\mathrm{Nu}_{w,\mathrm{nonequil}}} \tag{51}$$

This results in the following expressions.

Case I: Adiabatic boundary condition

$$E = \frac{3}{(1+\kappa)\mathrm{Bi}\psi}\left[1 - \frac{1}{\lambda}\frac{e^{2\lambda} - 1}{e^{2\lambda} + 1}\right] \tag{52}$$

Case II: Constant wall temperature boundary condition

$$E = \frac{\left\{6 + \left\{-5 + \dfrac{12\left(1 - \dfrac{2}{\lambda}\dfrac{e^{\lambda} - 1}{e^{\lambda} + 1}\right)}{(1+\kappa)\mathrm{Bi}}\right\}\times\left[\dfrac{k_{s,\mathrm{eff}}(1+\kappa)}{q_w H}(T_{w,\mathrm{up}} - T_{w,x=0}) + 1\right]\exp\left[\dfrac{-12\mathrm{Bi}k_{s,\mathrm{eff}}(1+\kappa)^2 x}{\rho c_p u_e H^2\left(7\mathrm{Bi}(1+\kappa) + 12\left(1 - \dfrac{2(e^{\lambda} - 1)}{\lambda(e^{\lambda} + 1)}\right)\right)}\right]}{6 - 5\left(\dfrac{k_{s,\mathrm{eff}}(1+\kappa)}{q_w H}(T_{w,\mathrm{up}} - T_{w,x=0}) + 1\right)\exp\left[\dfrac{-12k_{s,\mathrm{eff}}(1+\kappa)}{7\rho c_p u_e H^2}x\right]} - 1 \quad \text{for } \alpha = 0 \tag{53a}$$

$$E = \frac{1+\dfrac{12}{Bi\psi(1+\kappa)}\left(1-\dfrac{2}{\lambda}\dfrac{e^{\lambda}-1}{e^{\lambda}+1}\right)+\dfrac{k_{s,\mathrm{eff}}(1+\kappa)}{q_w H\sqrt{\psi}}\left(T_{w,\mathrm{up}}-T_w\right)\left\{-5+\dfrac{12}{Bi\psi(1+\kappa)}\left(1-\dfrac{2}{\lambda}\dfrac{e^{\lambda}-1}{e^{\lambda}+1}\right)\right\}}{1+\dfrac{5k_{s,\mathrm{eff}}(1+\kappa)}{1-\dfrac{12k_{s,\mathrm{eff}}(1+\kappa)}{7\rho c_p u_e H\tan(\alpha)}}\left[\dfrac{\dfrac{1}{7k_{s,\mathrm{eff}}(1+\kappa)}-}{\dfrac{12}{7\rho c_p u_e H\tan(\alpha)}}\right]-5\left[\begin{array}{l}\dfrac{k_{s,\mathrm{eff}}(1+\kappa)}{q_w H}\left(T_{w,\mathrm{up}}-T_{w,x=0}\right)+\\ \dfrac{k_{s,\mathrm{eff}}(1+\kappa)}{\left(1-\dfrac{12k_{s,\mathrm{eff}}(1+\kappa)}{7\rho c_p u_e H\tan(\alpha)}\right)}\times\\ \left(\dfrac{1}{7k_{s,\mathrm{eff}}(1+\kappa)}-\dfrac{12}{7\rho c_p u_e H\tan(\alpha)}\right)\end{array}\right]\times\psi^{\left(\frac{6k_{s,\mathrm{eff}}(1+\kappa)}{7\rho c_p u_e H\tan(\alpha)}-\frac{1}{2}\right)}} - 1$$

$$\text{for } \alpha \neq 0 \tag{53b}$$

3 Results and Discussion

The effect of pertinent parameters and their physical effects on fluid and solid phase temperature distributions and heat transfer are quite important in characterizing the production of an isothermal surface. The analytical temperature profiles are compared with the numerical results at different inclination angles and longitudinal locations, and also with the exact solutions by Lee and Vafai [28] and Marafie and Vafai [29] for a rectangular channel. In these studies [28,29], forced convection flow through a channel filled with a porous medium was investigated in which the upper and lower channel walls were subjected to a constant heat flux. Due to the symmetric geometry in these works [28,29], the channel centerline can be modeled as an adiabatic wall. As such, the

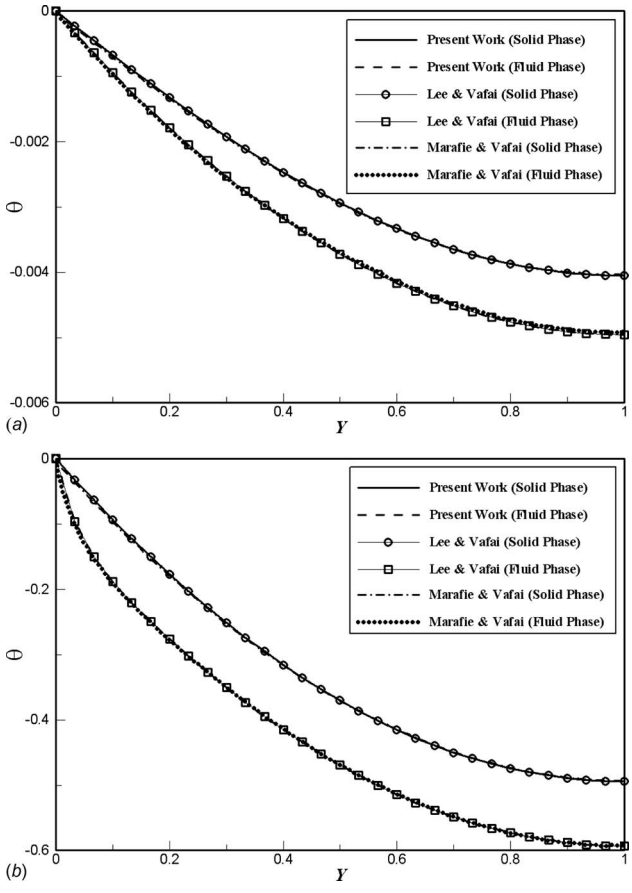

Fig. 2 Comparison of the present analytical temperature distributions for fluid and solid phases with analytical solutions by Lee and Vafai [28] and Marafie and Vafai [29] at α=0 deg and Bi=10. (*a*) κ=100 and (*b*) κ=0.01.

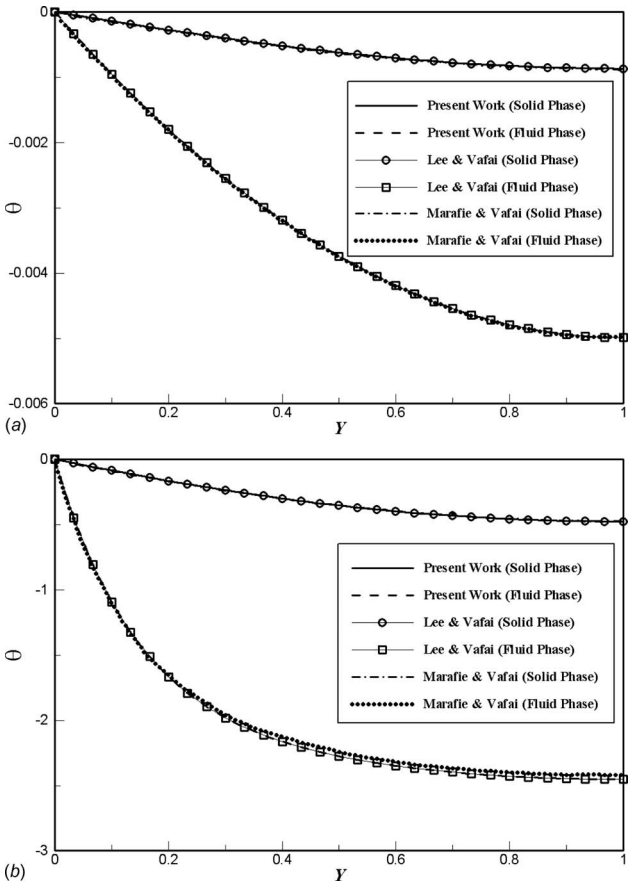

Fig. 3 Comparison of the present analytical temperature distributions for fluid and solid phases with analytical solutions by Lee and Vafai [28] and Marafie and Vafai [29] at α=0 deg and Bi=0.5. (*a*) κ=100 and (*b*) κ=0.01.

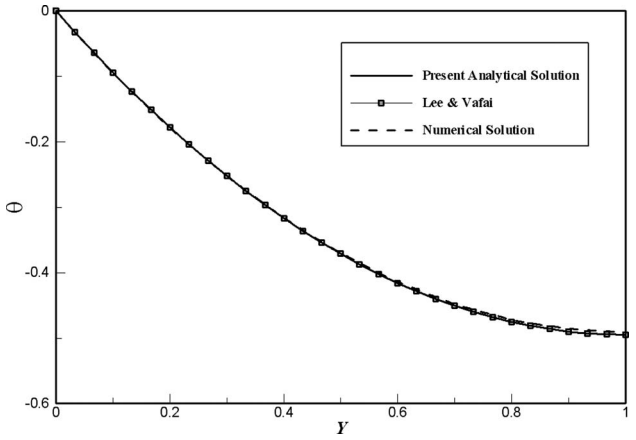

Fig. 4 Comparison of the temperature distribution for the one equation model obtained from the present analytical work, with the analytical solution of Lee and Vafai [28] and computational simulation for $\kappa=5\times10^{-5}$ and $\alpha=0$ deg

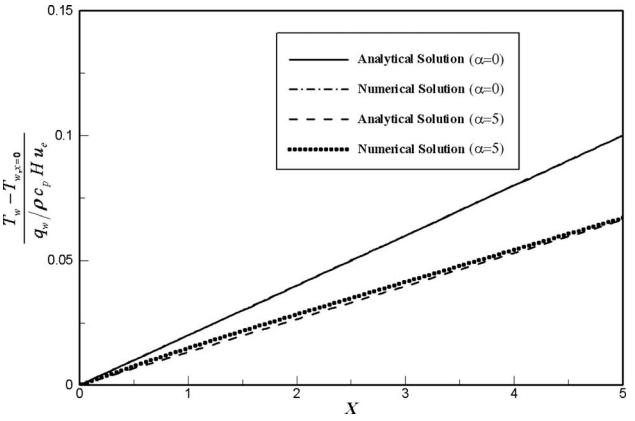

Fig. 6 Comparison between the wall temperature profile obtained from the present analytical solution and numerical simulation utilizing one equation model, at the inclination angles of 0 deg and 5 deg

results from Refs. [28,29] can be compared with the present exact solutions for zero inclination angle when an adiabatic boundary condition is employed for the upper wall of the channel. For numerical simulations, an implicit, pressure-based, cell-centered finite volume method is utilized to solve the coupled nonlinear governing equations. The governing equations including Darcy–Forchheimer–Brinkman momentum equation and the energy equation with local thermal equilibrium assumption are discretized and linearized, utilizing second order upwind method for the convection terms and central differencing for the diffusion terms. Resulting algebraic equations are solved sequentially using Gauss–Seidel point implicit linear equation solver in conjunction with an algebraic multigrid (AMG) method in order to reduce the dispersion errors while increasing the computational speed [41]. As such, first, the momentum equations are solved to obtain the velocity field. Next, the continuity equation is solved utilizing the SIMPLE algorithm for the pressure-velocity coupling to obtain and

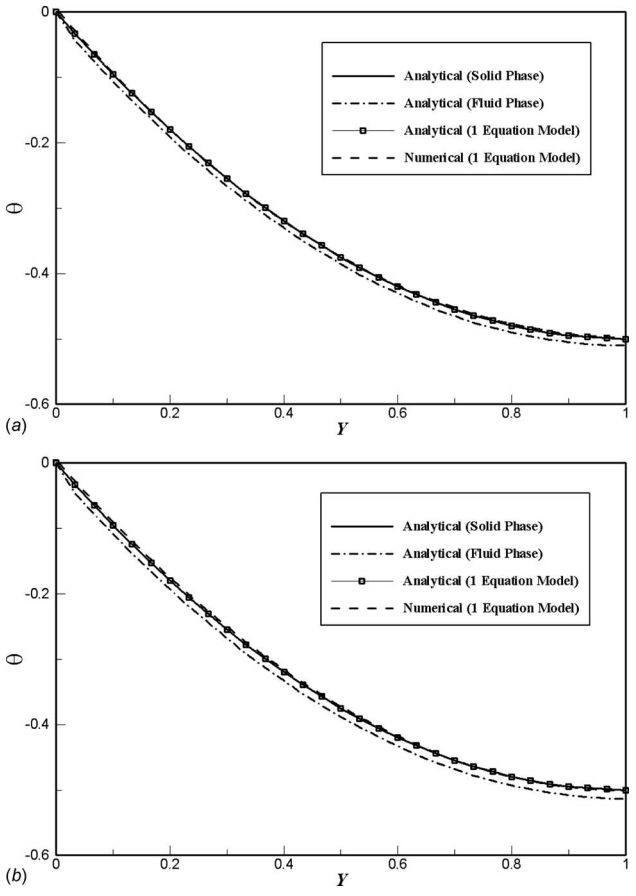

Fig. 5 Comparison of the present analytical temperature distributions (utilizing the exact solutions of two and one equation models) with the numerical simulations at $\alpha=2$ deg, Bi=100, and $\kappa=5\times10^{-5}$. (*a*) $X=1$ and (*b*) $X=4$.

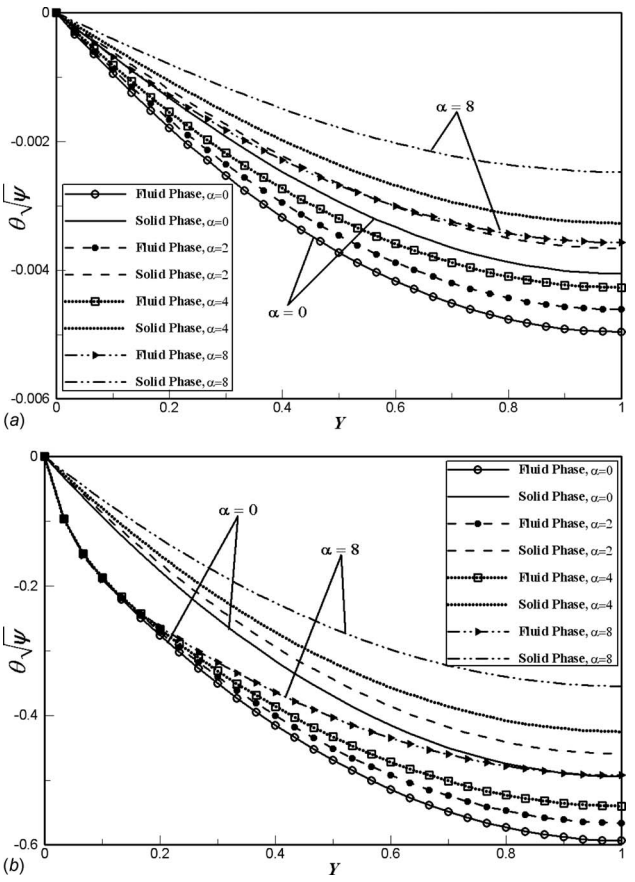

Fig. 7 Effect of inclination angle on fluid and solid temperature fields for Bi=10 at $X=2$. (*a*) $\kappa=100$ and (*b*) $\kappa=0.01$.

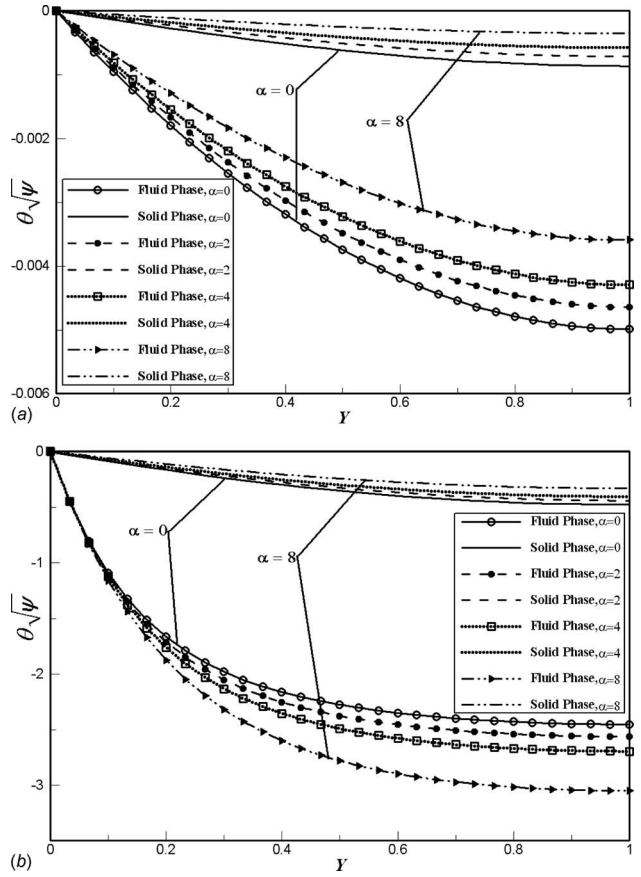

Fig. 8 Effect of inclination angle on fluid and solid temperature fields for Bi=0.5 at $X=2$. (*a*) $\kappa=100$ and (*b*) $\kappa=0.01$.

modify the pressure field, mass fluxes, and the velocity field [42]. Finally, the energy equation is solved to obtain the temperature field. An iterative procedure utilizing under-relaxation is used. Convergence is assumed when residuals become less than 10^{-6}.

Fluid and solid phase temperature distributions at zero inclination angle were found to be in excellent agreement with the analytical results by Lee and Vafai [28] and Marafie and Vafai [29]. The temperature profiles are compared with four sets of Biot numbers (Bi) and ratios of effective fluid to solid thermal conductivities (κ), as shown in Figs. 2 and 3. The small deviation in the

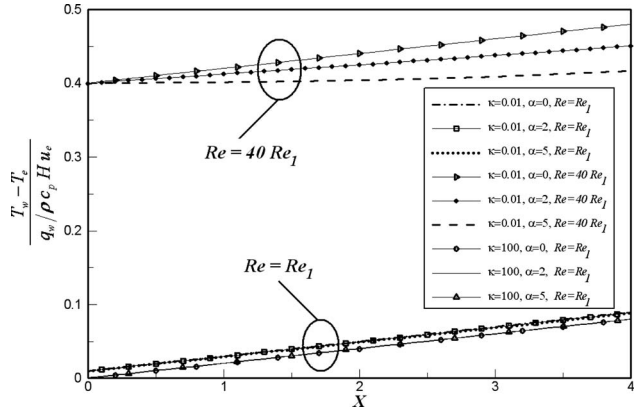

Fig. 9 Effect of the inclination angle (α), flow rate, and effective thermal conductivity ratio (κ) on the normalized wall temperature distribution for Bi=10

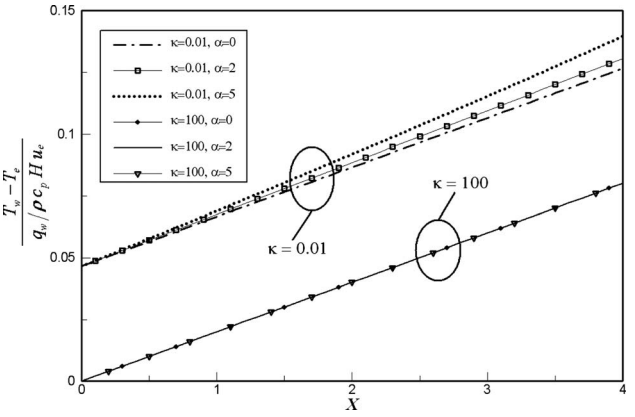

Fig. 10 Effect of the inclination angle (α) and effective thermal conductivity ratio (κ) on the normalized wall temperature distribution for Bi=0.5 and $Re=Re_1$

results is due to the utilization of generalized flow model to present fluid transport through porous medium in the work by Marafie and Vafai [29]. As expected, at lower values of the Biot number, a larger temperature difference is seen between the fluid and solid phases, due to a weak internal heat exchange between the fluid and solid. Next, the analytical temperature distribution for the case with an adiabatic upper wall is compared with the numerical results in Figs. 4 and 5. The comparisons indicate a very good agreement for the temperature profiles between the numerical and the analytical one equation model at different inclination angles (0 deg, 2 deg) and different longitudinal locations ($X=1,4$). The wall temperature distribution is also investigated to obtain a better understanding of the optimization and production of an isothermal surface. The analytical wall temperature distributions are compared with numerical simulations at different inclination angles in Fig. 6. Once again the analytical and numerical results are in excellent agreement.

To investigate the heat transfer aspects on production of an isothermal surface, the variations in the pertinent controlling parameters, such as inclination angle (α), Bi, and κ are investigated to illustrate their influence on the fluid and solid temperature distributions (Figs. 7 and 8). As can be seen in Figs. 7 and 8 an increase in the inclination angle, over a wide range, results in a more uniform solid temperature profile. The fluid temperature profile follows the same trend, except for low values of Bi and κ (Fig. 8(*b*)). For low values of κ, the heat exchange between the fluid and solid dominates over the conduction process as can be surmised from Eqs. (10) and (11). As such, an increase in the incli-

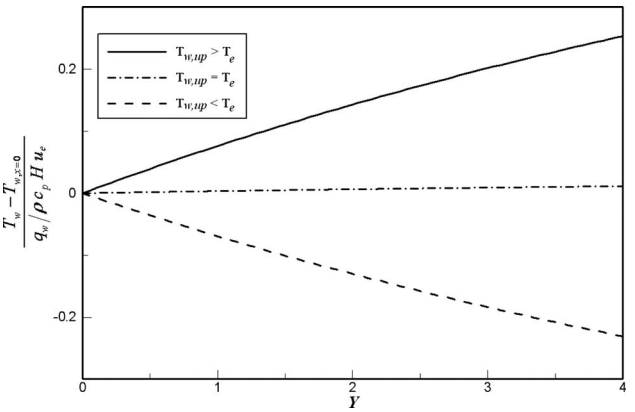

Fig. 11 Effect of the upper wall temperature (Case II) on the isothermal surface production for Bi=10, $\kappa=0.01$, and $\alpha=0$

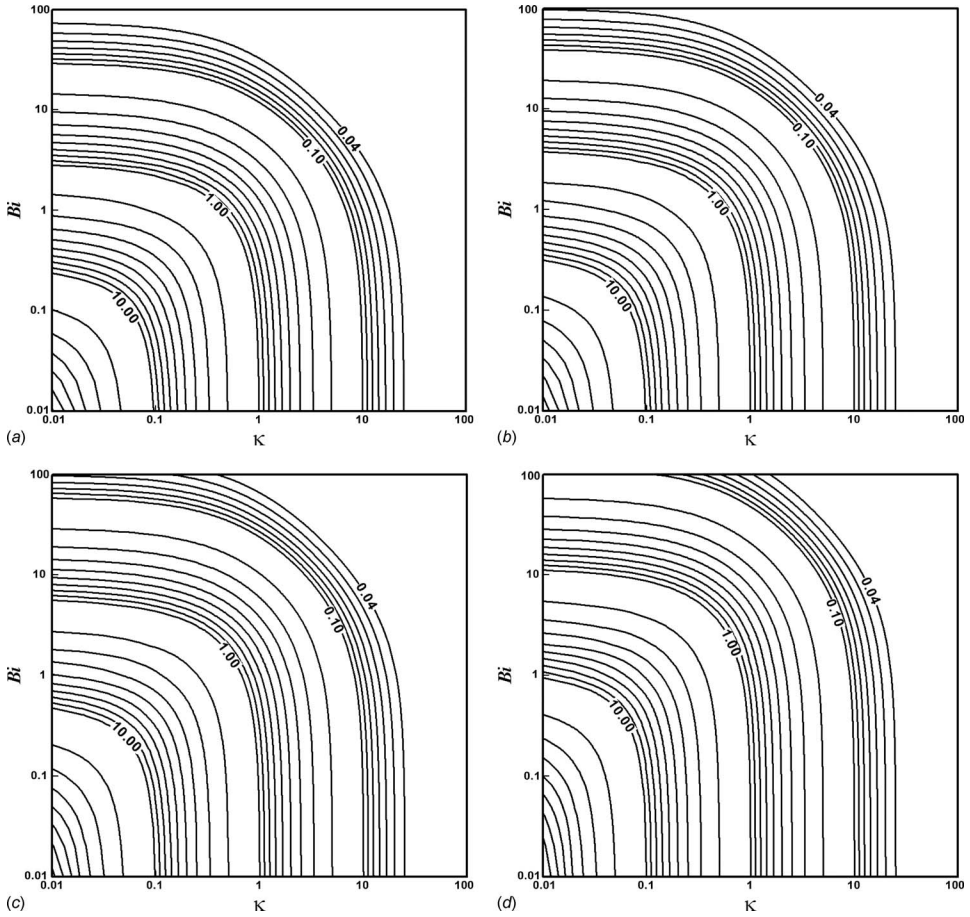

Fig. 12 Error maps on the validity of local thermal equilibrium model in the variable area channel heat exchanger: (*a*) ψ=1, (*b*) ψ=0.75, (*c*) ψ=0.5, and (*d*) ψ=0.25

nation angle at low Bi results in more deviation for the fluid phase temperature from that of the solid and the wall. However, at higher values of Bi, the inclination angle can be utilized as a valuable and effective parameter to control the wall temperature uniformity, as illustrated later in this work. The effect of Bi and κ on the temperature field at downstream locations is also investigated for nonzero inclination angles, which show trends that are similar to those shown in Figs. 7 and 8. Downstream locations are accompanied with a decrease in the channel thickness resulting in a larger convective term and heat exchange between the fluid and solid phases.

To illustrate characterization and production of an isothermal surface, the effects of the controlling parameters, $\psi(\alpha,x)$, Bi, and κ, on the wall temperature are shown in Figs. 9 and 10. Figures 9 and 10 indicate that for high effective thermal conductivity ratios (κ), changing the inclination angle does not considerably change the temperature uniformity, due to the dominating effect of the conduction over that of the fluid/solid heat exchange. However, at low thermal conductivity ratios (κ), increasing the inclination angle can modify the temperature profile. The effect of flow rate on the wall temperature distribution is also investigated in Fig. 9. The parameter Re_1 in this figure indicates a reference Reynolds number for investigating the flow rate effect. The results show that increasing the flow rate yields a more uniform temperature at the wall. For higher flow rates, the effects of inclination angle are quite substantial at high values of Bi and low values of κ. The effect of high flow rate in the cases with high value of κ can be very low due to the dominating effect of conduction in high κ.

A decrease in the effective thermal conductivity ratio can result in larger temperature values due to a decrease in heat exchange between the wall and the working fluid (Figs. 9 and 10). Also, at lower values of κ, a decrease in Biot number (at the same flow rate) results in larger wall temperature values due to a decrease in internal heat transport between the fluid and solid phases. Furthermore, for very low κ and Bi, an increase in the inclination angle can result in a slightly nonuniformity in the wall temperature (Fig. 10). For the second type of heat exchanger (Case II), the upper wall temperature also plays a role in isothermal surface production, while the effect of other parameters that have been studied earlier remains the same. Figure 11 indicates that an upper wall temperature smaller or larger than the entry temperature (T_e) can result in a more nonuniform temperature distribution, since as expected the upper wall is being employed to cool or heat the working fluid along the longitudinal direction.

To investigate the validity of local thermal equilibrium model, contour error maps are introduced based on the Nusselt number analytical expressions. As seen in Fig. 12, the error in utilizing the one equation model decreases for larger values of either the Biot number (Bi) or the effective thermal conductivity ratio (κ) or both. For larger interfacial fluid-solid heat exchange, the fluid and solid temperature distributions approach that of the one equation model indicating a small error when utilizing the one equation model. As Fig. 12 indicates, a decrease in the upper wall shape factor (ψ) reduces the validity of one equation model for a given Biot number.

4 Conclusions

Key issues in a number of thermal management devices, which may be required in biological, electronic, optical, laser, manufac-

turing, and solidification applications, are the production and regulation of an isothermal surface when it is subject to an imposed heat flux. In this work, analytical correlations are established to design a compact device capable of producing an isothermal surface. The analytical results were obtained considering negligible natural convection and radiation, hydraulically and thermally fully developed flow through the device, and homogenous and isotropic porous material. Exact solutions are presented for the fluid phase, porous substrate and surface temperature fields incorporating the local thermal nonequilibrium conditions. Nusselt number correlations are also established analytically for a generic variable cross sectional heat exchanger. These analytical results can be used as design formulas to prescribe the precise form of the setup for production of an isothermal surface. The investigation of the effect of the pertinent physical parameters indicate that the surface temperature uniformity can be regulated utilizing the inclination angle, especially for high flow rates and Biot numbers, due to larger heat exchange between the fluid and solid phases. It is established that an increase in the inclination angle results in a more uniform fluid and solid phase temperature distribution within the channel. At high effective fluid to solid thermal conductivity ratios, the fluid conduction dominates the effects of convection and the inclination angle. Utilization of the variable cross sectional area channel is also quite effective in augmenting the local Nusselt number and convective heat transfer coefficient on a surface subject to a constant heat flux. Both an insulated and a constant temperature sloped surface are considered in the analysis. It is found that utilization of local thermal equilibrium model leads to accurate results only at very high Biot numbers or at high effective fluid to solid thermal conductivities ratio. Furthermore, it is found that a decrease in the value of the upper wall shape factor (ψ) reduces the validity of the local thermal equilibrium model under the same physical conditions.

Acknowledgment

The grant from Ohio Supercomputer Center (OSC) is acknowledged and appreciated.

Nomenclature

a_{sf} = interfacial area per unit volume of porous media (m^{-1})
Bi = Biot number, $h_{sf}a_{sf}H^2/k_{s,\mathrm{eff}}$
c_p = specific heat of the working fluid ($J\,kg^{-1}\,K^{-1}$)
D_h = hydraulic diameter of the channel, $2H$(m)
E = error incurred in using the thermal equilibrium model $(\mathrm{Nu}_{w,\mathrm{equil}}-\mathrm{Nu}_{w,\mathrm{nonequil}})/\mathrm{Nu}_{w,\mathrm{nonequil}}$
h_{sf} = interstitial heat transfer coefficient ($W\,m^{-2}\,K^{-1}$)
$h_{w,\mathrm{nonequil}}$ = wall heat transfer coefficient for the thermal nonequilibrium model, $q_w/(T_w-T_{f,b})$ ($W\,m^{-2}\,K^{-1}$)
H = thickness of the channel entrance (m)
$k_{f,\mathrm{eff}}$ = effective thermal conductivity of the fluid phase ($W\,m^{-1}\,K^{-1}$)
$k_{s,\mathrm{eff}}$ = effective thermal conductivity of the solid phase ($W\,m^{-1}\,K^{-1}$)
$\mathrm{Nu}_{w,\mathrm{equil}}$ = Nusselt number of the wall subject to constant heat flux for the thermal equilibrium model
$\mathrm{Nu}_{w,\mathrm{nonequil}}$ = Nusselt number of the wall subject to constant heat flux for the thermal nonequilibrium model
q_w = heat flux at the wall ($W\,m^{-2}$)
Re = Reynolds number
T = temperature (K)
T_e = fluid temperature at the channel entrance (K)
$T_{f,b}$ = fluid bulk temperature (K)
T_w = temperature of the wall subjected to the constant heat flux (K)
$T_{w,\mathrm{up}}$ = temperature of the upper wall of the channel (K)
u = velocity ($m\,s^{-1}$)
u_e = velocity at the channel entrance ($m\,s^{-1}$)
$\bar{u}$ = nondimensional velocity, $\langle u\rangle/u_eH/(H-x\tan\alpha)$
x = longitudinal coordinate (m)
X = nondimensional longitudinal coordinate, x/H
y = transverse coordinate (m)
Y = nondimensional transverse coordinate, $y/H-x\tan\alpha$

Greek Symbols

α = inclination angle
κ = ratio of the effective fluid conductivity to that of the solid, $k_{f,\mathrm{eff}}/k_{s,\mathrm{eff}}$
θ = nondimensional temperature
$\theta_{f,b}$ = nondimensional fluid bulk temperature
$\theta_{w,\mathrm{up}}$ = nondimensional upper wall temperature, $k_{s,\mathrm{eff}}(T_{w,\mathrm{up}}-T_w)/[Hq_w\sqrt{\psi}+k_{s,\mathrm{eff}}(1+\kappa)(T_{w,\mathrm{up}}-T_w)]$
$\Delta\theta$ = nondimensional temperature difference between the solid and fluid phases
ρ = fluid density ($kg\,m^{-3}$)
λ = parameter, $\sqrt{\mathrm{Bi}\psi(1+\kappa)/\kappa}$
ψ = upper wall shape factor, $(H-x\tan\alpha)^2/H^2$

Subscripts/Superscripts

b = bulk
eff = effective property
f = fluid phase
s = solid phase
w = wall subjected to the constant heat flux
w,up = upper wall of the channel

Symbol

$\langle\rangle$ = "local volume average" of a quantity

References

[1] Zhu, N., and Vafai, K., 1998, "Analytical Modeling of the Startup Characteristics of Asymmetrical Flat-Plate and Disk-Shaped Heat Pipes," Int. J. Heat Mass Transfer, **41**, pp. 2619–2637.
[2] Wang, Y., and Vafai, K., 2000, "An Experimental Investigation of the Thermal Performance of an Asymmetrical Flat Plate Heat Pipe," Int. J. Heat Mass Transfer, **43**, pp. 2657–2668.
[3] Jiang, P. X., Fan, M. H., Si, G. S., and Ren, Z. P., 2001, "Thermal-Hydraulic Performance of Small Scale Micro-Channel and Porous-Media Heat-Exchangers," Int. J. Heat Mass Transfer, **44**(5), pp. 1039–1051.
[4] Lee, D. Y., and Vafai, K., 1999, "Comparative Analysis of Jet Impingement and Microchannel Cooling for High Heat Flux Applications," Int. J. Heat Mass Transfer, **42**, pp. 1555–1568.
[5] Vafai, K., and Zhu, L., 1999, "Analysis of a Two Layered Microchannel Heat Sink Concept in Electronic Cooling," Int. J. Heat Mass Transfer, **42**, pp. 2287–2297.
[6] Khaled, A. R., and Vafai, K., 2003, "The Role of Porous Media in Modeling Flow and Heat Transfer in Biological Tissues," Int. J. Heat Mass Transfer, **46**, pp. 4989–5003.
[7] Mahjoob, S., Vafai, K., and Beer, N. R., 2008, "Rapid Microfluidic Thermal Cycler for Polymerase Chain Reaction Nucleic Acid Amplification," Int. J. Heat Mass Transfer, **51**(9-10), pp. 2109–2122.
[8] Khanafer, K., and Vafai, K., 2001, "Isothermal Surface Production and Regulation for High Heat Flux Applications Utilizing Porous Inserts," Int. J. Heat Mass Transfer, **44**, pp. 2933–2947.
[9] Hetsroni, G., Mosyak, A., Segal, Z., and Ziskind, G., 2002, "A Uniform Temperature Heat Sink for Cooling of Electronic Devices," Int. J. Heat Mass Transfer, **45**(16), pp. 3275–3286.
[10] Erickson, D., and Li, D., 2004, "Integrated Microfluidic Devices," Anal. Chim. Acta, **507**(1), pp. 11–26.
[11] Mahjoob, S., and Vafai, K., 2008, "Analytical Characterization of Heat Transport Through Biological Media Incorporating Hyperthermia Treatment," Int. J. Heat Mass Transfer, in press.
[12] Kupchella, K., Clemons, C. B., Golovaty, D., and Young, G. W., 2006, "An Asymptotic Analysis for Directional Solidification of a Diffusion-Dominated Binary System," J. Cryst. Growth, **292**(1), pp. 111–124.
[13] Brown, R. A., 1988, "Theory of Transport Processes in Single Crystal Growth from the Melt," AIChE J., **34**(6), pp. 881–911.

[14] McLean, M., 1983, *Directionally Solidified Materials for High Temperature Service*, The Metals Society, London.
[15] Kermanpur, A., Rappaz, M., Varahram, N., and Davami, P., 2000, "Thermal and Grain-Structure Simulation in a Land-Based Turbine Blade Directionally Solidified With the Liquid Metal Cooling Process," Metall. Mater. Trans. B, **31**(6), pp. 1293–1304.
[16] Wang, Y., Amiri, A., and Vafai, K., 1999, "An Experimental Investigation of the Melting Process in a Rectangular Enclosure," Int. J. Heat Mass Transfer, **42**, pp. 3659–3672.
[17] Desai, C. P., and Vafai, K., 1993, "A Unified Critical Re-examination of the Melting Process in a Cavity," ASME J. Heat Transfer, **115**, pp. 1072–1075.
[18] Wilson, R. N., 1999, *Reflecting Telescope Optics II: Manufacture, Testing, Alignment, Modern Techniques*, Springer, New York.
[19] Barnes, W. P., 1966, "Some Effects of Aerospace Thermal Environments on High-Acuity Optical Systems," Appl. Opt., **5**(5), pp. 701–711.
[20] Sozen, M., and Vafai, K., 1990, "Analysis of the Non-Thermal Equilibrium Condensing Flow of a Gas Through a Packed Bed," Int. J. Heat Mass Transfer, **33**, pp. 1247–1261.
[21] Vafai, K., and Sozen, M., 1990, "Analysis of Energy and Momentum Transport for Fluid Flow Through a Porous Bed," ASME J. Heat Transfer, **112**, pp. 690–699.
[22] Sozen, M., and Vafai, K., 1993, "Longitudinal Heat Dispersion in Packed Beds with Real Gas Flow," J. Thermophys. Heat Transfer, **7**, pp. 153–157.
[23] Sozen, M., and Vafai, K., 1991, "Analysis of Oscillating Compressible Flow Through a Packed Bed," Int. J. Heat Fluid Flow, **12**, pp. 130–136.
[24] Vafai, K., and Sozen, M., 1990, "An Investigation of a Latent Heat Storage Packed Bed and Condensing Flow Through it," ASME J. Heat Transfer, **112**, pp. 1014–1022.
[25] Amiri, A., and Vafai, K., 1994, "Analysis of Dispersion Effects and Non-Thermal Equilibrium, Non-Darcian, Variable Porosity Incompressible Flow Through Porous Medium," Int. J. Heat Mass Transfer, **37**, pp. 939–954.
[26] Amiri, A., Vafai, K., and Kuzay, T. M., 1995, "Effect of Boundary Conditions on Non-Darcian Heat Transfer Through Porous Media and Experimental Comparisons," Numer. Heat Transfer, Part A, **27**, pp. 651–664.
[27] Alazmi, B., and Vafai, K., 2002, "Constant Wall Heat Flux Boundary Conditions in Porous Media Under Local Thermal Non-Equilibrium Conditions," Int. J. Heat Mass Transfer, **45**, pp. 3071–3087.
[28] Lee, D. Y., and Vafai, K., 1999, "Analytical Characterization and Conceptual Assessment of Solid and Fluid Temperature Differentials in Porous Media," Int. J. Heat Mass Transfer, **42**, pp. 423–435.
[29] Marafie, A., and Vafai, K., 2001, "Analysis of Non-Darcian Effects on Temperature Differentials in Porous Media," Int. J. Heat Mass Transfer, **44**, pp. 4401–4411.
[30] Poulikakos, D., and Renken, K., 1987, "Forced Convection in a Channel Filled With Porous Medium, Including the Effects of Flow Inertia, Variable Porosity, and Brinkman Friction," ASME J. Heat Transfer, **109**(4), pp. 880–888.
[31] Vafai, K., and Kim, S., 1989, "Forced Convection in a Channel Filled With Porous Medium—An Exact Solution," ASME J. Heat Transfer, **111**, pp. 1103–1106.
[32] Hunt, M. L., and Tien, C. L., 1988, "Effects of Thermal Dispersion on Forced Convection in Fibrous Media," Int. J. Heat Mass Transfer, **31**(2), pp. 301–309.
[33] Mahjoob, S., and Vafai, K., 2008, "A Synthesis of Fluid and Thermal Transport Models for Metal Foam Heat Exchangers," Int. J. Heat Mass Transfer, **51**(15-16), pp. 3701–3711.
[34] Calmidi, V. V., and Mahajan, R. L., 2000, "Forced Convection in High Porosity Metal Foams," ASME J. Heat Transfer, **122**, pp. 557–565.
[35] Phanikumar, M. S., and Mahajan, R. L., 2002, "Non-Darcy Natural Convection in High Porosity Metal Foams," Int. J. Heat Mass Transfer, **45**, pp. 3781–3793.
[36] Combarnous, M. A., and Bories, S. A., 1975, "Hydrothermal Convection in Saturated Porous Media," Adv. Hydrosci., **10**, pp. 231–307.
[37] Cheng, P., 1978, "Heat Transfer in Geothermal Systems," Adv. Heat Transfer, **14**, pp. 1–105.
[38] Tien, C. L., and Vafai, K., 1989, "Convective and Radiative Heat Transfer in Porous Media," Adv. Appl. Mech., **27**, pp. 225–282.
[39] Hadim, H., and Vafai, K., 2000, "Overview of Current Computational Studies of Heat Transfer in Porous Media and their Applications—Forced Convection and Multiphase Transport," *Advances in Numerical Heat Transfer*, Taylor & Francis, New York, pp. 291–330.
[40] Vafai, K., and Hadim, H., 2000, "Overview of Current Computational Studies of Heat Transfer in Porous Media and their Applications—Natural Convection and Mixed Convection," *Advances in Numerical Heat Transfer*, Taylor & Francis, New York, pp. 331–371.
[41] 2006, FLUENT 6.3 User's Guide, Lebanon US.
[42] Patankar, S. V., 1980, *Numerical Heat Transfer and Fluid Flow*, McGraw-Hill, New York.

Discrete Ordinates and Monte Carlo Methods for Radiative Transfer Simulation Applied to Computational Fluid Dynamics Combustion Modeling

David Joseph

Patrice Perez

Centre de Recherche d'Albi en génie des Procédés des Solides Divisés, de l'Energie et de l'Environnement, 81000 Albi, France;
HPC-SA, 3 Chemin du Pigeonnier de la Cépière, 31100 Toulouse, France

Mouna El Hafi
Centre de Recherche d'Albi en génie des Procédés des Solides Divisés, de l'Energie et de l'Environnement, 81013 Albi, France
e-mail: elhafi@enstimac.fr

Bénédicte Cuenot
CERFACS, 42 Avenue Gaspard Coriolis, 31057 Toulouse, France

Modeling radiative heat transfer in combustion applications involving complex geometries and detailed spectral properties of radiative gaseous species remains a difficult challenge, especially when full coupling with detailed chemistry and fluid dynamics is required. The Monte Carlo method (MCM) usually considered as a reference "exact" method for the computation of radiative transfer is however very demanding in CPU-time. An alternative is the discrete ordinates method (DOM), based on a finite volume approach, that is more suitable for a direct coupling with computational fluid dynamics but may lack accuracy. The aim of the present paper is to propose and demonstrate the efficiency of a methodology for radiative transfer calculation, combining the advantages of both MCM and DOM. In this approach, the fast DOM is used to compute the radiative solution, and its accuracy is controlled by comparison with the exact MCM solution at a selected controlling points. A first application of the proposed methodology to an industrial burner prototype shows its validity and potential for the direct coupling of radiation calculations with unsteady reacting flow computations. [DOI: 10.1115/1.3013832]

Keywords: radiative heat transfer, unsteady combustion, Monte Carlo, discrete ordinates, three-dimensional geometries

1 Introduction

Combustion simulation involves the treatment of coupled phenomena such as detailed chemistry, fluid mechanics and heat transfer for three-dimensional systems in complex geometries. The accurate treatment of thermal radiation is crucial if the aim is to predict the concentration of minor species, soot or wall heat fluxes that are highly dependent on temperature levels. However, the detailed calculation of radiative transfer leads to prohibitive computing time. This is even more critical for unsteady combustion simulations, where the full coupling with radiation is required.

The optically thin assumption is commonly used for the calculation of radiation in combustion simulations. In this approximation, the absorption of the gas mixture is neglected and only the emitted part of the radiative flux is considered, which considerably simplifies the calculation. This assumption may be justified in small scale non-sooty flames, although it may introduce significant errors in the prediction of pollutants [1]. In larger scale flames such as fire pools or furnaces, radiative absorption must be represented with good accuracy to predict radiative heat fluxes. In smaller industrial burners, it is known that the NO_x emission and soot production are very sensitive to radiation [2,3]. Wall heat fluxes are also critical parameters in burner design and should include radiative heat transfer [4].

In a recent work, Jensen et al. [5] compared the usual numerical methods for solving the radiative transfer equation (RTE). The ray tracing and Monte Carlo methods (MCMs) [6–9] allow to calculate quasiexact solutions and are considered as reference methods. In addition, MCM also provides estimates of the errors associated to the solution. It is able to treat high levels of complexity (complex geometries, reflective walls, scattering medium, gas spectral properties, etc.) and there is no conceptual difficulties to realize the coupling with flow dynamics. However these methods are complex and result in very high CPU costs. Many interesting ideas are actually under progress to reduce the computation time. Among them, the sensitivity approach (using first order of Taylor expansion) has been already tested in several applications [10,11] and showed good potential. Despite these improvements, the direct coupling of MCM with flow simulations is still not possible. On the contrary, the moment method [12], discrete ordinates method (DOM) [13,14], and the discrete transfer method [15] are fast and easy to couple with fluid dynamics, but they give approximate solutions. In particular the DOM is highly sensitive to the angular (ray effect) and spatial discretization. In Ref. [5], it is shown however that the DOM using the S_4 quadrature (24 discrete directions) already offers a very good compromise between CPU-time and accuracy and that the use of a higher order quadrature, such as the LC_{11} (96 discrete directions), provides accuracy levels comparable to the quasiexact methods (MCM and ray tracing).

It is possible to take advantage of the availability of the two classes of methods by combining them in a global methodology, allowing fast radiation calculations with a systematic estimation and control of the error. The simultaneous use of the pair DOM (for the radiation computation)/MCM (for the a posteriori error control) is then an optimal compromise between CPU cost and accuracy in view of coupled combustion-radiation simulations. The benefit of this approach is double: First, it allows to validate the DOM solution, and second it determines the level of accuracy of the various approximations in order to optimize the set of parameters (number of directions, discretization scheme, etc.). The objective of the present paper is to describe the proposed approach

Contributed by the Heat Transfer Division of ASME for publication in the JOURNAL OF HEAT TRANSFER. Manuscript received February 29, 2008; final manuscript received October 9, 2008; published online March 19, 2009. Review conducted by Ofodike A. Ezekoye.

and demonstrate its validity and potential for future coupled radiation-combustion simulations on different test cases.

Compared with most existing radiation codes, the coupling of radiation with combustion requires additional developments. First, the complexity of real industrial geometries requires the use of unstructured grids. For an efficient coupling, the radiative transfer model should be able to work on the same mesh as the combustion simulation and therefore handle unstructured meshes. Second, the description of the gaseous radiative properties has to be in accordance with the combustion simulations accuracy. In this context, two radiative transfer codes, DOMASIUM (based on DOM) and MCRAD (based on MCM), have been developed and applied to an unsteady combustion application following the above methodology.

In Sec. 2, the DOM and the MCM are briefly described. In Sec. 3, the DOM code, specifically developed for unstructured meshes, is validated against MCM on a nonisothermal and nonhomogeneous test case in a cylindrical geometry. Section 3.2 is devoted to the computation of thermal radiation in a real combustion chamber involving a complex geometry with an unstructured grid, using the combination of both DOM and MCM as explained above.

2 Mathematical Formulation

The two radiation codes DOMASIUM and MCRAD used in the present study were initially developed by Joseph [1] and Perez [16]. DOMASIUM is detailed in Ref. [14]. MCRAD has been utilized for benchmark publications and is described in Refs. [7] and [8]. The two codes have also been used in a pool fire problem where they have been compared with a ray tracing method, a discrete transfer method and a moment method [5], showing a good agreement with the reference solutions.

In all calculations presented in this paper, the same gas radiation property model (the statistical narrowband correlated-K model [17,18]) has been used. It is also described below.

2.1 Discrete Ordinates Method (DOM). DOMASIUM [5,14] has been designed to simulate the radiative heat transfer in coupled simulations with flow dynamics, involving unstructured grids. In the following and for the sake of clarity, the intensities and radiative properties are expressed for a single wave number (monochromatic case), but the formulation can be easily extended to a full spectrum.

The discrete ordinates method has been introduced first by Chandrashekhar [19] and have been widely used in radiative transfer applications. Considering an absorbing-emitting and nonscattering gray medium, the variation in the radiative intensity $I(\mathbf{s})$ along a line of sight can be written as

$$\frac{dI(\mathbf{s})}{ds} = \kappa I_b - \kappa I(\mathbf{s}) \tag{1}$$

where $I(\mathbf{s})$ is the radiative intensity along the directional coordinate $\mathbf{s}$, I_b is the blackbody radiative intensity, and κ is the absorption coefficient. Boundary conditions for diffuse surfaces are taken from the relation giving the intensity leaving the wall I_w as a function of the blackbody intensity of the wall $I_{b,w}$ and of the incident radiative intensity.

$$I_w(\mathbf{s}) = \epsilon_w I_{b,w} + \frac{\rho_w}{\pi} \int_{\mathbf{n}\cdot\mathbf{s}'<0} I_w(\mathbf{s}')|\mathbf{n}\cdot\mathbf{s}'|d\Omega' \tag{2}$$

where ϵ_w is the wall emissivity, ρ_w is the wall reflectivity, $\mathbf{n}$ is the unit vector normal to the wall, and $\mathbf{s}'$ is the direction of propagation of the incident radiation confined within a solid angle $d\Omega'$.

2.1.1 Angular Discretization. In the DOM, the calculation of a radiative source term at a given point is based on the discretization of the radiative transfer equation (Eq. (1)) according to a chosen number N_{dir} of discrete directions $\mathbf{s}_i(\mu_i, \eta_i, \xi_i)$, associated with the corresponding weights w_i, contained in the solid angle 4π, and where (μ_i, η_i, ξ_i) are directional cosines. Different angular discretizations may be used. In a recent study, Koch and Becker [20] compared the efficiency of several types of angular quadratures. They recommend the LC_{11} quadrature for its better accuracy. However calculations performed with the S_4 quadrature satisfy a good compromise between accuracy and rapidity as shown in Ref. [5], and may also be used.

2.1.2 Spatial Discretization for Hybrid Grids. The RTE (Eq. (1)) is solved for every discrete direction $\mathbf{s}_i$ using a finite volume approach. The integration of the RTE over the volume V of an element limited by a surface Σ, and the application of the divergence theorem yields

$$\int_{\Sigma} I(\mathbf{s}_i)\cdot\mathbf{s}_i\cdot\mathbf{n}d\Sigma = \int_V (\kappa I_b - \kappa I(\mathbf{s}_i))dV \tag{3}$$

The domain is discretized in three-dimensional control volumes V. It is assumed that I_b and $I(\mathbf{s}_i)$ are constants over the volume V and that the intensities I_j at the faces are constant over each face. Considering that I_j is the averaged intensity over the jth face, associated with the center of the corresponding face, that $I_{b,P}$ and I_P are the averaged intensities over the volume V, associated with the center of the cell, and assuming plane faces and vertices linked by straight lines, Eq. (3) can be discretized as follows:

$$\sum_{j=1}^{N_{\text{face}}} I_j(\mathbf{s}_i)\cdot(\mathbf{s}_i\cdot\mathbf{n}_j)A_j = \kappa V(I_{b,P} - I_P(\mathbf{s}_i)) \tag{4}$$

where $\mathbf{n}_j$ is the outer unit normal vector of the surface j.

The scalar product of the ith discrete direction vector with the normal vector of the jth face of the considered cell is defined by D_{ij} as

$$D_{ij} = \mathbf{s}_i\cdot\mathbf{n}_j = \mu_i n_{xj} + \eta_i n_{yj} + \xi_i n_{zj} \tag{5}$$

The discretization of the boundary condition (Eq. (2)) is straightforward.

$$I_w = \epsilon_w I_{b,w} + \frac{1-\epsilon_w}{\pi} \sum_{\mathbf{n}\cdot\mathbf{s}_i<0} w_i I(\mathbf{s}_i)|\mathbf{n}\cdot\mathbf{s}_i| \tag{6}$$

For each cell, the incident radiation G is evaluated as follows:

$$G = \int_{4\pi} I(\mathbf{s})d\Omega \simeq \sum_{i=1}^{N_{dir}} w_i I(\mathbf{s}_i) \tag{7}$$

and the incident heat flux H_w at the wall surfaces is

$$H_w = \int_{\mathbf{n}\cdot\mathbf{s}<0} I(\mathbf{s})|\mathbf{n}\cdot\mathbf{s}|d\Omega \simeq \sum_{\mathbf{n}\cdot\mathbf{s}_i<0} w_i I_i|\mathbf{n}\cdot\mathbf{s}_i| \tag{8}$$

For a gray medium, the radiative source term S_r is given by

$$S_r = \nabla\cdot Q_r = \kappa(4\pi I_b - G) \tag{9}$$

where Q_r is the radiative heat flux, and the radiative net heat flux at the wall is

$$Q_w = \epsilon\pi I_{b,w} - H \tag{10}$$

For the evaluation of the radiative intensity $I(\mathbf{s}_i)$ in Eqs. (6)–(10), Ströhle et al. [21] proposed a simple spatial differencing scheme based on the mean flux scheme that proved to be very efficient in the case of hybrid grids. This scheme relies on the following formulation:

$$I_P = \alpha\overline{I_{\text{out}}} + (1-\alpha)\overline{I_{\text{in}}} \tag{11}$$

where $\overline{I_{\text{in}}}$ and $\overline{I_{\text{out}}}$ are, respectively, the intensities averaged over the entering and the exit faces of the considered cell. α is a weighting number between 0 and 1. Substituting $\overline{I_{\text{out}}}$ from Eq. (11) into Eq. (4) yields (for more details see Ref. [14])

$$I_P = \frac{\alpha V \kappa I_b - \sum_{\substack{j \\ D_{ij}<0}} D_{ij} A_j I_j}{\alpha \kappa V + \sum_{\substack{j \\ D_{ij}>0}} D_{ij} A_j} \tag{12}$$

The case $\alpha=1$ corresponds to the Step scheme used by Liu et al. [13]. The case $\alpha=0.5$ is called the diamond mean flux scheme (DMFS), which is formally more accurate than the step scheme. After calculation of I_P from Eq. (12), the radiation intensities at cell faces such that $D_{ij}>0$ are set equal to $\overline{I_{\text{out}}}$, obtained from Eq. (11). For a given discrete direction, each face of each cell is placed either upstream or downstream of the considered cell center (a face parallel to the considered discrete direction plays no role). The control volumes are treated following a sweeping order such as the radiation intensities at upstream cell faces are known. This order depends on the discrete direction under consideration. An algorithm for the optimization of the sweeping order has been implemented [14]. Note that this sweeping order is stored for each discrete direction and only depends on the chosen grid and the angular quadrature, i.e., it is independent of the physical parameters or the flow and may be calculated only once, prior to the full computation.

2.1.3 Spectral Gas Properties. The absorption coefficient κ of the combustion products is highly dependent on the wave number ν, as shown by line spectra of radiative gases (H_2O, CO_2, and CO). To take this spectral dependency into account, the absorption coefficient of each species is here represented by the *SNB-ck* model [18,22,23]. For the gas mixture composed of different species, the same model is used, building data according to the mixing model exposed by Liu et al. [23]. The radiative solutions are obtained by computing $N_{\text{bands}} \times N_{\text{quad}}$ independent calculations where $N_{\text{bands}}=367$ is the number of narrowbands of spectral width $\Delta\eta=25$ cm^{-1}, describing the spectral properties in the range 150–9300 cm^{-1}, and $N_{\text{quad}}=5$ is the number of the Gauss–Legendre quadrature points used for the spectral integration over each narrowband. For nongray media, introducing spectral dependencies in Eq. (9) gives for the following source term:

$$S_{r,\text{DOM}} = \sum_{i=1}^{N_{\text{band}}} \sum_{j=1}^{N_{\text{quad}}} \Delta\nu_i w_{ij} \kappa_{ij} (4\pi \bar{I}_{b,ij} - G_{ij}) \tag{13}$$

where G_{ij} is obtained from Eq. (7).

The computational efficiency of such a model is strongly linked to the number of bands N_{bands} that has to be optimized depending on the studied case.

2.2 Monte Carlo Method–Net Exchange Formulation (MCM–NEF). The code MCRAD [5,7] is based on MCM and uses computer graphics algorithms. It provides the radiative source terms and the wall heat fluxes as well as their associated statistical error estimates. One of the main features of the MCM used here is the net exchange formulation (NEF). This NEF presents some similarities with the zonal method proposed by Hottel and Sarofim [24]. This formulation that satisfies the reciprocity principle was first introduced by Green [25] in 1967. It has been applied to one-dimensional radiative heat transfer problems [6,26], to multidimensional problems [7,8], and very recently, to fires for benchmark solutions [5]. The NEF is the integral formulation of the radiative heat transfer, using shape factors between two volumes (Eq. (14)), a surface and a volume (Eq. (15)), or two surfaces (Eq. (16)), respectively.

$$\zeta_{ij,\nu}^{VV} = \int_{V_j} \int_{V_i} \frac{\kappa_i \kappa_j \tau_{\nu,ij}}{s_{ij}^2} dV_i dV_j \tag{14}$$

$$\zeta_{ij,\nu}^{VS} = \int_{S_j} \int_{V_i} \frac{\kappa_i \cdot |\mathbf{n}_j \cdot \mathbf{s}| \cdot \tau_{\nu,ij}}{s_{ij}^2} dV_i dS_j \tag{15}$$

$$\zeta_{ij,\nu}^{SS} = \int_{S_j} \int_{S_i} \frac{|\mathbf{n}_i \cdot \mathbf{s}| \cdot |\mathbf{n}_j \cdot \mathbf{s}| \cdot \tau_{\nu,ij}}{s_{ij}^2} dS_i dS_j \tag{16}$$

with $\tau_\nu(s_{ij})$ the spectral transmissivity along a straight line between two points P_i and P_j expressed as

$$\tau_\nu(s_{ij}) = \exp\left[-\int_{s_i}^{s_j} \kappa_\nu(s) ds \right] \tag{17}$$

and $\Delta I_{b,\nu}$ the black intensity difference between these points,

$$\Delta I_{b,\nu} = I_{b,\nu}(P_i) - I_{b,\nu}(P_j) \tag{18}$$

These definitions allow the respective net exchange calculation:

$$\varphi_{(V_i,V_j)} = \int_0^\infty \zeta_{ij,\nu}^{VV} \Delta I_{b,\nu} d\nu \tag{19}$$

$$\varphi_{(V_i,S_j)} = \int_0^\infty \zeta_{ij,\nu}^{VS} \Delta I_{b,\nu} d\nu \tag{20}$$

$$\varphi_{(S_i,S_j)} = \int_0^\infty \zeta_{ij,\nu}^{SS} \Delta I_{b,\nu} d\nu \tag{21}$$

where φ represents the net radiative exchange between two volumes, a volume and a surface, or two surfaces. For the sake of clarity, this formulation is presented in the case of black walls. However, the generalization of these terms to nonblack walls can be found in Ref. [8]. The radiative source term for a volume V_i or the net heat flux at a surface S_i are computed by summing their radiative exchanges with all the other volumes and surfaces.

$$\int_{V_i} S_r(\mathbf{r}_{P_i}) dV_i = \sum_{j=1}^{N_s} \varphi_{(V_i,S_j)} + \sum_{j=1}^{N_v} \varphi_{(V_i,V_j)} \tag{22}$$

and

$$q_{w,\text{net},i} = \frac{\sum_{j=1}^{N_s} \varphi_{(S_i,S_j)} + \sum_{j=1}^{N_v} \varphi_{(S_i,V_j)}}{S_i} \tag{23}$$

where N_s is the number of surfaces, and N_v is the number of volumes. The multiple integrals encountered in Eqs. (19)–(21) are calculated with a Monte Carlo method [16]. Each radiative exchange can be represented as an integral $\mathbf{I}$ of a function g on the domain D. Defining an arbitrary probability density function p and a random variable X distributed according to p, $g(X)$ is also a random variable and $\mathbf{I}$ is the expectation of $g(X)$. $\mathbf{I}$ will be estimated with N samples of $g(X)$.

$$\mathbf{I} = E[g(X)] \approx \frac{1}{N} \sum_{i=1}^{N} g(x_i) = \langle g(X) \rangle_N$$

where x_i is a realization of X. This statistical approach provides the radiative source term and the wall heat flux with an error estimate. The standard deviation of the estimate is

$$\sigma(\langle g(X) \rangle_N) = \frac{1}{\sqrt{N}} \sigma(g(X)) \tag{24}$$

where $\sigma(g(X))$ is the standard deviation of $g(X)$ and is approximated as

$$\sigma(\mathbf{I}) \approx \frac{1}{\sqrt{N}} \sqrt{[\langle g(X)^2 \rangle_N - \langle g(X) \rangle_N^2]} \tag{25}$$

Note that MCRAD uses a suitable pdf p that significantly reduces the CPU-time [6].

2.2.1 Spectral Gas Properties and k-Distribution Formulation. The spectral integrations in Eqs. (19)–(21) are carried out over narrowbands, and the k-distribution method is employed within each band. According to this method, any radiative quantity A depending on κ_ν is averaged over a band of width $\Delta\nu$ as

$$\bar{A} = \frac{1}{\Delta\nu}\int_{\Delta\nu} A(\kappa_\nu)d\nu = \int_0^\infty f(\kappa)A(\kappa)d\kappa \tag{26}$$

where $f(\kappa)$ is the distribution function of the absorption coefficient within a spectral narrowband [27]. In the case of gas mixture, the absorption coefficient at a given wave number is computed as the sum of the absorption coefficients of all gas species. For a mixture of H_2O, CO_2, and CO, one obtains

$$\bar{A} = \frac{1}{\Delta\nu}\int_{\delta\nu} A(\kappa_{\nu,H_2O} + \kappa_{\nu,CO_2} + \kappa_{\nu,CO})d\nu \tag{27}$$

The correlated-k assumption is considered for nonhomogeneous media treatment in each narrowband, so that Eqs. (19)–(21) become

$$\varphi_{(V_i,V_j)} = \sum_{n=1}^{n_b}\Delta\nu_n\int_0^1 dg\int_{V_i} dV_i\int_{V_j} dV_j\frac{1}{l_{ij}^2}\kappa(g) \times \exp\left[-\int_{l_i}^{l_j}\kappa(g)dl\right]\kappa(g)\Delta I_{b,\nu}$$

$$\varphi_{(V_i,S_j)} = \sum_{n=1}^{n_b}\Delta\nu_n\int_0^1 dg\int_{V_i} dV_i\int_{S_j} dS_j\frac{\boldsymbol{u}\cdot\boldsymbol{n}_j}{l_{ij}^2}\kappa(g) \times \exp\left[-\int_{l_i}^{l_j}\kappa(g)dl\right]\Delta I_{b,\nu}$$

$$\varphi_{(S_i,S_j)} = \sum_{n=1}^{n_b}\Delta\nu_n\int_0^1 dg\int_{S_i} dS_i\int_{S_j} dS_j\frac{(\boldsymbol{u}\cdot\boldsymbol{n}_i)(\boldsymbol{u}\cdot\boldsymbol{n}_j)}{l_{ij}^2} \times \exp\left[-\int_{l_i}^{l_j}\kappa(g)dl\right]\Delta I_{b,\nu} \tag{28}$$

where l_{ij} is the length between points i and j, n_i and n_j are normal vectors to surfaces at points i and j, and $\boldsymbol{u}$ is the directional vector between i and j.

2.3 Accurate Solutions by MCM. In the proposed approach, the radiative solution is calculated with the DOM using either the S_4 or LC_{11} quadrature, allowing a fast and robust computation. However the obtained solution is not exact and the error associated to each point is unknown. To evaluate the accuracy of the DOM solution, the MCM is also run at selected representative points to calculate the reference solution at these points, which play the role of probes and are chosen according to the reacting flow field topology. Finally, the analysis of the DOM results in the light of the MCM exact solutions at the probes gives a good evaluation of the full radiation field.

3 Results

3.1 Validation Test Case. The test case presented here has already been described in detail in Ref. [7] where the MCM used in MCRAD, a ray tracing method and a DOM for structured grids were compared. Here the same test case is used to compare the DOM solution on unstructured grids, performed on DOMASIUM, with the reference MCM solution.

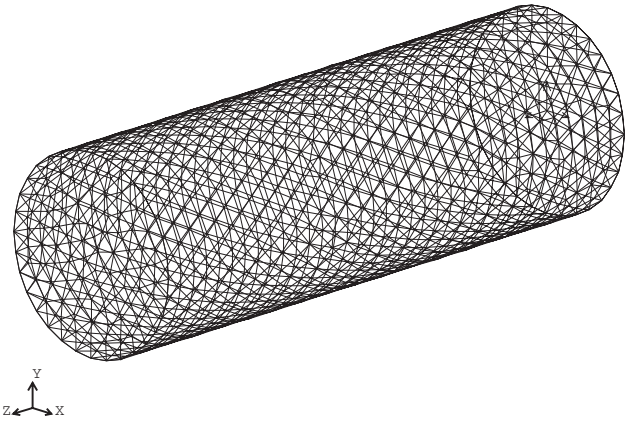

Fig. 1 Cylindrical grid (100,000 cells)

The configuration is a cylindrical black walled enclosure of length L containing a mixture of water vapor, carbon dioxide, and nitrogen at atmospheric pressure. The geometrical characteristics are $L=1.2$ m and the radius is $R=0.3$ m. The wall temperature is 800 K, except at $z=L$ where it is 300 K. The temperature and concentration fields are described by the following analytical functions.

$$T(z,r) = 800 + 1200(1 - r/R)(z/L) \tag{29}$$

$$X_{H_2O}(z,r) = 0.05\cdot[1 - 2(z/L - 0.5)^2]\cdot(2 - r/R) \tag{30}$$

$$X_{CO_2}(z,r) = 0.04\cdot[1 - 3(z/L - 0.5)^2]\cdot(2.5 - r/R) \tag{31}$$

The DOM calculation is performed using the LC_{11} quadrature and about 100,000 cells for the grid (Fig. 1).

The radiative source term along the central axis and the radiative heat flux at the wall are shown, respectively, in Figs. 2 and 3, where the results from both methods DOM and MCM are plotted. The associated relative errors obtained with MCM are presented in Figs. 4 and 5. Due to the fact that the unstructured grid used for the DOM calculation does not coincide with the location of the points calculated with the MCM, an interpolation procedure is needed to allow the comparison. From the MCM error estimates, the averaged relative error is found to be about 1.13% for the radiative source term and 1.98% for the radiative heat flux. Figure 3 demonstrates the high accuracy of the DOM for the wall heat

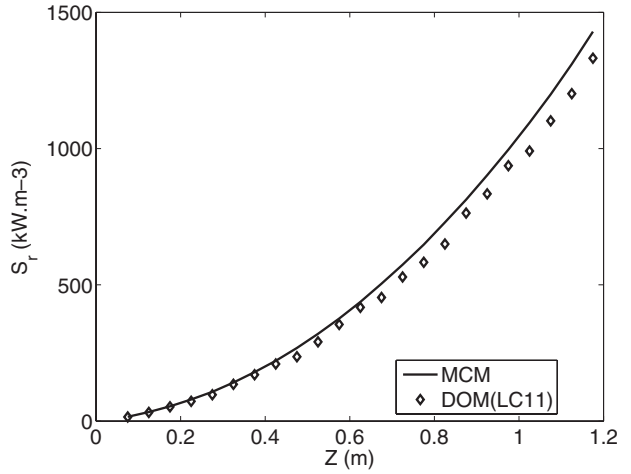

Fig. 2 Radiative source term along the central axis of the cylinder

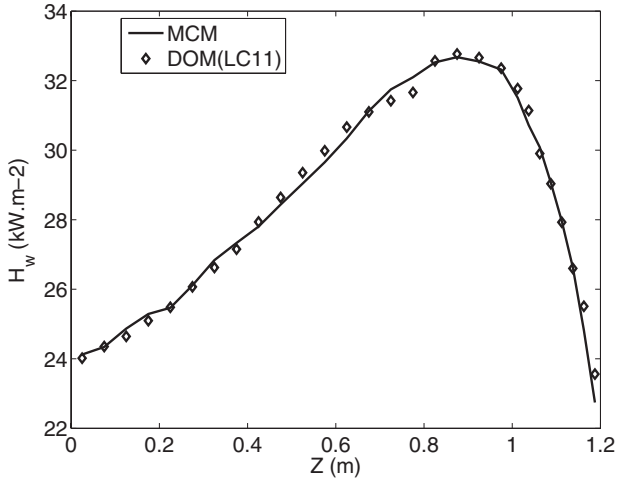

Fig. 3 Incident radiative heat flux at the wall of the cylinder

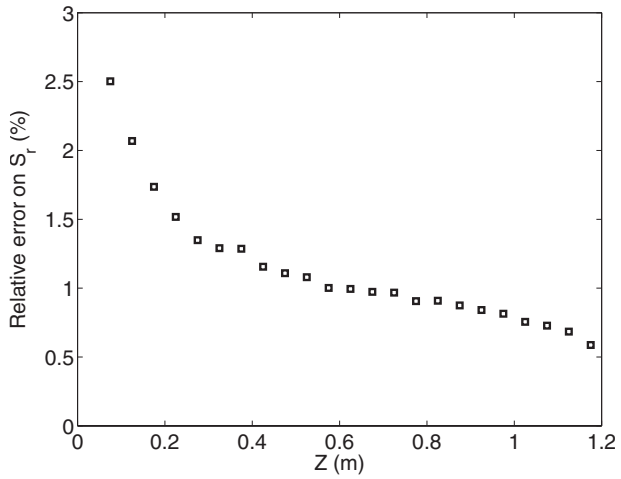

Fig. 4 Relative error associated to the MCM radiative source term along the central axis of the cylinder

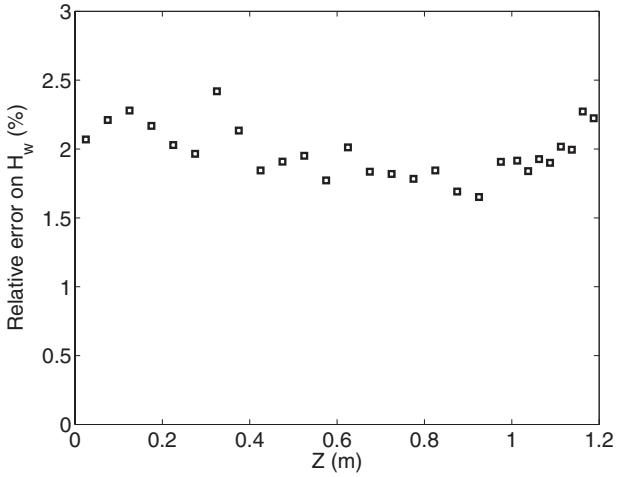

Fig. 5 Relative error associated to the MCM incident radiative heat flux at the wall of the cylinder

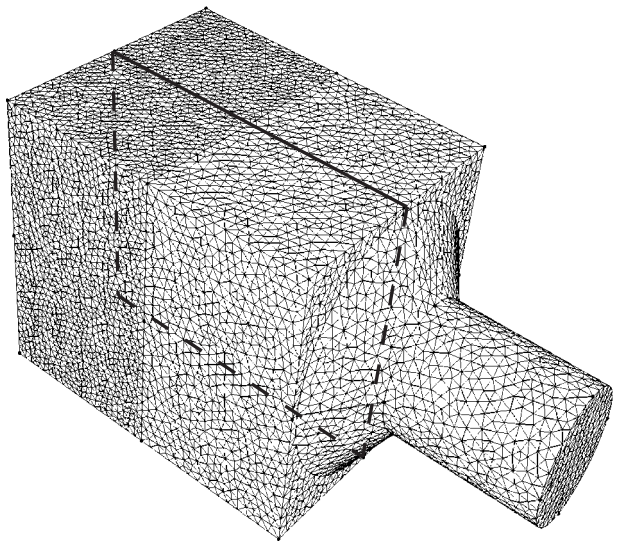

Fig. 6 Grid of the combustion chamber

flux. The source term (Fig. 2) calculated with DOM is also very accurate at the cold side of the cylinder, but a small increasing discrepancy with the MCM reference solution appears in the hot half. This discrepancy however does not exceed 10%. A first explanation may be due to the insufficient spatial discretization called "false scattering," as explained in the parametric study of Joseph [1]. He shows that false scattering increases in DOM for increasing optical thickness. In the present case, the temperature and concentration fields (Eqs. (29) and (30)) lead to higher optical thicknesses on the hot side of the cylinder and false scattering is therefore likely to appear. Another reason for the difference between DOM and MCM may be attributed to the calculation of the species molar concentration and temperature fields themselves, which are discretized in the DOM but exactly computed from Eqs. (29) and (30) in the MCM.

3.2 Application to a Real Combustion Chamber. This approach using the DOM method with the calibration by MCM is now performed on a complex 3D configuration of a realistic combustion chamber (Fig. 6).

Flow solutions are provided by a combustion code based on the large eddy simulation (LES) approach [28,29]: Here precomputed temperatures and concentration profiles are used to calculate the radiative source term, which means that calculation is performed in a noncoupled way. In this test case, a swirled turbulent premixed flame is stabilized on a methane/air injection at a stoichiometric ratio of 0.75, an air flow rate of 12 g/s, and a temperature of 300 K for a thermal power of 27 kW. The chamber has a square cross section of 86×86 mm^2 and its length is 110 mm. It ends into an exhaust duct with a 6:1 contraction. It is assumed that walls are adiabatic and may be considered as perfect radiative black bodies.

The flame/turbulence interaction is modeled by the thickened flame/efficiency function model [30,31] and the chemical scheme for combustion takes into account two reactions with six species (CH_4, O_2, CO_2, CO, H_2O, and N_2) [32]. The molar concentrations of CO_2, CO, H_2O, O_2, and N_2 are used to determine the radiative spectral properties of the mixture. Figure 7 shows a 2D view in the cutting median plane defined on Fig. 6 of the temperature and radiative species molar fractions fields obtained from the LES and used for the radiation calculation. The corresponding heat release $\dot{\omega}$ is shown on Fig. 8.

The flame has the classical conical shape found in this type of burners. It is attached to the injector and deviated from the central axis by the swirling flow that creates a central recirculation zone. The maximum heat release is of the order of 7×10^8 J m^{-3} s^{-1},

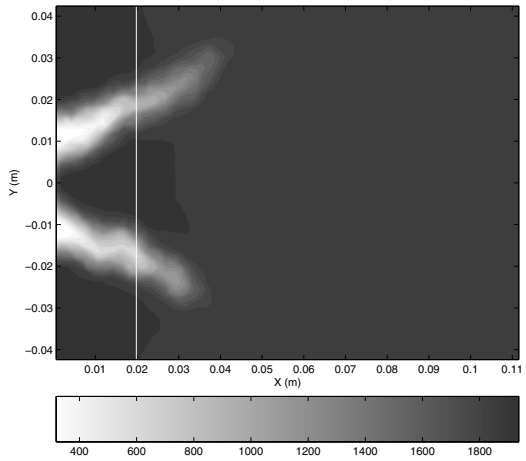

(a)The temperature

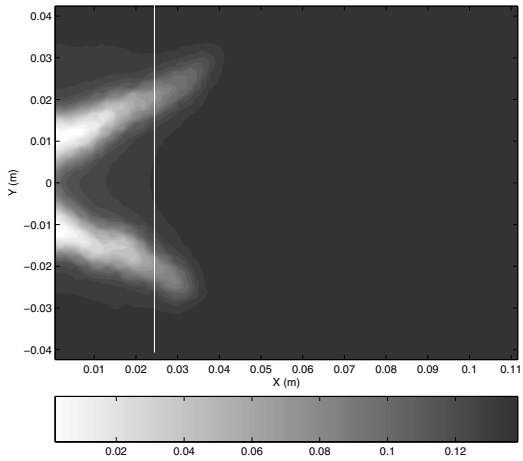

(b)X_{H_2O} profile

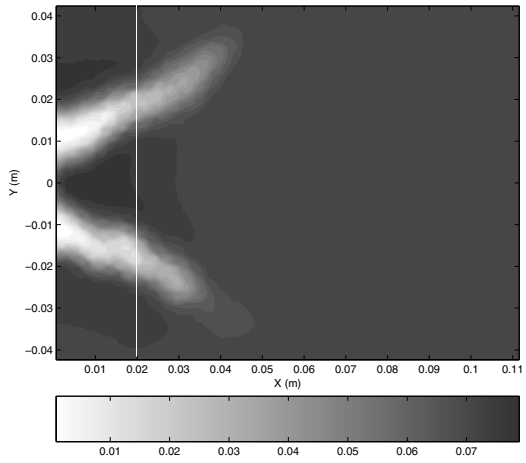

(c)X_{CO_2} profile

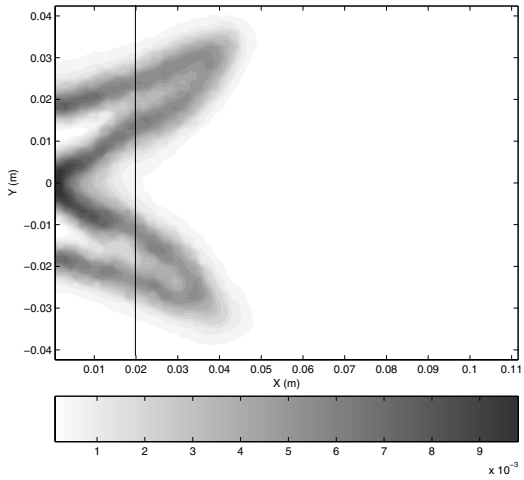

(d)X_{CO} profile

Fig. 7 Instantaneous solution fields in the median cutting plane of the combustion chamber: temperature and radiative species concentration; (*a*) temperature profile, (*b*) X_{H_2O} profile, (*c*) X_{CO_2} profile, and (*d*) X_{CO} profile

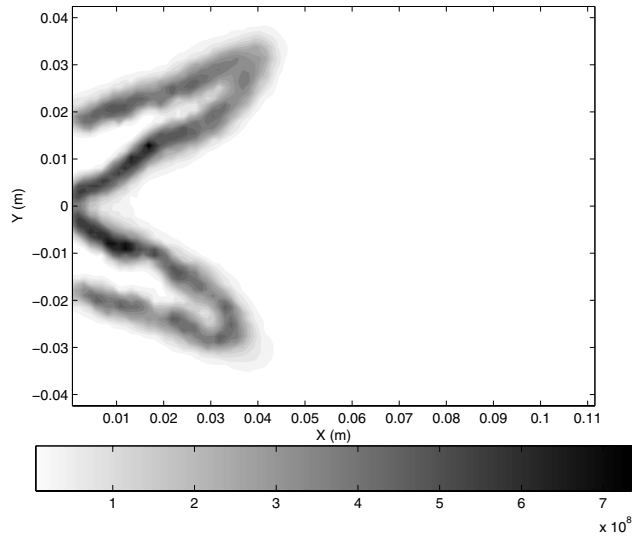

Fig. 8 Instantaneous heat release $\dot{\omega}$ in the median cutting plane of the combustion chamber

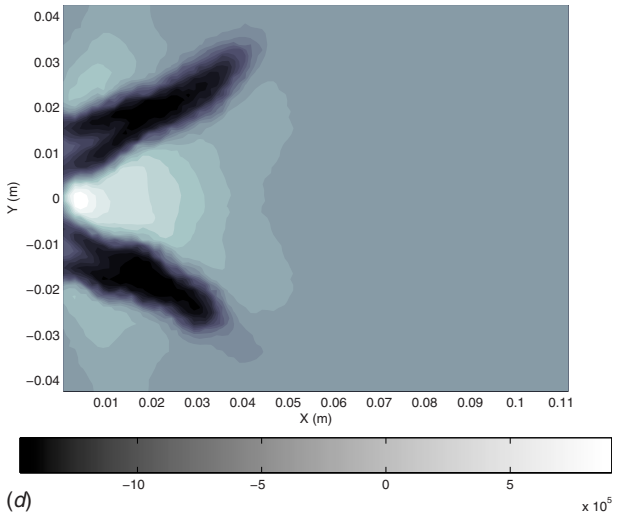

(*d*)

Fig. 9 Instantaneous radiative source term in the median cutting plane of the combustion chamber; calculation with DOM-S_4 quadrature

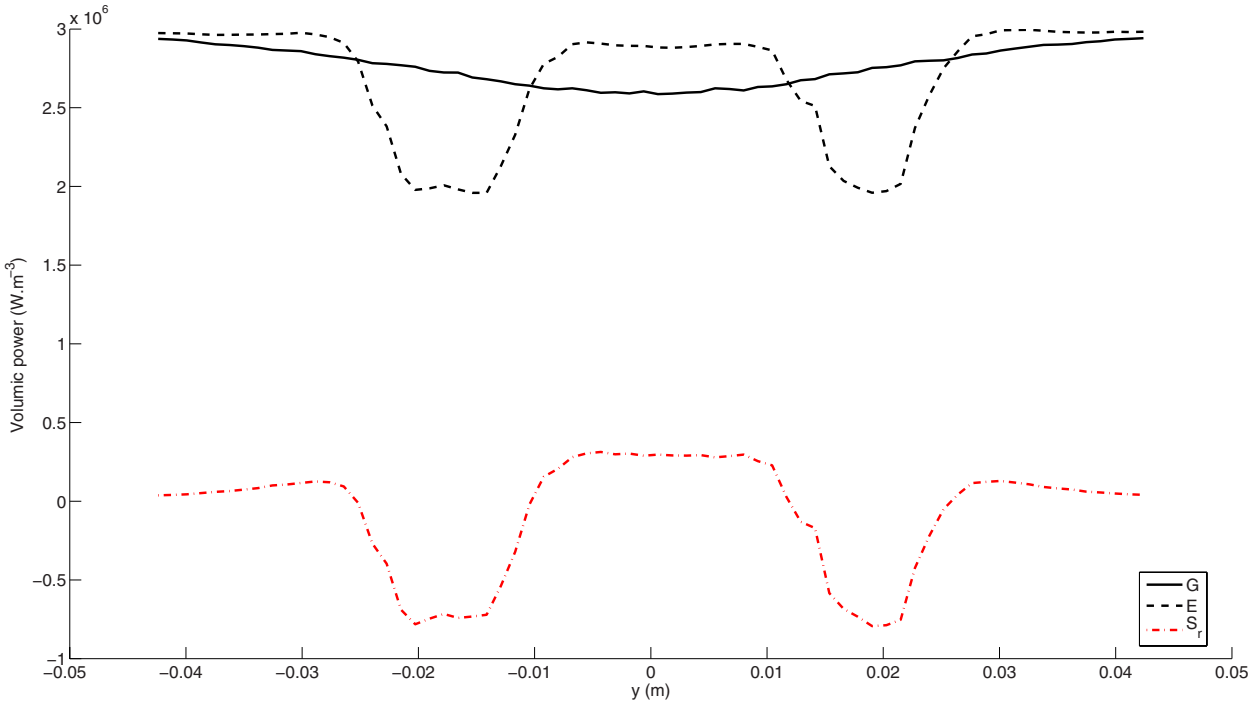

Fig. 10 Radiative incident heat flux *G*, radiative emitted heat flux *E*, and radiative source term S_r along the *y*-axis located at $x=0.02$ m in the median plane of the combustion chamber; calculation with DOM-LC_{11} quadrature

leading to a maximum temperature of about 1900 K.

Figure 9 represents the corresponding instantaneous radiative source term obtained from DOM with the S_4 quadrature. The maximum value is of the order of 10^6 J m^{-3} s^{-1}, i.e., two orders of magnitude smaller than the maximum heat release.

However it is interesting to note that the location of the maxima of these two energy source terms is completely different: the heat release is maximum at the flame front location, i.e., at the frontier between cold and hot gases, whereas the absolute value of the radiative source term is highest in the cold gas region, where there is strong absorption. This is due to the presence of absorbing chemical species (combustion products that have diffused in the unburnt gas) in these regions at a low temperature. This may give locally a significant contribution to the total gas energy, and fi-

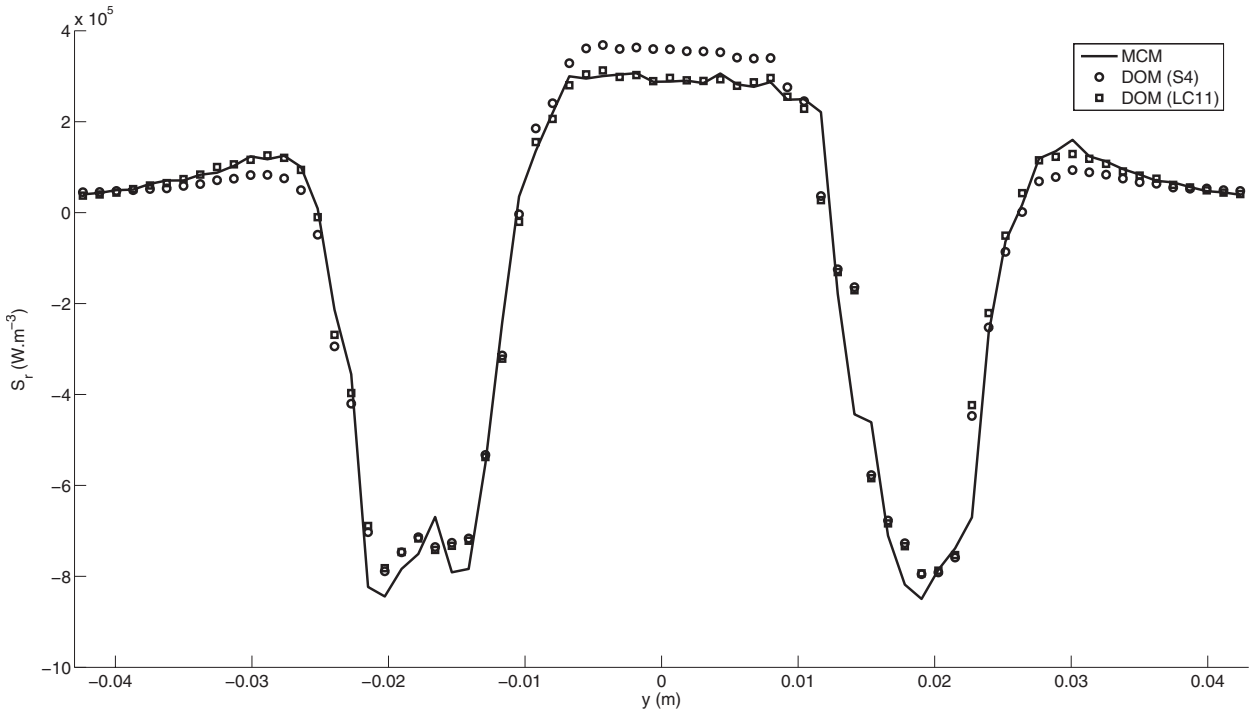

Fig. 11 Radiative source term along the *y*-axis located at $x=0.02$ m in the median plane of the combustion chamber; calculation with DOM-S_4 quadrature, DOM-LC_{11} quadrature, and MCM

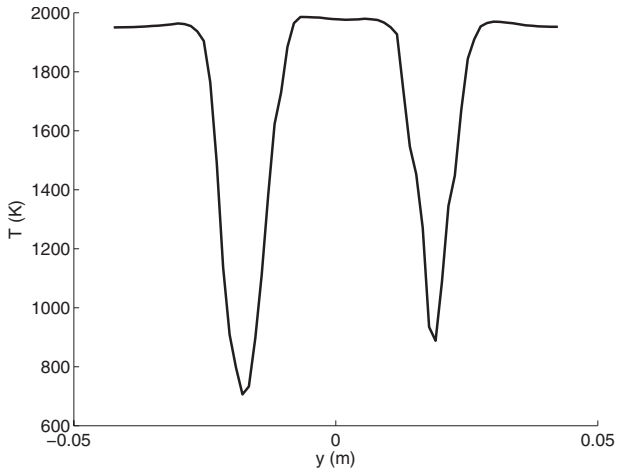

Fig. 12 Temperature profile along the *y*-axis located at $x = 0.02$ m in the median plane of the combustion chamber

nally lead to a potential high impact on the flame structure and the flow. Figure 10 represents the emitted part E and the incident part G of the radiative heat fluxes that sum to the radiative source term S_r. It appears that the radiative exchanges E and G are of the same order of magnitude and that both are higher than the source term.

Therefore in this case, a simple model based on emission only (as the optically thin model) would clearly lead to a wrong source term, which is expected to have a strong impact on minor species prediction.

The same calculation was also performed with the LC_{11} quadrature and a comparison is shown on Fig. 11, where the radiative source term (Fig. 9) is plotted along a line at $x=0.02$ m for the two DOMs (S_4 and LC_{11}) and the MCM calculations. The corresponding temperature and radiative species molar fractions profiles are represented along the same axis in Figs. 12 and 13. The averaged relative error on the MCM solution is found to be 3.17%.

The flame impact is well represented by the three methods. The solution modeled with the LC_{11} (96 discrete directions) is in excellent agreement with the reference solution, with a maximum error of 3%, confirming the already known high accuracy of this method. As expected the S_4 quadrature calculation is less accurate, in particular, in the vicinity of the flame fronts. Note that the radiative source term is either underestimated (outside the conical flame) or overestimated (inside the conic flame), although the temperature and species concentrations, and as a consequence, the emission E are nearly constant in these zones (Figs. 12, 13, and 10).

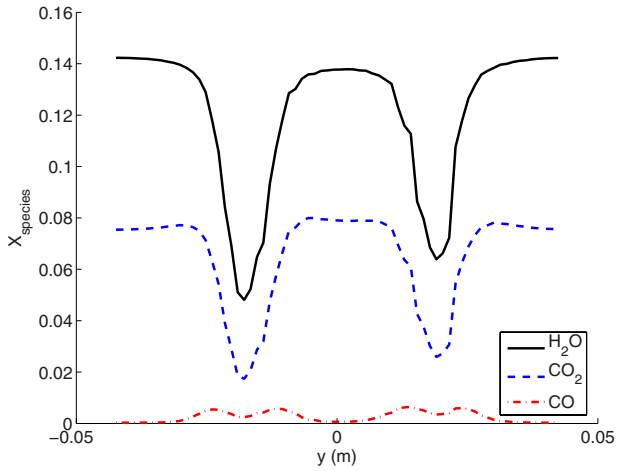

Fig. 13 Radiative species molar fractions profiles along the *y*-axis located at $x=0.02$ m in the median plane of the combustion chamber

The underestimation and the overestimation of the radiative source term S_r obtained with the S_4 quadrature are located in zones where the temperature and radiative species concentrations are maximum. This is an indication for the source error, probably due to a lack of angular resolution, and illustrates clearly the benefit of using the DOM with MCM error control. Without the reference solution, it would be impossible to identify and estimate such an error. Still the maximum error does not exceed 20% in very localized zones, and one may conclude that for most combustion applications, the accuracy of the DOM with the S_4 (24 discrete directions) quadrature is sufficient.

In the perspective of coupling radiation calculations with unsteady combustion simulations, the advantages of the DOM with MCM error control approach appear also clearly in the light of CPU cost. While for the present case, the DOM takes 4 ms/cell for each discrete direction, the MCM calculation time is of the order of a few seconds per point on the same computer.

4 Conclusions

The full coupling of radiation with unsteady combustion is a key point in the development of predictive simulation tools for industrial burners. It requires fast and accurate radiative models, in accordance with the needs of the combustion models. In this context, a DOM with MCM error control is proposed, which cumulates the advantages of both classes of methods. The validity and potential of this methodology is demonstrated on both academic and complex industrial test cases. It is shown how the effective accuracy of an approximate DOM solution is estimated with the MCM, leading to an optimal choice of parameters of the DOM and the best compromise between accuracy and efficiency.

The next step toward radiation-combustion coupled simulations is the improvement of computational resources management and an automatic control procedure using MCM probe solutions. Simpler and faster spectral radiative property models will also reduce the radiation computing time without a significant loss of accuracy, down to a time of the same order of magnitude than the combustion simulations. These developments are currently in progress and first attempts of coupled simulations have already been successful [33–36].

Acknowledgment

The support of Turbomeca and the EC project PRECCINSTA (EU Contract No. ENK5-CT-2000-00060) is gratefully acknowledged for providing the CFD data.

Special thanks to Professor Fournier of the University Paul Sabatier for his guidance and fruitful discussions.

References

[1] Joseph, D., 2004, "Modélisation des transferts radiatifs en combustion par méthode aux ordonnées discrètes sur des maillages non structurés tridimensionnels," Institut National Polytechnique de Toulouse.

[2] Beltrame, A., Porshnev, P., Merchan-Merchan, W., Savelier, A., Kennedy, L. A., Petrova, O., Zhdanok, S., Amouri, F., and Charon, O., 2001, "Soot and NO Formation in Methane-Oxygen Enriched Diffusion Flames," Combust. Flame, **124**, pp. 295–310.

[3] Hall, R. J., Smooke, M. D., and Colket, M. B., 1997, "Predictions of Soot Dynamics in Opposites Jets Diffusion Flames," *Physical and Chemical Aspects of Combustion: A Tribute to Irvin Glassman*, Academic, New York.

[4] Mbiock, M., and Weber, R., 2000, *Radiation in Enclosures*, Springer-Verlag, Berlin.

[5] Jensen, K. A., Ripoll, J. F., Wray, A. A., Joseph, D., and El Hafi, M., 2007, "On Various Modeling Approaches for Radiative Heat Transfer in Pool Fires," Combust. Flame, **148**(4), pp. 263–279.

[6] de Lataillade, A., Dufresne, J. L., El Hafi, M., Eymet, V., and Fournier, R., 2002, "A Net Exchange Monte Carlo Approach to Radiation in Optically Thick Systems," J. Quant. Spectrosc. Radiat. Transf., **74**(5), pp. 563–584.

[7] Coelho, P. J., Perez, P., and El Hafi, M., 2003, "Benchmark Numerical Solutions for Radiative Heat Transfer in Two-Dimensional Axisymmetric Enclo-

sures With Nongray Sooting Media," Numer. Heat Transfer, Part B, **43**, pp. 425–444.
[8] Perez, P., El Hafi, M., Coelho, P. J., and Fournier, R., 2005, "Accurate Solutions for Radiative Heat Transfer in Two-Dimensional Axisymmetric Enclosures With Gas Radiation and Reflective Surfaces," Numer. Heat Transfer, Part B, **47**, pp. 39–63.
[9] Tessé, L., Dupoirieux, F., and Taine, J., 2004, "Monte Carlo Modeling of Radiative Transfer in a Turbulent Sooty Flame," Int. J. Heat Mass Transfer, **47**, pp. 555–572.
[10] De Lataillade, A., Blanco, S., Clergent, Y., Dufresne, J. L., El Hafi, M., and Fournier, R., 2002, "Monte Carlo Methods and Sensitivity Estimations," J. Quant. Spectrosc. Radiat. Transf., **75**, pp. 529–538.
[11] Roger, M., Blanco, S., El Hafi, M., and Fournier, R., 2005, "Monte Carlo Estimates of Domain Deformation Sensitivities," Phys. Rev. Lett., **95**, p. 180601.
[12] Modest, M. F., 2003, *Radiative Heat Transfer*, 3rd ed., McGraw-Hill, New York.
[13] Liu, J., Shang, H. M., Chen, Y. S., and Wang, T. S., 2000, "Development of an Unstructured Radiation Model Applicable for Two Dimensional Planar, Axisymmetric and 3-Dimensional Geometries," J. Quant. Spectrosc. Radiat. Transf., **66**, pp. 17–33.
[14] Joseph, D., El Hafi, M., Fournier, R., and Cuenot, B., 2005, "Comparison of Three Spatial Differencing Schemes in Discrete Ordinates Method Using Three-Dimensional Unstructured Meshes," Int. J. Therm. Sci., **44**(9), pp. 851–864.
[15] Lockwood, F. C., and Shah, N. G., 1981, "A New Radiation Solution Method for Incorporation in General Combustion Prediction Procedures," 18th Symposium (International) on Combustion, The Combustion Institute, pp. 1405–1409.
[16] Perez, P., 2003, "Algorithmes de synthèse d'images et propriétés spectrales des gaz de combustion: méthode de Monte Carlo pour la simulation des transferts radiatifs dans les procédés à haute température," Institut National Polytechnique de Toulouse.
[17] Liu F., 1999, "Numerical Solutions of Three-Dimensional Non-Grey Gas Radiative Transfer Using the Statistical Narrow-Band Model," ASME J. Heat Transfer, **121**, pp. 200–203.
[18] Soufiani, A., and Taine, J., 1997, "High Temperature Gas Radiative Property Parameters of Statistical Narrow Band Model for H_2O, CO_2 and CO and Correlated-*K* Model for H_2O and CO_2," Int. J. Heat Mass Transfer, **40**(4), pp. 987–991.
[19] Chandrashekhar, S., 1950, *Radiative Transfer*, Clarendon, Oxford.
[20] Koch, R., and Becker, R., 2003, "Evaluation of the Quadrature Schemes for the Discrete Ordinates Method," *Proceedings of Eurotherm73 on Computational Thermal Radiation in Participating Media*, Eurotherm Series No. 11, P. Lybaert, V. Feldheim, D. Lemonnier, and N. Selçuk, eds., Elsevier, Paris, pp. 59–74.
[21] Ströhle, J., Schnell, U., and Hein, K. R. G., 2001, "A Mean Flux Discrete Ordinates Interpolation Scheme for General Coordinates," Third International Conference on Heat Transfer, Antalya.
[22] Liu, F., Smallwood, G. J., and Gülder, Ö. L., 2000, "Application of the Statistical Narrow-Band Correlated-*k* Method to Low-Resolution Spectral Intensity and Radiative Heat Transfer Calculations—Effects of the Quadrature Scheme," Int. J. Heat Mass Transfer, **43**, pp. 3119–3135.
[23] Liu, F., Smallwood, G. J., and Gülder, Ö. L., 2001, "Application of the Statistical Narrow-Band Correlated-*k* Method to Non-Grey Gas Radiation in CO_2–H_2O Mixtures: Approximate Treatments of Overlapping Bands," J. Quant. Spectrosc. Radiat. Transf., **68**, pp. 401–417.
[24] Hottel, H. C., and Sarofim, A. F., 1967, *Radiative Transfer*, McGraw-Hill, New York.
[25] Green, J. S. A., 1967, "Division of Radiative Streams Into Internal Transfer and Cooling to Space," Q. J. R. Meteorol. Soc., **93**, pp. 371–372.
[26] Cherkaoui, M., Dufresne, J. L., Fournier, R., Grandpeix, J. Y., and Lahellec, A., 1996, "Monte Carlo Simulation of Radiation in Gases With a Narrow-Band Model and a Net-Exchange Formulation," ASME J. Heat Transfer, **118**, pp. 401–407.
[27] Dufresne, J.-L., Fournier, R., and Grandpeix, J.-Y., 1999, "Inverse Gaussian *K*-Distributions," J. Quant. Spectrosc. Radiat. Transf., **61**, pp. 433–441.
[28] Schönfeld, T., and Rudgyard, M., 1999, "Steady and Unsteady Flows Simulations Using the Hybrid Flow Solver AVBP," AIAA J., **37**(11), pp. 1378–1385.
[29] Roux, S., Lartigue, G., Poinsot, T., Meier, U., and Bérat, C., 2005, "Studies of Mean and Unsteady Flow in a Swirled Combustor Using Experiments, Acoustic Analysis and Large Eddy Simulations," Combust. Flame, **141**, pp. 40–54.
[30] Angelberger, C., Egolfopoulos, F., and Veynante, D., 2000, "Large Eddy Simulations of Chemical and Acoustic Forcing of a Premixed Dump Combustor," Flow, Turbul. Combust., **65**(2), pp. 205–222.
[31] Colin, O., Ducros, F., Veynante, D., and Poinsot, T., 2000, "A Thickened Flame Model for Large Eddy Simulations of Turbulent Premixed Combustion," Phys. Fluids, **12**(7), pp. 1843–1863.
[32] Selle, L., Lartigue, G., Poinsot, T., Koch, R., Schildmacher, K. U., Krebs, W., Prade, B., Kaufmann, P., and Veynante, D., 2004, "Compressible Large Eddy Simulations of Turbulent Combustion on Complex Geometries on Unstructured Meshes," Combust. Flame, **137**, pp. 489–505.
[33] Goncalves dos Santos, R., Lecanu, M., Ducruix, S., Gicquel, O., and Veynante, D., 2005, "Large Eddy Simulations of Combustion/Radiative Heat Transfers Coupling Using the Specialized Communication Language CORBA," The Cyprus International Symposium on Complex Effects in Large Eddy Simulations, Limassol, Cyprus, Sept. 20–25.
[34] Gonçalves dos Santos, R., Ducruix, S., Gicquel, O., and Veynante, D., 2006, "Large Eddy Simulations of Turbulent Combustion Including Radiative Heat Transfers Using Specialised Communication Languages," 11th International Conference on Numerical Combustion, Granada, Spain.
[35] Gonçalves dos Santos, R., Ducruix, S., Gicquel, O., Joseph, D., El Hafi, M., and Veynante, D., 2007, "Large-Eddy Simulations Including Radiative Heat Transfer," Third European Combustion Meeting, Chania, Crete, Apr. 11–13, Paper No. 23–3.
[36] Goncalves dos Santos, R., Lecanu, M., Ducruix, S., Gicquel, O., Iacona, E., and Veynante, D., 2008, "Coupled Large Eddy Simulations of Turbulent Combustion and Radiative Heat Transfer," Combust. Flame, **152**(3), pp. 387–400.

A Simple Model for Transient Heat Conduction in an Infinite Cylinder With Convective Boundary Conditions

Messaoud Guellal
Laboratoire de Génie des Procédés Chimiques,
Université of Sétif,
Route Maâbouda,
Sétif 19000, Algéria

Hamou Sadat
Laboratoire d'Etudes Thermiques,
Université of Poitiers,
40 Avenue du Recteur Pineau,
86022 Poitiers, France

Christian Prax
Laboratoire d'Etudes Aérodynamiques,
Université of Poitiers,
40 Avenue du Recteur Pineau,
86022 Poitiers, France

A perturbation method is used to solve an unsteady one-dimensional heat conduction problem in a cylinder. A simple second order explicit solution is obtained. It is shown that this solution is accurate even for high values of the Biot number in a region surrounding the center of the cylinder.
[DOI: 10.1115/1.3082428]

Keywords: heat conduction, perturbation method, step response, cylinder, lumped capacitance model

1 Introduction

Heat conduction in cylindrical and spherical geometries may appear in many practical situations of engineering interest [1]. Analytical solution to transient heat conduction problem in a cylinder with convective boundary condition has been developed for many years in the form of infinite series whose calculation necessitates the solution of a characteristic equation involving Bessel functions for each value of the considered Biot number [2]. Furthermore, this analytical solution requires sometimes the calculation of several hundreds terms in the series in order to reach the expected accuracy [3]. In many practical situations (control, system identification, inverse problems, etc.), simpler models are very useful. When the Biot number is small (typically lower than 0.1) the classical lumped model gives a good approximation of the surface temperature [4]. It has been shown that the lumped model can be improved by using a perturbation method [5]. A second order model has then been developed for the plate configuration [6]. In this paper, we present first and second order models for the infinite cylinder. The accuracy and the limitations of these models are examined. It is shown that accurate enough solutions are obtained when using the second order model in a region surrounding the center of the cylinder.

Contributed by the Heat Transfer Division of ASME for publication in the JOURNAL OF HEAT TRANSFER. Manuscript received December 3, 2007; final manuscript received October 24, 2008; published online March 17, 2009. Review conducted by Yogendra Joshi.

2 Mathematical Formulation

We consider the heat conduction problem in an infinitely long cylinder of radius R initially at a uniform temperature T_i. The cylinder exchanges heat by convection with a medium, which is at a variable temperature $f(t)$. The convection coefficient h is constant on the whole external surface of the solid, and the thermophysical properties are assumed constant. With these assumptions, the heat equation and boundary conditions can be written in dimensionless form as

$$\frac{\partial\theta}{\partial\tau}=\frac{1}{x}\frac{\partial}{\partial x}\left(x\frac{\partial\theta}{\partial x}\right) \tag{1}$$

$$\theta(x,0)=0 \quad \text{at} \quad \tau=0$$

$$\frac{\partial\theta}{\partial x}=0 \quad \text{at} \quad x=0$$

$$-\frac{\partial\theta}{\partial x}=\mathrm{Bi}(\theta-F) \quad \text{at} \quad x=1 \tag{2}$$

where we have introduced the following dimensionless variables:

$$\theta=\frac{T-T_i}{T_\infty-T_i}, \quad \tau=\mathrm{Fo}=\frac{\alpha t}{R^2}, \quad x=\frac{r}{R}$$

$$F=\frac{f-T_i}{T_\infty-T_i}, \quad \mathrm{Bi}=\frac{hR}{\lambda} \tag{3}$$

T_∞ is a reference temperature, which will be later the fluid constant temperature.

When the fluid temperature is constant ($f(t)=T_\infty$ and $F=(f-T_i)/(T_\infty-T_i)=1$), the analytical solution of the problem defined by Eqs. (1) and (2) can be calculated by employing the separation of variables technique [2,3]. This solution is obtained as

$$\theta(x,\tau)=\sum_{i=1}^{\infty}\frac{2J_1(n_i)}{n_i[J_0^2(n_i)+J_1^2(n_i)]}J_0^2(n_i\,.\,x)\exp(-n_i^2\tau) \tag{4}$$

where the characteristic values n_i are the roots of the transcendental equation

$$n_iJ_1(n_i)-\mathrm{Bi}\;J_0(n_i)=0 \tag{5}$$

and where J_0 and J_1 are the Bessel functions of the first kind of order zero and order one, respectively.

3 Perturbation Solution

By introducing the perturbation parameter ε, the heat conduction equation is written as follows:

$$\varepsilon\frac{\partial\theta}{\partial\tau}=\frac{1}{x}\frac{\partial}{\partial x}\left(x\frac{\partial\theta}{\partial x}\right) \tag{6}$$

The solution can then be written in the form of an infinite series

$$\theta(x,\tau)=\sum_{n=0}^{\infty}\varepsilon^n\psi_n(x)F_n(\tau) \tag{7}$$

where $\psi_n(x)$ and $F_n(\tau)$ are the nth order of spatial and time functions, respectively.

By introducing the temperature expression (7) in Eq. (6) and applying the initial and boundary conditions (2), one obtains

$$\begin{aligned}&\frac{1}{x}\frac{d}{dx}\left(x\frac{d\psi_0}{dx}\right)=0\\&\psi_{n-1}=\frac{1}{x}\frac{d}{dx}\left(x\frac{d\psi_n}{dx}\right), \quad n>0\end{aligned} \tag{8}$$

and

$$\frac{d\psi_n}{dx} = 0 \qquad \text{at } x = 0$$

$$-\frac{d\psi_0}{dx} = \mathrm{Bi}(\psi_0 - 1) \quad \text{at } x = 1 \text{ for } n = 0 \tag{9}$$

$$-\frac{\partial\psi_n}{\partial x} = \mathrm{Bi}\ \psi_n \qquad \text{at } x = 1 \text{ for } n > 0$$

By truncating the series (7), temperature can be expressed at order 1 and order 2 as follows:

$$\theta(x,\tau) = F(\tau) + \psi_1(x)\frac{dF}{d\tau} \tag{10}$$

$$\theta(x,\tau) = F(\tau) + \psi_1(x)\frac{dF}{d\tau} + \psi_2(x)\frac{d^2F}{d\tau^2} \tag{11}$$

where

$$\psi_0 = 1 \tag{12}$$

$$\psi_1 = \frac{1}{4}\left(x^2 - \frac{\mathrm{Bi}+2}{2\ \mathrm{Bi}}\right) \tag{13}$$

$$\psi_2 = \frac{1}{4}\left(\frac{x^4}{16} - \frac{\mathrm{Bi}+2}{4\ \mathrm{Bi}}x^2\right) + \frac{3\ \mathrm{Bi}^2 + 12\ \mathrm{Bi} + 16}{64\ \mathrm{Bi}^2} \tag{14}$$

3.1 First Order Model. The general solution (10) cannot be used directly to determine step response. So, by using the concept of transfer function H_1, and taking the Laplace transform of the equation, we get

$$\bar{\theta}(x,p) = H_1\bar{F}(p) \tag{15}$$

where H_1 is given by

$$H_1 = 1 + p\psi_1(x) \tag{16}$$

$\bar{\theta}$ and $\bar{F}$ are the Laplace transforms of θ and F, respectively.

The transfer function (16) is now approximated (by carrying a polynomial division) as follows:

$$H_1^* = \frac{1}{1 - p\psi_1} \tag{17}$$

We can now use the inverse Laplace transform to obtain the first order temperature response

$$\theta_1(x,\tau) = 1 - \exp\left[-\frac{\tau}{\frac{1}{4}\left(\frac{\mathrm{Bi}+2}{\mathrm{Bi}} - x^2\right)}\right] \tag{18}$$

The following special cases can be derived for the center and the surface of the cylinder and for an infinite Biot number, respectively:

(i) at the cylinder center ($x=0$)

$$\theta_{1c}(\tau) = 1 - \exp\left(-\tau\frac{4\ \mathrm{Bi}}{\mathrm{Bi}+2}\right) \tag{19}$$

(ii) on the cylinder surface ($x=1$)

$$\theta_{1S}(\tau) = 1 - \exp(-2\ \mathrm{Bi}\ \tau) \tag{20}$$

(iii) for an infinite Biot number

$$\theta_1(x,\tau) = 1 - \exp\left(\frac{4}{x^2-1}\cdot\tau\right) \tag{21}$$

3.2 Second Order Model. The second order approximation leads to the following approximate transfer function:

$$H_2^* = \frac{1}{a(x)\left[\left(\frac{1}{a(x)}\right) + \left(\frac{b(x)}{a(x)}\right)p + p^2\right]} \tag{22}$$

where

$$a(x) = \frac{3}{64}x^4 - \frac{\mathrm{Bi}+2}{16\ \mathrm{Bi}}x^2 + \frac{\mathrm{Bi}+4}{64\ \mathrm{Bi}}$$
$$b(x) = -\frac{1}{4}\left(x^2 - \frac{\mathrm{Bi}+2}{\mathrm{Bi}}\right) \tag{23}$$

We can now perform the inverse Laplace transform to obtain the second order temperature response

$$\theta_2(x,\tau) = \left(\frac{1}{ap_1p_2}\right) + \left(\frac{1}{ap_1(p_1-p_2)}\right)\exp(p_1\tau) - \left(\frac{1}{ap_2(p_1-p_2)}\right)\exp(p_2\tau) \tag{24}$$

where the two poles p_1 and p_2 and the discriminant Δ are defined by

$$p_1(x) = \frac{1}{2}\left[-\left(\frac{b}{a}\right) + \sqrt{\Delta}\right] \tag{25a}$$

$$p_2(x) = \frac{1}{2}\left[-\left(\frac{b}{a}\right) - \sqrt{\Delta}\right] \tag{25b}$$

$$\Delta = \left(\frac{b}{a}\right)^2 - \frac{4}{a} = \frac{b^2 - 4a}{a^2} \tag{26}$$

For an infinite Biot number, the expressions of the two poles simplify to

$$p_1 = \frac{8}{(3x^2-1)} + 8\sqrt{\frac{2x^2}{(3x^2-1)^2(1-x^2)}} \tag{27a}$$

$$p_2 = \frac{8}{(3x^2-1)} - 8\sqrt{\frac{2x^2}{(3x^2-1)^2(1-x^2)}} \tag{27b}$$

Notice that when $x=0$, these poles degenerate to $p_1=p_2=-8$. It is worth noting here that these low order explicit models can be used for any value of the Biot number without calculating the eigenvalues.

4 Results and Discussion

The second order model can be used if the two poles are negative. We therefore discuss in this section the sign of the poles by considering the function $a(x)$ and the following function $f(x)$:

$$f(x) = b^2 - 4a = \frac{1}{8\ \mathrm{Bi}^2}(-\mathrm{Bi}^2\ x^4 + \mathrm{Bi}(\mathrm{Bi}+2)x^2 + 2)$$

It can be easily shown that this function is always positive for all Biot number values, as shown in Fig. 1.

On the other hand, function $a(x)$ is equal to zero for a singular value of x given by

$$x = x_b = \sqrt{\frac{2(\mathrm{Bi}+2) - \sqrt{\mathrm{Bi}^2 + 4\ \mathrm{Bi} + 16}}{3\ \mathrm{Bi}}}$$

For an infinite Biot number this singular position is $x_b = 1/\sqrt{3}$.

It can be shown that, while the second pole p_2 is always negative (Fig. 2), the first pole is positive beyond x_b ($x > x_b$) for all Biot numbers, as shown in Fig. 3. One may thus conclude that the second order can be used only in the region of the cylinder comprised between $x=0$ and $x=x_b$.

In order to demonstrate the validity of the second order model, we get the results obtained for three values of the Biot number, namely, Bi=0.1, Bi=10, and Bi=∞ (which is the worst case).

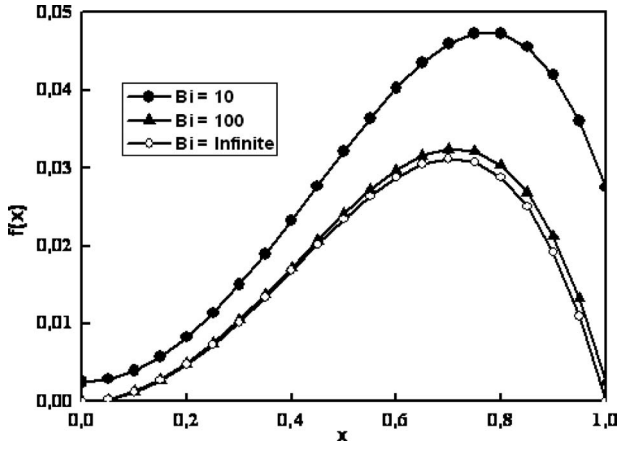

Fig. 1 Function $f(x)$ for Bi=10, Bi=100, and Bi=∞

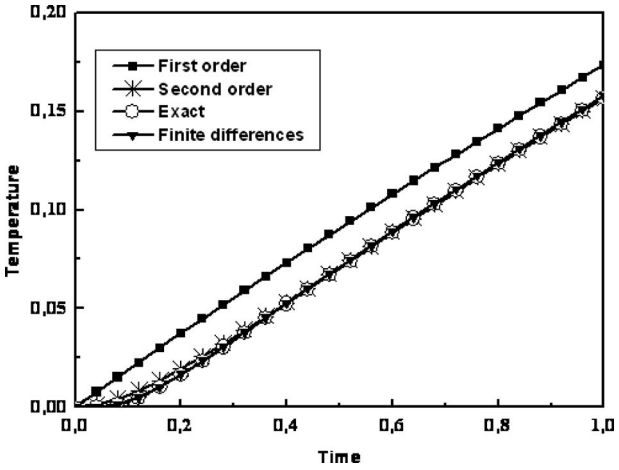

Fig. 4 Step response at $x=0$ for Bi=0.1

Figures 4 and 5, which represent the step response for Bi=0.1 at the center and at $x=0.3$, calculated by using the first and second order models together with the analytical solution and a finite difference numerical solution, show that the second order model gives accurate results and is better than the first order one, as expected. Figures 6 and 7, (Bi=10, $x=0$) and (Bi=∞, $x=0.3$), respectively, show that even for high values of the Biot number, the second order responses remain very close to the exact solutions and can therefore be used in engineering calculations.

Finally, in order to assess the accuracy of these low order models, we present in Fig. 8 the absolute relative error (in comparison with the exact analytical solution) as a function of time. The maximum error is 2.3% when using the second order perturbation method against 13.7% when using the first one.

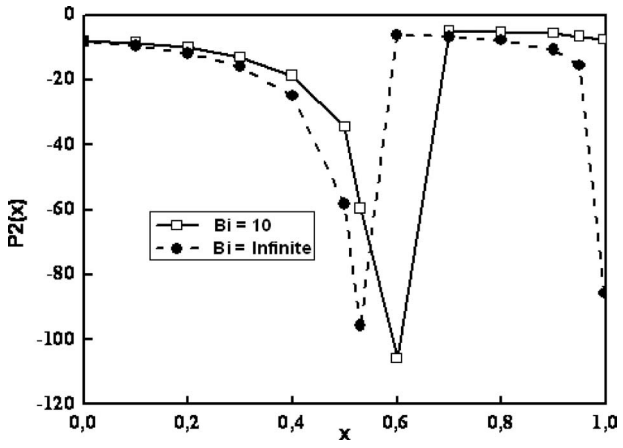

Fig. 2 Second pole for Bi=10 and Bi=∞

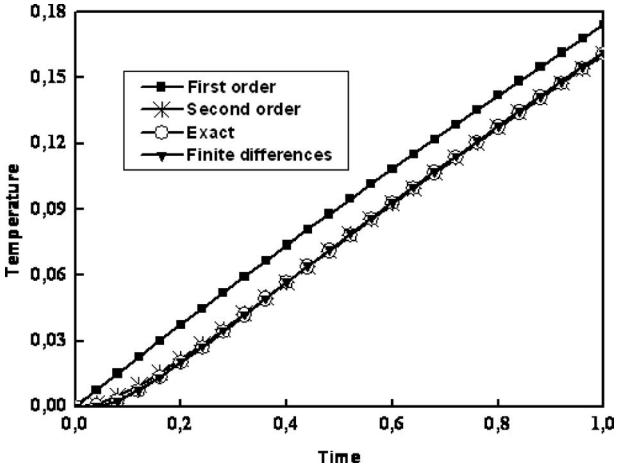

Fig. 5 Step response at $x=0.3$ for Bi=0.1

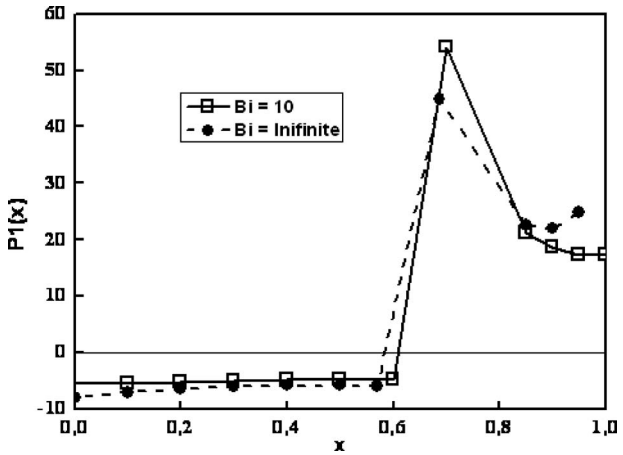

Fig. 3 First pole for Bi=10 and Bi=∞

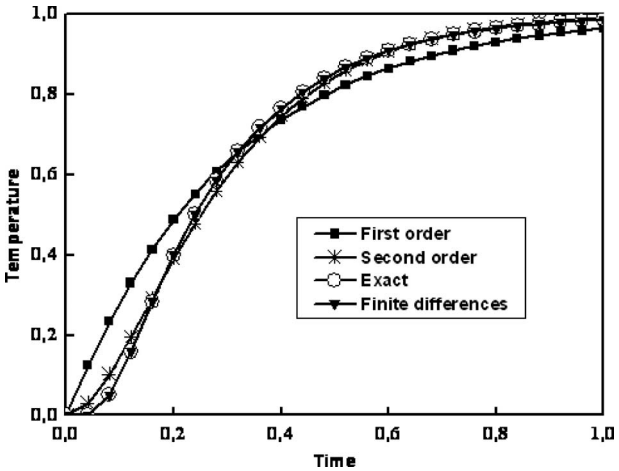

Fig. 6 Step response at $x=0$ for Bi=10

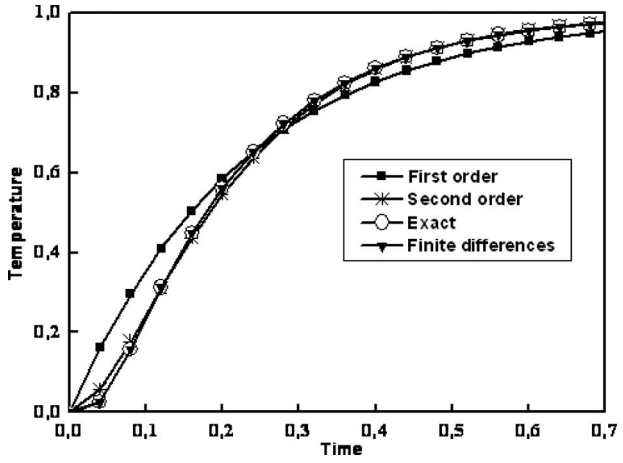

Fig. 7 Step response at $x=0.3$ for Bi$=\infty$

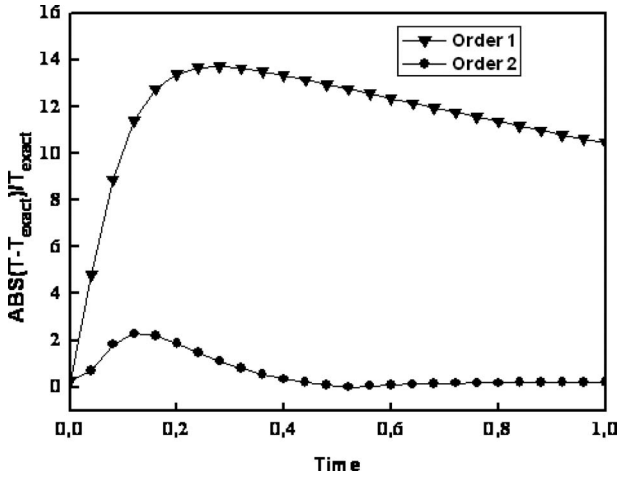

Fig. 8 Relative error of the low order models

5 Conclusion

A perturbation method applied to one-dimensional heat conduction in an infinite cylinder with convective boundary condition has been presented. It has been shown that a second order model can be used with a sufficient accuracy for engineering calculations in a region surrounding the center of the cylinder. The limits of this region have been given.

Nomenclature

Bi = Biot number
$f(t)$ = fluid temperature
Fo = Fourier number
$F(t)$ = dimensionless fluid temperature
$F_n(t)$ = time functions
h = heat convection coefficient (W m^{-2} K^{-1})
H = transfer function
H^* = approximate transfer function
n_i = transcendental equation roots
p = Laplace variable
r = radial coordinate (m)
R = radius (m)
t = time (s)
T = temperature (°C)
x = dimensionless radial coordinate

Greek Symbols

α = thermal diffusivity (m^2 s^{-1})
λ = thermal conductivity (W m^{-1} K^{-1})
ε = perturbation parameter
τ = dimensionless time
θ = dimensionless temperature
ψ_n = nth order spatial function

Subscripts

i = initial
∞ = infinite

References

[1] Atefi, G., and Moghimi, M., 2006, "A Temperature Fourier Series Solution for a Hollow Sphere," ASME J. Heat Transfer, **128**(9), pp. 963–968.
[2] Arpaci, V., 1996, *Conduction Heat Transfer*, Addison-Wesley, Reading, MA.
[3] Bairi, A., and Laraqi, N., 2003, "Diagrams for Fast Transient Conduction in Sphere and Long Cylinder Subject to Sudden and Violent Thermal Effects on Its Surface," Appl. Therm. Eng., **23**, pp. 1373–1390.
[4] Alhama, F., and Campo, A., 2001, "The Connection Between the Distributed and Lumped Models for Asymmetric Cooling of Long Slabs by Heat Convection," Int. Commun. Heat Mass Transfer, **28**(1), pp. 127–137.
[5] Sadat, H., 2005, "A General Lumped Model for Transient Heat Conduction in One Dimensional Geometries," Appl. Therm. Eng., **25**, pp. 567–576.
[6] Sadat, H., 2006, "A Second Order Model for Transient Heat Conduction in a Slab With Convective Boundary Conditions," Appl. Therm. Eng., **26**, pp. 962–965.

Analytical Solutions of Nusselt Number for Thermally Developing Radial Flow Through Small Gap Between Two Parallel Disks

Achintya Mukhopadhyay
Department of Mechanical Engineering,
Jadavpur University,
Kolkata 700 032, India
e-mail: amukhopadhyay@mech.jdvu.ac.in

Closed form solutions are developed for heat transfer due to radial flow through small gap between two parallel isothermal disks. The thermal entrance length increases with an increase in Peclet number and decrease in the inner radius of the circular disks. The attainment of fully developed Nusselt number is slower for slug flow than for fully developed creeping flow. The effect of disk rotation can be incorporated through an effective pressure gradient. The presence of disk rotation increases the thermal entrance length. [DOI: 10.1115/1.3013826]

Keywords: thermally developing flow, radial flow, parallel disks, analytical

1 Introduction

Heat transfer through thermally developing flows in conduits is important for understanding the fundamentals of convective heat transfer and also for various engineering applications. Excellent reviews on the subject are available [1,2]. The geometries most frequently investigated are circular ducts and channels formed by two parallel plates. Rectangular and triangular ducts and ducts of arbitrary cross sections have also been investigated. However, radial flow through the gap between two circular disks has received much less attention. Radial flow and heat transfer are relevant for diverse technological applications like automatic valves of reciprocating compressors [3], chemical vapor deposition (CVD) [4], and thrust bearings [5]. Impingement cooling of electronic devices [6] and a novel design of microscale combustors [7] also involve radial flow between two heated disks. These applications require accurate estimation of local heat transfer from the plates. Although some numerical simulations of fluid flow and heat transfer are available [6,8], exact solutions of heat transfer equations are not available. The objective of the present work is to obtain closed form expressions for Nusselt number in the thermally developing region.

2 Analysis

The configuration investigated consists of two coaxial disks placed parallel to each other. The fluid flows radially, entering at the inner radius, r_i, with temperature, T_i. The walls are maintained at a constant temperature, T_w. The analysis is made with the following assumptions.

1. Flow is only in the radial direction.
2. Diffusion is neglected in the radial direction, as the spacing between the plates is much smaller than the outer radius of the plates.

Contributed by the Heat Transfer Division of ASME for publication in the JOURNAL OF HEAT TRANSFER. Manuscript received November 6, 2007; final manuscript received September 14, 2008; published online March 17, 2009. Review conducted by Minking Chyu.

The governing energy equation is expressed in the following form:

$$u(r,z)\frac{\partial T}{\partial r} = \alpha\frac{\partial^2 T}{\partial z^2} \tag{1}$$

The boundary conditions for the problem are given as

$$r = r_i : T = T_i \tag{2a}$$

$$z = \pm b : T = T_w \tag{2b}$$

In this configuration, the velocity decreases along the radial direction. However, the flow rate through the plate is constant. The flow rate is given by

$$Q = 2\pi b\bar{u}r \tag{3}$$

We use the following scaling to nondimensionalize the problem:

$$\theta = \frac{T - T_w}{T_i - T_w}, \quad Z = \frac{z}{b}, \quad R = \frac{r}{b} \tag{4}$$

The problem is expressed in dimensionless form as

$$\frac{\mathrm{Pe}}{R}U\frac{\partial\theta}{\partial R} = \frac{\partial^2\theta}{\partial Z^2} \tag{5}$$

with

$$R = R_i : \theta = 1 \tag{6a}$$

$$Z = \pm 1 : \theta = 0 \tag{6b}$$

In Eq. (5), Peclet number, Pe, is defined as $\mathrm{Pe} = \bar{u}r/\alpha = u_i r_i/\alpha$. It is to be noted that Eq. (3) implies that $u_i r_i = \bar{u}r$. This definition ensures a constant value of Peclet number. Two flow configurations are studied here, namely, slug flow and fully developed creeping flow for which exact solutions for the velocity profile are possible. However, for radial flow through short channels, sufficient upstream radial length is not available for the flow to become hydrodynamically fully developed before thermal boundary conditions are applied. Consequently, for such configuration, thermal and hydrodynamic developments take place simultaneously. Such flow is beyond the scope of the present analytical treatment. However, the two cases considered here, namely, slug flow and fully developed flow, represent limiting cases of the hydrodynamically developing velocity profile. Thus the Nusselt numbers obtained in these two cases represent the bounds within which the actual Nusselt number for hydrodynamically and thermally developing flow is expected to occur.

Case 1: Slug Flow ($U = 1$). For slug flow, Eq. (5) becomes

$$\frac{\mathrm{Pe}}{R}\frac{\partial\theta}{\partial R} = \frac{\partial^2\theta}{\partial Z^2}$$

Using separation of variables, the solution to the above equation using the boundary conditions, Eqs. (6*a*) and (6*b*), is given as

$$\theta(R,Z) = \sum_{n=1}^{\infty}\frac{\sin\lambda_n}{\lambda_n}\exp\left[-\frac{\lambda_n^2(R^2 - R_i^2)}{2\mathrm{Pe}}\right]\cos\lambda_n Z \tag{7}$$

The eigenvalues of the problem are $\lambda_n = (2n-1)\pi/2$.

The local Nusselt number is defined as

$$\mathrm{Nu}(R) = -\frac{2}{\theta_b(R)}\left.\frac{\partial\theta(R,Z)}{\partial Z}\right|_{Z=1} \tag{8}$$

The local bulk mean temperature, $\theta_b(R)$, is defined as

$$\theta_b(R) = \frac{1}{2}\int_{-1}^{1}\theta(R,Z)dZ \tag{9}$$

Substituting the expression of $\theta(R,Z)$ in Eqs. (8) and (9), the

expression for Nusselt number becomes

$$\mathrm{Nu}(R) = \frac{2\sum_{n=1}^{\infty} \sin^2 \lambda_n \exp\left[-\frac{\lambda_n^2}{2\mathrm{Pe}}(R^2 - R_i^2)\right]}{\sum_{n=1}^{\infty} \frac{\sin^2 \lambda_n}{\lambda_n^2} \exp\left[-\frac{\lambda_n^2}{2\mathrm{Pe}}(R^2 - R_i^2)\right]} \tag{10}$$

The Nusselt number in the fully developed region is obtained as the final converged value of the above series as

$$\mathrm{Nu}_\infty = \lim_{R\to\infty} \frac{2 \sin^2 \lambda_1 \exp\left[-\frac{\lambda_1^2}{2\mathrm{Pe}}(R^2 - R_i^2)\right]}{\frac{\sin^2 \lambda_1}{\lambda_1^2} \exp\left[-\frac{\lambda_1^2}{2\mathrm{Pe}}(R^2 - R_i^2)\right]} = \frac{\pi^2}{2} = 4.935$$

Case 2: Fully Developed Creeping Flow. The velocity profile for this case is determined following the procedure outlined by Bird et al. [9]. Since $v=0$ everywhere in the domain, from continuity equation we have $\partial/\partial r(ru)=0$ which implies that ru is a function of z only, i.e., $ru=\varphi(z)$. Using the above simplifications, the momentum equation becomes [9]

$$-\frac{\rho\varphi^2}{r^3} = -\frac{dp}{dr} + \frac{\mu}{r}\frac{d^2\varphi}{dz^2} \tag{11}$$

Closed form solution of Eq. (11) is possible only for creeping flow [9], i.e., neglecting the inertia term on the left hand side (LHS) of Eq. (11). The equation of motion becomes

$$-\frac{dp}{dr} + \frac{\mu}{r}\frac{d^2\varphi}{dz^2} = 0 \tag{12}$$

Integrating Eq. (12) with the boundary condition $\varphi=0$ at $z=\pm b$, we obtain

$$\varphi(z) = \frac{\Delta p b^2}{2\mu \ln\frac{r_0}{r_i}}\left(1 - \frac{z^2}{b^2}\right) \tag{13}$$

The volume rate through the disk is given by

$$Q = \int_{-b}^{b} 2\pi r u dz = \frac{4\pi\Delta p b^3}{3\mu \ln\frac{r_0}{r_i}} \tag{14}$$

The average velocity is obtained as $\bar{u}=Q/4\pi br$. Using Eqs. (13) and (14), for this case the expression for U in Eq. (5) becomes

$$U = \tfrac{3}{2}(1 - Z^2) \tag{15}$$

Equation (5) thus becomes

$$\frac{3}{2}\frac{(1-Z^2)}{R\mathrm{Pe}}\frac{\partial\theta}{\partial R} = \frac{\partial^2\theta}{\partial Z^2}$$

The solution to the above equation subject to boundary conditions given by Eq. (6) is given by

$$\theta(R,Z) = \sum_{n=1}^{\infty} C_n \exp\left[-\frac{\lambda_n^2 R^2}{3\mathrm{Pe}}\right] F(\lambda_n Z) \tag{16}$$

where $F(\lambda_n Z)$ is the eigenvector corresponding to the eigenvalue λ_n, which is obtained from the equation $d^2G/dZ^2 + (1-Z^2)\lambda^2 G = 0$ with $G=0$ at $Z=\pm 1$. These eigenvalues are identical to those of thermally developing forced convection in channels with constant wall temperature [10,11].

The constants C_n are given by

$$C_n' = C_n \exp\left(\frac{-\lambda_n^2 R_i^2}{3\mathrm{Pe}}\right) = \frac{\int_{-1}^{1} (1-Z^2) F(\lambda_n Z) dZ}{\int_{-1}^{1} (1-Z^2)[F(\lambda_n Z)]^2 dZ} \tag{17}$$

The bulk mean temperature is given as

$$\theta_b = \frac{1}{2}\int_{-1}^{1} \frac{3}{2}(1-Z^2)\theta dZ$$

$$= -\frac{3}{2}\sum_{n=1}^{\infty} \exp\left[-\frac{\lambda_n^2}{2\mathrm{Pe}}(R^2 - R_i^2)\right]\frac{1}{\lambda_n^2} C_n' \left.\frac{dF(\lambda_n Z)}{dZ}\right|_{Z=1} \tag{18}$$

The Nusselt number is finally obtained as

$$\mathrm{Nu}(R) = \frac{\frac{4}{3}\sum_{n=1}^{\infty} \exp\left[-\frac{\lambda_n^2}{2\mathrm{Pe}}(R^2 - R_i^2)\right] C_n' \left.\frac{dF(\lambda_n Z)}{dZ}\right|_{Z=1}}{\sum_{n=1}^{\infty} \frac{1}{\lambda_n^2} \exp\left[-\frac{\lambda_n^2}{2\mathrm{Pe}}(R^2 - R_i^2)\right] C_n' \left.\frac{dF(\lambda_n Z)}{dZ}\right|_{Z=1}} \tag{19}$$

The fully developed Nusselt number is obtained, as before, as the converged values of the series

$$\mathrm{Nu}_\infty = \lim_{R\to\infty} \frac{4}{3}\frac{\exp\left[-\frac{\lambda_1^2}{2\mathrm{Pe}}(R^2 - R_i^2)\right] C_1' \left.\frac{dF(\lambda_1 Z)}{dZ}\right|_{Z=1}}{\frac{1}{\lambda_1^2}\exp\left[-\frac{\lambda_1^2}{2\mathrm{Pe}}(R^2 - R_i^2)\right] C_1' \left.\frac{dF(\lambda_1 Z)}{dZ}\right|_{Z=1}} = \frac{4}{3}\lambda_1^2 \tag{20}$$

The values of λ_n and C_n' $(dF(\lambda_n Z)dZ)|_{Z=1}$ are obtained from Ref. [10]. Using these values, the fully developed Nusselt number becomes 3.77, which is expectedly in agreement with that for channel between two parallel plates [11]. The expressions of velocity profile and Nusselt number are also valid in the presence of disk rotation, provided an effective Peclet number is defined incorporating the effect of rotation, as shown in the Appendix.

3 Results and Discussions

Comparison With Earlier Studies. At first the results from the present work are compared with that of Prata et al. [8] The flow in Ref. [8] involves impingement of the axially feeding jet on the disk. This makes direct comparison of their results with the present solution difficult. Moreover, the finite radius of the disks introduces end effects, which are not observed in the present work. Figure 1 shows the local Nusselt number for the case depicted in Fig. 7 of Ref. [8]. In spite of the discrepancies mentioned above, there is excellent qualitative and reasonably good quantitative agreement with both the experimental and numerical results of Prata et al. [8].

Slug Flow. Figure 2 shows the local Nusselt number along the radial coordinate for slug flow for different Peclet numbers. From the figure, it is observed that as expected, at large radial distances, the local Nusselt number converges to the value of fully developed Nusselt number for all the cases. However, the distance required for the flow to become thermally fully developed increases with Peclet number.

The effect of curvature on the thermal development for slug flow is shown in Fig. 3. For $r_i \to \infty$, the present configuration approaches a channel between two parallel plates. Figure 3 shows that the thermal development length increases with a decrease in the value of r_i. For a large value of the inner radius, $r_i=100$, the local Nusselt number distribution coincides with that of a parallel

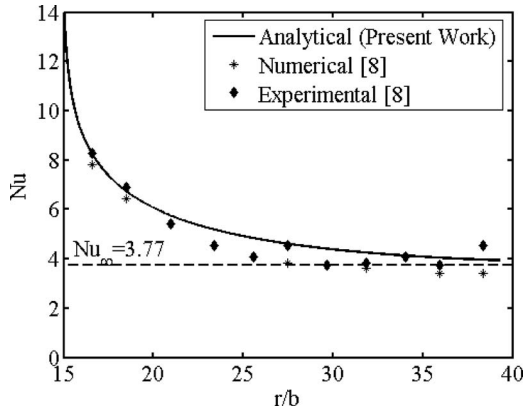

Fig. 1 Comparison of local Nusselt number with the results of Ref. 8

plate channel. Figure 3 shows that thermal development of the flow is much slower for radial disk compared to straight channels.

Fully Developed Flow. Figure 4 shows the effect of Peclet number on the variation in local Nusselt number for fully developed creeping flow. It is to be noted that the high Peclet numbers for creeping flows imply high Prandtl numbers, as encountered in oils. The variation is qualitatively similar to that for slug flow. However, the development is much faster than that for slug flows. For this flow configuration also, at large values of r_i, the distribution of local Nusselt number approaches that of the parallel plate channel. The effect of inner radius is also qualitatively similar to that for slug flow.

A comparison of the results for slug flow and fully developed flow shows that for slug flow, the thermal entrance length and Nusselt numbers in the developing and fully developed regions are higher than those for the fully developed flow. Since these velocity profiles are limiting cases of velocity field for a hydrodynamically developing flow, the actual Nusselt number for a short channel in the developing region should lie between the local Nusselt numbers in the developing region for these two cases. However, the fully developed Nusselt number in the actual case would be equal to that for the hydrodynamically fully developed flow while near the entrance region, the local Nusselt number should be closer to the same for slug flow at the corresponding location.

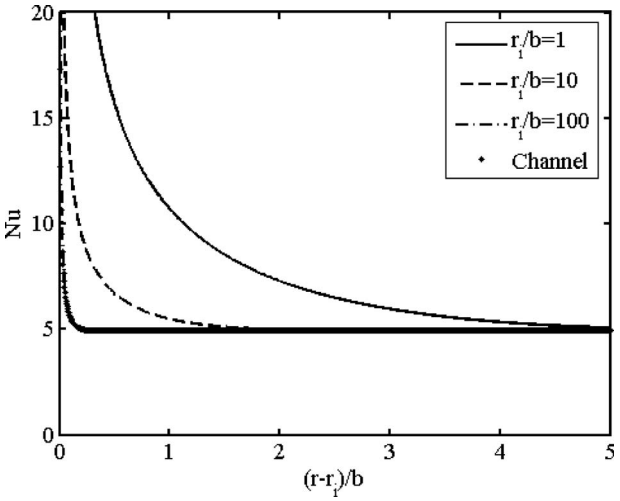

Fig. 3 Effect of inner radius on local Nusselt number for slug flow at Pe=100

4 Conclusions

An analytical model for thermally developing radial flow and heat transfer between two parallel plates is developed for slug flow and fully developed creeping flow. The major conclusions from the work are as follows.

- Fully developed Nusselt number for radial flow between two parallel disks is identical to that of parallel plate channels.
- Thermal development for radial flow passages is slower than for parallel plate channels. The thermal development length increases with decreasing values of inner radius.
- Greater thermal development length is necessary at higher Peclet numbers.
- Although the qualitative trend for the variation in Nusselt number is similar for the two types of flows, thermal entrance length is much shorter for the latter.
- In the presence of disk rotation, thermal entrance length increases.

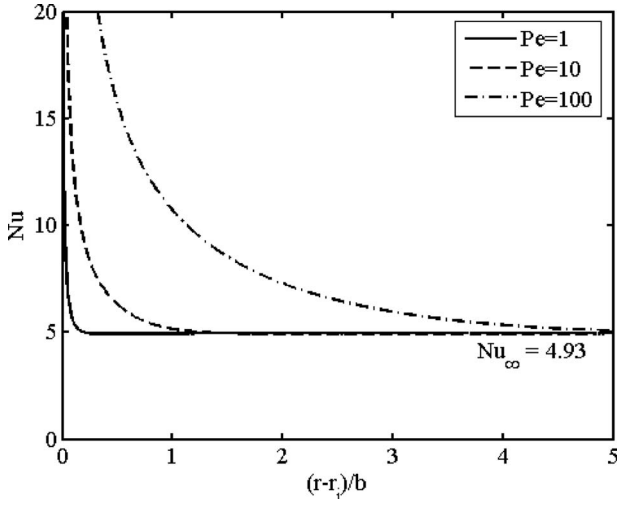

Fig. 2 Effect of Peclet number on local Nusselt number for slug flow at $r_i/b=1$

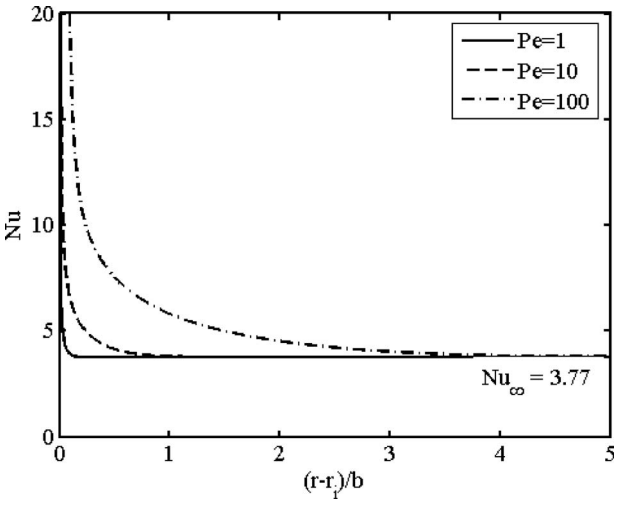

Fig. 4 Effect of Peclet number on local Nusselt number for fully developed creeping flow at $r_i/b=1$

Nomenclature

b = half width of radial channel (m)
h = heat transfer coefficient (W/m^2K)
k = thermal conductivity of fluid (W/mK)
Nu = nusselt number ($=h2b/k$) (dimensionless)
Nu_∞ = fully developed Nusselt number (dimensionless)
p = pressure (Pa)
Δp = pressure drop across radial channel (Pa)
Pe = Peclet number (dimensionless)
Q = volume flow rate (m^3/s)
r = radial coordinate (m)
r_i = inner radius (m)
r_o = outer radius (m)
R = dimensionless radial coordinate
R_i = dimensionless inner radius ($=r_i/b$) (dimensionless)
T = temperature (K)
T_i = fluid temperature at the channel inlet (K)
T_w = wall temperature (K)
u = radial velocity (m/s)
$\bar{u}$ = average radial velocity (m/s)
u_i = radial velocity at the channel inlet (m/s)
U = dimensionless radial velocity ($=u/\bar{u}$) (dimensionless)
v = axial velocity (m/s)

Greek Symbols

α = thermal diffusivity (m^2/s)
ϕ = $ru(m^2/s)$
λ = eigenvalue (dimensionless)
μ = viscosity (Pa s)
θ = dimensionless temperature
θ_b = dimensionless bulk temperature
ρ = density (kg/m^3)
ω = angular speed (rad/s)

Appendix: Effect of Disk Rotation

For the case of rotation of the disk(s) about the axis, the governing equations are [12] as follows:

$$\frac{1}{r}\frac{\partial}{\partial r}(ru) + \frac{\partial v}{\partial z} = 0 \tag{A1}$$

$$\frac{1}{r}\frac{\partial}{\partial r}(ru^2) + \frac{\partial}{\partial z}(uv) = -\frac{1}{\rho}\frac{\partial p}{\partial r} + r\omega^2 + \nu\left[\frac{\partial^2 u}{\partial z^2} + \frac{1}{r}\frac{\partial}{\partial r}\left(r\frac{\partial u}{\partial r}\right) - \frac{u}{r^2}\right] \tag{A2}$$

$$\frac{1}{r}\frac{\partial}{\partial r}(ruT) + \frac{\partial}{\partial z}(vT) = \alpha\left[\frac{\partial^2 T}{\partial z^2} + \frac{1}{r}\frac{\partial}{\partial r}\left(r\frac{\partial T}{\partial r}\right)\right] \tag{A3}$$

Using the assumptions involved in the derivation of Eqs. (1) and (12), the continuity and energy equations remain unchanged while the momentum equation (A2) becomes

$$-\frac{dp}{dr} + \frac{\mu}{r}\frac{d^2\varphi}{dz^2} + \rho\omega^2 r = 0 \tag{A4}$$

Integrating with respect to r from r_i to r_o, we obtain

$$\frac{d^2\varphi}{dz^2} = -\frac{\Delta p + \frac{1}{2}\rho\omega^2(r_o^2 - r_i^2)}{\mu \ln\frac{r_o}{r_i}} \tag{A5}$$

The two terms in the numerator can be combined to define an effective pressure drop $\Delta p^* = \Delta p + \frac{1}{2}\rho\omega^2(r_o^2 - r_i^2)$. With this effective pressure drop, the velocity profile and discharge can be expressed using the same expressions developed earlier (Eqs. (13) and (14)). Thus the dimensionless velocity profile and the Nusselt number can be obtained from Eqs. (15) and (19), respectively. However, since the effect of rotation is to increase the effective pressure gradient, the effective Peclet number would also be increased in the presence of rotation. Since the thermal entrance length increases with an increase in Peclet number, attainment of thermally fully developed condition is delayed in the presence of rotation.

References

[1] Shah, R. K., and London, A. L., 1978, *Laminar Flow Forced Convection in Ducts*, Academic, New York, Chaps. V and VI.
[2] Kays, W. M., and Crawford, M. E., 1993, *Convective Heat and Mass Transfer*, McGraw-Hill, New York.
[3] Possamai, F. C., Perreira, R. C., and Prata, A. T., 2001, "Pressure Distribution in Laminar Radial Flow Through Inclined Disks," Int. J. Heat Fluid Flow, **22**, pp. 440–449.
[4] Nakabayashi, K., Ichikawa, T., and Morinshi, Y., 2002, "Size of Annular Separation Bubble Around the Inlet Corner and Viscous Flow Structure Between Two Parallel Disks," Exp. Fluids, **32**, pp. 425–433.
[5] Tashtoush, B., Tahat, M., and Probert, D., 2001, "Heat Transfers and Radial Flows via a Viscous Fluid Squeezed Between Two Parallel Disks," Appl. Energy, **68**, pp. 275–288.
[6] Palm, S. J., Roy, G., and Nguyen, C. T., 2006, "Heat Transfer Enhancement With the Use of Nanofluids in Radial Flow Cooling Systems Considering Temperature-Dependent Properties," Appl. Therm. Eng., **26**, pp. 2209–2218.
[7] Kumar, S., Maruta, K., and Minaev, S., 2007, "Experimental Investigations on the Combustion Behavior of Methane-Air Mixtures in a Micro-Scale Radial Combustor Configuration," J. Micromech. Microeng., **17**, pp. 900–908.
[8] Prata, A. T., Pilichi, C. D. M., and Ferreira, R. T. S., 1995, "Local Heat Transfer in Axially Feeding Radial Flow Between Parallel Plates," ASME J. Heat Transfer, **117**, pp. 47—53.
[9] Bird, R. B., Stewart, W. E., and Lightfoot, E. N., 1960, *Transport Phenomena*, Wiley International ed., Wiley, New York, Chap. 3, p. 114.
[10] Shah, R. K., and Bhatti, M. S., 1987, "Laminar Convective Heat Transfer in Ducts," *Handbook of Single Phase Convective Heat Transfer*, S. Kakac, R. K. Shah, and W. Aung, eds., Wiley, New York, Chap. 3.
[11] Arpaci, V. S., 1966, *Conduction Heat Transfer*, Addison-Wesley, Reading, MA, Chap. 4, p. 209.
[12] Basu, S., and Cetegen, B. M., 2007, "Effect of Hydraulic Jump on Hydrodynamics and Heat Transfer in a Thin Liquid Film Flowing Over a Rotating Disk Analyzed by Integral Method," ASME J. Heat Transfer, **129**, pp. 657–663.

Effect of Absorptive Coating of the Hot Fluid Passage of a Heat Exchanger Employing Exergy-Optimized Pin Fins in High Temperature Applications

Nwosu P. Nwachukwu[1]
e-mail: pn_nwosu@yahoo.com, ebere_ay@yahoo.com

Samuel O. Onyegegbu

Department of Mechanical Engineering,
National Center for Energy Research and Development (NCERD),
University of Nigeria,
Nsukka, Nigeria

*An expression for the optimum pin fin dimension is derived on exergy basis for a high temperature exchanger employing pin fins. The present result differs from that obtained by Poulikakos and Bejan (1982, "Fin Geometry for Minimum Entropy Generation in Forced Convection," ASME J. Heat Transfer, **104**, pp. 616–623) for a low temperature heat recovery application. Also, a simple relation is established between the amounts the base temperature of the optimized pin fin is raised for a range of absorptive coating values. Employing this relation, if the absorptivity of the coating, the plate emissivity, the number of protruding fins, and some area and fluid parameters are known, the corresponding value for the base temperature of the fin is immediately obtained. The analysis shows that the thermal performance of the exchanger improves substantially with a high absorptivity coating hence can be seen as a heat transfer enhancement feature of the exchanger operating with radiation dominance.* [DOI: 10.1115/1.3013827]

Keywords: heat exchanger, coating, pin fin, radiation dominance, entropy generation number, exergy

1 Introduction

The task of a heat exchanger is to deliver heat from a warmer fluid to a colder fluid. The task may be defined, in a convenient format, by the rate of flow of an extensive thermodynamic property associated with one or both fluids, e.g., entropy, enthalpy, and free energy. A heat exchanger design is concerned with accomplishing the task of smooth thermal energy transfer and thus requires the minimization of thermodynamic irreversibility (entropy production) within its functional units. Useful energy loss in heat exchangers, in deference to thermodynamic optimization, can be minimized by the exergy-conservation design philosophy [1] to the system components, notably for a pin fin heat exchanger. Various studies concerning the thermal optimization of fins have been undertaken [2–5]. In high temperature exhaust application of the exchanger, a hot stream of hydrocarbon exhaust passes through the hot fluid channel of the exchanger and dissipates its heat chiefly by radiation [6], which falls on a surface of limited absorptive envelope. It may be argued that the application of a "paycoat" may be more advantageous than extending the exchanger general dimensions for the sole purpose of absorbing more of the radiant heat energy emanating from the hot fluid. The limited absorptive potential of the hot-side heat exchange surface provides an incentive for a material to be employed to entrap the radiant thermal energy incident on this surface; a coating material of a selective nature (high absorptivity α_c and very low emissivity ε_c) could provide a means of reducing the loss of useful energy in the exchanger operating with a high temperature exhaust fluid. The purpose of this paper is to obtain an exergy-based expression for the dimensions of a pin fin, which is used as a basic heat transfer augmentation feature in some heat exchangers. Although some fundamental work on pin fin optimization with bias to exergy has been undertaken by Poulikakos and Bejan, here we are approaching the optimization process with emphasis on the high temperature application of the exchanger where the ratio $[\theta_b/T_\infty]$ is high thus requires the derivation of the optimum pin fin length expression owing to this outcome since the optimum pin fin length expression, as obtained in the previous work, is relatively inadequate. In addition, this work examines the influence of absorptive coatings on the heat extraction potential of a pin fin heat exchanger system, and as a result, establish a relation for the amounts of the incident radiation that would be absorbed by the system for a range of coating absorptivity values and hence rely on this as a route toward reducing useful energy loss in the system.

2 Problem Formulation

Consider a pin fin of overall length L and diameter D contained in a cross-flow arrangement attached to a base coated with a material of absorptivity α_c and emissivity ε_c on the heat exchange surface contiguous to the hot stream (Fig. 1). The dimensions of the pin fin satisfy the condition $L/D \gg 1$. The equation for the computation of the entropy generation rate of a single fin in cross-flow is given by [1]

$$S_{\text{gen}} = \frac{q_b \theta_b}{T_\infty^2\left(1 + \dfrac{\theta_b}{T_\infty}\right)} + \frac{F_D U_\infty}{T_\infty} \tag{1}$$

where S_{gen} is the entropy generation rate associated with the fin and the fluid flow arrangement, θ_b is the difference between the fin base temperature T_b and the free stream temperature T_∞, and F_D is the net drag force transmitted through the fin to the base wall. The unidirectional fin conduction model satisfies the validity criterion [6]

$$\left(\frac{hD}{k}\right)^{1/2} \ll 1 \tag{2}$$

The relationship between the fin base heat flux and stream temperature difference is [1,7]

$$\theta_b = \frac{q_b}{(\pi/4)kD^2 m \tanh ml} \tag{3}$$

where

$$m = \left(\frac{4h}{kD}\right)^{1/2}$$

With the specification of S_{gen} and the fin base temperature difference relations, the entropy generation number N_s associated with the fin for design purposes can be determined by [1,8]

$$N_s = \frac{S_{\text{gen}}}{\left(\dfrac{q_b^2 U_\infty}{k\nu T_\infty^2}\right)} \tag{4}$$

The entropy generation number N_s is the ratio of entropy production rate in a heat exchanger passage to the stream-to-stream heat transfer rate to the passage. This dimensionless group is defined as the entropy production rate or irreversibility rate present in a heat

[1]Corresponding author.

Contributed by the Heat Transfer Division of ASME for publication in the JOURNAL OF HEAT TRANSFER. Manuscript received November 10, 2007; final manuscript received September 9, 2008; published online March 17, 2009. Review conducted by Gautam Biswas.

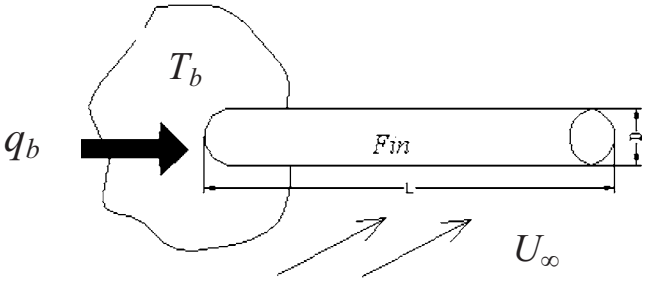

Fig. 1 Pin fin nomenclature

exchanger channel [8]; N_s approaching zero implies an almost ideal heat exchanger channel. Combining Eqs. (1), (3), and (4) and simplifying, N_s becomes

$$N_s = \frac{1}{\left[\frac{\pi}{4} D\,\mathrm{Re}_D m \tanh ml + \frac{q_b U_\infty}{k\nu T_\infty}\right]} + (1/2) Q C_D\,\mathrm{Re}_L\,\mathrm{Re}_D \quad (5)$$

where Q represents the fluid friction coefficient and C_D represents the drag coefficient; they are defined by

$$Q = \frac{\rho k T_\infty \nu^3}{q_b^2} \quad (6)$$

$$C_D = \frac{F_D}{(1/2)\rho U_\infty^2 DL} \quad (7)$$

The fluid friction coefficient Q is a function of the base heat transfer rate q_b. The Reynolds number is used as a dimensionless notation for the two geometries of the fin for the external flow consideration: Re_D and Re_L. The optimum fin length in its dimensionless form denoted as $\mathrm{Re}_{L\mathrm{opt}}$ is computed by solving $\partial N_s / \partial\,\mathrm{Re}_L = 0$. $\mathrm{Re}_{L\mathrm{opt}}$ is obtained as

$$\mathrm{Re}_{L\mathrm{opt}} = \frac{\mathrm{Re}_D (k/\lambda)^{1/2}}{2\mathrm{Nu}^{1/2}} \cosh^{-1}\left[\left(\frac{\varphi^{1/2}}{A \tanh(A''\,\mathrm{Re}_{L\mathrm{opt}}) + A'}\right)\right] \quad (8)$$

The equation above differs from the result obtained in Ref. [1], where the assumption based on "enhanced thermal contact" was made, which is unique to counterflow liquefiers and cannot be employed in some other applications of the fin. However, the result obtained here is generic thus could be used to obtain the optimum fin length on thermodynamic grounds for different applications. The optimum pin fin dimension, on thermodynamic grounds, is one that transfers the maximum quantity of heat to the cold fluid while generating the least entropy (i.e., conservation of exergy). The major design consideration for the high temperature application of the fin is that the ratio θ_b / T_∞ is significant thus the complete S_{gen} equation that gave way to the result in Eq. (8) is more adequate and embodies a better engineering approximation when compared with a modification to the same approximation undertaken by Poulikakos and Bejan [1]. Clearly the ratio $[\theta_b / T_\infty]$ is very significant in high temperature application of the fin; the neglect of this ratio in the work presents the need to obtain an expression for the optimum pin fin length on exergy grounds for high to intermediate temperature heat recovery applications. The $\mathrm{Re}_{L\mathrm{opt}}$ equation is computed from the fin and the cold fluid properties; the dimensionless groups represented in the equation are

$$\varphi = \frac{2\pi\,\mathrm{Nu}(\lambda/k)}{Q C_D\,\mathrm{Re}_D}$$

$$A = (\pi/2)\mathrm{Re}_D\,\mathrm{Nu}^{1/2}\left(\frac{\lambda}{k}\right)^{1/2}$$

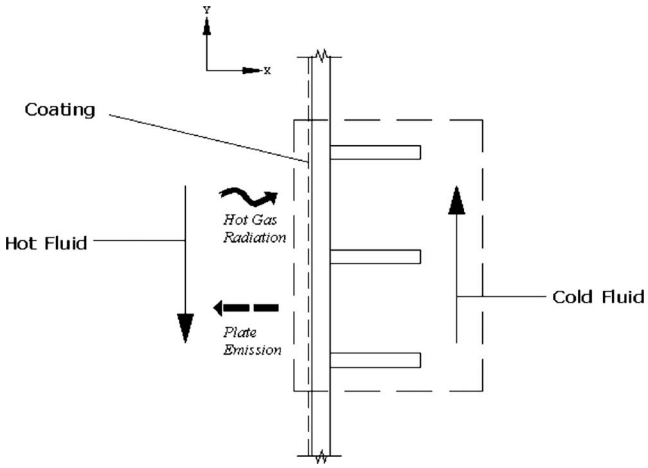

Fig. 2 Schematic of a pin fin attached to a plate with prescribed heat duty

$$A' = q_B U_\infty / k\nu T_\infty$$

$$A'' = 2\mathrm{Nu}^{1/2}(\lambda/k)^{1/2}/\mathrm{Re}_D \quad (9)$$

φ and A' are combined property parameters they give in various proportions of the magnitude the fin heat duty relative to the fin thermal conductivity. Parametric ratios A and A'' give the heat extraction potential of the cold fluid weighed against the fin thermal conductivity for a given flow prescription. For a slender pin fin congruent with the unidirectional fin conduction model, the Nusselt number Nu and the drag coefficient C_D can be evaluated from results developed for a single cylinder in cross-flow [9,10].

3 Derivation of the Governing Equation for the Coated Plate

Consider a basic section of a pin fin-plate arrangement incorporating N fins in the cold channel (Fig. 2). It is assumed that the thermal conductivity of the plate (including the fins) and the thermophysical properties of the fluid moving across the bank of fins are constant. Also, the plate surface contiguous to the hot fluid (hydrocarbon exhaust gases) is coated with a material, which has emissivity ε_c and absorptivity α_c. The hydrocarbon exhaust mixture has a temperature T_g and emissivity ε_g. The mixture embodies participating media [6]—gases that absorb and scatter incident radiation while emitting radiation of their own, examples are CO_2 and H_2O. The emissivity of the constituent gases is characterized by temperature of the mixture T_g, the partial pressure of the constituent gases (p), equivalent length (L), and the total pressure of the mixture (P). The overall gas emissivity is given by [6]

$$\varepsilon_g = \varepsilon_{\mathrm{CO_2}} + \varepsilon_{\mathrm{H_2O}} - \Delta\varepsilon \quad (10)$$

where $\varepsilon_{\mathrm{CO_2}}$ is the emissivity of CO_2 and $\varepsilon_{\mathrm{H_2O}}$ is the emissivity of H_2O. The correction $\Delta\varepsilon$ modifies the cumulative emissive property of the mixture so as to obtain an effective value. The individual gas emissivity and the correction information are obtainable [6]. The dominant mode of heat transfer from the hot stream of hydrocarbon gases is radiation [5]. We can account for the net rate of heat transfer from the gas mixture to the coated plate by considering the radiation emanating from the hydrocarbon exhaust gas mixture to the coated surface and also the portion that is emitted by the coated surface to the gas stream. If we assume that the material of which the fins and the prime (i.e., unfinned) area are built is an excellent conductor, a thermal energy balance yields

$$\alpha_c \varepsilon_g \sigma T_g^4 A_s - \varepsilon_c \sigma T_b^4 A_s = \varepsilon \sigma A_t [T_b^4 - T_\infty^4] + h A_t \left[1 - \frac{N A_f (1 - \eta_f)}{A_t} \right] \theta_b \tag{11}$$

The relation above gives the absorbed radiation from the hot fluid as well as the net heat gain of the cold fluid by convection and radiation mechanisms. The quantity h is equivalent to the average coefficient of convection heat transfer for the length of the exchanger for approximately uniform T_b. Defining the various dimensionless ratios as follows:

$$\theta_z = \frac{T_b}{T_\infty}, \quad \phi = \frac{A_s}{A_t}$$

$$\xi = \frac{\sigma T_\infty^3}{\tau}, \quad \zeta = \frac{\sigma T_g^4}{\tau T_\infty} \tag{12}$$

and the value of the parameter τ is defined by

$$\tau = \frac{h[A_t - N A_f (1 - \eta_f)]}{A_t}$$

Above, the dimensionless group ζ is indicative of the flame gases (i.e., the hot fluid) radiation potential relative to cold fluid convection potential for prescribed exchanger material properties. If T_∞ is prescribed, as is often the case, a variation in τ becomes an indication of varying convection heat transfer coefficient h of the cold fluid, which is contingent on the cold fluid velocity. The resulting nondimensional governing equation for θ_z (i.e., the dimensionless fin base temperature) is obtained by combining Eqs. (11) and (12) to get

$$\theta_z = \left[\frac{\alpha_c \varepsilon_g \zeta \phi + \varepsilon \xi + 1}{\varepsilon \xi + \varepsilon_c \phi \xi + 1/\theta_z^3} \right]^{1/4} \tag{13}$$

Supposing we have a film with absorptivity α_c and established the parameters defined in Eq. (13), we can compute θ_z using any suitable numerical methods and hence predict the coating effect on the heat exchange process. The dimensionless base temperature of the fin can also be related to the entropy generation rate of the fin expressed by Eq. (1), consequently

$$S_{\text{gen}} = \frac{1}{T_\infty} \left[q_b \left(1 - \frac{1}{\theta_z} \right) + F_D U_\infty \right] \tag{14}$$

If $\theta_z = 1$ in the above equation, there is no discernible heat transfer i.e., $T_b = T_\infty$: entropy generation in the arrangement is only an outcome of frictional pressure losses as a consequence of the $F_D U_\infty / T_\infty$ term. Should θ_z be less than unity then the fluid stream at T_∞ transfers heat to the plate-fin arrangement at approximately T_b, which is an undesired design goal.

4 Discussion

In Fig. 3, it is seen that the result of Poulikakos and Bejan [1] gives higher values of $\text{Re}_{L\text{opt}}$ for lower Nu values than the present result (Eq. (8)); we see a maximum deviation in this regard suggesting that in applications where Nu is very low the present result gives a more economical (i.e., cost-effective) accurate fin-sizing formula from a thermodynamic standpoint than the result in Ref. [1]. The corresponding increase in $\text{Re}_{L\text{opt}}$ with Nu for different values of Q shows a strong thermodynamic interaction. The convective heat transfer coefficient is used to build the Nu; hence higher Nu values suggest higher heat transfer coefficients, though heat transfer coefficients are relatively small in laminar flows. A quantitative explanation for the $\text{Re}_{L\text{opt}}$-Nu-Q relationship in the figure is that the fin heat transfer area grows higher for flow velocities yielding lower heat transfer coefficients and for increased heat transfer rate q_b to the fin base. Essentially, higher values of $\text{Re}_{L\text{opt}}$ for lower Q values for a given Nu shows that the size (length) of an individual fin is enhanced due to an improved heat transfer rate to its base, and this *minor* increase in the fin geometry provides an additional heat transfer "outlet" for the improved rate. Note that parameter Q varies as the square of the reciprocal of the fin base heat transfer rate q_b.

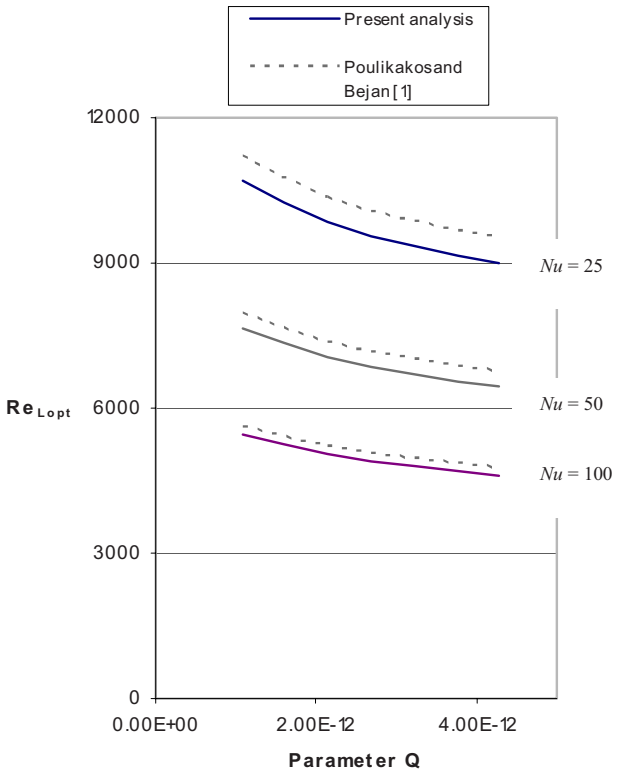

Fig. 3 Comparison of $\text{Re}_{L\text{opt}}$ results in laminar flow for various Nu values

Solving the energy balance relation for selected values and plotting the results of Eq. (13), we obtain Fig. 4. In the figure, θ_z increases with α_c/ε showing the relative importance of a superior coating application on the heat recovery surface of the exchanger; this would improve heat absorption especially in high temperature applications. Parameter ζ expresses the hot fluid radiation, which is a function of its absolute temperature, relative to the cold fluid potential for absorbing this heat: for high values of the parameter ($\zeta \gg 1$), radiation from the hot fluid is much greater than convection heat transfer. Figure 5 shows the evolution of the entropy generation number N_s with α_c/ε and ζ. The result shows that N_s increases with α_c/ε as a result of the S_{gen}-θ_z relationship (in Eq. (14)); however since N_s values are well below unity this shows an improved net heat gain and a good heat exchange channel [8]. The results of a developed model [11] and the thermodynamic optimization with respect to the sizing of the pin fin, as well as the effect of the coating, have been shown and are in agreement for a heat exchanger employing pin fins as heat transfer enhancement features.

5 Conclusion

Thermodynamic optimization leads to designs coming closer to utilizing available work (exergy), which factually leads to more profitable designs in the long run. We have applied the minimization of the entropy generation concept to the design of the extended surface. The possibility of reducing useful energy waste on account of the application of an absorptive coating has been demonstrated. This paper gives the expression for the optimum pin fin dimension on the exergy basis in a heat recovery application where the ratio $[\theta_b / T_\infty]$ is high. This expression shows clearly a difference from the result of Poulikakos and Bejan obtained for a low temperature heat recovery application where the ratio is mar-

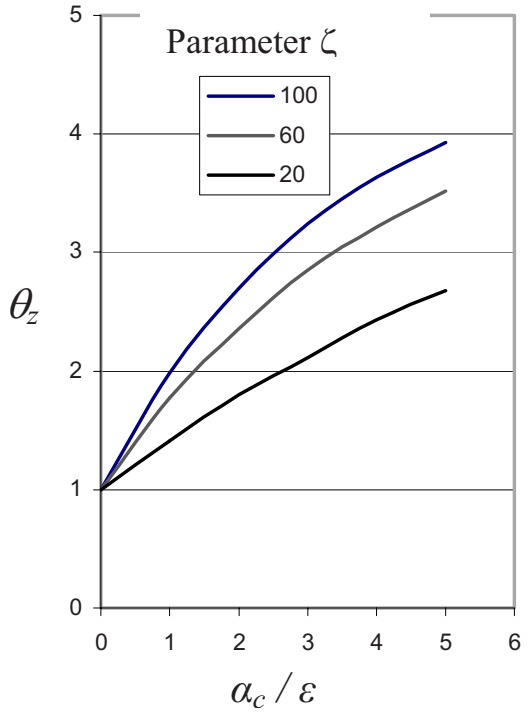

Fig. 4 Effect of α_c/ε and parameter ζ on the dimensionless fin base temperature θ_z

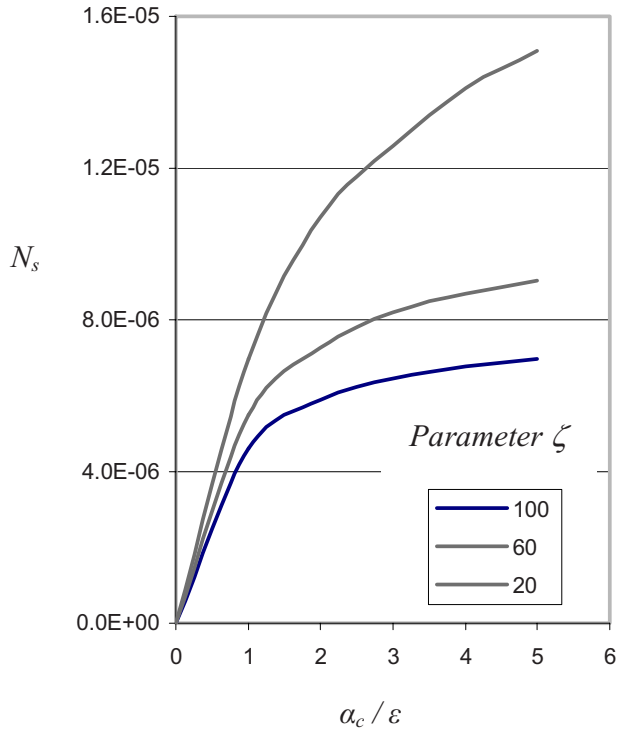

Fig. 5 Evolution of N_s with α_c/ε and parameter ζ

ginal; although both results compare well in high Nu conditions, the present result is more accurate and nonspecific. In combination with the optimum pin fin dimension expression, the theory presented here supports also the prospect of raising the fin base temperature by the application of a superior heat-absorbing coating on the hot fluid heat exchange surface so as to improve heat transfer from the fin to the cold stream, and this is appropriate for systems with high temperature employ of hydrocarbon exhaust fluid, where radiative heat transfer overwhelms convection heat transfer. The optimum application of the heat-absorbing film would improve the heat extraction rate of the surface to which it is applied.

Nomenclature

A_f = surface area of fin (m^2)
A_s = coated hot-side wall area (m^2)
A_t = total cold-side surface e area (m^2)
D = pin fin diameter (m)
Q = fluid friction irreversibility coefficient
F_D = drag force (N)
h = cold fluid heat transfer coefficient (W/m^2 K)
k = thermal conductivity of material (W/m K)
L = fin length (m)
m = fin conduction parameter
Nu = Nusselt number, hD/λ
Pr = Prandtl number
q_b = base surface heat transfer rate (W)
q_f = fin surface heat transfer (W)
Re_x = Reynolds number, $x(U_\infty/v)$
S_{gen} = entropy generation rate (W/K)
T_b = temperature of fin base (K)
U_∞ = cold stream velocity (m/s)
T_∞ = cold steam temperature (K)
λ = thermal conductivity of cold fluid (W/m K)
ρ = density of cold fluid (kg/m^3)
η = fin efficiency
v = kinetic viscosity (m^2/s)
σ = Stefan–Boltzmann constant
ε = emissivity of plate (cold side)
ε_c = emissivity of coating
ε_g = emissivity of gas
α_c = absorptivity of coating
θ_b = base-stream temperature difference (K)
θ_z = dimensionless fin base temperature

References

[1] Poulikakos, D., and Bejan, A., 1982, "Fin Geometry for Minimum Entropy Generation in Forced Convection," ASME J. Heat Transfer, **104**, pp. 616–623.
[2] Khan, W. A., Culham, J. R., and Yovanovich, M. M., 2004, "Optimization of Pin-Fin Heat Sinks Using Entropy Generation Minimization," Thermal and Thermomechanical Phenomena in Electronic Systems, **1**, pp. 259–267.
[3] Dul'kin, I. N., and Garask'o, G. I., 2008, "Analysis of the 1D Heat Conduction Problem for a Single Fin With Temperature Dependent Heat Transfer Coefficient—Part II. Optimum Characteristics of Straight Plate and Cylindrical Pin Fins," Int. J. Heat Mass Transfer, **51**, pp. 3325–3341.
[4] Gerencser, D. S., and Razani, A., 1995, "Optimization of Radiative-Convective Arrays of Pin Fins Including Mutual Irradiation Between Fins," Int. J. Heat Mass Transfer, **38**(5), pp. 899–907.
[5] Gray, W. A., and Kilham, J. K., 1976, *Heat Transfer From Flames*, Elek Science, London, p. 108.
[6] Bejan, A., 1993, *Heat Transfer*, Wiley, New York, pp. 65–69.
[7] Kern, F., and Bohn, S. M., 1992, *Principles of Heat Transfer*, Harper and Row, New York, p. 417.
[8] Bejan, A., 1978, "General Criterion for Rating Heat Exchanger Performance," Int. J. Heat Mass Transfer, **21**, pp. 655–665.
[9] Gebhart, B., 1971, *Heat Transfer*, McGraw-Hill, New York, pp. 212–214.
[10] Incropera, F. P., and Dewitt, D. P., 1996, *Fundamentals of Heat and Mass Transfer*, 4th ed., Wiley, New York.
[11] Nwosu, P. N., 2005, "Heat Transfer Analysis and Computer-Aided Design of a Pin-Fin Heat Exchanger With Internal Coating," M.Eng. thesis, University of Nigeria, Nsukka, Nigeria.